Segmental Rotor Switched Reluctance Drives

Tuncay Celik

A thesis submitted for the degree of

Doctor of Philosophy

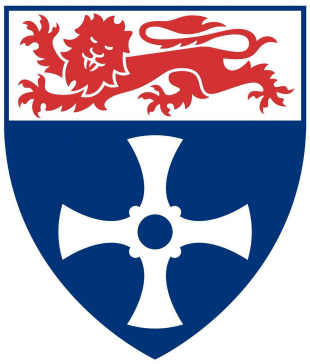

University of Newcastle upon Tyne

School of Electrical, Electronic and Computer Engineering

To my wife, Azime
and son, Tymur

Abstract

One of the well-known drawbacks of switched reluctance machines is the relatively high output torque ripple. Techniques aiming to reduce machine torque ripple either compromise the machine performance or the simplicity of the inverter and the controller. The work presented in this thesis shows that low torque ripple over a wide speed range can be achieved without severe penalties in terms of the machine performance and the size, cost and complexity of the power electronics and the controller. This is achieved by designing a 6-phase machine and driving it from a three-phase full bridge circuit.

Switched reluctance motors with segmented rotors are a relatively recent advancement in the electromagnetic design of doubly-salient reluctance motors, having only been introduced in 2002. By replacing the conventional toothed rotor with individual segments, it has been proven that higher torque density than conventional switched reluctance machines could be achieved. Early work by Mecrow and El-Kharashi has demonstrated the operation of prototype machines with short-pitched and fully-pitched windings. The machine design work presented here builds on this early work by examining aspects of the machine design and its operation. Two six-phase machines – one with a segmented rotor and the other with a toothed rotor - have been designed. Performance comparisons have been made between the two six-phase machines and a three phase segmented rotor machine that was previously designed at Newcastle University.

Additionally, a three phase single tooth winding and a two phase segmented rotor switched reluctance machine have been studied in simulation and experimentally. Detailed comparison of inverter ratings and machine efficiencies are made under equal conditions for a 2-phase machine driven from h-bridge and asymmetric half-bridge inverters. This is achieved with results from a test rig and the use of accurate dynamic simulation. Simulation models for 3-phase and 6-phase machines have also been generated. Detailed comparison of inverter ratings and machine efficiencies are made under equal conditions for the 3-phase and 6-phase drives in the dynamic simulation.

Comparisons between simulated and measured results are shown to be very good for all of the drives.

Table of Contents

List of Figures

Chapter-1

Chapter-2

Chapter-3

Chapter-4

Chapter-5

Chapter-6

Chapter-7

Chapter-8

Chapter-9

Chapter-10

Appendix A

Appendix B

Appendix C

List of Tables

Chapter-3

Chapter-4

Chapter-6

Chapter-7

Chapter-8

Chapter-9

Chapter-10

Appendix D

Acknowledgements

Just to be writing the Acknowledgements of this thesis means that it is the end of a very long era of my life which is almost surreal. At times, it has been very difficult. Without the help, support and encouragement of many people, it could not have happened.

First of all, my biggest thanks go to my supervisor Professor Barrie Mecrow and my dear wife Azime. I feel very lucky to have been the student of Barrie – to be able to have direct access to his expertise and experience in all aspects of electric machines and drives. His support has always been more than technical throughout the years (and I mean, a lot of years!). Thank you - Barrie, for believing in me when things looked gloomy. I felt the luckiest man when I met Azime and I still do more than ever. She has sacrificed many things for this PhD. It has been tough on her within the last few months. I cannot thank her enough; she is the most understanding, supportive and loving person in my life. Don't worry dear; the balance will revert back to 90-10 again.

Another short but big thanks go to my one year old boy Tymur for giving me the biggest incentive to finish writing-up my PhD after a very long time. Of course, many thanks go to my family for their support throughout my student life and always accepting what I do and never doubting me in my student life.

This PhD also involved a lot of building and stripping of test rigs which would not be possible without the help of the technicians at the mechanical workshop. Thanks to all the academic staff one way or another involved in my PhD during my time in Newcastle.

I am especially grateful to my proof-reader, Steve Greetham for taking the time to read this thesis despite his own busy life and for providing invaluable feedback. Special thanks to Mark Leaver and Yu Chen for continued talks, support and encouragement they gave me at Dyson Ltd.

Finally, big thanks to all the nice people of Geordie-land for making me feel like home and making my time in Newcastle so enjoyable.

List of Symbols

Symbols

1, 2, 3	Subscripts referring to slot quantities
A, B, C	Subscripts referring to tooth quantities
g	Air-gap
I_{dem}	Demand current
R	Resistance
T	Torque
T	Tesla – unit of flux density
V	Voltage
A	Ampere
V_{star} or Vstar	Star point potential
V_{DC} or V_{dclink}	DC Link Voltage
12/10 or 12-10	Denotes a machine with 12 stator and 10 rotor poles
12/8 or 12-8	Denotes a machine with 12 stator and 8 rotor poles
4/2 or 4-2	Denotes a machine with 4 stator and 2 rotor poles
6/4 or 6-4	Denotes a machine with 6 stator and 4 rotor poles
8/6 or 8-6	Denotes a machine with 8 stator and 6 rotor poles
I_{star} or Istar	Current flowing into the star point
t/λ	Tooth-width to pole pitch ratio
ψ	Flux-linkage
λ_s	Stator pole pitch
λ_r	Rotor pole pitch
Nm	Newton-meter
MW	Mega Watt
kW	Kilo Watt
W	Watt
RPM / rpm	Revolutions per Minute
kg	Kilogram

max	Maximum
min	Minimum
ρ	Resistivity
Pshaft / Psh	Shaft power
η	Efficiency
μ_o	Permeability of air
B	Magnetic flux density
Tmax	Maximum torque
Tmin	Minimum torque
Tave or Taverage	Average torque
Tripple	Torque ripple in [%]
Lmax	Maximum inductance (aligned position)
Lmin	Minimum inductance (unaligned position)
t	Tooth-width
Lg	Air-gap length
Vref	The voltage reference value defining the required duty cycle to be applied to the phase windings
MagNet	The name of the finite element analysis software package from Infolytica Corporation
N_r	Number of rotor poles
N_s	Number of stator poles
N_{ph}	Number of machine phases
W	Stator tooth width
Mk	Mark
P_{Fe} or $P_{fe\text{-}specific}$	Total specific iron loss
$P_{fe\text{-}machine}$	Total machine iron loss
f	Frequency
B_{max}	Maximum flux density
α	Steinmetz constant
K_h	Hysteresis loss coefficient
K_e	Eddy loss coefficient
$M_{machine}$	Total machine mass
OptDesign	Number that is used to quantify how good a machine design is

ToutRatio	Percentage comparison of the design options in terms of average output torque
ToutPcuRatio	Percentage comparison of the design options in terms of average output torque per machine copper loss
ToutMassRatio	Percentage comparison of the design options in terms of average output torque per total machine mass
IndRatio	Percentage comparison of the design options in terms of unaligned linear inductance
Φ	Magnetic flux
N	Number of turns
$v(t)$	Instantaneous terminal voltage
$i(t)$	Instantaneous phase current
$\psi(t)$	Instantaneous flux-linkage
ψ_0	Initial flux-linkage
uF	Micro-farads
Ω	Ohms
CBD_S	Stator Core-Back Depth
TW_S	Stator Tooth Width
λ_S	Stator Pole Pitch
Φ_S	Stator Bore Diameter
Φ_{R1}	Rotor Outside Diameter
Φ_{R2}	Rotor Inside Diameter
Φ_{shaft}	Shaft Diameter
CBD_R	Rotor Core-Back Depth
TW_R	Rotor Tooth Width
L_g	Air-gap Length
Φ_{OUT}	Machine Outside Diameter
h_S	Stator Tooth Height
h_R	Rotor Tooth Height
R_{phase}	Phase resistance
L	Mean of the total length of a coil winding
D	Bare conductor diameter with no insulation layer
σ	Conductivity of copper

W	Co-energy
Pos_{rotor}	Rotor position with respect to a phase
Vtri	PWM carrier signal
I_Line	Line current
IPhA or IphaseA or Ia	Current flowing in phase A
IPhB or IphaseB or Ib	Current flowing in phase B
IPhC or IphaseC or Id	Current flowing in phase C
IPhD or IphaseD or Id	Current flowing in phase D
IPhE or IphaseE or Ie	Current flowing in phase E
IPhF or IphaseF or If	Current flowing in phase F
Eon	Energy per switch at turn-on
Eoff	Energy per switch at turn-off
Iu	Current flowing in Line U
Iv	Current flowing in Line V
Iw	Current flowing in Line W
I_LineX	Current flowing in Line X
I_LineY	Current flowing in Line Y
I_LineZ	Current flowing in Line Z
di/dt	Rate of change of current
$Dcond_{calculated}$	Calculated total conductor diameter
sff	Slot Fill Factor
A_{slot}	Total available winding area
N_{turns}	Number of turns per slot
P_{copper} or P_{cu}	Copper losses

Abbreviations

2D	Two-dimensional
3D	Three-dimensional
PI	Proportional-Integral
PID	Proportional-Integral-Derivative
DC / dc	Direct current
AC / ac	Alternating Current
BDCM	Brushless Direct Current Machine
CSA	Cross-Sectional Area
PM	Permanent Magnet
BLDC	Brushless Direct Current
DSP	Digital Signal Processor
BEMF	Back Electromotive Force
PCB	Printed Circuit Board
EMF	Electro Motive Force
FE	Finite Element
FEA	Finite Element Analysis
FPGA	Field Programmable Gate Array
IGBT	Insulated Gate Bipolar Transistor
MMF	Magneto Motive Force
MPL	Mean Path Length
MOSFET	Metal Oxide Field Effect Transistor
SCR	Silicon Controlled Rectifier
PID	Proportional, Integral, Derivative (current controller parameters)
PWM	Pulse Width Modulations
SP	Short Pitched
FP	Fully Pitched
SR	Switched Reluctance
SRM	Switched Reluctance Machine
VA	Volt-Ampere
kVA	Kilo Volt-Ampere

TW	Tooth-Width
GUI	Graphical User Interface
EU	European Union
USA	United States of America
US	United States
UK	United Kingdom
MagFine	Name derived from the combination of 'MAGnet' and the 'FINE' structure of d-HDDR magnet powder
VAT	Value Added Tax
NdFeB	Neodymium-Iron-Boron
InD	Rotor outer diameter
OutD	Stator outer diameter
Hz	Hertz
MHz	Mega Hertz
kHz	Kilo Hertz
CBD	Core-Back Depth
ROD	Rotor Outer Diameter
SOD	Stator Outer Diameter
PhA	Phase A
PhB	Phase B
PhC	Phase C
PhD	Phase D
PhE	Phase E
PhF	Phase F
FRFS	Flux-Reversal-Free-Stator
RMS or rms	Root Mean Square
A2D	Analogue to Digital
EMI	Electromagnetic Interference
PEDM	Power Electronics Drives and Machines
mm	Milimeter
m	Meter
SD	Segment Depth
VB	Visual Basic
PC	Personal Computer

SMC	Soft Magnetic Composite
DAC	Digital to Analog Conversion
LED	Light Emitting Diode
ADC	Analogue to Digital Conversion
MEC	Magnetic Equivalent Circuit
CPU	Centra Processing Unit
At	Ampere-turn

CHAPTER 1

1 - Introduction

1.1 INTRODUCTION

With advancements in power electronic devices, microcontroller technology, manufacturing processes and materials science, the use of electric motors in every sector from the aerospace industry to domestic appliances has been rapidly increasing. Electric motors now account for more than 60% of total energy consumption in industry within the EU and the USA. Consequently the design requirements of electric motors have become more demanding than ever. The main driving factors for the design requirements are cost, efficiency, size and torque density. There are more application specific requirements such as torque ripple, wide operating speed range, thermal performance, fault tolerance and acoustic noise that also need consideration and continuous development.

At the start of this PhD, previous academic study of segmental rotor SRMs was conducted in a PhD at Newcastle University and resulted in two 3-phase machines, one with multi-tooth phase windings, spanning more than one stator tooth, and the other with single-tooth phase windings. Fundamental operating principles were investigated on a single phase rectilinear model and design rules were established. As a result two 3-phase prototype machines were built and tested. Both of these machines were very successful and resulted in approximately 40% more output torque compared to conventional SRMs.

The author was involved in the dynamic measurements taken from these prototype machines at the beginning of this PhD project.

1.2 SWITCHED RELUCTANCE MACHINES IN INDUSTRY

Switched reluctance drives are no novelty and have been around since the 1800s. However, until the 1960s the optimum operation of an SR drive was somewhat impossible as control of SR motors was heavily dependant on sophisticated switching control. Although it is yet to have a significant share in the marketplace, with advancements in power electronics and materials technology the switched reluctance machine has entered into the electric machines and motor drives market. Compared to other conventional drive solutions, such as ac and permanent magnet based drives, SR drives have a small share in domestic and industrial applications. Well known issues of high torque ripple, high acoustic noise and vibration, cost and (potential) complexity of the power converter prohibit the SRM's greater market penetration. In simple terms, SRMs are still not perceived as "good value for money". On the other hand, advantages such as simple and low cost machine construction due to the absence of rotor windings, rotor cage or permanent magnets, low rotor inertia, high torque to inertia ratio and high starting torque without excessive inrush current make the SRM an attractive alternative for several applications.

Academic research continues to drive SRM technology forwards (see for example the works of Prof. R. Krishnan in Virginia, Prof. B. C. Mecrow in Newcastle, Prof. T. J. E. Miller in Glasgow, Prof. D. A. Torrey in Rensselaer, Prof. M. Ehsani in Texas, Prof. I. Husain in Akron, Prof. C.Pollock in Leicester). However, this is not reflected in the industry. In fact, the use of SRMs in industry has been in decline in recent years. This is partly because of the fact that the same technological advancements making SRMs attractive also allow other machine technologies to develop further and maintain or even increase their market dominance. For example, recent years have seen an exponential increase in the development of permanent magnets that are both mechanically and magnetically stronger (e.g. MagFine compression and injection molded anisotropic bonded magnets from Aichi Steel Corporation) than their earlier counterparts. These new permanent magnets also tolerate operating temperatures as high as 150^{o}C without significant flux loss (typically 4-5%). Moreover, as the number of magnet manufacturers increases, the cost of permanent magnets has reduced. Because of their high torque density, permanent magnet machines have started to dominate some sectors of the

industry. They are the primary candidate for high efficiency / small size domestic appliances (see for example the new generation Dyson Digital Motor used in handheld products – DC30 and DC31) and have a significant share in the wind turbine generators market (V112-3.0 MW of Vestas Wind Systems, GE's 2.5MW wind turbines, G128-4.5 MW of Gamesa, etc.). However, a recent rise in rare earth material cost, along with concerns over security of supply has led to debate over whether permanent magnet machines will continue to dominate.

The AC induction machine is still the preferred option for many industrial applications. However, it is well known to have problems with heat extraction from the rotor, as the rotor also carries windings and current. There is also concern over the induction machine's efficiency over a wide speed and power range.

Until the performance issues of SRMs are resolved in an economical fashion this motor drive technology will struggle to have a deeper penetration and a larger market share of either industrial or domestic applications. Significant improvements are required in the field of converter topologies, control algorithms, torque ripple, acoustic noise reduction and sensorless operation.

1.2.1 Target Industries for SR Motor Drive Technology

The author believes that there are four target sectors in order to achieve greater penetration for the SR motor drive technology. These can be summarised as follows:

- **Energy**:

The level of interest in the use of SR machine technology in the energy sector has risen over the years but activity has mainly remained at research level in academia [1-4]. Wind power is growing at an annual rate of 30%, with a worldwide installed capacity of 157,900 MW in 2009, and is widely used in Europe, Asia, and the U.S.A. During the five-years from the end of 2004 through to 2009, worldwide renewable energy capacity grew at rates of 10 to 60 percent annually for many technologies. For wind power and many other renewable technologies, growth accelerated in 2009 relative to the previous four years; more wind power capacity was added during 2009 than any other renewable technology. Nowadays, 19% of the electricity used in Denmark is supplied by wind

power generators. This is 9% in Spain and Portugal, and 6% in Germany and the Republic of Ireland [5]. The United States is an important growth area and installed U.S. wind power capacity reached 25,170 MW at the end of 2008 [6]. Unfortunately when it comes to machine drive technologies employed in the wind power industry, the top 10 wind turbine generator manufacturers opt for either permanent magnet synchronous machine or squirrel cage / wound rotor induction machine technologies. However, the potential of the SRM for this type of application is high [1]: the SR generator has been considered for wind power applications for a long time [2].

Much of the research on SR generators has so far focussed on aircraft [7-11]. Greater penetration of SR machine technology into the energy sector can be achieved with further research aiming to improve the behaviour of SRMs in generator mode, specifically in wind power applications. However, it must be said that unless significant improvements are to be made, penetration into the wind turbine generator market is quite difficult. There are two mains reasons to this: first of all, new generator concepts of MW scale are very expensive to prototype and secondly, new production lines can require enormous investment, prohibiting companies investing in SRM technology.

- **Domestic Appliances**:

Domestic energy consumption has been increasing with continuously growing rates since 1990s. As the number of households, population and household disposable income increase, the demand for energy by households also amplifies. Furthermore, as the number of appliances owned per household increases and more functionality is demanded from new products, the energy consumption by the domestic appliances and its impact on our environment has become very important. There are new EU legislations imposing strict energy limits to some of the household appliances and there will be a greater need for more efficient and compact electric motor drives in the domestic appliances sector. From the companies' point of view, these new products will also need to be financially feasible.

SRMs offer much greater efficiency than brushed motors: if magnet costs continue to rise they may start to displace permanent magnet brushless products.

- **Automotive**:

There are now over one billion cars on our planet. There is an undeniable reasoning to develop vehicles that are clean, efficient and sustainable. This is driven by environmental,

as well as economical, issues. For an era when reducing carbon emissions and controlling global warming is one of the biggest driving factors, the exhaust emissions of conventional internal combustion engine vehicles are deemed to be unacceptable. Moreover, as the oil reserves of the planet diminish, alternative ways to run these vehicles are paramount for the automotive industry. High efficiency electric motor drive technologies provide the means for a clean, efficient and environmentally friendly urban transportation system.

There are incentives given by governments to promote the use of electric vehicles such as: reduced VAT and other taxes, insurance facilities, parking and battery charging facilities (including free recharging on street or in the parking areas), toll free travel on motorways and exemption from congestion charging.

SRMs are much more amenable to field weakening than permanent magnet motors: they offer good competition to induction motors and may be superior to permanent magnet motors in the extended constant power range.

- **Aerospace**:

Once again the sector and the motor drive technology's link to the sector are both driven by the global aim of minimising carbon emissions. SRMs have a big advantage because they are inherently fault tolerant, i.e. the drive will continue to work even when one or more of the phases of the machine fail. The aircraft industry is moving towards an increased use of electrical auxiliaries, particularly to replace hydraulic and mechanically powered systems. As well as very high performance, the industry requires extremely reliable and fault tolerant systems. Albeit continued interest, it is still early days for the more electric aircraft and continuous commitment from the industry and research institutes is paramount to the increased use of electrically driven systems in the aerospace industry.

1.2.2 Examples of SR Drives in Industry

There are only a few companies specialising in SR motor and drive system development. The foremost example is SR Drives in Harrogate, UK. SR Drives was a start-up company founded by the pioneering works of Prof. Lawrenson and his colleagues at Leeds University. Many of the specific industrial examples of SR machines and drives given within the next few pages are developed by SR Drives.

Rocky Mountain Technologies Inc. in Montana, USA was incorporated in 2000 with a strong focus on SR motors and drives. The company produces series of three and four phase SR motor drives ranging from 0.4kW to 25kW for motion and alternative energy applications.

VS Technology Corporation (VST) in Texas, U.S.A develops switched reluctance drives and drive-trains for small to large applications including vehicles. VST has been working in the automotive field since 1990 and in 2007 acquired all of the advanced motor drives technology from Honeywell Corporation, expanding its reach. VST has a range of vehicle traction motors from 20kW to 200kW and wind turbine generators from 50kW to Megawatts. They also develop high speed motors up to 100,000 rpm.

Technelec Ltd. was established in 1992 by Professor Charles Pollock, aiming to exploit his work in Warwick and Leicester Universities. The company specialises in design and development of electronically controlled switched reluctance machines, flux switching machines and hybrid stepping motors.

Specific examples of SR machines and drives in the market place are summarised below.

1. DOMESTIC & COMMERCIAL APPLIANCES:

- *Dyson DigitalMotor*:

Used in Japanese Vacuum Cleaners (DC12) and Airblade (AB01 and AB03). It is a high efficiency (more than 80%) 1600W motor, capable of spinning at 100000 rpm with a lifetime of 1000 hours in constant use. The drive has built-in electronics resulting in compact size.

- *AMETEK Blower Motors*:

Blower motors from the Infin-A-Tek series of AMETEK Lamb Electric operating from 24V, 26V and 48V DC, and 120V and 230V AC use SR drive technology. The use of SR drive in this application is claimed to have increased the service life three to five times longer than designs commonly utilising series universal motors.

- *Beckman Instruments Inc*:

SR drive technology is used to power Beckman's AVANTI® J & JE series of high-speed centrifuge systems. The system is claimed to be a major improvement on conventional high-speed centrifuges, providing faster acceleration, faster deceleration and higher g-forces.

2. TRANSPORTATION AND AUTOMOTIVE APPLICATIONS:

- *Green Propulsion*:

In Green Propulsion's (a Belgian company specialising in developing cleaner prototype vehicles) 'Series and Parallel' hybrid transmission scheme, two switched reluctance motor-generators were utilised for a hybrid power-train; a 50kW and a 160kW SR drive both working in conjunction with a 2.5 litre diesel engine.

- *Renault*:

Renault's TIVA system (Transmission Infiniment Variable) uses two switched reluctance drives linked via a two-stage epicyclic gearbox. This is a hybrid vehicle with the main power source being a diesel combustion engine.

- *Caterpillar*:

The US Department of Energy has provided funding to Caterpillar to investigate the benefits of increased electrical auxiliaries for highway trucks. Electrical auxiliaries include the oil pump, the water pump, the air compressor for the vehicle brake system and an electric HVAC (Heating Ventilation & Air Conditioning) system. The heart of the system is an SRM based starter/generator unit (340V, 1200Nm, 30kW) which is mounted on the crankshaft between the engine and gearbox. The intention of the starter/generator is both to provide a direct-drive functionality to start the engine and also to generate the required electrical power for the various auxiliaries on board.

- *Deutsche Bahn AG*:

German railway company Deutsche Bahn AG uses switched reluctance motor technology in the heart of the air conditioning system for its ICE 3 high speed passenger trains. At maximum cooling, the motor power is 40kW operating at a speed of 23,000rpm. The unit

weighs less than a conventional air conditioning unit, which allows it to be entirely roof mounted.

3. INDUSTRIAL APPLICATIONS:

- *CompAir Ltd*:

CompAir Ltd. specialises in compressed air equipment. Designed by SR Drives® Ltd., SR motor drives are used in its LSR and D-HSR series of variable-speed rotary-screw compressors and are said to achieve high efficiency.

- *Drax Power Ltd*:

Drax Power Ltd. operates the UK's largest coal-fired power station**.** As part of a £1 million investment in plant modifications, Drax Power Ltd has installed a fuel blending plant which allows a variety of alternative fuels to be accurately blended with the main coal feed. This was achieved with five SR Drive systems, ranging from 40kW to 160kW. Two of these were new installations and three replaced fixed speed induction motors.

- *Picanol*:

Based in Ieper, Belgium, Picanol is recognized as the world's leading company in the design and production of weaving machines. Picanol has been using switched reluctance drive technology (named the "Sumo" motor) since 2000 with its OMNI*plus* range.

- *LeTourneau Inc*:

Based in Longview, Texas, LeTourneau Inc. employs SR Drive® technology in its latest 50 Series 'digital' loaders. The L-1350 electric-wheel loader is the first machine of its type to be fitted with an SR drive system that provides independent traction for each wheel. Four 300kW SR motors were used. Relative to the original brushed DC motors, a major increase in service and inspection life has been achieved (from around 500 hours to 20,000 hours) due to the absence of brushes and a commutator.

1.3 SWITCHED RELUCTANCE MACHINES WITH SEGMENTAL ROTORS

Conventionally both the stator and the rotor of an SRM are made up of toothed steel laminations. However, the toothed rotor structure is known to suffer from poor utilisation of the machine's magnetic circuit. A measure of the magnetic utilisation of the machine is often indicated by the tooth width to pole pitch ratio (t/λ). t/λ gives an idea of how much of an excited rotor pole carries magnetic flux. With conventional toothed rotor structures this ratio is optimally around 0.42. Once the ratio is over 0.5 there is always an overlap between the rotor and the stator teeth which results in increased unaligned inductance [12].

Mecrow et al in 2002 [12] suggested that the segmental rotor arrangement was very well suited to the concentrated stator MMFs of SRMs. Unlike the conventional toothed structure, the rotor of a segmental SRM is constructed from a series of discrete segments. A segmental design does not suffer like the toothed design when t/λ is increased beyond 0.5. In fact t/λ values of beyond 0.7 are easily achievable without compromising the unaligned inductance. With the segmental rotor design magnetic utilisation of the machine is increased, i.e. the proportion of the air carrying flux is greatly increased. Although segmental rotor structures are similar to that of segmental rotor synchronous reluctance motors there are three major differences:

1. The phase windings of the segmental rotor SRM are concentrated.
2. There is negligible magnetic coupling between the phases of the segmental rotor SRM.
3. The segmental rotor SRM is excited with direct current pulses, rather than sinusoidal AC.

With the conventional toothed rotor SRM the stator teeth permeances are regulated as the rotor rotates cyclically. In the case of the segmental rotor SRM, torque is generated as the rotor segments modulate slot permeances. Slot permeance is minimised when the segments are centred under a stator tooth (unaligned position) and maximised when the segments bridge a slot opening (aligned position).

The rotor structure of a segmental SRM only permits neighbouring teeth to be magnetically linked, which requires the magnetic flux to enclose a single stator slot. This was achieved with two different winding arrangements:

1.3.1 Multi-tooth Winding Segmental Rotor SRM

Each coil spans more than one stator tooth (as many teeth as the number of phases). Rectilinear representation of a 3-phase multi-tooth winding segmental rotor SRM in the aligned position is depicted in Figure 1. Use of coils spanning more than one stator teeth result in substantial end-winding lengths. This reduces the electric loading, which makes the design impractical for applications that combine short lamination stack length with a large pole pitch. Nevertheless, 40% more torque within a given frame size was achieved compared to the conventional toothed rotor SRM [12].

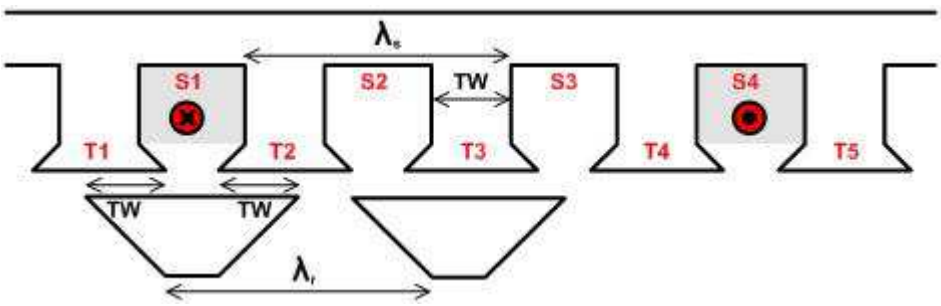

Figure 1 Rectilinear representation of a 3-phase multi-tooth winding segmental rotor SRM in the aligned position

1.3.2 Single-tooth Winding Segmental Rotor SRM

Slots S2 and S3 and tooth T3 in Figure 1 were removed to have a segmental rotor design where any one slot is still occupied by windings of a single phase. Each coil of the stator is now wound around a single tooth which achieves short and non-overlapping end-windings. With the single-tooth winding arrangement only every other stator tooth accommodates phase windings. The wound teeth span a complete rotor pole. The rectilinear representation of a 3-phase single-tooth winding segmental rotor SRM in the aligned position is illustrated in Figure 2. The width of the stator teeth carrying phase windings is doubled compared to the stator teeth with no phase windings. The stator teeth with no windings act as the return path for the flux generated by the slot MMFs. The

single-tooth winding arrangement has a poorer magnetic utilisation compared to the multi-tooth winding arrangement. However the advantage of the single-tooth winding design is the shortened end-windings. Overall, the single-tooth winding design has similar performance to the multi-tooth winding design but requires less copper windings.

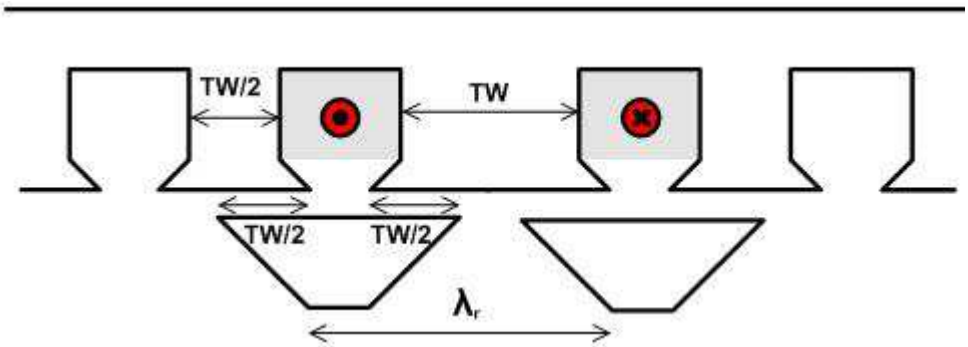

Figure 2 Rectilinear representation of a 3-phase single-tooth winding segmental rotor SRM in the aligned position

As the rotor depth is shallow, another advantage of the segmental design is that it can be suitable for applications where machines with large shafts are required.

1.4 CONVERTERS AND CONTROLLERS FOR SWITCHED RELUCTANCE MACHINES

The performance and cost of an SR drive is highly affected by the chosen converter topology and the control method. It is well known that the direction of current has no effect on torque production in a switched reluctance machine. This means that an SR drive can operate with unipolar phase currents which, along with phase independence opens up the possibility of using single switch per phase converters. As a result many different converter topologies are currently available to drive switched reluctance machines. The converter topologies usually differ in the way they handle the stored magnetic energy at the end of each stroke. Some of the topologies return the stored magnetic energy back to the supply, some use this energy to charge a capacitor to aid with the turn-on and turn-off of phase windings, some use it to energise a closely coupled second winding and some simply dissipate this energy across resistors. Each converter topology has its own advantages and disadvantages. It is best to match the converter to

the specific application requirements. There is always a trade-off between the performance, cost and the complexity of the converter circuit and the controller.
For example an asymmetric half-bridge converter has the maximum control flexibility (it is able to control phases separately and provide positive, zero and negative voltage loops) but requires two devices per phase, increasing the size and cost of the drive. A bifilar winding converter requires only a single switch per phase but the ratings of the devices are high; the C-dump converter offers fast demagnetisation of phases during commutation but requires complicated control. Basic requirements of a converter topology can be summarised as follows:

- Provide positive voltage to increase the flux in a phase.
- Have the ability to control the flux when the required level of current is reached.
- Provide negative voltage to reduce the phase current to zero.

The Volt-Ampere (VA) rating of the converter is usually used as a measure to indicate how effectively the ratings of the power switches have been utilised and, hence, the relative cost of the converter circuit. This is clearly a very crude model: for example it incorrectly suggests that a converter with fewer switches does not necessarily reduce the cost of the power electronics if the switches require higher current, voltage and / or power dissipation ratings.
Use of the 3-phase bridge circuit with SR drives has already been demonstrated by Clothier et al [13] with a 3-phase fully-pitched winding conventional toothed rotor SRM. When driven from a 3-phase full-bridge circuit the machine can be connected in star (Figure 3) or in delta (Figure 4) configuration. There are two phases conducting at any given time with a 3-phase full-bridge circuit driven machine. There are distinct advantages to using the 3-phase full-bridge circuit, which can be summarised as:

- The 3-phase full-bridge circuit is one of the most commonly known and readily available topologies. The volume of production of 3-phase full bridge converters dwarfs any other topology available for SR drives. They usually come with the current transducers and the controller electronics.
- With the 3-phase full bridge circuit, devices with internally packaged diodes can be used.

- The line currents, rather than the phase currents, can be controlled. As a result, the number of current transducers can be reduced to two for a three phase machine (based on the fact that the line currents should sum to zero).
- The number of connections between the motor and the converter are reduced to three.
- The controller can be separated and placed far away from the motor.

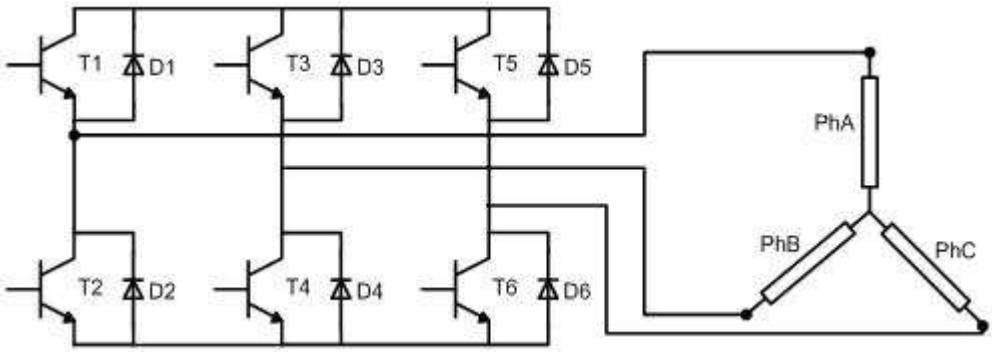

Figure 3 Star-connected 3-phase fully-pitched winding SRM driven from 3-phase full bridge inverter

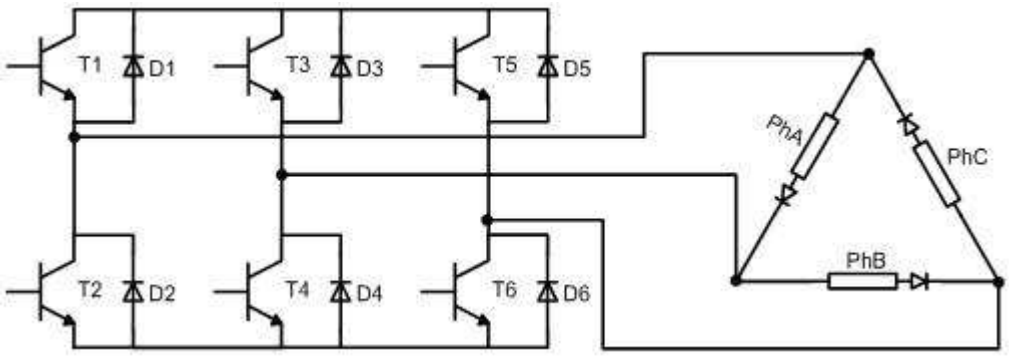

Figure 4 Delta-connected 3-phase fully-pitched winding SRM driven from 3-phase full bridge inverter

The disadvantages of using the 3-phase full bridge circuit for driving SRMs are:

- There is no inherent shoot-through protection.
- The line currents are restricted in that they must sum to zero.
- There are additional diode losses.

1.5 SWITCHED RELUCTANCE MACHINES vs. PERMANENT MAGNET BRUSHLESS DC MACHINES

With recent advances made in the magnet material and manufacturing technologies, permanent magnet brushless dc machines (PM BLDC) have become the first choice for many applications. The competition is a tough one, especially in the aerospace, automotive and renewable energy sectors (wind turbine generators specifically).

It is possible to compare the performance of machines using the flux-linkage versus current characteristics. Per phase flux-linkage versus current locus for an SRM is only in a single quadrant. On the other hand, for a PM machine the flux-linkage versus current locus occupies four quadrants. This is illustrated in Figure 5 for the 3-phase 12-8 and 12-10 segmental rotor designs [12], 3-phase 12-8 conventional toothed rotor design and a 3-phase PM BLDC design (that has 12 slots and 8 poles with Neodymium-Iron-Boron (NdFeB) magnets with each coil wound around a single tooth). In Figure 5 all machines are running under current control, generating similar amounts of copper losses and, when loaded, the peak machine flux density levels in all the machines are identical. The locus for the PM machine is shown for one half cycle of conduction, with the machine connected in a star configuration. The areas of flux/MMF loci are directly related to torque production (it should be stated that the 12-10 design will be traversing its loop 25% more times than the others and hence produces 25% more torque per unit area of locus).

Each SRM phase conducts for 1/3 of a cycle whereas each of the phases of a PM machine conducts for 2/3 of an electrical cycle. PM machines have greater power to weight ratios and are generally more efficient than SR machines. Furthermore, the ripple content of the total output torque in a PM machine is significantly lower than that can be achieved with an SRM, hence making the PM machine the preferred option in torque ripple sensitive applications. SRMs have inherent fault tolerance, as the phases can be physically (by winding each phase coil around a single stator tooth), electrically (by driving them from separate half-bridges) and magnetically (by having little or no mutual coupling) isolated. Moreover, as the SR machines are singly excited, fault current will not continue to be driven into a faulted phase, once excitation to that phase is removed.

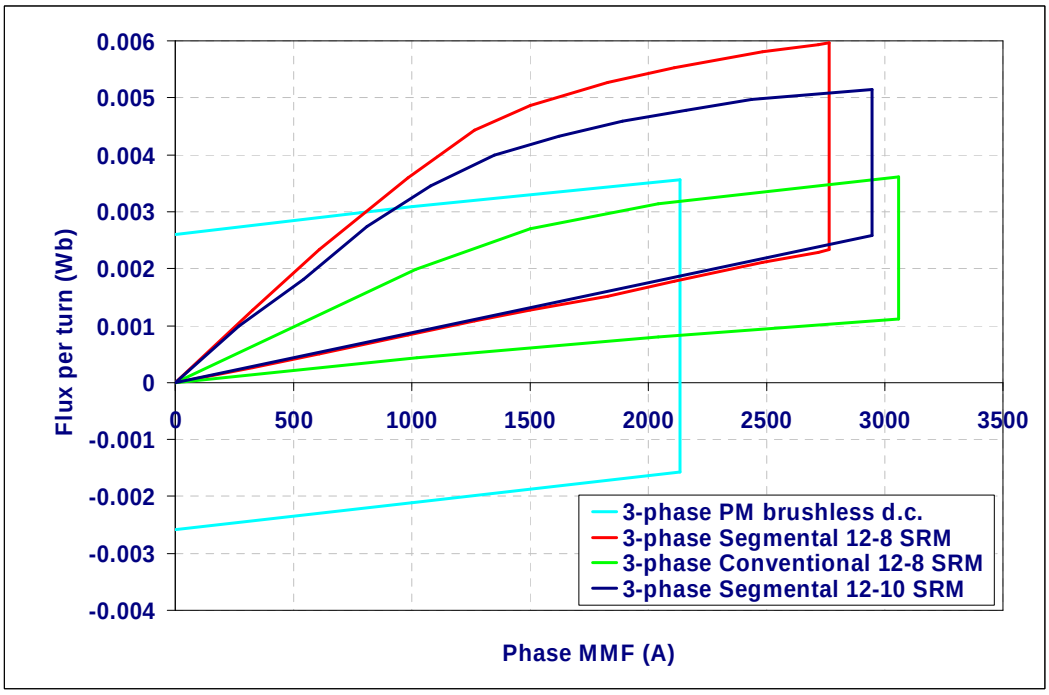

Figure 5 Flux-Linkage loci for the 3-phase segmental rotor 12-10 SRM (in dark blue), 3-phase segmental rotor 12-8 SRM (in red), 3-phase conventional toothed rotor 12-8 SRM (in green) and a brushless d.c. PM machine (in light blue), operating under current control

With careful design PM machines can achieve a similar degree of fault tolerance with higher torque densities (although the potential torque density is compromised to achieve fault tolerance) which is a very significant merit especially in the aerospace industry where total mass is crucial [14].

High performance permanent magnets are from the group of elements on the periodic table known as rare earth materials. The supply risk and the price volatility (in 2008 there was a shortage of Neodymium and Praseodymium for use in permanent magnets and the price rose by a factor of five to a peak of $50/kg for Neodymium [15]) of these materials must be highlighted here. As the Chinese leader Deng Xiaoping famously stated in 1992: "The Middle East has oil, China has rare earths", currently China dominates the world supply of rare earth magnet raw materials. Added to the sheer size of available rare earth resources, highly developed separation and processing power resulted in China representing over 95% of the world's rare earth materials supply. Rare earth materials are not only used in the electric motors industry. Published global production and consumption estimates show that as early as 2015 Asia alone could consume almost all of the world production for many of the rare earth materials if no new production facilities are established.

The Chinese rare earth industry is government controlled and can easily control the pricing of rare earth materials to eliminate competition in mining, separation and processing of rare earth materials. Recently China increased taxes and imposed export restrictions and VAT penalties on all Chinese exporters of rare earth materials.
There will inevitably be a growth in demand for rare earth materials for permanent magnets in the near future with growing numbers of hybrid and electric vehicles and high performance wind turbine generators. Where permanent magnet motors fall short due to price volatility, or purely because of insufficient materials resources, the SR machines will be the prime candidate to substitute them.

1.6 OBJECTIVES AND CONTRIBUTION TO KNOWLEDGE

This PhD thesis aims to reduce the torque ripple of SRMs by simply increasing the number of phases. The number of power devices, current transducers and the number of connections between the machine and the converter are kept to a minimum by connecting phase windings of the machine back-to-back and driving them from a conventional 3-phase full bridge circuit. Instead of controlling the phase currents, the controller deals with the line currents, reducing the number of current transducers needed to two as the third line current can be derived from the other two line currents.

The research conducted during this PhD study contributes to knowledge in the following areas:

- A comprehensive assessment of segmental rotor SRMs and comparison against other machine types.
- Approaches which enable SRMs to be driven from conventional three phase bridge inverters.
- A concept which enables six phase SRMs to be employed, whilst only having three wires connecting the SRM to the power inverter.
- Machine construction methods which allow greater slot fill factors.
- A concept which allows reduction of torque ripple in a switched reluctance machine.
- A method which enables driving a two-phase SRM with a single current transducer.

- Simulation methods which enable accurate modelling of various machine and inverter topologies.
- A set of matrix transformations which enables modelling of SRMs even when there is strong mutual coupling between phases.

1.7 THESIS OVERVIEW

This thesis is divided into eight chapters and appendices.

Various SR machine design topologies centred on the conventional toothed stator and rotor structures are reviewed in **Chapter 2 – SR Machine Topologies.** The same chapter also reviews the concept of employing a segmented rotor design in a doubly salient reluctance motor. Fundamental design principles are given and two demonstrator machines are compared with conventional and axially laminated SRMs.

A review of drive topologies and control methods for switched reluctance machines is discussed in **Chapter 3 – SR Drives**. Converter topologies that are commonly employed in SR drives are presented and basic operating principles are explained.

Chapter 4 – Machine Design and Testing describes the detailed design processes of 6-phase 12-10 segmental and conventional toothed rotor SRMs. Measurements of the flux-linkage characteristics, static torque and thermal characteristics are all presented.

In **Chapter 5 – Machine Construction Techniques** the method of constructing stator for prototype machines is explained. The method of constructing stators from separate cores is decribed and discussed.

Chapter 6 – Simulation Models describes the simulation models developed to model various parts of the drive system. The prototype segmental rotor machine has strong mutual coupling between phases. A set of matrix transformations is presented to de-couple the phase quantities into slot quantities.

In **Chapter 7 – Machine Operation and Comparison to Simulation – Two Phase Drives –** a two phase configuration is used to compare the performance of asymmetric half-bridge and h-bridge inverters. Dynamic measurement results under various operating conditions are presented and compared to the dynamic simulation results.

In **Chapter 8 – Machine Operation and Comparison to Simulation – Three Phase Drives –** dynamic measurement results under various operating conditions for the three phase 12-10 single tooth segmental rotor SRM are presented. These measurements are also used to validate the dynamic simulation and deduce inverter rating requirements.

In **Chapter 9 – Machine Operation and Comparison to Simulation – Six Phase Drives –** the six phase 12-10 segmental rotor SRM is connected in star and driven from a 3-phase full bridge circuit. Dynamic measurement results are presented and analysed.

In **Chapter 10 – Comparison of Machine Performances –** the torque ripple and inverter VA requirements of the six phase 12-10 segmental and toothed rotor SRMs are compared against those of the 3-phase 12-10 single tooth segmental rotor SRM.

With the final chapter, **Chapter 11 – Conclusion and Future Work** the overall aims are revisited and major achievements and shortcomings of the research are highlighted. Suggested future work arising from the research carried out in this PhD thesis is provided and an overall assessment of the obtained results is presented in this chapter.

CHAPTER 2

2 - SRM Topologies

2.1 INTRODUCTION

With the development of new materials, continuing advancements and cost reduction in power semiconductors, more effective use of mathematical optimisation techniques and increased capabilities of 2D and 3D FE analysis, interest in both commercial development and research in switched reluctance machine based drive systems has continued to produce new concepts in recent years. Early development of switched reluctance machines was driven by the activities of Bedford [16, 17] at General Electric Company in Schenectady, of Lawrenson and Stephenson [18] at Leeds University, of Byrne and his colleagues [19] at University College in Dublin and of Ray and Davis [20] at Nottingham University. In [18] Lawrenson et al outline the basic operating and design principles of doubly salient reluctance motors. Pioneering work of Lawrenson, Stephenson, Ray and Davis from Leeds and Nottingham Universities has grown into a commercial establishment in the name of *SR Drives Ltd* founded in 1980. Also the work of the SPEED Laboratory led by Prof. Miller at the University of Glasgow, the Power Electronics Drives and Machines group of the University of Newcastle Upon Tyne, and Prof. Charles Pollock in Leicester and Warwick Universities have led the way in SR machine and drive research for the last three decades.

This chapter starts with a brief explanation of the torque ripple phenomenon in SRMs and gives an overview of torque ripple minimisation techniques in SR drives through the electromagnetic design of the machine. Recent papers by Mecrow et al [12, 23] have introduced the concept of employing segmented rotor design to SRMs. Instead of the

usual toothed arrangement, the rotor is constructed from a series of discrete segments, each of which is magnetically isolated from each other. Section 2.3.2 of this chapter reviews Mecrow's 3-phase designs. This chapter will also review various switched reluctance motor designs giving examples of some of the relevant work aiming to improve the performance of SRMs by altering the magnetic and / or electric design of the machine. Section 2.3.1 is dedicated to explaining several different design variations of the conventional toothed rotor structure. Section 2.3.3 covers recently published work on segmental rotor switched reluctance machines.

2.2 SRM TORQUE RIPPLE

In an ideal switched reluctance machine, reluctance varies linearly with tooth overlap and for a constant MMF, constant torque is produced. SRMs are designed to operate deep into the magnetic saturation zone of the lamination material to maximise the output torque density. Consequently in a real machine saturation and field fringing flux mean that the torque produced for a constant phase current is a non-linear function of position. Saturation and variation of magnetic reluctance in the SRM, due to its doubly salient structure, generate highly non-linear flux and torque characteristics. As a result generated torque can contain significant torque ripple. Torque ripple is not only a highly undesirable characteristic for many applications (i.e. direct drive electric power steering and robotics) on its own but is also believed to contribute significantly to another drawback of SR drives, *acoustic noise* [24]. Torque ripple in a drive system can be quantified by Equation 1.

$$Tripple\,(\%) = \frac{T\max - T\min}{Tave} \times 100 \qquad \textbf{Equation 1}$$

where $Tave$ is the average machine output torque.

Torque ripple minimisation can be realised by machine design and / or employing torque smoothing control strategies. The following subsection summarises the methods aiming to reduce the torque ripple in SR drives through machine electromagnetic design. A summary of methods relating to the drive control will be presented in the next chapter.

2.2.1 Torque Ripple Minimisation through Machine Design

As one phase gets closer to the end of its energisation cycle and the energisation of the next phase is about to start a torque dip appears. As a result, the majority of torque ripple is said to happen in this phase overlap region. The width of the overlapping region between torque outputs of adjacent phases depends on the pole overlap angle between the stator and rotor, material properties, number of poles and number of phases. Optimising the individual phase torque-angle characteristics by salient pole shape profiling [25], or skewing of the rotor axially [26] can help to minimise the inherent torque ripple. Increasing the number of phases appears to be a better approach in reducing torque ripple, since the higher the number of phases the higher the overlap will be as the phases get near the commutation zone. The obvious downside of having a machine with increased number of phases is the potentially increased cost and complexity of the drive system due to increased number of power devices required to drive the phases of the machine.

The vibration modes and torque ripple are associated with the level of air-gap flux density; it is believed that the higher the air-gap flux density level the worse the torque ripple, vibration (due to normal forces) and the acoustic noise levels. It now appears that to reduce the torque ripple, vibrations and consequently the acoustic noise, the air-gap length can be increased. However increasing the air-gap will compromise the power density and the efficiency of operation [27]. Another design method to reduce torque ripple is to employ an asymmetric rotor pole geometry [28]. However skewed rotor poles compromise the total output torque. In [29] adjacent rotor poles have unequal widths resulting in a two-stage flux pattern, which was believed to operate with a low torque ripple (more on this machine later in this chapter).

In [30] the authors analyse the effect of simple variations of the rotor pole face structure on the torque production of a 60kW - 6000rpm experimental SRM. A notable design procedure, focusing on torque ripple minimisation, is given in [31]. The design presented in [31] is heavily centred around the feasible design triangle given in [18]. In [32] authors use FE to analyse the effects of shaping the rotor and stator pole tips on the torque ripple in short-pitched and fully-pitched winding SRMs. In [33] stator and rotor pole arcs are optimised through a genetic algorithm based routine in order to reduce torque ripple, without reducing the average torque output of the machine. The paper deals with a specific design and appears to be (more of) an application of genetic algorithms rather

than a generalised approach for reducing torque ripple in switched reluctance machines. Other examples of torque ripple reduction through pole arc shape optimisation are given in [34, 35].

2.3 SRM TOPOLOGIES

Theory and general design considerations of switched reluctance machines are well documented in a number of papers [30, 36-58].

The performance of a drive comprising a switched reluctance motor heavily depends not only on the motor itself but also on how well the power electronic controller is matched to the particular motor design and application requirements. Therefore successful switched reluctance motor designs should take the converter and the motor as a whole, fulfilling the requirements of the specific application. A few examples of application specific switched reluctance machine design work are given in [59-67]. When a design is required for a specific application, often the design space and performance requirements are known parameters. What is left for the design engineer to do is to produce the optimal machine and controller design to fulfil the requirements. This obviously is not a trivial task. Optimal machine design can be regarded as a multi-dimensional optimisation problem and the solution can be found by using genetic algorithms [68-70], artificial neural networks [71] or non-linear optimisation methods [72].

2.3.1 Conventional Toothed Rotor SRMs

In simple terms, a switched reluctance machine has salient poles on both its stator and rotor, but has windings on its stator only (see Figure 6).

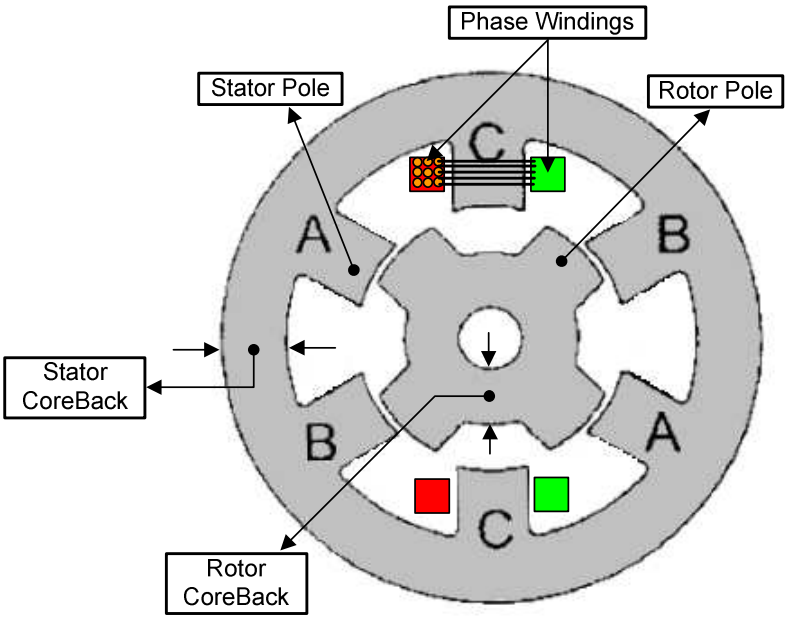

Figure 6 Schematic of a three-phase conventional switched reluctance machine showing various motor sections

Conventionally, the phase windings are short-pitched, with each coil wound around a single stator pole. Each phase has series and / or parallel connected coils forming stator poles. Use of short-pitched windings results in negligible magnetic coupling between phases, i.e. flux generated by a single phase current only links the windings of that phase. Of course, in reality there is some mutual coupling through core-back saturation and cross-slot leakage but this is generally considered to be negligible [49]. Similar to its stator structure, the rotor of a conventional SRM is formed from a toothed lamination structure. Motoring torque is generated when current flows into a phase when the rate of change of phase inductance is positive. Similarly, generating torque is achieved by injecting current into a phase when the rate of change of phase inductance is negative (see Figure 7).

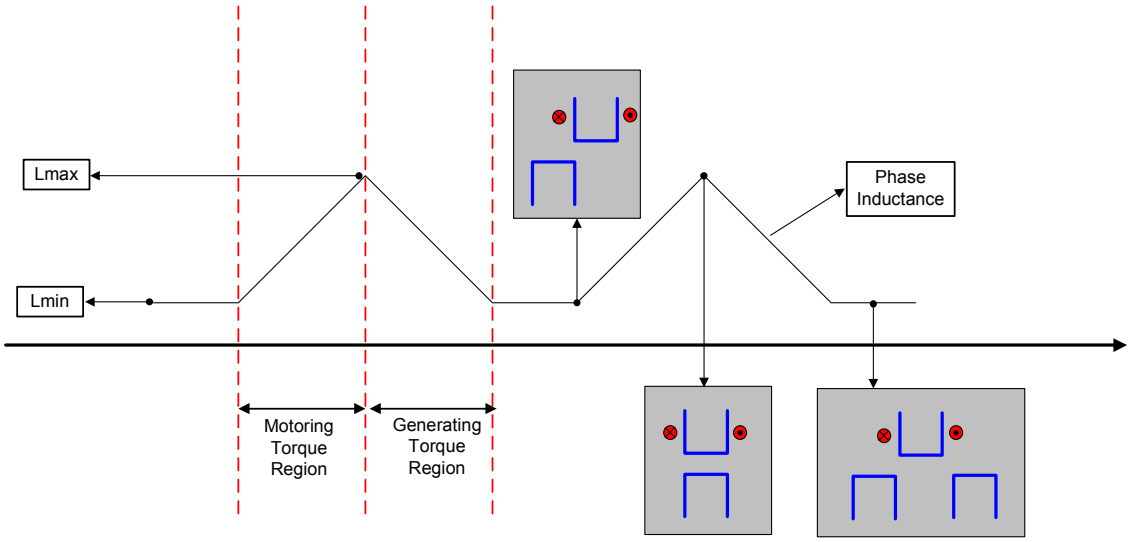

Figure 7 Variation of inductance and positive and negative torque production regions with ideal pulse unidirectional current. Lmax and Lmin are the maximum and minimum phase inductances, respectively

For the conventional toothed rotor structure in Figure 8 there are four main parameters that are considered to be of importance in its design. These are:

- Tooth width to pole pitch ratio (t/λ)
- Air-gap length(L_g)
- Ratio of stator and rotor outside diameters i.e. Split ratio ($\frac{SOD}{ROD}$)
- Ratio of core-back width to half of tooth width ($\frac{CBD}{t/2}$)

The dimensional abbreviations above are shown graphically in Figure 8.

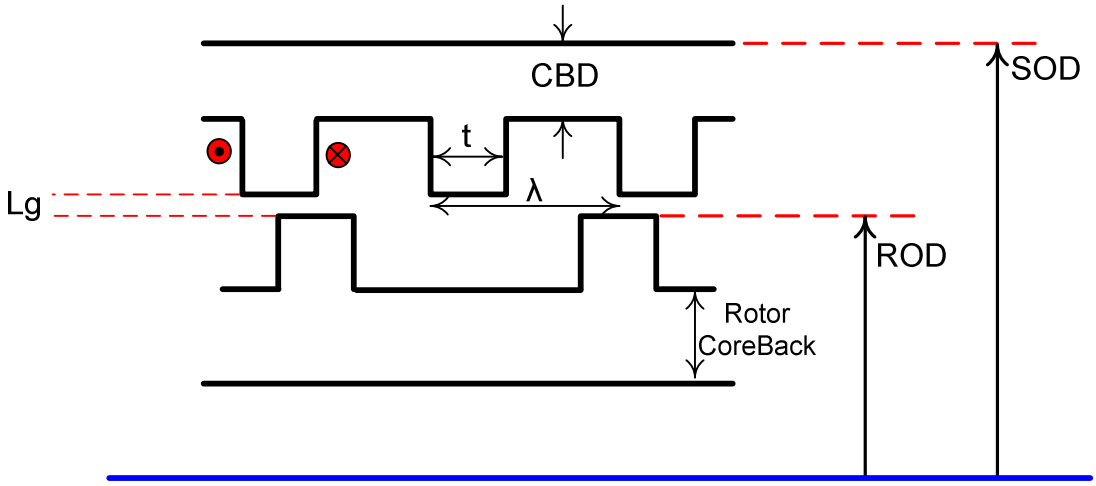

Figure 8 Description of several machine dimensions for a rectilinear representation of a conventional toothed rotor SRM

Tooth width to pole pitch ratio (t/λ - Figure 8) is often used as a measure of magnetic utilisation in switched reluctance machines because it gives a good measure of how much an excited rotor pole carries magnetic flux. The limitation with a toothed design is that t/λ cannot be increased beyond 0.5 as the stator and rotor poles start overlapping even at the unaligned position, increasing unaligned permeance and consequently reducing torque capability. Typical values of t/λ range from 0.3 to 0.45. An increased unaligned curve also increases the VA requirements of the drive as it becomes more difficult to drive the phase current when the minimum inductance of the machine is high. Higher converter VA requirements will compromise the size and the cost of the overall drive system.
Variations on the basic topology have emerged. Significant contributions include:

- Use of short flux paths [73-75]
- Flux reversal machines [76-78]
- Common pole E-cores [79]
- Staggered rotor teeth [29, 78]
- Flux switching motors [51, 80-82, 92]
- “Shark tooth” air-gaps [83-85]
- Multi-teeth per pole [86-88]
- Overlapping windings to exploit mutual coupling between phases [13, 51, 89-92]

2.3.2 Segmented Rotor Switched Reluctance Machines

The SRM design variations listed in the preceding section have all been attempts to alleviate various weaknesses and to improve the performance of switched reluctance machines i.e. output torque, efficiency, torque ripple, etc. However, the magnetic geometry of all these designs has been effectively fixed, employing a series of stator teeth with short-pitched or fully-pitched windings and a series of rotor teeth that are magnetically coupled through the stator and rotor back iron. The fundamental short-coming of the magnetic circuit of a conventional toothed rotor SRM is the limitation imposed on tooth pitch to pole pitch ratio (t/λ) by the unaligned inductance of the machine. If the ratio of (t/λ) was to be increased above 0.5 then there would be an overlap between stator and rotor teeth, even when the rotor was in the unaligned position. This would result in excessive unaligned inductance and reduce the aligned to unaligned inductance ratio, which in turn would reduce the output torque of the machine.

A patent in 2002 by Mecrow [93] and subsequent conference [94] and journal papers [12] by Mecrow et al have introduced the concept of using a segmental rotor in SR machines. The idea stems from the developments seen in synchronous reluctance motor magnetic design and aims at increasing the magnetic utilisation of switched reluctance motors by having more than half of the magnetic iron structure carry machine flux with short flux paths at any time during machine operation. Instead of the conventional toothed structure, the rotor is constructed from a series of discrete segments. Each rotor segment is magnetically isolated from its neighbour (Figure 9). As the stator phase windings are energised the rotor segments tend to move to a minimum reluctance position, modulating the stator slot permeances in the process. This is similar to a toothed structure where the rotor tooth moves to the minimum reluctance position, but differs in the fact that the slot permeances are modulated by rotor rotation, rather than teeth permeances in a conventional toothed structure.

Prior to Mecrow's segmental rotor structure there have been a couple of notable exceptions to the conventional toothed SRM design. Xu and Lipo's work [95], where they have examined the axially laminated rotor structures for variable reluctance motors and

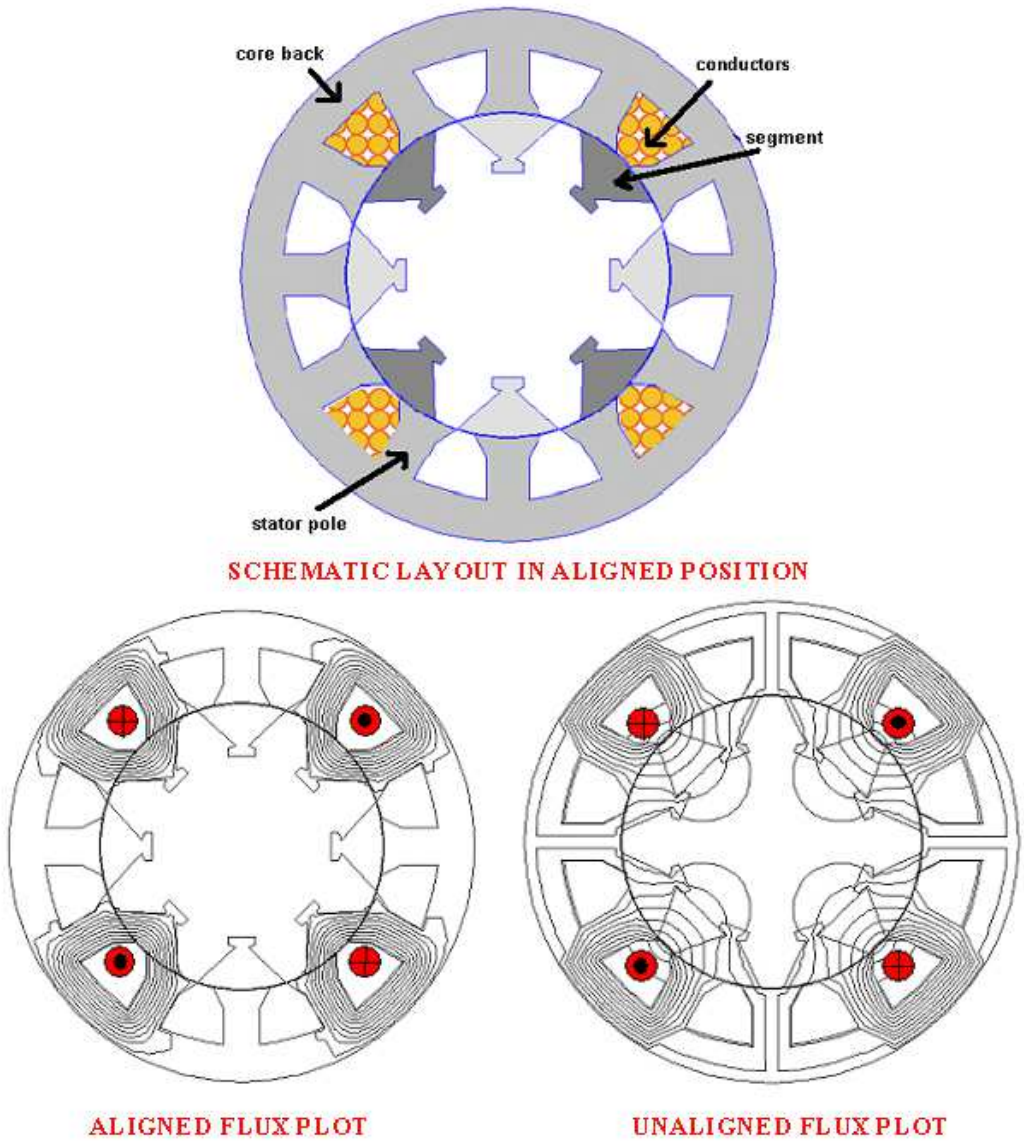

Figure 9 Three-phase segmental rotor prototype machine schematic layout and magnetic flux plots in aligned and unaligned rotor positions

Horst's patent [96], concerning the use of a segmented rotor design for unidirectional operation of two-phase SRMs, should be stated here as examples of designs towards changing the fundamental magnetic structure of conventional toothed SRMs. In [95] Xu and Lipo describe a new type of reluctance motor with concentrated windings and an axially laminated rotor driven by unidirectional currents. A cross-sectional view of their design is given in Figure 10. Although Xu and Lipo have called their machine a synchronous reluctance motor it had similarities with doubly salient switched reluctance machines in that it had concentrated windings and operated in a switched fashion with unipolar currents. Xu and Lipo were able to show that with axially laminated rotor

structure synchronous reluctance motors were able to generate higher torque densities. The machine in Figure 10 has its rotor laminations bent to produce paths of minimum reluctance in the direction of laminations and maximum reluctance in the path normal to the laminations.

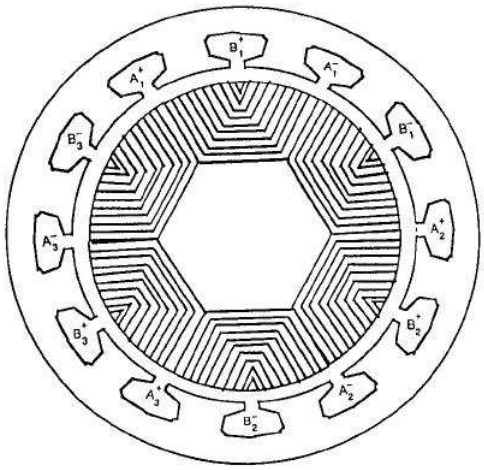

Figure 10 Cross-sectional view of Xu and Lipo's axially laminated single salient variable reluctance motor [95]

A cross-sectional view of Horst's two-phase segmental SRM is shown in Figure 11. Horst was aiming to increase the power density of the machine by having shorter flux paths and using all salient poles simultaneously. As can be seen from Figure 11 the air-gap was distorted to achieve a preferred direction of rotation. It is not clear from the patent, which is limited to two phase machines, whether a prototype was ever built.

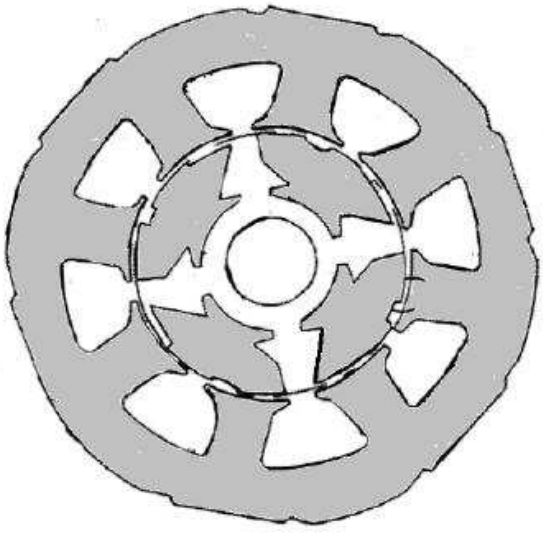

Figure 11 Cross-sectional view of Horst's two-phase segmental rotor SRM [96]

In [12] Mecrow et al demonstrated that SRMs with segmental rotors outperform reluctance machines with axially laminated rotors. In [12] Mecrow states: *"… It can be concluded that axially laminated rotors work well with the distributed MMF pattern of a synchronous reluctance motor, but do not offer the best solution for an SRM. With an SRM the MMF is concentrated, and it is better to have a rotor magnetic circuit which has an equally concentrated reluctance, as displayed by the segmental design*". Mecrow's work produced two successful prototype machines with segmental rotors. The first prototype was called a multi-tooth winding segmental rotor SRM and the second one was called a single-tooth winding segmental rotor SRM. The following two sections will discuss these two prototypes in more detail.

2.3.2.1 Segmented Rotor Switched Reluctance Motors with Fully-Pitched Windings

The first prototype designed and built by Mecrow et al was a 3-phase machine with 12 stator teeth and 8 rotor segments [12]. Initial design work was carried out on a single phase rectilinear machine (Figure 12) to determine the advantages of employing segmental rotors in switched reluctance motors. To reveal the principles of the new design, the geometry is simplified as much as possible. For this reason a single phase, simple rectilinear model with a segmented rotor has been considered initially. This is illustrated in Figure 12 along with the magnetic flux plots for aligned and unaligned positions.

In Figure 12 the magnetic flux flows down one tooth, through a rotor segment and returns via the adjacent stator tooth. All the conductors in each slot only couple with flux driven by their own magneto-motive force, with very little mutual coupling between one slot and another. Torque production can therefore be considered on a per slot basis in which the slot permeance is modulated by the rotor segments [12]. In the aligned position the rotor segments magnetically short the stator slots, producing a high permeance, whilst in the unaligned position the segments are located over the tooth tips so that the unaligned permeance is limited by the slot opening [12].

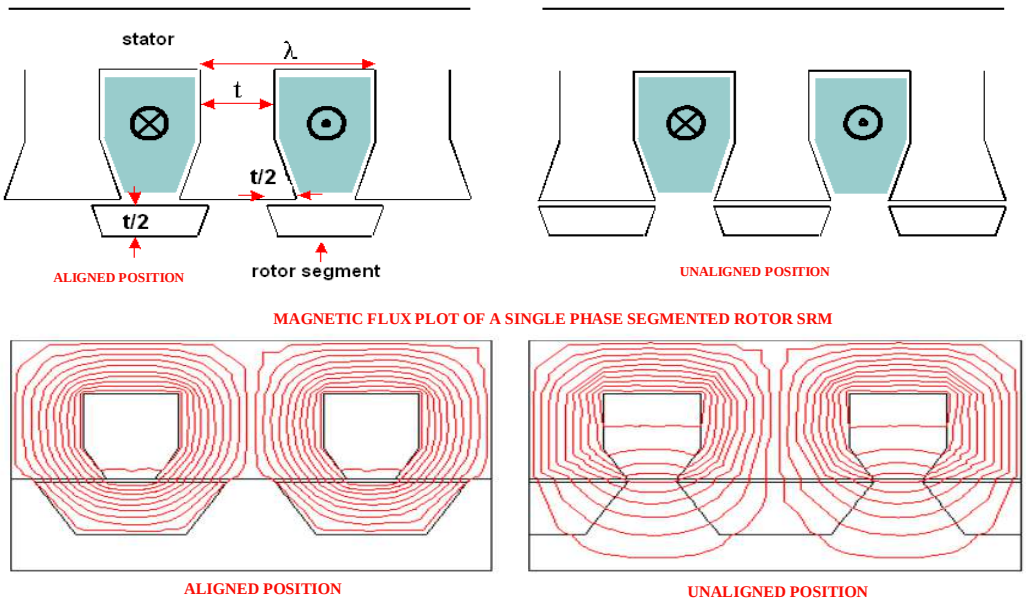

Figure 12 Rectilinear representation of a single phase segmental rotor SRM with 2D flux plots in aligned and unaligned positions [23]

The definition of *tooth width* (t) for this machine is the width in the main body of the tooth, not at the tooth tip as is the case for conventional toothed structures. As in the conventional toothed SRMs "λ" is the pole pitch. Contrary to conventional toothed rotor designs the segmental design has been shown to have the ability to maintain a low unaligned permeance, even when the effective t/λ is greater than 0.7, thereby resulting in a much greater torque capability. Magnetisation characteristics at the maximum permeance (i.e. aligned) position for both conventional toothed rotor SRMs and segmented rotor SRMs correspond closely with each other. The real difference is observed in the minimum permeance (i.e. unaligned) magnetisation characteristics. When t/λ is less than 0.5 (Figure 13) the segmental design exhibits a higher unaligned flux-linkage, mainly due to the semi-closed nature of the slot, which increases the cross-slot flux. However, once t/λ is bigger than 0.5 (Figure 14) the opposite occurs and the segmental design exhibits a much lower unaligned flux-linkage characteristic.

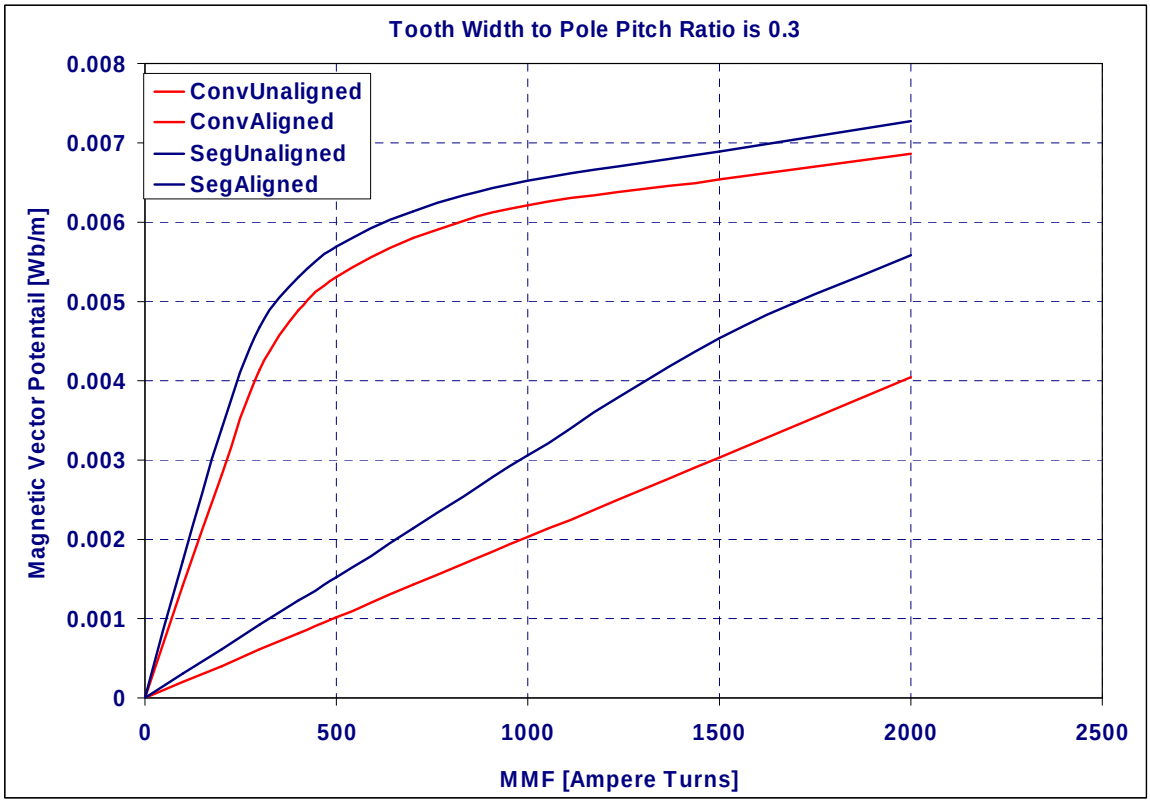

Figure 13 Comparison of aligned and unaligned magnetisation curves of toothed rotor (both red traces) and segmental rotor (both blue traces) when tooth width to pole pitch ratio is 0.3

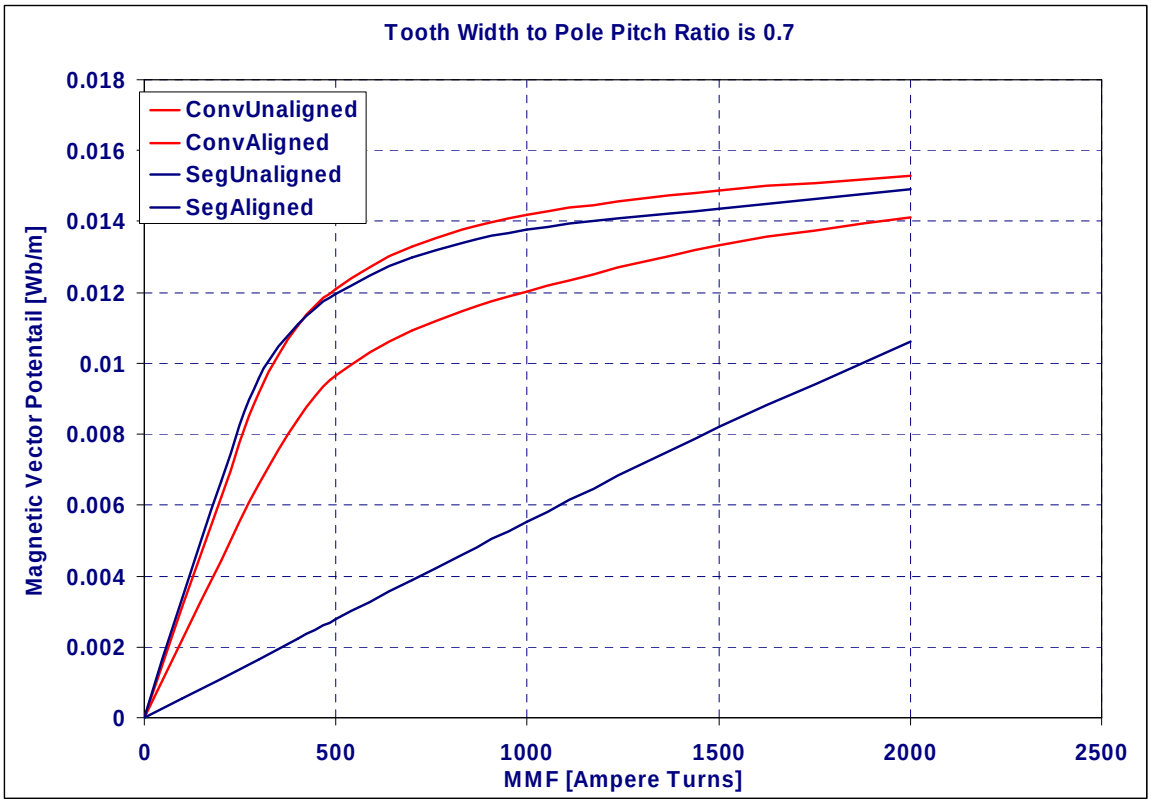

Figure 14 Comparison of aligned and unaligned magnetisation curves of toothed rotor (both red traces) and segmental rotor (both blue traces) when tooth width to pole pitch ratio is 0.7

The single phase rectilinear design comparison is useful to show that with a segmental rotor structure it is possible to substantially increase the torque capability of switched reluctance machines. The advantage of the segmental design becomes more apparent with increased tooth width to pole pitch ratio.

Mecrow et al demonstrated that although having a machine design with $t/\lambda > 0.5$ would be impractical (as this would leave insufficient room for the windings) in a rectilinear single phase machine example, this would not apply to a multi-phase machine. Figure 9 shows the three-phase 12-8 segmental rotor SRM in aligned and unaligned positions. Mecrow et al showed that the tooth width of the single phase design could be halved with the multi-phase design, which would allow enough room for phase windings whilst retaining a high value of tooth width to pole pitch ratio. This is due to the fact that in a three-phase design, with one phase excited, each stator tooth carries only the flux of one rotor segment [12]. Whereas in a single phase design, with one phase excited, each stator tooth has to carry the flux of two rotor segments (see Figure 12). The multi-tooth winding, three-phase design had 12 stator teeth and 8 rotor segments.

A tooth width to pole pitch ratio of 0.67 was achieved. This meant that the segmental rotor design could carry much more flux than the conventional toothed rotor design with similar machine dimensions having tooth width to pole pitch ratio of 0.33. Although the windings of the three-phase segmental design in [12] were fully-pitched, torque was produced as a result of changing self-inductance, not as a result of mutual inductance experienced with toothed rotor SRMs with fully-pitched windings [12]. Compared to a conventional toothed rotor SRMs with short-pitched windings, segmental rotor SRMs with fully-pitched windings have considerably longer end-windings, resulting in additional copper mass and winding loss. The importance of this additional loss depends on the machine axial length and pole number [12]. For a short stack length machine the ratio of end-winding length to overall winding length will be substantial.

Static torque results and comparison of the mean torque capability at thermal limit (i.e mean torque vs. winding copper loss) between fully-pitched segmental rotor, fully-pitched toothed rotor and short-pitched toothed rotor designs are given in [12] and are explained in more detail in [97].

2.3.2.2 Segmented Rotor Switched Reluctance Motors with Short-Pitched Windings

As described in the previous section, for SRMs with segmental rotors the flux-linkage per phase is doubled and hence torque as a function of electric loading is doubled (flux of a single phase is carried by two-thirds of stator teeth rather than one-third used in a conventional toothed rotor SRM). However, as the coils spanned as many stator teeth as the number of phases the end-winding length was increased. For a prototype machine this additional end-winding length resulted in 20% reduction in electric loading at thermal limit [12, 23]. Overall a net increase of 40% in the measured torque per unit volume at thermal limit was achieved compared to that achieved by conventional toothed rotor SRMs within a given frame size. However, the torque per unit winding mass of the multitooth winding prototype was raised only modestly compared to conventional toothed rotor SRM.

To develop a three-phase design which is suitable for short stack length machines it is essential that the windings span a single tooth to keep the end-windings short, whilst maintaining the condition that only the conductors of a single-phase occupy any one slot.

The idea is realised by Mecrow et al [23]. The design is depicted in its rectilinear form in Figure 15, along with the rectilinear form of the fully pitched design. The new short-pitched segmented rotor SRM (or single-tooth segmented rotor SRM) is achieved by removing the shaded regions from the fully pitched design (see Figure 15) as these regions carried no flux and their removal would not significantly influence the level of flux-linkage. In the short-pitched segmented design the coil spans a single rotor segment and have a shorter end-winding, wrapped around a single-tooth [23]. The unwound teeth of the short-pitched design are the same width as the width of the teeth of the fully pitched design, whilst the wound teeth are double this width. The reason is that the wound teeth now carry the flux of two adjacent slots.

Two-dimensional flux plots of the prototype single tooth winding segmental rotor SRM in the aligned and unaligned positions are given in Figure 16.

Figure 17 shows two-dimensional finite element predictions of magnetization curves for both segmental rotor designs and an equivalent conventional toothed rotor design. Once again it is quite obvious from this figure that with a conventional toothed rotor design, only half of the flux-linkage of segmental designs can be achieved. Inspection of Figure 17 also reveals that the flux-linkage characteristics of multitooth and single tooth winding

segmental rotor designs are virtually identical. In the aligned position the difference is about 3%, whereas in the unaligned position the difference between the magnetisation curves of single tooth and multitooth segmental designs is as low as 1%. This suggests that the force produced by one phase is identical with a multitooth and a single tooth segmental design. However, the force exerted per unit area of airgap is reduced by 20% compared to a multitooth winding design when the MMF per phase is fixed. This is due to the fact that the single tooth winding design requires more space for the wound teeth, which require being twice as wide. A set of design rules for single tooth winding segmental design is given in [23]. The assembly method for the single tooth designs is similar to that employed for multitooth designs. For both multitooth and single tooth winding designs static torque curves are somewhat different to those usually experienced with conventional toothed rotor SRMs.

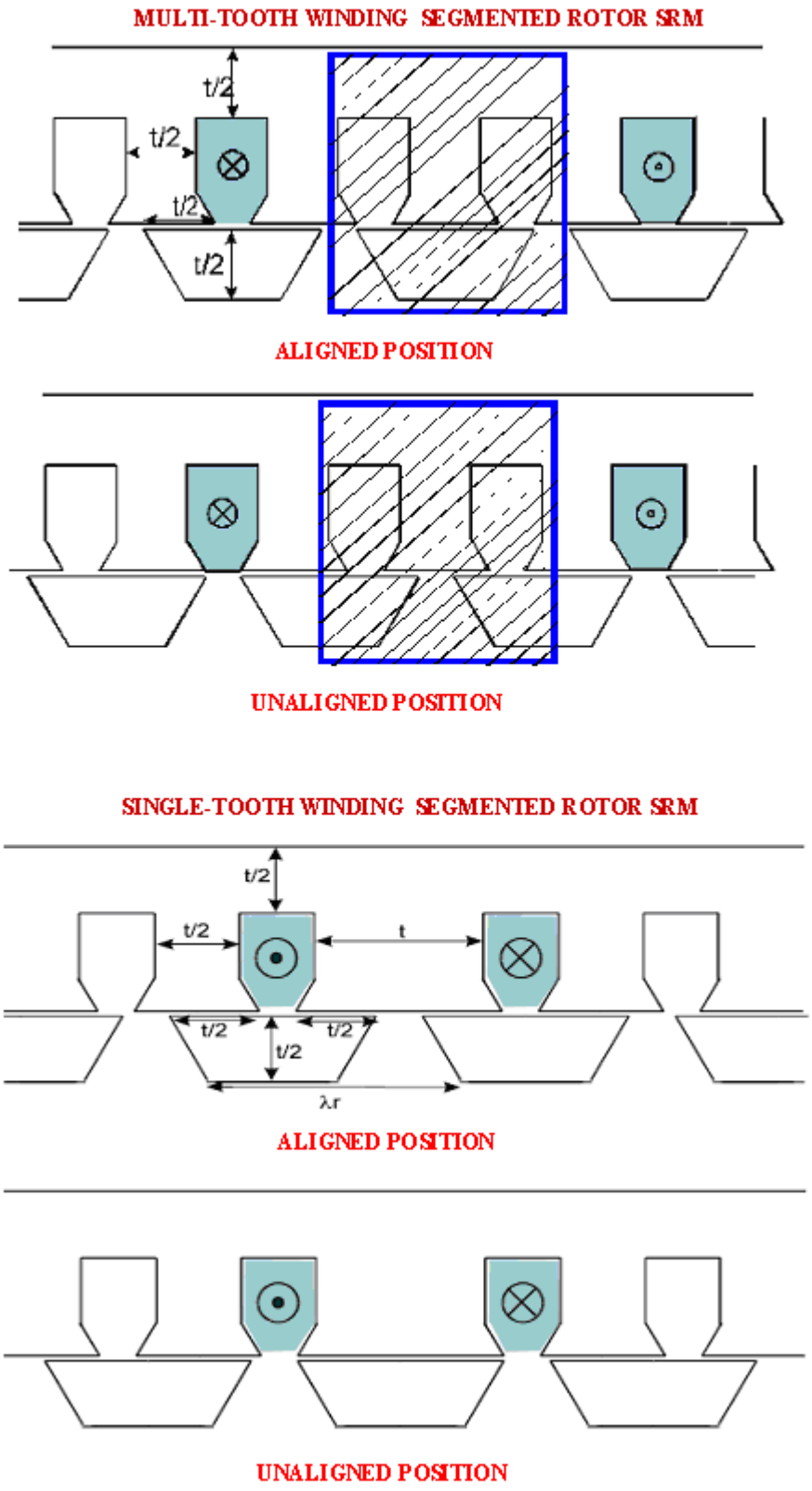

Figure 15 Rectilinear representation of three-phase segmented rotor SRMs [23]

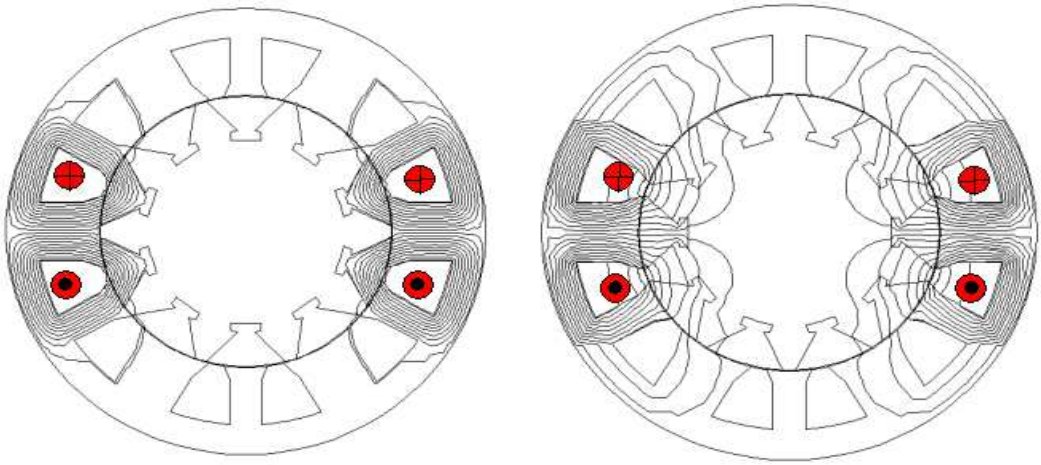

ALIGNED FLUX PLOT UNALIGNED FLUX PLOT

Figure 16 Three-phase 12/10 segmental rotor SRM with single-tooth windings - shown in aligned position

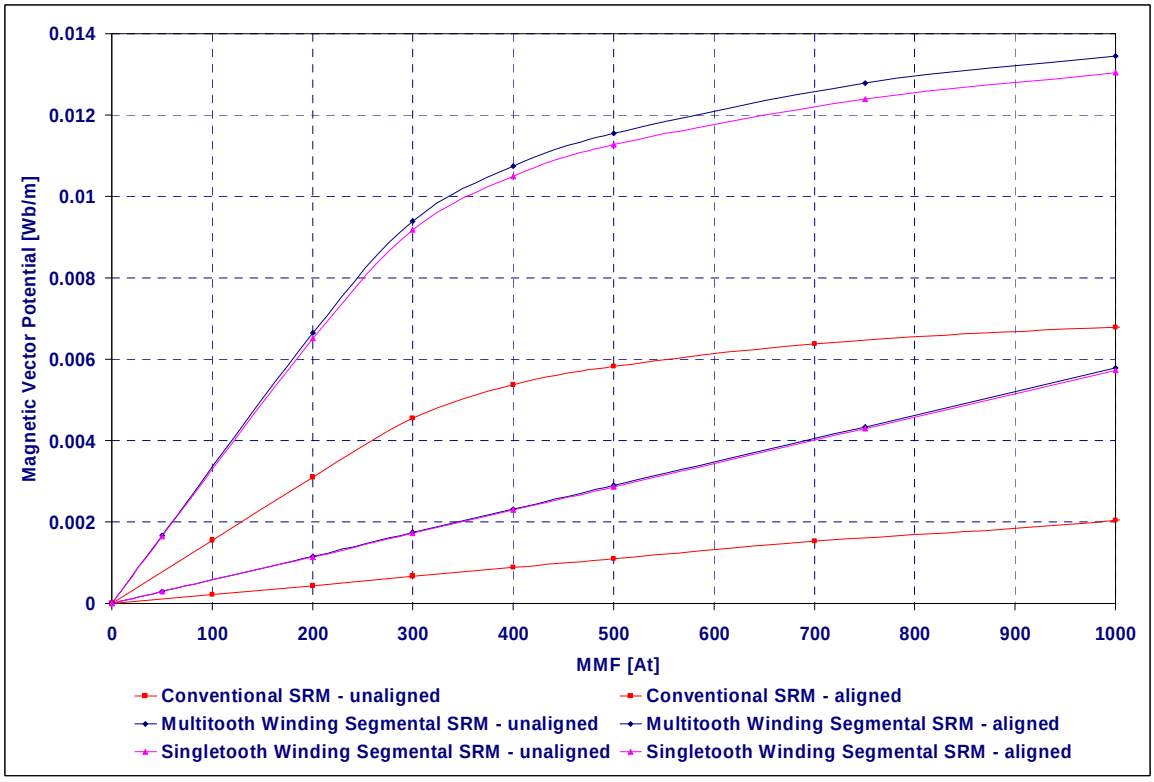

Figure 17 Magnetic vector potential of a phase coil as a function of coil MMF for both segmental designs and a conventional SRM

This is explained with the aid of Figure 18. At high excitation levels the form of the static torque curves are similar to those of a conventional toothed rotor machine when the machine is saturated. However, the shape differs significantly when the machine is in the unsaturated region (i.e. low excitation levels). This difference is due to the permeance variation experienced with the segmental rotor structure as the rotor moves from the unaligned to the aligned position. With a segmental design the area of overlap between stator teeth and rotor segments increases on one side of the magnetic circuit but it decreases on the other. This results in a static torque which rises to reach a peak at approximately 12.0 degrees from the aligned position. Running waveforms of a single tooth winding segmental rotor have been presented in [23], where the machine phases were energised with an asymmetric half-bridge converter.

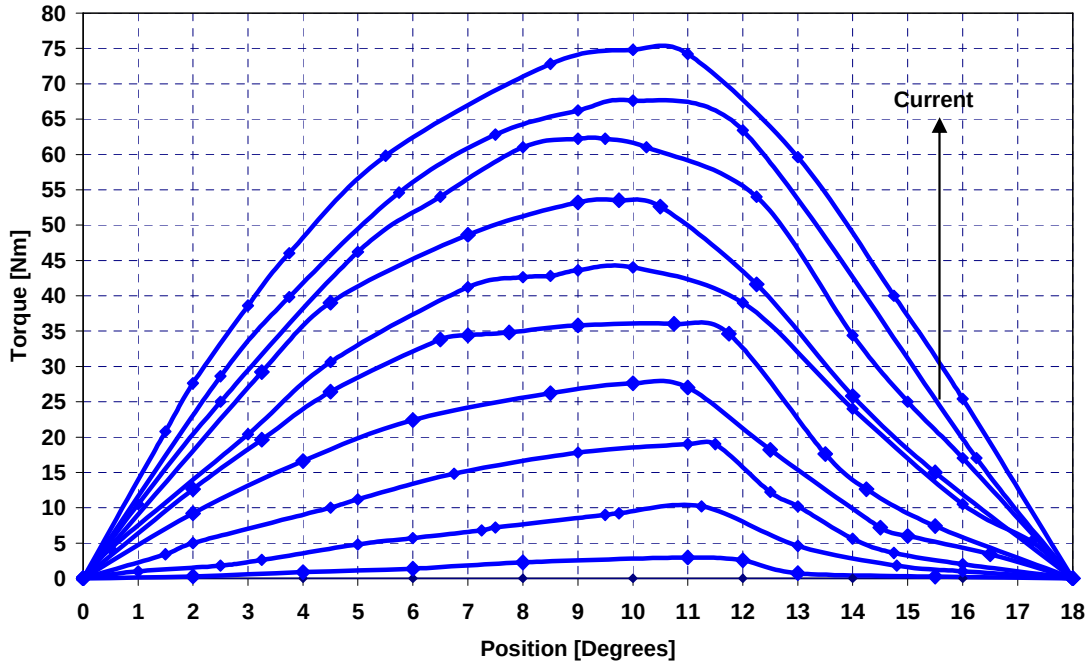

Figure 18 Measured static torque characteristics of 12/10 single tooth design with a single phase excited. Each curve is for a constant current, rising in 2.0A steps to 20.0A [97]

In [23] the effect of orientation of magnetisation is briefly explained. Apparent from the magnetic flux plots of Figure 16 there is minimal coupling between individual phase coils of a phase. Therefore, it can be said that the magnetic characteristics of any one phase are independent of the polarity of the two coils. The orientation of magnetisation can be any of the forms depicted in Figure 19 without having a measurable effect on phase

parameters. Mutual coupling between the phases of the single-tooth winding segmental rotor SRM has been shown to be minimal [23].

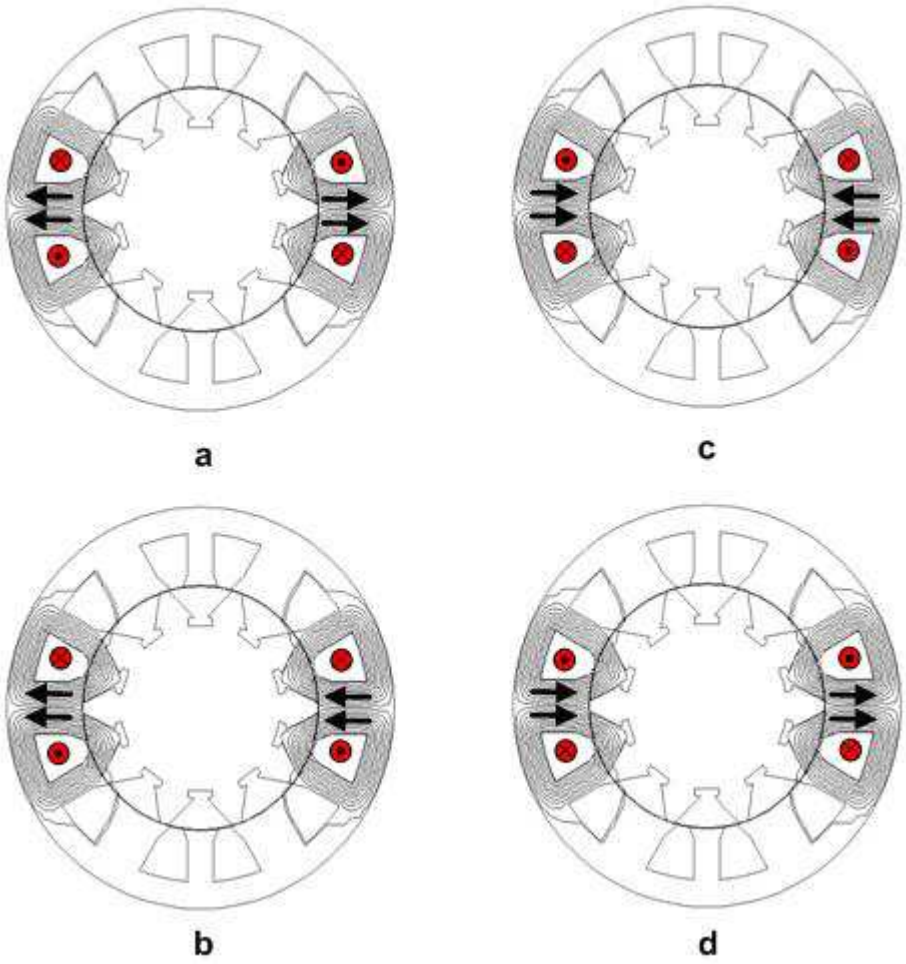

Figure 19 Possible orientation of magnetisation for single tooth winding segmental rotor SRM (all shown in aligned position)

Direction of energisation for each phase coil becomes an important factor when two phases are excited simultaneously, which is most likely to occur when the machine is operating under voltage control and a positive voltage is applied for more than one third of a cycle (for a three-phase machine). There are two possible scenarios:

- The unwound teeth of the machine are dimensioned to take only the flux of a single phase. If the two phases are excited simultaneously and the direction of energisation in adjacent phase coils both act in the same direction, i.e. both inwards or both outwards, the unwound teeth will have to take the sum of the fluxes from two phases.

This will result in saturation of the unwound teeth (cross-saturation) resulting in reduced torque.

- If the direction of energisation in adjacent phase coils acts in opposite directions, i.e. inwards, outwards, inwards, outwards, etc. the unwound teeth will carry the difference between the fluxes of adjacent coils. Therefore simultaneous excitation of two phases will actually reduce the saturation conditions. However, this time the unwound teeth will experience bi-directional flux.

With both of the above scenarios the direction of the stator coil MMFs will influence the iron loss in the machine.

2.3.2.3 Other Segmented Rotor Switched Reluctance Motor Designs

After the introduction of new segmental rotor SRMs by Mecrow, several researchers used the idea of segmental rotors in their designs. In [98] Oyama et al present a 3-phase design with 6 stator teeth and 4 rotor segments with fully-pitched phase windings. This work is heavily based on the principles outlined by Mecrow et al. The only difference appears to be the way the segments are held together and the shape of the segments. An aluminium block is used to hold the segments in place but there is no discussion of mechanical strength. A cross-sectional view of Oyama et al's machine is given in Figure 20.

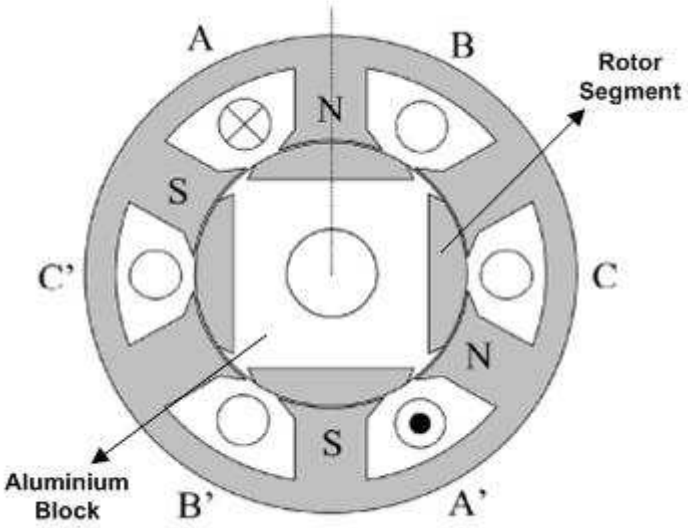

Figure 20 Cross-sectional view of Oyama et al's segmental rotor SRM with segments embedded in an aluminium block [98]

Another piece of interesting work utilising segmental rotors in SRMs is that of Vattikuti et al [99]. A cross-sectional view of Vattikuti's segmental rotor SRM is shown in Figure 21. The machine illustrated in Figure 21 has circular stator slots with fully-pitched windings. In this design the flux is forced to flow in a circular path. Due to long end-windings of the fully-pitched winding distribution, the design is unlikely to be suitable for designs with short stack lengths. Furthermore, all the analysis was based on FE analysis and none of this theoretical work was proven with measurements from a prototype.

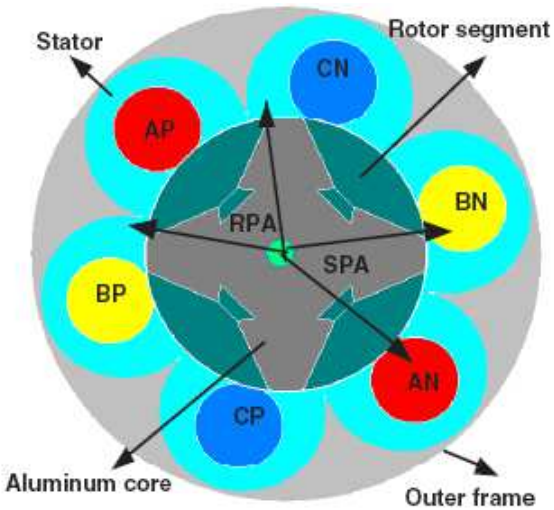

Figure 21 Segmental rotor SRM with circular stator teeth – work of Vattikuti et al [99]

In [8] Hall et al employ a segmented rotor structure for an embedded aero-engine starter / generator application. The design was driven by the requirements / limitations imposed by the application, such as the available space, operating speed, operating temperature and power. An outer rotating segmental rotor SRM with 18 stator teeth and 15 rotor segments was the chosen machine topology which was able to satisfy fault tolerance, power, operating temperature and speed requirements of the application. A cross-sectional view of the design is given in Figure 22.

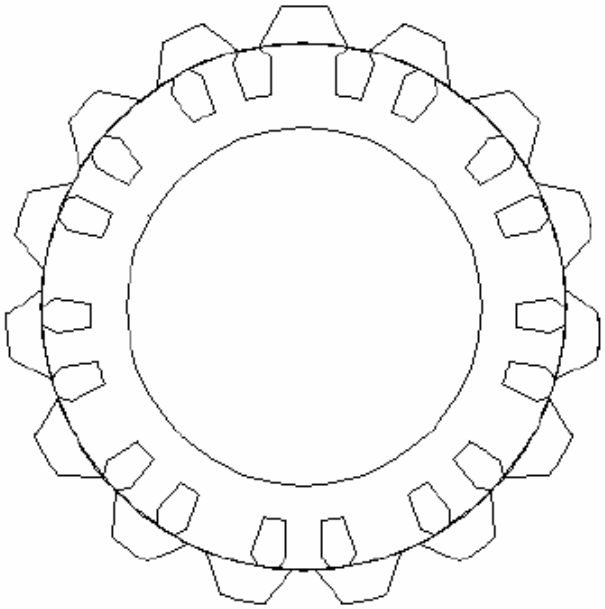

Figure 22 Outer rotating segmental rotor SRM with 18 stator teeth and 15 rotor segments for use in aero-engine embedded starte / generator application - R.Hall et al [8]

2.4 SUMMARY

Fundamentals of the magnetic structure of switched reluctance motors have been effectively unchanged for decades. Almost without exception both the stator and the rotor of an SRM are of the toothed form (Figure 6). Design principles of these conventional toothed rotor structures are well established in literature. The effects of variations in various design parameters of these conventional toothed rotor machines on machine performance (such as torque output, torque ripple, acoustic noise) are all well documented. Some of the important design work on the conventional toothed rotor structure is summarised in this chapter.

Mecrow et al introduced the concept of segmental rotors for use in switched reluctance motors by applying some of the developments of synchronous reluctance motor magnetic design (with modification). This segmental rotor design better utilises the magnetic circuit and increases the torque output of the machine. The multitooth winding version has the drawback of increased end-winding length. As a result, only a small gain is achieved in torque per copper volume and loss compared to the conventional toothed rotor SRMs of the same frame size. Consequently, for a short stack length application a multitooth winding segmental rotor SRM would not be the preferred option. Segmental rotor SRMs with single tooth windings are aimed to overcome the long end-winding penalty of the multitooth winding option by having every other tooth wound with concentrated windings. Consequently, a single tooth winding segmental design has much shorter end-windings compared to a multitooth winding segmental design. Mecrow et al showed that a single tooth winding segmental design could be designed with 29% less copper compared to a multitooth winding segmental design of the same frame size [23]. Moreover, single tooth winding solutions would be more suitable for fault tolerant applications as the windings are magnetically, thermally and mechanically isolated from each other to a greater degree than they are in a conventional toothed rotor and multitooth winding segmental rotor SRMs. Recently a few designs using the segmental rotor principle have been reported, aiming to ease the manufacturing process as well as increasing the performance of the machine compared to conventional toothed rotor options.

CHAPTER 3

3– SR Drive Topologies

3.1 INTRODUCTION

The performance and the cost of any motor drive system are highly affected by the performance of the selected converter topology. Probably more so than the other drive systems, the relatively low cost of manufacturing the core SR motor for an SR drive system is counter-balanced by the potentially high power electronics costs. One often comes across the phrase “matching the converter to the particular application” for an SR drive. Indeed, the type of converter required for a particular SR motor drive is intimately related to motor construction and number of phases. In other words, a designer is faced with a decision to find the most appropriate combination of motor and power electronic converter for a particular application. For this reason no single combination of motor and power electronic converter has become the standard for SR drives.

For an SR machine the direction of the generated torque does not depend on the signs or the values of the flux-linkage and current. As a matter of fact the torque generated by an SR motor only depends on the sign of the rate of change of phase inductance with rotor position. This feature of SR machines along with phase independence has been extensively used to the advantage of SR drives and resulted in many different converter topologies over the years. As there are many topologies to choose from for an SR drive, there is always a trade-off between gaining some of the advantages and losing some with each topology. Whatever the chosen converter topology is, the power electronic converter for an SR drive is required to build the flux in a phase winding from zero at each stroke by providing a positive voltage loop; it must then be able to reduce the applied voltage if

the desired current level is reached. Finally it must be able to provide a negative voltage loop at turn-off to quickly return the phase current to zero before the sign of rate of change of inductance changes. For an SR drive, at the end of each stroke the power electronic converter must provide a path to recover the stored energy in the magnetic field. SR converters differ in terms of how they achieve this. Some of the converters dissipate the energy, whereas others use magnetic or capacitive recovery techniques. It is also beneficial to have a converter topology which is capable of generating a zero-voltage loop (i.e. freewheeling period) before phase commutation instances. In freewheeling mode the phase current is circulated through the power electronic devices and phase windings instead of being returned back to the supply with a negative voltage loop. This mode of operation has the potential to reduce the current ripple. It also reduces the circulating energy from the dc bus and the machine phases, increases efficiency and reduces frequent energy reversals in the machine phases. Energy reversals are believed to be a significant acoustic noise source. Elimination of these energy reversals during the phase energisation cycle by introducing a freewheeling period just before the commutation point potentially eliminates noise associated with them altogether [101].

In Chapter 2, it was mentioned that there were two distinct ways to tackle the torque ripple problem in SR drives and the methods relating to the electromagnetic design of the machine were summarised. In this chapter, the torque ripple minimisation techniques relating to the control strategy employed in an SR drive system will be presented. Consequently, section 2 of this chapter summarises the work focusing on current profiling techniques.

Section 3 of this chapter summarises:

- The SR drives based on the number of machine phases
- The drive control methods e.g. high speed PWM control, advanced flux-linkage contol and sensorless control, etc.
- Some of the most common converter topologies used to drive SR machines, e.g. asymmetric half-bridge converter, C-dump converter, etc.

Finally in section 4 a summary of the chapter is presented.

3.2 TORQUE RIPPLE MINIMISATION THROUGH DRIVE CONTROL

As torque is a nonlinear function of phase current and rotor position, the flat topped phase current is believed to be far from ideal in terms of generating ripple free output torque in an SR drive. Furthermore, due to the non-linear relationship between rotor position, torque and current, no reference frame transformation can be applied to SR machine control. This necessitates instantaneous torque control in order to reduce torque ripple if electronic control is used [102]. Several notable papers have been published by researchers investigating ways of defining and generating ideal phase current waveforms which result in minimal output torque ripple. Lack of space precludes a detailed description of all methods adopted, but interested readers are referred to references [103-127].

3.2.1 Measuring Torque Ripple

Torque ripple can be measured using in-line torque transducers, strain gauge bridges, observer algorithms or accelerometers measuring vibrations of the drive housing. Methods of measuring torque ripple are given in [24]. In [128] off-line static torque measurements are used to estimate the running torque waveforms from measured currents and rotor position. Absolute accuracy of the method in [128] is questionable, as it depends on the bandwidth of the current sensor, A2D sampling rate, encoder resolution, accuracy of the initial static torque measurements, accuracy of the encoder and the accuracy of current transducers. However, it is believed to be a simple and effective way of measuring the dynamic torque ripple of the drive system for comparative analysis. In [129] Corda et al outline how to determine machine torque during operation. Torque ripple measurement can be done by storing static torque characteristics and measuring phase current and rotor position to look-up an instantaneous torque value.

An interesting solution to determination of torque ripple in mass-produced switched reluctance drives is presented in [130]. In [130] Koenig and Pekarek present a specially designed piezoelectric washer that is attached to an anchor bolt (used to mount the machine to the mechanical structure) and senses harmonics resulting from machine

torsional vibrations (i.e. torque ripple). The method seems to be more suitable for large machines, where the relative cost of the sensor is low.

3.3 DRIVE TOPOLOGIES

For the majority of SR machines the phases are said to be magnetically de-coupled, permitting independent control of phase windings. At very high speeds, this is especially beneficial as considerable overlapping between adjacent phase currents is present. However, lack of mutual coupling means that the stored magnetic field energy during the energisation of the phase windings needs to be provided with a path during commutation of a phase. This stored energy can be handled in a number of different ways [131-134].

As torque is independent of the direction of the current for an SR machine, the flux-linkage and the current, as well as the topology of the inverter circuit, may be unipolar. This mode of operation is preferred because it permits a simpler form of controller. Ability to operate with unipolar currents and the need to have a path for the stored magnetic energy at the end of each stroke resulted in considerable amount of unique converter topologies for an SR drive system.

It is highly desirable to have a simple form of torque control in electric drives. In DC drives this is achieved naturally by simply controlling the product of flux and current in the machine. The simplicity of a DC drive torque control comes from the fact that the flux and current are independently controllable. In most AC machines the principles of DC machine torque control is achieved with the use of field-oriented control, which is based on some form of mathematical transformation. Generally speaking in classical DC and AC machines, control of the flux is maintained constant while the current is varied in response to the torque demand. The SRM is a highly non-linear machine in its nature with torque a nonlinear function of not only the phase current but also of the rotor position. Moreover, for a machine with mutually coupled phases - such as a fully-pitched winding machine - torque is dependant on the rotor position and current in all of the machine phase windings. Therefore there is no simple torque constant for an SRM.

3.3.1 Review of Drives

This section is a brief summary of SR drives based on the machine number of phases. Single phase SR drives are the simplest, with fewest connections between the machine and electronics. However, they cannot produce positive torque at all angular positions. Starting problems can be overcome by the introduction of a permanent magnet in the stator [135] or by using a graded air-gap (i.e. graded reluctance) to extend the angle over which positive torque is available [65].

With two phase drives problems of starting are reduced, but still pose challenges. Methods used include stepping the air-gap, or providing asymmetry in the rotor poles [136]. This machine may be of interest where the cost of winding connections is important, but again high torque ripple may be detrimental, with the torque falling close to zero at some rotor positions. Compared to a three-phase drive, a two-phase drive requires two thirds the number of power devices and the switching frequency is reduced for a given rotor speed, lowering the losses in the two phase drive [82]. If cost is the primary concern and the performance is not measured in terms of torque ripple and starting ability, single and two phase drives can be of interest.

Three and four phase drives offer the simplest solution to starting without resorting to high numbers of phases. Significant torque can be developed at all rotor positions, but torque ripple is still much higher than in a conventional 3 phase ac machine.

Compared to three and four phase drives, the torque ripple is greatly reduced with a 6 phase drive. The output torque is made up of six pulses per electrical cycle, as in a 3-phase PM motor drive. However, as the number of phases is higher, the number of power devices and the number of connections between the inverter and the motor are also higher. An example of the torque ripple reduction with a 6-phase drive is given in Figure 23. The top trace shows the torque output from a 3-phase 12-10 segmented rotor SRM whereas the bottom trace shows the total output torque from a 6-phase 12-10 segmented rotor SRM. In both cases perfect current control is assumed. Both machines are running @ 200rpm under current control. Control angles are adjusted for both drives in order to achieve similar average output torque values.

It is concluded that an SRM will only approach the low torque ripple of a conventional PM when there are six pulses of torque per electrical cycle. This requires a 6 phase SRM

but, with conventional converter topologies, this will not be cost effective: there will be 12 controlled power switches and 12 cables connecting the inverter with the machine, compared to 6 switches and three cables in a conventional ac machine. The challenge posed is "Can a 6 phase SRM be run with only 6 power switches and 3 cables between motor and inverter?"

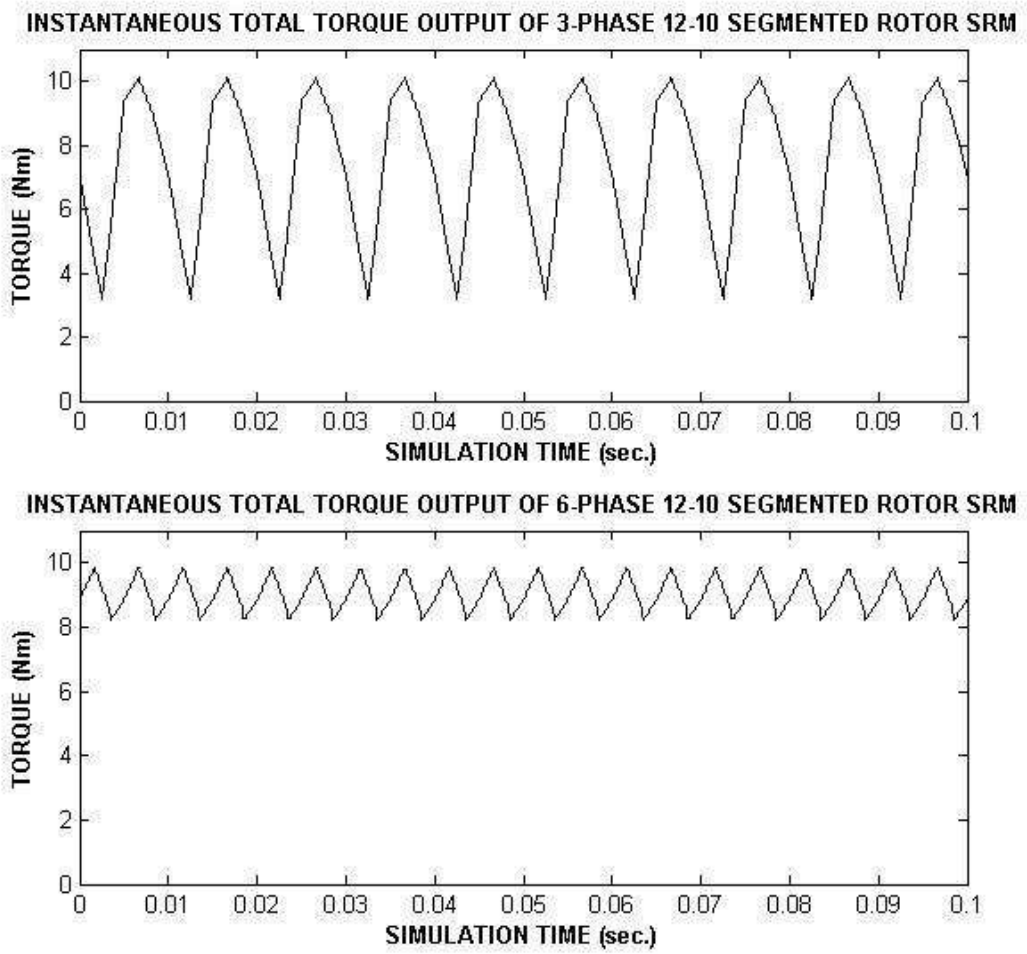

Figure 23 Simulation of 3-phase and 6-phase 12-10 segmented rotor SRMs under perfect current control

3.3.2 Review of Control Methods

In general, torque is directly related to the currents flowing in phase windings. Therefore in most electric drives phase current is the controlled variable and it is often designed to track a pre-defined reference value to achieve the required output torque. However the

overall shape of the current waveform is not only dependant on the average torque required but also on the torque ripple requirements of the drive system.

The next step is to decide on the control method. With the right choice, the drive performance can be significantly improved. With good controller design:

- Motor performance can be improved.
- Overall efficiency of the drive system can be increased.
- A quieter drive operation can be achieved.
- The drive system can operate more reliably.
- The size and the number of components required in the system can be reduced.

Some of the most common control methods used for SR machines are summarised below.

3.3.2.1 Hysteresis Current Control

At low speeds the phase current has to be constrained to protect the electronics because of the high available Volt-seconds. This is typically achieved by hysteresis current chopping where the power transistors are switched off and on according to whether the current is greater or less than a reference current. As the upper and lower current thresholds are control parameters, this chopping current strategy allows a very precise current control. However, as the switching frequency is not fixed, acoustic and electromagnetic noise is difficult to filter [49].

3.3.2.2 PWM Control

Current control can also be achieved by an advanced PID controller combined with a PWM voltage control strategy. Current chopping can be achieved either by varying the applied voltage from negative to positive or from negative to zero and then to positive. The former method is called hard-chopping and the latter one is called soft chopping [24]. In terms of current control, SR machines differ from commonly used ac and dc machines. As the effective phase inductance varies significantly with the rotor position the controller will only be tuned optimally at one point and for all other points the system response will be over or under damped, making stable operation difficult [89, 137].

Above base speed the phase current potentially cannot reach the desired level and the phase needs to be energised before the phase inductance starts rising (i.e. advancing of commutation point). Eventually a speed is reached where the phase is energised for the entire commutation interval. This form of operation is often called “Single Pulse” mode as there is no phase voltage chopping, but a continuous energisation of the phase windings for the entire conduction period.

3.3.2.3 Current Profiling

Due to the highly non-linear characteristics of the SR machine, a current waveform tracking a constant current reference will result in high torque ripple. By profiling the current a constant shaft torque with minimal torque ripple can be achieved. Since torque cannot be controlled directly, due to the lack of adequate torque sensors, this can only be accomplished using a priori information about the torque-current-angle characteristics of the motor. Additionally these characteristics must be known fairly accurately in order to achieve satisfactory results. The torque control strategy is based on following a contour for each of the phases of the SR motor such that the sum of torque produced by each phase is constant and equals the desired torque.

The principle of current profiling can be extended and used with a flux-linkage controller. Barrass [110] successfully applied the use of flux-based control to 3-phase short-pitched and fully-pitched SR machines. In this method 2D look-up tables are used to estimate machine flux-linkage from current and rotor position in real time. The flux-linkage controller is de-coupled from the dc-link voltage variations and phase winding temperature variations. Flux-linkage controllers are said to have a fast and well-damped response [110] and are well suited for constant torque operation.

3.3.3 Review of Converter Topologies

Although SRMs are conventionally easy to manufacture and relatively cheap to make, the largest cost of an SR drive system is its power electronic converter. Therefore, performance of the converter plays an important role in cost and performance of the overall drive system.

The cost and size of power electronic drives vary significantly for an SRM. The selection of a converter, as mentioned earlier, depends upon the application. The elements of cost associated with the power electronics side of an SR drive system can be summarised as follows:

- Number and rating of power semiconductor switches and diodes.
- Cooling system related to the power electronic losses. The higher the losses the more costly the cooling system will be.
- The amount of passive components needed i.e. dc-link capacitors, filter inductors. This can be a significant factor for applications with strong EMI-restrictions.
- Gate drive circuits. If the number of floating point gate-drive circuits is high, the cost of the drive will be higher than a converter with fewer floating point and more grounded switches.
- Control logic (including sensors).

Following the above statements it is important to match the converter to the particular application for an SR drive application. A large number of converter topologies and their advanced versions are available for an SR drive. This is due to:

- The phase independence.
- The unipolar current requirement.
- Different methods of dealing with the stored magnetic field energy at the end of each stroke of the machine.

Of particular interest are the simplicity, flexibility and the cost of the converter for a given application. A few of the most common topologies are reviewed below.

3.3.3.1 Asymmetric Half-Bridge Converter

Converters with a single switch per phase can be used but by far the most common converter topology for controlling SRMs is the asymmetric half-bridge converter. A simple diagram of an asymmetric half-bridge converter is given in Figure 24. In an asymmetric half-bridge converter, the power devices are connected to either side of the dc

link rail and in series with a phase winding (e.g. T1 and T2 in Figure 24) and two diodes (e.g. D1 and D2 in Figure 24) form the return path for the phase current. The diodes cannot be anti-parallel (i.e. already packaged within the power switches). This adds to the cost of the drive. Requirement of separate freewheeling diodes is not so much of an issue at high power levels, as the inverter switches do not usually come with anti-parallel diodes as a single package [142].

On the plus side an asymmetric half-bridge configuration is inherently immune to shoot-though faults, as there is always a phase winding in series with power devices

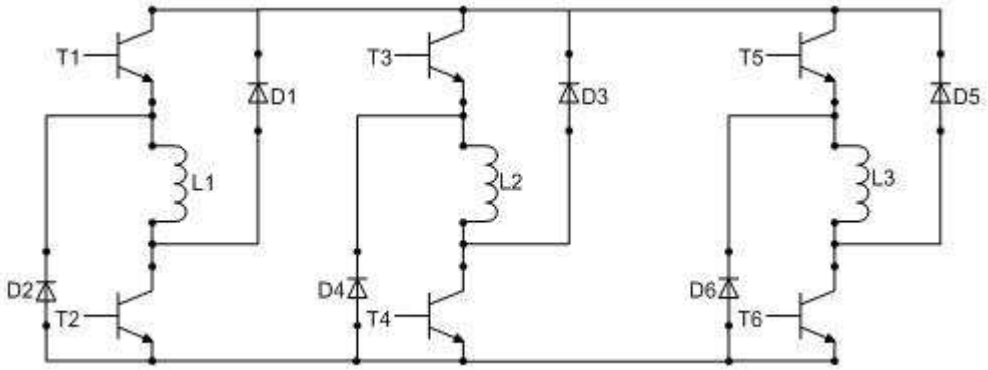

Figure 24 Asymmetric half-bridge converter driving a three-phase machine

Asymmetric half-bridge converters provide maximum control flexibility and are able to apply all of the available dc-link voltage (minus the power electronic device voltage drops) across the phase windings [49]. This is a significant advantage in controlling the current in the phase windings. With an asymmetric half-bridge converter each phase can be controlled independently and power devices are rated only at the dc link voltage.

On the negative side, the total component count is high as each phase requires two switches and two diodes and two connections between inverter and motor. This increases the size and the cost of the system.

The asymmetric half-bridge converter is able to supply all three operating modes. These are:

1. *Positive Voltage Loop*: where a positive voltage is applied across the phase windings to increase the current. Both top and bottom devices are turned on and conducting current in this loop.

2. *Zero Voltage Loop*: where the phase current is freewheeled through a diode and a power device rather than returned back to the supply. This mode of operation is advantageous as it is believed to generate less torque ripple, and hence less machine noise. It also minimises the ripple content of the phase current and potentially reduces the dc-link capacitor RMS ripple current rating, making it smaller.

3. *Negative Voltage Loop*: where at the end of a phase energisation cycle a negative supply voltage is applied across the phase winding to reduce the phase current down to zero before the rate of change of inductance reverses direction. Both power switches are turned off and negative supply voltage appears across phase windings (anti-parallel diodes are conducting the current) quickly reducing the current down to zero.

In terms of cost, size and the number of connections between the motor and the converter, as there are two switches per phase the asymmetric half-bridge circuit is more suitable for machines with fewer phase windings. Moreover, as there are always two series connected devices conducting current; the asymmetric half-bridge topology is unsuitable for low voltage applications.

3.3.3.2 Shared Switch Converter (Miller Circuit)

A schematic of this converter topology is given in Figure 25. With this circuit converter switches and diodes are shared between windings of more than one phase, reducing the number of switches used per phase. First reported by Miller [144] with this converter topology, one power device is common to all phases of the machine [Switch Q in Figure 25]. It is this device which performs the chopping of the phase current. The main drawback of this topology is that phases cannot be controlled independently. Once a motor phase is turned off the on-coming phase becomes the priority. As the phase current starts falling in the off-going phase and rising in the on-going phase, the current controller will try controlling the current in the newly energised phase. When the current controller starts chopping the on-coming phase this will affect the reverse voltage available to completely de-flux the off-going phase. This inevitably slows down the de-energisation

process and results in a tail current in the off-going phase. This becomes more of a problem at higher speeds, where the amount of time available to energise and de-energise a phase is significantly reduced. The tail current will last into the region where the phase inductance reduces. This will generate negative torque and reduce the output power and the efficiency of the drive system.

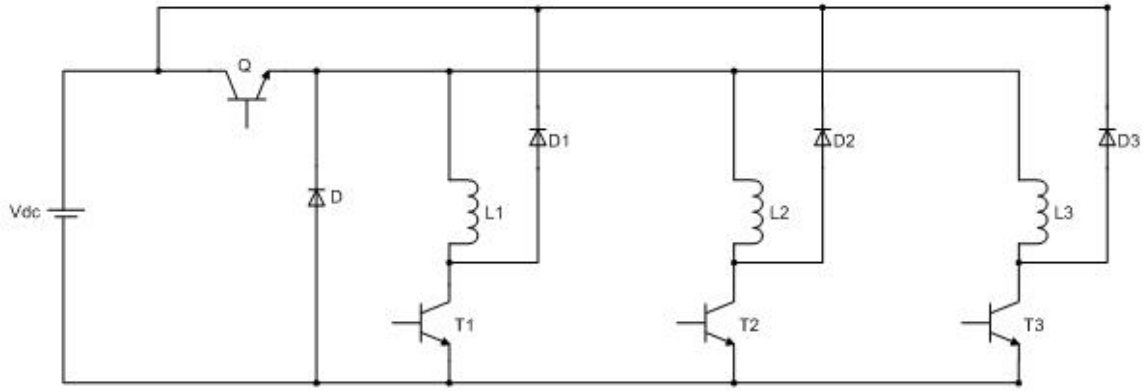

Figure 25 Shared switch converter driving a three-phase machine

3.3.3.3 C-Dump Converter

For an SRM, flux in a phase is built up from zero at the beginning of a cycle and returned to zero before the end. Stored energy at the end of each stroke needs to be provided with a path to travel. In the case of a C-dump converter the stored energy is dumped into a capacitor [Cx in Figure 26] and returned back to the supply through the chopper circuit consisting Tc, Dc and Lc in Figure 26. Like the Miller circuit, this topology also requires an additional switch [Tc in Figure 26] on top of a single switch per phase. A chopper, the operation of which is based on the buck principle, is used to discharge the additional capacitor [131]. With the dump capacitor a faster demagnetisation of phases is possible. With this topology, the number of passive components is high and the control complexity (requires the monitoring of the dump capacitor voltage and control of the chopper switch) makes the converter expensive and rather complicated. As more components are added to the system and the control method complexity is increased, there is the compromise of adding more tolerances to the overall system. This means that the system performance becomes more susceptible to component and/or parameter value variations. This is not a desired feature for a high volume application.

Moreover the voltage ratings of the dc-link capacitor and switching devices are high (the average voltage across the dump capacitor is approximately twice the voltage across the dc-link capacitor in order to have equal magnetizing and demagnetizing voltages), which potentially increases the cost and the overall size of the drive system. The system has potential reliability issues as any control failure will lead to over-charging of the dump capacitor and over-stressing the power devices, leading to their failure. Modified versions of this topology have been proposed [145, 146].

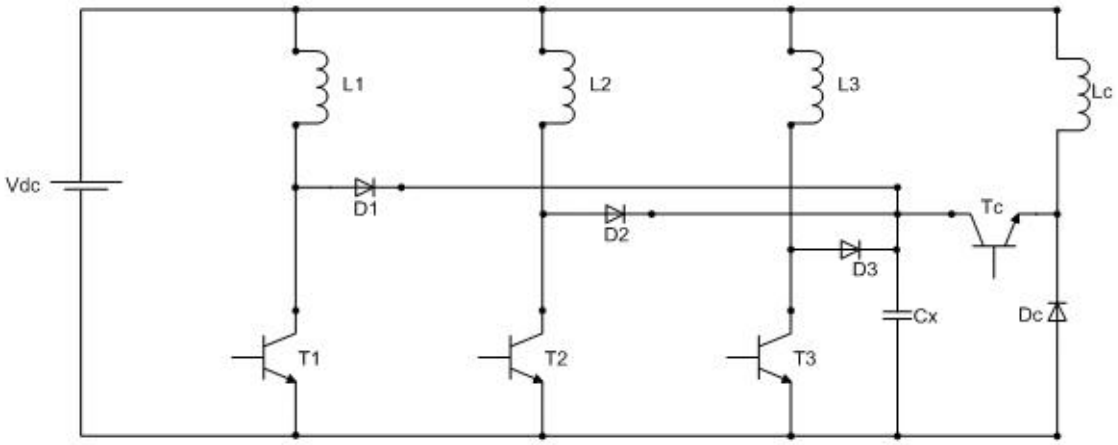

Figure 26 C-dump converter driving a three-phase machine

3.3.3.4 Split DC-Link Converter

As the name suggests, the single dc-link capacitor is split into two capacitors in series. This circuit topology is only suitable for machines with an even number of phases, as in Figure 38. Although the power devices are rated at the supply voltage, they are only capable of supplying half of the supply voltage.

This converter uses one extra capacitive component in the supply rail, which will potentially increase the cost and the size of the drive and potentially reduce the overall drive efficiency. It is also intolerant to phase unbalance. Under such a case there is dangerous voltage build-up in the split dc-link capacitors [145]. Therefore the control circuit must balance the phase currents to keep the centre point voltage at the correct level.

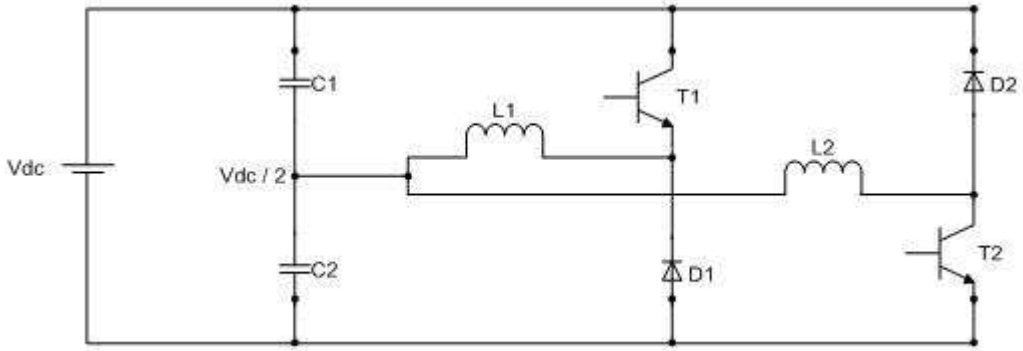

Figure 27 Split dc-link converter driving a two-phase machine

3.3.3.5 Bifilar Winding Converter

As with the split dc link converter, at first glance this converter seems very attractive as it only requires a single switch per phase (Figure 28). An extra winding is used in each phase to recover the stored energy during commutation. Although the converter has one power switch per phase, the switch needs to be rated at least twice the supply voltage level, because when the secondary windings conduct negative dc-link voltage is induced across the primary windings. This converter also suffers from reduced efficiency, as only one of the bifilar windings carries current at any time, resulting in poor copper utilisation for the machine [145]. Three to four electrical connections per phase are needed compared to the usual two connections per phase for other drive circuits. Furthermore, snubber circuitry is required to protect the power devices against large di/dt effects in case of leakage. Overall this converter is a good example to show that a single switch per phase drive is not necessarily a cheap and an efficient solution.

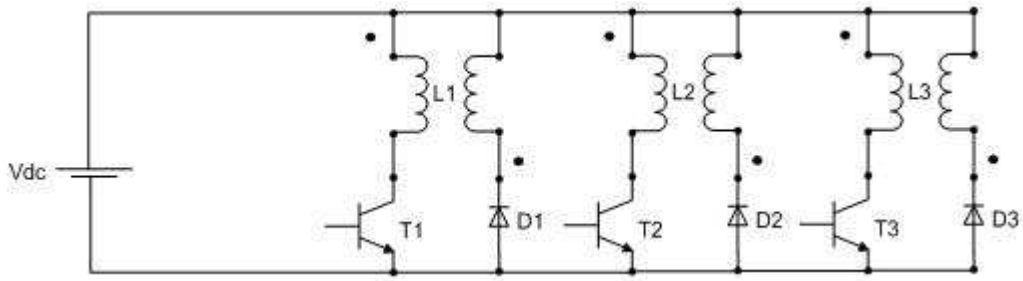

Figure 28 Three-phase bifilar winding converter

3.3.3.6 H-Bridge Converter

An H-bridge converter for SR drives is generally used in the format given in Figure 29. In this format the h-bridge circuit meets the minimum switch per phase requirement for SR drives and is suitable for 4-phase machines. Like the split dc-link circuit it can only utilise half of the dc-link voltage. Obvious, from Figure 29, two phases are always on simultaneously. However, only one of these phases may be contributing to torque production at any instant. Therefore torque per copper loss is degraded [145].

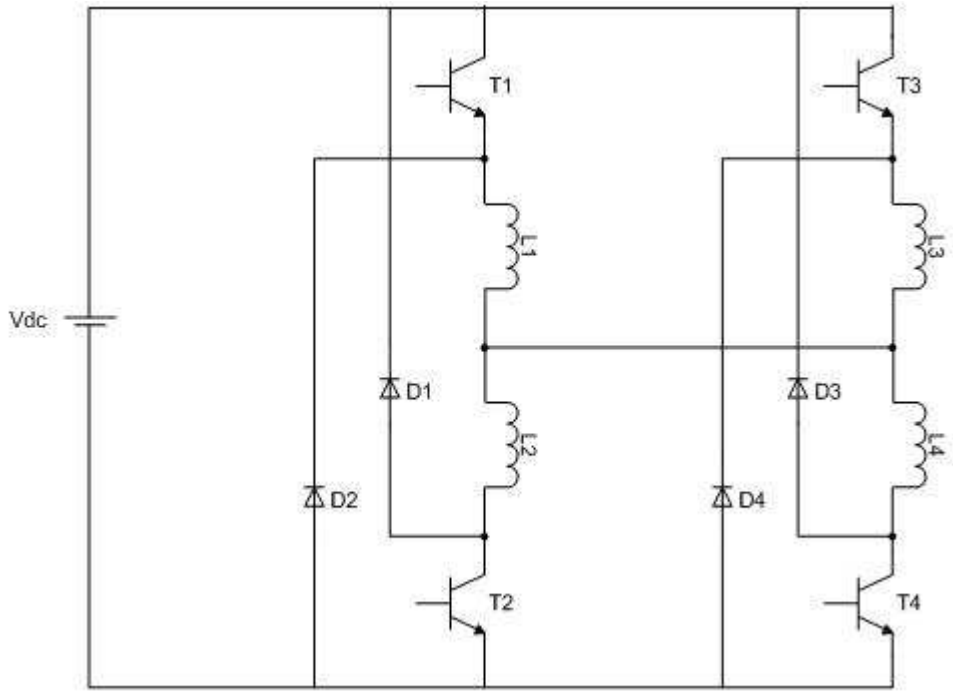

Figure 29 H-bridge converter driving a four-phase machine

An alternative H-bridge converter is implemented in this PhD project. Figure 30 illustrates an h-bridge circuit for a two phase SRM where phase windings are connected back-to-back through two diodes (named as phase diodes hereafter). The phase diodes are used to achieve operation with unipolar phase currents, prohibiting the flow of phase current in the reverse direction when the direction of applied phase voltage is reversed. Therefore, when a phase is de-energised, its current decays to zero and stays at zero until the next positive voltage cycle. The control can be achieved either with a single current transducer, measuring the difference between adjoining phase currents (line current), or with two current transducers measuring each phase current separately. With the arrangement in Figure 30 the loss in power transistors is reduced as each converter phase

leg only conducts the difference between adjoining phase currents. The remainder of the current simply circulates within the phases. Unfortunately the use of a h-bridge converter in this manner is only suitable for machines with even number of phases. Moreover the diodes in series with the windings of each phase increase the total inverter losses. Simulation results and lab measurements of the h-bridge circuit driving a two-phase SRM where phases are connected back to back are given in Chapter 7.

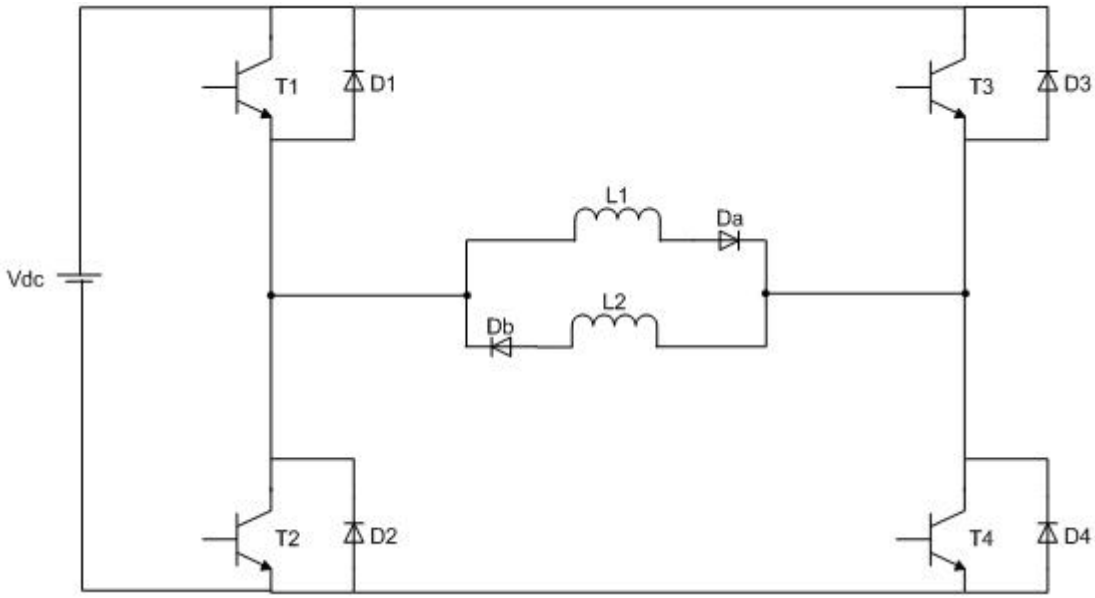

Figure 30 H-bridge converter driving a back-to-back connected two-phase machine

3.3.3.7 Three-Phase Full Bridge Converter

A three-phase full bridge converter generates AC currents and is commonly used for AC drives. It cannot directly supply the unipolar currents desired for almost all SR machines. With a delta connected drive, unipolar phase currents can be achieved with alternating line currents so long as a circulating current can be maintained by the circuit. The basic delta connection prevents a net voltage being applied around the delta, so the circulating current cannot be maintained.

It was shown [89] that the circulating current in the delta configuration could be maintained by placing diodes in series with each of the phase windings (Figure 31).

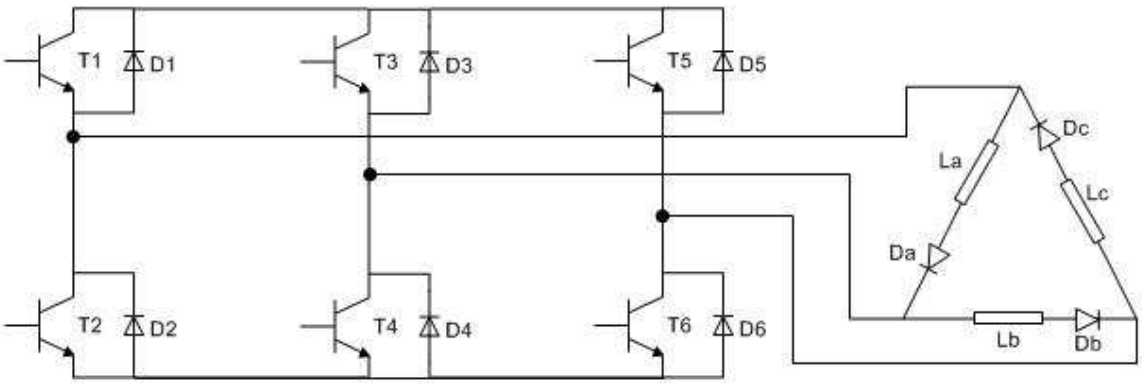

Figure 31 Three-phase full bridge circuit driving a delta connected machine

With the use of the three-phase full-bridge circuit, the number of connections between the motor and the inverter is reduced to only three. Providing that the phase diodes are connected at the motor end, the converter and the motor can be far away from each other. As opposed to the asymmetric half-bridge inverter, which directly controls the phase voltages, the standard three-phase inverter can only control the line quantities.

In [148] another use of three-phase bridge inverter for driving a switched reluctance motor was given. In this paper, the three phase bridge was used to drive a short-pitched winding machine. The machine was connected in star. Unlike the basic star-connection the star point was connected at the mid point of two dc-link capacitors. Two phases were energised in order to keep the voltage balance between the dc-link capacitors. In this configuration, one of the energised phases did not contribute to torque production (in fact producing negative torque and hence reducing the total output torque of the machine) and generated extra copper losses.

Earlier in this chapter, the challenge was identified as *running a 6-phase SRM with only 6 power devices and 3 cables between motor and inverter*. Within this research the concept of using a three phase bridge is extended to six phase drives in an attempt to reduce torque ripple, without resorting to large numbers of power devices or motor connections. Two drive concepts have been introduced, which are briefly explained in the next two sub-sections.

A. Six-Phase Star Connected Drive:

The phases of the machine have been paired and connected back-to-back through series connected diodes. The diodes in series with the phase windings have been called “phase diodes” and were used to prohibit the flow of bipolar phase currents. The paired phases form a “module”. The three modules were then connected in star and driven from the three-phase bridge inverter. The star point has been left unconnected, forcing the sum of the three line currents to be zero. The star-connected six phase drive is illustrated in Figure 32.

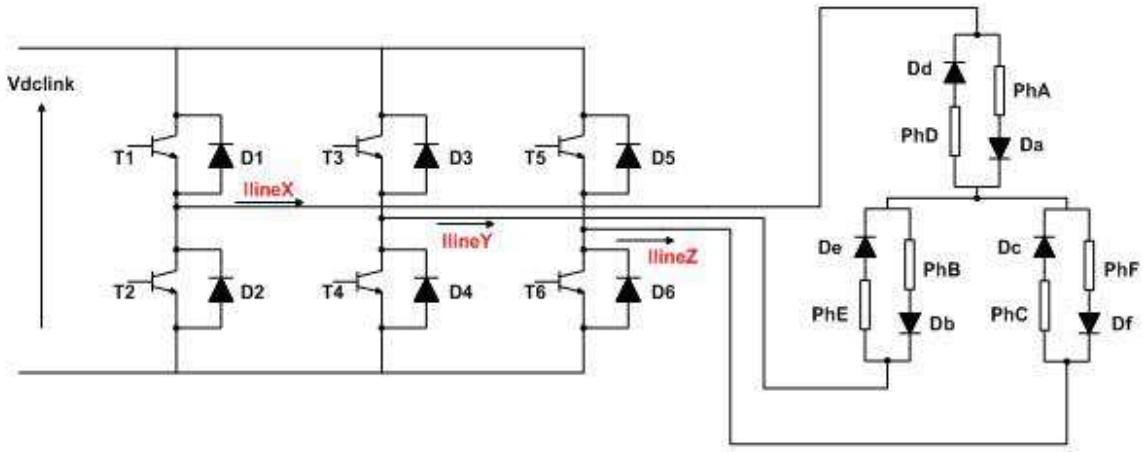

Figure 32 Star-connected six-phase machine driven by a 3-phase full bridge circuit

B. Six-Phase Delta Connected Drive:

In the case of the delta connected six-phase drive, the modules were connected in delta configuration. This drive circuitry is depicted in Figure 33. The voltage applied to any one module directly affects the voltage available to be supplied to the other two modules. This affects the ability of the converter to supply voltage to phases on different modules.

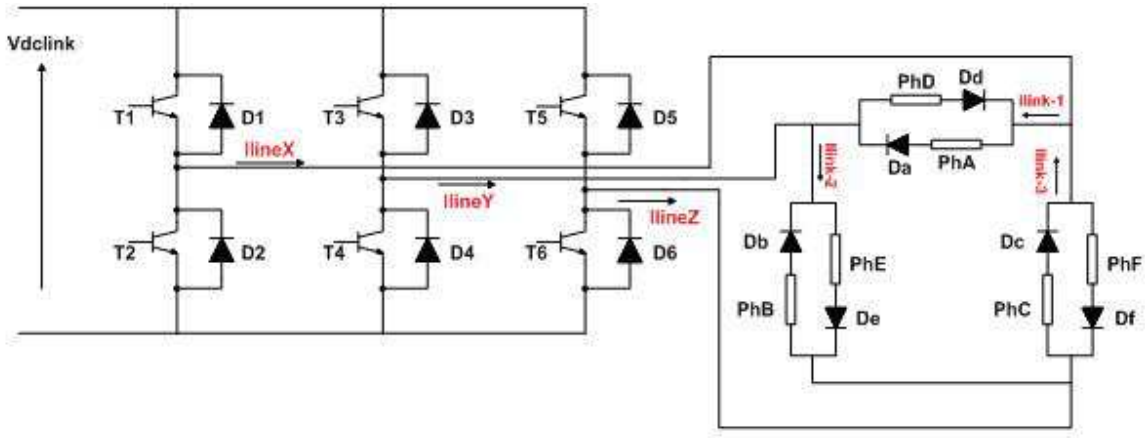

Figure 33 Delta-connected six-phase SRM operated from a conventional 3-phase bridge circuit

For both the star (Figure 32) and delta (Figure 33) connected drives the current controller can be based on phase currents or line currents. Within this research, line current based control has been implemented as it required two current transducers, rather than six (third line current can be derived from the other two). Another advantage of measuring line currents instead of phase currents is that the current sensors do not need to be at the machine end and can be close to the inverter with short cabling and better noise immunity. A controller based on line currents requires a separate PID and a PWM controller for each line. The controller controls the potentials at points U, V, and W in Figure 34. The line demand current is compared with the measured current (Iu, Iv or Iw in Figure 34) and the error is fed to the PID controller. Depending on the error current and the PID controller gains, the PID controller of each line only produces a positive reference voltage (Vref), which is then compared to the triangular wave (Vtri) in the PWM controller**.** The top transistors of each bridge leg (T1-T2, T3-T4 or T5-T6) are switched on if Vref of the corresponding leg is greater than Vtri. If not, the bottom transistors are switched on. Table 1 summarises the useful switching states and potentials at points U, V, and W for each condition.

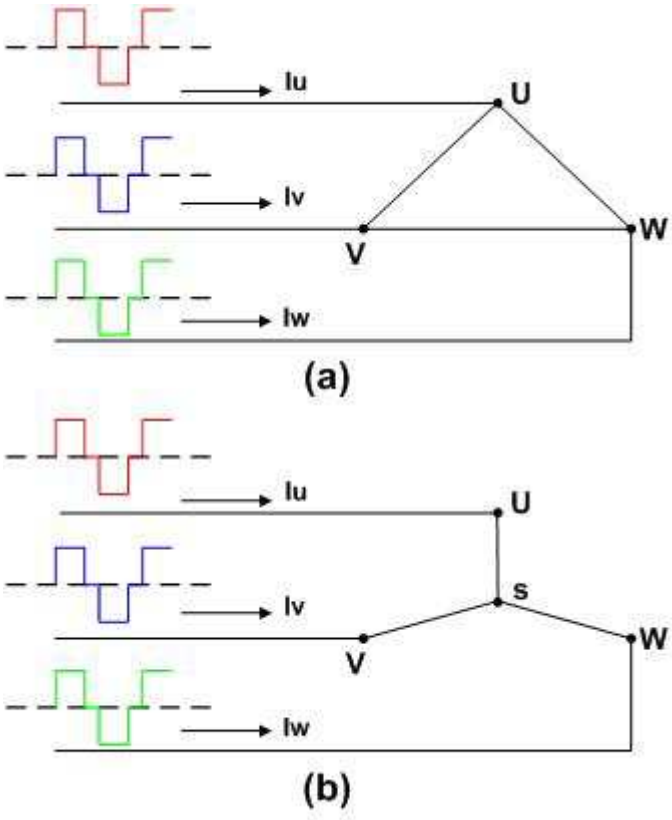

Figure 34 Ideal line currents for the delta (a) and star (b) connected six-phase drives

Table 1 Summary of the useful switching states and potentials at points U, V, and W for each operating condition for the 6-phase star and delta connected drives.

PHASES DESIRED ON	SWITCH STATES						DIRECTION OF LINE CURRENT	POTENTIALS AT POINTS U, V, W		
	LEG 1		LEG 2		LEG 3					
	T1	T2	T3	T4	T5	T6		Vu	Vv	Vw
F & A	ON	OFF	OFF	OFF	OFF	ON	Iv > 0 D4 conducts	V(+)	V(-)	V(-)
							Iv < 0 D3 conducts	V(+)	V(+)	V(-)
A & B	ON	OFF	OFF	ON	OFF	OFF	Iw > 0 D6 conducts	V(+)	V(-)	V(-)
							Iw < 0 D5 conducts	V(+)	V(-)	V(+)
B & C	OFF	OFF	OFF	ON	ON	OFF	Iu > 0 D2 conducts	V(-)	V(-)	V(+)
							Iu > 0 D1 conducts	V(+)	V(-)	V(+)
C & D	OFF	ON	OFF	OFF	ON	OFF	Iv > 0 D4 conducts	V(-)	V(-)	V(+)
							Iv < 0 D3 conducts	V(-)	V(+)	V(+)
D & E	OFF	ON	ON	OFF	OFF	OFF	Iw > 0 D6 conducts	V(-)	V(+)	V(-)
							Iw < 0 D5 conducts	V(-)	V(+)	V(+)
E & F	OFF	OFF	ON	OFF	OFF	ON	Iu > 0 D2 conducts	V(-)	V(+)	V(-)
							Iu > 0 D1 conducts	V(+)	V(+)	V(-)

Dynamic simulation of the star and delta connected six-phase machines driven from three-phase full bridge circuit will be presented in Chapter 6. Simulated and measured results of the 6-phase star and delta connected drives will be presented in Chapter 9.

3.4 SUMMARY

AC electrical machines produce two pulses of torque per phase per electrical cycle. Hence a 3-phase AC machine has 6 pulses of torque per cycle. The pulses overlap strongly and consequently the level of torque ripple produced is generally low (of the order 1%-10%). SRMs, on the other hand, produce one pulse of torque per phase per electrical cycle. Hence a 3-phase SRM has only 3 pulses of torque per electrical cycle. Moreover, in the periods between peaks of pulses the output torque dips considerably, producing torque ripple in the order of 30-100% of the mean torque value. For many applications the high level of torque ripple is unacceptable and can only be easily rectified by increasing the number of phases of the machine to six or more; thereby making it comparable to a 3-phase AC machine. However, a negative consequence of a high phase number is both the large number of power electronic components and electrical connections between the motor and the converter, i.e. increased drive cost.

Alternative converter arrangements have been reviewed: these all reduce the number of power devices, but also reduce the level of controllability of phase voltage and current. Earlier work which used a conventional three phase bridge for a 3 phase SRM is reviewed and it is postulated that this concept may be suitable for a 6 phase drive. Consequently, two drive topologies have been introduced; one with the phases of the machine connected in star and the other in delta.

CHAPTER 4

4– Machine Design & Testing

4.1 INTRODUCTION

It is the aim of this work to produce a high phase number SRM generating low torque ripple, without resorting to complex power electronic supplies or control strategies. The machine designed and constructed for this PhD project is a 6-phase SRM with 12 separate stator cores and 10 rotor segments. The details of the machine construction are given in this chapter.

Prototype designs were evaluated with the aid of 2D finite element analysis to generate the flux linkage characteristics. Both a commercially available FE package (MagNet of Infolytica Corp.) and the FEA package of the Newcastle University's Power Electronics, Drives and Machines (PEDM) group were used to model both segmental and toothed rotor 6-phase designs. Early FE analysis was carried out in the FE package of PEDM and the design space analysis was carried out in Infolytica's MagNet. Results of magnetic and thermal testing of prototype machines are also presented in this chapter.

4.2 DESIGN OF THE 6-PHASE SEGMENTED ROTOR SRM

For direct comparison, the 6-phase segmented design has its outer diameter, inner diameter, air-gap length and lamination stack length equal to those of the three phase segmented rotor machines designed by Mecrow et al. These are summarised in Table 2. For 3-phase multi-tooth and single-tooth winding segmented rotor SRMs presented in [12] and [23], respectively, each stator coil enclosed a single-tooth, which resulted in very little coupling between one slot and another.

For a 6-phase design where each slot contains only the windings of a single phase, the machine would require 24 stator teeth and 22 rotor segments. A 12 stator teeth and 11 rotor segments arrangement could also be possible. However, this would produce unbalanced magnetic pull, resulting in increased acoustic noise and potentially reduced bearing life. To limit the switching frequency and to avoid excessive core losses, 12 stator teeth and 10 rotor segments were chosen for the 6-phase design.

Table 2 List of dimensions of 6-phase segmented design that are kept the same as those of the 3-phase single-tooth segmented design of Mecrow et al

Stator Outside Diameter [mm]	150.00
Stator Bore Diameter [mm]	91.40
Rotor Outside Diameter [mm]	90.80
Air-gap Length [mm]	0.30
Lamination Stack Length [mm]	150.00

Choosing a 12-10 arrangement for a 6-phase design requires each stator slot to contain windings of two phases, with each coil of a phase wound around a single tooth, resulting in short-pitched windings. As will be explained in the following chapters, at any one time during the machine operation, the 6-phase design will have two phases conducting current simultaneously. Simultaneous conduction of two separate phases has an effect on the machine design, especially in the definition of the aligned and unaligned positions for this machine. In Figure 35 the 6-phase segmented rotor machine is shown in the unaligned position. Note that this unaligned position is shown with respect to phases A and F

conducting simultaneously. As two phases will be conducting at any one time, in the unaligned position the gap z in Figure 35 should be as large as possible to minimise the machine unaligned inductance. This ensures that neither the rotor nor the stator excessively contribute to the unaligned flux-linkage. Y1 and Y2 in Figure 35 are the stator tooth tip arc angle and the rotor segment arc angle, respectively. The direction of current flow in each coil is highlighted by the conventional dot / cross representation in Figure 35.

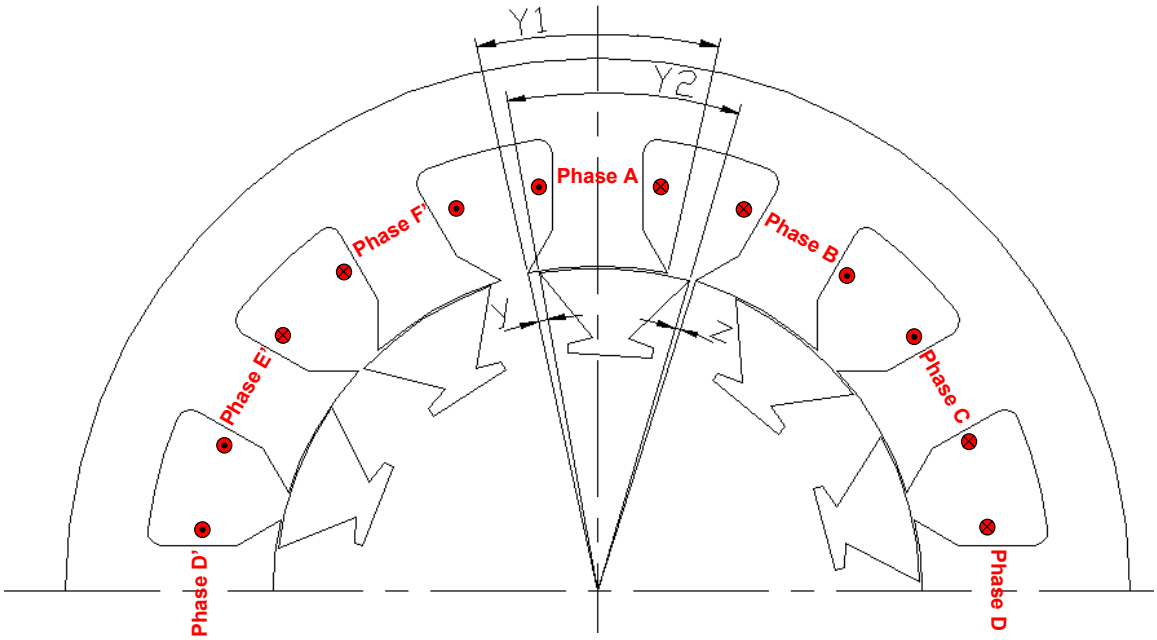

Figure 35 Drawing of the 6-phase 12-10 short-pitched segmented rotor SRM (to establish design rules and equations) in the unaligned position with respect to conduction of Phases A and F

Similarly in Figure 36 the machine is shown in the aligned position. Flux plots for the unaligned and aligned positions in Figure 35 and Figure 36 are depicted in Figure 37 and Figure 38, respectively.

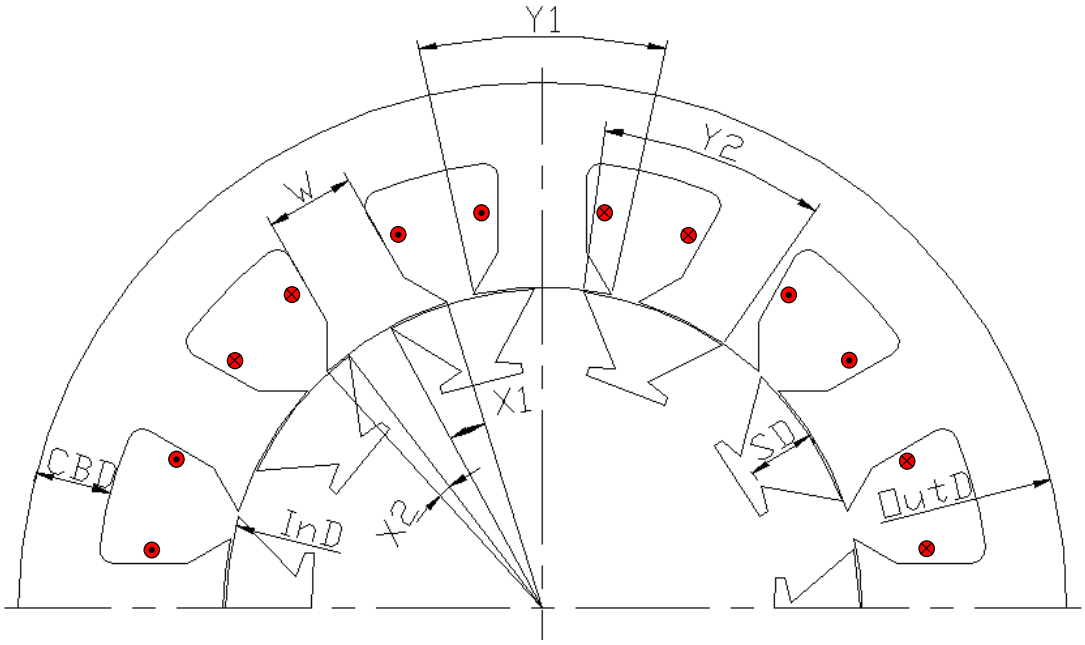

Figure 36 Drawing of the 6-phase 12-10 short-pitched segmented rotor SRM (to establish design rules and equations) in the aligned position with respect to conduction of Phases A and F. Phase configuration is the same as shown in Figure 35

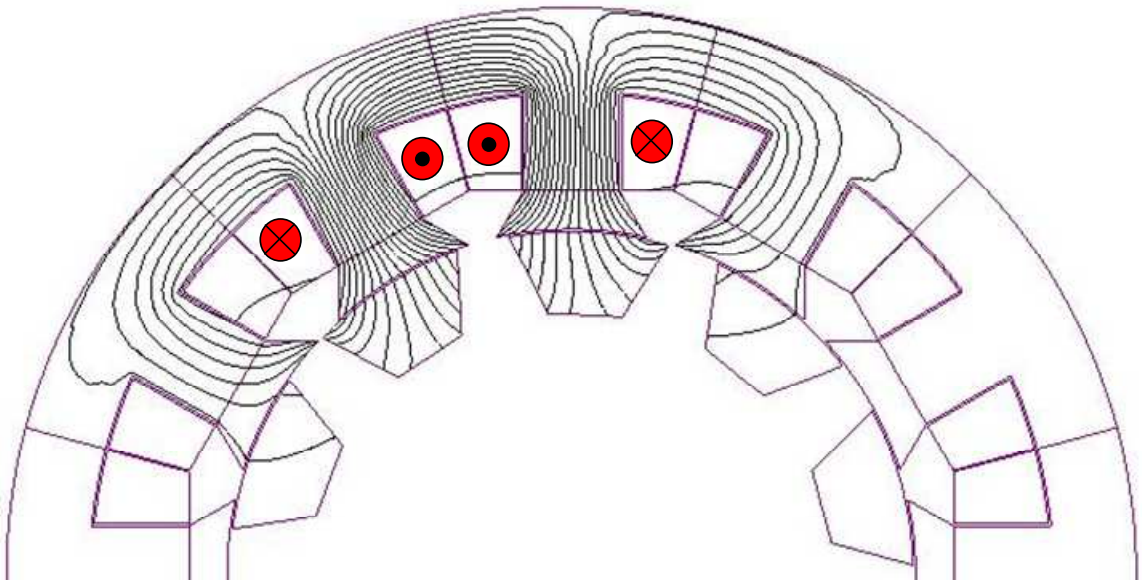

Figure 37 Flux plot of the 6-phase segmental rotor 12-10 SRM in the unaligned position. The energised coils are shown with the conventional dot / cross representation. Only one half of the machine is shown

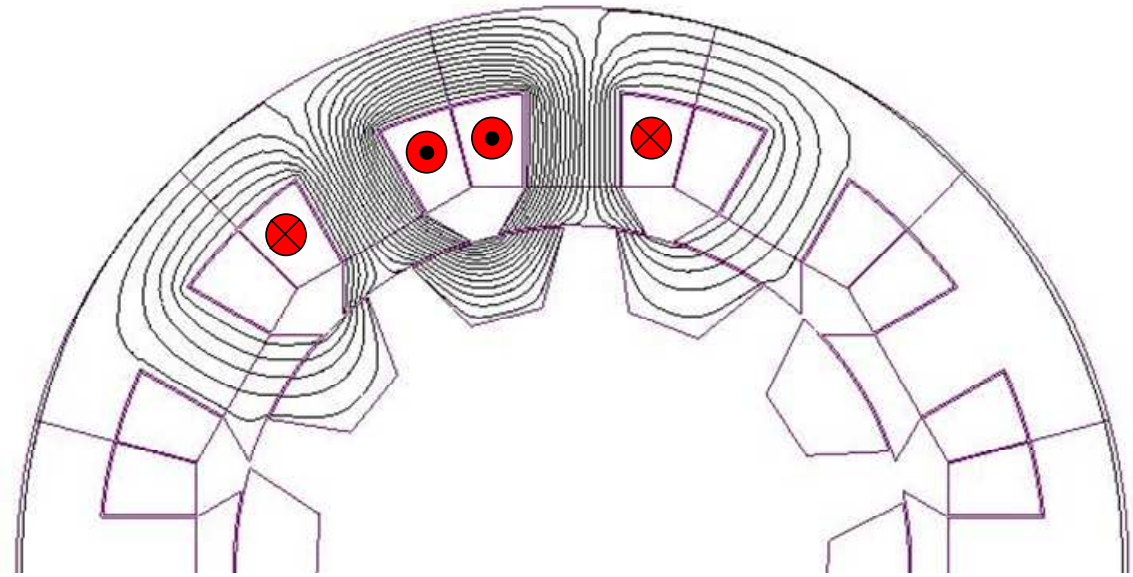

c

Figure 38 Flux plot of the 6-phase segmental rotor 12-10 SRM in the aligned position. The energised coils are shown with the conventional dot / cross representation. Only one half of the machine is shown

Figure 39 shows a rectilinear representation of the 6-phase 12-10 segmented rotor SRM with slots labelled as a, b, c, d, e, and f and teeth labelled as 1, 2, 3, 4, 5, and 6. In Figure 39 the arrows pointing up and down from one stator tooth to the next indicate the direction of flux. The labelling of slots and teeth will be used in Chapter 6.

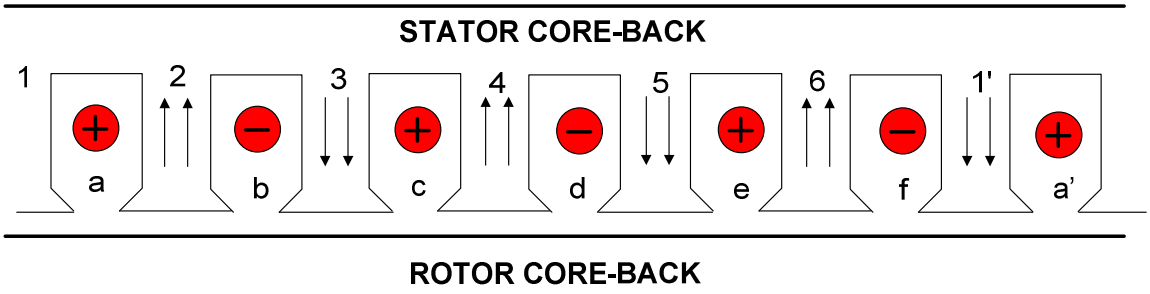

Figure 39 2D rectilinear representation of six-phase SRM showing the direction of slot MMFs and teeth fluxes

In the aligned position the overlap angles (X1 and X2 in Figure 36) between the stator teeth and the rotor segments should be as large as possible to maximise the machine aligned inductance. In Figure 36, W is the stator tooth width, SD is the active rotor segment depth (excluding the dovetail section), OutD is the stator outer diameter, InD is

the rotor outer diameter, and CBD is the stator core-back depth. The relationships between the variables given in Figure 35 and Figure 36 are established from Equation 2 to Equation 7, with dimensions chosen to:

(a) Have all magnetic components carrying a similar peak flux density, so that no one component creates early onset of magnetic saturation.
(b) Maximising the difference between the unsaturated aligned and unaligned inductances.

The gap angle *y* in the unaligned position (shown in Figure 35) is the angle between the rotor segment tip and one of the energised stator tooth tip and is calculated by Equation 2.

$$y = \frac{(\frac{360}{N_r} - \frac{360}{N_s}) - (Y2 - Y1)}{2} = 3 - \frac{Y2 - Y1}{2}$$ **Equation 2**

where N_s is the total number of stator teeth and N_r is the total number of rotor segments.

The gap angle *z* in the unaligned position (shown in Figure 35) is the angle between the rotor segment tip and the closest non-energised stator tooth tip and is calculated by Equation 3.

$$z = \frac{360}{N_s} - Y2 - y = 30 - Y2 - y$$ **Equation 3**

$$X1 = \frac{Y2 - (\frac{360}{Ns} - Y1)}{2}$$ **Equation 4**

$$X2 = Y1 - (\frac{360}{Nr} - Y2) - X1$$ **Equation 5**

The stator tooth width - W should be equal to the overlap between stator teeth and rotor segments in the aligned position. This ensures similar levels of magnetic saturation throughout the magnetic circuit and yields Equation 6.

$$W = \frac{2\pi \times \left(\frac{InD}{2}\right) \times (X1 + X2)}{360} = \frac{2\pi \times \left(\frac{InD}{2}\right) \times (Y1 + Y2 - \frac{360}{Nr})}{360}$$ **Equation 6**

where W is the stator tooth width and InD is the rotor outside diameter.

From Figure 38, it is evident that the stator core-back and the rotor segment carry similar levels of flux. The level of flux carried by the stator core-back and the rotor segments is somewhat less than that carried by the stator teeth. However, inspection of Figure 37 and Figure 38 reveals that the core-back of the fully energised slot (where coils of both phases carry current – the slot with two dots in Figure 38) is required to carry more flux than the half energised slots (the slots with a single cross in Figure 38). Therefore, Equation 7 is used to calculate the stator core-back and the rotor segment depths (excluding the dovetail section) where they are made larger than half the stator tooth width.

$$CBD = SD = 0.7 \times W$$ **Equation 7**

In Equation 7, CBD is the stator core-back depth, SD is the segment depth and W is the stator tooth width. The final values of stator core-back depth and the rotor segment depth are further increased. The stator core-back is made deeper in order to increase the stiffness of the machine aiming to reduce the stator vibrations and acoustic noise (but not too deep which would reduce the available winding area and result in increased copper losses for the same slot MMF), whereas the rotor segment depth is made bigger to have better retention against circumferential forces which will allow (mechanically) higher speed operation.

The electromagnetic limit of torque output of the machine can be increased by changing the stator tooth width (W), the stator tooth tip arc angle ($Y1$) and / or the rotor segment arc angle ($Y2$). However the machine torque output per copper loss can be reduced as a result of the changes in the available slot area, the number of turns, and / or the conductor diameter. To be able to characterise the torque output vs. total machine copper loss one needs to calculate the total slot area with a good degree of accuracy. Detailed calculation steps of the total slot area, conductor diameter and the phase resistance are given in Appendix D.

4.2.1 Determining the Machine Dimensions

Design equations for the prototype 6-phase segmented rotor SRM with 12 stator teeth and 10 rotor segments were listed from Equation 2 to Equation 7. The arc angle of the rotor segment (Y2 in Figure 35 and Figure 36) was varied from 20^o to 30^o by steps of 1^o. For each angle the arc angle of the stator tooth tip (Y1 in Figure 35 and Figure 36) was also varied from 20^o to 30^o. The designs, which had good overlap (i.e. maximum X1 + X2 in Figure 35 and Figure 36) in the aligned position (Figure 36) and also had the maximum values for y and z (Figure 35 and Figure 36) in the unaligned position (Figure 35), were selected and compared, based upon their torque capability.

Aligned and unaligned flux/MMF curves for this design are presented in Figure 40 and the mean torque/MMF curve is shown in Figure 41.

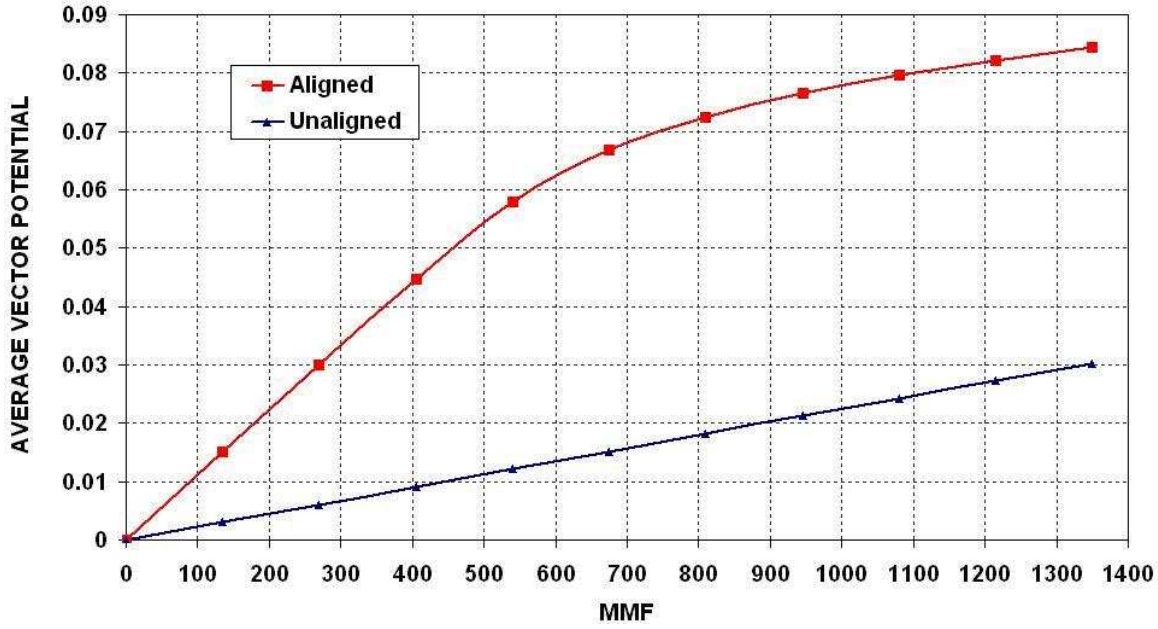

Figure 40 Aligned and unaligned average vector potential vs. MMF c urves for the prototype machine

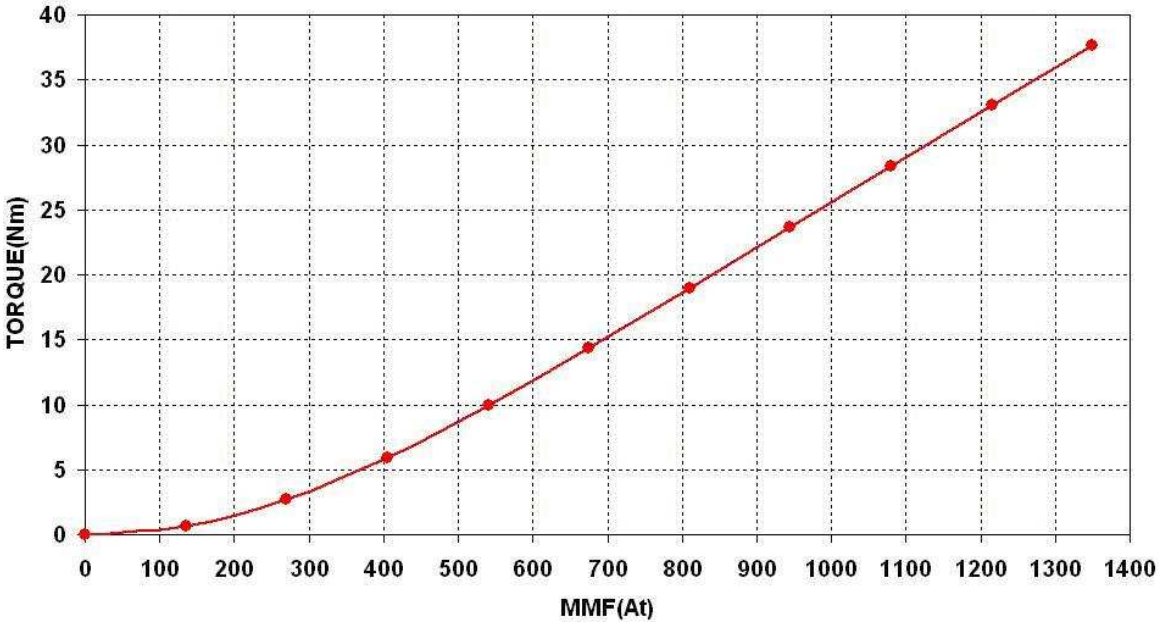

Figure 41 Mean torque vs. MMF curve for the prototype machine

Flux plots for this design in the aligned and unaligned positions are given in Figure 42a and Figure 42b, respectively. The dimensions of this machine were not produced using formal optimisation, but rather through the use of the design rules discussed earlier and through comparisons between different similar designs. The final design was judged to be good, and selected for manufacture.

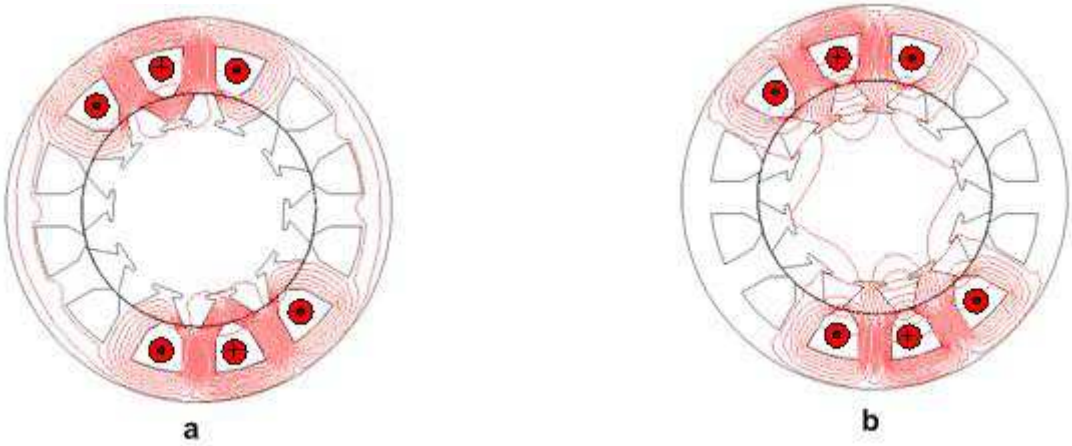

Figure 42 Magnetic flux plots for the 6-phase 12-10 short-pitched segmented rotor SRM with two phases excited simultaneously in the aligned position (a) and in the unaligned position (b)

The chosen design dimensions are given in Table 3.

Table 3 Full list of design parameters of the prototype machine

Number of phases	6
Stator bore diameter [mm]	91.40
Air-gap length [mm]	0.30
Rotor outside diameter [mm]	90.80
Number of stator teeth	12
Number of rotor segments	10
Stator tooth tip taper angle [Degrees]	60.00
Rotor segment taper angle [Degrees]	60.00
Lamination stack length [mm]	150.00
Stator Tooth Tip Arc Angle - Y1 [Degrees]	25.00
Rotor Segment Arc Angle - Y2 [Degrees]	27.00
Gap in unaligned position - y [Degrees]	2.00
Gap in unaligned position - z [Degrees]	1.00
Overlap in aligned position - X1 [Degrees]	11.00
Overlap in aligned position - X2 [Degrees]	5.00
Stator Tooth width [mm]	12.68
Stator core-back depth [mm]	11.00
Rotor segment depth [mm]	9.72
Estimated total slot area [mm^2]	273.65
Total conductor diameter [mm]	1.40
Number of turns per coil	44
Slot fill factor (approximately)	0.50
Estimated phase resistance [Ω]	0.36
Estimated end-winding length [mm]	45.74

4.2.2 Design Space Analysis

At a later stage of this PhD project a commercially available electro-magnetic finite element analysis package called “MagNet” from Infolytica Corporation became available. In MagNet, by programming at the command level with VBScript or VBA (visual basic scripting languages) it is possible to automate the process of generating models by using

design equations (in this case Equation 2 to Equation 7). The script can create the model, set model meshing options, run the simulation and extract and save results in spreadsheet or text format once the simulation is finished. This allows relative comparison of many different design possibilities within the given design space and requirements in a relatively short amount of time. This method was used to judge the quality of the design selected above for manufacture.

The computation time of using 3D FE analysis would be very large, so two dimensional finite element modelling was performed allowing flux-linkage vs. current characteristics of the machine to be generated quickly. This is beneficial for a comparative design process as effects of different machine dimensions can be analysed very quickly and an optimum design decision can be made. Among others, end winding leakage effects are not taken into account in 2D FE analysis. End winding leakage effects can become significant when the machine is in the unaligned position, especially when the machine has a short stack length. Simulations with two dimensional models will underestimate the magnetisation curve in the unaligned position. The amount of underestimation will depend on the ratio of the total end-winding length to the lamination stack length. However, for comparative analysis of design possibilities within the available design space, using 2D FE analysis can still be considered a valid approach.

This section summarises the work carried out for machine design space mapping by varying the stator tooth tip arc angle (Y1 angle in Figure 35) and the rotor segment arc angle (Y2 angle in Figure 35). As the stator tooth tip and rotor segment arc angles are varied the following machine parameters change:

- The stator tooth width (W in Figure 36).
- The stator core-back depth (CBD in Figure 36).
- Available stator slot, and, hence, winding area.
- The overlap angles (X1 and X2 in Figure 36) between the stator teeth and the rotor segments in the aligned position.
- The separation angles (y and z in Figure 35) between the stator teeth and the rotor segments in the unaligned position.
- Rotor segment depth (SD in Figure 36).

The analysis is based on three factors:

1. **Magnetisation curves** in the aligned and unaligned rotor positions and the area covered between these two curves. This gives a direct indication of output torque capability of a particular design.

2. **Per phase copper losses**. As the stator tooth tip and the rotor segment arc angles are varied the stator tooth width widens and narrows, changing the available slot area in the process. For a given conductor diameter this will change the number of turns per coil and the slot fill factor or for a given slot fill factor it will change the conductor diameter and the number of turns per coil. In both cases per coil winding resistance will be changing, directly affecting the copper losses in the process. Comparisons are made using the assumption of perfect current control.

3. **Unaligned magnetisation curve**. Although the area between the aligned and unaligned curves is a good indicator of the output torque capability of the machine, one cannot ignore the effect of the unaligned curve in the converter VA requirements. A design with an increased unaligned magnetisation curve and an overall increased area between the aligned and unaligned curves (aligned curve increases more than the unaligned) may not always be the preferred choice just because it can generate more torque. Increased unaligned inductance will make it more difficult to inject the desired current into the phase windings within the required amount of time. This can increase the VA requirements of the drive system and make it more difficult to achieve the desired level of output torque at a given operating speed of the motor.

In order to assess how good the chosen design is, in terms of absolute torque output, total output torque per total loss and unaligned inductance within the given design space, stator tooth tip arc angle and rotor segment arc angle have been varied from 20^o to 30^o in steps of 1^o. This has resulted in 121 different design possibilities. However many of these possibilities were eliminated before any FE work was carried out, simply due to practical limits (e.g. too narrow / wide slot area, thin stator core-back depth or narrow slot opening, etc.). Six potential designs have been chosen for further analysis including the one corresponding to the design chosen for manufacture.

The following parameters have been kept the same for all six design possibilities:

1. Slot fill factor (same as the manufactured design).
2. Number of turns per coil (same as the manufactured design).
3. Lamination stack length.
4. Stator outside diameter.
5. Stator bore diameter.
6. Air-gap length.
7. Number of stator teeth.
8. Number of rotor segments.
9. Stator tooth tip taper angle.
10. Rotor segment taper angle.

The stator tooth tip arc angle and rotor segment arc angle of six possible designs are tabulated in Table 4.

Table 4 Stator tooth tip and rotor segment arc angles for chosen design possibilities for the 6-phase segmented rotor SRM for further analysis

	Stator Tooth Tip Arc Angle Y1 [Degrees]	Rotor Segment Arc Angle Y2 [Degrees]
Option - 1	24	24
Option - 2	25	25
Option - 3 (prototype design)	25	27
Option - 4	25	28
Option - 5	25	29
Option - 6	26	27

Using Equation 2 to Equation 7, stator tooth width, overlap angles (X1 and X2) in the aligned position and gap angles (y and z) in the unaligned position have been calculated for each design. These are listed in Table 5 for each design option.

Table 5 Stator tooth width and overlap and gap angles for each design option

	Stator Tooth Width [mm]	Gap Angle in the unaligned position - y [Degrees]	Gap Angle in the unaligned position - z [Degrees]	Overlap Angle in the aligned position - X1 [Degrees]	Overlap Angle in the aligned position - X2 [Degrees]
Option - 1	9.51	3	3	9	3
Option - 2	11.09	3	2	10	4
Option - 3 (Mk3 design)	12.68	2	1	11	5
Option - 4	13.47	1.5	0.5	11.5	5.5
Option - 5	14.26	1	0	12	6
Option - 6	13.47	2.5	0.5	11.5	5.5

All FE work has been carried out in MagNet .Using a script written in Visual Basic, an FE model for each design was automatically generated, the 2D FE simulation for each design was run, and the flux-linkage characteristics in the aligned and unaligned positions were extracted for each design. A comparison of aligned and unaligned magnetisation curves for each design option is illustrated in Figure 43, which shows the total flux-linkage against per coil current, where two adjacent coils (i.e. two adjacent phases) are energised simultaneously. Unsurprisingly, as the gap angles (y and z) reduce the unaligned inductance increases. Likewise when the overlap angles (X1 and X2) and the stator tooth width increase, the aligned magnetisation curve also increases.

In Figure 43, the aligned curves for designs Option-4 and Option-6 are identical. This is because both designs have the same stator tooth width, stator core-back depth, rotor segment depth and overlap angles in the aligned position (note that they also have the same slot MMFs).

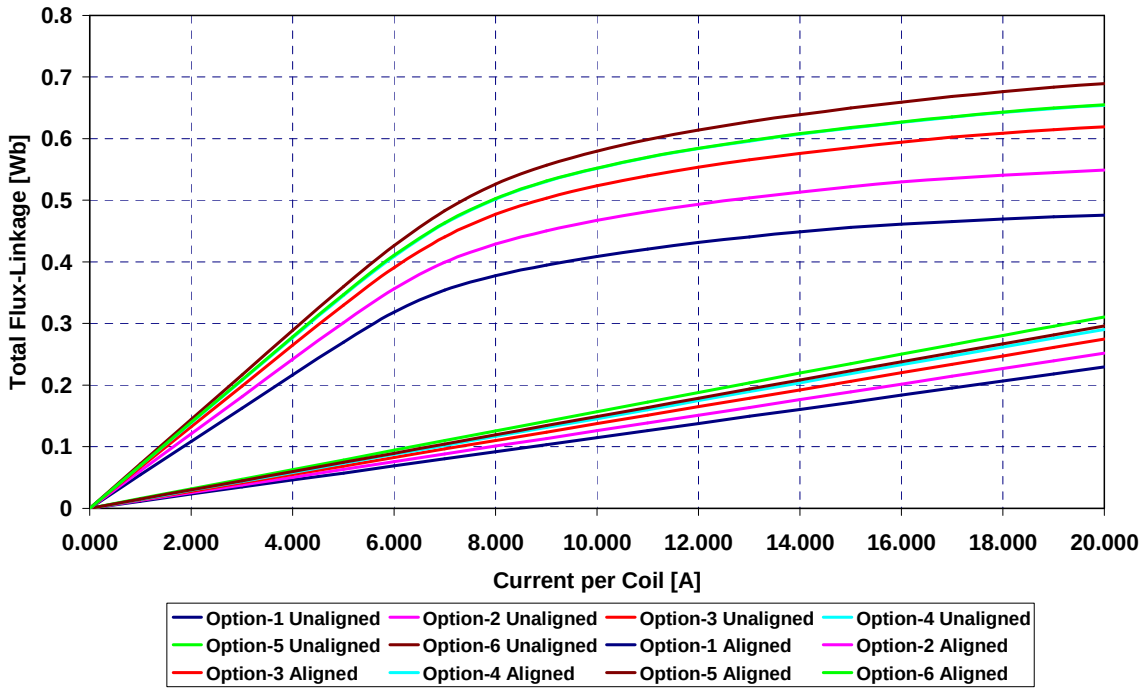

Figure 43 Aligned and unaligned magnetisation curves for each design option where the slot fill factor and the number of turns per coil are fixed

In practice the design choice depends on the application and can involve factors such as those listed (but not limited to) below:

- Target minimum output torque.
- Target cost for the drive system.
- Operating environment and available cooling options.
- Target maximum output torque ripple.
- Target minimum drive efficiency.

The best machine design solution may not satisfy all of the above and is usually a compromise depending on the design requirements of the application. At the start of this PhD project, there were no strict design requirements in terms of the machine design. The comparison between the six design options was based on five factors (objective functions) listed below.

- **Mean output torque capability**: Theoretically, a design option can have a high torque per copper loss value but it can also have a low **average output torque** level. Therefore, as well as the torque per copper loss, the actual average output torque capability should be considered in the comparison of different design options.

- **Mean output torque per copper loss**: Every machine will have a thermal limit, the limit where the drive operation becomes unrealistic due to increased temperature of one or more parts of the drive system. In this context, **torque per loss** is an important parameter in electric motor design, as it describes a motor's ability to produce torque as a function of heat. Winding copper loss is generally the predominant factor in generating the heat in an electric motor unless the machine is running at very high speeds where the level of iron losses becomes significant due to the increased operating frequency.

- **Mean output torque per machine total mass (iron laminations and copper windings)**: The weight of the electric motor can also be considered an important design criterion and is especially significant in application areas such as the automotive and domestic appliances sectors. Therefore, another comparison factor - the **torque per total machine mass** should be considered.

- **Size and cost of the power electronics based on estimating the VA requirements from the linear unaligned inductance**: The size and cost of a motor drive is generally represented by its Volt-Ampere (VA) requirements. In the case of the SRM **the unaligned linear inductance of the machine** has a direct impact on the VA requirements of the drive system (The higher the unaligned inductance the larger the VA requirements). For this reason, the unaligned inductance of each design option at the same current level (10A) has also been taken into consideration whilst comparing the performance of different design options. It must be said that the machine design with the lowest unaligned inductance does not necessarily result in a reduction in the cost and the size of the power electronics. The device selection has a quantized characteristic. There needs to be a step change in voltage and / or current requirements before a device from the next available family is required (larger or smaller).

- **Relative comparison of iron losses**: Copper loss is certainly not the only electrical loss encountered in an electric machine. The iron core of the machine is also a source of loss. The absolute values for both the hysteresis and the eddy current losses have not been calculated, but by using the flux density levels and the loss coefficients for the eddy current and hysteresis losses in various parts of the magnetic circuit the iron losses for each design option have been estimated relatively with respect to Design Option-3.

Table 6 summarises the comparison of the six design options. Results in Table 6 have been normalised with respect to the prototype design. Except the unaligned inductance ratio, all results in Table 6 have been generated for a fixed coil current of 20A. The unaligned inductance ratio has been given at 10A of coil current in order to ensure comparison is based on the linear part of the unaligned curve.

Table 6 Summary of the performance comparison of the six design options (results normalised with respect to the prototype design)

MACHINE DESIGN OPTION	Mean Output Torque Capability Ratio [%]	Torque per Copper Loss Ratio [%]	Torque per Total Machine Mass Ratio [%]	Unaligned Inductance Ratio [%]	Eddy Current Loss Ratio [%]	Hysteresis Loss Ratio [%]
Option - 1	-23.71	5.64	-18.17	-16.53	-19.27	-19.19
Option - 2	-11.42	2.87	-8.04	-8.34	-10.38	-10.24
Option - 3 (prototype design)	0.00	0.00	0.00	0.00	0.00	0.00
Option - 4	5.01	-3.07	3.06	5.94	4.25	4.29
Option - 5	9.10	-8.66	5.10	14.06	8.61	8.72
Option - 6	4.28	-6.15	3.09	8.36	3.11	3.22

As the above mentioned objective functions that help with choosing the optimum machine design can be of conflicting nature, ultimately the design choice turns into a multi-objective optimisation exercise that aims to maximise the average torque output, minimise the copper and iron losses for the same output power, increase the average torque output per unit machine mass and minimise the VA requirements of the drive. Note that there can be other design requirements depending on the application. Unfortunately it is unlikely that there is a single solution that simultaneously minimises or

maximises each objective to its fullest. There usually is a set of solutions with trade-offs to be made. For example a design solution might have the highest average output torque at the expense of increased copper losses.

Given that there were no specific design targets at the beginning of this PhD project, in an attempt to combine all of the objective functions into a single functional form and aid with the decision making in choosing a machine design option out of six possibilities, Equation 8 has been proposed.

$$OptDesign = ToutRatio + ToutPcuRatio + ToutMassRatio + IndRatio \times (-1) \qquad \textbf{Equation 8}$$

All values used in Equation 8 are in [%] with respect to Design Option-3, the higher the *OptDesign* value the more favourable the design option. In Equation 8 *OptDesign* ("Optimum Design") is a number that is used to quantify how good a particular machine design is. *ToutRatio* is the percentage comparison of the design options in terms of average output torque, *ToutPcuRatio* is the percentage comparison of the design options in terms of average output torque per machine copper loss, *ToutMassRatio* is the percentage comparison of the design options in terms of average output torque per total machine mass, and *IndRatio* is the percentage comparison of the design options in terms of unaligned linear inductance (representing VA requirements of the motor drive). *IndRatio* has been multiplied by (-1) in order to address the fact that the unaligned inductance should ideally be minimised. Each variable in Equation 8 can have a weighting factor depending on the application. For example, if the cost and size of the power electronics is the primary concern, then the *IndRatio* value can be multiplied with a number bigger than 1.0 to increase its influence on the final machine design. Here no distinction has been made between the four factors (i.e. all factors has been given the same importance and consequently each uses a weighting factor of 1.0). The results for *OptDesign* value for each design option are tabulated in Table 7. Note that the eddy current and hysteresis losses are not part of Equation 8 and their effects are not reflected in Table 7, as the actual values for these loss components were not calculated. However, both core loss components can still be of help in choosing the ultimate machine design.

Table 7 Comparison of OptDesign parameters for each design (results are normalised with respect to Design Option-3)

MACHINE DESIGN OPTION	OPTIMUM PERCENTAGE [%]
Option - 1	-19.7112
Option - 2	-8.2552
Option - 3 (Mk3 design)	0.0000
Option - 4	-0.9366
Option - 5	-8.5256
Option - 6	-7.1397

According to Table 7 Design Option-3 is the best solution but only marginally compared to Design Option-4. However, considering the results presented for the comparison of the eddy current and the hysteresis losses in Table 6 (Design Option-3 will potentially generate approximately 4.3% less eddy current and hysteresis losses compared to Design Option-4) Design Option-3 becomes the preferred option for the final design. Design Option-3 was indeed the prototype design.

The flux density plot of the prototype design in the aligned position with 20A of coil current is depicted in Figure 44.

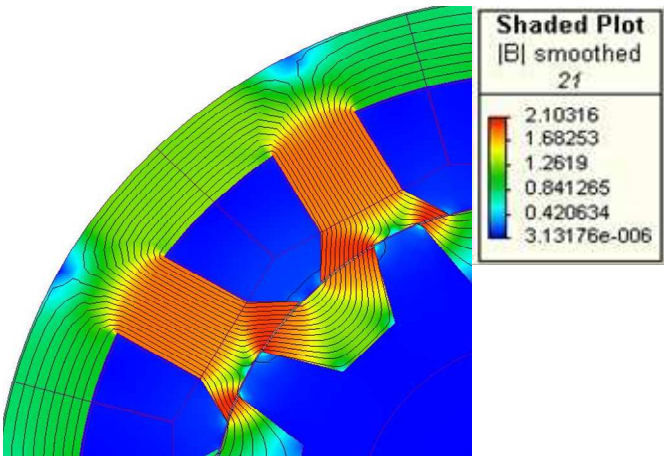

Figure 44 Flux density plot of Mk3 design in the aligned position with 20A of coil current (adjacent coils are excited simultaneously)

4.3 DESIGN OF THE 6-PHASE TOOTHED ROTOR SRM

To be able to compare the 6-phase segmented rotor prototype SRM with a conventional toothed rotor SRM, a 6-phase conventional toothed rotor SRM has been designed. Many papers have been published outlining the design of conventional toothed rotor SRMs [18, 40, 41].

The basic design ratios are given as:

- Tooth width to pole pitch ratio.
- Split ratio (ratio of stator outside diameter to rotor outside diameter).
- Ratio of stator core-back depth to half of the stator tooth width.
- Air-gap length.

A rectilinear model of the conventional design with the critical dimensions listed in Table 8 is given in Figure 45. To be able to carry out a direct comparison with the segmented design, the machine outer diameter (Φ_{OUT}), outer rotor diameter (Φ_{R1}), the stator core back depth (CBD_S), the air-gap length (L_g) and the lamination stack length are all kept the same as those of the segmented design. Tooth width to pole pitch ratio (TW_S / λ_S) has been set towards the upper end of the suggested ranges to maximise the torque production capability of the machine [38]. Thus TW_S / λ_S is selected to be 0.4 for this design, which yields a stator tooth width of 11.41mm.

The recommended ratio of stator core-back depth to half of stator tooth width was in the range of 1.1 to 1.3, which would give approximately 6.3mm to 7.4mm of stator core-back depth. However this took no account of the acoustic noise. The rotor tooth width has been selected to be equal to the stator tooth width. Initially the rotor core-back depth (CBD_R) has been set equal to the stator core-back depth (CBD_S). Initial dimensioning of the toothed rotor design is tabulated in Table 9.

Table 8 Critical design parameters for the conventional toothed rotor 6-phase SRM

CBD_S	Stator Core-Back Depth
TW_S	Stator Tooth Width
λ_S	Stator Pole Pitch
Φ_S	Stator Bore Diameter
Φ_{R1}	Rotor Outside Diameter
Φ_{R2}	Rotor Inside Diameter
Φ_{shaft}	Shaft Diameter
CBD_R	Rotor Core-Back Depth
TW_R	Rotor Tooth Width
L_g	Air-gap Length
Φ_{OUT}	Machine Outside Diameter
h_S	Stator Tooth Height
h_R	Rotor Tooth Height

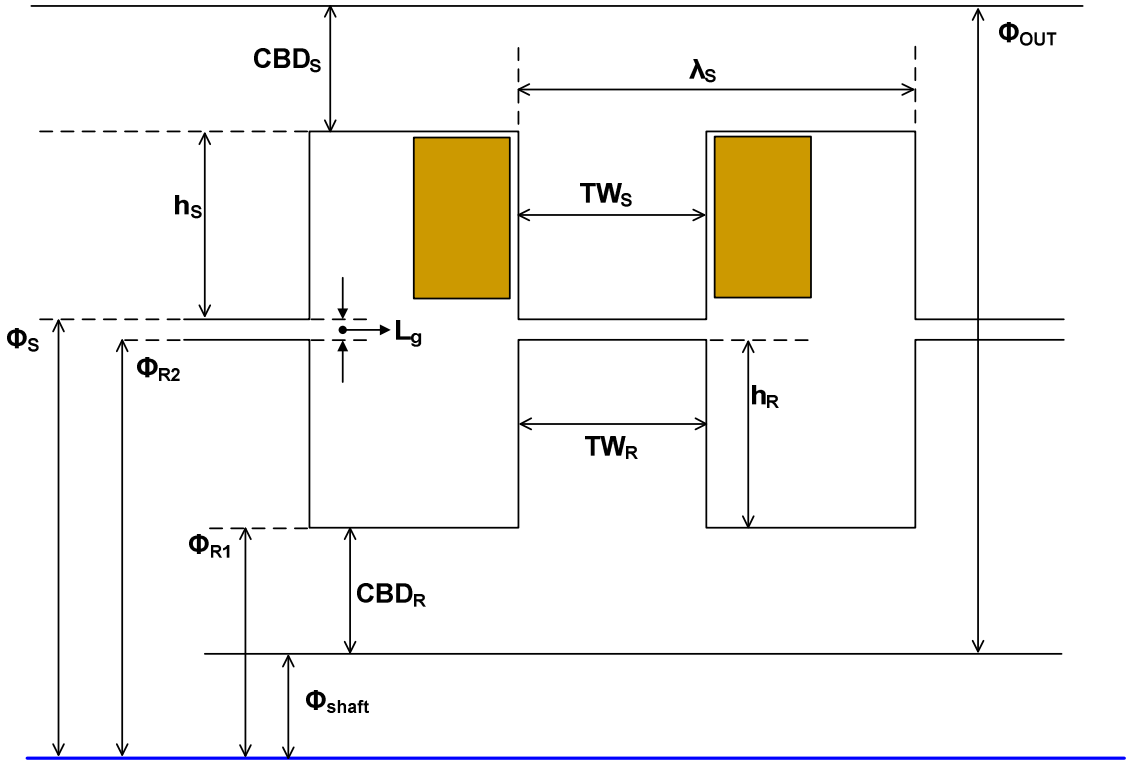

Figure 45 Rectilinear representation of the toothed rotor machine design variables

Table 9 Machine dimensions for the 6-phase SRM with conventional toothed rotor

CBD_S [mm]	11.0
TW_S [mm]	11.41
λ_S [mm]	28.525 (Stator Pole Pitch)
Φ_S [mm]	91.4
Φ_{R1} [mm]	90.8
Φ_{R2} [mm]	58.0
Φ_{shaft} [mm]	36.0
CBD_R[mm]	11.0
TW_R [mm]	11.41
L_g [mm]	0.3
Φ_{OUT} [mm]	150
h_S [mm]	18.3
h_R [mm]	16.4

Similar to the method used for the segmented rotor design, the conductor diameter and the number of turns per coil have been calculated assuming a peak current density of 10.0 [A/mm^2] and a peak phase current of 25.0 [A]. The conductor diameter is calculated to be 1.4mm and the number of turns per coil is 50. A slot fill factor of approximately 0.5 can be achieved.

The design with the machine dimensions listed in Table 9 has been modelled in 2D FE. Like the segmented rotor design, two adjacent phases have been energised simultaneously in the FE simulation. Figure 46 illustrates the average vector potential against MMF curves for the 6-phase toothed rotor design with 11.0mm rotor core-back depth.

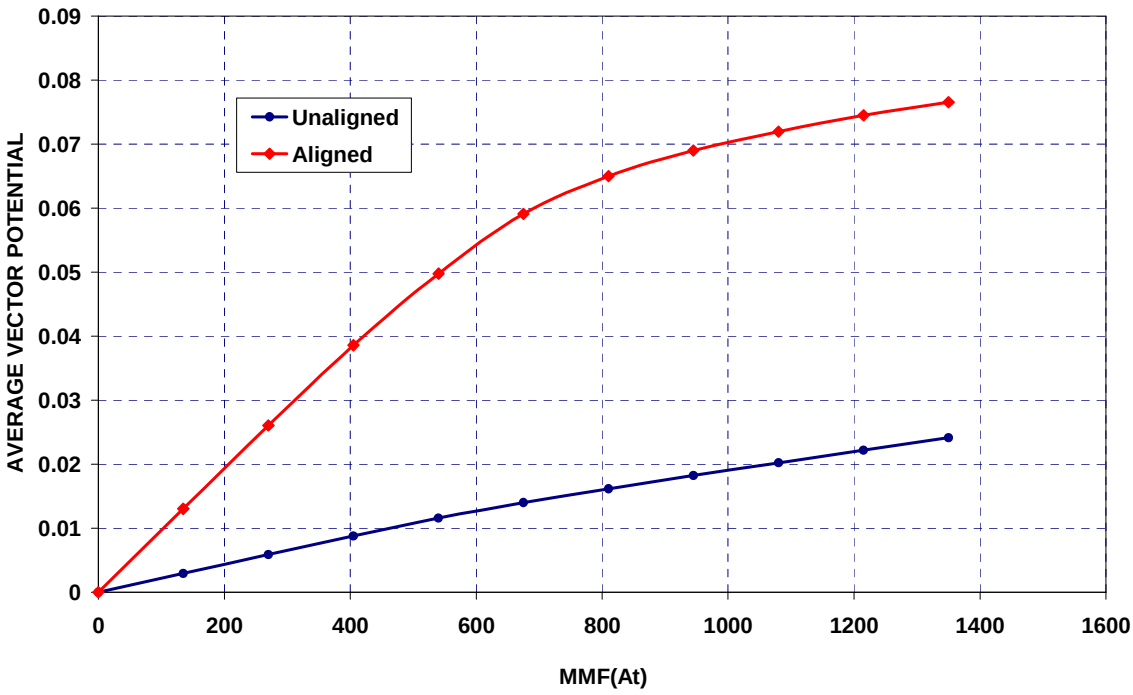

Figure 46 Magnetisation curves in the aligned and unaligned positions for the conventional toothed rotor 6-phase SRM with 11.00mm of rotor core-back depth

Initially the rotor core-back depth (CBD_R) is selected to be equal to the stator core-back depth (CBD_S). In order to have a mechanically stiffer rotor design, the core back depth was increased without affecting the unaligned curve considerably. It was consequently found that the rotor core-back depth could be increased to as much as 18mm without affecting the aligned and unaligned magnetisation curves significantly.

As can be seen in Figure 47 the tooth tip contains a "tang", the main purpose of which is to locate a wedge to hold the windings in place. The tang will slightly raise the unaligned curve as in this position it shortens the gap between the stator and rotor teeth at a time when they should be as far apart as possible. However, the tang will slightly increase the aligned curve as well, since the overlap angle between rotor and stator teeth increases in this position. Therefore these two effects are expected to cancel each other out.

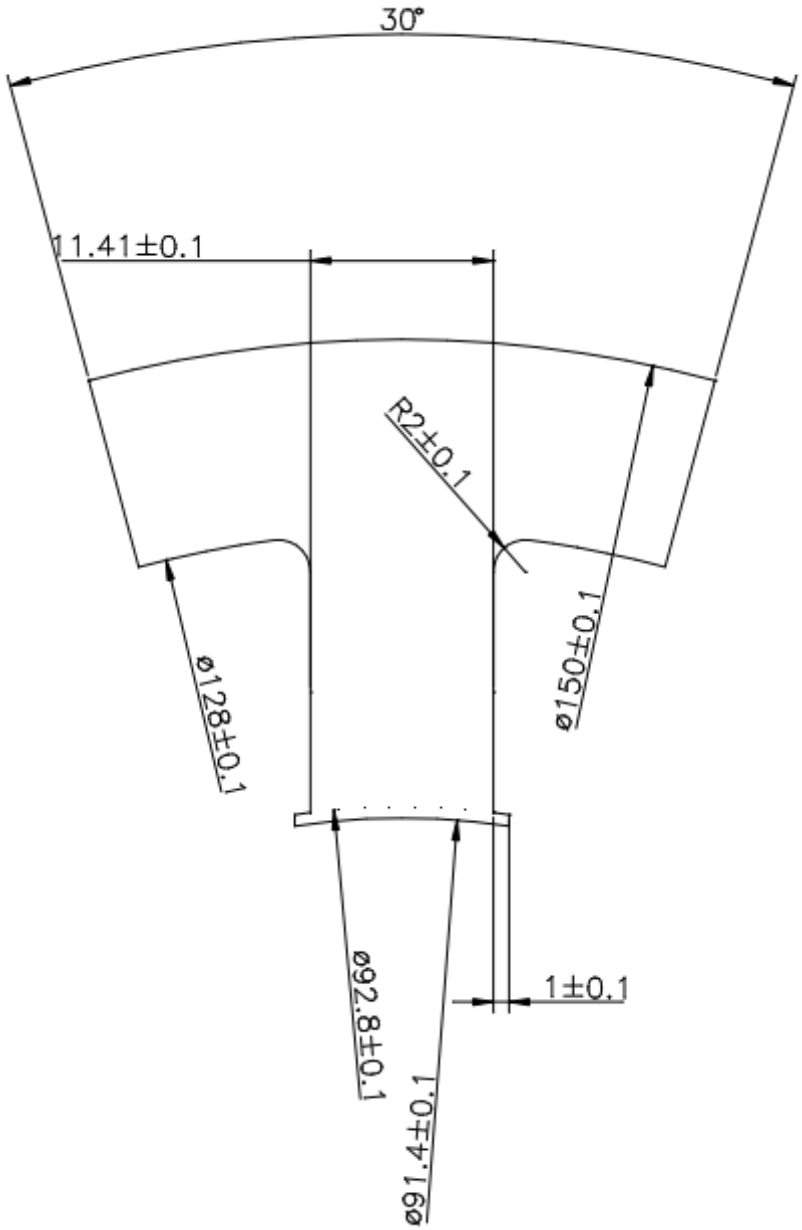

Figure 47 A Single stator tooth of the 6-phase conventional toothed rotor SRM showing the stator tooth tip tang

2D magnetic flux plots of the 6-phase conventional rotor machine in the aligned and unaligned rotor positions are presented in Figure 48a and Figure 48b, respectively. Figure 49 depicts the magnetisation curves of the 6-phase conventional rotor machine from unaligned to aligned rotor position.

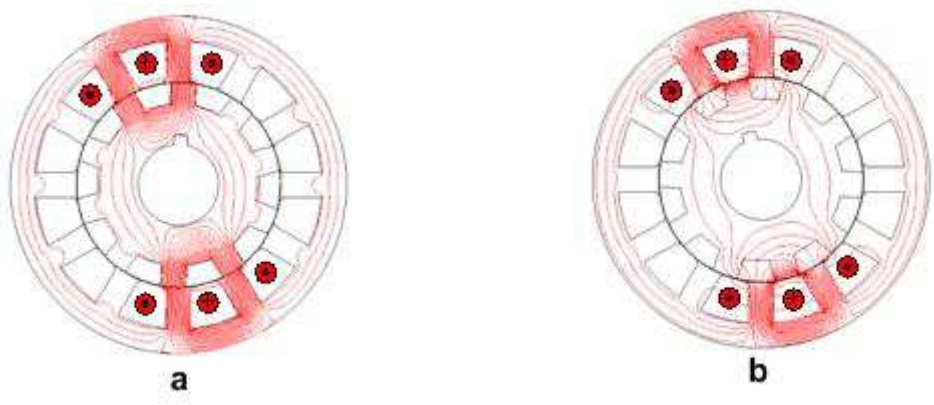

Figure 48 Magnetic flux plots of the 6-phase 12-10 short-pitched conventional toothed rotor SRM with two phases excited simultaneously in the aligned position (a) and in the unaligned position (b)

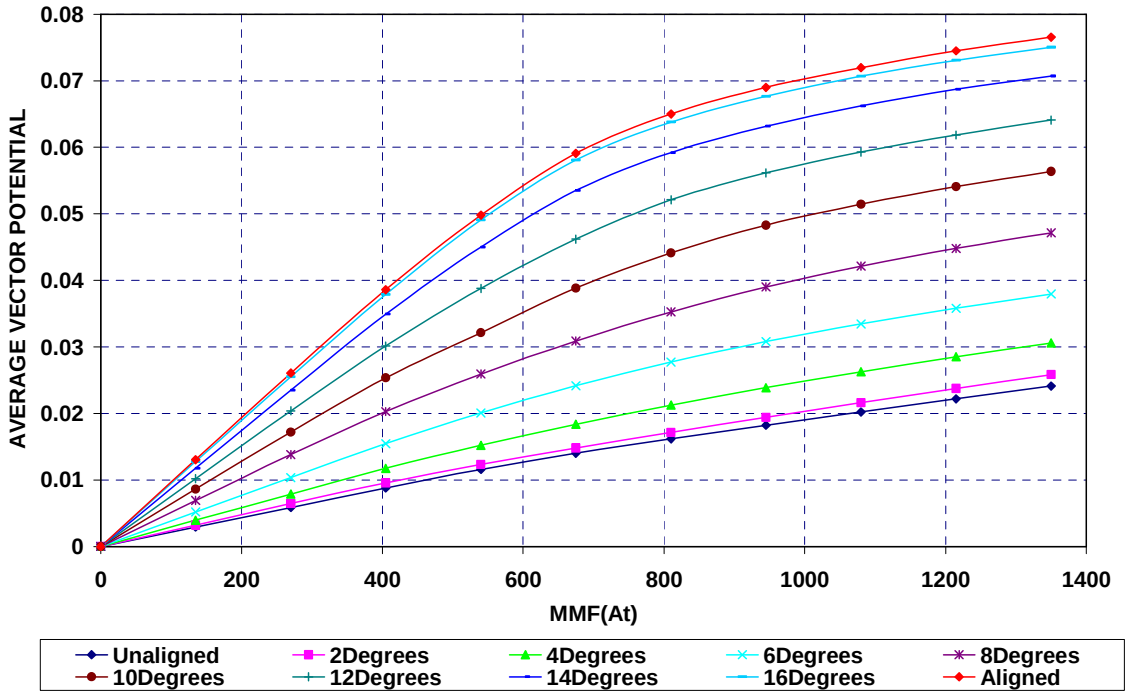

Figure 49 Magnetisation curves of the 6-phase 12-10 SRM with conventional toothed rotor. Magnetisation curves from unaligned to aligned position with 2^{o} stepping shown

The comparison of the segmental and toothed rotor designs will be presented in Chapter 10.

4.4 SUMMARY

Design processes for the six-phase segmental and toothed rotor 6-phase SRMs have been presented in this chapter. Initial design for the segmental rotor machine based on simple design equations has been verified against the design options available within the design space. The design options have been compared based on several performance parameters and an equation based on these performance parameters has been recommended in order to help with choosing the best design option for the segmental rotor machine. The toothed rotor machine design has been based on well-known design equations sourced from several publications. The rotor core-back of the toothed rotor has been made as large as possible without compromising the torque capability of the machine. Stator core-back depths of both segmental and toothed rotor machines have been intentionally made larger than the electromagnetically needed values. This was to increase the stiffness of the machine and consequently reduce the acoustic noise of the designs.

CHAPTER 5

5– Machine Construction Techniques and Test Rig Description

5.1 MACHINE with SEPARATE STATOR CORES

Regardless of windings being multi-tooth or single-tooth, the achievable slot fill factor for conventional stator structures is usually no more than 40%. This is due to the narrow space available to thread a winding nozzle on the inside of the stator, which imposes constraints on the tightness of the coils and also on the speed of the winding operation. The effect gets worse with increased slot number as the dead space rate within a slot increases. Also with increased slot number, the electromagnetic designer is limited to a slot opening width of at least the size of the winding nozzle, as otherwise winding operation cannot be possible. A typical winding process on a conventional stator structure with a nozzle is depicted in Figure 50.

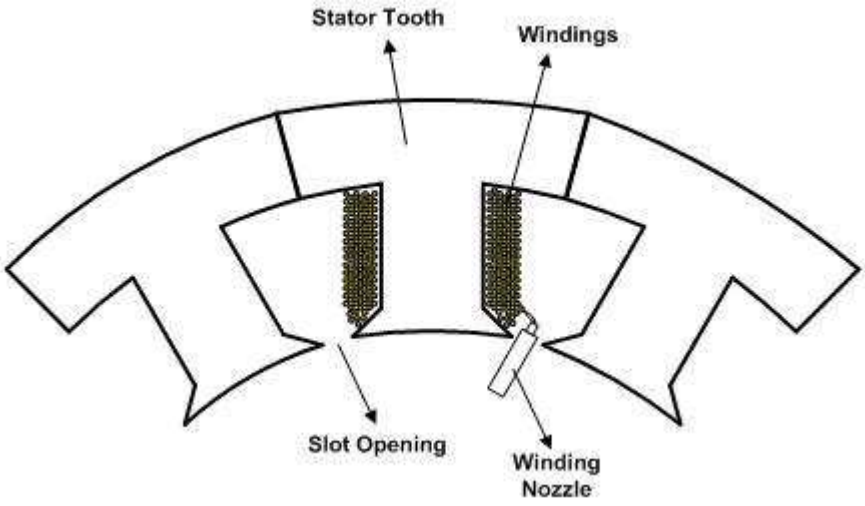

Figure 50 Graphical representation of typical winding operation with a nozzle threaded through the stator slot opening

For a given number of turns, if the slot fill factor can be increased, one can potentially increase the conductor diameter and reduce the coil resistance. Having shorter end-windings can also reduce the total length of windings. Compared to single-tooth windings multi-tooth windings inherently have longer axial overhangs and hence are more resistive. Therefore using single-tooth windings will also reduce the coil resistance and hence the copper losses.

Separating the stator core into separate pieces in order to increase the slot fill factor is certainly not a novelty in the electric motors world. As well as increasing the slot fill factor, separating the stator core also simplifies the coil winding and insertion process and reduces the assembly time and cost. Hoefer and Jack [157] have successfully used the separated stator core principle for a high-speed brushless permanent magnet (PM) motor for a vacuum pump using soft magnetic composites (SMC) as the stator core material. This high-speed PM motor used three separate stator teeth, each carrying a separate winding. A two-piece back iron clamp was used to hold the stator teeth together. This motor is depicted in Figure 51.

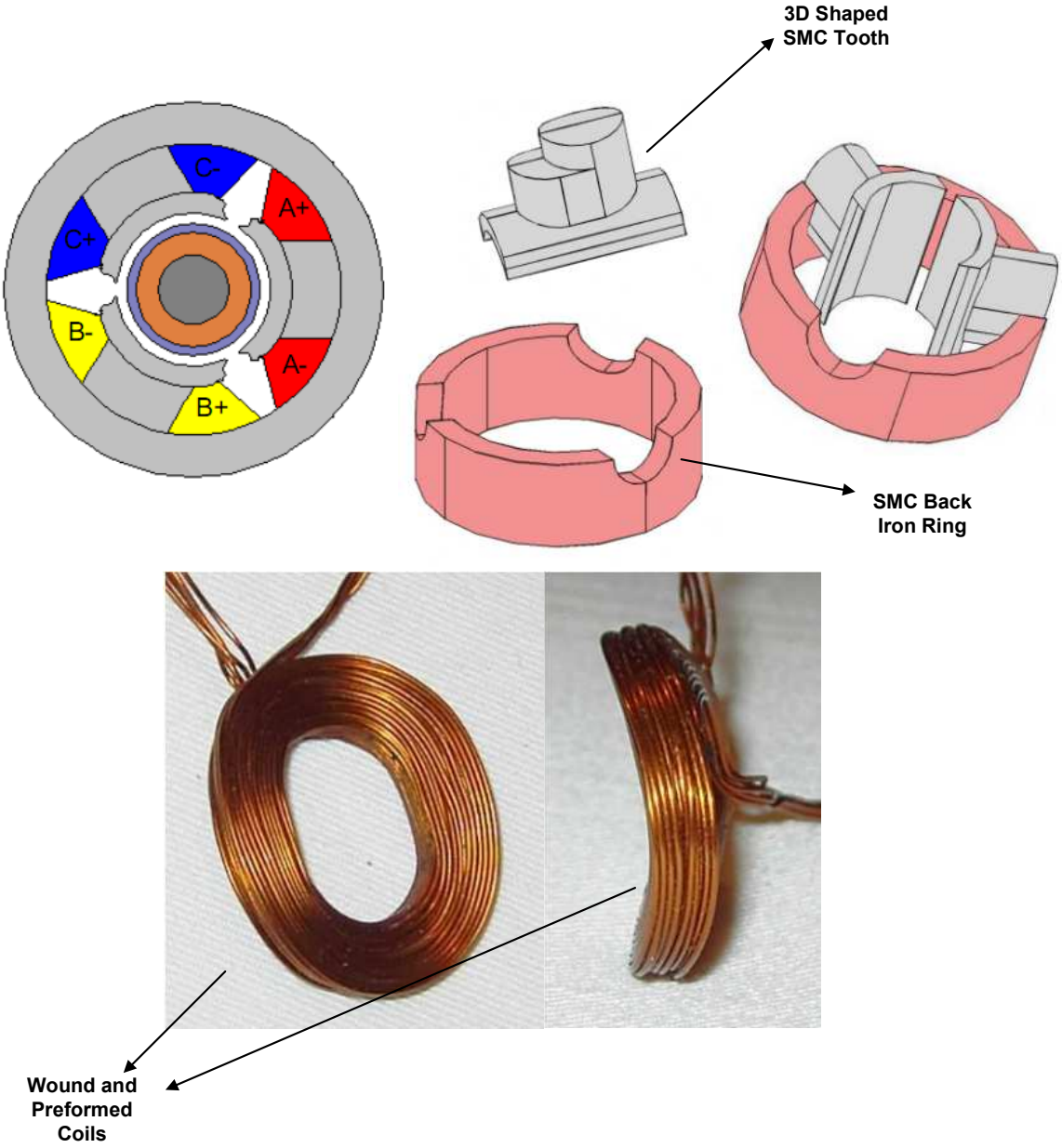

Figure 51 Ulrike Hoefer's high speed permanent magnet vacuum pump motor made of SMC core with three separate teeth, two back-iron rings and preformed windings [157]

Concerning productivity, the non-separate core consists of a small number of parts, thus assembly is relatively easy. As the separate core consists of a large number of parts, assembly is difficult, and productivity is unfortunately poor. The number of parts also influences the core precision [158]. Because a conventional stator core structure is stamped by one singular punch, the circularity is precise. On the other hand, in the separate core case, the processing errors in the contact surfaces can accumulate, and as a result, it is not easy to make the circularity high. In terms of motor characteristics, along

with the rigidity, high circularity of the core is important for having small noise and small vibration. In mass production, keeping the circularity costs a lot for separate core structures.

Mitsubishi has been successful in utilising separated stator core structures in a number of their commercial motors. Researchers at Mitsubishi claimed that by winding at high-density and carefully redesigning the motor electro-magnetically they were able to reduce the copper losses by 32.2 % and iron losses by 11.9 % [158]. The copper loss reduction was achieved by having approximately 75 % slot fill factor compared to 59 % attainable with conventional single punch stator structures thanks to the ingenious “joint-lapped” core. Mitsubishi since used the joint-lapped core approach in a wide range of their commercial products such as air-conditioner compressor motors, elevator motors, and exhaust gas re-circulation valve motors [159-161]. The joint-lapped core principle has made it possible to solve the problems of divided cores, securing the same amount of space for the winding operations as in the divided-core approach without impacting the ease of assembly and connectivity. With joint-lapping the core, the opening angle of the teeth is increased. Effectively, joint-lapping allows opening up a core section for high speed, high density winding operation and once the winding on a tooth is completed another section of the core is bent back and opened up for winding. Once all teeth are wound in similar fashion the complete unit is bent back to form a round shape. As a result, even thick wires can be wound in alignment without coil distortion, which is common in separate cores. The start and end of the joint-lapped core are connected together by welding, caulking or shrink fitting into the frame. Moreover joint lapping can allow the use of narrower slot openings if it is desired for the design as well as increasing the speed of winding operation by using a circular motion flyer. The winding process on a joint-lapped core and a picture of such a core are depicted in Figure 52.

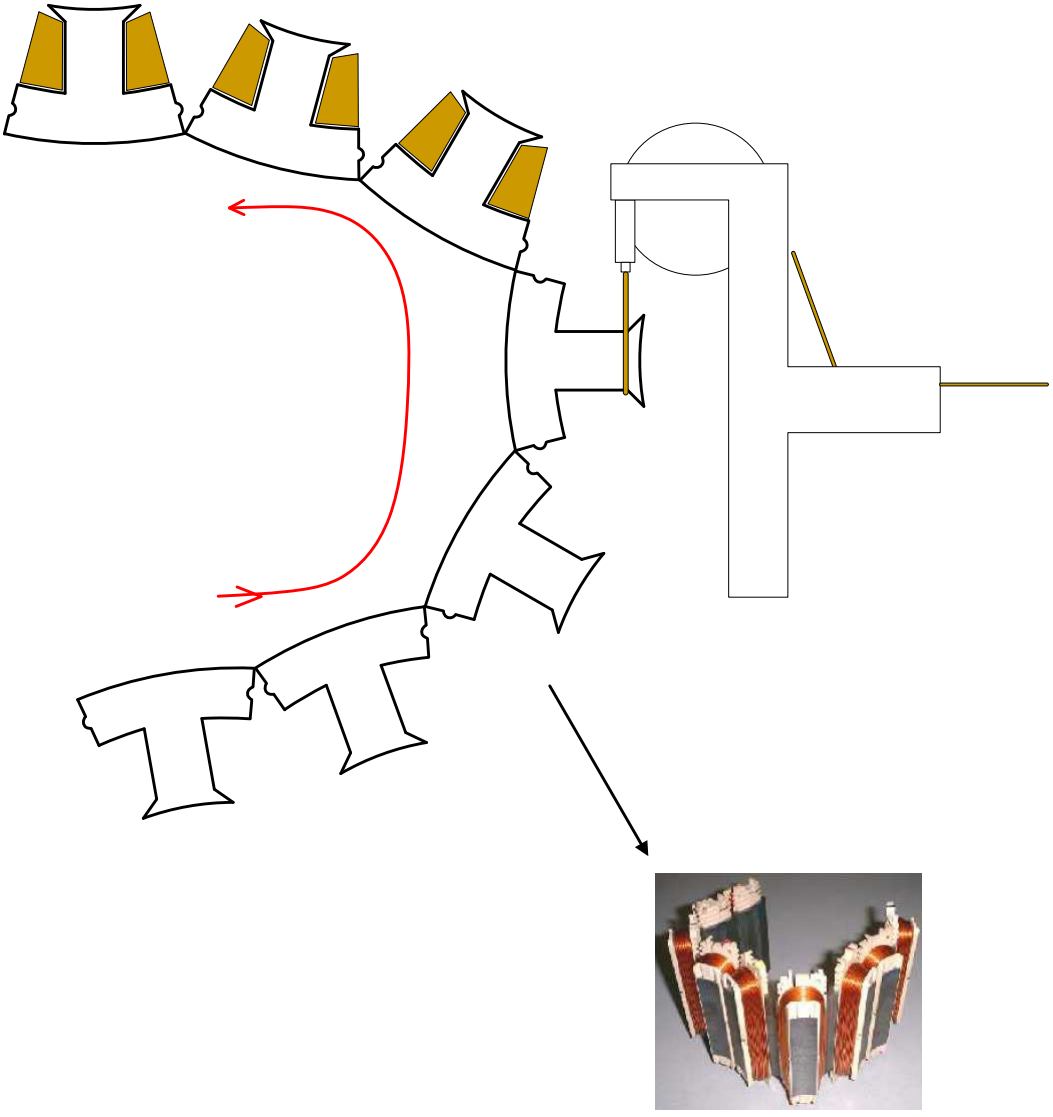

Figure 52 Winding process with joint lapped core and picture of joint lapped core [158]

5.2 CONSTRUCTION OF THE PROTOTYPE MACHINE

The prototype machine has six phases with an inner rotor formed by 10 discrete segments and an outer stator formed by 12 separate cores. Rotor and stator laminations were both laser cut. Standard 0.5mm lamination steel (M250-35A) was used.

5.2.1 Stator Construction

The temperature of the stator windings is the limiting factor for the maximum output torque of an SRM. This temperature is mainly determined by the copper losses and the thermal resistance between the windings and the stator laminations, assuming that the laminations are sufficiently cooled. Furthermore, machine efficiency will be affected adversely by excessive winding losses [162]

The use of separate tooth laminations greatly increases the possible slot fill factor, but does introduce a series of joints around the core back of the stator. These joints create small gaps, which increase the reluctance of the flux path and are detrimental to performance. In conventional SRMs the magnetic flux has to cross a series of these joints and the subsequent reduction in performance is often thought to outweigh the benfits of increased slot fill. However, for segmental rotor SRMs the flux paths are very short and flux only ever has to cross a single joint. This method of construction was consequently selected.

The machine stator was constructed from 12 separate cores: no joints were used to hold the separate stator cores together, as it was believed that the forces exerted by the machine frame structure would be enough to hold the divided core pieces together. Each stator core occupied 30 mechanical degrees. A single stator core is illustrated in Figure 53.

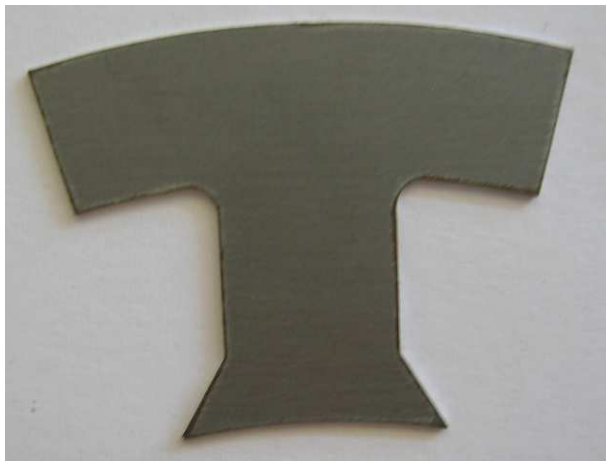

Figure 53 Picture of single stator core lamination for the 6-phase 12-10 segmented rotor prototype machine

The stator of the prototype machine was constructed in three stages: Assuming a lamination packing factor of 97 % (3% occupied by glue, air and iron lamination coating), each stator tooth of length 150mm required around 291 laminations, each nominally 0.5 mm thick.

Gluing 291 laminations all at once and controlling their radial and horizontal alignment required a systematic approach. To ease gluing stator laminations and forming of 150mm stacks, the process was divided into two stages. In the first stage a jig (Figure 54) was designed to glue together 50mm long stator tooth pieces.

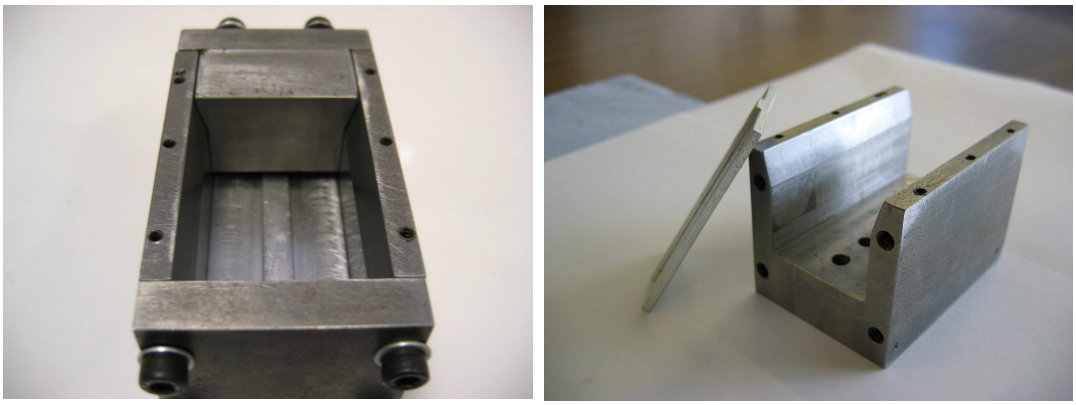

Figure 54 Jig used to produce the 50mm long stator tooth pieces

Each 0.5mm thick lamination was coated with a thin layer of adhesive and then placed inside the 50mm long jig. Then the glued laminations were cured in an air-circulating oven at 80^{o}C for about an hour. Pictures of the 50mm piece inside the jig and finished piece are given in Figure 55.

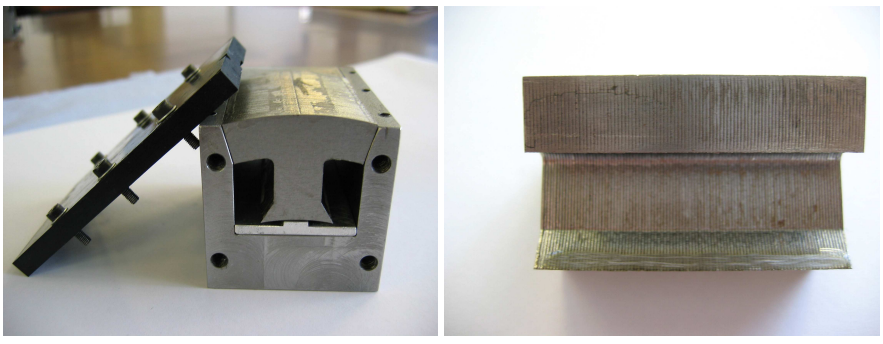

Figure 55 50mm stator piece inside the jig and a close-up on the glued and cured 50mm piece

To achieve satisfactory bond strength with the 50mm pieces as well as the final 150mm pieces, the glue used was a formulated epoxy adhesive from Magna-Tac® that was ideal

for bonding laminations. To form twelve 150mm long stator teeth, 36 of these 50mm tooth pieces were needed. Before bonding the 50mm laminations to form the stator teeth, excess glue on the laminations was carefully removed. Another jig (Figure 56) was then used to produce the 12 stator teeth.

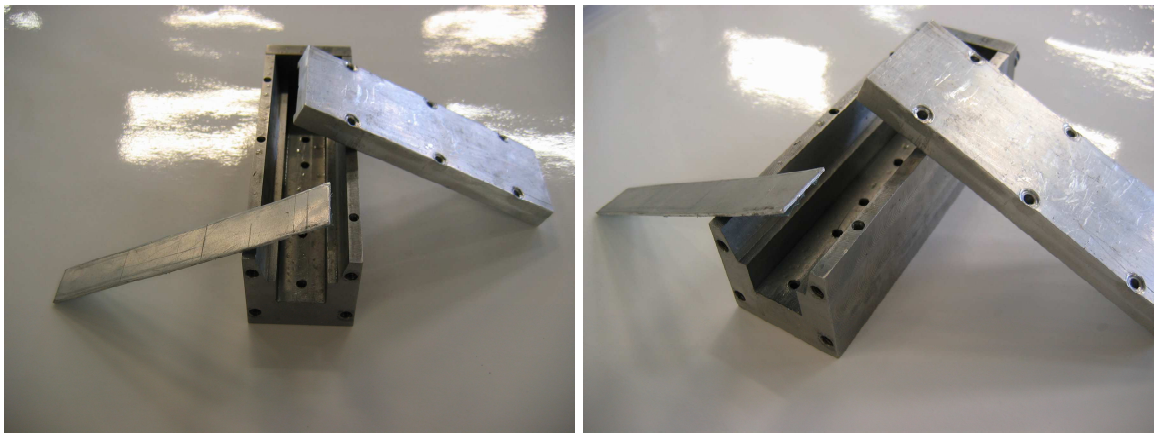

Figure 56 Pictures of the jig used to produce the 150mm long stator tooth pieces

It was required to thoroughly dry the adhesive before curing for optimum bonding. This was accomplished by forced drying in an air-circulating oven at approximately 90^{o}C for about 15 minutes. The adhesive could be cured without a prior drying period, however for optimal results drying was highly recommended [163]. After coating 50mm laminations with the adhesive and drying thoroughly, three 50mm long lamination stacks were put together and cured at 170^{o}C for at least two hours. The final product at the end of this stage is pictured in Figure 57.

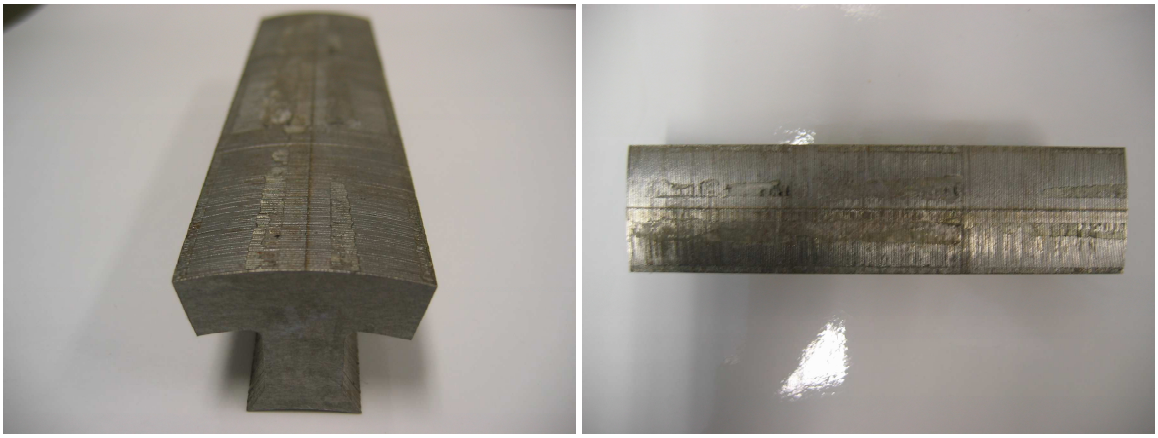

Figure 57 Pictures of the complete stator tooth pieces

Note that the positioning of the pole face of each lamination was controlled as well as two side faces (where the teeth would be glued together to form the complete stator assembly).

5.2.2 Windings

A slot fill factor of 0.5 was thought to be realistic without being too optimistic for calculating the initial conductor diameter. The maximum permissible current density was chosen to be 10A/mm^2, with a peak current of 25A a wire of diameter of 1.36mm was required. The nearest wire size to this was 1.4mm, corresponding to 44 turns per coil in a slot area of 270 mm^2.

The above fill factor was achieved with difficulty. Bulging and curving of conductors due to the relatively long machine axial length and the relatively thick conductor diameter of 1.4mm greatly affected the maximum achievable slot fill factor. It is hypothetically mentioned in [156] that the curve of coils is caused when the wires are drawn and wound in such a manner that the residual distortion is not eliminated completely due to the tension.

In the same paper the reasoning for the bulge in wires is attributed to the hardening due to continuous plastic deformation during winding process. The curving and bulging of wires are depicted in Figure 58a and Figure 58b, respectively. The author believes that with a more careful winding approach the slot fill factor can easily be increased further. A self-bonding enamelled wire with thermosetting bond coat from VonRoll-Isola was selected. The aim was to increase the retention of windings around separate stator cores and to keep the bulging of windings to a minimum. Before the winding operation, inside surfaces of each stator tooth were covered with slot liners to avoid shorting between stator windings and stator core. Figure 59 pictures a stator tooth covered with slot-liner.

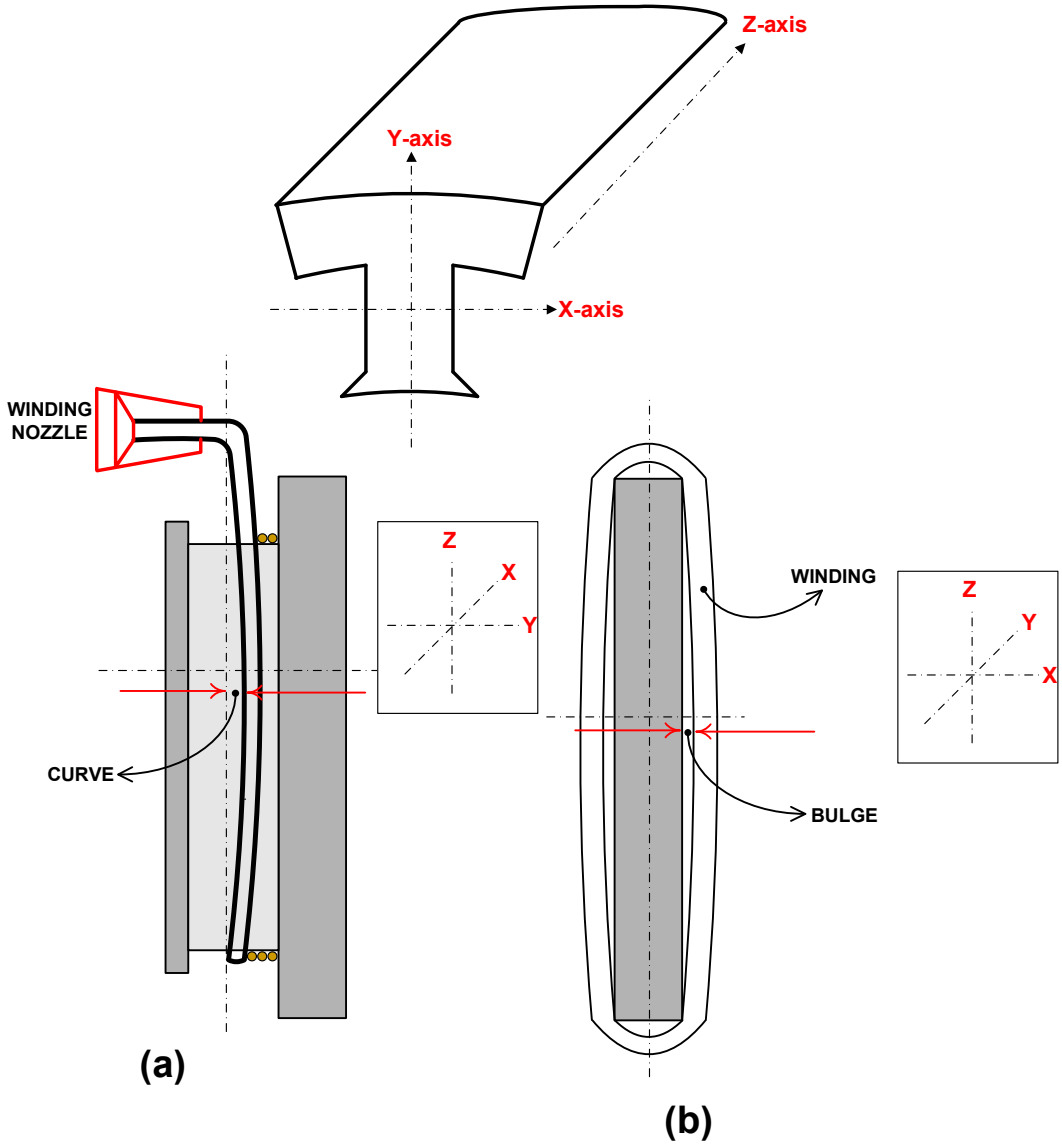

Figure 58 Curving and bulging of conductors during winding operation

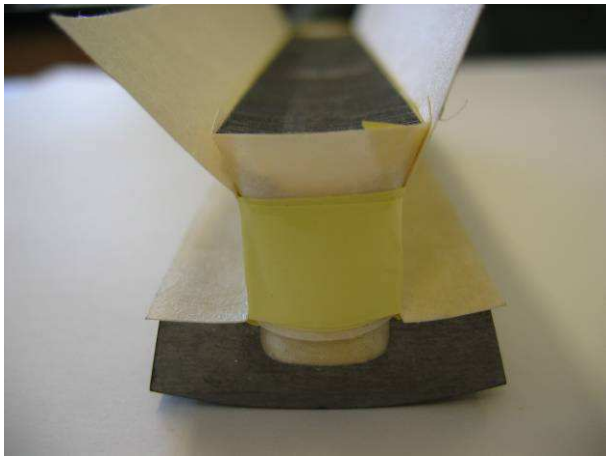

Figure 59 Stator tooth piece covered with slot liner against winding to lamination shorts

A small plastic piece cut to the shape of the stator tooth is glued to both ends of the stator and can be seen in Figure 59. This is to ease the winding operation and also to protect the windings against the sharp edges of stator laminations. The windings were hand-wound using the arrangement pictured in Figure 60.

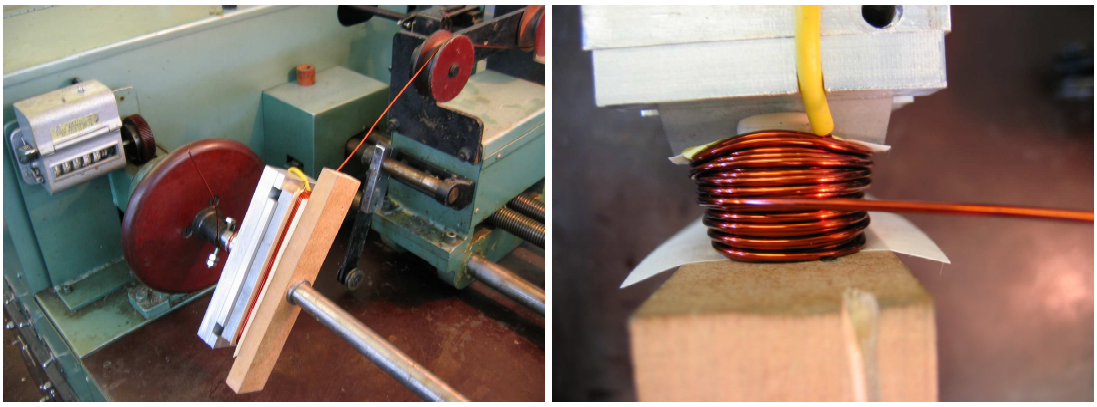

Figure 60 Manual winding of the stator pieces

Another jig (Figure 61) was used to press the bulging windings from both sides. Once tightly placed inside this jig, the bonding of the wires (Figure 62) was achieved by applying energising the coil. The temperature of the wires was raised within 30-60 seconds to about 230^{o}C and kept at this temperature for about 2-3 minutes. The final form of a stator tooth after winding and curing is pictured in Figure 63.

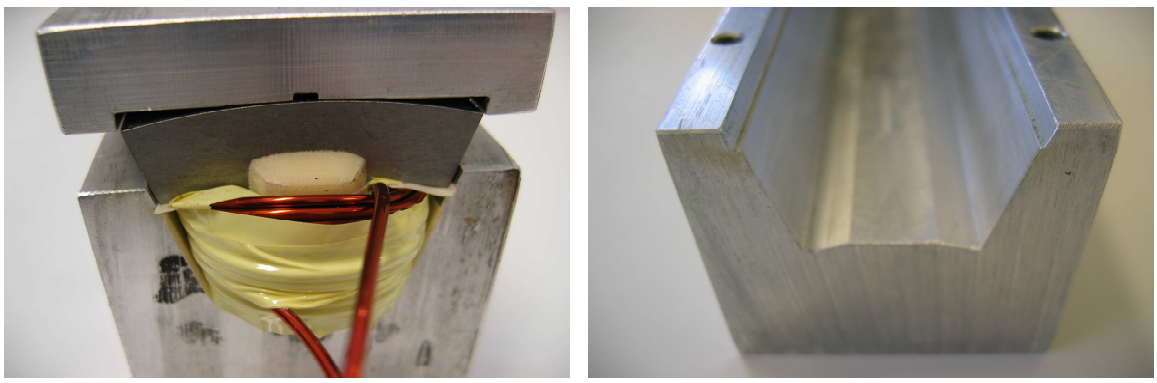

Figure 61 Jig used to press the bulging windings and make them ready for bonding

Figure 62 Bonding of wires through applying a current surge

Figure 63 Stator tooth with bonded windings

Once 12 teeth were wound they were glued and shrink fitted into the aluminium frame of the machine, pictured in Figure 64. Finally both ends of each coil were brought out of the frame to allow full flexibility in the way the coils could be connected together (e.g. series, parallel, series and parallel).

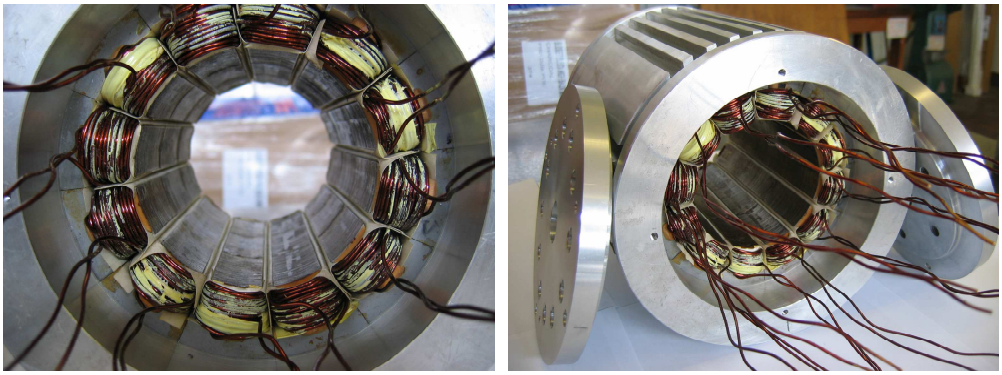

Figure 64 Frame and stator assembly - each coil connection brought out to have full flexibility in connection

5.2.3 Rotor Construction

The rotor construction process was the same as the one used for prototyping the three phase segmental designs [12, 23]. The segment laminations were mounted on a steel shaft, which was non-magnetic. Having a non-magnetic steel shaft ensures that there is no magnetic flux path formed between the rotor segments that can affect the flux-linkage characteristics and hence the performance of the motor adversely. Circumferential location was achieved by using flat bottoms on the rotor segment laminations. Radial retention of the rotor segments was achieved by non-magnetic steel wedges, which were dovetailed into protrusions at the bottom of each segment, and then bolted on to the rotor shaft. The construction process is shown pictorially in Figure 65 and the final form of the rotor after assembling and machining is given in Figure 66. For the same inner and outer machine dimensions and approximately the same output torque, dovetailing rotor segments in [12] allowed safe operation up to a speed of 6000 rpm.

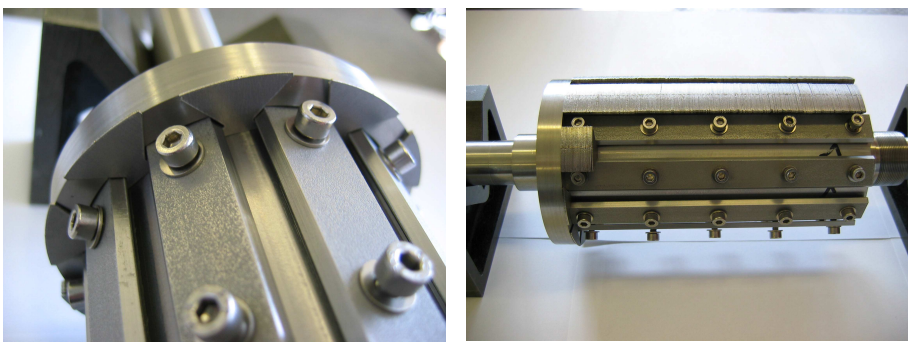

Figure 65 Construction of the segmented rotor of the prototype 6-phase 12-10 SR machine

Figure 66 Finished and machined segmented rotor assembly of the prototype 6-phase 12-10 SR machine

This rotor design is also used successfully in [136] as an alternative to Pollock's flux switching machine.

5.3 TEST RIG DESCRIPTION

The test rig used for the prototype 6-phase segmented rotor SRM comprises the following main components:

- Segmented rotor SRM.
- High voltage power converter.
- DSP based control electronics.
- Mechanical load.
- Host PC and DSP emulator.

A schematic representation of the test rig is illustrated in Figure 67. This section briefly discusses the main parts of the drive system along with the auxiliary equipments used for measurements and protection.

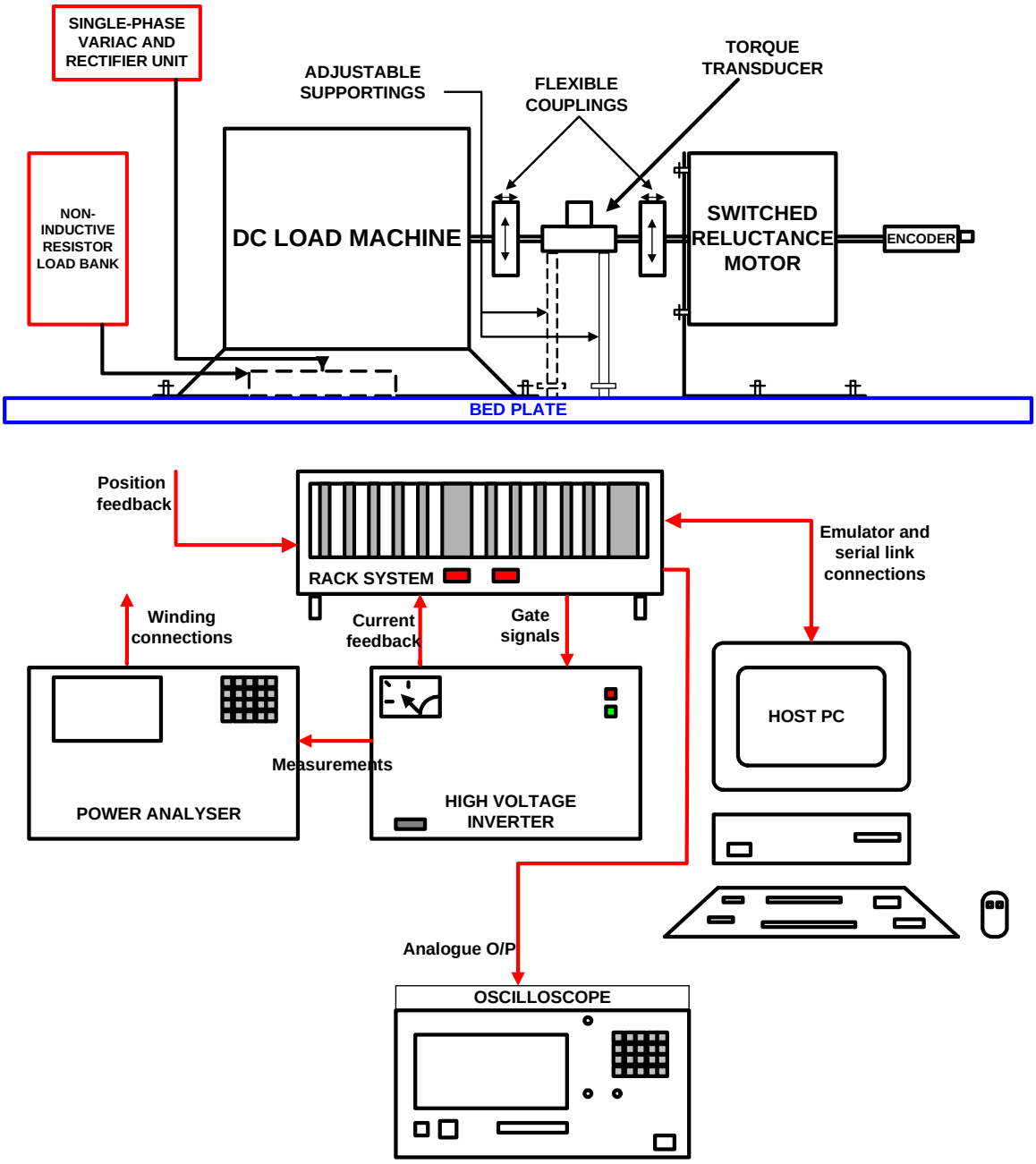

Figure 67 Schematic representation of the test rig

5.3.1 Load Arrangement

Throughout this work a separately excited, brushed DC machine was used as the load machine in parallel with a non-inductive load bank as the load system to test the prototype machines. The load torque could be adjusted via the armature current or by changing the stator electric field. The armature was connected via a load bank connected in parallel with the DC machine; the field excitation was supplied via a variable single-phase

transformer and a rectifier. Figure 68 shows the schematic layout of the load arrangement. A torque transducer capable of measuring rated torque up to 50 Nm was used to measure the torque output of the electrical machine. To monitor the voltage, current and torque waveforms 2-channel oscilloscopes were used. Finally for power flow measurements a power analyser was used as part of the test rig.

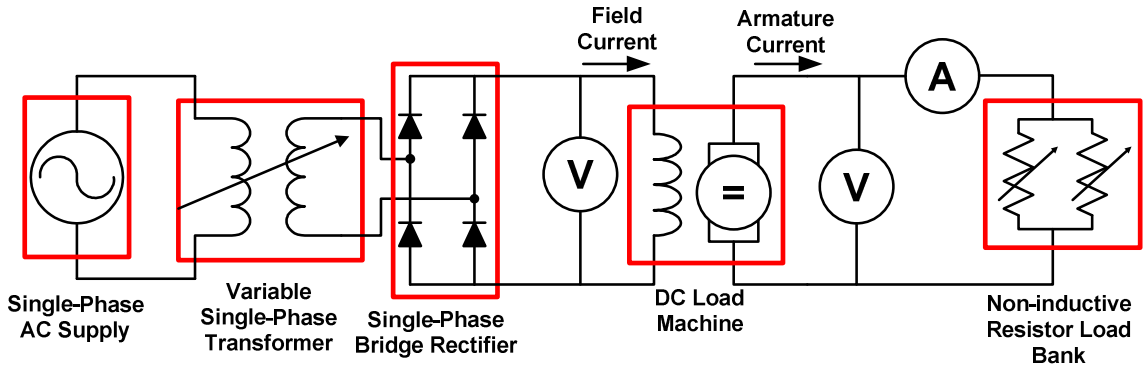

Figure 68 Schematic description of the load arrangement – dc machine with a resistive load bank connected in parallel

5.3.2 High Voltage Power Converter

The electrical power converter consisted of an input rectifier, a dc link filter, a dc link dump and inverter bridges (Figure 69). The input voltage to the power converter was supplied via a three-phase variac connected to the input of the converter. The three-phase variac was effectively used to adjust the level of dc-link voltage. A simple three-phase diode bridge was used to rectify the three-phase supply and to provide the dc-link voltage. Each leg of the rectifier consisted of a single-phase diode bridge, with diodes connected in pairs and in parallel, thus increasing the current rating of the device.

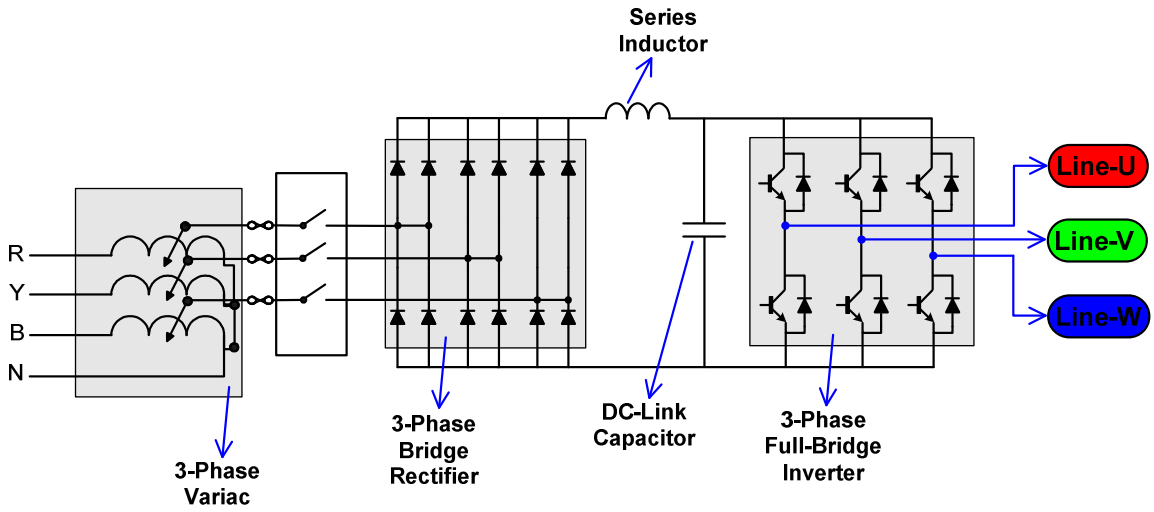

Figure 69 Electric power converter

A series inductor was used to limit the inrush current and to improve the line current form factor. In conjunction with the dc-link capacitor, the inductor formed the dc-link filter, which reduced voltage and current ripple. The main functions of the dc-link capacitor were to act as an energy storage reservoir and to present low supply impedance to the inverter bridges.

Diodes (phase diodes) were connected in series with phase windings to eliminate bi-polar phase currents. These diodes were mounted in an aluminium box near the motor end of the drive system. The connections were then taken out of this metal box (terminal box - Figure 70) to have flexibility in connecting the phase windings. As mentioned earlier both ends of all machine coils were brought out to have full flexibility in connecting the phase windings (Figure 71).

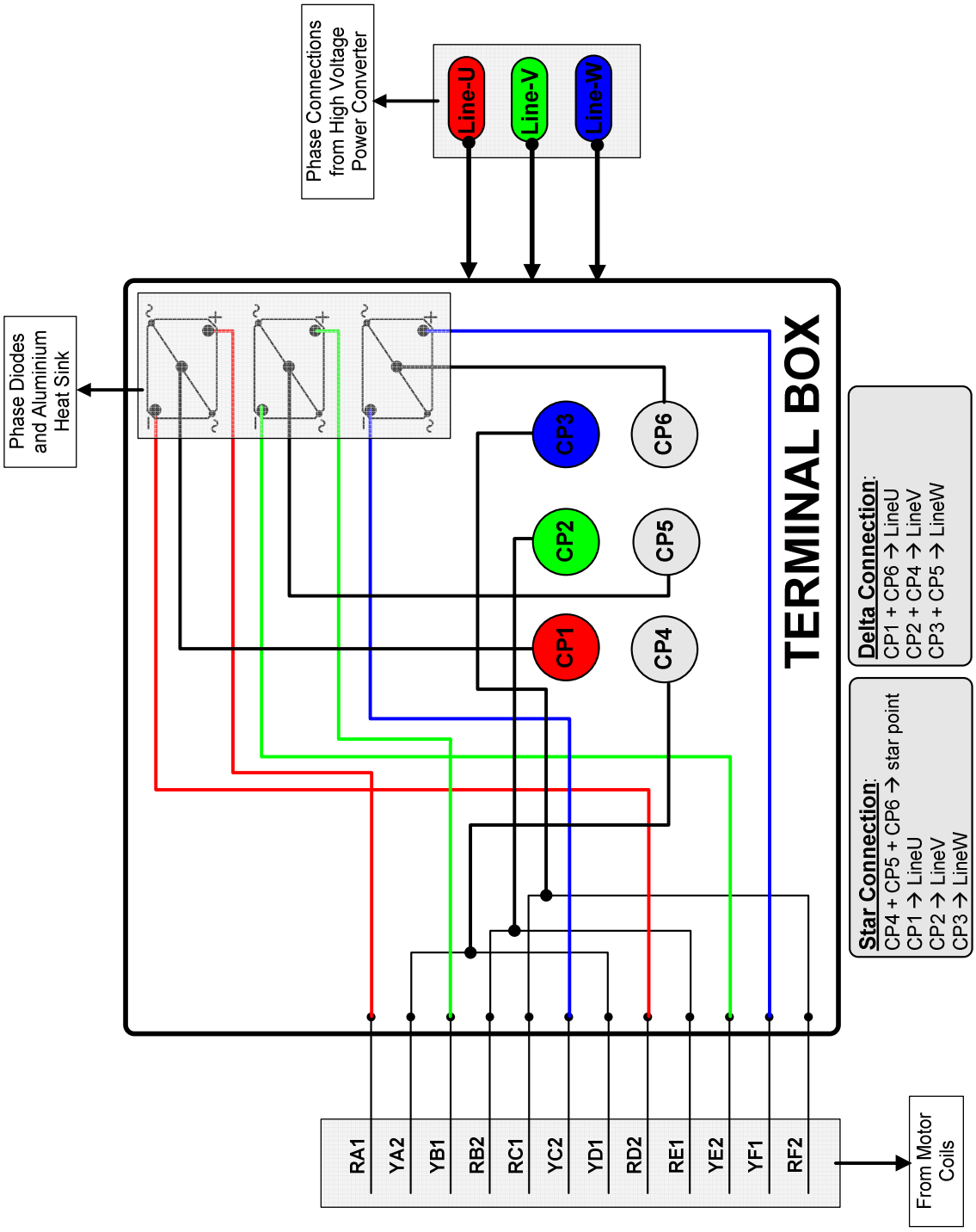

Figure 70 Terminal box connections - phase diodes are mounted on an aluminium sheet in this box and all coil connections are brought inside this box

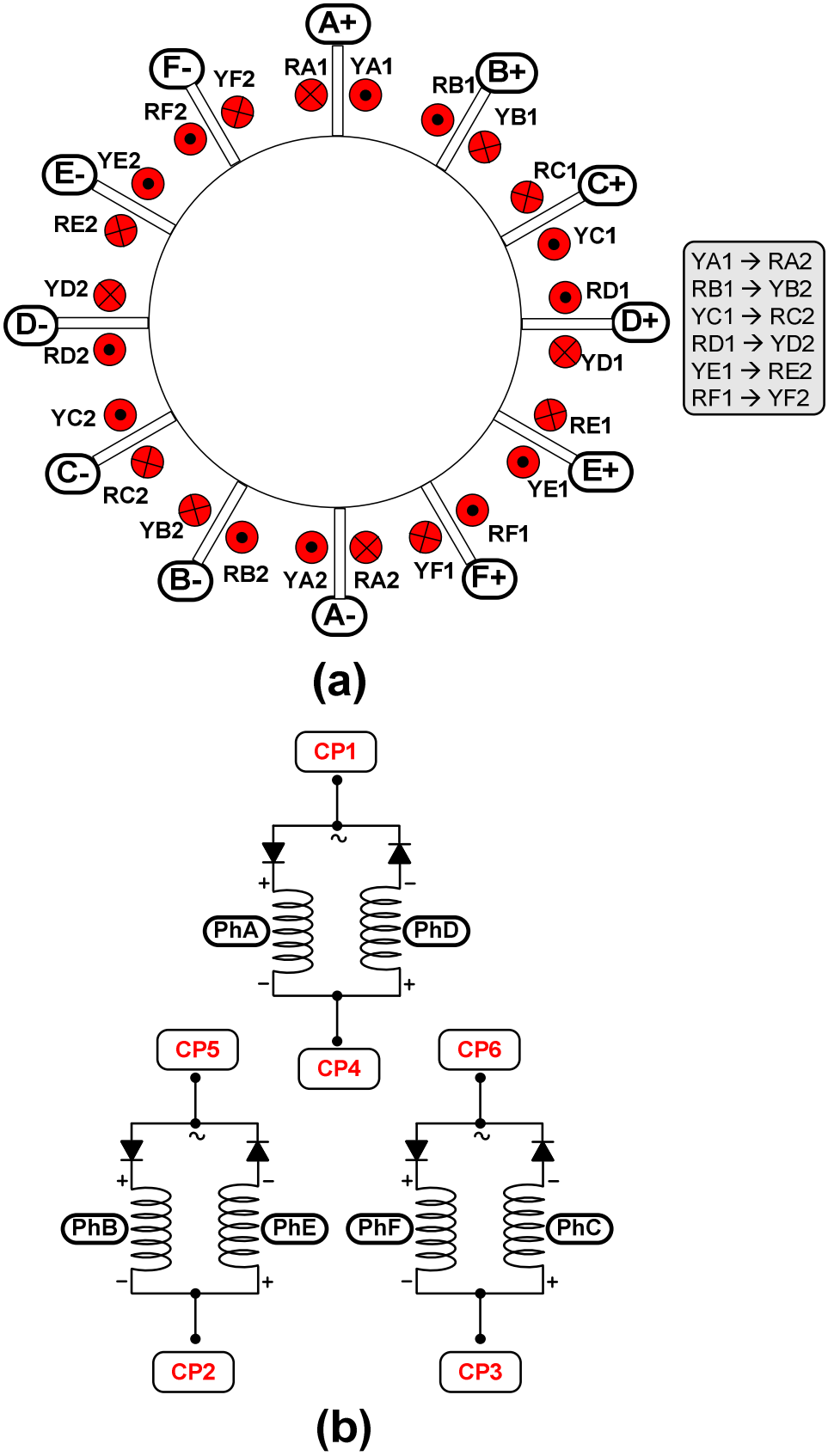

Figure 71 Phase connections – see Figure 70 in relation to some of the labelling

5.3.3 Control Electronics

Control was centred on the Texas Instruments TMS320C31 DSP. This was a 32-bit floating point processor operating at 40MHz. Other major parts of the control electronics were the analogue/digital input card, the power device control card, over-current and over-voltage monitoring cards and the analogue output card. All cards were produced by previous research projects [89, 165]. The cards communicated via a 2x32 backplane and were mounted in a 19” rack cabinet, with connections to the host PC, speed encoder and power converter. Each card was mapped to the main control software as memory blocks in the DSP. The host computer was used for storing files and writing, compiling and downloading programs to the control electronics. A serial connection to the DSP allowed for data to be transferred from the DSP to the PC.

Rotor position was measured using a 12-bit gray code output absolute encoder. Gray code output of the encoder was decoded into binary format with a look-up table within the control software.

The controller DSP was supported by a Field Programmable Gate Array (FPGA) based PWM card. The PWM card was capable of controlling up to 6 pairs of devices independently with PWM frequencies of up to 40 kHz. PWM control parameters such as triangular waveform resolution, dead-time, etc. were all software programmable. The PWM card was also able to produce a synchronisation pulse once per PWM cycle to allow the phase currents to be sampled at the correct instants. Schematic explanation of the parts of the control electronics is given in Figure 72.

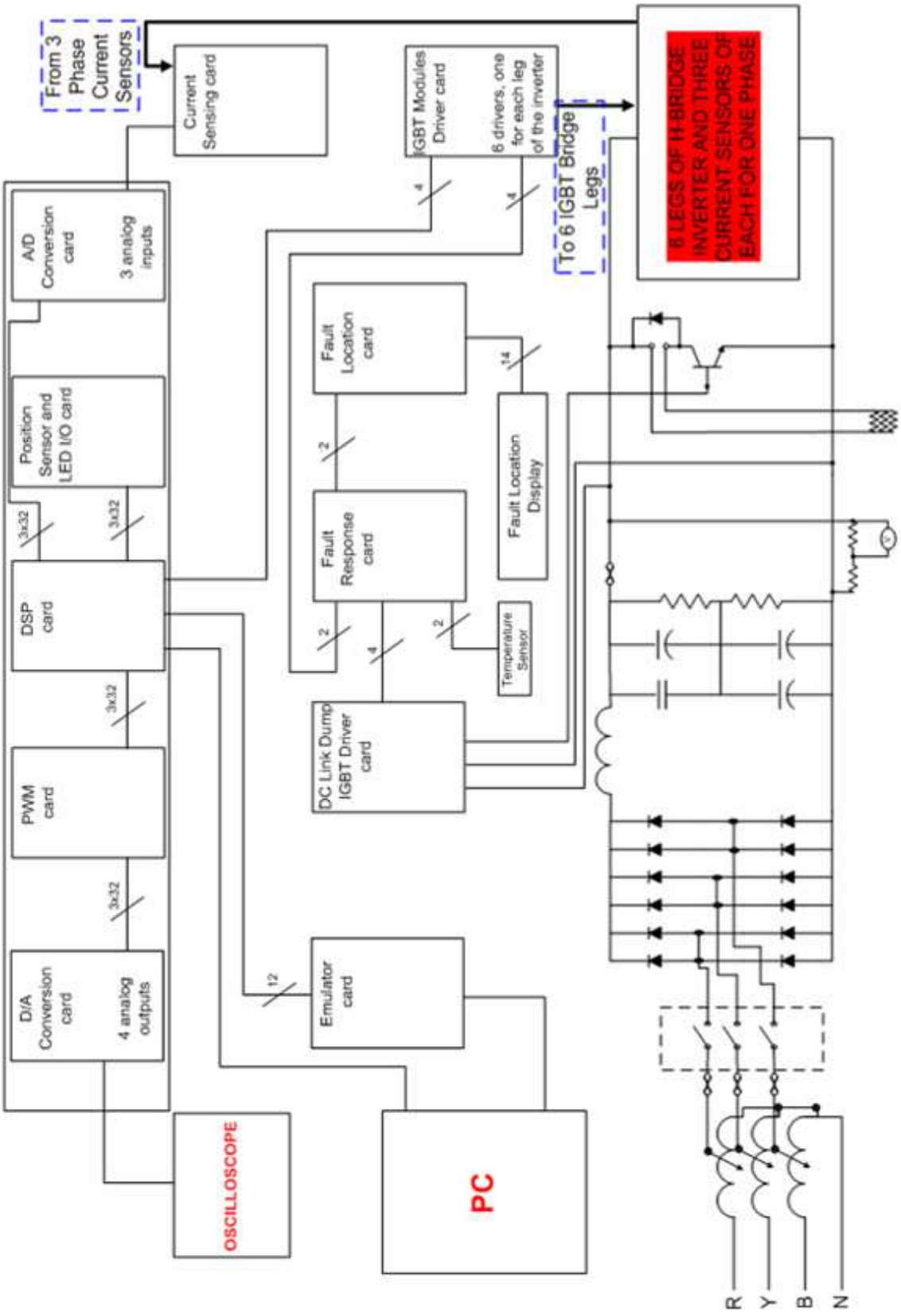

Figure 72 Control electronics

Three analogue-to-digital conversion (ADC) cards were used to transform the three-phase current signals into 10-bit digital code. A Matlab based GUI (Graphical User Interface) was created to set control variables such as current demand, PID controller gains, and conduction and advance angles.

Three single and one multiple output digital-to-analogue conversion (DAC) cards were used to output and monitor signals such as phase current, torque, and flux. Other cards were: the LED display variable input or output card, the speed encoder card and the power supply card.

An over-current and over-voltage monitor card worked in parallel with the over-current and over-voltage detection circuits and were used to protect the system by forcing the gate commands inactive, and thus forcing some or all of the power devices to turn off. Over-current detection was achieved by monitoring the analogue output of each current transducer and continuously comparing it to a threshold value. A similar comparison was made on the DC link voltage to check for over-voltage conditions caused by excessive regenerative braking of the machine during test.

5.3.4 Drive Software Explanation

French [166], Clothier [89] and Weiner [137] have all previously contributed to the programming work of the test-rig. The whole control system was synchronised to the triangle wave on the PWM card, with synchronisation pulses sent out at the peak of every triangular wave to initiate the first current control loop in the DSP. The function of this loop was to sample the encoder position and determine the phase current demands. The second control loop was the one that actually contained the PID current control. This was initiated internally in the DSP by a software timer, which in turn was set by the hardware interrupt supplied by the synchronisation pulse. This software timer also output a hardware pulse to the ADC cards that initiated the sampling of currents at this point. The current error(s) could then be calculated, and voltage references generated via the PID gains. Finally these references were sent to the PWM controller card and were implemented there at the next synchronisation pulse [89].

The drive system software required the initial unaligned position of the machine. To determine the initial rotor position for the 6-phase 12-10 machine a pair of phases were energised when the machine was stationary. The DSP was used to output the rotor

position in digits. (between 0 and 4096 (12 bits) for a 12-10 machine). This initial unaligned position in digits was then entered into the relevant part of the control software. During operation, the position information was read by the 12-bit gray-code encoder. The encoder reading then went through a look-up table where the gray-code was converted into binary. Depending on the initial position value, the number of phases, advance angle and the rotor position, the software decided which pair of phases needed to conduct. Each line current was controlled separately and each had its own PID reference voltage and control routine. Once the pair of phases which needed conducting was determined, each line current demand was defined and with the user-defined PID gains and measured line current values, line reference voltages were generated based on each line current error. These reference voltages (with 8-bit resolution) were then written to the PWM card where they were compared with an 8-bit 20kHz reference triangular waveform. Depending on the outcome of this comparison MOSFET gate signals were generated and sent to the relevant MOSFET modules. This process is explained schematically in Figure 73. The phases of the 12-10 machine go through energisation, freewheeling and de-fluxing cycles 10 times in each mechanical cycle.

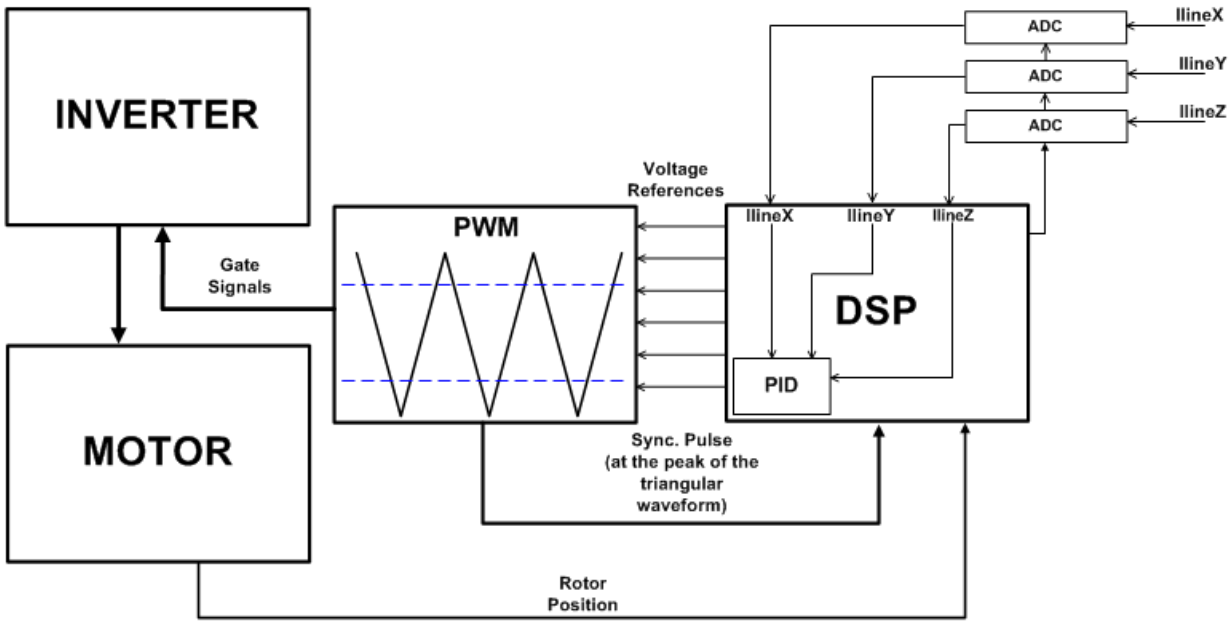

Figure 73 Implementation of current control with the drive software

5.3.5 Prototype Testing

This section discusses the static magnetic and thermal characterisation of the prototype 6-phase segmented rotor SRM.

5.3.5.1 Flux-Linkage Measurements

Flux-linkage is the product of magnetic flux (φ) and the number of turns (N) linked by that flux and is used as a key factor in determining the physical characteristics of any machine, such as the torque capability. The flux-linkage characteristics of a machine also play an important part during control system development (flux control, current shaping for low torque ripple operation, etc.) and validating the performance of simulation tools. It is thus important to obtain a full set of accurate flux-linkage characteristics. Measured flux-linkage characteristics can also be used for verifying the machine design process. The prototype motor has 12 stator teeth and 10 rotor segments. Therefore one electrical cycle lasts 36^o mechanical and complete characteristics of the motor can be obtained by taking measurements within this range. Flux-linkage measurements in this work are based on the "Volt-Seconds" method, where stator flux linkage is calculated from voltage and current measurements on the phase winding circuit [154]. This can be achieved simply by applying a voltage source to the phase winding, after which the corresponding instantaneous terminal voltage $v(t)$ and instantaneous current $i(t)$ measurements are taken. The instantaneous flux linkage $\psi(t)$ can then be calculated by Equation 9.

$$\psi(t) = \int_0^t (v(t) - i(t)R)dt + \psi_0 \qquad \textbf{Equation 9}$$

where R is the measured resistance of the phase windings and ψ_0 represents the initial flux linkage. The initial value of the flux-linkage ψ_0 is very significant only in electromagnetic circuits containing remnant fluxes, such as permanent magnets. In the case of an SRM, this initial value is 0 as there is no magnetic flux in the steady state when no current is applied.

A GUI has been created to assist with the calculation of the flux-linkage characteristics of the prototype motor from captured voltage and current scope traces. Details of the operation of the "Flux-Linkage Viewer" GUI are given in the Appendix A. A full set of magnetisation curves for the prototype 6-phase segmented rotor SRM is given in Figure 74.

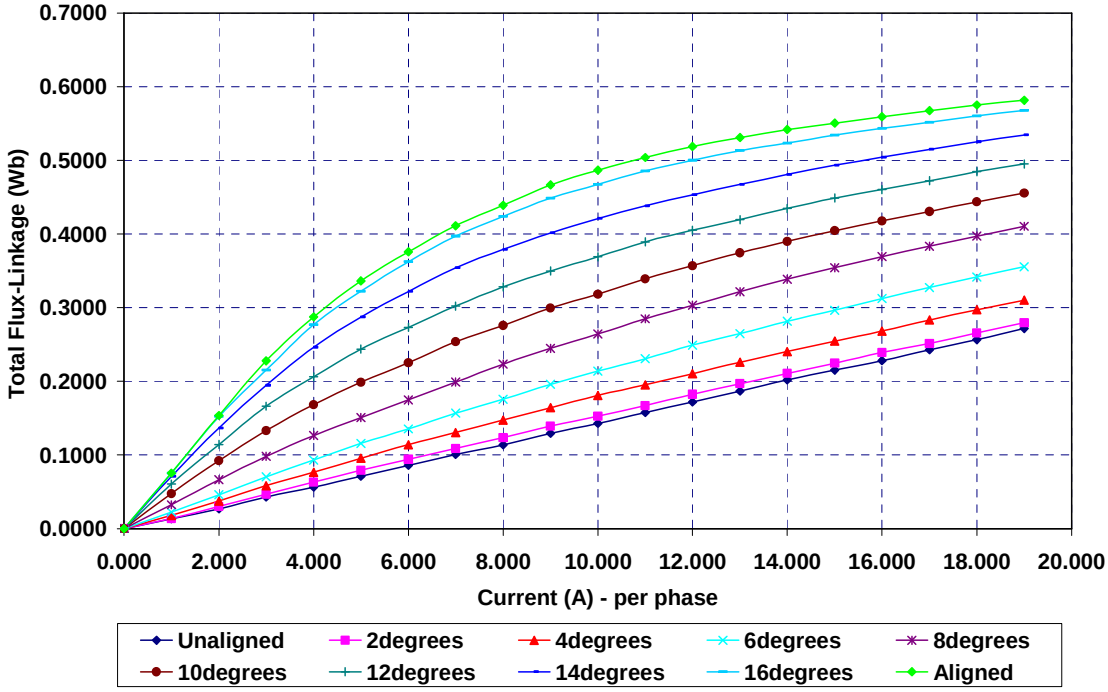

Figure 74 Measured flux-linkage curves for the prototype 6-phase 12-10 segmented rotor SRM (Mk3 design) with two phases excited at the same time. Each curve is at a constant position, running from unaligned to aligned in 2.0 degree steps

Comparison of the aligned and unaligned magnetisation curves obtained from measurements to those predicted in two-dimensional FE analysis is given in Figure 75. The differences between the two sets of flux-linkage results are believed to be due to the following reasons:

- The unaligned inductance is higher in reality due to the end winding leakage effects. When the rotor is at or near the unaligned position the inductance can increase by 20-30% due to *fringing* of magnetic flux in the axial direction. Unfortunately 2D FE analysis cannot take this into account and results in underestimation of the magnetisation curve at the unaligned position.

- The inductance in the unsaturated section of the aligned curve is higher than predicted. This is thought to be due to the air gap being smaller than the desired value of 0.3mm. This can be explained by the nature of building the machine. It is believed that the wire erosion process that was used to form the geometry of the lamination, the machining process to achieve the correct stator and rotor bore diameters and the method of locating the rotor within the stator all have an effect on having an air-gap other than the desired value of 0.3mm.

- There is a difference between the measured and theoretical results in the region of saturation of the teeth and the core back in the aligned magnetisation curve. In this case the measured results are lower. This can be attributed to two factors. One is that the achieved lamination packing factor is different to the one assumed in the FE analysis and the other is that the BH characteristics of the core material in the FEA package has finite amount of error, especially in the saturation region.

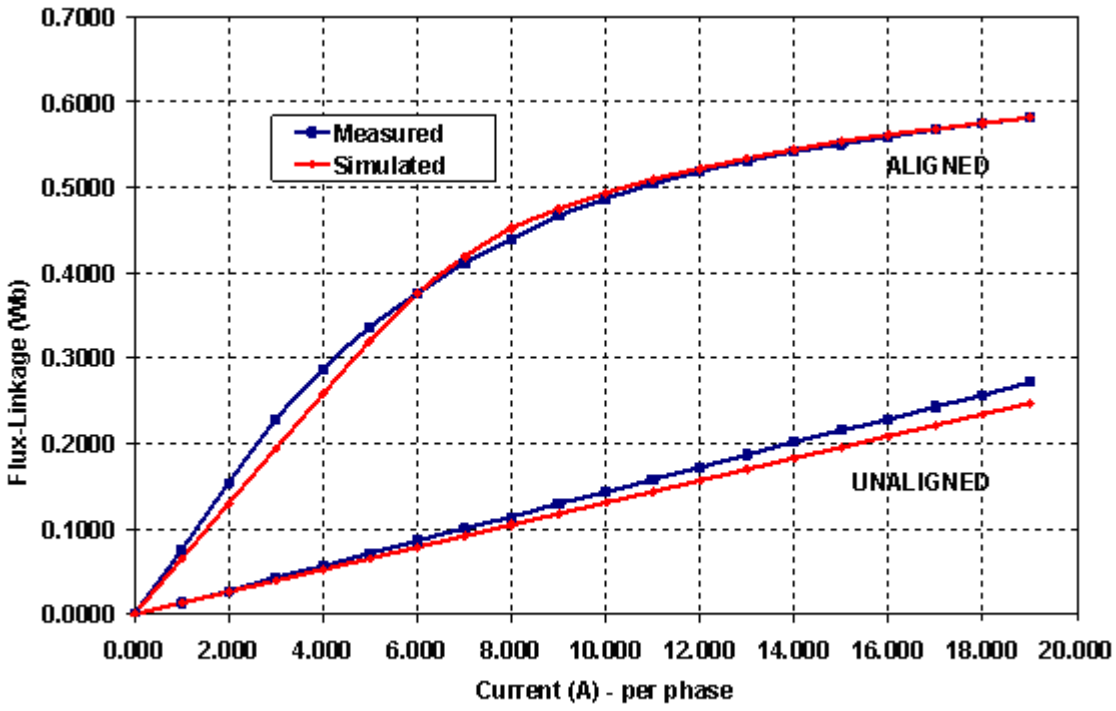

Figure 75 Comparison of 2D FE predicted aligned and unaligned magnetisation curves with those of measurements

5.3.5.2 Static Torque Measurements

Torque characterisation for an SRM can be achieved either indirectly by using other measured motor parameters or directly by using torque transducers as torque sensing elements. The former method exploits the close relationship between the flux-linkage, co-energy and torque characteristics of an SRM. Knowing that torque is a function of co-energy, which is in turn a function of flux linkage, it is possible to derive the torque characteristics from the flux linkage characteristics. However, such indirect torque characterisation methods can be inaccurate in nature due to errors that arise in the methods in which the flux-linkage is obtained. This can be experimental or through mathematical calculations using Finite Element Analysis (FEA) tools. Even though the errors in flux-linkage data are low, these will be accumulated and further amplified onto the calculated torque characteristics when integration and differentiation are performed on the flux-linkage data. Direct measurement techniques do not have errors introduced by mathematical calculation or approximation. By attaching various sensors to the SRM and performing measurements at different operating points, it is possible to collect torque, current, and rotor angle data and form the torque characteristics of an SRM. Of course, direct measurements will have measurement errors. However, these can be kept to a minimum by careful consideration of the test set-up and measurements taken.

Windings of two phases of the prototype machine were connected in series and excited simultaneously. The rotor angle was varied between the unaligned and the aligned positions for a number of excitation levels, and the torques measured with a torque transducer coupled to the shaft of the motor. The DSP and the position encoder were once again used to continuously monitor the rotor position. Using the flux-linkage characteristics produced by the FE method, torque-position characteristics are predicted and a comparison made between the predicted and measured results. This is shown in Figure 76. It can be seen that there is a good correlation between measured and predicted static torque curves. Full static torque characteristics are given in Figure 77.

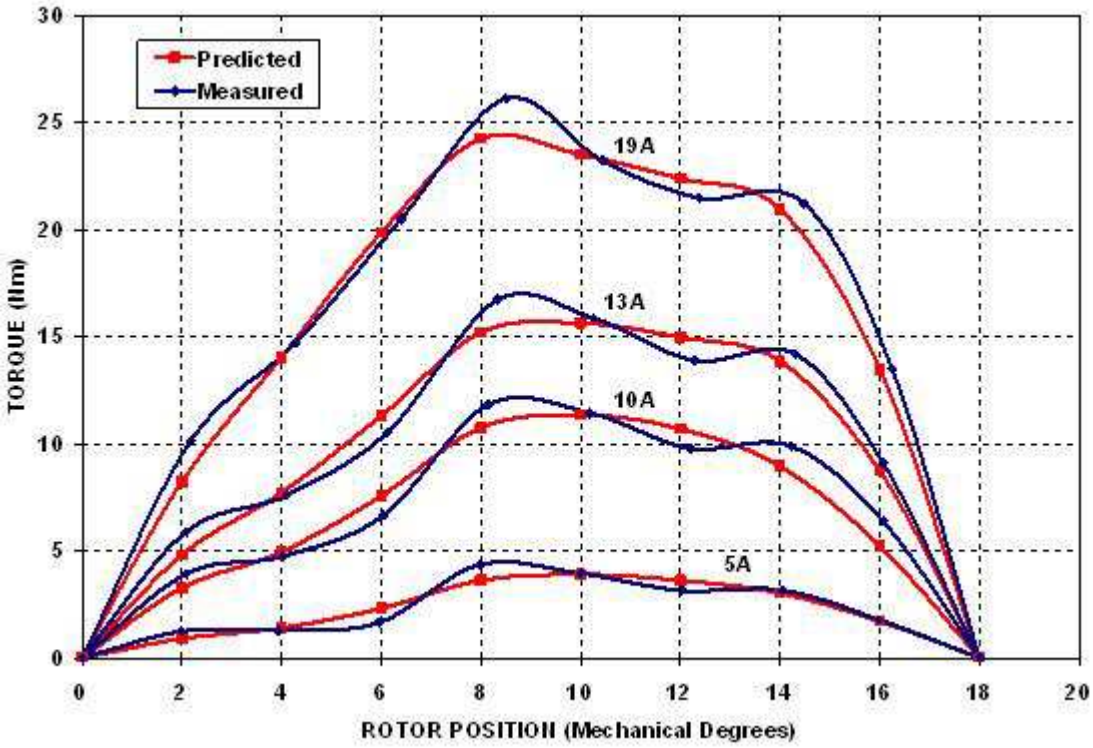

Figure 76 Measured vs. predicted static torque characteristics of the prototype 6-phase segmented rotor SRM at various excitation levels

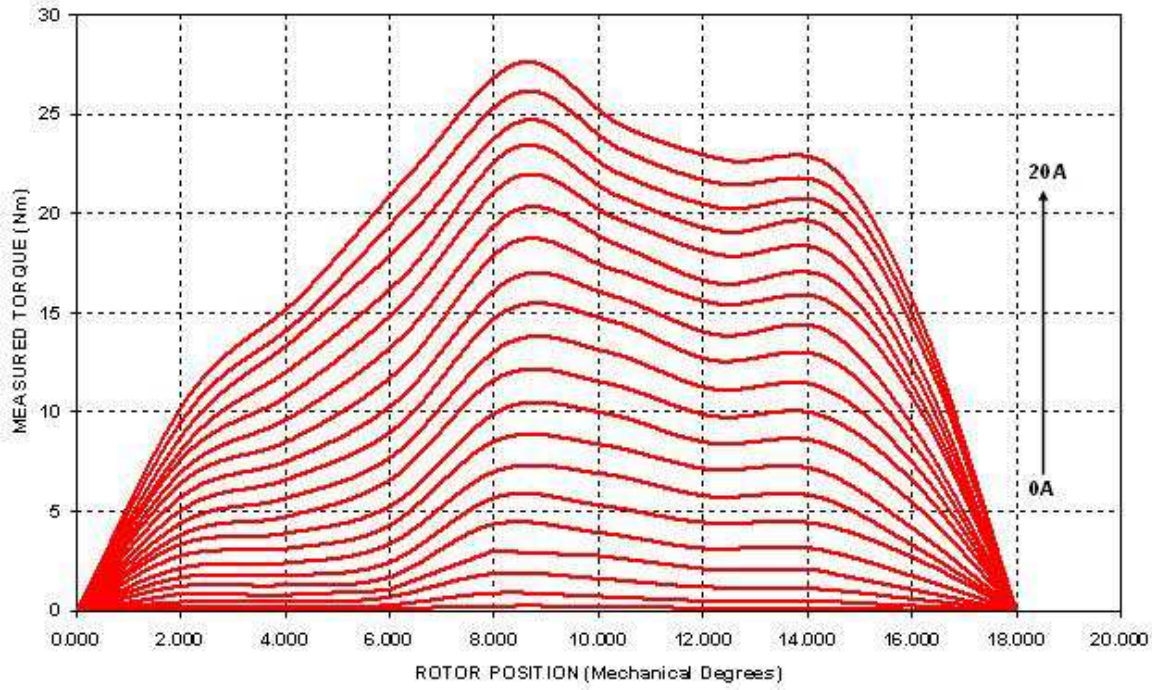

Figure 77 Measured static torque characteristics of the prototype 6-phase segmented rotor SRM up to 20A of excitation

5.3.5.3 Thermal Characterisation of the Prototype Machine

Lastly, the thermal characteristics of the machine have been determined. A temperature probe was placed on the frame of the machine and another one was embedded within the phase windings. A DC power supply was used in constant current mode and the current was set to 6.5A. All six phases were connected in series. Power was injected into the machine for ninety minutes. The motor was subjected to forced-cooling with a fan. Temperatures on two probes as well as applied voltage and current were recorded with a data logger connected to serial port of a PC. The machine exhibited two thermal time constants: one of approximately thirty minutes associated with the bulk heating of the entire machine and frame and accounting for 28% of the steady-state temperature rise, and one of approximately five minutes associated with heating of the winding and accounting for 72% of the temperature rise. Based on the results it was determined that 100 degrees centigrade rise in winding temperature corresponded to approximately 459W loss and an RMS current of 13.6A.

Accuracy of the thermal time constants derived from measurements can be observed in Figure 78, where the lumped parameter curves are superimposed on top of the measured results.

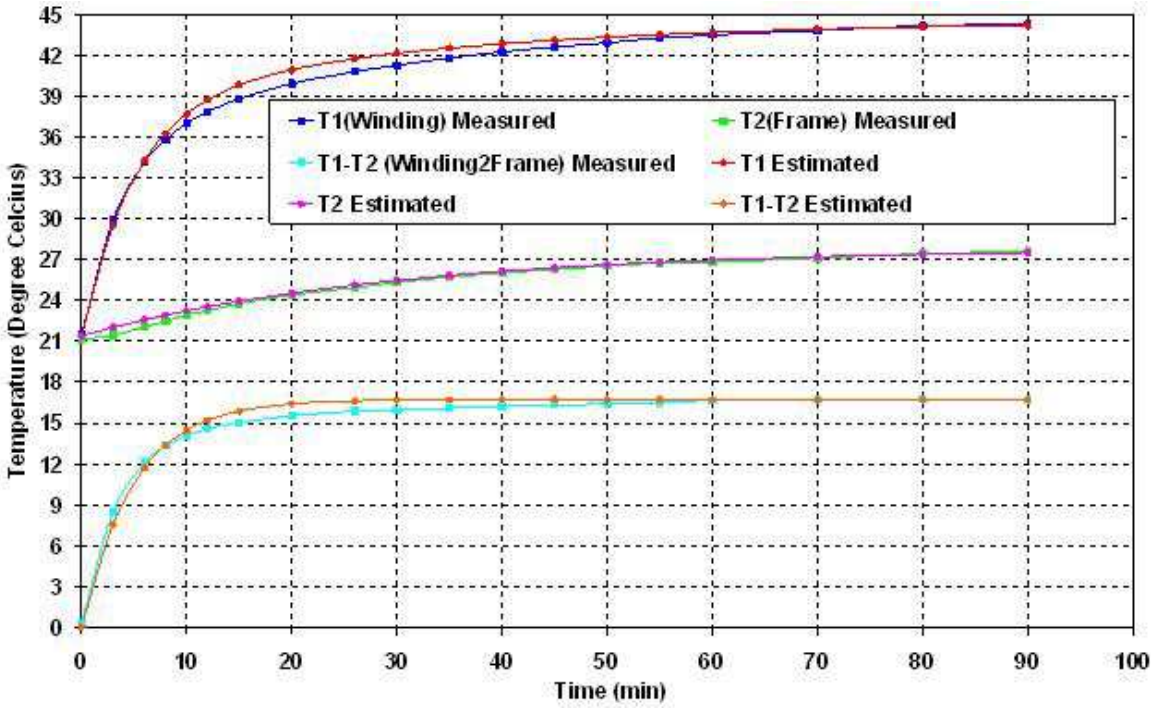

Figure 78 Measured and predicted temperature measurements of the windings and the machine frame

5.4 SUMMARY

Construction of the prototype segmental rotor 6-phase machine has been explained. The stator of the prototype was built from separate cores in order to increase the slot fill factor of the machine; a fill factor of approximately 0.5 has been achieved. The fill factor could be further improved if the bulging and curving of the conductors could be controlled in a better way. It is believed that with designs where thin conductors are required and the machine design has a short stack length the fill factor can be improved to values above 0.6.

The components of the test rig including the control software have been briefly described. The segmental rotor machine has been built and the static flux-linkage and torque measurements have been verified against those predicted using 2D FE analysis. The themal characteristics of the prototype machine have also been determined and presented in this chapter.

CHAPTER 6

6– Simulation Models

6.1 INTRODUCTION

In conjunction with finite element analysis, simulating a drive system is highly desirable as it permits going through many different design variations such as machine geometries, inverter topologies and excitation patterns without having to physically construct and test all of them. A simulation with high results accuracy and short simulation time is ideal. In many cases though, there is a compromise between the accuracy and the simulation time. Although every effort is made to achieve a fast simulation, the accuracy of the simulation has been the main motive for this PhD project. A simulation which is accurate enough to predict the experimental results will help in:

- Eliminating lengthy experimental procedures.
- Shortening the product development process.
- Determining the optimal system design (including the machine, electronics and the controller) easily by allowing the assessment of the system behaviour in response to design modifications such as controller resolution, machine number of turns, combinations of control angles (advance and total conduction angles), etc.
- Reducing the risks associated with prototyping.

The simulation can be divided into distinct sections:

1. Input stage (rectifier and filtering)

2. Controller stage
3. Converter stage
4. Machine stage (including the mechanical system)

In this PhD the simulation work was focussed on the controller, converter and machine modelling.

Simulation of an SRM can be developed with a low level programming language such as FORTRAN or C/C++. However any additional module requirement will lengthen the model development greatly. Spice, VisSim, MathCad, and MATLAB® / Simulink® are other likely candidates to simulate an electrical machine drive system. Spice has the disadvantage of being biased towards electronics simulation. MATLAB® is a matrix based programming and simulation environment. It is very flexible and offers different solver options and has the ability to work with large data sets. These features make MATLAB® a strong candidate for electrical drive system simulation.

The simulation package introduced here is developed in the MATLAB® / Simulink® environment. The main part of the simulation is realised in Simulink® supported by scripting in MATLAB® m-file format. A Graphical User Interface (GUI) was also generated to ease the interaction between the user and the simulation models. Simulink® is an environment where mathematical models of systems are represented with a customisable set of block libraries connected together that establish mathematical relationships between the blocks (based on the mathematical model of the system), simulating and testing a wide variety of time-varying systems. Creating a simulation model is as simple as dragging and dropping the necessary blocks from the library browser of Simulink® onto the graphical editor and connecting them with lines. Simulink® is integrated with Matlab®, providing immediate access to an extensive range of tools for algorithm development, analysis and creating batch processing scripts to run simulations back to back. As mentioned earlier, Simulink® provides different solvers (computing the system dynamics over time using information contained in the model) to support the simulation of a broad range of systems, including continuous-time (analog), discrete-time (digital), hybrid (mixed-signal), and multi-rate systems of any size. Both fixed step size and variable step size simulations are possible in a Simulink® based simulation.

6.2 SRM MODELLING and SIMULATION

6.2.1 Background

In contrast with other electrical machines, SRMs operate in high saturation with a strongly non-linear current-flux relationship. Therefore the classical equivalent circuit representations usually applied to the modelling of electrical machines cannot be easily employed to SRMs as the inductance of the circuit is highly dependant on the rotor position and the phase current. When modelling short-pitched winding SRMs, the current in any one phase almost always falls to zero within an electrical cycle. Because this current is the only source of flux for that phase, the phase flux also falls to zero when the phase current falls to zero. The states are known at the start and at the end of any electrical cycle. Thus each electrical cycle can be viewed in isolation. This makes the simulation of short-pitched SRMs particularly simple, as the initial conditions of phase flux and phase current are known at the start of fluxing any phase of the machine. This eliminates the need for long transient simulation. Unfortunately, the same does not apply to SRMs with mutually coupled phase windings. There are still periods of zero phase current. However, due to mutual coupling, the flux in any one phase is a function of currents in all other phases [91]. Therefore a phase with no current flowing in its windings does not necessarily have zero flux linking them as well. Thus, at the start of each cycle, the initial conditions are unknown and a number of cycles are needed until steady-state operation is reached. Although when compared to simple short-pitched SRMs this might seem as a nuisance, compared to other machine types it is not. For brushless DC machines the initial conditions are usually unknown. As a result, a number of cycles of simulation are needed in order to evaluate the performance under steady-state conditions.

6.2.2 Review of SRM Simulation Methods

6.2.2.1 Early Work

In this section some of the early work relating to the modelling and simulation of SR machines and drives is presented. Methods for the performance prediction of both short-pitched and fully pitched winding SRMs have been extensively developed over the past two decades. Many methods have been proposed for modelling the torque-current relationship of SRMs. Almost all of the early work relating to SRMs in general came from Stephenson, Lawrenson and their colleagues in Leeds University. Work in [18, 167, 168] can all be seen as seminal examples defining the way for modelling and ultimately simulation of SR machines and drives. Studying the motor's magnetic property is essential for accurate modelling and control of an SRM. Generally speaking, if the aim is to assess the motor performance, rather than the performance of an individual converter topology and the associated controller, then the simulation is aimed at accurate modelling of the motor magnetic characteristics with a simple but accurate modelling of the controller.

Real-time simulations of SRMs are given in [169 and 170]. The model in [170] takes the magnetic non-linearity of the SRM into account. However, the magnetisation curves were approximated by polynomial functions. In this paper, the authors first obtained the magnetisation curves from FE analysis and then approximated these curves with polynomial functions in their Spice simulation. Moreover, only a single example was given to compare phase current and voltage waveforms of the simulation and real-life measurements. In [171] the SABER simulation package has been used to generate a non-linear model of an SR drive system with an asymmetric half bridge inverter. The effects of magnetic saturation, the results on motor performance with typical changes in supply voltage, winding turns and switching angles were presented for a particular 2-stator-pole / 2-rotor-pole motor. With the use of SABER, Pollock et al [171] were able to account for dynamic properties of devices such as voltage spikes, high frequency oscillatory features caused by reverse recovery and stray capacitance. The claim was the ability to rapidly change the control strategies and try different circuit topologies and assess their effect on motor performance in SABER.

In [172] Pulle claims to have improved the method described by Stephenson and Corda with the use of cubic splines. The method aims to represent the magnetisation curves of

an SRM with the use of cubic splines and deals with fitting segments of a curve representing the flux linkage/current relationship with third order polynomials and matching the first and second derivatives at the knots where the segments meet**.** The generated flux-linkage curves correlate favourably with experimental data and are used to simulate the motor as per the method described by Stephenson and Corda. Radun proposed two separate analytical models based on basic magnetic field laws for computing the magnetisation curves of SRM [173, 174]. In [174] Radun computes the flux-linkage characteristics of SRMs for the aligned position and for the intermediate rotor positions. The model proposed is not empirical and does not require any data from the modelled machine or any FEA results. Radun predicts the unaligned curve of SRM in [173] using the idea introduced in [174]. Even though the methods are analytically straightforward and easy to implement with a computer program the methods do not provide a unified theory of predicting the flux-linkage characteristics of SRMs. It requires two different methods to generate the full set of magnetisation curves of SRMs.

Torrey *et al* [175, 176] focused on finding an analytical expression for the flux-linkage / current / position data which would provide all of the flux-linkage-current information for every rotor position in one summary equation. They derived a single equation to embody the flux-linkage characteristics of an SRM and used the Fourier cosine series to represent the coefficients of the equation. Although they achieved good curve fittings, the method of representing the fitting coefficients introduced higher order harmonics that added ripple to the predicted instantaneous torque production because of their rapid spatial variation.

Miller *et al* [177] introduced an interesting method for the modelling and design of SRMs. Their aim was to reduce the computation time substantially and generate a rapid computer aided design at the expense of accuracy. Instead of representing the magnetisation data of the machine by flux-linkage as a function of current, they modelled the SRM by analytical piecewise first or second-order functions of flux-linkage against rotor position with current as an undetermined parameter. The formulation was empirical and the data for position other than the aligned and unaligned positions was found by interpolation. The model forms the basis of the popular PC-SRD program. However, the idea of modelling by the empirical equations presented by Miller *et al* in [177] is not easy to comprehend and incorporate into new methods of modelling SRMs.

Xue *et al* [178] have introduced the application of two-dimensional bi-cubic spline interpolation functions to the modelling and simulation of SRMs. Compared with the other techniques they claimed that the new algorithm has given more accurate results.

None of the above mentioned methods for modelling and simulating the SRMs considered the mutual coupling between phases. Lipo and Moreira [179] argued that the presence of the mutual coupling between phases of a short-pitched winding SRM has significant influence on the open circuit voltage waveform across each phase winding and the turn-off time of the phase current (which would reduce torque and introduce more losses). They also stated that the mutual coupling can also contribute to unwanted conduction during the nominal OFF period of a phase winding, hence, also contributing extra losses together with undesirable torque components. To address the issue, they introduced a coupled circuit model and simulated a four-phase SRM with short-pitched windings. Another example where the mutual coupling between machines was taken into account during the modelling of the machine is given in [180]. Shuyu and Tseng developed their model using a few sets of FE computed phase flux linkage/current/position data under the condition of simultaneous excitation of two neighbouring phases. The combination of piecewise Hermite cubic spline and Fourier series techniques was then used to represent each FE calculated flux linkage data set in the dynamic simulation. The model was implemented in SABER for a 4-phase SRM driven from a split dc-link inverter.

Unlike the short-pitched winding SRM, in a fully pitched winding machine the majority of torque is produced from the variation of mutual inductance with position. This means that the mutual coupling must be modelled very accurately, including the full effects of saturation within these terms. As the flux linkage of any one winding is a non-linear function of rotor position and currents in all phases, machines with fully pitched windings are more difficult to model and study. Mecrow et al [91] proposed transformation matrices to simplify the modelling of fully pitched winding SRMs. They broke down the instantaneous flux-linkages and currents in each phase to give the flux and magneto motive force (MMF) in each tooth of the machine. The flux and MMF could then be linked in the model by a simple look-up table, determined from either simulation or measurement. By having the transformation matrices, simulation of each phase could be de-coupled from the other phases of the machine. Barrass [90] described a simulation model for the fully pitched winding SRM where he utilised the idea of transformation matrices in his simulation model.

Torrey and Xu [181] stated that the approach of Mecrow *et al* to the modelling and simulation of fully pitched SRMs did not lead to a deeper understanding of the fully pitched SRM. They used an FE circuit coupled simulation to eliminate the difficulty of modelling mutually coupled phases of the fully pitched winding machine. They used an FE solver (Flux2D) and a circuit simulator (Simplorer) simultaneously. However, their machine model in FE was solved with a 2D solver ignoring 3D effects. Furthermore, the overall simulation time was increased by the use of circuit-coupled FE simulation as at every time step the simulation ran the FE model.

In [182] Torrey and Kokernak used flux tubes to generate a nonlinear magnetic circuit model for a mutually coupled SRM. The solution was analogous to solving for node potentials in an electric circuit. The model was claimed to be also suitable for conventional short-pitched SRM geometries that required consideration of mutual coupling effects. They added pole tips (that could get saturated) to the model to overcome the difficulties associated with the rotor and stator pole permeances when they exhibit partial overlap. The idea of adding saturable pole tips needs further analysis to make the recommended model suitable for different machine geometries.

Other examples of modelling and simulating the performance of SRMs are: [183] where Liu and Stiebler suggested an analytical model based on per-unit (p.u.) system and [184] where Hossain and Husain presented the development of a simple analytical model of SRMs, which is mostly suitable for real time implementation. In [171] the authors describe how a decision was made to adopt the SABER simulation package for the simulation of switched reluctance motor drives.

6.2.2.2 Recent Work

In this section some of the recent work relating to the modelling and simulation of SR machines and drives is presented. There have been many other simulation methods recently adopted, including neural networks [185-187], genetic algorithms [188] and finite element analysis [189]. In [190] Stephenson et al incorporated iron losses and its effect on the current waveform into the dynamic modelling of the SRM. Mutual coupling between phases due to shared portions of the magnetic circuit and leakage flux was also implemented in their modelling. Finally, [191] is a relatively recent example for use of cubic splines in representing the magnetization characteristics of SRMs.

Use of Matlab® / Simulink® for the realisation of the complete electric drive system simulation is becoming more and more common. Some of the recent examples relating to modelling and simulation of SR drives are [150, 192]. In [150] FE generated magnetic characteristics were used in a Simulink® based dynamic simulation of a super-high-speed 4/2 switched reluctance motor. The simulation was used to assist with maximising the starting torque of the machine. The paper uses static characteristics of the machine in order to predict the behaviour of the machine in (arguably) the most dynamic operating region: start-up. Another example for a Matlab / Simulink based simulation is [193], where magnetisation curves were measured and then stored in look-up tables in the simulation. In this paper, flux-linkage measurements were taken by locking the rotor, applying dc volts to the phase windings and measuring this voltage and the resulting phase current. This information was then used to generate the static torque characteristics of the motor as well. Flux-linkage and torque characteristics of the motor were then stored in look-up tables in the dynamic simulation model that were realised in Simulink®. In [194] the authors use Matlab® / Simulink® in order to model the dynamic behaviour of a magnetic levitated switched reluctance linear actuator along with the control algorithm. There are, however, no real measurements to validate and support the conclusions drawn from the simulation results. In [195] Matlab® / Simulink® was used to simulate a 3-phase asymmetric half-bridge converter in order to determine the optimum snubber capacitor so that the efficiency of the converter can be improved. However, the method was only useful for low speed operation where the current was under chopping mode control. In [196] the authors design and simulate a 3-phase 12-10 switched reluctance motor with asymmetrical stator poles and short flux paths. In [196] the simulation is used to analyse and verify the machine design in order to guide the design and the production of the machine. However, no validation of the machine design and the simulation was presented to the readers. In [149] authors use Matlab® / Simulink® to simulate the dynamic behaviour of an SRM based drive system for an electric vehicle application. Rather than using FE generated or measured flux-linkage characteristics of an SRM, the authors chose to estimate the magnetisation curves with analytical methods. Unfortunately there is not a great deal of explanation as to how this analytical method was derived and how well it represents the magnetic characteristics of the machine.

Due to the high computational time and resources associated with the FE analysis, especially during the initial design stage, an analytical approach may be favoured to narrow down the options within the available design space. FE analysis is favoured at the

later stages of the design stage where accurate results are required to verify the machine design against measurements. Analytical methods aim to generate a "Magnetic Equivalent Circuit" (MEC) of the machine for rapid analysis of machine magnetic characteristics. The advantage of using the MEC approach is the fast solution time, which in turn allows the designer to examine hundreds of topologies very quickly. Examples of simulation models using machine characteristics that are generated by using analytical methods are [197-202]. In [198] authors present a "new" analytical nonlinear model for rapid SRM modelling. It is claimed that the method is satisfactory both in accuracy and in calculation speed. The machine model based on the presented analytical model was then integrated into the modelling of an "Airborne Power System" that was implemented in Dymola / Modelica. In [201] various different control strategies were simulated for a 3-phase 6/4 switched reluctance machine. The model involved a non-linear dynamic model of the machine based on Fourier series phase self inductance characterisation and a double closed loop; comprising a chopping controller in the current control loop and fuzzy logic plus PI controller in the speed control loop. In [203] 2D FEA generated magnetisation characteristics of an SR machine is used to construct a dynamic equivalent circuit model in Simplorer to predict the machine's dynamic behaviour.

There have been a few examples of real-time simulation of SRMs as well. A d-SPACE based real-time simulation of a 4-phase 8/6 SR drive in Simulink® environment is presented in [204]. The study ultimately aims to be the stepping stone in developing a sensorless controller for the SRM by using additional toolboxes that are available in Matlab® / Simulink®. Another example of a real-time simulation attempt is [205] where CPU-based real-time simulation results of a 60-kW current-controlled 6/4 SRM are presented. The real-time simulation of the drive was conducted on the RT-LAB real-time simulation platform using "SimPowerSystems" in the Simulink® environment.

6.3 SIMULATION DATABASE

The main parts of a model aiming to simulate the operation of electric machines and drives can be summarised as follows.

1. **The Power electronics**: Depending on the detail of the simulation this includes:

- The front-end bridge rectifier
- The front-end filter components, i.e. series inductor and parallel dc-link capacitor
- The inverter

2. **The Machine**: Here, means of representing the electromagnetic characteristics of the machine is required. More specifically, the flux-linkage-position-current and torque-position-current relationships are used to model the machine's electromagnetic behaviour.

3. **The Control**: This can be anything from a control scheme combining PID and PWM controllers to more complex schemes like neural network based controllers.

Based on the simple partitioning of the simulation model listed above, the simulation model of an electric machine and its drive can be viewed as a multilevel modelling problem. All the components of the drive system were considered and it was decided that a model generated in the Matlab® / Simulink® environment would give the highest flexibility in creating different parts of the model to a high enough accuracy. As a result of this decision, the simulation package presented below is based on several detailed Simulink® models which are controlled by a Graphical User Interface (GUI) and supported by several m-file scripts (M-files are text files that contain Matlab® programs) and functions. Details of the simulation database are presented in Appendix C.

6.3.1 Machine Model

A numerical approach to the simulation of SRMs is introduced by Stephenson and Corda [167] that is used to characterise the relationship between flux-linkage, current and rotor position. This method eliminates the need of using differentiating terms. This way, the errors introduced by differentiation are eliminated.

Usually for a conventional SRM the only shared parts for flux flowing in the machine iron are the stator and rotor core-backs. Compared to the saturation levels seen in the stator teeth the saturation of stator and rotor core-back is small and can usually be ignored. This means that the mutual coupling introduced by the core-back saturation can also be ignored. The flux-linkage of any one phase can therefore be assumed to vary with

the rotor position and current flowing in that phase only. This greatly simplifies the simulation and a block diagram can be drawn as the one given in Figure 79. This block diagram model can simply be copied over for each phase of the machine to model the machine's electromagnetic characteristics.

Using Stephenson and Corda's method, position and flux-linkage information are used to obtain the phase current from a 2-dimensional look-up table. The data used in the 2-dimensional look-up table can be produced by direct measurement of the flux-linkage characteristics of the machine or by finite element simulation. The calculated phase current value is then used in the next time step to calculate the resistive voltage drop and, hence, to update the flux-linkage value by using Equation 10.

$$\psi_n = \int (v_n - R \times i\,(\theta, \psi)_{n-1})\, dt \qquad \textbf{Equation 10}$$

Intermediate values of the flux-linkage are derived by quadratic interpolation. The flux-linkage characteristics are inverted using successive approximation to give a table of $i(\theta, \psi)$. Flux-linkage characteristics depicted in Figure 80 are converted into current characteristics of the form given in Figure 81. The flux-linkage and position signals are used to calculate the phase current at each simulation time step. Data interpolation and extrapolation of current/flux-linkage/position data during simulation is based on a cubic-spline fit.

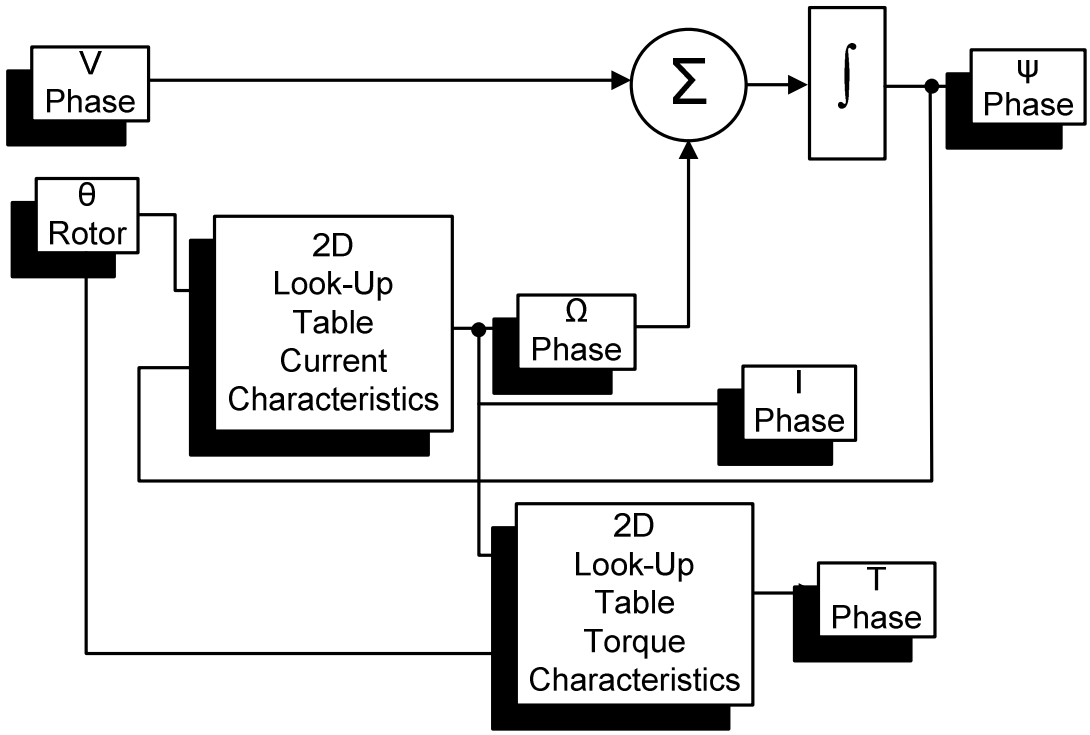

Figure 79 Schematic representation of modelling one phase of a conventional SRM

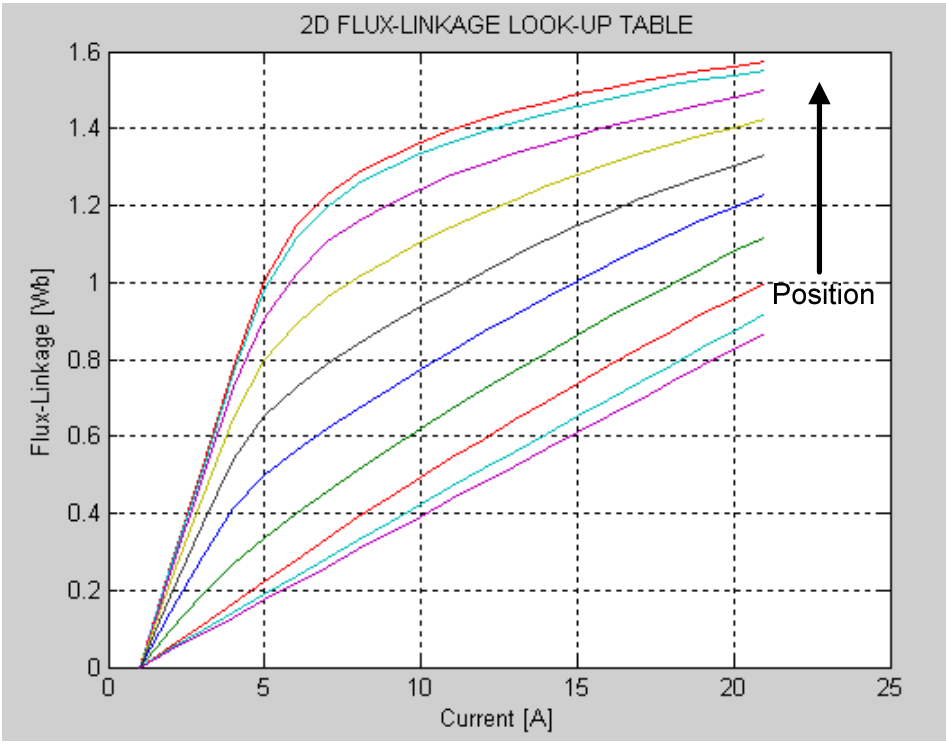

Figure 80 Fl ux-linkage - Current - Position characteristics

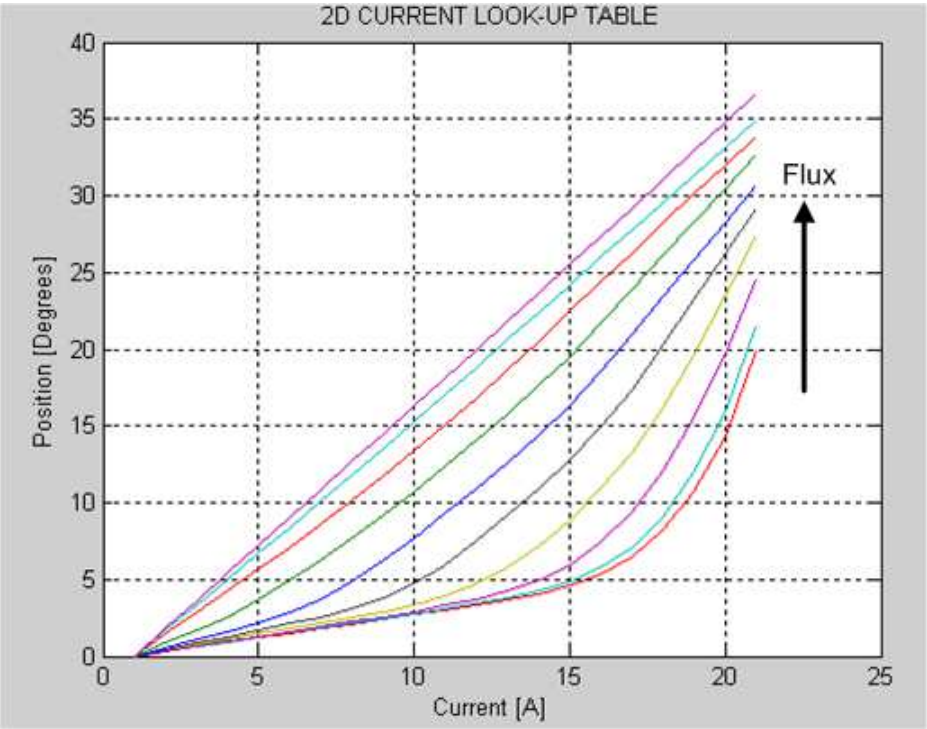

Figure 81 Current - Position - Flux-Linkage characteristics created from Flux-Linkage - Current - Position characteristics

The torque is stored in another look-up table and can be obtained either directly by measurement or indirectly by evaluating the co-energy of the machine. In the latter method, a table of co-energy is obtained by numerically integrating the flux-linkage with respect to phase current.

$$\overline{W}(\theta,i) = \int_0^i \psi(\theta,i)\, di \Big|^{\theta=const.} \qquad \textbf{Equation 11}$$

The intermediate values of co-energy are again found by quadratic interpolation and the torque is calculated by a numerical differentiation of the co-energy:

$$T(\theta,i) = \frac{d\overline{W}(\theta,i)}{d\theta} \Big|^{i=const.} \qquad \textbf{Equation 12}$$

Using Equation 11 and Equation 12 the flux-linkage characteristics of the form given in Figure 82 are converted to static torque characteristics of the form given in Figure 83.

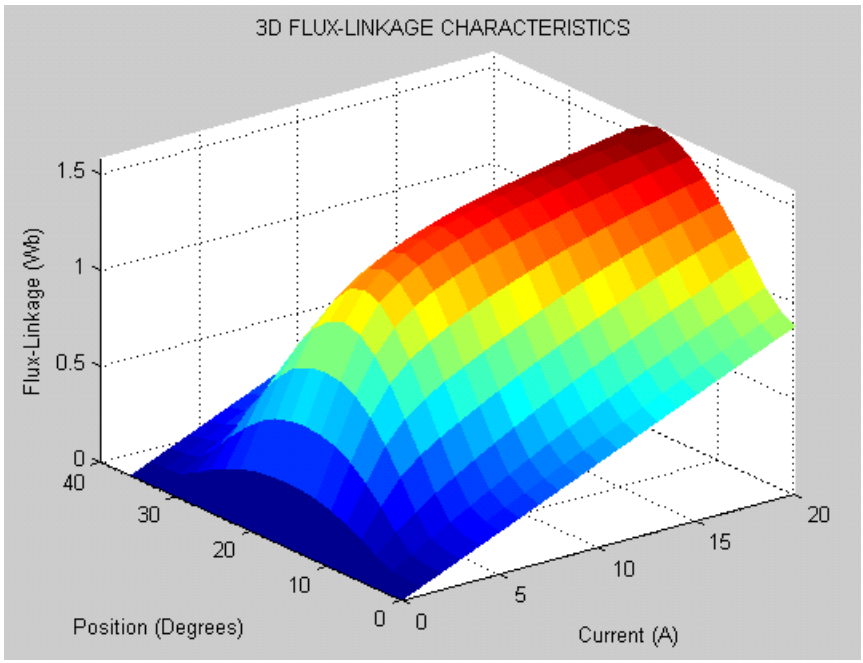

Figure 82 3D Flux-linkage characteristics

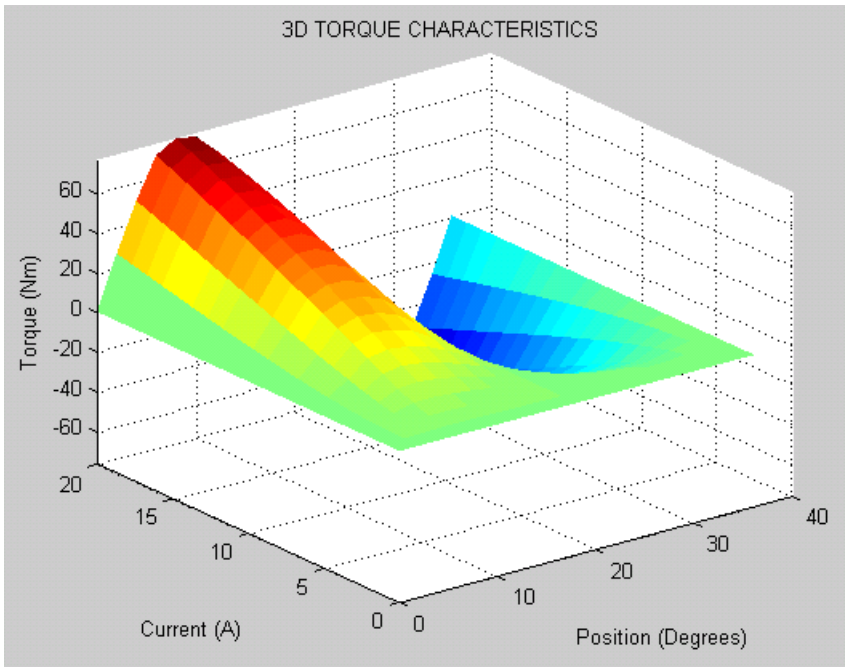

Figure 83 3D Static torque characteristics

Once again data interpolation and extrapolation of current/flux-linkage/position data during simulation is based on a cubic spline fit.

Creating the look-up tables used in the Simulink® model is done offline, i.e. it is not done whilst the simulation is running. The transformation starts with flux-linkage

characteristics of the machine and using Matlab® scripting functionality torque-current and current-position relationships are created as 2D look-up tables. The screenshots of look-up tables used in simulation model are given in Figure 84.

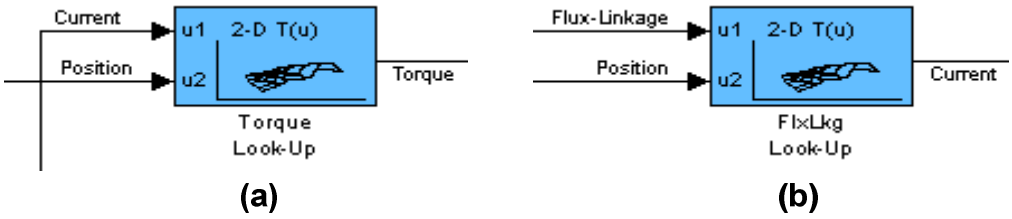

Figure 84 (a) 2D torque-current-position look-up table in Simulink®
(b) 2D current-flux linkage-position look-up table in Simulink®

6.3.2 Control Modelling

A considerable number of Simulink® models for control modelling have been built. The internal structure of these models varies, depending on machine type, power circuit configuration and control algorithm. An in-depth description of the internal structure of all the different models would exceed the objectives of this chapter. However, all drive systems are constructed from basic inverter and control blocks which are summarised in the following sections. Delays associated with signal processing in real drive systems, such as the time spent during analogue to digital sampling and conversion and the time delay between generating the PID reference voltage and updating of this reference voltage in the PWM controller, are not modelled in the simulation. DC-link voltage ripple and the voltage drops across the power devices are negligible for most high voltage, high current drives and have not been factored in the simulation.

6.3.2.1 Angle and Speed Calculations

Phase selection is dependant on rotor position and control angles (i.e. advance angle and total conduction angle). Zero rotor position is defined as the instance where a phase stator pole opposes a rotor segment as shown in Figure 85, i.e. unaligned position. All discussion in this chapter relating to rotor position is based on electrical degrees rather

than mechanical. Rotor position with respect to the first phase (Phase-A) is calculated. This signal is in the form given in Figure 86. Rotor position with respect to the rest of the machine phases is calculated simply by phase shifting the position signal of Phase-A. The simulation always starts at the unaligned position for Phase-A.

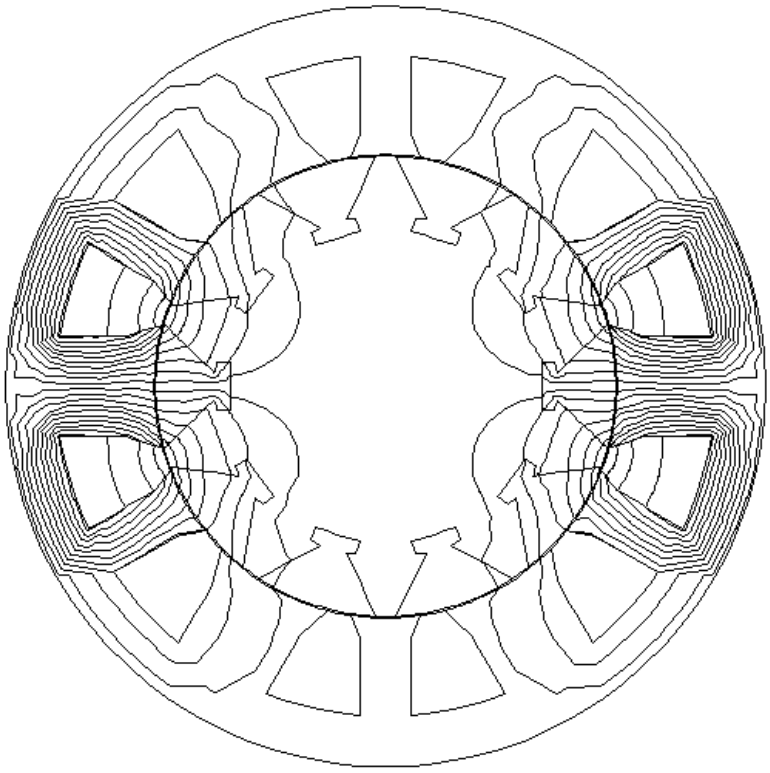

Figure 85 Magnetic flux plots for a 12-10 single tooth winding segmental rotor machine with a single phase excited illustrating the zero position implementation in simulation

The position signal given in Figure 86 is calculated from the rotor speed by utilising Equation 13.

$$Pos_{rotor} = Speed\ x \frac{360}{60} x\ N_r\ [Elect.\ Degrees] \qquad \textbf{Equation 13}$$

where

Pos_{rotor} : Rotor position with respect to a phase,

$Speed$: Rotor speed of rotation,

N_r : Total number of machine rotor poles.

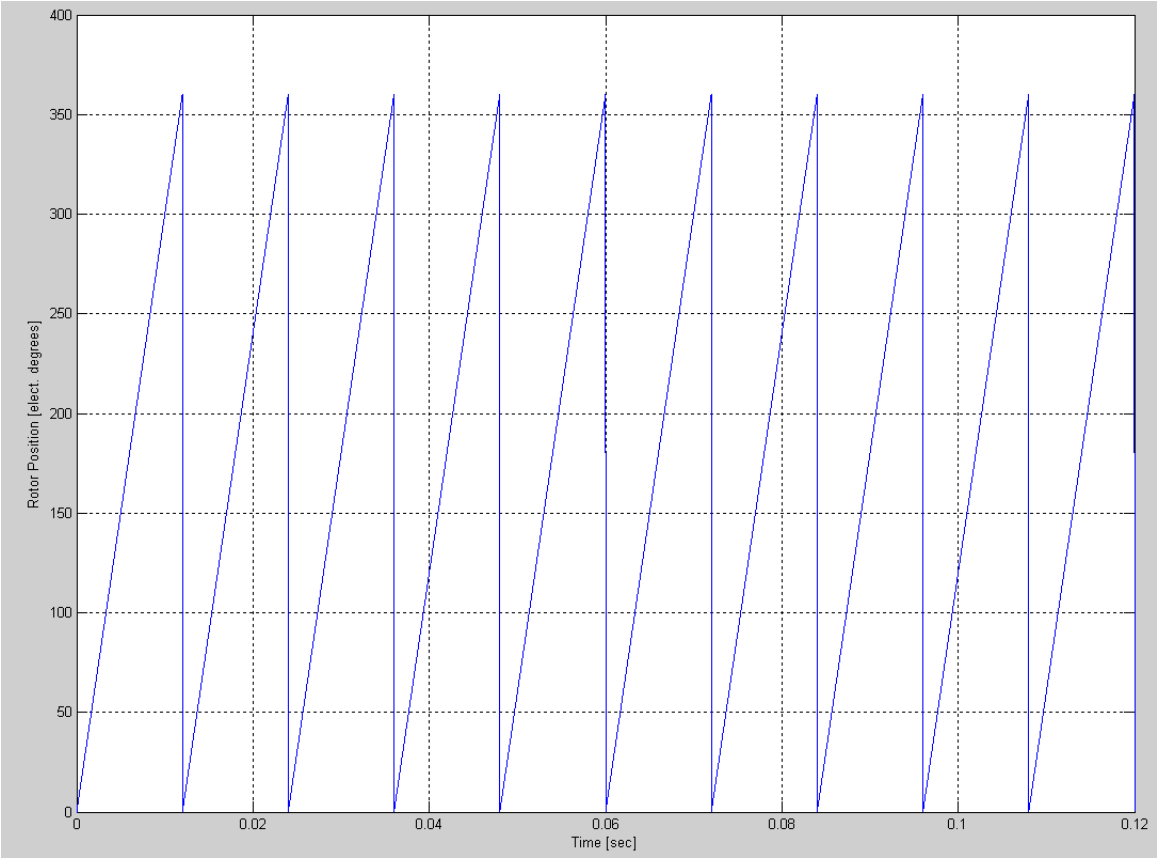

Figure 86 Rotor position signal with respect to Phase-A of the machine in simulation

Once the rotor position is determined for a phase then the energisation signal, i.e. when that phase is switched on and off with respect to rotor position, is calculated. This is done by comparing the rotor position signal for that phase with the advance and conduction angles requested by the user. Advancing is when a phase energisation starts before the unaligned position for that phase is reached and retarding is when a phase energisation starts after the unaligned position for that phase is passed.

Phase energisation signal(s) not only define the energisation region for the machine phase(s) but are also used to inhibit bridge legs and calculate current demand signal for certain converter topologies and switching strategies.

6.3.2.2 Current Sampling

In the real drive system there are three 160A rated current transducers available to measure drive currents. Three analogue-to-digital conversion (ADC) cards are used to transform the measured current signals into 10-bit digital code. The sampling rates of the ADC cards were 20 kHz. Digital sampling is modelled by using zero-order hold blocks in Simulink®. The sampled currents also have a conversion ratio. This ratio is simply modelled by a gain block in Simulink®. In the real drive, the line current demands are software defined (for the 3-phase full bridge circuit) and are based on the commutation points calculated from a 12-bit encoder position feedback signal.

6.3.2.3 PID Controller

PID controllers are commonly implemented in microcontroller or DSP based drive systems to maintain the current within a desired level. The controlled current is fed back into the controller where the sampling of the current and comparing to the reference value are implemented. Once the current error signal is calculated it is then sent to the PID controller. Based on the error signal the PID controller generates the reference voltage(s). Depending on the type of the converter and the switching strategy, the PID controller either generates a single reference voltage or two reference voltages, one of them being the complimentary of the other. An integral anti windup is also included in the PID modelling of the simulation.

The value of the reference voltage generated by the PID controller is limited to the resolution of the PWM triangular waveform. The PWM waveform has a peak value of 255 $(2^8 - 1)$ and so has the PID controller reference voltage. If complimentary switching is to be employed, the PID controller also generates a negative reference voltage (in digital terms a complimentary signal with respect to controller resolution). An example of the operation of the PID controller in simulation is given in Figure 87.

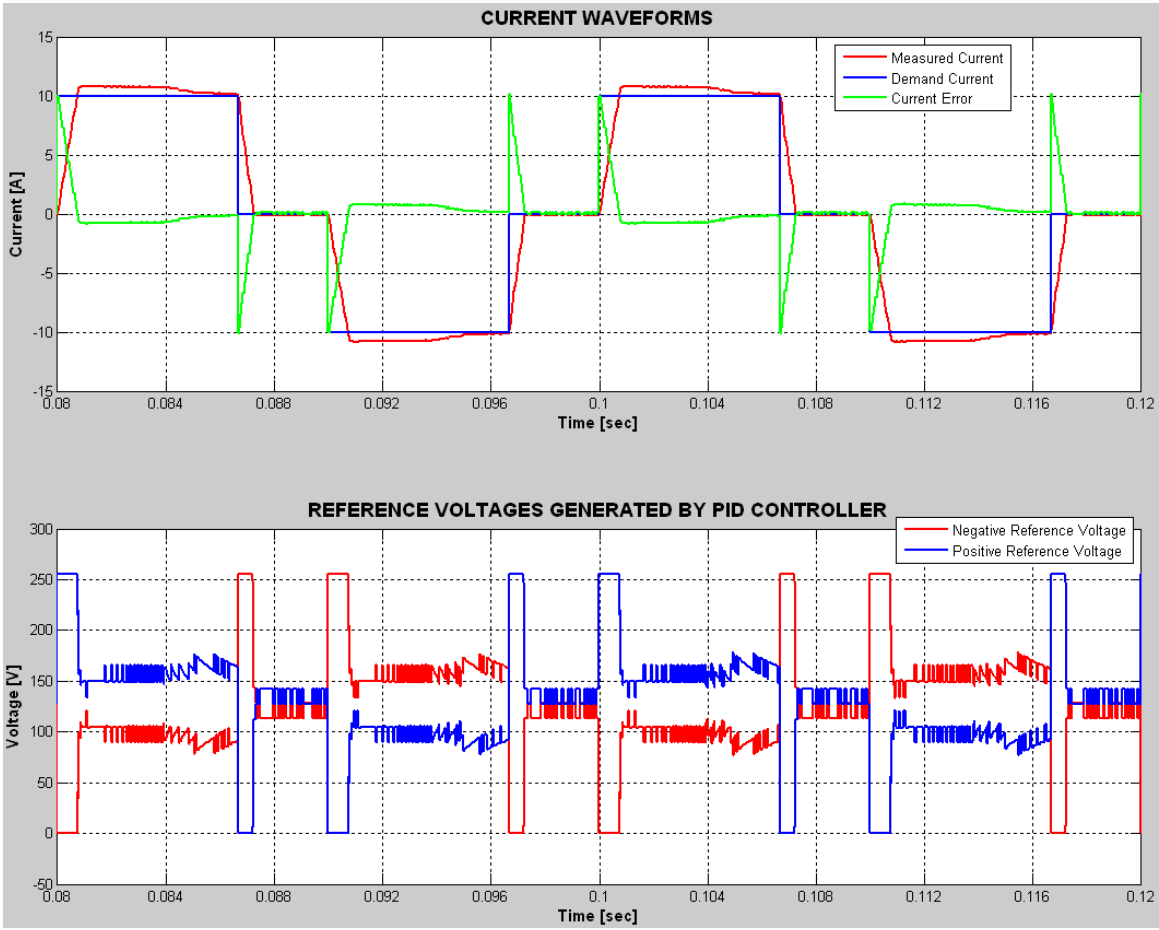

Figure 87 Operation of PID controller in simulation of a 2-phase machine driven by an h-bridge converter shown for a few electrical cycles

In this example, the simulation was of a two-phase machine driven by an h-bridge converter where phases were connected back-to-back (see Chapter-3 for a description of this circuit topology). Motor speed is 300rpm, current demand is 10A, and phases are energised at the unaligned position for 120 electrical degrees. The top trace in Figure 87 shows the demand current in blue, measured current in red and current error signal in green. The bottom trace shows the positive and negative reference voltages. When there is positive demand current the PID controller saturates at its maximum value and this can be seen from the generated reference voltages. As the current gets closer to the demanded level the error current reduces and the PID controller tries to keep the current at the desired level. The digitised nature of the measured current can be seen in Figure 88.

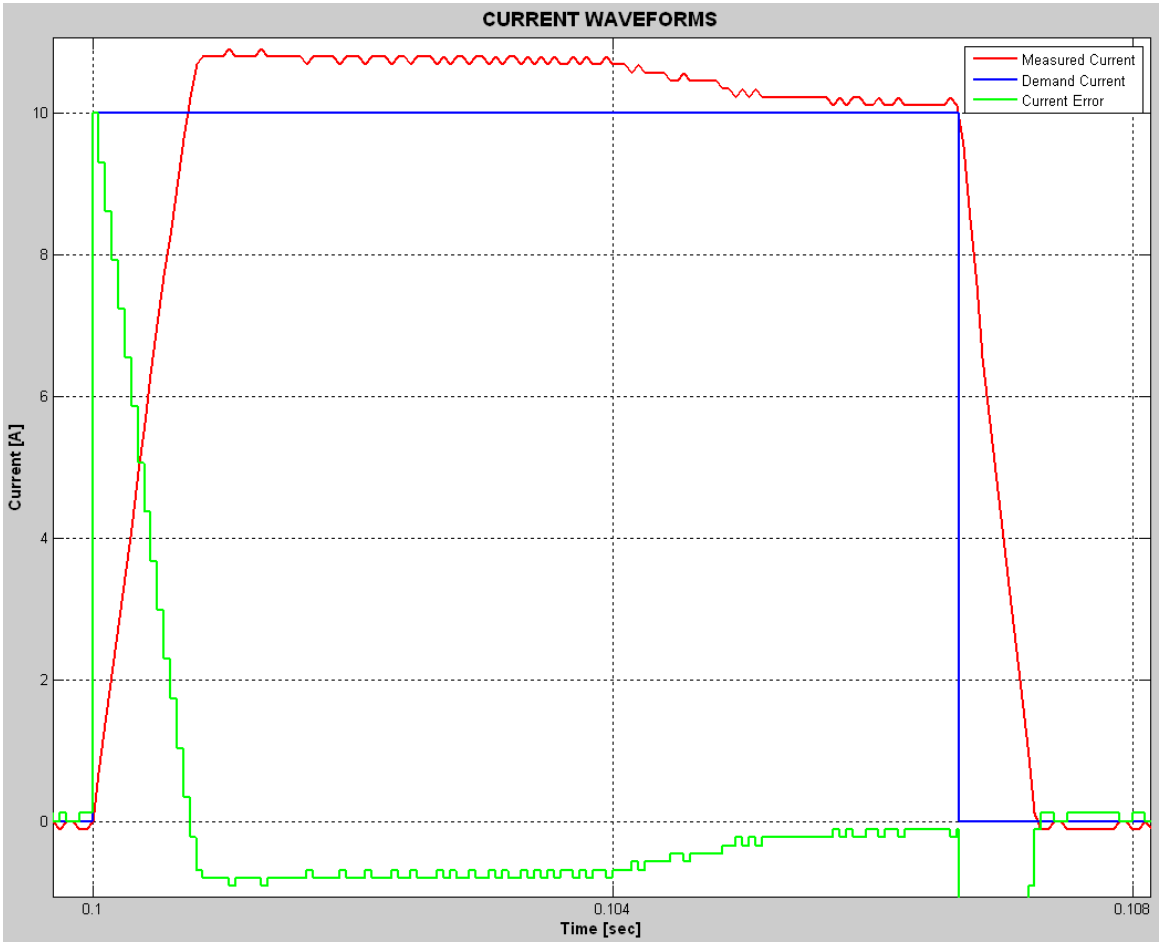

Figure 88 Zoomed version of measured and demanded current signals (along with the error signal in green) showing the digitised nature of the measured current

6.3.2.4 PWM Controller

Fixed frequency PWM controllers are usually implemented along with PID control. The reference voltages generated by the PID controller are fed into the fixed frequency PWM controller where it is compared to a triangular wave and the inverter switches are turned on or off accordingly.

The PWM controller converts the voltage reference signals (Vref: the voltage reference value defining the required duty cycle to be applied to the winding) fed by the PID controller into gate signals for the transistors. In [137] the PWM controller is simply modelled as an amplifier. Even though modelling the PWM controller as an amplifier simplifies the model and reduces the simulation time, it makes the switching patterns of power devices unclear to the user. This no doubt complicates the part of the simulation

where the device losses and voltage drops are calculated. With the method followed in this PhD project, the switching states of each power device are readily available. The model can then simply use the device voltage drops and loss models to calculate the voltage drops and power losses across each device.

The PWM reference voltage is a triangular one. The resolution of this voltage and the reference voltage(s) - Vref generated by the PID controller both have a resolution of 8 bits. An example of how the gate signals are generated for an H-bridge (see Figure 89) converter from the triangular PWM reference voltage and PID Vref voltage is depicted in Figure 90.

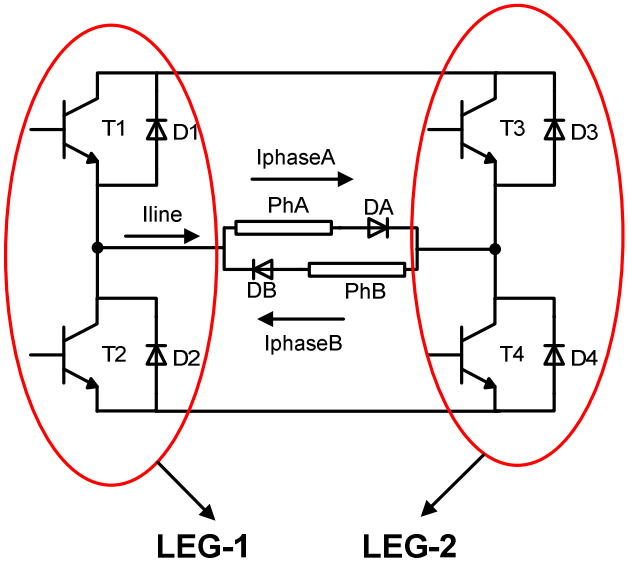

Figure 89 Back-to-back connected two-phase SRM driven by an H-Bridge inverter

For leg 1 of the bridge, top device (T1) is switched on when Vref (generated by the PID controller) is greater than Vtri (PWM carrier signal) and bottom device (T2) is switched on when Vref is smaller than Vtri. For leg 2 of the bridge top device (T3) is switched on when –Vref (again, generated by the PID controller) is greater than Vtri and bottom device (T4) is switched on when Vtri is greater than –Vref. The PWM strategy ensures that two switches of the bridge will always be conducting at any one time and both switches of any one leg cannot be on at the same time. A schematic representation of the PWM controller for an H-bridge converter in Simulink® is given in Figure 91.

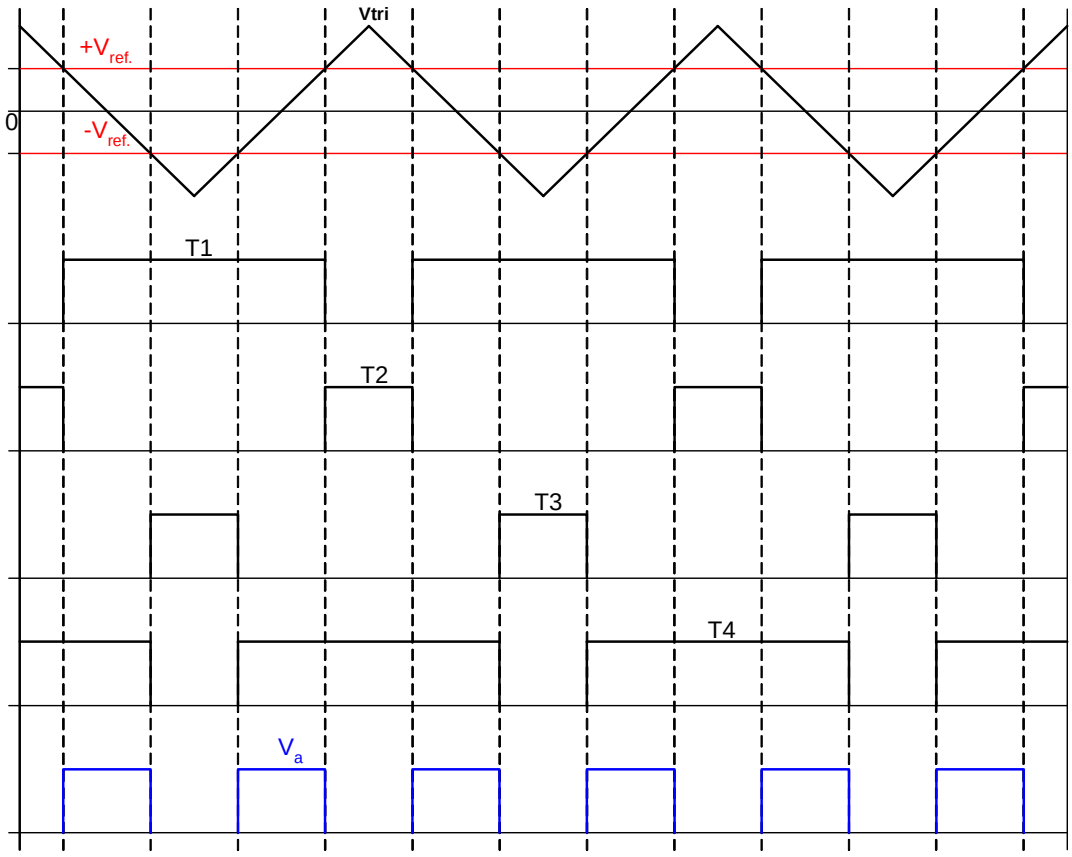

Figure 90 PWM control of H-bridge inverter. +Vref and –Vref are the voltage control signals generated by the PID controller. T1, T2, T3, T4 are the transistor gate signals, Va is the voltage subsequently imposed on the winding

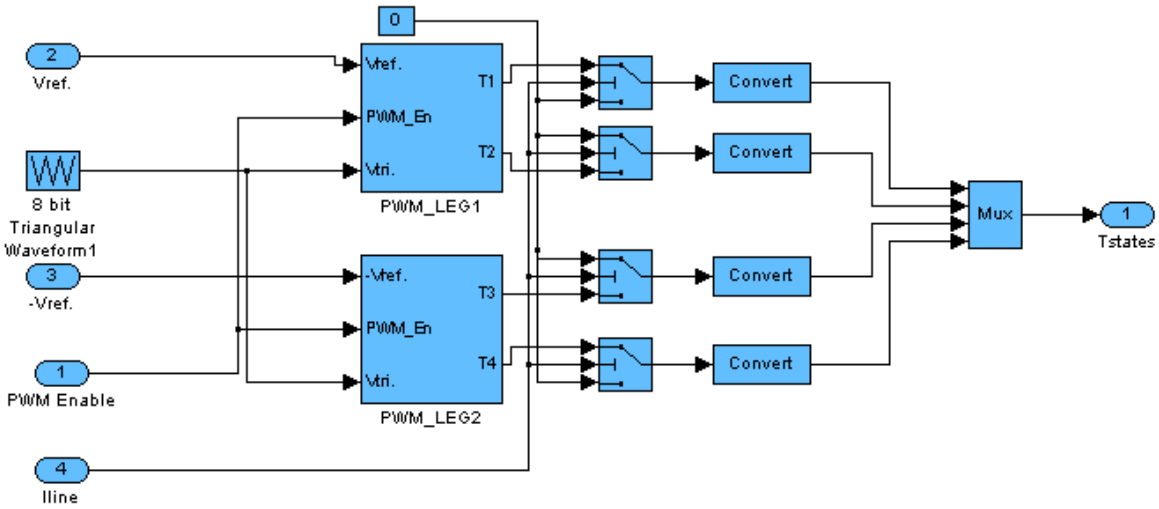

Figure 91 Screenshot of the PWM controller model in Simulink®

An example of the PWM controller operation in simulation is given in Figure 92. The top trace in Figure 92 contains the triangular PWM reference voltage in red, positive

reference voltage in green and negative reference voltage in blue. The other four traces show the switching states of each power device of an h-bridge converter. In this example the top left and bottom right devices appear to be switching and conducting the phase current. It is also obvious from this example that the switching strategy balances the switching of top and bottom devices. Therefore the device losses are balanced between the top and bottom devices of the circuit. In Figure 93 the waveforms in Figure 92 are shown for a few PWM cycles for clarity.

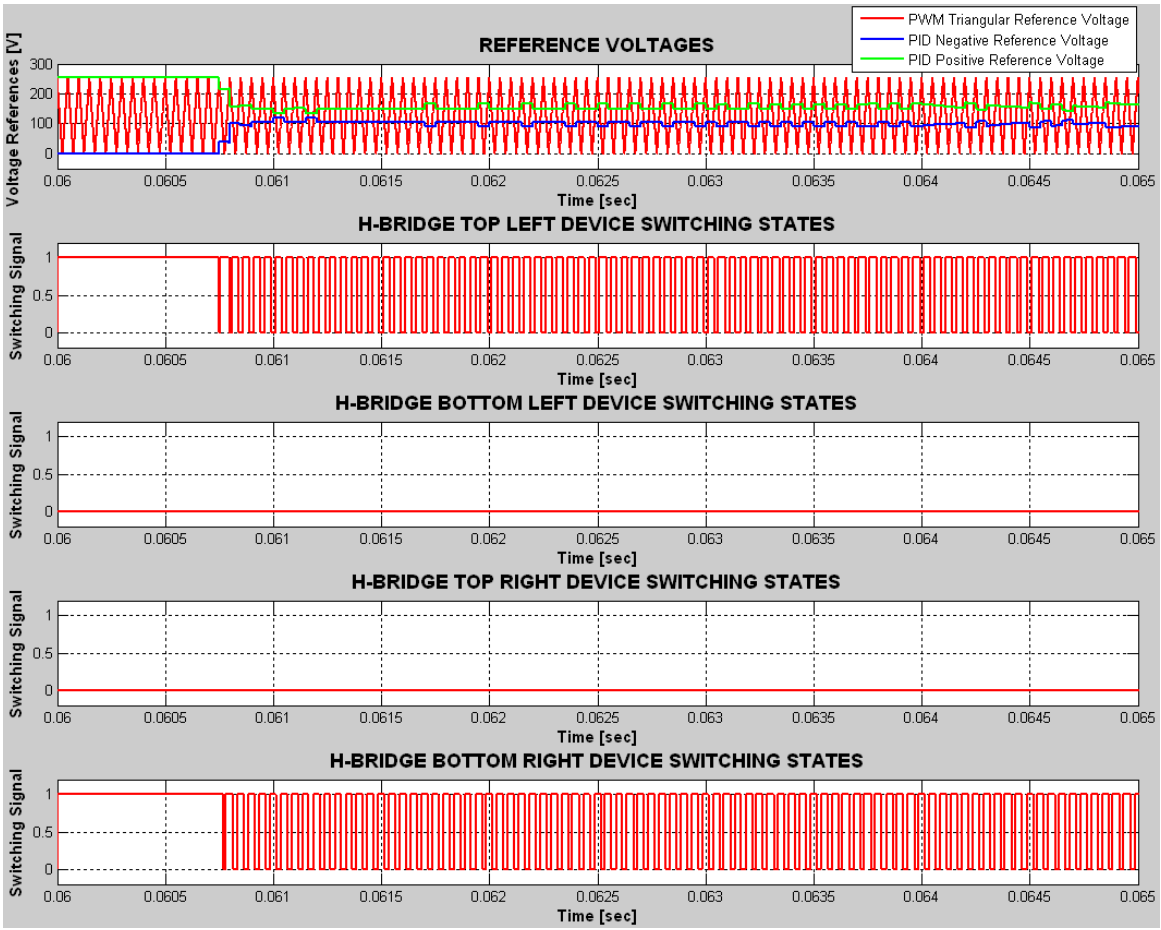

Figure 92 PWM controller operation in simulation - Simulation inputs are rotor speed = 300rpm, advance angle = 0 degrees, conduction angle = 120 degrees, current demand = 10A

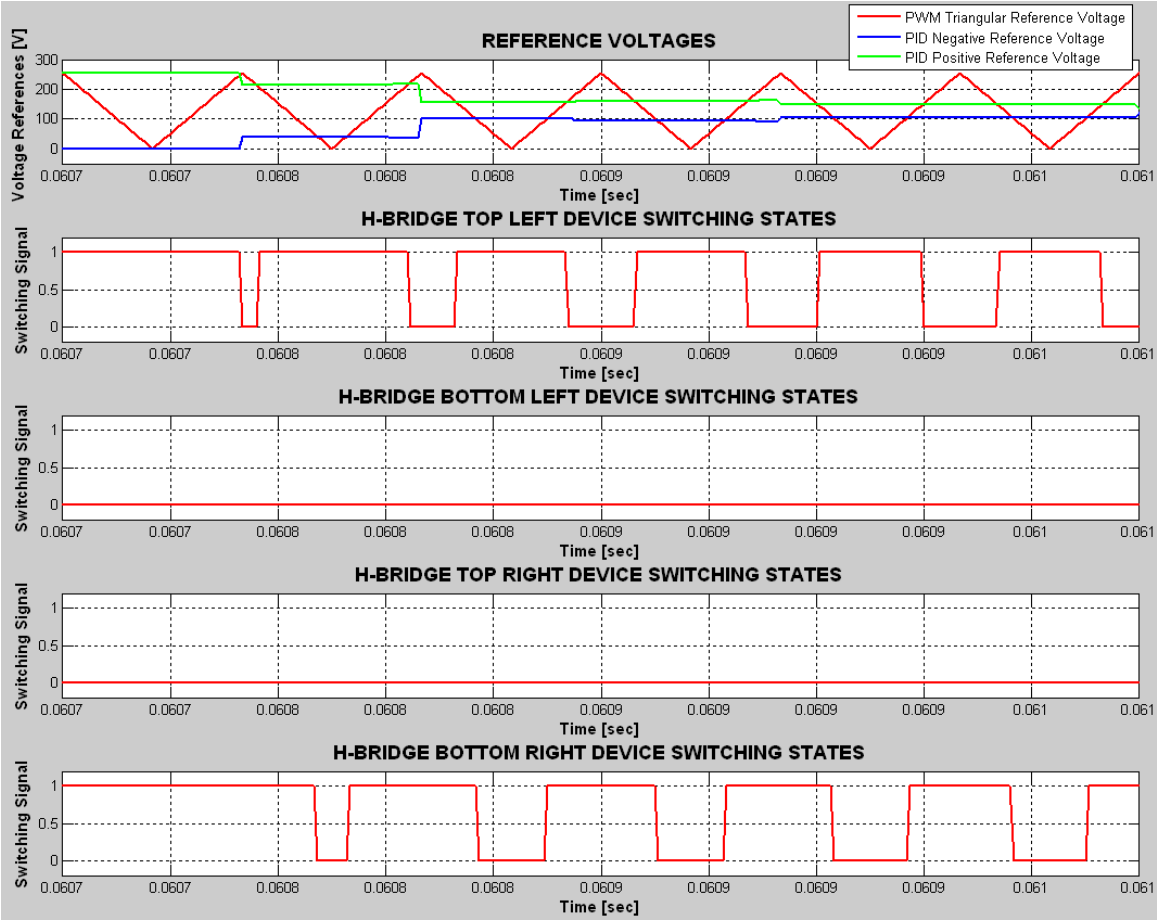

Figure 93 Traces in Figure 92 shown for a few PWM cycles

As mentioned earlier in the chapter, time lags between the output of the PID controller and the input of the PWM controller and also between the current sampling and PID controller are not modelled in the simulation. In reality the voltage reference output generated by the PID controller is fixed for one entire PWM period. Also there is a finite amount of time between the sampling of the phase current(s) and PID output(s). It was believed that omission of these time delays did not spoil the performance analysis based on simulation results and kept the simulation model simple but accurate.

6.3.2.5 Converter Modelling

The voltage applied to each phase is determined by the states of the devices in the power electronic converter. A simulation database is able to model several different converter topologies, namely asymmetric half-bridge, h-bridge and 3-phase full-bridge converters.

Rather than modelling the dynamic operation of each power device the states of each device are determined.

A device is either in a high state (i.e. able to conduct current) or in a low state (i.e. does not conduct current). Any one device can be in a high state but this on its own does not suggest that it actually conducts current. Depending on the states of other devices, rotor position and phase or line currents, the simulation decides whether a power device conducts current or not. Once the conduction state of each power device is determined, the voltage applied to each phase can then be decided. For example, in Figure 89 the phases of a two-phase SRM are connected back-to-back and operated from a PID controlled H-bridge inverter. The diodes (phase diodes) connected in series with the phase windings are used to achieve unidirectional current flow. Control can be achieved by sampling the phase currents (IphaseA and IphaseB in Figure 89) or the line current (I_Line in Figure 89) and comparing to a reference value (current demand). Sampling the line current is shown here. Line current control requires only one current sensor as opposed to two needed for controlling the phase currents separately. Therefore it is likely to be the preferred method in real-time applications. The PID controller supplies positive Vref to control leg 1, comprising switches T1 and T2 and negative Vref to control leg 2 of the bridge, comprising switches T3 and T4. As a result of complimentary switching, conduction and switching losses are shared equally between each transistor. The schematic explanation of the controller is given in Figure 94.

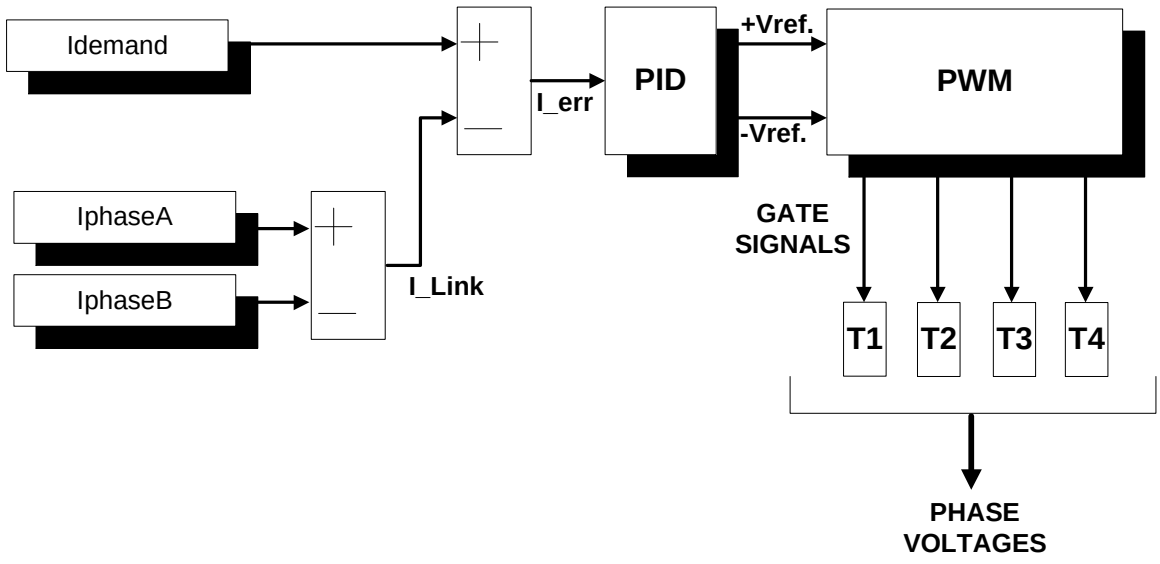

Figure 94 Schematic of controller for the two-phase drive given in Figure 89

All possible switching states and corresponding operating conditions are summarised in Table 10.

Table 10 All possible switching states of the transistors in the H-Bridge inverter of the 2-phase SRM model and operating conditions depending on the states of the power switches

T1	T2	T3	T4	OPERATING CONDITION
0	0	0	0	If I_Line > 0 (Ia>Ib) D2 – DA – D3 conducts and phaseA freewheels. 0 volts to both phases
0	0	0	1	NOT POSSIBLE (two switches should be on at any one time)
0	0	1	0	NOT POSSIBLE (two switches should be on at any one time)
0	0	1	1	NOT POSSIBLE (switches of any one leg cannot be on at the same time)
0	1	0	0	NOT POSSIBLE (two switches should be on at any one time
0	1	0	1	If Ia>Ib T4 - DA - D2 conducts and phaseA freewheels. If Ia<Ib T2 – DB – D4 conducts and phase B freewheels. 0 volts applied to both phases.
0	1	1	0	Phase B energised and receives positive volts whereas Phase A is de-fluxed and receives negative volts.
0	1	1	1	NOT POSSIBLE (too many switches on)
1	0	0	0	NOT POSSIBLE (two switches should be on at any one time
1	0	0	1	Phase A energised and receives positive volts whereas Phase B is de-fluxed and receives negative volts.
1	0	1	0	If Ia>Ib T1 - DA – D3 conducts and phaseA freewheels. If Ia<Ib T3 – DB – D1 conducts and phase B freewheels. 0 volts applied to both phases.
1	0	1	1	NOT POSSIBLE (too many switches on)
1	1	0	0	NOT POSSIBLE (switches of any one leg cannot be on at the same time)
1	1	0	1	NOT POSSIBLE (too many switches on)
1	1	1	0	NOT POSSIBLE (too many switches on)
1	1	1	1	NOT POSSIBLE (too many switches on)

A schematic of the subsystem in Simulink® is given in Figure 95 where the switching states of power devices and applied phase voltages are determined.

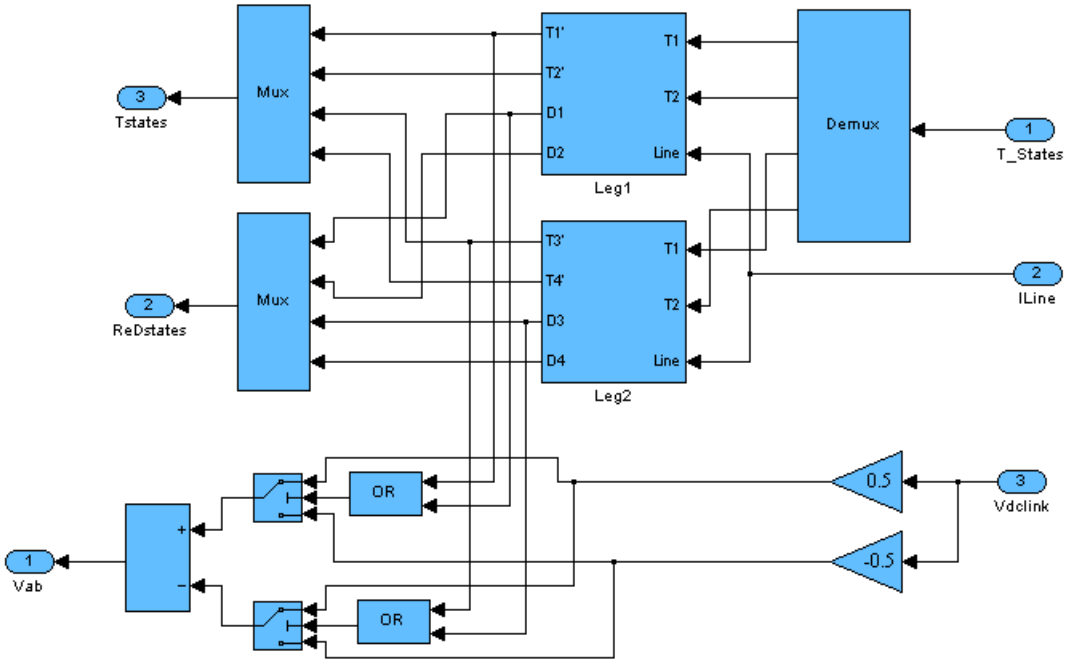

Figure 95 Screenshot of simulation subsystem calculating phase voltages and power device switching states

Dead-time is required to prevent turning on the upper and lower devices on the same leg of the converter simultaneously. Here, the simulation assumes that the switching of power devices is ideal, i.e. when a switching command is generated; the device reacts and turns on or off immediately. Therefore there is no need to model the dead-time effects. In reality the dead-time will affect the available voltage applied to the on-coming phase and off-going phase during commutation and somewhat distort the waveforms (during dead-time negative voltage is applied to the commutation spike instead of the tail current that results in a shorter commutation spike but a longer tail current). This will result in an overshoot in phase current when the inverter is controlled by line-current sensors rather than phase current sensors [89].

6.3.2.6 Phase Diode Modelling

For models where a diode is connected in series with the phase windings to avoid bi-polar current flow through the phase windings, the operation of this diode (called the phase diode in the simulations) needs to be modelled correctly. In the simulation, the phase diode should operate, i.e. block phase current flow in reverse direction if the phase energisation signal is OFF (phase conduction period has completed) and the phase current has decayed to zero. The simulation detects the positive to negative zero-crossing of the phase current and simultaneously checks the phase energisation signal. If the phase is in the OFF state then the *Phase Diode* operates and blocks the phase current flowing in the reverse direction. Figure 96 is a schematic of the phase diode modelling in Simulink®.

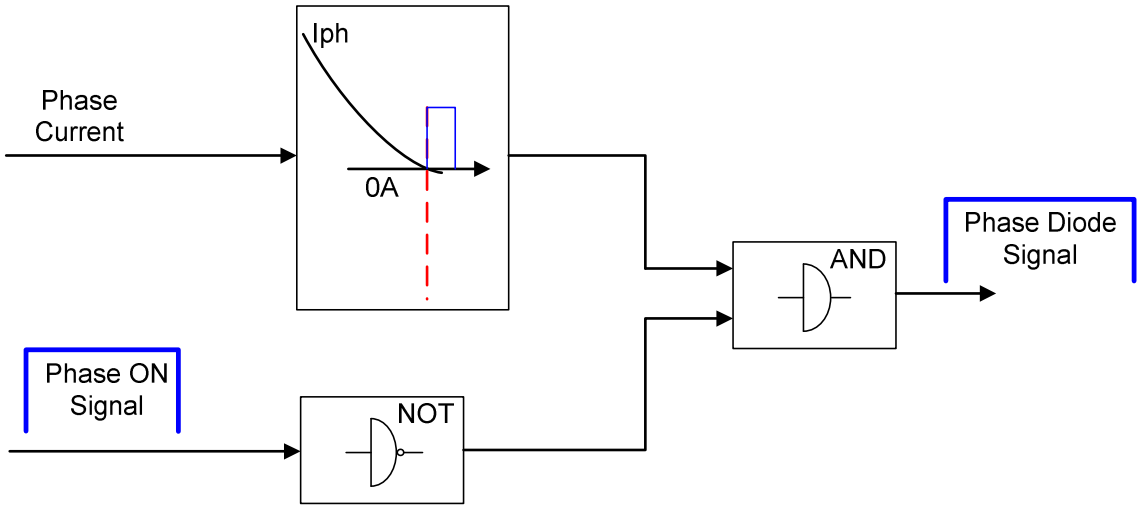

Figure 96 Phase Diode Modelling in Simulink® (Inputs are phase current and phase energisation signal, output is HIGH when Phase Diode operates, i.e. blocks the phase current reverse direction)

6.3.2.7 Electronics Loss Modelling

If the simulation is to be used to determine the performance of the power devices and some device related design parameters such as peak device voltage, current stresses, switching losses and electromagnetic interference (EMI) due to switching action, then it is desirable to model the device dynamically. That is to use the device transient equivalent models in the simulation environment [142].

The aim of the inverter loss calculation was to be able to perform comparative studies between different drives and assess their impact on power electronic ratings in terms of

device loss as well as device peak/rms current. For this reason, devices were characterised only in a reasonably simple way as it was the comparative performance of the drive rather than the comparative performance of individual devices that were being assessed. Nevertheless it is best to use the loss curve illustrating the highest junction temperature as this will give the most accurate representation of the device in real life.

Conduction loss of a diode, IGBT or MOSFET was based on a linear model in the form of $y = mx + c$ equation. Therefore, in the case of an IGBT, three parameters were entered as shown in Figure 97. Vce (on) and Ic at (V_2, I_2) and Vce (on) at (V_1, I_1). I_1 is always 0 amps [89].

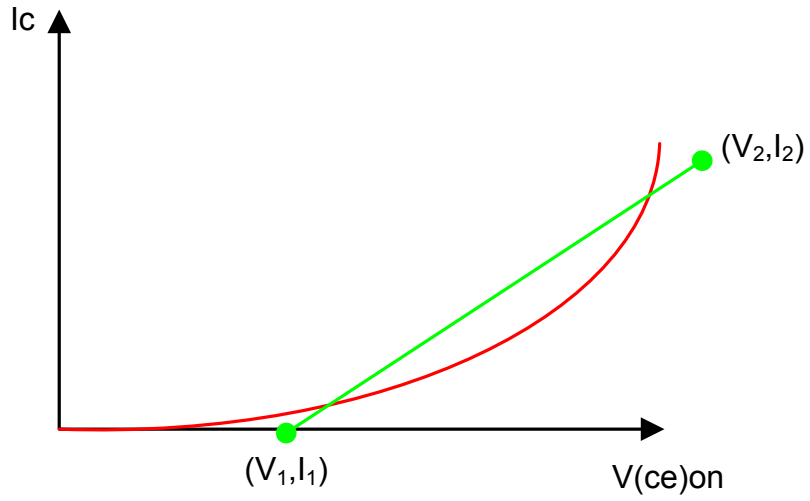

Figure 97 IGBT conduction loss characterisation – Red trace is a representation of the forward VI curve from the datasheet and green trace is the linear approximation within the operating current range of the application

This is a first order approximation to the non-linear characteristic which is typically of the form given in Figure 97. If the device operates at a limited current range then the linear approximation is such that only the operating range of the device in the application is taken into account. This way, the accuracy of the linear approximation is maximised.

A choice of the method to calculate switching loss of an IGBT or MOSFET is offered. One way is to enter the energy per switch at turn on (Eon) and the energy per switch at turn off (Eoff). The device current and volts that this energy is based on is also entered. E(on) and E(off) are then scaled proportionally in the simulation to suit the actual currents and voltages being used. This method is particularly suitable for IGBTs and the energy

per switch value quoted in the data sheet includes 'tail' losses and the reverse recovery current effect of the diode.

The model is able to detect the switching instances of any device. Also the type of switching is distinguishable in the simulation so that the coefficients for turn-on and turn-off losses can be applied correctly to the right instance of switching.

6.3.3 Inverter Modelling

6.3.3.1 Asymmetric Half-Bridge Inverter Drive

This requires knowledge of the voltage across the phase at all times. During the turn off process, the two transistors controlling one particular phase are simply turned off. With positive current still continuing to flow, the diodes conduct the current and the phase windings see a negative voltage bringing the phase current down to zero. However, once at zero, the current does not reverse direction. Therefore, the voltage that is applied to the winding by the diodes is not known and hence flux linkage cannot be calculated. It is therefore necessary in the simulation to control the current to zero by setting the current demand to zero during the off period. This way, the current controller knows the voltage being applied and therefore the problem is overcome.

6.3.3.2 Six-Phase Delta Connected Drive

The delta connected drive (Figure 33 repeated in Figure 98) presents no problem to the simulation as unlike the star connected inverter, the controller directly controls the voltage across each phase winding. Therefore the phase voltage is known at every time step for a delta connected inverter, so solving for phase currents and flux linkages is relatively straightforward. The only difficulty comes with the methodology used in the current controller itself. In the case of modelling a six-phase SRM where phases are paired and connected back-to-back through so-called phase diodes, the voltage applied to any one module directly affects the voltage available to be supplied to the other two modules. This will affect the ability of the converter to supply voltage to phases on different modules.

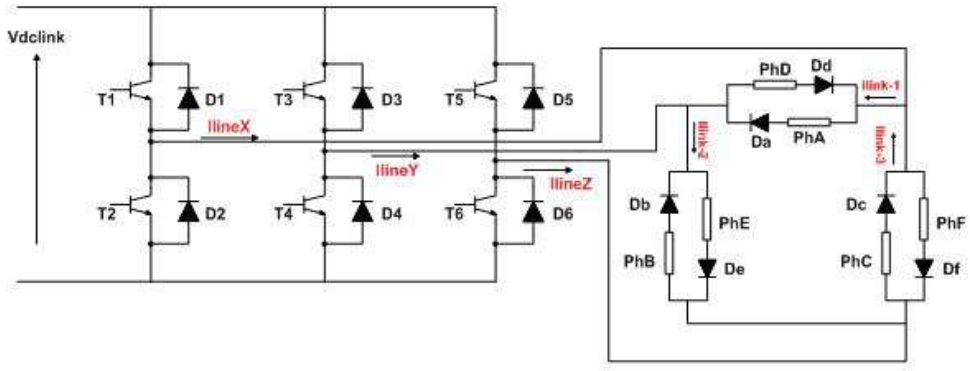

Figure 98 Delta-connected six-phase SRM operated from a conventional 3-phase bridge circuit

The phase voltages of the delta connected 6-phase machine driven from the 3-phase full bridge circuit are calculated as:

$$Vx - Vy = VphaseA = -VphaseD$$
$$Vy - Vz = VphaseE = -VphaseB$$
$$Vz - Vx = VphaseC = -VphaseF$$

Equation 14

Simulation results of the 6-phase delta-connected SRM with magnetically de-coupled phase windings working under current and voltage control are presented in Chapter 9.

6.3.3.3 Six-Phase Star Connected Drive

The star connected drive (Figure 32 repeated in Figure 99) is an unusual case for the simulation. Phase currents must sum to zero at the star point. Moreover, the star point is not directly controlled by the current controller, and hence, its voltage is unknown to the controller. Unlike the delta-connected drive, the controller in simulation requires the star point voltage so that it can calculate the phase voltages and consequently flux-linkages, currents and torques. In [89] Clothier uses an iterative method to calculate the star point voltage at every time step of the simulation. The principle is based on the fact that the sum of the currents flowing into the star point must be zero. With the star point voltage from the previous time step, the new time step is entered. Inevitably an error current is produced at the star point. The star point voltage is then adjusted in the appropriate direction by a calculated amount and the whole time step restarted until the sum of the currents is zero (or within a specified error band).

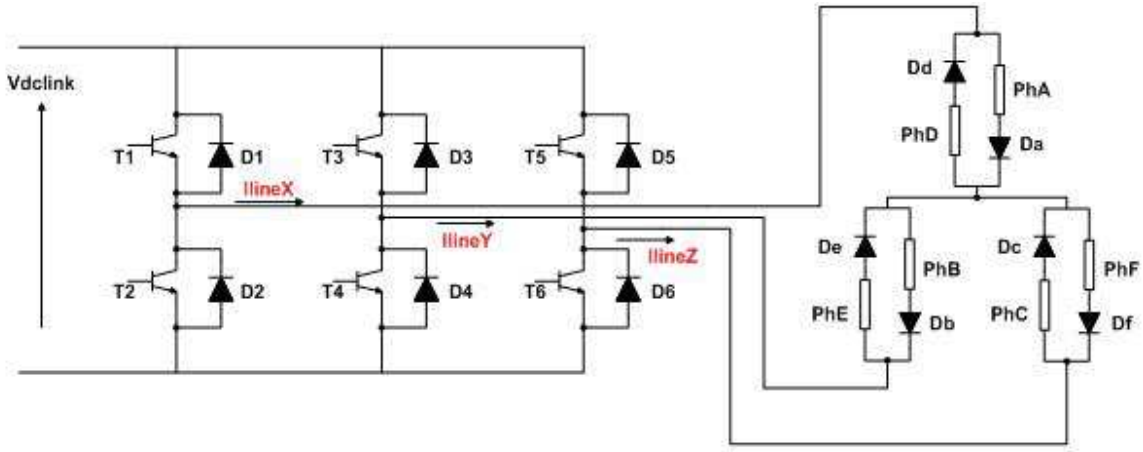

Figure 99 Star-connected six-phase machine driven by a 3-phase full bridge circuit

The method applied in this project also aims to minimise the current error at the star point. However, this is achieved with a slightly different method. All phase flux-linkages and phase currents along with the dc-link voltage, phase resistance and simulation time-step are all transferred into an m-file at each time step during the simulation. Within this m-file the phase inductance is assumed to be linear. The star point voltage is varied between $-V_{dclink}/2$ and $+V_{dclink}/2$. The value which minimises the star point current is selected as the star point voltage and used in the next time step of the simulation. An example of star-point voltage calculated in the simulation is given in Figure 100. In Figure 100 the blue trace is the star-point voltage calculated during the simulation and the red trace is a filtered version of the same voltage waveform. The filtering is done by a simple moving average filter. The depth of the filter was selected so that there was no significant loss to the waveform (both the phase and the amplitude of the filtered waveform are believed to be relatively accurate). The star-point current calculated (with the star-point voltage in Figure 100) is given in Figure 101. The current demand was set to 10A for this simulation.

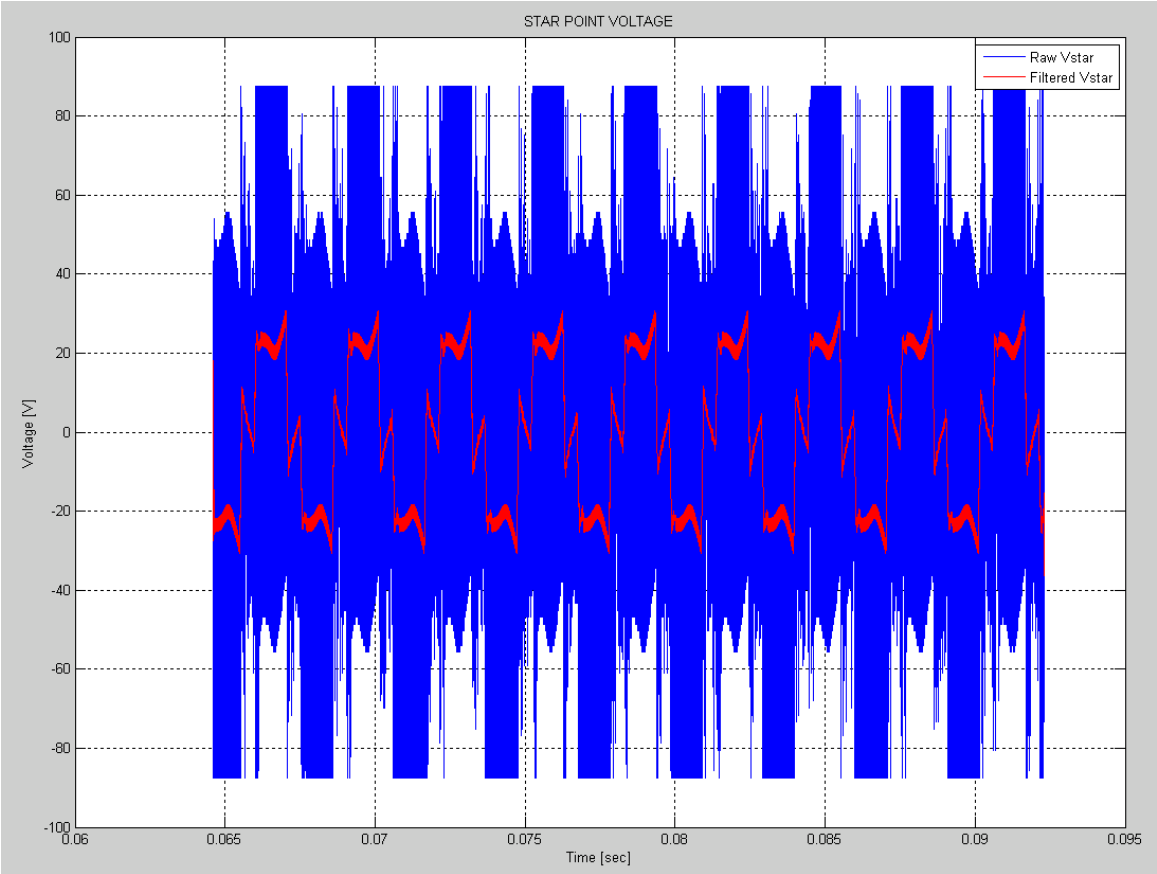

Figure 100 Raw and filtered star point voltage waveforms from simulation of 6-phase SRM driven by a 3-phase full-bridge inverter – Blue trace: Raw star-point voltage; Red trace: Filtered star-point voltage

Looking at Figure 101 the error in star point current is approximately 0.3% of the current demand at any time step. The controller works the same as for line current controlled delta-connected drive. The PID controller generates positive reference voltages for each line of the bridge. These values are then compared to the PWM triangular reference voltage and the switching states of the power devices are determined. Then depending on the switching states of the devices and the direction of current, the devices which actually conduct current are determined. Once the current conducting power devices are known the line voltages can be determined easily. Once the star-point voltage and the line voltages (controlled by the controller) are known, module voltages and, hence, phase voltages can be calculated. Simulation results of the 6-phase line current controlled star-connected SRM with magnetically de-coupled phase windings working under current and voltage control are presented in Chapter 9.

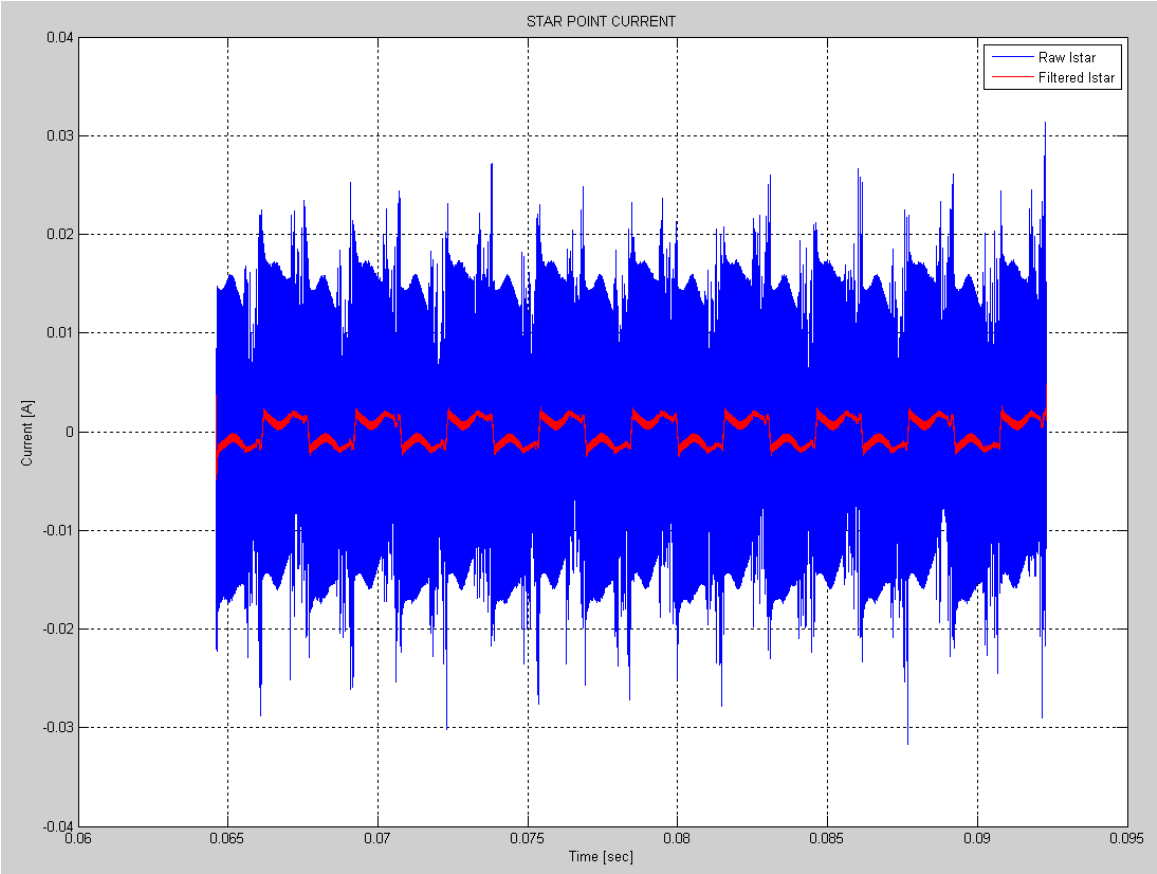

Figure 101 Raw and filtered star point current waveforms from simulation of 6-phase SRM driven by a 3-phase full-bridge inverter (Star-point voltage in Figure 100– Blue trace: Raw star-point current; Red trace: Filtered star-point current

6.4 MODELLING OF SRMs WITH MUTUALLY COUPLED PHASE WINDINGS

Conventional SRMs with short-pitched windings and some segmental rotor SRMs are assumed to be magnetically de-coupled and the mutual saturation of the core-back is considered to be of no significance. The flux-linkage of any one phase is therefore assumed to be solely a function of phase current and rotor position of that phase (operation of any one phase has no effect on other phases of the machine). This assumption allows modelling of each phase separately. When an SRM has a segmental rotor construction, the magnetic flux paths enclose a single slot and the magnitude of the flux is a function of the segment position and the total MMF in the slot. For many designs each slot contains two coils of adjacent phases – consequently there is strong mutual coupling between phases. Moreover, the prototype 6-phase segmental rotor machine that

is presented in this thesis will always have two adjacent phases conducting at the same time during operation, when the machine is connected in either a star or delta configuration. Mutual coupling means that the flux linking each coil is a non-linear function of rotor position and currents flowing in all other phases. Therefore, the circuit equation of each phase cannot be solved independently, from a single non-linear differential equation. Modelling becomes complex because flux-linkage is a function of multiple phase currents and rotor position, resulting in a three or more dimensional look-up table.

In other words, the techniques used to model the magnetically de-coupled SRMs cannot be used to simulate the 6-phase machine with mutually coupled phases. To ease the difficulty faced with the simulation of the machine with mutually coupled phases, an alternative network relating flux and MMF in the magnetically coupled 6-phase machine to those in an equivalent magnetically de-coupled 6-phase machine is needed. Use of transformation matrices to de-couple the mutual coupling between phases has previously been successfully used for conventional toothed rotor SRMs with fully pitched windings [91] The idea is simple: "*Use a set of so-called transformation matrices in order to de-couple the mutually coupled nature of phase quantities such as MMF and flux-linkage into equivalent but mutually de-coupled quantities so that the analysis, understanding and the simulation of the machine are simplified [91]*."

The flux-linkage characteristics obtained from 2-D FE analysis (the end-winding length to stack length ratio is relatively small) can be used to characterise the machine at different rotor positions. It then becomes a relatively simple problem to solve for the phase current, flux-linkage and torque values. In the case of a short-pitched 6-phase segmented rotor SRM, where phases are connected back-to-back and then connected in star or delta, the flux-linkage in a phase is a non-linear function of rotor position and the currents in all phases. It is rather difficult to solve for each phase current, flux-linkage and torque due to the mutual coupling between phases. It makes the machine both very difficult to simulate and difficult to understand.

A set of transformation matrices has been generated to convert current and flux-linkage values into corresponding values in a magnetically de-coupled machine. A more appropriate terminology for "magnetically de-coupled machine" parameters, in this case is perhaps "slot" parameters. For a segmented rotor SRM the torque is produced as the rotor segments modulate the stator slot permeance and magnetic flux paths enclose stator slots, therefore it is more appropriate to think in terms of permeance variation per slot

rather than the permeance variation per tooth, which is evaluated in conventional SRMs. Once the transformations are completed it is then possible to apply the techniques used to simulate a conventional SRM with de-coupled phases to the 6-phase delta / star connected segmented rotor SRM with magnetically coupled phases.

The aim is to:

1. Develop a set of equations that convert teeth MMFs to slot MMFs.

2. Check that the 6x6 matrix formed by combining the transformation equations that are found in 1 has an inverse (i.e. determinant of the matrix is non zero). This is to be able to convert slot MMFs into teeth MMFs in the simulation. The magnetic characteristics that will be used in the simulation will be relating flux circulating around one of the machine slots against the MMF in that slot for varying rotor positions. However, the ultimate aim of the simulation is to calculate the phase currents at every time step. Therefore the slot MMFs determined from the magnetisation characteristics of the slot (flux and rotor position required) will need to be converted to teeth MMFs so that the phase currents can be determined (using number of turns). This is demonstrated with Equation 15.

$$V_{PHASE} \Rightarrow [\psi]_{PHASE} \Rightarrow [\psi]_{SLOT} \overset{POSITION}{\Rightarrow} [MMF]_{SLOT} \Rightarrow [i]_{PHASE} \qquad \textbf{Equation 15}$$

3. Develop a set of equations that convert slot fluxes to teeth fluxes.

4. Check that the 6x6 matrix formed by combining the transformation equations that are found in 3 has an inverse. This is to be able to convert teeth fluxes (relating to phase flux-linkage via the number of turns) into slot fluxes. Slot fluxes along with the rotor position are required to be known at every time step of the simulation so that the slot MMFs can be determined (Equation 16). Next, the slot MMFs and the rotor position can be used to calculate the torque contribution of each slot. Slot MMFs are then converted into teeth MMFs and finally phase currents to be used at the next time step of the simulation are determined.

$$[\phi]_{SLOT} = [C]_{FLX} \bullet [\phi]_{TOOTH} \qquad \textbf{Equation 16}$$

It would be a good idea at this stage to present the schematic explanation of the simulation for the 6-phase prototype with mutually coupled phases. This is done in Figure 102 for the simulation of the star-connected 6-phase segmental rotor SRM. The same schematic can be used to represent the delta-connected drive as well. The only modification to the schematics in Figure 102 would then be the method used to calculate the phase voltages from line voltages (Vx, Vy and Vz).

$$[MMF]_{TOOTH} = [C]_{MMF} \bullet [MMF]_{SLOT} \qquad \textbf{Equation 17}$$

$[\phi]_{TOOTH}$ in Equation 16 and $[MMF]_{TOOTH}$ in Equation 17 can be linked to $[\psi]_{PHASE}$ and $[i]_{PHASE}$ in Equation 15 via the number of turns per tooth.

By examining Figure 103 (Figure 39 repeated here for clarity) the slot currents can be written as

$$\begin{bmatrix} Ia \\ Ib \\ Ic \\ Id \\ Ie \\ If \end{bmatrix} = \begin{bmatrix} 1 & 1 & 0 & 0 & 0 & 0 \\ 0 & 1 & 1 & 0 & 0 & 0 \\ 0 & 0 & 1 & 1 & 0 & 0 \\ 0 & 0 & 0 & 1 & 1 & 0 \\ 0 & 0 & 0 & 0 & 1 & 1 \\ 1 & 0 & 0 & 0 & 0 & 1 \end{bmatrix} \bullet \begin{bmatrix} I1 \\ I2 \\ I3 \\ I4 \\ I5 \\ I6 \end{bmatrix} \qquad \textbf{Equation 18}$$

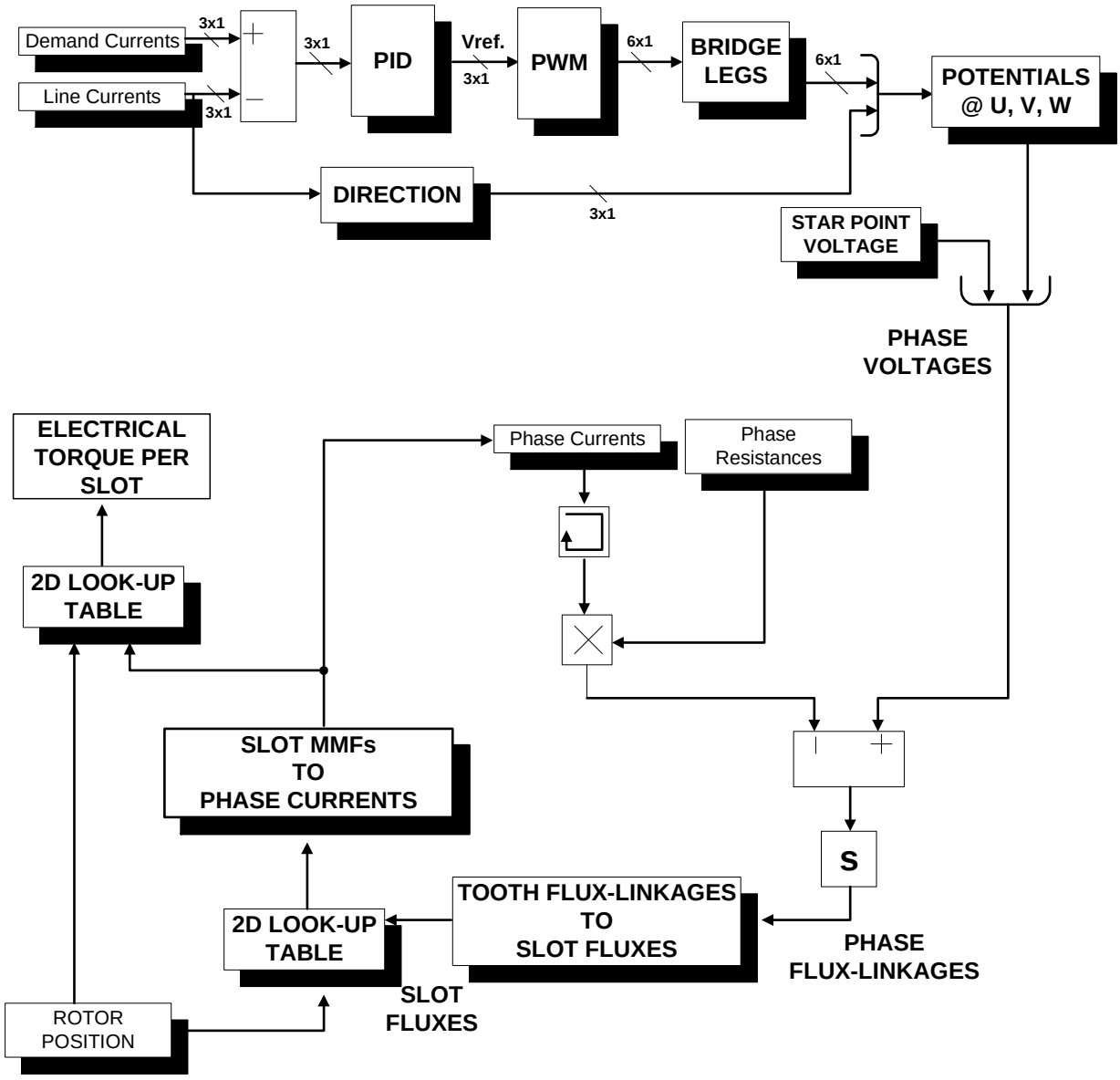

Figure 102 Schematic explanation of simulation of six-phase SRM with mutually coupled phase windings

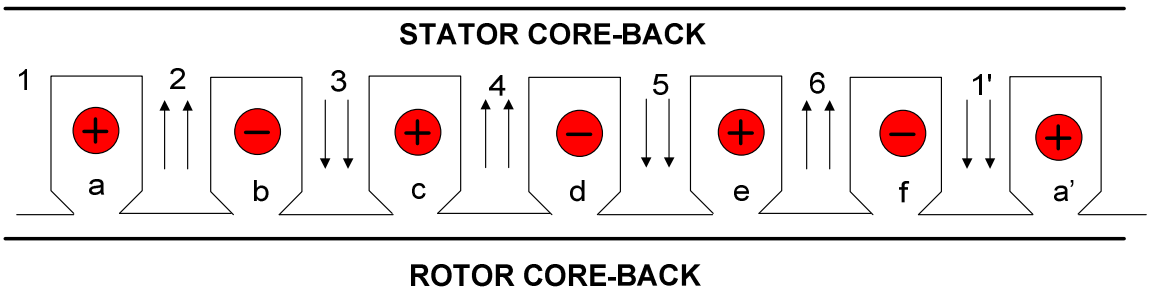

Figure 103 2D rectilinear representation of six-phase SRM showing the direction of slot MMFs and teeth fluxes

From Equation 17 and Equation 18 the transformation matrix for converting teeth currents into slot currents is given in Equation 19.

$$[C]_{MMF} = \begin{bmatrix} 1 & 1 & 0 & 0 & 0 & 0 \\ 0 & 1 & 1 & 0 & 0 & 0 \\ 0 & 0 & 1 & 1 & 0 & 0 \\ 0 & 0 & 0 & 1 & 1 & 0 \\ 0 & 0 & 0 & 0 & 1 & 1 \\ 1 & 0 & 0 & 0 & 0 & 1 \end{bmatrix} \quad \textbf{Equation 19}$$

In order to convert slot MMFs to teeth MMFs, $[C]_{MMF}$ in Equation 19 must be a non-singular matrix (the determinant of $[C]_{MMF}$ must be non-zero). However, it is possible to obtain any one row or any one column of $[C]_{MMF}$ from a linear combination of other rows or columns of the same matrix. This means that the determinant of $[C]_{MMF}$ is 0, and, hence $[C]_{MMF}$ does not have an inverse matrix. The transformation matrix in Equation 19 is of no use on its own and additional equations are required in order to overcome the problem of matrix singularity.

In Figure 103 the net slot MMF should equal zero. Therefore,

$$Ia - Ib + Ic - Id + Ie - If = 0 \quad \textbf{Equation 20}$$

However, Equation 20 can be solved implicitly from Equation 18.

Additionally for a star connected machine as shown in Figure 32, module currents must sum up to zero at the star point.

$$I1 + I3 + I5 - I2 - I4 - I6 = 0 \quad \textbf{Equation 21}$$

As current in any one phase can be calculated from currents in the other five phases, the first row and column of the matrix in Equation 19 can be removed (this is not a rule, it can be the second row and column, etc.). However, the first column cannot be removed directly as the current in Phase-F (i.e. If) cannot be calculated without the first column of the matrix. However from Equation 21 $I1$ can be rewritten as

$$I1 = I2 + I4 + I6 - I3 - I5$$ **Equation 22**

Removing the first column and row from Equation 18 and using Equation 22, the new transformation matrix can be written as in Equation 23.

$$\begin{bmatrix} Ib \\ Ic \\ Id \\ Ie \\ If \end{bmatrix} = \begin{bmatrix} 1 & 1 & 0 & 0 & 0 \\ 0 & 1 & 1 & 0 & 0 \\ 0 & 0 & 1 & 1 & 0 \\ 0 & 0 & 0 & 1 & 1 \\ 1 & -1 & 1 & -1 & 2 \end{bmatrix} \bullet \begin{bmatrix} I2 \\ I3 \\ I4 \\ I5 \\ I6 \end{bmatrix}$$ **Equation 23**

The 5 by 5 matrix in Equation 23 is non-singular and has an inverse of the form given in Equation 24.

$$\begin{bmatrix} I2 \\ I3 \\ I4 \\ I5 \\ I6 \end{bmatrix} = \begin{bmatrix} 0 & 0 & -1 & -1 & -1 \\ -1 & 0 & 0 & -1 & -1 \\ -1 & -1 & 0 & 0 & -1 \\ -1 & -1 & -1 & 0 & 0 \\ 0 & -2 & 0 & -2 & 1 \end{bmatrix} \bullet \begin{bmatrix} Ib \\ Ic \\ Id \\ Ie \\ If \end{bmatrix}$$ **Equation 24**

Using Equation 24 and Equation 22 all phase currents can be calculated.

The above transformation is valid for the star-connected drive.
Once again by examining Figure 103 the teeth fluxes can be written as in Equation 25.

$$\begin{bmatrix} \phi 1 \\ \phi 2 \\ \phi 3 \\ \phi 4 \\ \phi 5 \\ \phi 6 \end{bmatrix} = \begin{bmatrix} 1 & 0 & 0 & 0 & 0 & 1 \\ 1 & 1 & 0 & 0 & 0 & 0 \\ 0 & 1 & 1 & 0 & 0 & 0 \\ 0 & 0 & 1 & 1 & 0 & 0 \\ 0 & 0 & 0 & 1 & 1 & 0 \\ 0 & 0 & 0 & 0 & 1 & 1 \end{bmatrix} \bullet \begin{bmatrix} \phi a \\ \phi b \\ \phi c \\ \phi d \\ \phi e \\ \phi f \end{bmatrix}$$ **Equation 25**

Similar to the transformation matrix in Equation 19, any one row or column of the transformation matrix in Equation 25 can be calculated by linear combination of others, i.e. there is no inverse of the matrix. For the machine in Figure 39, the net flux flowing through the stator teeth should sum up to zero. This can be represented by Equation 26.

$$\phi 1 + \phi 3 + \phi 5 - \phi 2 - \phi 4 - \phi 6 = 0 \qquad \textbf{Equation 26}$$

However, Equation 26 can be solved implicitly from Equation 25.

The net flux enclosing the stator slots should also sum up to zero. This necessitates Equation 27 to be satisfied.

$$\phi a + \phi b + \phi c + \phi d + \phi e + \phi f = 0 \qquad \textbf{Equation 27}$$

From Equation 27 the flux circulating around slot-a (i.e. ϕa) can be rewritten as given in Equation 28.

$$\phi a = -\phi b - \phi c - \phi d - \phi e - \phi f \qquad \textbf{Equation 28}$$

Similar to the process of calculating the current transformation matrix, the first row and column of the 6 by 6 matrix in Equation 25 are removed. From Equation 25 and Equation 28 the following transformation matrix is devised (Equation 29).

$$\begin{bmatrix} \phi 2 \\ \phi 3 \\ \phi 4 \\ \phi 5 \\ \phi 6 \end{bmatrix} = \begin{bmatrix} 0 & -1 & -1 & -1 & -1 \\ 1 & 1 & 0 & 0 & 0 \\ 0 & 1 & 1 & 0 & 0 \\ 0 & 0 & 1 & 1 & 0 \\ 0 & 0 & 0 & 1 & 1 \end{bmatrix} \bullet \begin{bmatrix} \phi b \\ \phi c \\ \phi d \\ \phi e \\ \phi f \end{bmatrix} \qquad \textbf{Equation 29}$$

The 5 by 5 matrix in Equation 29 is non-singular and has an inverse of the form given in Equation 30.

$$\begin{bmatrix} \phi b \\ \phi c \\ \phi d \\ \phi e \\ \phi f \end{bmatrix} = \begin{bmatrix} -1 & -2 & -2 & -2 & -2 \\ 0 & 0 & -1 & -1 & -1 \\ -1 & 0 & 0 & -1 & -1 \\ -1 & -1 & 0 & 0 & -1 \\ -1 & -1 & -1 & 0 & 0 \end{bmatrix} \bullet \begin{bmatrix} \phi 2 \\ \phi 3 \\ \phi 4 \\ \phi 5 \\ \phi 6 \end{bmatrix} \qquad \textbf{Equation 30}$$

Using Equation 28 and Equation 30 all slot fluxes can be determined. As the transformation matrix in Equation 25 is the transpose of the transformation matrix in Equation 18, the transformations are power invariant (flux transformation relates directly to voltage transformation and power is the product of current and voltage). Once the transformations are completed, it is then possible to apply the techniques used to simulate a segmented rotor SRM with de-coupled phases to the 6-phase delta / star connected segmented rotor SRM.

As mentioned earlier, due to the mutual coupling between phases, flux-linkage in a phase is not necessarily zero even if the current in that phase is zero. In the simulation of the machines with mutually de-coupled phases the phase flux-linkages are all forced to stay at zero until the beginning of the next energisation cycle of the phases once the phase currents fall to zero. However, with the machine where the phases are mutually coupled, any change in a phase current will result in a change to the flux linking all six phases. Therefore, the phase flux-linkages should not be zeroed when the phase currents fall to zero. It should be noted that at the periods where the phase current is zero and the phase energisation cycle is finished the phase diode still operates and stops the current reversing direction. Moreover, unlike the short-pitched SRMs with mutually de-coupled phases where the flux-linkage is always positive, the flux-linkage of a phase may need to go negative during the off period of a phase. This is again due to the mutual coupling effects.

It has been already mentioned that the simulation model requires the knowledge of the flux vs. MMF characteristics of one of the machine slots at different rotor positions as well as the transformation matrices. These characteristics used in the simulation are obtained in the FE package. The method used to generate these characteristics is explained in detail in Chapter 9.

The transformation matrix used to transform tooth fluxes into equivalent slot fluxes of a star-connected machine can also be utilised for the delta-connected machine. However the transformation matrix derived for transforming the slot MMFs into phase currents cannot be used for the delta-connected drive as the module currents do not necessarily sum up to

zero. Therefore another equation is needed for the delta-connected machine to create the MMF/Current transformation matrix. At the time of writing this thesis the transformation matrices for the delta-connected drive were not completed.

6.5 PERFORMANCE CALCULATIONS

At the end of a simulation, the results are transferred into a script by feeding the required signals into individual output ports at the highest level of the Simulink® model. Each output port is given a name (Figure 104). The names given to the output ports are then input into the "Data Import / Export" part of the *Configuration Parameters* (Figure 105 - the order of occurrence should be kept the same as the one in the Simulink® model).

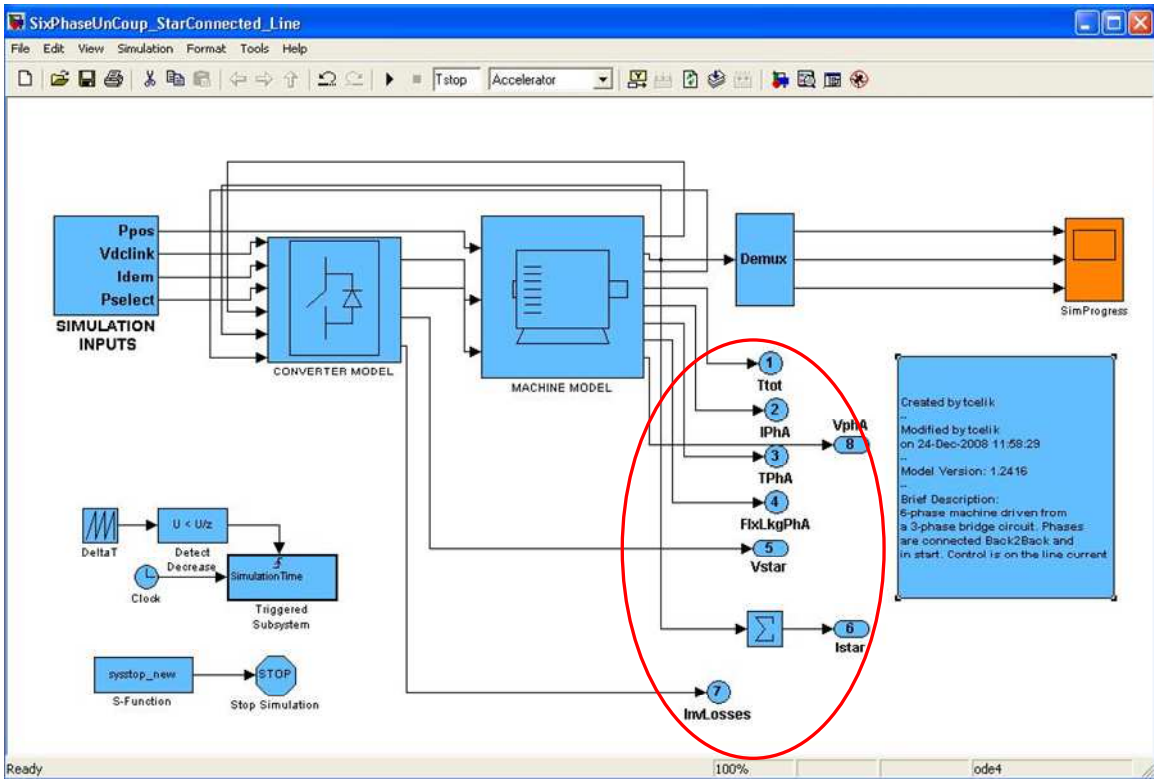

Figure 104 Data Exporting for Offline Statistical Calculations Once the Simulation Has Completed (Output Ports Circled in Red)

These results are then used to carry out statistical calculations such as inverter losses, average machine torque, torque ripple, inverter VA ratings and machine copper losses. Once the simulation completes, statistical calculations are carried out over the last three

complete electrical cycles. For this reason, the M-file script first extracts the last three electrical cycles of every simulation output waveform.

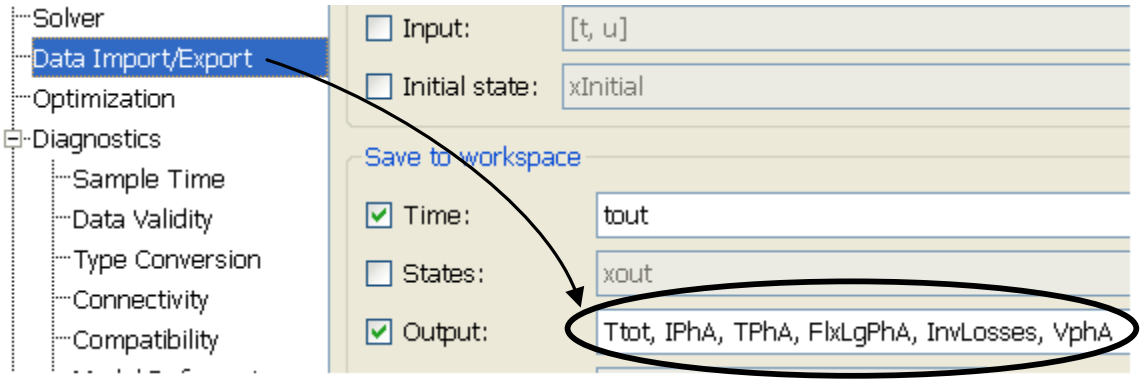

Figure 105 Configuration parameters pane used for data importing / exporting in Simulink®

Power electronics loss calculations vary depending on the converter topology used. However the principle of the performance calculations is the same for all of the converter topologies. IGBT conduction, switching losses and diode conduction losses are all calculated at each time step within the simulation. The averaging of these losses, on the other hand, is done offline once the simulation finishes and these waveforms are available for the post-processing code.

Instantaneous torque is calculated at every time step of the simulation for each phase of the machine. Total electric machine torque is then calculated by summing instantaneous torque values of each phase of the machine.

6.6 SUMMARY

A simulation database has been developed that is able to model SR machines for different machine geometries and phase numbers by employing the machine's flux-linkage characteristics, either obtained from measurements or from finite element analysis. As the flux-linkage characteristics accurately describe the way flux varies with position and current, they can be used to correctly model the magnetic saturation in any switched reluctance machine. Simulation models for two-phase, three-phase and six-phase SRMs have been generated. Asymmetric half-bridge, 3-phase full bridge and h-bridge converters have also been modelled in the simulation package. The simulation model is flexible - any

simulation model can be changed to run with a different converter or controller without having to re-create the entire model.

For six phase segmental rotor machine modelling, an approach has been taken which is similar to the one employed for modelling of fully-pitched winding machines. For this, a set of transformation matrices have been generated in order to ease the modelling of six phase segmental rotor machines by de-coupling phase quantities into slot quantities. Magnetic saturation is modelled by using a combination of the machine's flux-linkage / current / angle relationship and a suitable time-stepping solution.

For the time-stepping solution, a fourth order Runge-Kutta solver readily available in Simulink® has been chosen which generates accurate simulation results without compromising the speed of simulation. The time stepping routine is able to determine how the current in the machine is affected at any instance in time by the switching states of the inverter and the position of the rotor. A GUI has also been developed to ease the running of any simulation for the user. All of the essential parameters needed for the simulation are presented in a window so that the user does not have to know the details of the simulation to be able to drive it. The details of the GUI are presented in Appendix C. The user interface is also able to carry out statistical calculations including inverter losses, copper losses and torque ripple based on simulation results, in addition to producing waveforms such as instantaneous output torque and phase current.

In Chapters 7, 8, and 9 simulation results along with measurements will be presented for the 2-phase, 3-phase and 6-phase drives, respectively.

CHAPTER 7

7– Machine Operation and Comparison to Simulation - Two Phase Drives -

7.1 INTRODUCTION

This chapter contains the dynamic measurement and simulation results of two-phase segmental rotor machine drives. A two-phase machine was not designed; instead the phases of the six-phase segmental machine were connected such that it could be run as a two phase machine. The operational principles of the asymmetric half-bridge and h-bridge converters were both presented in Chapter 3; the description of the test rig was given in Chapter 5. The inverter of the test rig was configured to drive:

- The two-phase segmental rotor machine from the asymmetric half-bridge converter.
- The two-phase segmental rotor machine from the h-bridge converter with series diodes.

In the next section, the simulated results will be compared against those measured for the h-bridge and asymmetric half-bridge driven two-phase machine. Matlab® based scripts were used to analyse the measured waveforms in order to predict some of the performance parameters of the drive systems and ease the comparison against simulated

waveforms and simulated performance parameters. Examples at low and high speeds are presented.

Following on from the comparison of simulated results against measurements, section 7.3 focuses on the relative performance comparison of the asymmetric half-bridge and h-bridge driven 2-phase machine in the dynamic simulation environment. The section looks at how well the two topologies compare in terms of:

- The total inverter loss at high and low speeds.
- Overall drive efficiency at high and low speeds.

7.2 MEASUREMENTS AND SIMULATION RESULTS

A segmental rotor machine with two-phases has not been designed; instead the phases of the six-phase segmental machine were connected such that it could be run as a two phase machine. A schematic description of the six-phase machine configured as a two-phase machine is given in Figure 106.

Phases A and F and phases C and D of the six phase machine have been paired together to form Phase-1 and Phase-2 of the two-phase segmental machine, respectively. Phase B and phase E of the six-phase machine have been left unconnected. There is no need to measure the flux-linkage characteristics of the two-phase machine as the flux-linkage measurements taken from the six-phase machine by connecting two adjacent phases in series are equivalent to the per phase flux-linkage characteristics of the newly configured two phase machine.

The inverter legs of the drive system (explained in Chapter 5) have been configured to drive the two phase machine from an h-bridge and an asymmetric half bridge inverter. The operating principles of both asymmetric half-bridge and h-bridge inverters have been given in Chapter 3. Only the measured and simulated waveforms are presented in this section. In the h-bridge driven case the phases of the two-phase machine were connected back-to-back through phase diodes (which are used to force the phase currents to be unipolar). Instead of controlling phase currents separately, the line current was controlled

with a single current transducer. This is thought to be beneficial in terms of drive simplicity and cost.

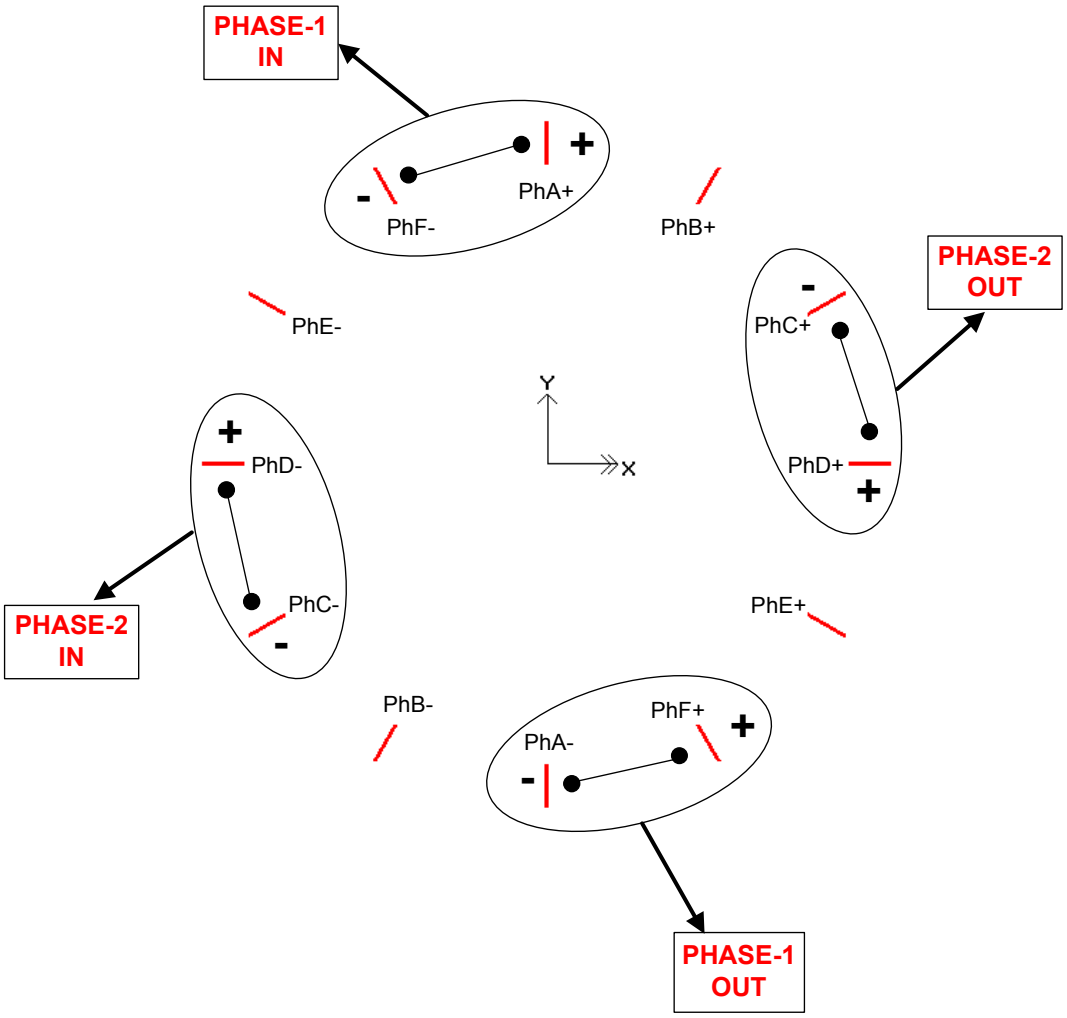

Figure 106 Six-phase segmental rotor machine configured to run as a two-phase machine

A Matlab® based script was written to analyse the oscilloscope captured running waveforms and indirectly calculate performance parameters such as total output torque and copper losses. The script takes the phase current waveform, switch-on angle, phase resistance, number of phases and estimated winding temperature during test as inputs and is able to identify / calculate the following parameters:

- The total duration of phase energisation i.e. conduction angle
- Torque generated by a phase
- Total machine output torque

- Torque ripple
- Running speed
- Shaft power
- Peak phase current
- RMS phase current
- Copper loss
- Flux-linkage locus
- Line current waveform for h-bridge connected drive

The test rig had a torque-meter coupled to the shaft of the machine in test. The torque-meter was capable of providing average shaft torque measurement. However, the instantaneous torque waveform analysis was not possible with the torque-meter, except at very low speed. The above mentioned Matlab script is very useful for deriving the torque waveforms. The script uses the flux-linkage-current-position (ψ-i-θ) characteristics of the machine to calculate the phase flux-linkage and the torque-current-position (T-i-θ) characteristics to calculate the torque generated by the phase. Both (ψ-i-θ) and (T-i-θ) characteristics can be obtained by measurements or by FE simulations. Phase quantities are then phase shifted (depending on the number of phases and the number of rotor poles) to calculate the contribution of all phases to torque production. The total instantaneous electromagnetic torque for the machine is then the sum of the torques for each phase. The torque calculated by this technique does not include rotational losses, nor does it include the magnetic saturation of one phase affecting the characteristics of another. The result generated by the script can therefore be higher than the shaft torque actually delivered by the machine. Rotational losses increase with speed. As a result, the discrepancy is expected to be larger at higher speeds.

7.2.1 Two-Phase Machine Driven by H-Bridge Inverter

Simulating the H-bridge drive shown in Figure 107 is beneficial in that it can be used as a building block for the more complicated six-phase drive system simulation. Both the six-phase drive and the two-phase h-bridge drive have two phases connected back to back through phase diodes.

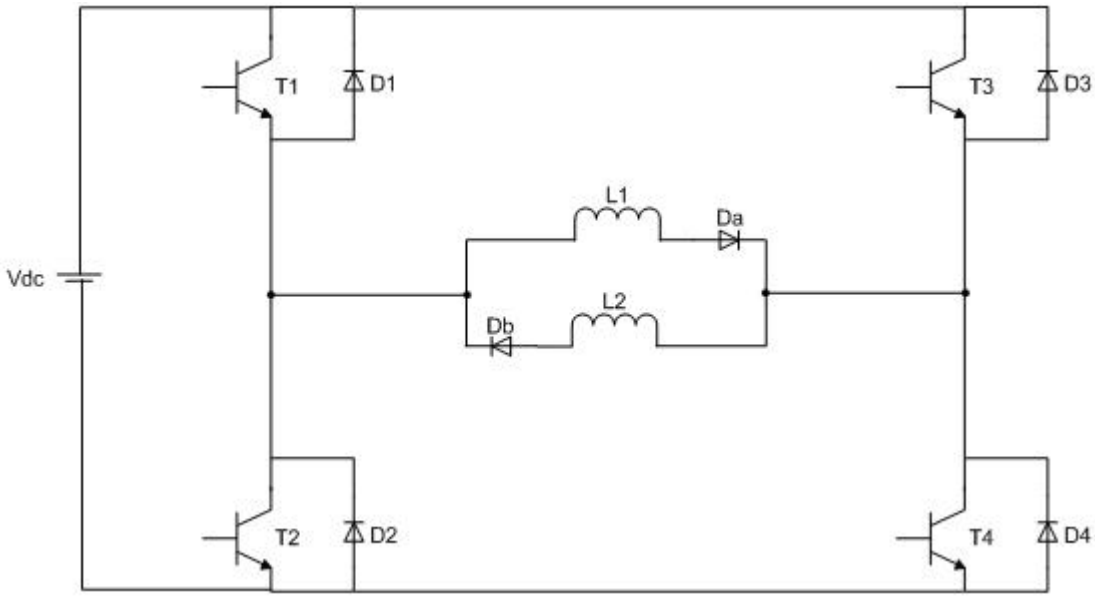

Figure 107 H-bridge converter driving a back-to-back connected two-phase machine

Simulation techniques used to model the two-phase h-bridge drive can then ease the modelling of the six-phase drive.

To explain the operation of the H-bridge inverter driving the 2-phase SRM with its phases connected back-to-back through phase diodes, the simulated waveforms in Figure 108 and Figure 109 are used. In Figure 108 and Figure 109 the machine is under current control and voltage control, respectively. In both Figure 108 and Figure 109 the conduction angles are 120^{o} (electrical), the phases are energised at the unaligned position, the line current demands are 30A and the dc-link voltages are 175V. The phase voltage trace in both figures depicts two plots: in red is the actual phase voltage applied during simulation and the plot in blue is the filtered (with a moving average filter) version of this simulated phase voltage.

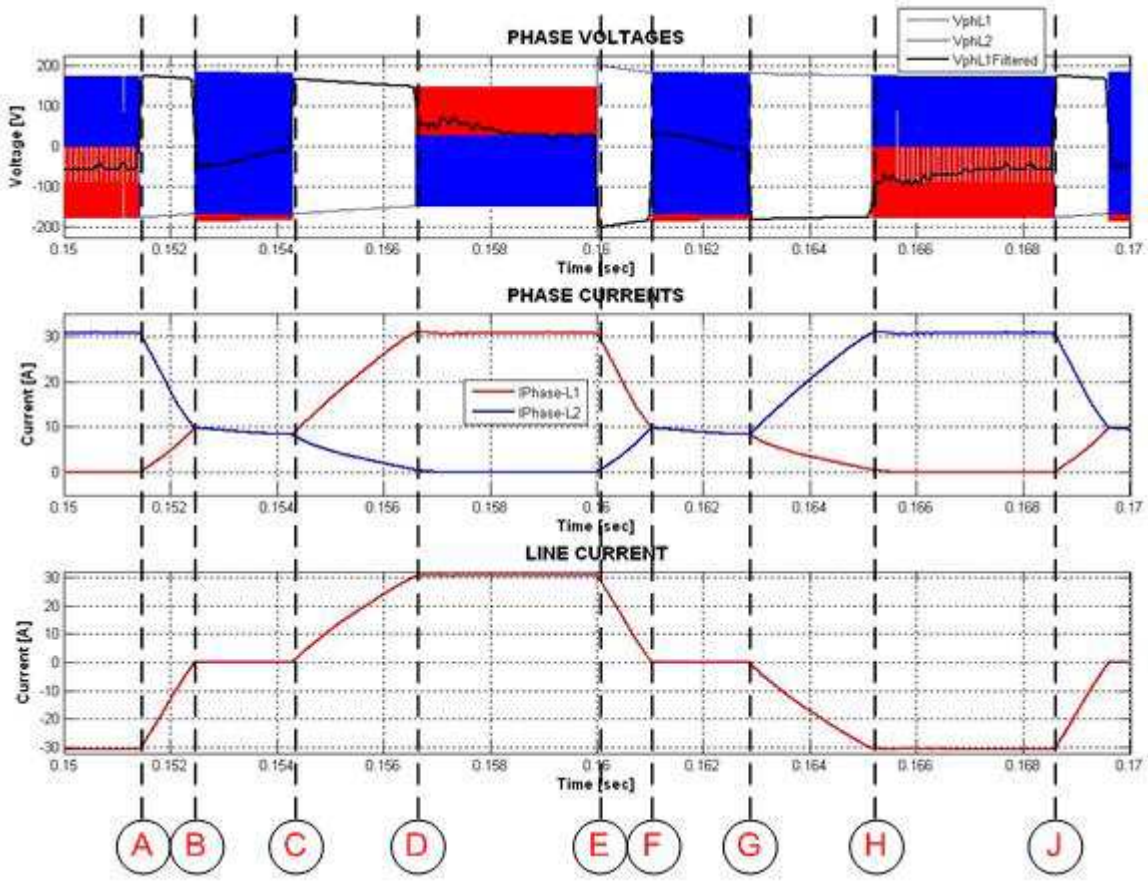

Figure 108 Simulation results of the two-phase machine driven from an H-bridge inverter under current control. Conduction angle is 120 degrees (electrical), no advancing, current demand is 30A and the dc-link voltage is 175V. Top trace = phase voltages – red for L1, blue for L2, black for filtered L1 voltage; middle trace = phase currents – red for L1, blue for L2; bottom trace = line current. Speed of operation is 350RPM

With respect to Figure 107, in Figure 108:

Point A: Phase L2 starts to turn off. Phase L1 is not turned on at this point. However, the negative voltage across phase L2 (Figure 108 waveform in blue in top trace) to de-flux the phase is seen as positive voltage across phase L1 (Figure 108 waveforms in red and black in top trace). The line current falls (Figure 108 bottom trace) to zero whereas the current in phase L1 (waveform in red in middle trace) rises until point B.

Point B: Line current falls to zero. The controller in the simulation aims to keep the line current at zero until point C (where phase L1 is turned on) by applying positive and negative dc-link voltage across both phases. The current in phase L1 drops slightly due to the resistive voltage drop across phase windings.

Point C: Phase L1 is turned on. Both the line current and the phase L1 current rises rapidly with the positive voltage across phase L1 windings.

Point D: The current demand is reached. The machine is under current control. The controller in the simulation aims to keep the current at the demand level by applying positive and zero volts across phase L1 windings. The positive voltage across phase L1 is seen as a negative voltage across the phase L2 windings. The diode (Db in Figure 30) is reverse-biased and does not allow the current in phase L2 to flow in the reverse direction.

Point E: Phase L1 starts to turn off. The controller applies negative volts across phase L1 windings and its current falls to zero. Phase L2 current (similar to the rise in phase L1 current between points A and B) starts rising due to positive volts seen across phase L2 windings.

Point F: Line current falls to zero once again. The controller works similar to the way it did between points B and C.

Point G: Phase L2 is energised and its current rises rapidly until the line current demand is reached at point H, as between points C and D.

Point H: Line current demand is reached and controlled, in an identical manner to point D.

Point J: Back to point A.

The only difference in traces in Figure 109 compared to those in Figure 108 is the fact that the machine is running under voltage control. The line current demand of 30A is not reached and the controller applies positive volts for the entire duration of the conduction period. Similar to Figure 108, when the line current falls to zero, the controller aims to keep the current at zero by applying positive and negative volts across phases until the next energisation point of either phase. From Figure 110 to Figure 113 the simulation results of the h-bridge driven two-phase machine are compared to the measurements taken from the test rig under various operating conditions. The red trace in each figure is

the measured waveform and the blue trace is the simulated waveform. The instantaneous measured torque waveform is not actually measured. It is calculated with the Matlab® script by using the rotor position information (which is also calculated) and the phase current. Negative advance angles in the figures are when the phase is energised after the unaligned position.

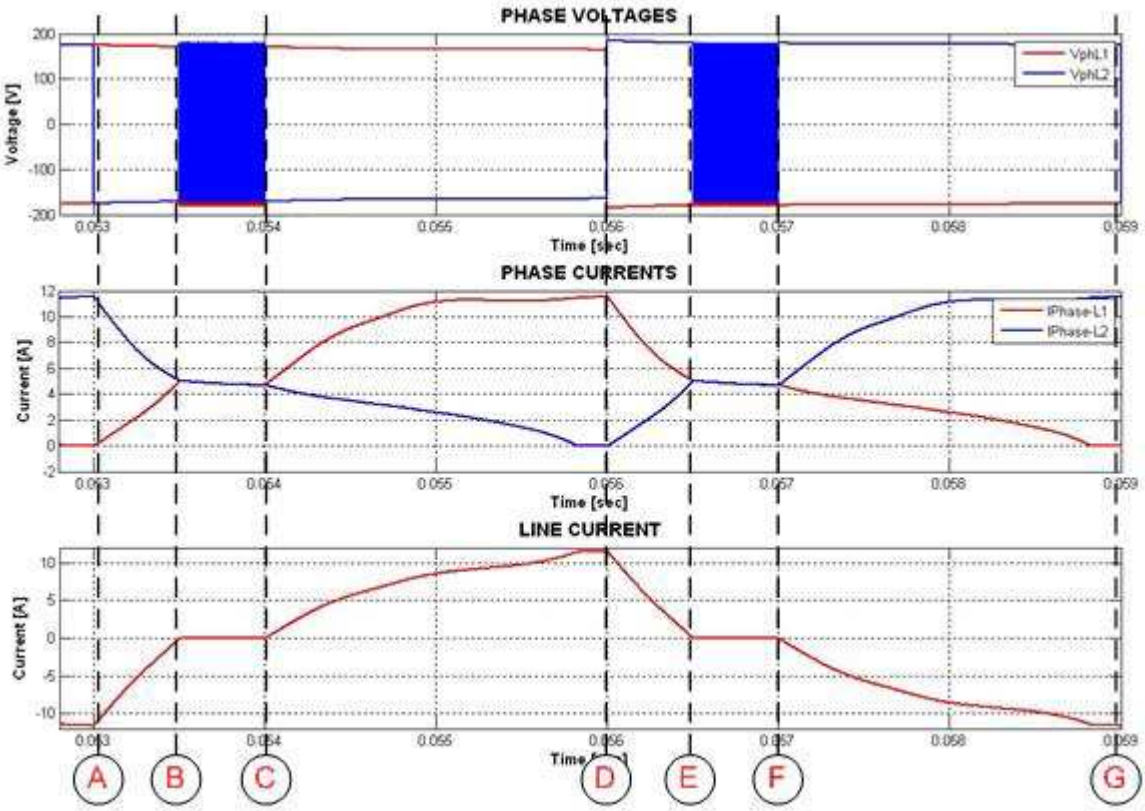

Figure 109 Simulation results of the two-phase machine driven from an H-bridge inverter under voltage control. Conduction angle is 120 degrees (electrical), no advancing, current demand is 30A and the dc-link voltage is 175V. Top trace = phase voltages (red for L1, blue for L2); middle trace = phase currents (red for L1, blue for L2); bottom trace = line current. Speed of operation is 1000RPM

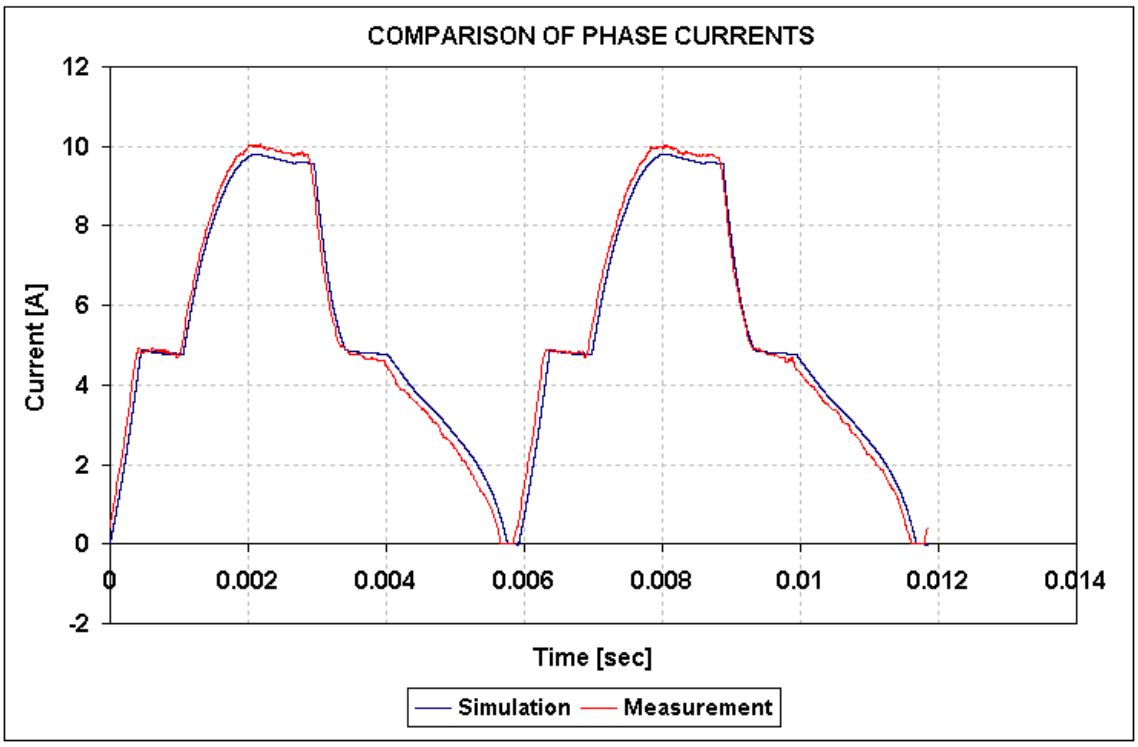

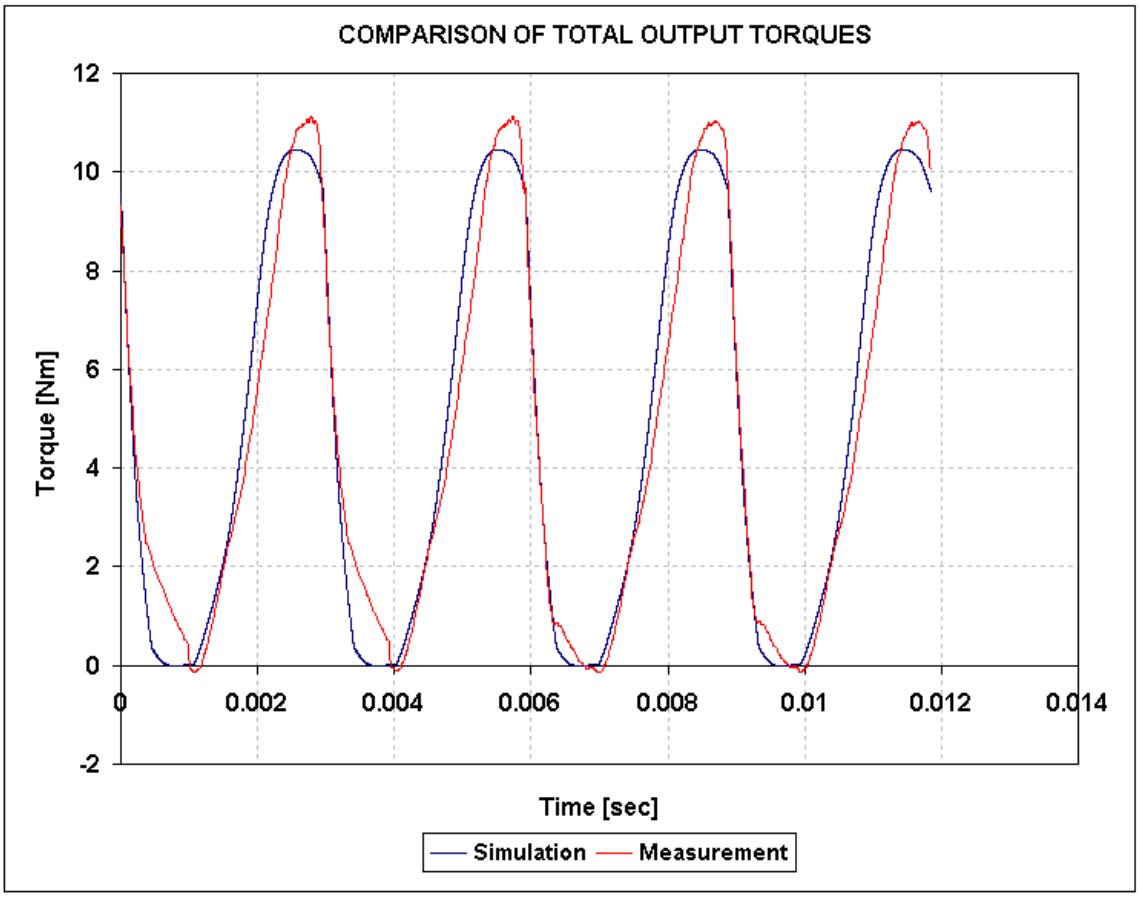

Figure 110 Phase current and machine total output torque comparison of simulated and measured results for h-bridge inverter with Advance Angle = 10Degrees; Conduction Angle = 115.4Degrees; Speed = 1013.5RPM; Current Demand = 30A; Vdclink = 175V

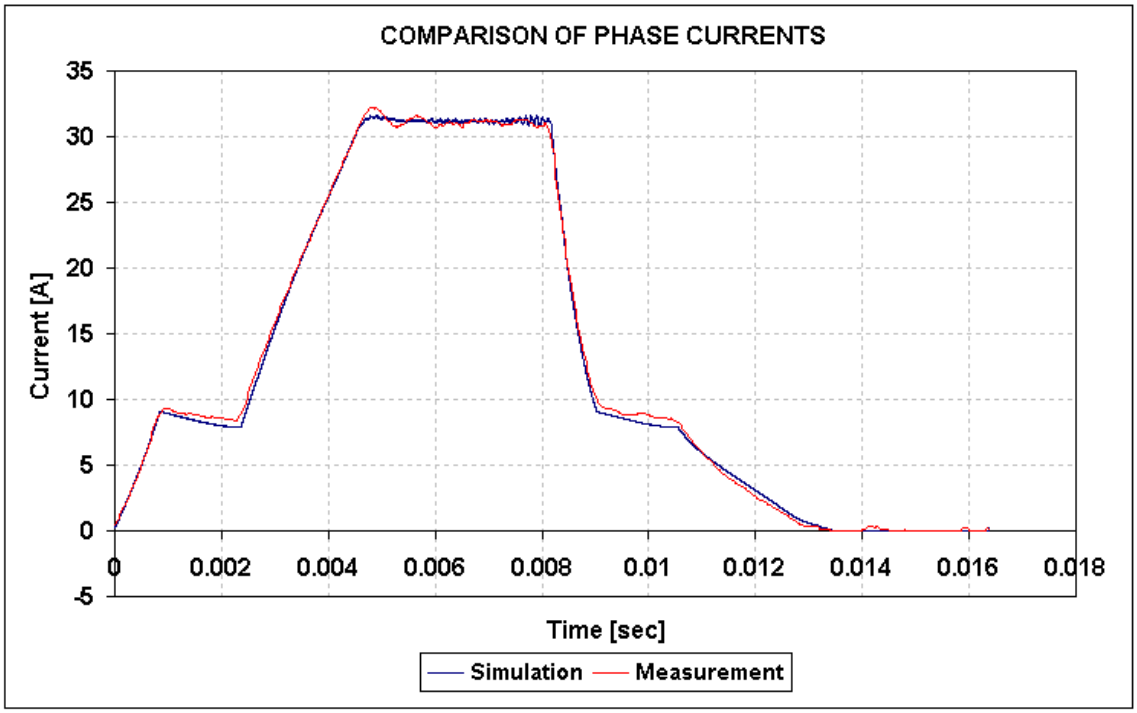

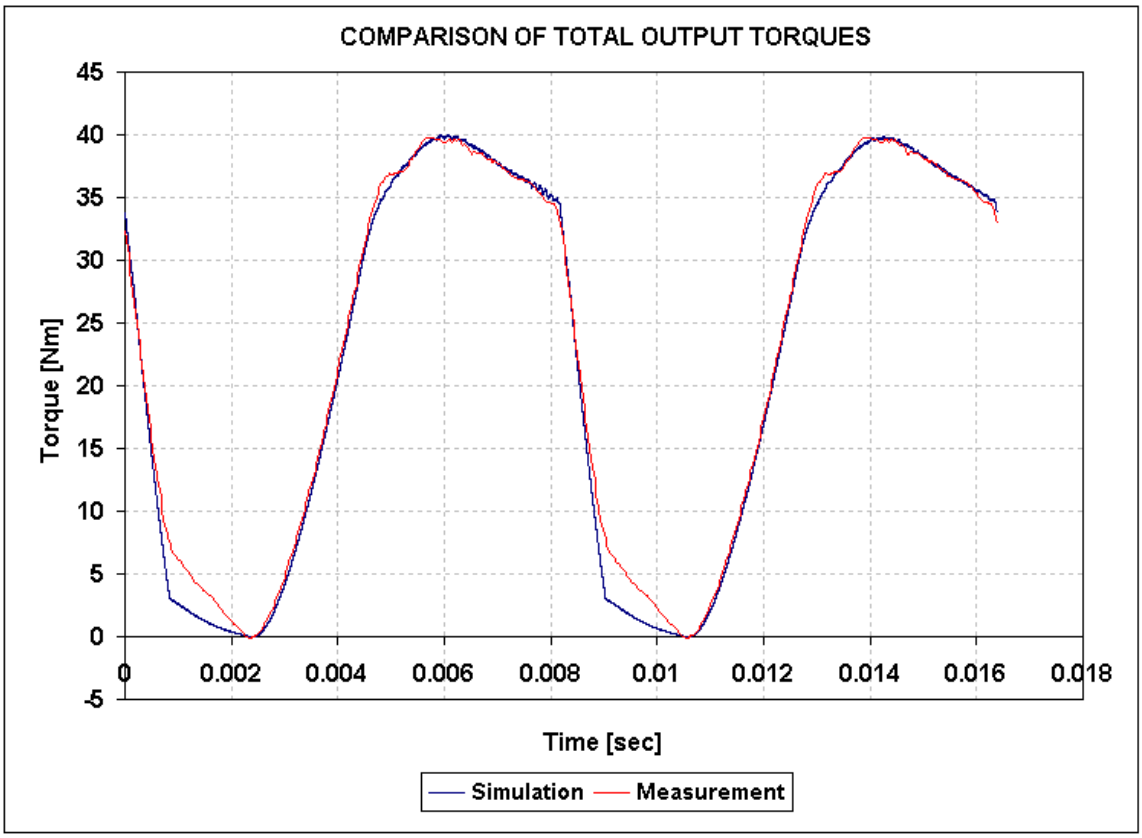

Figure 111 Phase current and machine total output torque comparison of simulated and measured results for h-bridge inverter with Advance Angle = 0Degrees; Conduction Angle = 127.7Degrees; Speed = 366.2RPM; Current Demand = 30A; Vdclink = 175V

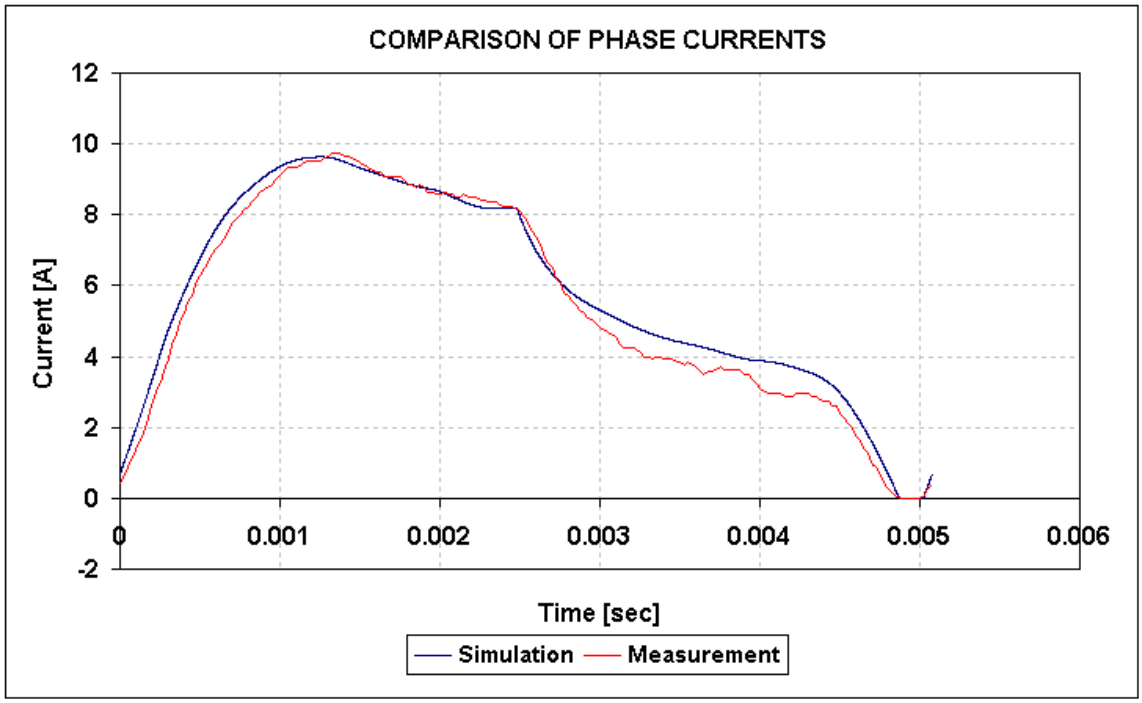

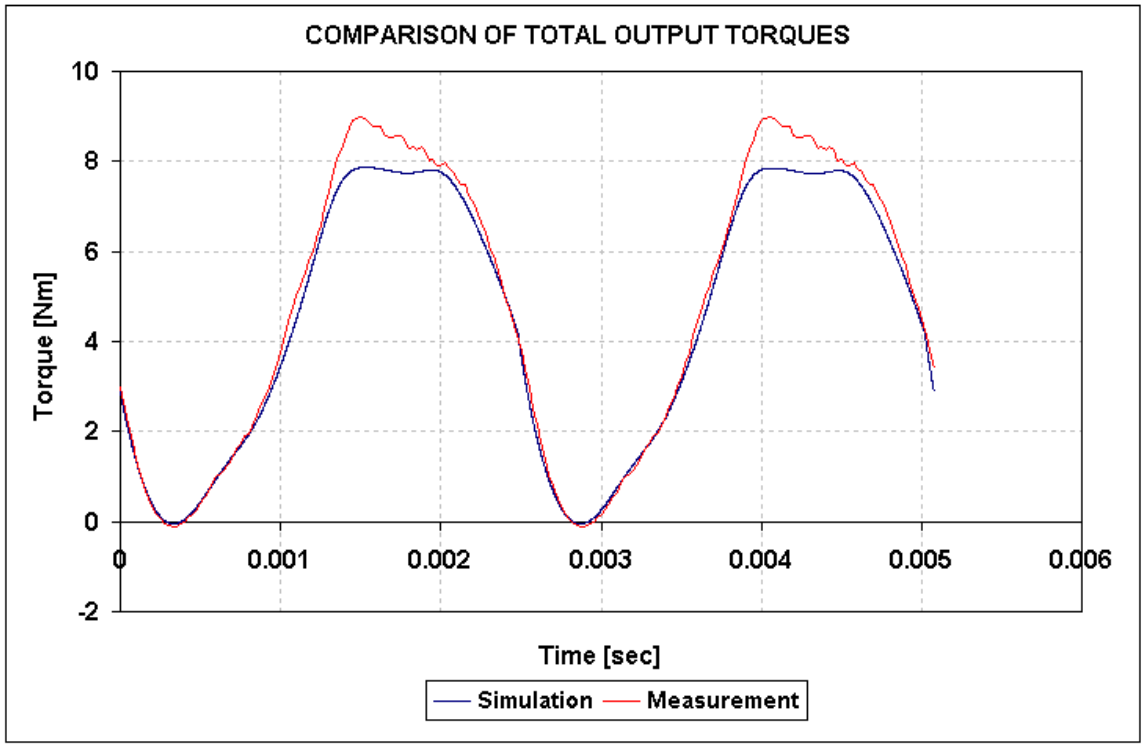

Figure 112 Phase current and machine total output torque comparison of simulated and measured results for h-bridge inverter with Advance Angle = 20Degrees; Conduction Angle = 175.6Degrees; Speed = 1181.7RPM; Current Demand = 30A; Vdclink = 175V

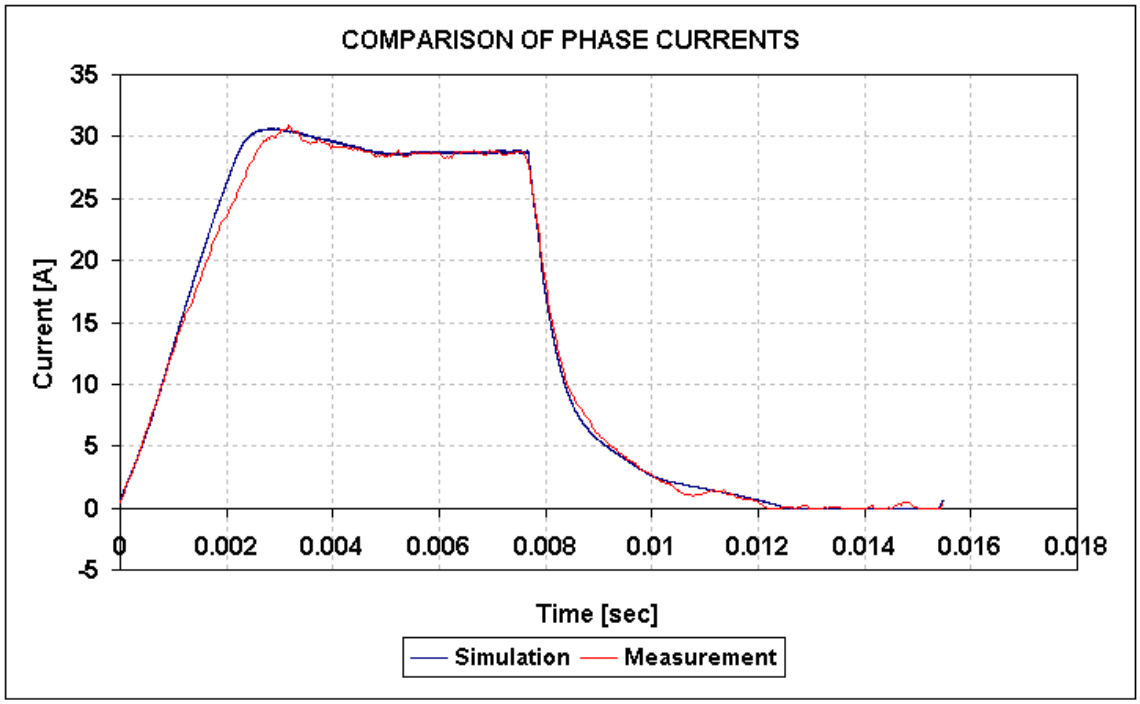

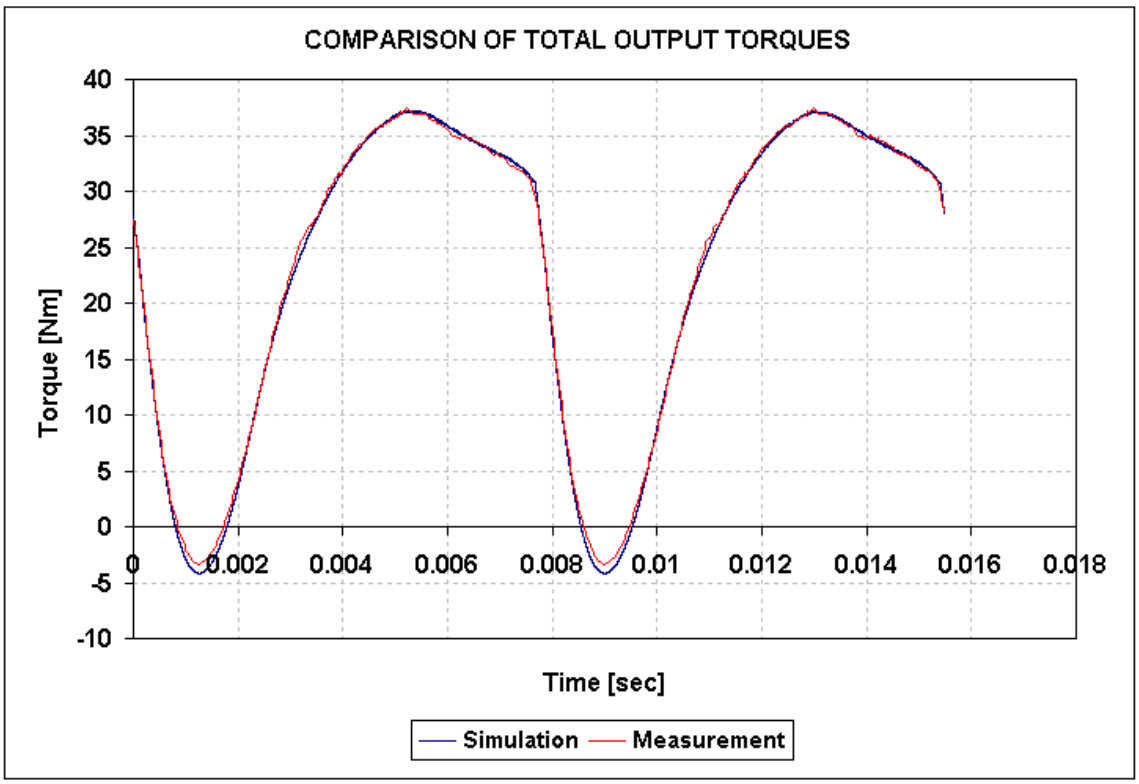

Figure 113 Phase current and machine total output torque comparison of simulated and measured results for h-bridge inverter with Advance Angle = 40Degrees; Conduction Angle = 176.8Degrees; Speed = 387.5RPM; Current Demand = 30A; Vdclink = 175V

The Matlab® script mentioned at the beginning of this section is used to calculate performance parameters. The results of the Matlab® script for each of the comparison figures (i.e. Figure 110 to Figure 113) are compared to those of the measurements and the simulation in Table 11. Test-1, Test-2, Test-3 and Test-4 in Table 11 correspond to Figure 110, Figure 111, Figure 112 and Figure 113, respectively.

Table 11 Comparison of results obtained from direct measurements, predictions from the Matlab® script and the simulation for the h-bridge driven two-phase machine

		TEST-1	TEST-2	TEST-3	TEST-4
MEASURED	Speed [RPM]	1017	365	1179	387
	Torque [Nm]	4.10	20.60	4.20	23.00
	Iphase RMS [A]	6.30	17.80	6.90	18.30
SCRIPT	Speed [RPM]	1014	366	1186	388
	Torque [Nm]	4.60	22.60	4.77	23.20
	Iphase RMS [A]	6.16	17.63	6.25	18.70
	Error-1 [%]	12.20	9.71	13.57	0.87
SIMULATED	Speed [RPM]	1013.50	366.20	1181.70	387.50
	Torque [Nm]	4.90	21.90	4.47	23.00
	Iphase RMS [A]	6.23	17.57	6.45	19.00
	Error-2 [%]	19.51	6.31	6.31	0.00

Error-1 in Table 11 is the percentage difference between the measured total average output torque of the machine and the predicted average output torque of the machine from the Matlab® script. Likewise, Error-2 in Table 11 is the percentage difference between the measured total average output torque of the machine and the simulated average output torque of the machine from the dynamic simulation in Simulink.

Overall, the simulated and measured waveforms correlate favourably, which is also backed-up by the performance parameter calculations from the Matlab® script and the dynamic simulation in Simulink. In Table 12 some of the Matlab® script calculated performance parameters are presented for the measurements given in Table 11.

Table 12 Script calculated performance parameters for the 2-phase 12-10 segmental rotor machine driven from the asymmetric half-bridge inverter

	TEST-1	TEST-2	TEST-3	TEST-4
Advance Angle [Elect.Deg.]	10	0	20	40
Conduction Angle [Elect. Deg.]	115.4	127.7	175.6	176.8
Current Demand [A]	30	30	30	30
Speed [RPM]	1013.5	366.2	1181.7	387.5
RMS Phase Current [A]	6.16	17.63	6.25	18.69
Peak Phase Current [A]	10.04	32.23	9.72	30.90
Average Total Torque [Nm]	4.58	22.6	4.8	23.2
Maximum Total Torque [Nm]	11.08	39.8	8.99	37.50
Minimum Total Torque [Nm]	-0.14	-0.071	-0.11	-3.33
Torque Ripple - MEAN [%]	244.7	176.6	190.7	176.0
Torque Ripple - MAX [%]	101.3	100.2	101.2	108.9

"Torque Ripple – MEAN [%]" in Table 12 is calculated by

$$Tripple_{MEAN} = 100 \times \left(\frac{(T\max - T\min)}{Tave} \right) \qquad \textbf{Equation 31}$$

Where $Tripple_{MEAN}$ is the torque ripple based on peak-to-peak instantaneous torque variation and the average torque; $T\max$ is the maximum output torque; $T\min$ is the minimum output torque and $Tave$ is the average output torque.

"Torque Ripple – MAX [%]" in Table 12 is calculated by

$$Tripple_{MAX} = 100 \times \left(\frac{(T\max - T\min)}{T\max} \right) \qquad \textbf{Equation 32}$$

Where $Tripple_{MAX}$ is the torque ripple based on peak-to-peak instantaneous torque variation and the maximum output torque; $T\max$ is the maximum output torque and

T min is the minimum output torque. In Table 12 the "Torque Ripple – MAX [%]" values are all more than 100%. This can only happen if the T min value is negative (Minimum Total Torque in Table 12).

7.2.2 Two-Phase Machine Driven by Asymmetric Half-Bridge Inverter

The two-phase machine in section 7.2.1 has also been driven by an asymmetric half-bridge inverter of the form given in Figure 114. This section summarises the measurements taken from the drive system and the results obtained from the dynamic simulation.

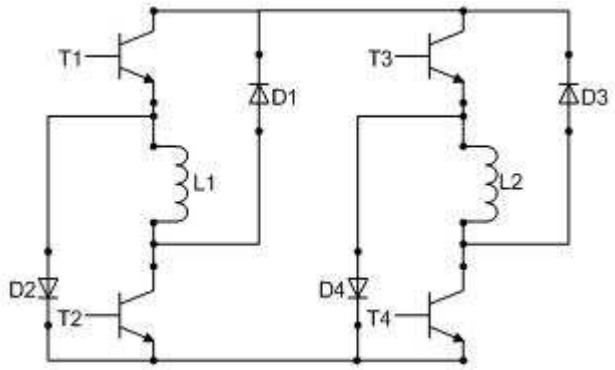

Figure 114 Asymmetric half-bridge converter driving a two-phase machine

From Figure 115 to Figure 118 the simulation results of the asymmetric half bridge driven two-phase machine are compared to the measurements taken from the test rig under various operating conditions. Once again the Matlab® script is used to calculate performance parameters. The results of the Matlab® script for each of the comparison figures (i.e. Figure 115 to Figure 118) are compared to those of the measurements and the simulation in Table 13. Test-1, Test-2, Test-3 and Test-4 in Table 13 correspond to Figure 115, Figure 116, Figure 117 and Figure 118, respectively.

Table 13 Comparison of results obtained from direct measurements, predictions from the Matlab® script and the simulation for the asymmetric half bridge driven two-phase machine

		TEST-1	TEST-2	TEST-3	TEST-4
MEASURED	Speed [RPM]	937.50	802.14	400.00	364.96
	Torque [Nm]	4.40	4.70	14.80	14.30
	Iphase RMS [A]	8.50	5.40	15.40	18.70
SCRIPT	Speed [RPM]	945.00	805.40	400.30	364.70
	Torque [Nm]	5.00	5.21	14.80	15.62
	Iphase RMS [A]	7.90	5.34	15.21	18.46
	Error-1 [%]	13.52	10.85	0.00	9.23
SIMULATED	Speed [RPM]	945.00	805.40	400.30	364.70
	Torque [Nm]	5.41	5.82	14.30	15.77
	Iphase RMS [A]	7.95	5.82	14.90	17.97
	Error-2 [%]	22.95	23.83	-3.38	10.28

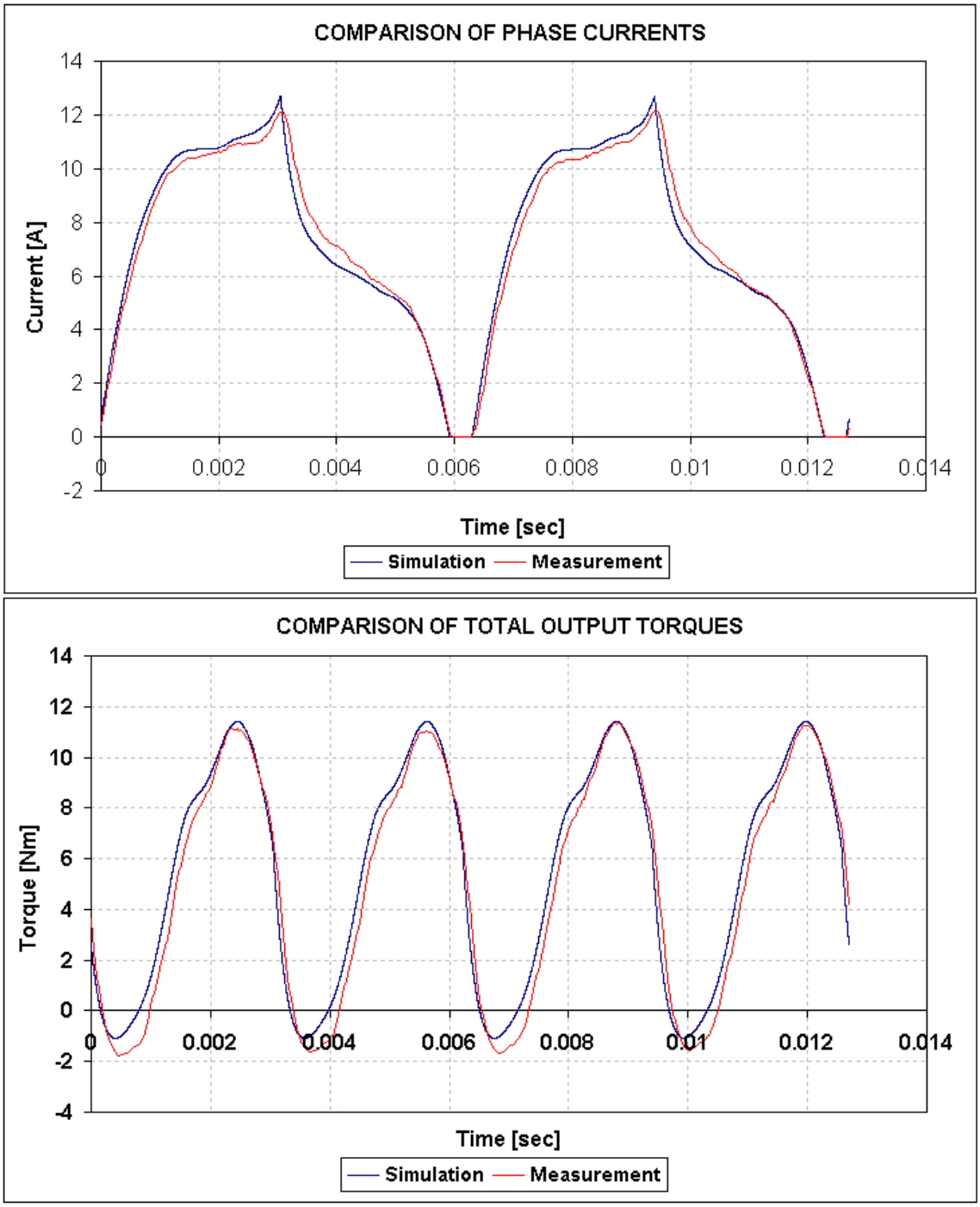

Figure 115 Phase current and machine total output torque comparison of simulated and measured results for asymmetric half-bridge inverter with Advance Angle = 12Degrees; Conduction Angle = 175.75Degrees; Speed = 945RPM; Current Demand = 30A; Vdclink = 175V

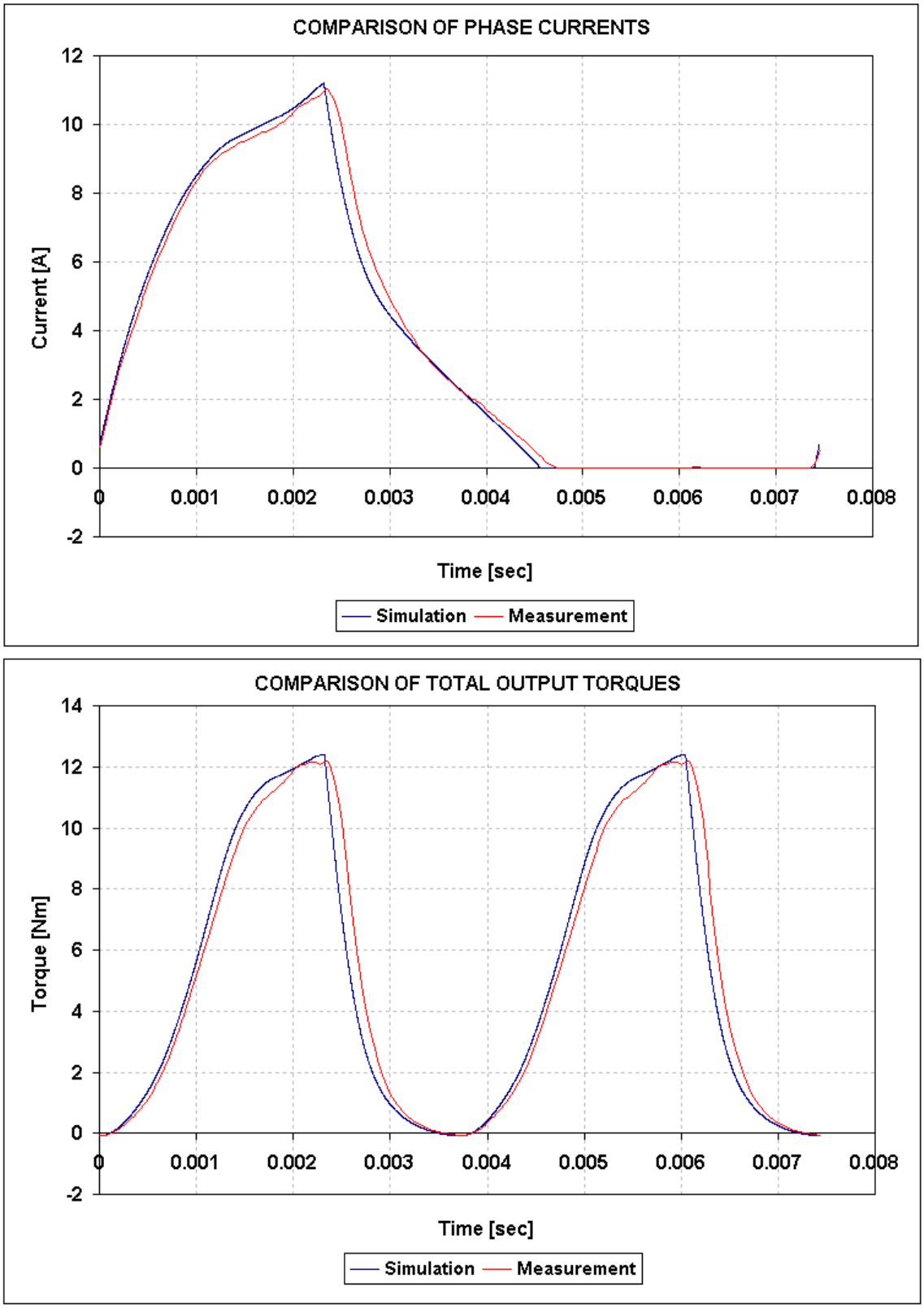

Figure 116 Phase current and machine total output torque comparison of simulated and measured results for asymmetric half-bridge inverter with Advance Angle = 0Degrees; Conduction Angle = 114.8Degrees; Speed = 805.4RPM; Current Demand = 30A; Vdclink = 175V

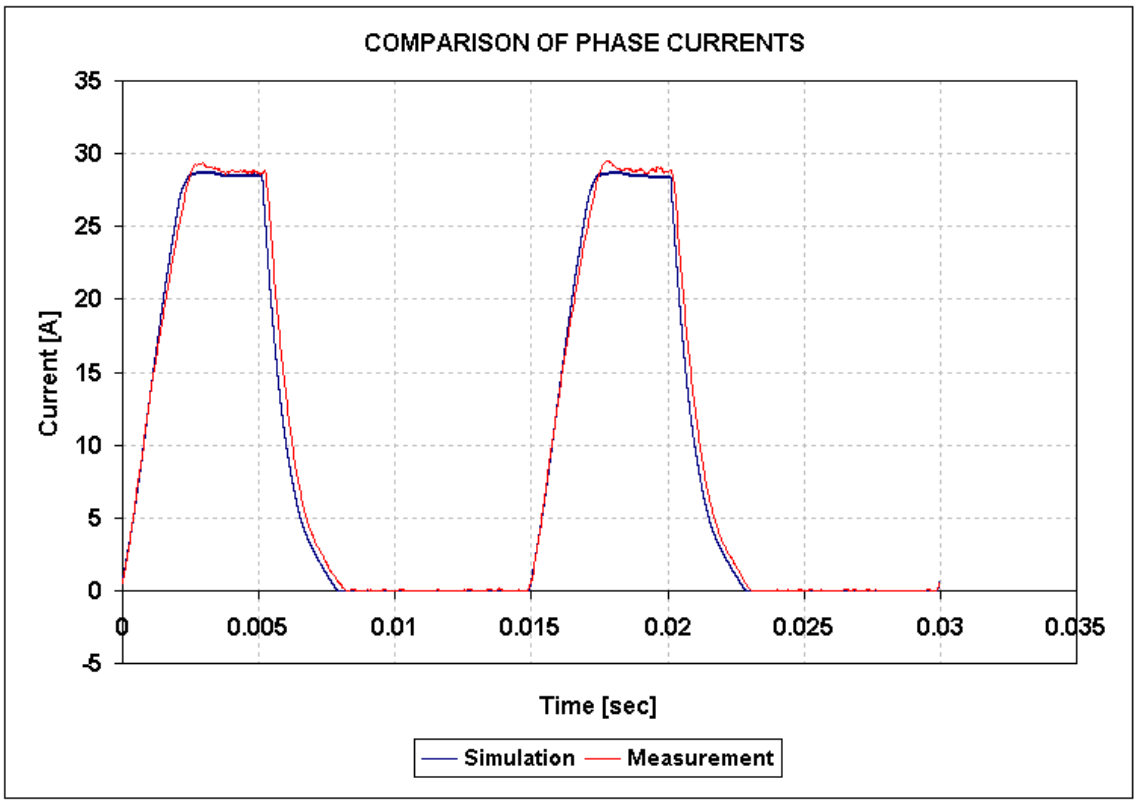

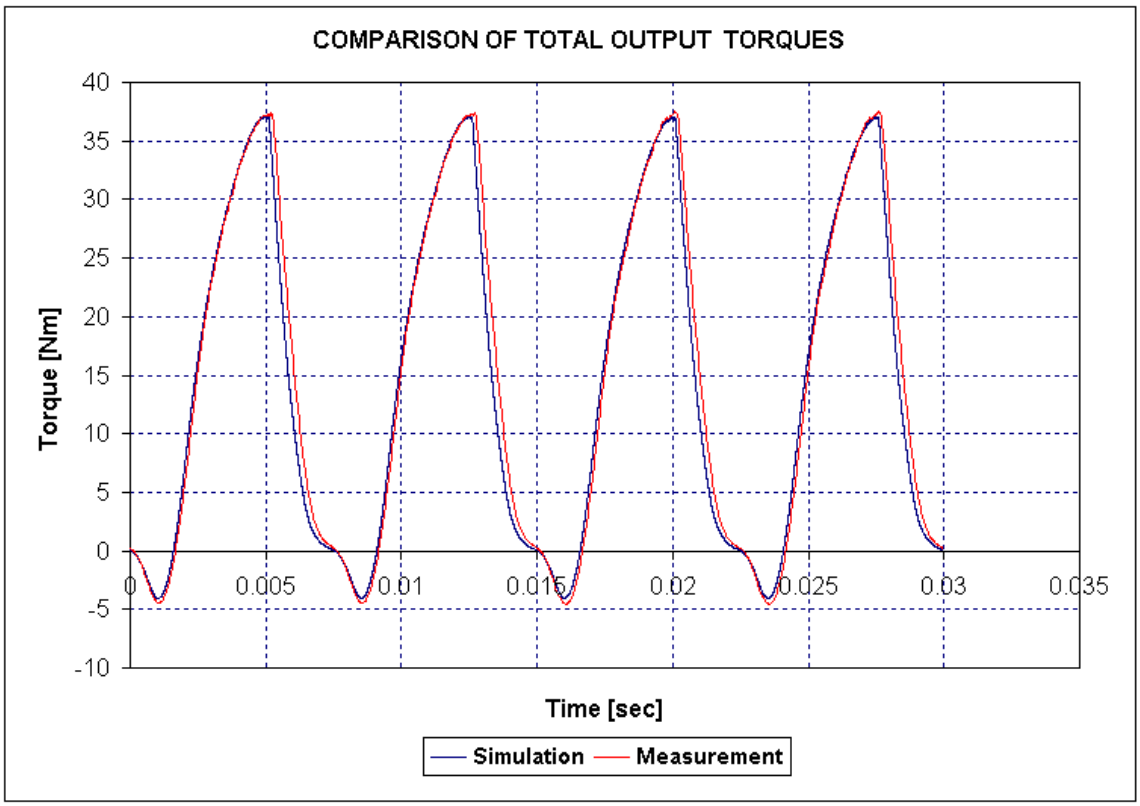

Figure 117 Phase current and machine total output torque comparison of simulated and measured results for asymmetric half-bridge inverter with Advance Angle = 40Degrees; Conduction Angle = 124.6Degrees; Speed = 400.3RPM; Current Demand = 30A; Vdclink = 175V

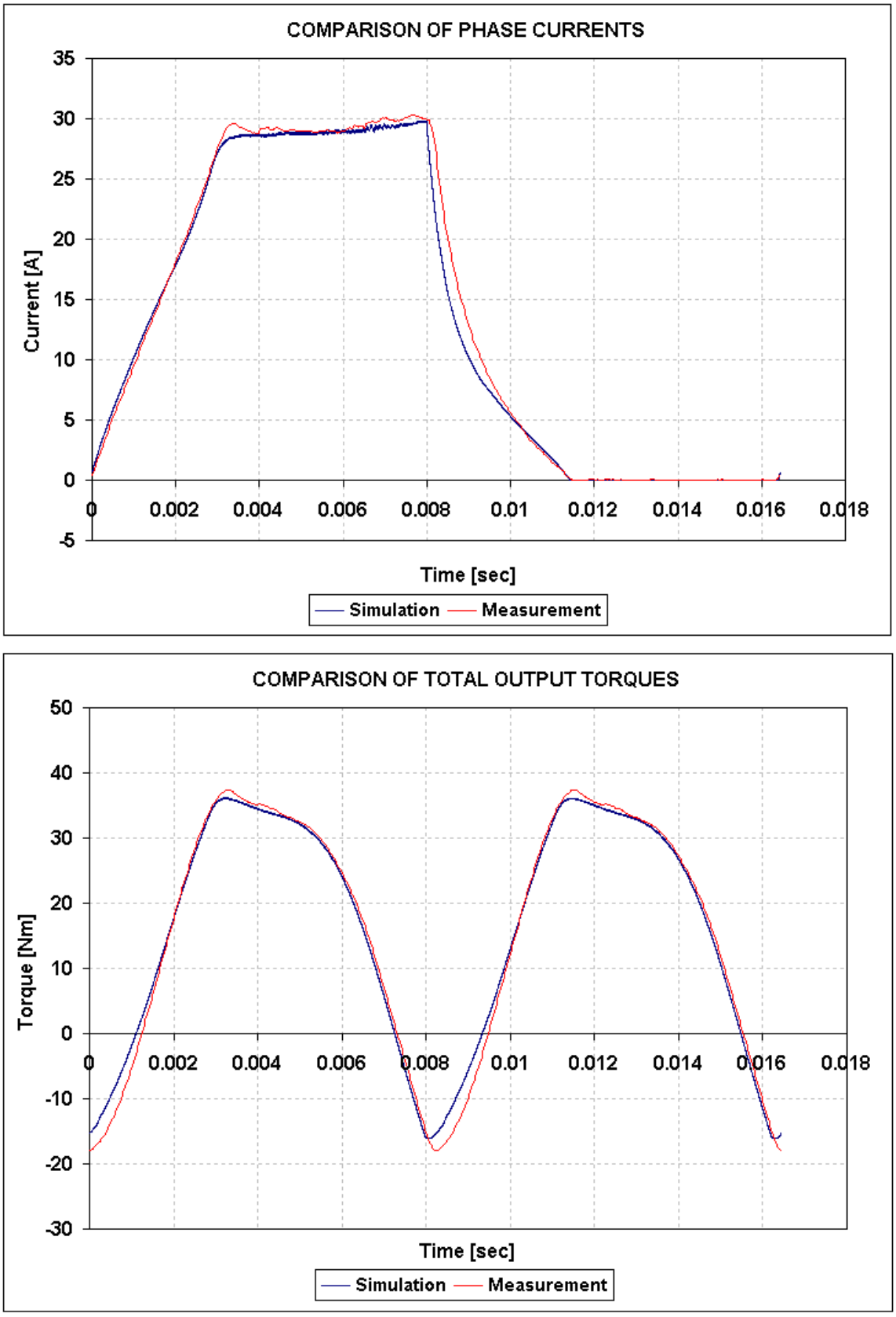

Figure 118 Phase current and machine total output torque comparison of simulated and measured results for asymmetric half-bridge inverter with Advance Angle = -20Degrees; Conduction Angle = 176.2Degrees; Speed = 364.7RPM; Current Demand = 30A; Vdclink = 175V

Once again, the correlation between the simulated and measured waveforms is good. The performance parameter predictions from the Matlab® script and the dynamic simulation are also good. In Table 14 some of the Matlab® script calculated performance parameters are presented for the measurements given in Table 13.

Table 14 Script calculated performance parameters for the 2-phase 12-10 segmental rotor machine driven from the h-bridge inverter

	TEST-1	TEST-2	TEST-3	TEST-4
Advance Angle [Elect.Deg.]	12	0	40	-20
Conduction Angle [Elect. Deg.]	175.75	114.8	124.6	176.2
Current Demand [A]	30	30	30	30
Speed [RPM]	945	805.4	400.3	364.7
RMS Phase Current [A]	7.90	5.34	15.21	18.46
Peak Phase Current [A]	12.12	11.03	29.43	30.28
Average Total Torque [Nm]	4.99	5.21	14.80	15.62
Maximum Total Torque [Nm]	11.25	12.63	37.46	37.35
Minimum Total Torque [Nm]	-1.72	-0.08	-4.48	-17.96
Torque Ripple - MEAN [%]	259.6	243.8	283.4	354.1
Torque Ripple - MAX [%]	115.3	100.6	111.9	148.1

“Torque Ripple – MAX [%]” and “Torque Ripple – MEAN [%]” in Table 14 are calculated by using Equation 31 and Equation 32, respectively. It is apparent from Equation 31 and Equation 32 that “Torque Ripple – MEAN [%]” will always be greater than “Torque Ripple – MAX [%]”.

The Matlab® script is also able to generate the flux-linkage locus for a given set of measurements. An example is given in Figure 119. The flux-linkage locus in Figure 119 was generated for the test condition given in Figure 113.

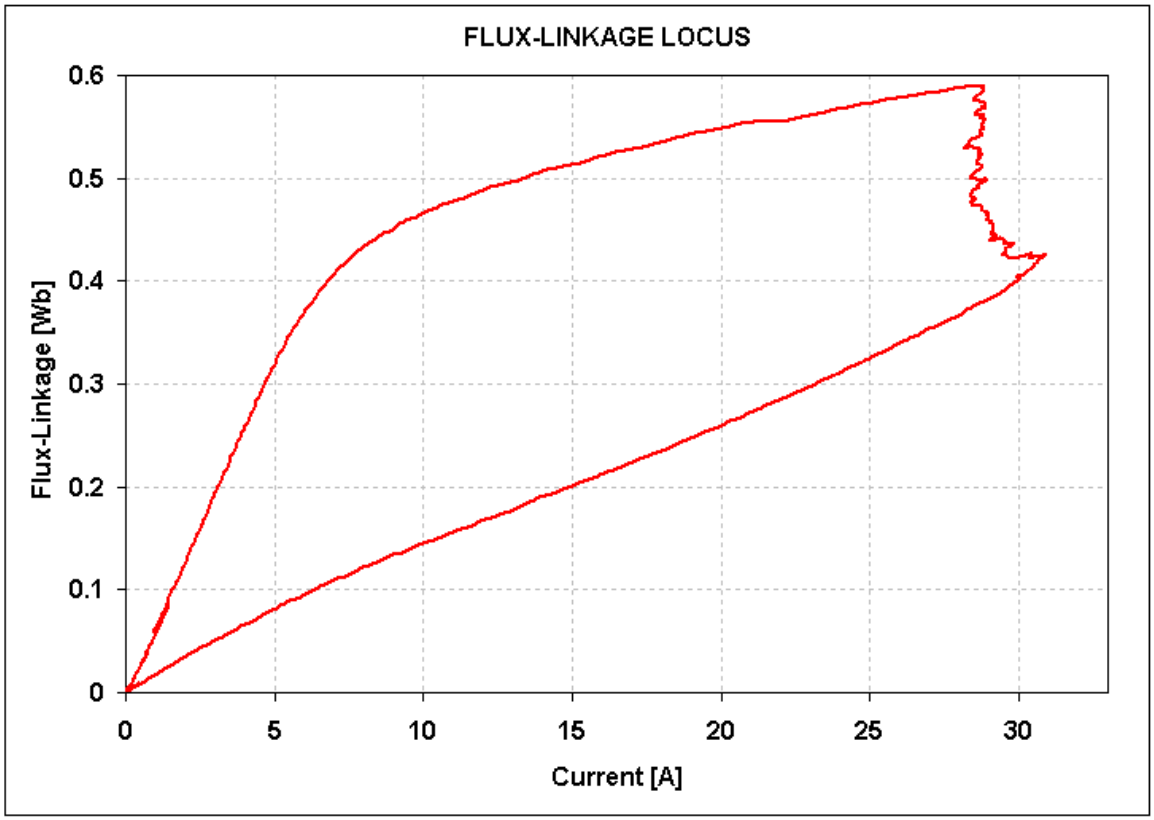

Figure 119 Estimated flux-linkage locus for h-bridge inverter driven system with Advance Angle = 40Degrees; Conduction Angle = 176.8Degrees; Speed = 387.5RPM; Current Demand = 30A; Vdclink = 175V

The discrepancies between measured and simulated results can be attributed to several factors:

1. Simulated results were based on FE simulated flux-linkage characteristics of the machine. The torque characteristics of the machine were also not measured but derived from the flux-linkage characteristics of the machine.

2. The real drive itself suffers from the discrete nature of its digital controller. A 100usec control cycle equates to an electrical rotation of 6.0^{o} at 1000 rpm operation (for the machine with 10 rotor segments). This means that the angle at which commutation takes place can be in error up to this amount.

3. It is likely that the position encoder of the drive system also suffers from a certain amount of lag due to the flexible nature of the coupling connecting it to the

machine. As a result, the sampled current waveform may be phase shifted towards the aligned position by a small angle.

7.3 INVERTER VA-RATING COMPARISON

The main cost of an SR drive system is its power electronic converter. Therefore, the performance of the converter plays a significant role in cost and performance of the overall drive system. After correlating the simulation models for the h-bridge and the asymmetric half-bridge inverter driven two-phase machine, comparison has been made between the performances of the two drive circuits. It must be underlined that the main aim here is not assessing how well a particular IGBT or MOSFET operates with one of the two inverter circuits, but is to analyse how the asymmetric half-bridge and h-bridge inverters perform compared to each other driving a two-phase machine.

The size and cost of an inverter drive are usually assessed by determining its rating. There are two commonly used techniques to evaluate the inverter rating of a drive system [206]:

1. The peak voltage and the current that each power electronic device must withstand are calculated. The peak voltage and current are then multiplied with the number of devices in the circuit. Inverter rating is then expressed in terms of kVA of inverter power per kW of motor output power.

2. A repeat of the first technique but instead of using the peak device current, the rms device current is used. The inverter rating is again expressed in terms of kVA per kW of motor output power.

The above methods result in different comparison results and the decision as to which method is more appropriate depends on the application. Ultimately, the main factor used to determine a suitable device for an application is the calculation of its peak junction temperature. This is determined by the losses in the device and its thermal resistance to the heatsink. The device junction temperature should be calculated at low and high speeds. In case of high speed operation, the device junction temperature is dominated by the average device losses. On the other hand, when the motor is operating at low speeds, the device junction temperature will reach its steady-state value within an electrical cycle

when the current is at its *peak (*assuming that the motor speed is low enough to reach this steady-state condition. Otherwise, more complex calculations involving the thermal time constant of the device are required.). This suggests that at low speeds it will be more appropriate to use the inverter rating comparison based on *peak* device current whereas at high speeds this should be based on *rms* device current. Clearly, the application conditions need to be known before the decision is made in choosing the method for determining the inverter rating.

In practice, the total cost and the size of an inverter drive requires additional considerations other than the peak / rms VA rating calculations. These can be summarised as follows:

1. **Number of Switches:** The cost of one device is not necessarily twice the cost of two devices of half the VA rating. The assessment should also include the available packaging space, cost relating to component assembly and additional circuitry required, e.g. the number of drive and control circuits. In general, an inverter with a lower switch count is preferable.

2. **Circuit Topology:** Indirect savings can be made by reducing the size of the PCB (through reduction in material cost), heatsink mounting area and assembly cost by using a different circuit topology. For example, if the freewheel diodes are in parallel with the power devices they can easily be placed within the same package and hence the component count can be reduced (note that the total cost of the power devices is not necessarily reduced). An inverter solution can also be favourable in terms of number of connections required between the motor and the inverter.

3. **Total Inverter Loss:** In a situation where the device rating is the same between two inverter topologies (based on the peak voltage and current requirements of individual devices) but the number of active devices (i.e. loss generating devices) at any given time is different, the heatsink requirements will be different. For example, in one drive two phases may be conducting at a time, and in the other only one phase, resulting in twice the inverter losses and hence twice the heatsink rating (which will cost more and take up more space).

The following two sections detail the VA-rating comparison of the two phase drives driven from the h-bridge and asymmetric half-bridge inverters using the two assessment techniques described above. It should be noted that the results are obtained from the validated dynamic simulation of the machine and controller. The use of the simulation is justified with the results presented in the preceding sections of this chapter where very good correlation has been demonstrated between the simulated and measured waveforms for both drives at high and low speeds. The first section below is the comparison of inverter VA-ratings when both drives operate under full voltage control (high speed operation). The second section follows on from the first one but looks at the comparison when both drives operate under current control (low speed operation). Negative advance in the following sections is when the phase is energised before the unaligned position and positive advance is when the phase is energised after the unaligned position. For all simulations the dc-link voltage is fixed at 175V. It should be noted that the drive efficiency calculations in the following two subsections do not include the machine iron losses. However, it is believed that the exclusion of iron loss values does not affect the relative comparison results severely.

7.3.1 Drive under Voltage Control

For the purposes of this comparison, both drives have been simulated at 1200rpm and the current demands were set to 50A in order to ensure operation under full voltage control with both drives. It should be noted that the current demand for the h-bridge circuit is set for the line current rather than the phase current. With both drives the machine rated output torque target was set to 10Nm. In order to maximise the output torque at high speed, the conduction angle was set to 180^{o} for both drives. The number of turns of the machine was then adjusted (by using the simulation GUI) in order to achieve 10Nm at 1200rpm with both drives. The aim here is to maximise the number of turns for the given speed and torque requirements in order to minimise the current in the circuit. This way, the inverter losses are minimised for the given speed and torque. The number of turns of the machine was reduced if the machine was not able to achieve the required torque and increased if the machine was more than able to achieve it. The final number of turns was chosen when the machine was *just* able to achieve the required torque at the specified speed when the advance angle was optimised for the specified conduction angle. It should

be noted that any change in the number of turns does not affect the machine copper losses. The same amount of stator slot area with the same slot fill factor is available to fill with copper. For example, if the number of turns was doubled the current demand would be halved and as a result the copper losses would remain constant because the conductor cross sectional area per turn would need to be halved for the same slot area and fill factor. Table 15 summarises the simulation results for the asymmetric half-bridge and h-bridge driven two phase machine when the drive is under voltage control at 1200rpm aiming to achieve 10Nm of output torque.

It is not surprising to see that both drives result in similar phase currents and consequently similar winding copper losses (number of turns is the same for both drives). This is due to the fact that the conduction angle is set to 180^o and with this conduction angle both drives work in a very similar way and generate the same phase currents. However the devices and the diodes of the h-bridge circuit do not see all of the phase current (due to circulation of current around the phase windings and the diodes) whereas all the phase current goes through the devices and diodes of the asymmetric half-bridge circuit. This can be observed in Figure 120. As a result, inverter ratings of the h-bridge topology compares favourably against those of the asymmetric half-bridge topology. The difference is especially large when the VA rating comparison is based on the RMS device current (almost 20% improvement). This is also reflected in the total inverter losses as the h-bridge generates more than 16.0W less inverter losses. However, the gain in the inverter losses is somewhat spoiled by the additional conduction losses generated by the diodes in series with the phases. As a result total power electronic losses of the h-bridge drive are only 6.0W less than those of the asymmetric half-bridge drive. In terms of overall drive efficiency both drives perform similarly. The h-bridge drive is less than 1.0% more efficient than the asymmetric half-bridge drive. In Table 15 torque ripple results are virtually the same, as the phase currents are the same for both drives.

Table 15 Summary of comparison of the performances of h-bridge and asymmetric half-bridge driven two-phase machine drive systems under voltage control

	H-Bridge	Asymmetric Half-Bridge	
Vdc_Link [V]	175	175	
Number of Motor Phases	2	2	
Speed [RPM]	1200	1200	
Average Output Torque [Nm]	10.0	10.0	
Output Power [W]	1257.0	1257.4	
Demand Current [A]	50	50	
Nturns per coil - ORIGINAL	88	88	
Nturns per coil - FINAL	87	87	
R_Phase [Ohms]	0.8582	0.8582	
Advance Angle [Deg.]	-83.5	-83.5	
Conduction Angle [Deg.]	180	180	
			Percentage Difference [%]
Iphase_RMS [A]	10.85	10.85	
Winding Cu Losses [W]	202.0	202.2	0.09
Iphase_PEAK [A]	18.82	18.82	
Total Inverter Losses [W]	50.7	66.4	
Total Phase Diode Losses [W]	10.0	0.00	
Total Power Electronic Losses [W]	60.8	66.4	
Drive Efficiency [%]	82.7	82.4	
Swt_VARating_Peak [kVA / kW]	9.8	10.5	6.91
Swt_VARating_RMS [kVA / kW]	5.0	5.6	12.69
Dio_VARating_Peak [kVA / kW]	9.6	9.6	-0.06
Dio_VARating_RMS [kVA / kW]	1.8	2.3	28.17
Total Peak VA Rating [kVA / kW]	19.4	20.1	3.46
Total RMS VA Rating [kVA / kW]	6.7	7.9	16.78
Torque Ripple Pk-2-Pk [%]	114.1	114.1	0.00
Torque Ripple Ave-2-Pk [%]	257.4	257.3	-0.04

Some of the abbreviations in Table 15 are described in Table 16. The “Percentage Difference [%]” column in Table 15 is calculated by dividing the value under the “Asymmetric Half-Bridge” column with that under the “H-Bridge” column.

Table 16 Explanation of abbreviations used in Table 15 and Table 17

Vdc_Link	Available DC-Link Voltage
Nturns	Number of turns
R_Phase	Phase resistance at room temperature
Iphase_RMS	RMS phase current
Iphase_PEAK	Peak phase current
Cu	Copper
Swt_VARating_Peak	VA rating of IGBTs based on Peak Current
Swt_VARating_RMS	VA rating of IGBTs based on RMS Current
Dio_VARating_Peak	VA rating of Recovery Diodes based on Peak Current
Dio_VARating_RMS	VA rating of Recovery Diodes based on RMS Current

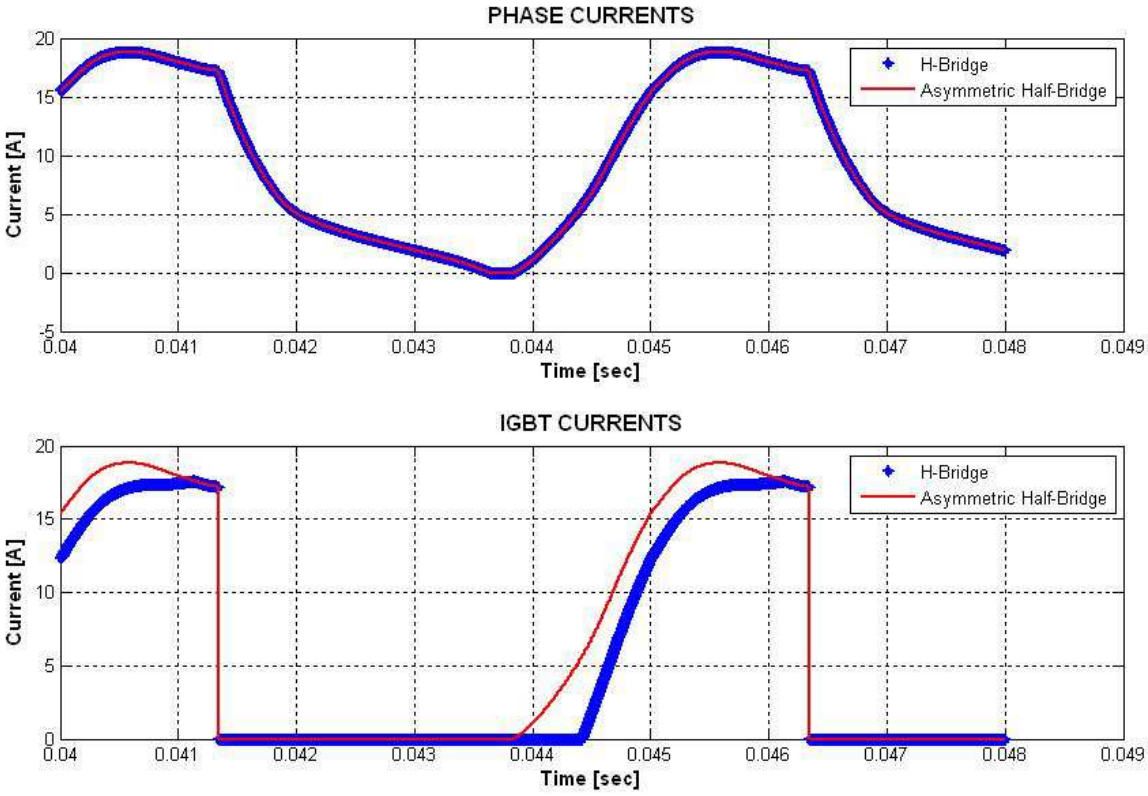

Figure 120 Phase and IGBT currents for the h-bridge and asymmetric half-bridge inverter two-phase drives at 1200 rpm with 175V dc-link and 50A of current demand

7.3.2 Drive under Current Control

The motor speed was reduced to 100rpm. The number of turns determined when the drives were under voltage control (in the previous section) is used. The controllers now work under current control. Both drives use the same PID controller parameters. It should be noted that the h-bridge drive is line controlled, i.e. the sum of the two phase currents is controlled by the controller. In order to maximise the torque per unit copper loss the conduction angle was limited to 120^o for both asymmetric half-bridge and h-bridge driven machine. The current demands and the advance angles for both drives were then optimised in order to achieve the required output torque (same as the previous section – 10Nm). Table 17 tabulates the comparison based on the simulation results for the asymmetric half-bridge and h-bridge driven two phase machine when the drive is under current control at 100rpm, aiming to achieve 10Nm of output torque.

From Table 17, in terms of VA ratings, both inverters perform similarly. This is reflected in the total inverter losses as well, as the switches and diodes do not experience the circulating phase current in the h-bridge driven machine (see Figure 121 and Figure 122). However, the total power electronic losses are higher with the h-bridge topology as the diodes in series with phase windings incur additional conduction losses.

Furthermore, due to the circulating currents and the long phase tail currents with the h-bridge circuit, the rms phase current is higher with the h-bridge drive (see Figure 121). This results in increased copper losses. To understand this, one needs to go back to Figure 108 and analyse the region between Points B and C. In this region the line current is zero and the controller aims to keep this current at zero by applying positive and negative dc-link voltage across the phases. As no voltage is applied across the phases on average, the phase current only drops slightly due to resistive voltage drop and results in longer tail current (although the line current is zero, the phase currents circulate around the phases through the phase windings and the phase diodes). Moreover, phases start conducting before their energisation cycles begin. This can again be explained by the help of Figure 108 (region between points A and B). Negative voltage applied across the turning-off phase results in positive voltage applied across the off-phase. This positive voltage results in the off phase start conducting long before the start of its actual energisation cycle. Consequently the rms phase current is increased with the h-bridge inverter, resulting in more copper losses.

Table 17 Summary of comparison of the performances of h-bridge and asymmetric half-bridge driven two-phase machine drive systems under current control

	H-Bridge	Asymmetric Half-Bridge	
Vdc_Link [V]	175	175	
Number of Motor Phases	2	2	
Speed [RPM]	100	100	
Average Output Torque [Nm]	10.0	10.0	
Output Power [W]	104.7	104.7	
Demand Current [A]	13.8	14	
Nturns per coil - ORIGINAL	88	88	
Nturns per coil - FINAL	87	87	
R_Phase [Ohms]	0.8582	0.8582	
Advance Angle [Deg.]	40.0	40.0	
Conduction Angle [Deg.]	120	120	
P	10	10	
I	0.5	0.5	
D	0	0	
			Percentage Difference [%]
Iphase_RMS [A]	9.12	8.26	
Winding Cu Losses [W]	142.8	117.1	-17.98
Iphase_PEAK [A]	17.15	15.24	
Total Inverter Losses [W]	77.9	78.5	
Total Phase Diode Losses [W]	8.35	0.00	
Total Power Electronic Losses [W]	86.2	78.5	
Drive Efficiency [%]	31.4	34.9	
Swt_VARating_Peak [kVA / kW]	101.6	101.8	0.18
Swt_VARating_RMS [kVA / kW]	41.1	41.8	1.66
Dio_VARating_Peak [kVA / kW]	101.6	101.81	0.18
Dio_VARating_RMS [kVA / kW]	35.3	36.0	1.90
Total Peak VA Rating [kVA / kW]	203.3	203.6	0.18
Total RMS VA Rating [kVA / kW]	76.5	77.8	1.77
Torque Ripple Pk-2-Pk [%]	106.9	100.0	-6.43
Torque Ripple Ave-2-Pk [%]	191.9	192.9	0.47

Combination of extra diode losses and higher copper losses result in the h-bridge drive operating approximately 3.5% less efficient.

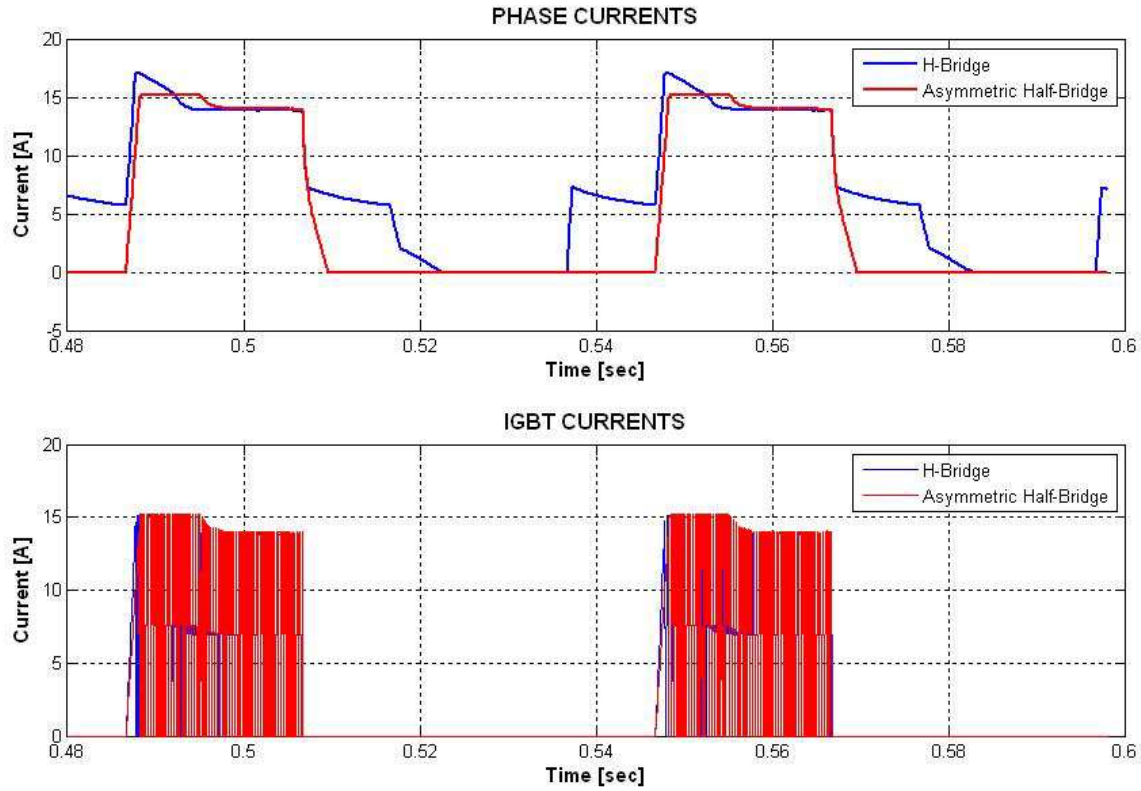

Figure 121 Phase and IGBT currents for the h-bridge and asymmetric half-bridge inverter two-phase drives at 100 rpm with 175V dc-link

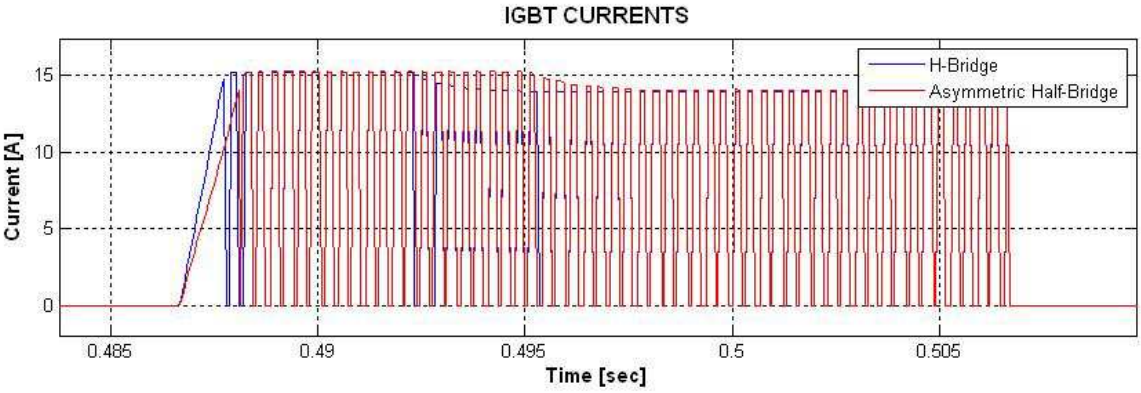

Figure 122 Zoomed-in IGBT currents for the h-bridge and asymmetric half-bridge inverter two-phase drives at 100 rpm with 175V dc-link

7.4 SUMMARY

Before the more complicated simulation of the 6-phase drives, two phase drives were analysed in this chapter. In terms of circuit topology, the h-bridge inverter has similarities with the 6-phase drive topologies studied in this thesis. Using the test rig explained in *Chapter 5 – Machine Construction Techniques and Test Rig Description* and rearranging the phase winding connections, the six phase segmental rotor SRM has been successfully driven from the asymmetric half-bridge and h-bridge inverters as a 2-phase machine. With the h-bridge circuit, the line current was the controlled parameter, whereas both phase currents were controlled with the asymmetric half-bridge inverter. Both drives were run under voltage and current control and measurements under various operating points from both 2-phase drives have been presented. Matlab® scripts were written to analyse captured waveforms from both 2-phase drives. These scripts were able to estimate some of the performance parameters such as phase RMS currents, conduction angles, running speed (from the period of phase current), instantaneous phase torques, average total output torque, torque ripple, shaft power and total machine copper losses (assuming winding temperature of 100^{o}C during steady-state operation). Measured conditions were then simulated in the dynamic simulation package in the Matlab® environment (see *Chapter 6 – Simulation Models*). The simulated waveforms were compared with the measured ones and good correlation was achieved with both 2-phase drives under voltage and current controlled conditions.

Once the simulations of both the h-bridge and asymmetric half-bridge driven 2-phase machines were verified against the measurements, further comparison between the two drive circuits was carried out by using the dynamic simulation package. Performance of the 2-phase machine driven by the asymmetric half-bridge and h-bridge inverters was then compared.

It has been discussed that many factors (the number of switches, circuit topology, indirectly affecting the size of the PCB and the heatsink requirements) affect the size of the inverter of a drive system. Two methods of calculating inverter size were presented in this chapter – VA rating and inverter losses. VA rating comparison in itself can be done in two different ways – one considering peak device current and the other considering the RMS device current. It is worth noting that the relevance of each inverter size comparison method changes with application.

To enable meaningful comparison of inverter VA ratings of the 2-phase drives, two points in the operating range were selected for comparison. The drives were first compared at 1200rpm when the controllers of both inverters were under voltage control. The number of turns and the advance angles were adjusted to achieve the target output torque of 10Nm. The number of turns was then fixed and the current demands and the advance angles were adjusted at 100rpm where both controllers were under current control.

The overall conclusion from Table 15 and Table 17 is that the h-bridge and asymmetric half-bridge driven two-phase segmental rotor SR drives perform very similarly under voltage and current control. There is a slight gain with the asymmetric half-bridge topology when the drive is under current control in terms of overall drive efficiency. However, with h-bridge circuit, the number of required current transducers is reduced from two to one. Furthermore, the total number of connections between the inverter and the motor is reduced from four to two with the h-bridge inverter (assuming phase diodes are mounted at the motor end). Under both voltage and current control, the VA rating comparison based on peak device and diode currents suggest that the inverter topologies behave in a similar manner. However, when the comparison is based on the rms device and diode currents, the h-bridge topology is favourable (only very slightly under current control). On the negative side, the h-bridge topology requires two additional phase diodes in order to achieve unipolar phase currents. However, this is somewhat compensated as the bridge recovery diodes can be part of the power devices with the h-bridge circuit, whereas the asymmetric half-bridge topology requires separate recovery diodes. It must be said that the phase diodes of the h-bridge arrangement do not need to be fast diodes and as a result, can be relatively cheap. Although with 1/3 of an electrical cycle conduction both drives perform similarly, the h-bridge drive outperforms the asymmetric half-bridge drive (in terms of inverter VA ratings –especially rms current based comparison) at higher speeds when the conduction period is extended to 1/2 of an electrical cycle. Therefore, the overall cost of the h-bridge circuit is likely to be less than the asymmetric half-bridge circuit.

For both the asymmetric half-bridge and h-bridge inverters the drive system performance can be optimised by adjusting the advance and conduction angles as the speed of the machine changes. The relative importance of inverter size and machine efficiency depends on the specific application. In terms of assessing the size of the inverter, it also

depends on the individual application that will determine the most appropriate method: inverter loss or peak / rms VA.

Finally, torque ripple results have shown that there is not a significant difference between the asymmetric half-bridge and h-bridge driven two-phase SR drives.

CHAPTER 8

8– Machine Operation and Comparison to Simulation – Three Phase Drives -

8.1 INTRODUCTION

This chapter contains the dynamic measurement and simulation results of the three-phase single tooth winding (12-10) segmental rotor machine drive. The results of the 3-phase drive have been presented in this chapter as they will form the basis of comparison between the 3-phase drive and the 6-phase one in one of the later chapters. The results of this comparison will be presented in Chapter 10. The 3-phase segmental rotor machine was designed as part of a previous PhD project in the Newcastle University, U.K [97]. The 3-phase segmental rotor machine has been used as the baseline (throughout this thesis) for comparing the performance of the 6-phase segmental and conventional rotor SRMs designed as part of this PhD project. The inverter of the test rig has been configured to drive the three phase machine from a 3-phase asymmetric half-bridge inverter.

In the next section, the simulated results will be compared against those measured. As for the two-phase drives, Matlab® based scripts were used to analyse the measured waveforms in order to predict some of the performance parameters of the drive system and ease the comparison against simulated waveforms and performance parameters. Examples at low and high speeds are presented. Inverter VA-rating assessment (based on

rms and peak device currents) under various operating conditions for the three-phase drive is also presented in this chapter. Dynamic torque-speed characteristics of the three-phase segmental rotor machine have been measured and presented in section 2.2 of this chapter.

8.2 MEASUREMENTS AND SIMULATION RESULTS

A dynamic simulation model for the three-phase asymmetric half-bridge inverter driven machine has been created and the model has been correlated against the measurements taken from the three-phase single tooth winding (12-10) segmental rotor SRM. The measured and simulated instantaneous phase current and total output torque waveforms were plotted on top of each other. The results of the Matlab® script were compared to those of the measurements and the simulation in the following sub-sections for several tests. Similar to the analysis of the 2-phase drive measurements, a Matlab® based script was written to analyse the scope-captured data and generate instantaneous torque waveforms based on phase currents and positions using FE generated flux-linkage characteristics.

8.2.1 Comparison of Measurements against Simulations

Four different operating conditions are presented here. Test-1 and Test-4 are when the drive is under full voltage control and Test-2 and Test-3 are when the drive is under current control. Table 18 summarises the operating conditions of the measurements presented in the proceeding sections.

Table 18 Tabulated summary of test conditions for the measurements presented in the proceeding sections

	TEST-1	TEST-2	TEST-3	TEST-4
Advance Angle [Elect.Deg.]	12	-8.8	0	-10
Conduction Angle [Elect. Deg.]	119.2	164.6	118.6	154.4
Current Demand [A]	10	10	10	10
Speed [RPM]	978.8	1047	588.2	1109.1

When the drive is under full voltage control the Matlab® script is additionally able to determine the power device and diode currents from the measured line current and calculate the VA rating of the inverter. The same could not be done for the drive under current control as neither the switching states of the devices nor the actual device currents were measured. However, for all of the examples below, the script determines the advance angle and conduction angle applied by the controller and the resulting operating speed and average output torque. The script is also able to determine performance parameters, such as the rms and peak phase currents, and the maximum and minimum instantaneous total torque. The advance angle, conduction angle, and speed determined by the Matlab® script and the drive current demand are then input into the dynamic simulation. Power device and diode VA ratings are determined, based on rms and peak values of currents as well as total inverter losses and total machine copper losses. The drive efficiency quoted under the "Simulated" column in the tables within the following sections is calculated by Equation 33.

$$\eta = 100 \times \frac{(T_{ave} \times (2 \times \pi \times N_s / 60))}{(T_{ave} \times (2 \times \pi \times N_s / 60)) + P_{inv} + P_{cu}} \qquad \textbf{Equation 33}$$

Where T_{ave} is the average total output torque in [Nm], N_s is the operating speed in [rpm], P_{inv} is the total inverter losses (conduction + switching) in [W], and P_{cu} is the total machine copper losses in [W]. For the total machine copper losses, it was assumed that the windings were running at 100^{o}C. Equation 33 does not include the machine iron losses. However, it was believed that Equation 33 could be still be used as an indicator for the overall drive efficiency.

8.2.1.1 Test-1 (Voltage Control)

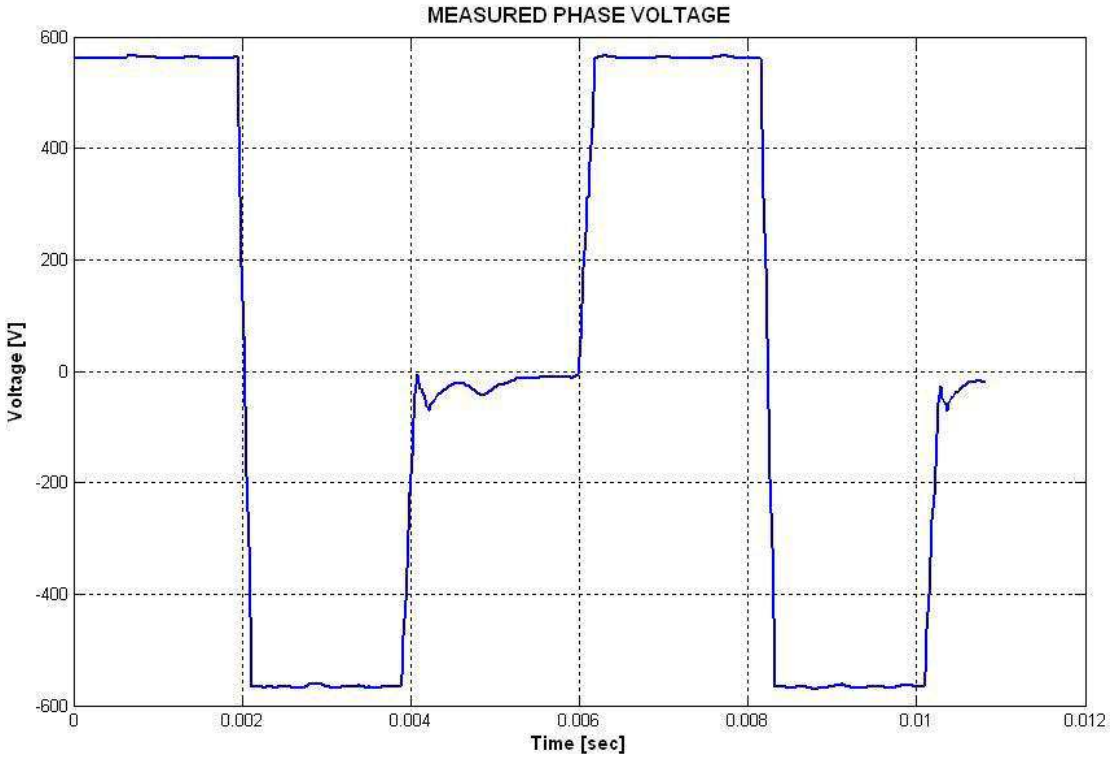

Figure 123 Phase voltage waveform with Advance Angle = 12°; Conduction Angle = 119.2°; Speed = 978.8RPM; Current Demand = 10A; Vdclink = 562V

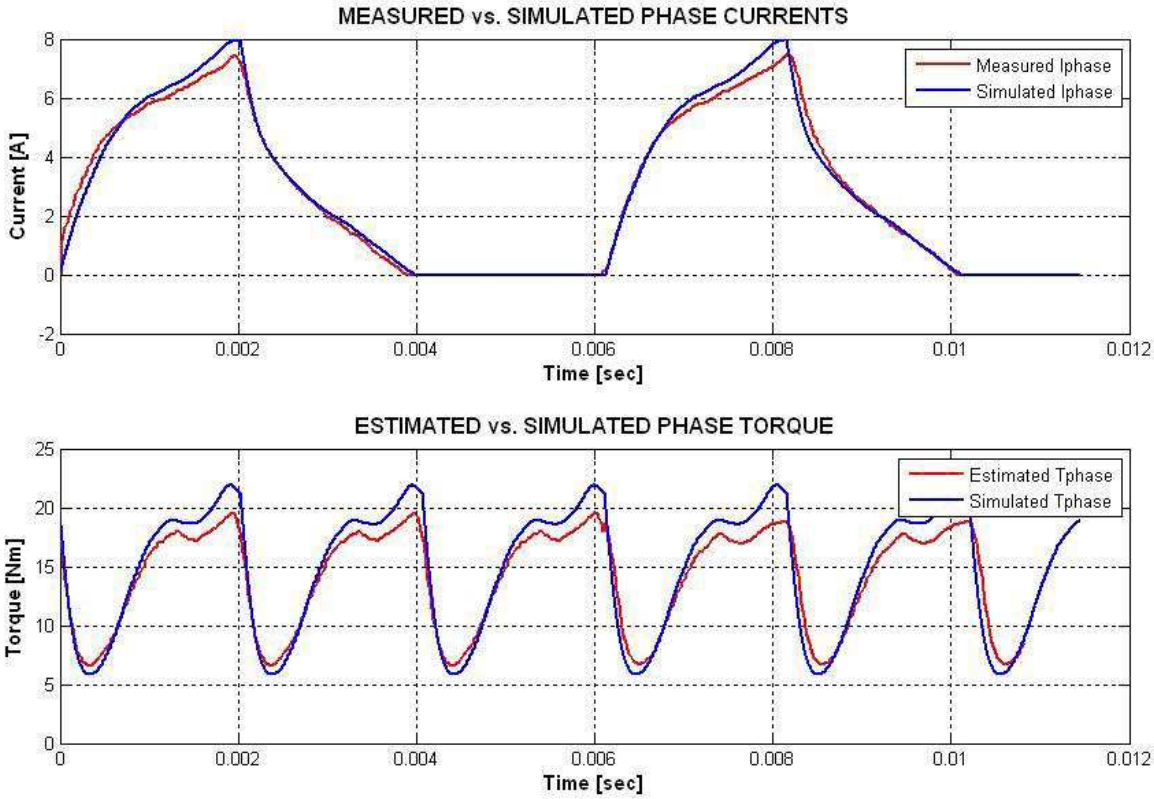

Figure 124 Comparison of simulated and measured phase current and torque with Advance Angle = 12°; Conduction Angle = 119.2°; Speed = 978.8RPM; Current Demand = 10A; Vdclink = 562V

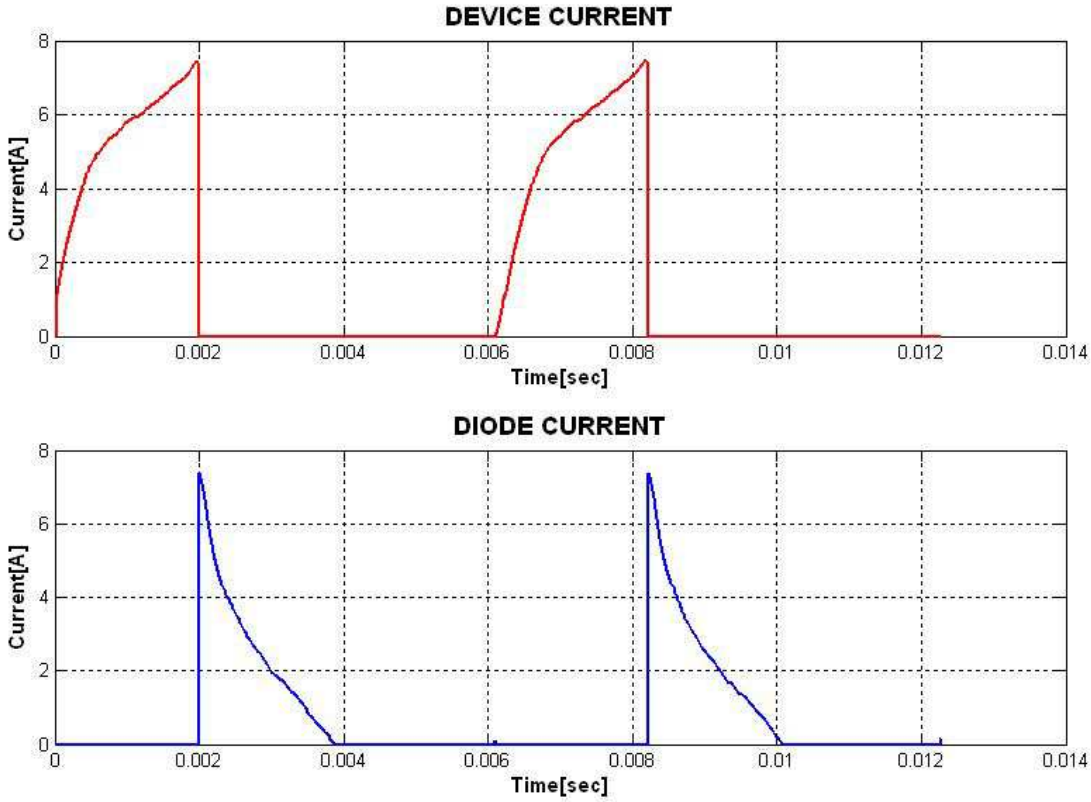

Figure 125 IGBT and recovery diode currents with Advance Angle = 12°; Conduction Angle = 119.2°; Speed = 978.8RPM; Current Demand = 10A; Vdclink = 562V

During Test-1, the machine is running relatively fast. As the turn-on point of the phase is delayed past the unaligned rotor position and the conduction angle is limited to approximately 1/3 of an electrical cycle, the current never reaches the required level. The resistive voltage drop across the phase windings becomes negligible and all of the available voltage is consumed by the change in the phase flux-linkage. At the end of the energisation cycle the power devices are turned-off and the phase current decays to zero. However, the current decay gets slower and slower as the phase inductance rises when the rotor position approaches alignment. This is reflected in the output torque waveform (Figure 124) as a relatively high torque ripple is experienced under Test-1.

Table 19 Summary of measured, script and simulation determined results for Test-1 where Advance Angle = 12°; Conduction Angle = 119.2°; Speed = 978.8RPM; Current Demand = 10A; Vdclink = 562V

	Measured	Script	Simulated
Advance Angle [Elect.Deg.]		12	12
Conduction Angle [Elect. Deg.]		119.2	119.2
Current Demand [A]	10	10	10
Speed [RPM]	969	978.8	978.8
RMS Phase Current [A]	3.64	3.64	3.58
Peak Phase Current [A]	7.46	7.46	7.5
RMS Device Current [A]			3.2
Peak Device Current [A]			7.5
RMS Diode Current [A]			1.71
Peak Diode Current [A]			7.5
Average Total Torque [Nm]	14.6	14.26	13.83
Maximum Total Torque [Nm]		19.2	19.81
Minimum Total Torque [Nm]		6.63	5.66
Torque Ripple - MEAN [%]		88.15	102.31
Torque Ripple - MAX [%]		65.47	71.43
Total Device RMS VA [kVA / kW]		7.2827	7.51
Total Device PEAK VA [kVA / kW]		17.04	17.8
Total Diode RMS VA [kVA / kW]		4.03	4.0
Total Diode PEAK VA [kVA / kW]		16.8	17.8
Total Inverter Losses [W]			26.83
Total Copper Losses [W]			99.0
Shaft Power [W]	1481.51	1461.65	1418
Drive Efficiency [%]			91.9
Torque per Copper Loss [Nm/W]			**0.1402**
Torque per Total Loss [Nm/W]			**0.1102**

8.2.1.2 Test-2 (Current Control)

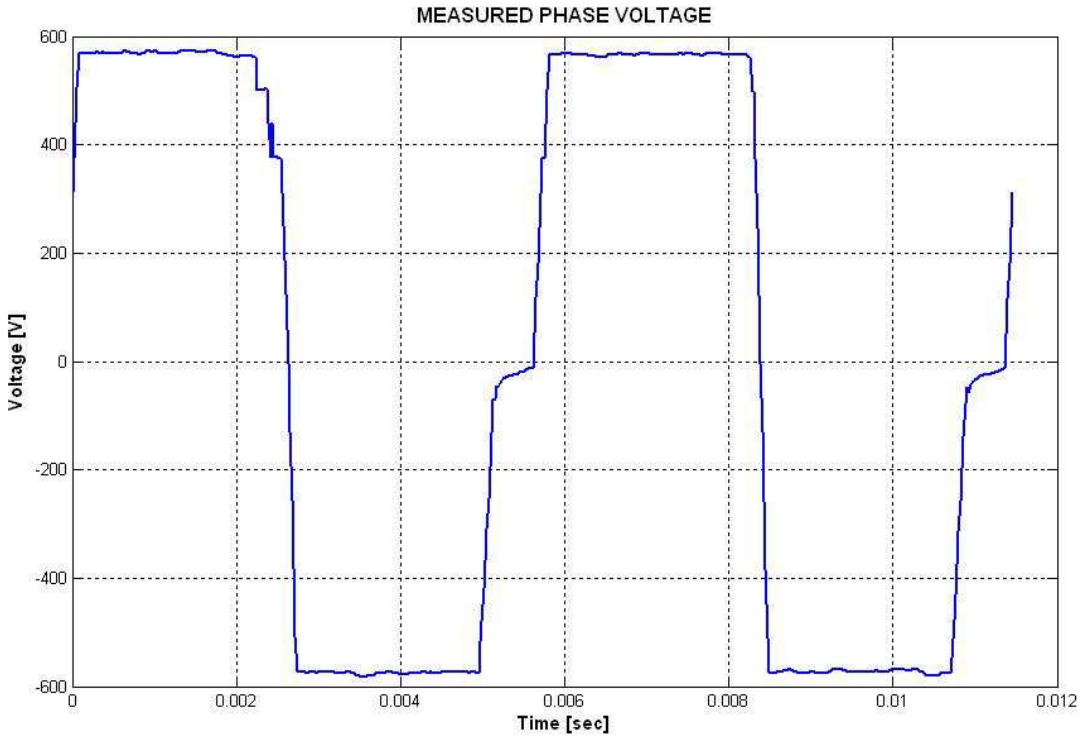

Figure 126 Phase voltage waveform with Advance Angle = -8.8°; Conduction Angle = 164.6°; Speed = 1047RPM; Current Demand = 10A; Vdclink = 567V

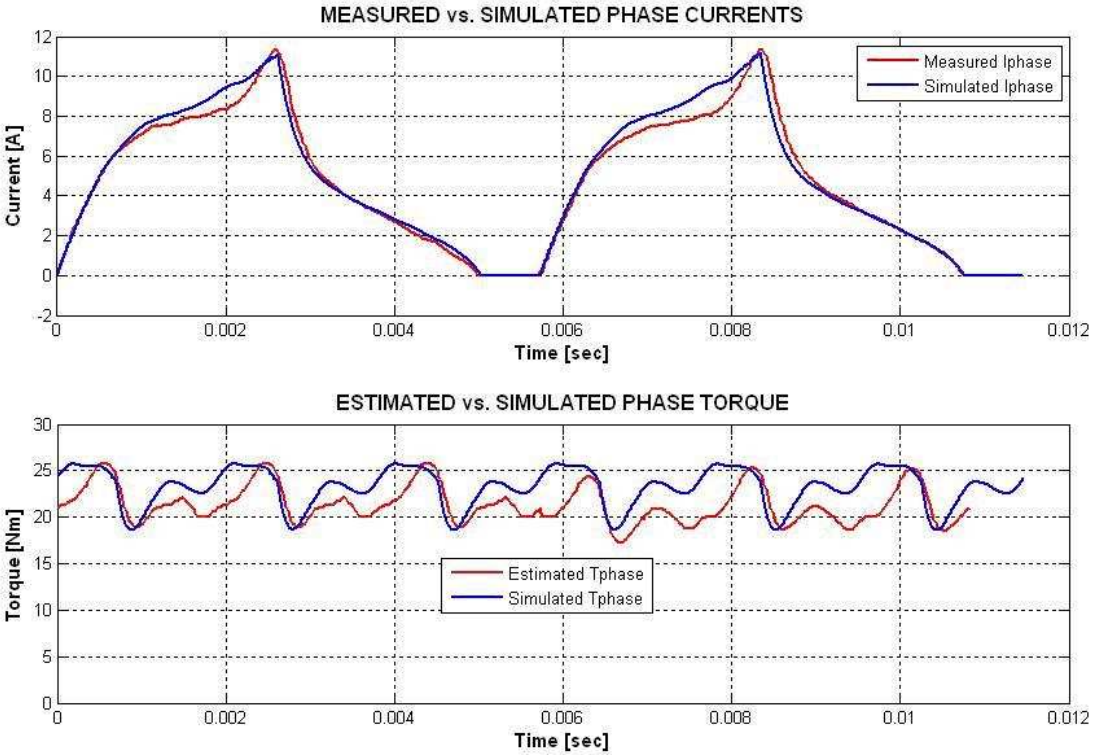

Figure 127 Comparison of simulated and measured phase current and torque with Advance Angle = -8.8°; Conduction Angle = 164.6°; Speed = 1047RPM; Current Demand = 10A; Vdclink = 567V

Table 20 Summary of measured, script and simulation determined results for Test-2 where Advance Angle = -8.8°; Conduction Angle = 164.6°; Speed = 1047RPM; Current Demand = 10A; Vdclink = 567V

	Measured	Script	Simulated
Advance Angle [Elect.Deg.]		-8.8	-8.8
Conduction Angle [Elect. Deg.]		164.6	164.6
Current Demand [A]	10	10	10
Speed [RPM]	1061	1047	1047
RMS Phase Current [A]	5.74	5.74	5.93
Peak Phase Current [A]	11.35	11.35	11.15
RMS Device Current [A]			5.55
Peak Device Current [A]			11.15
RMS Diode Current [A]			3.0497
Peak Diode Current [A]			11.13
Average Total Torque [Nm]	20.5	21.3	23.24
Maximum Total Torque [Nm]		25.61	25.73
Minimum Total Torque [Nm]		18.07	18.6
Torque Ripple - MEAN [%]		35.40	30.68
Torque Ripple - MAX [%]		29.44	27.71
Total Device RMS VA [kVA / kW]			6.92
Total Device PEAK VA [kVA / kW]			14.9
Total Diode RMS VA [kVA / kW]			3.84
Total Diode PEAK VA [kVA / kW]			14.87
Total Inverter Losses [W]			79.2
Total Copper Losses [W]			269.4
Shaft Power [W]	2277.71	2335.37	2548.1
Drive Efficiency [%]			87.97
Torque per Copper Loss [Nm/W]			**0.0863**
Torque per Total Loss [Nm/W]			**0.0667**

During Test-2, the controller enters into current control mode right at the end of the energisation cycle. This can be clearly seen in the figures for the device and diode currents of Test-2 in Figure 134 and Figure 135, respectively (red traces in both figures). This is not as obvious in Figure 126. The reason the simulation predicts a longer chopping period under Test-2 is believed to be due to the difficulty in ensuring the PID controller gains in the current controller of both the simulation and the actual drive are identical.

8.2.1.3 Test-3 (Current Control)

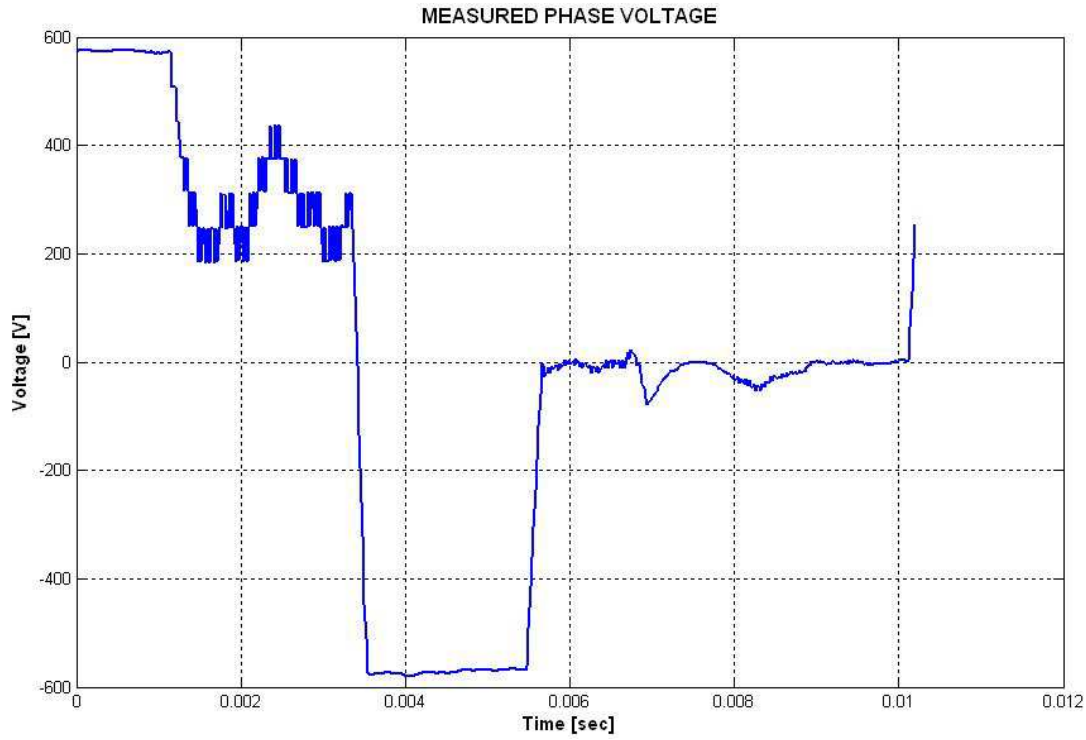

Figure 128 Phase voltage waveform with Advance Angle = 0°; Conduction Angle = 118.6°; Speed = 588.2RPM; Current Demand = 10A; Vdclink = 575V

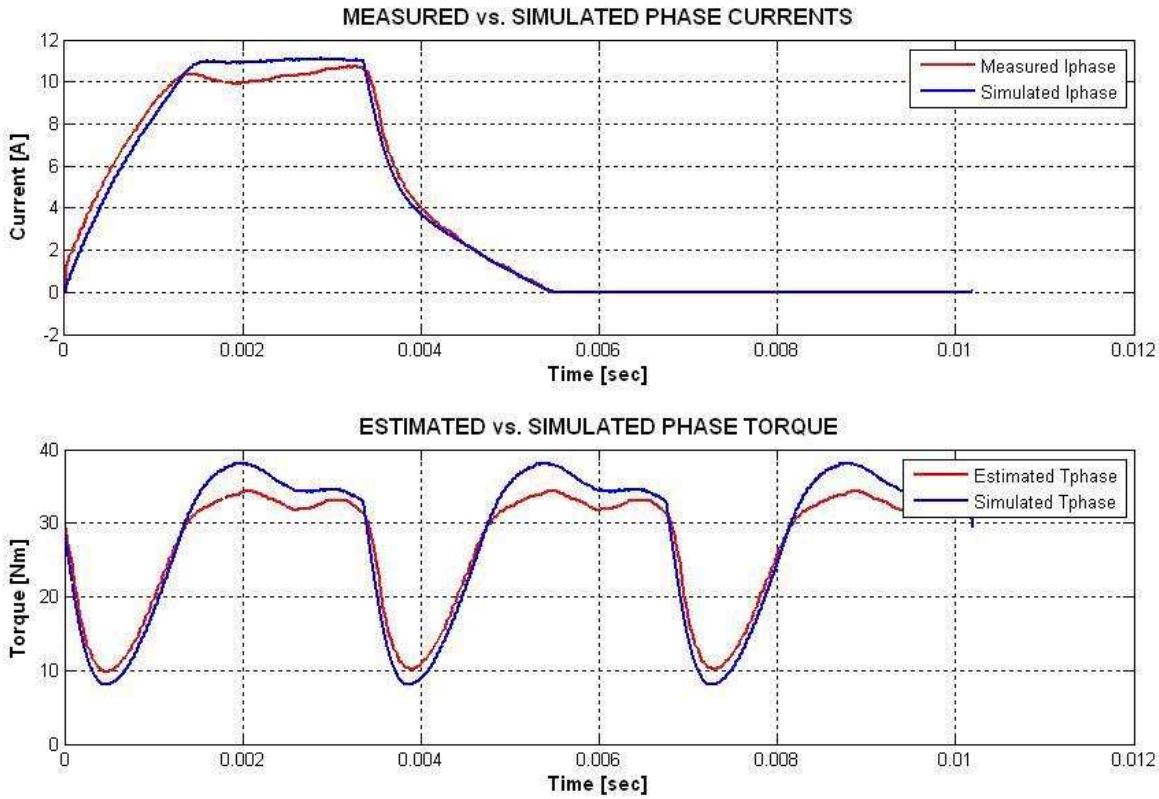

Figure 129 Comparison of simulated and measured phase current and torque with Advance Angle = 0°; Conduction Angle = 118.6°; Speed = 588.2RPM; Current Demand = 10A; Vdclink = 575V

Table 21 Summary of measured, script and simulation determined results for Test-3 where Advance Angle = 0°; Conduction Angle = 118.6°; Speed = 588.2RPM; Current Demand = 10A; Vdclink = 575V

	Measured	Script	Simulated
Advance Angle [Elect.Deg.]		0	0
Conduction Angle [Elect. Deg.]		118.6	118.6
Current Demand [A]	10	10	10
Speed [RPM]	586	588.2	588.2
RMS Phase Current [A]	5.6	5.6	5.641
Peak Phase Current [A]	10.75	10.75	10.73
RMS Device Current [A]			4.93
Peak Device Current [A]			10.72
RMS Diode Current [A]			2.87
Peak Diode Current [A]			10.71
Average Total Torque [Nm]	27.5	26.8	26.06
Maximum Total Torque [Nm]		34.4	36.9
Minimum Total Torque [Nm]		9.84	7.04
Torque Ripple - MEAN [%]		91.64	114.43
Torque Ripple - MAX [%]		71.40	80.90
Total Device RMS VA [kVA / kW]			10.1
Total Device PEAK VA [kVA / kW]			23.03
Total Diode RMS VA [kVA / kW]			6.7
Total Diode PEAK VA [kVA / kW]			23.03
Total Inverter Losses [W]			168.4
Total Copper Losses [W]			244.7
Shaft Power [W]	1687.56	1650.78	1605.3
Drive Efficiency [%]			79.53
Torque per Copper Loss [Nm/W]			**0.1065**
Torque per Total Loss [Nm/W]			**0.0631**

During Test-3, the machine is running relatively slowly compared to other tests presented in this chapter. The controller has enough time to build the phase current and reach the required value before the phase inductance starts limiting the rate of change of current. The current rises rapidly against a small inductance around the unaligned rotor position. Later in the energisation cycle the rate of rise and fall of current is reduced in the PWM cycle as the inductance increases. Once the demand current is reached, the controller enters into current control mode and aims to keep the phase current at the same level until the end of the energisation period. This can be seen in Figure 134 and Figure 135. Once the conduction period is elapsed, the controller turns off the devices and negative voltage is applied across the phase windings to de-flux the phase before the aligned position is reached.

8.2.1.4 Test-4 (Voltage Control)

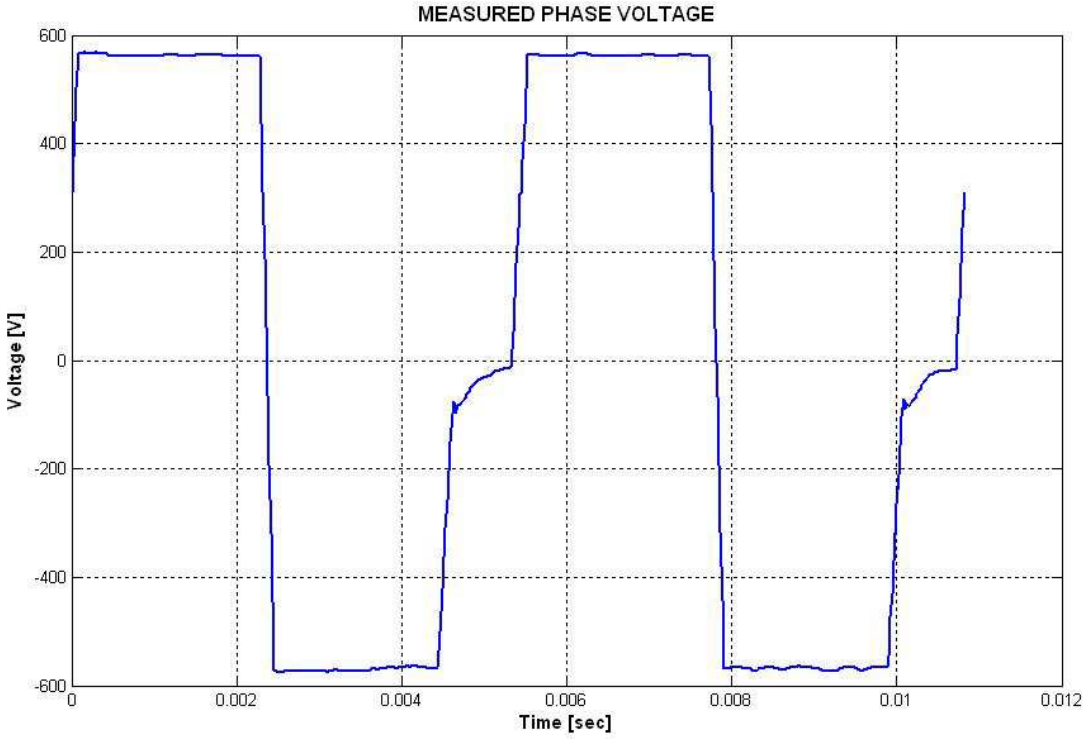

Figure 130 Phase voltage waveform with Advance Angle = -10°; Conduction Angle = 154.4°; Speed = 1109.1RPM; Current Demand = 10A; Vdclink = 567V

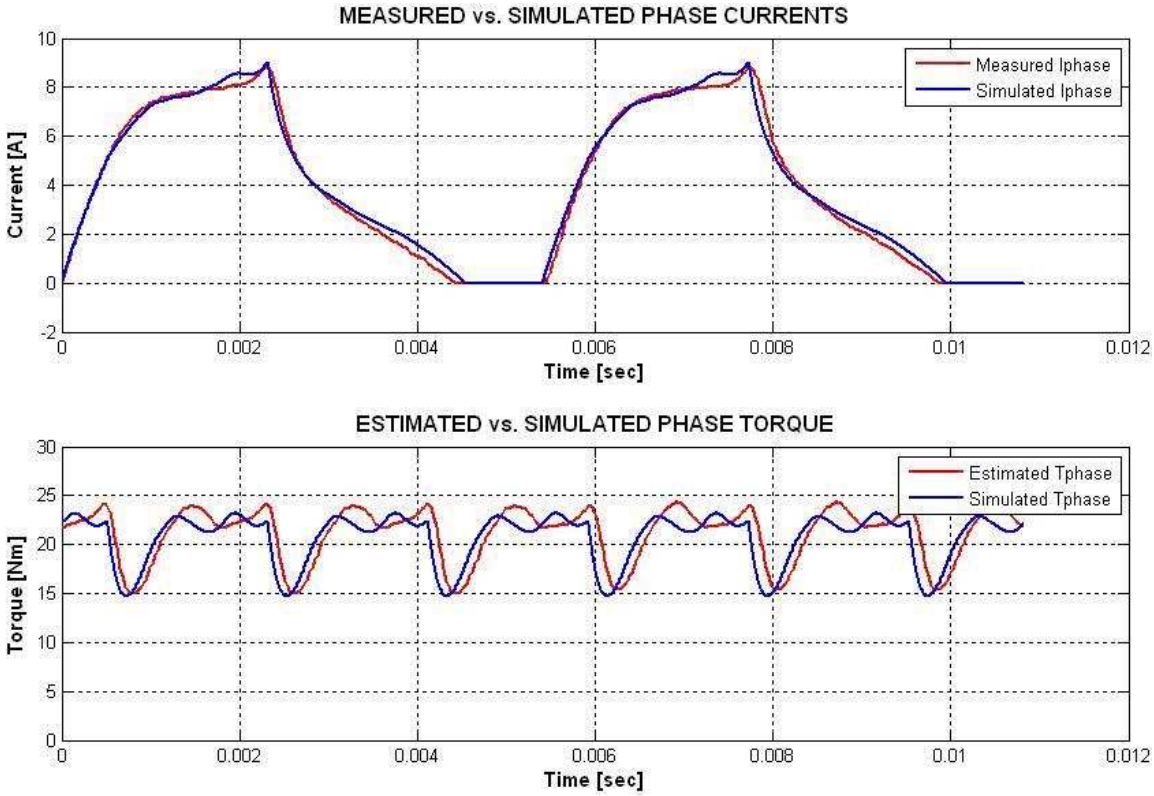

Figure 131 Comparison of simulated and measured phase current and torque with Advance Angle = -10°; Conduction Angle = 154.4°; Speed = 1109.1RPM; Current Demand = 10A; Vdclink = 567V

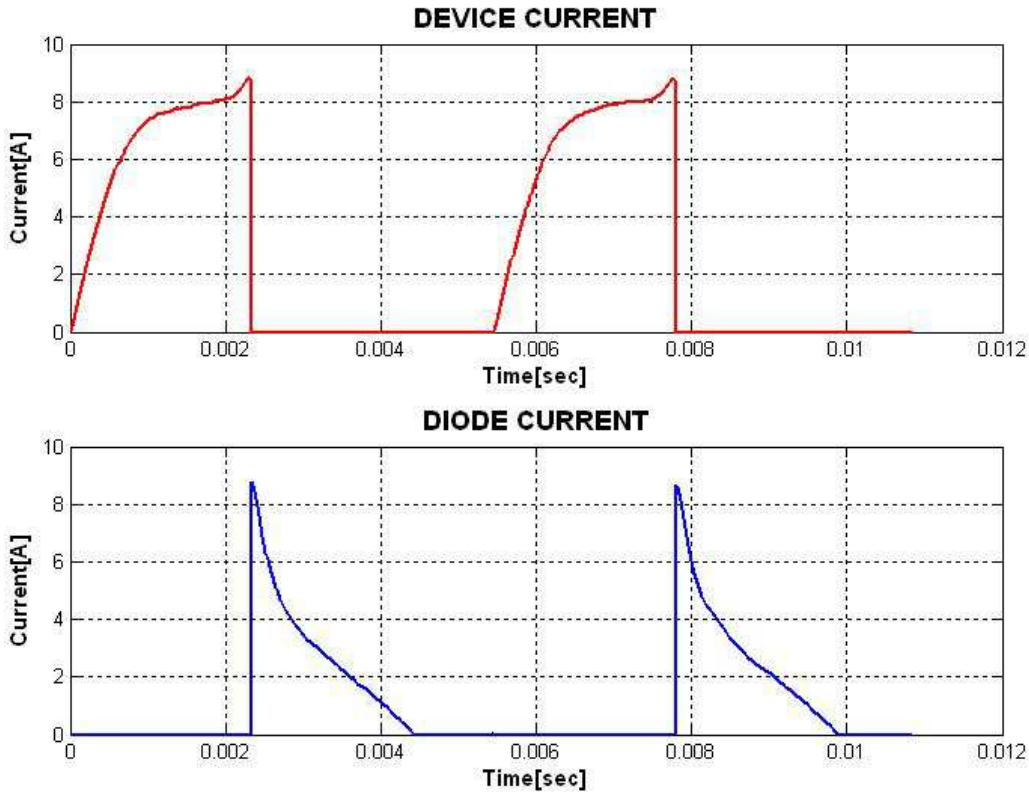

Figure 132 IGBT and recovery diode currents with Advance Angle = -10°; Conduction Angle = 154.4°; Speed = 1109.1RPM; Current Demand = 10A; Vdclink = 567V

Similar to Test-1, the machine is running relatively fast during Test-4. Unlike Test-1, the turn-on point of the phase is in advance of the unaligned rotor position and the conduction angle approaches 1/2 of an electrical cycle. Although compared to Test-1, the phase energisation is advanced and the phase is allowed to conduct longer, the current still never reaches the required level of 10A and the controller is under voltage control.

Table 22 Summary of measured, script and simulation determined results for Test-4 where Advance Angle = -10°; Conduction Angle = 154.4°; Speed = 1109.1RPM; Current Demand = 10A; Vdclink = 567V

	Measured	Script	Simulated
Advance Angle [Elect.Deg.]		-10	-10
Conduction Angle [Elect. Deg.]		154.4	154.4
Current Demand [A]	10	10	10
Speed [RPM]	1100	1109.1	1109.1
RMS Phase Current [A]	5.03	5.03	5.04
Peak Phase Current [A]	8.81	8.81	9.03
RMS Device Current [A]			4.6761
Peak Device Current [A]			9.02
RMS Diode Current [A]			2.37
Peak Diode Current [A]			9.02
Average Total Torque [Nm]	23.7	21.16	20.65
Maximum Total Torque [Nm]		24.32	23.2
Minimum Total Torque [Nm]		15.17	14.73
Torque Ripple - MEAN [%]		43.24	41.02
Torque Ripple - MAX [%]		37.62	36.51
Total Device RMS VA [kVA / kW]		6.0943	6.38
Total Device PEAK VA [kVA / kW]		11.9372	12.81
Total Diode RMS VA [kVA / kW]		3.0348	3.22
Total Diode PEAK VA [kVA / kW]		11.8196	12.81
Total Inverter Losses [W]			42.9
Total Copper Losses [W]			195
Shaft Power [W]	2730.04	2457.62	2398.4
Drive Efficiency [%]			90.98
Torque per Copper Loss [Nm/W]			**0.1059**
Torque per Total Loss [Nm/W]			**0.0868**

Based on the results obtained from the four test conditions presented above, the correlation between the simulated and measured waveforms is very good. From Table 19 to Table 22 the performance parameter predictions from the Matlab® script and the dynamic simulation also correlate very well with each other. Phase, device and diode currents from all four test conditions are plotted in the same figure in Figure 133, Figure 134, and Figure 135, respectively.

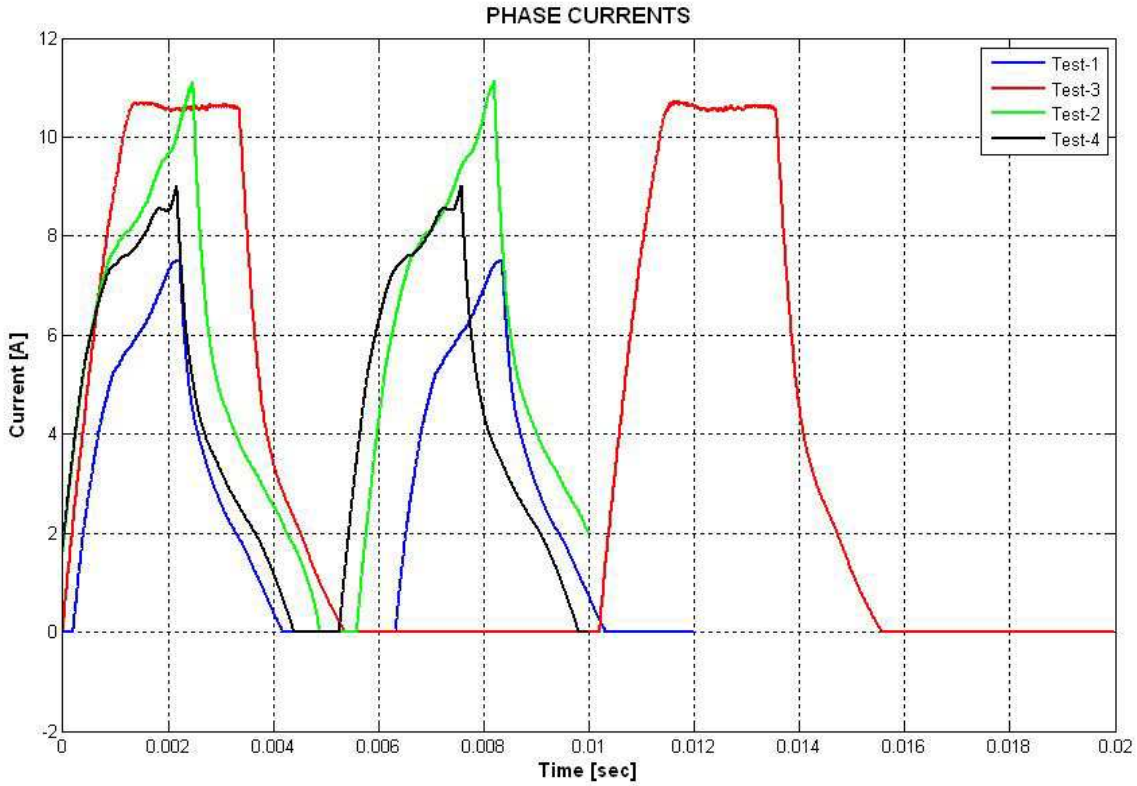

Figure 133 Simulated phase currents of Test-1, Test-2, Test-3 and Test-4

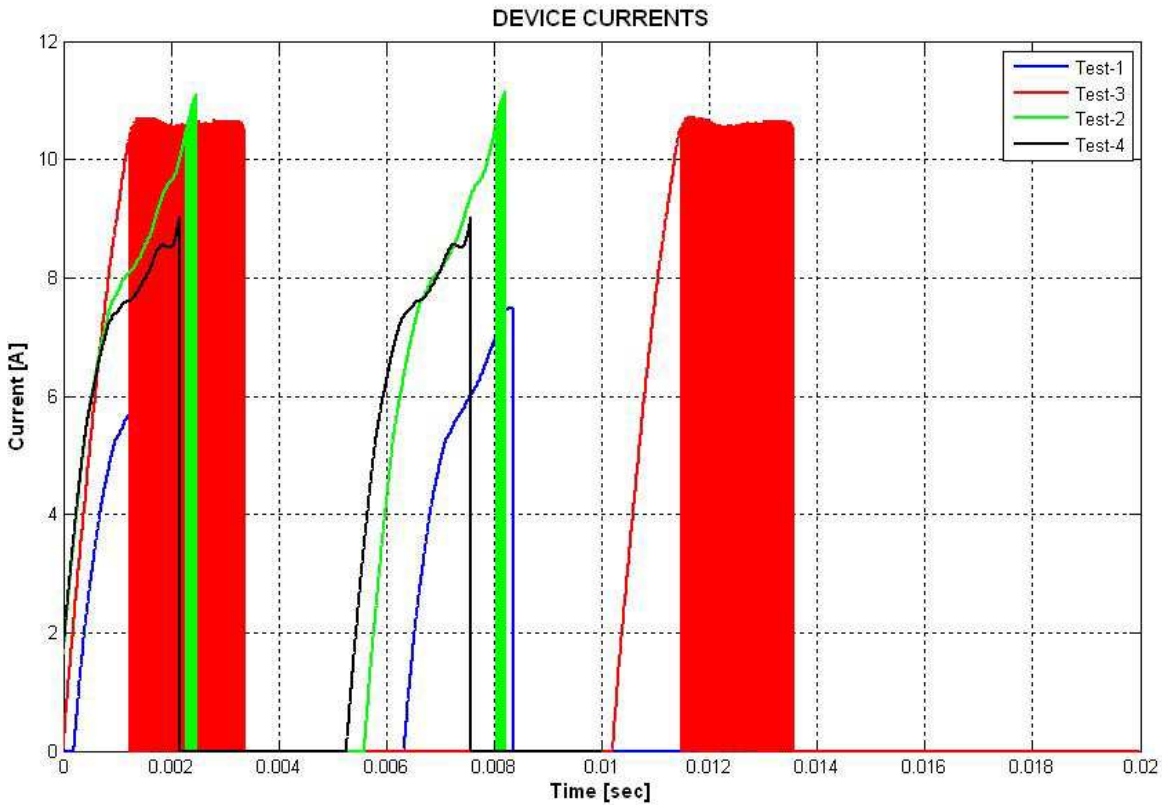

Figure 134 Simulated device currents of Test-1, Test-2, Test-3 and Test-4

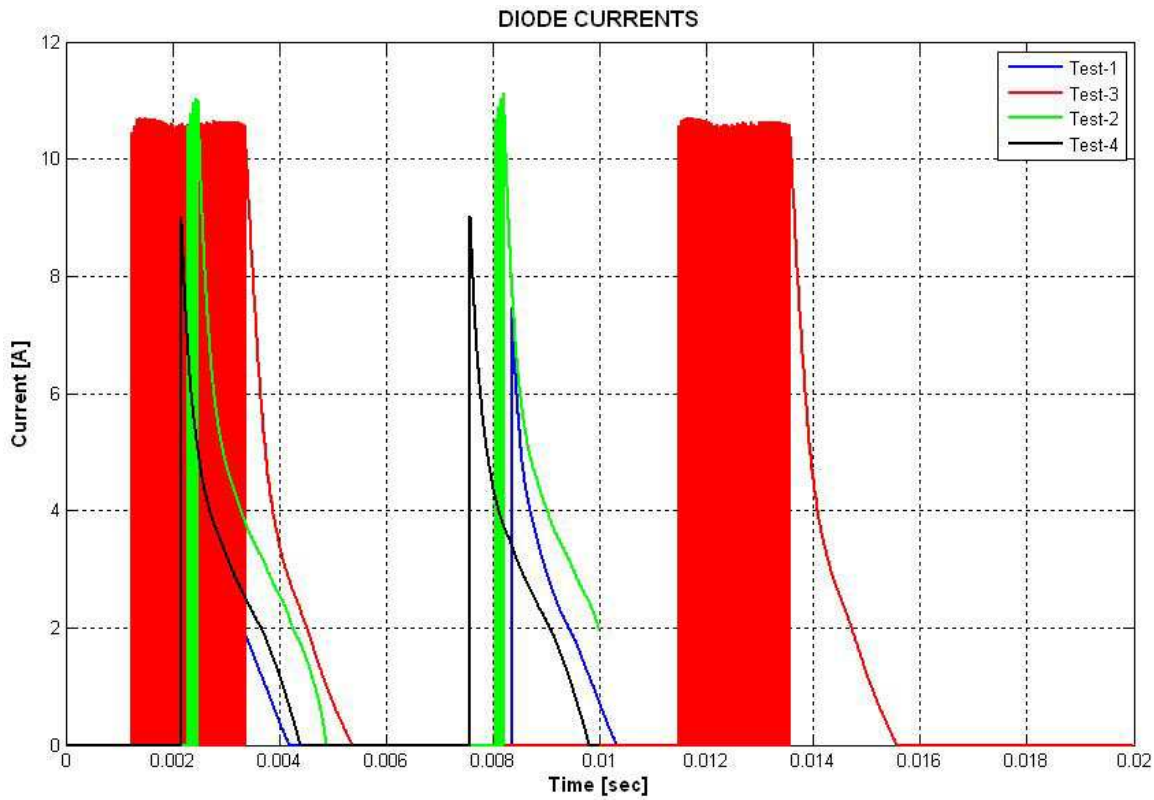

Figure 135 Simulated diode currents of Test-1, Test-2, Test-3 and Test-4

The drive efficiency is higher when the machine is running faster and the controller is under full voltage control. This is typical of SR drives. Although the drive under Test1, Test2 and Test-4 operates approximately at the same speed (978.8rpm, 1047rpm and 1109.1rpm, respectively) the average output torques and the drive efficiencies are different. As the conduction angle is increased the motor is able to generate more output torque. However the machine efficiency is comprised as more current flows through the power devices and the phase windings, increasing the total inverter and copper losses. Although the peak and rms device and diode currents are the lowest during Test-1 (see Figure 134 and Figure 135), the inverter VA rating based on both peak and rms currents is the second worst after Test-3. This is due to the reduced shaft power during Test-1. A much better performance is achieved under Test-4 in terms of shaft power, output torque ripple and inverter VA rating by energising the phase earlier and prolonging the conduction period. The compromise is the reduced drive efficiency due to the increased copper and inverter losses. However, the drop in drive efficiency between Test-1 and Test-4 is only 0.9%.

8.2.2 Dynamic Torque vs. Speed Characteristics

Torque/speed characteristics of the 3-phase single-tooth winding segmental rotor SRM were measured on the test rig for various conduction angles. The advance angle has been varied for each conduction angle and measurements taken at different speeds for each advance angle. The speed was varied by varying the load (see *Chapter 5 – Machine Construction Techniques and Test Rig Description* for the description of the load used in the test rig). The measurements were taken with a dc-link voltage of 580V. Phase current was controlled and the demanded current level was fixed at 10A. The results are presented in Figure 136. The conduction angle was varied from one third of an electrical cycle (i.e. 120^o) to half of an electrical cycle (i.e. 180^o). For each conduction angle, the advance angle was varied from 60^o before the unaligned position to 60^o after the unaligned position with 20^o steps. The aim was to see the effects of control angles (i.e. advance and conduction angles) on the torque vs. speed characteristics of the machine.

In general, advancing the phase energisation instance with respect to the unaligned position of the phase is beneficial in torque production as the speed increases. As the speed reduces, delaying the phase energisation instance after the unaligned position helps with torque production, so that, with high conduction angles, a delay angle as high as 60^o is helpful in torque production. However, no matter what the conduction angle is, as the speed increases the torque production reduces rapidly with high delay angles. This is because it starts to become too late for the controller to energise the phase windings and increase the phase current to the required level, as well as keeping the negative torque low enough to generate high average output torque. As a consequence, the phase current stays positive for longer and longer. There is still positive current flowing in the phase windings even when the rate of change of inductance changes direction, resulting in a large amount of negative torque.

Until approximately 170^o of conduction angle, switching the phases 60^o before the unaligned position results in a flat torque-speed characteristics. This means that the machine output power increases with speed (however, the actual torque level and the speed range where the power increases is somewhat limited). Although generally with higher conduction angles more torque is possible, this comes with a significant compromise in the total machine copper losses.

With longer conduction periods the rms phase currents are also increased, resulting in elevated total machine copper losses. At low speed, it is often more advantageous to increase the current demand when more torque is required (from the point of view of copper and inverter losses) rather than extending the phase energisation period. At higher speeds, the controller operates under full voltage control and increasing the current demand will not have any effect on the machine output torque. The only way to increase the torque then, is to increase the conduction angle and to advance the switching-on instance of the phases before the unaligned rotor position. The general conclusion from the torque vs. speed curves given in Figure 136 is that there is an optimum energisation instance with respect to the unaligned position to generate the highest average output torque for a given operating condition (i.e. conduction angle and speed) without compromising the drive efficiency and the inverter VA-rating significantly.

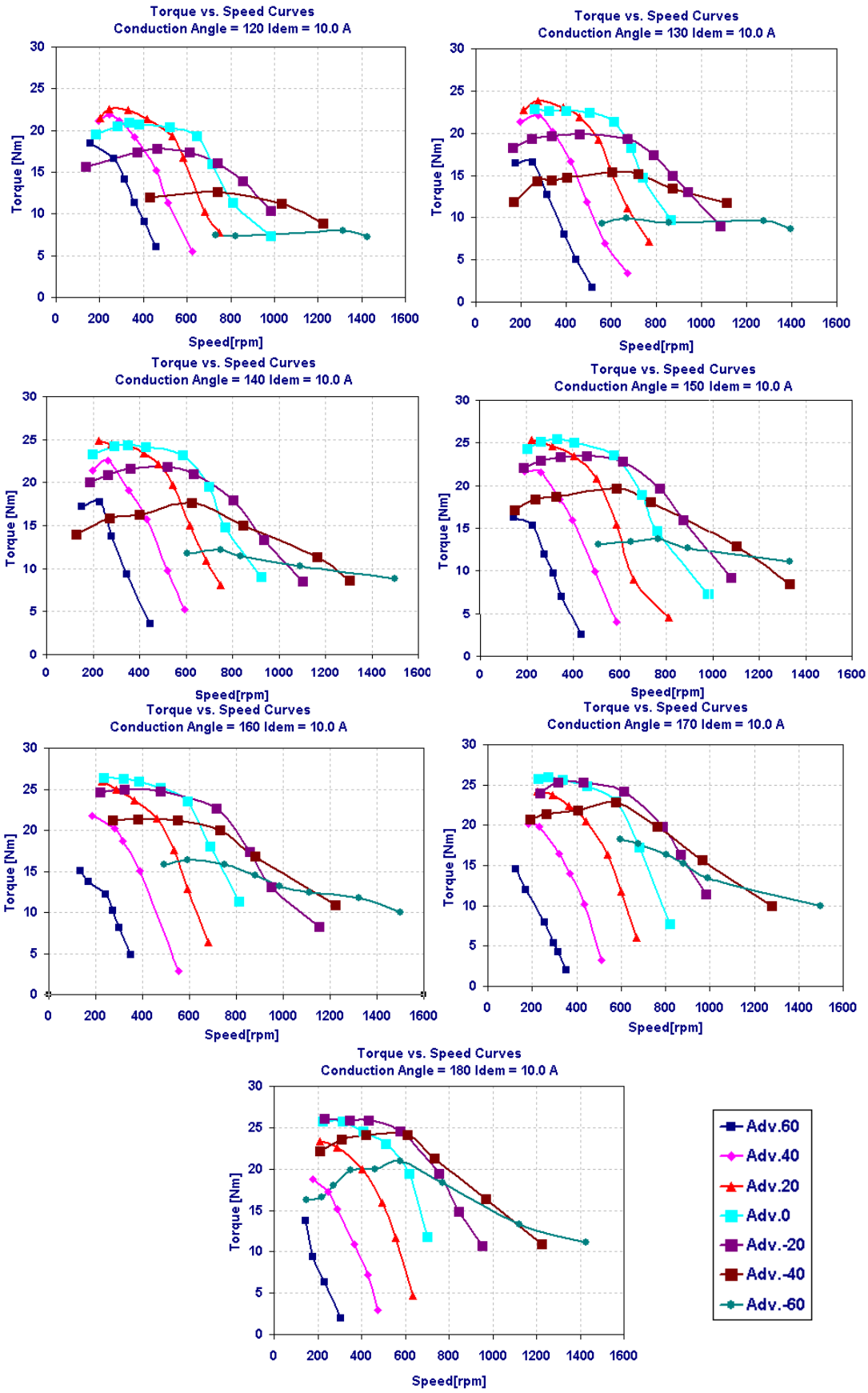

Figure 136 Measured torque-speed curves of 3-phase single-tooth segmental rotor SRM. Conduction angle varied from 120 degrees to 180 degrees. Phase current demand was fixed at 10A and dc-link voltage was 580V

8.3 SUMMARY

Several measurements taken from the 3-phase segmental machine, driven from the three-phase asymmetric half-bridge circuit, have been presented. The simulated waveforms were compared with the measured ones and good correlation was achieved throughout, including current and voltage control modes involving significant magnetic saturation. Good correlation between the measured and simulated waveforms also suggest that the subtleties introduced by the digital PWM control system can be ignored and satisfactory simulation results can still be achieved.

At low speeds, the conduction angle should be limited (e.g. 120^{o}) to minimise the copper losses. At low speeds, the machine BEMF is relatively low and there is plenty of time to build the phase current from zero to the required level. As a result, the controller operates under current control and the applied phase voltage is chopped in order to maintain the current at the required level. The current demand is usually determined by considering the load torque. At higher speeds, the machine BEMF is increased and there is a limited amount of time to increase the phase current to the required level. Therefore, the conduction angle is maximised (e.g. 180^{o}) in order to fully utilise the available dc-link voltage and generate the required torque. Furthermore, under voltage control, the phase energisation is advanced in order to increase the current when the phase inductance is at its minimum. However, the torque ripple is likely to increase for a given conduction angle as more negative torque is likely to be generated with increased advance angles. Under voltage control the drive efficiency is usually higher compared to current control (as constant output power can be maintained even tough the output torque is reduced). With increased conduction angle, the total inverter and machine copper losses are compromised. However, as the region, where the output torque of individual phases overlap is increased, the output torque ripple is reduced with increased conduction angles.

CHAPTER 9

9– Machine Operation and Simulation - Six Phase Drives -

9.1 INTRODUCTION

In the two preceding chapters dynamic simulation and measurement results for the 2-phase and 3-phase drives were presented. This chapter is dedicated to the dynamic measurement and simulation results of the prototype six-phase (12-10) segmental rotor machine drive. Simulation models of the star and delta connected six phase machine were created. These models are believed to be valid where the phases of the machine were mutually de-coupled. These simulation results would not be accurate for the six-phase segmental rotor machine with its strong mutual coupling effects between phases and hence were not compared against the dynamic measurements taken from the segmental rotor prototype machine. However, the six-phase 12-10 conventional rotor machine (designed as part of this PhD project) had mutually de-coupled phases and could be analysed using these simulation models. The phases of the machine were connected in pairs and in parallel through phase diodes, these pairs of phases were connected in star. The inverter of the test rig has been configured to drive the six phase machine from a 3-phase full bridge circuit.

Matlab® based scripts were used to analyse the measured waveforms in order to predict some of the performance parameters of the drive. Particular attention was paid to the instantaneous output torque waveform in order to assess the torque ripple performance of the six-phase drive.

Dynamic simulation results of a six-phase SRM with mutually de-coupled phases, connected in both star (Figure 137) and delta (Figure 138) configuration, operating under current and voltage conditions are given in section 9.2.

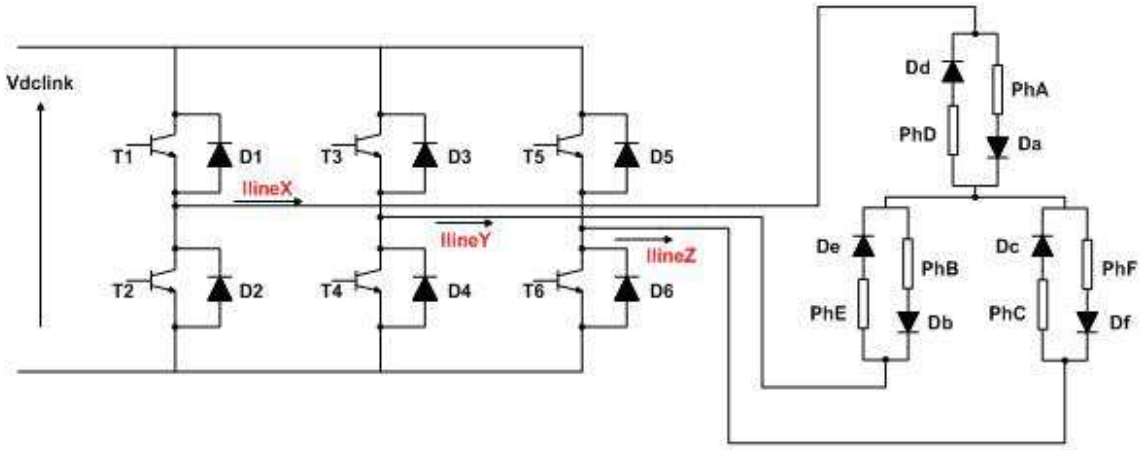

Figure 137 Star-connected six-phase machine driven by a 3-phase full bridge circuit

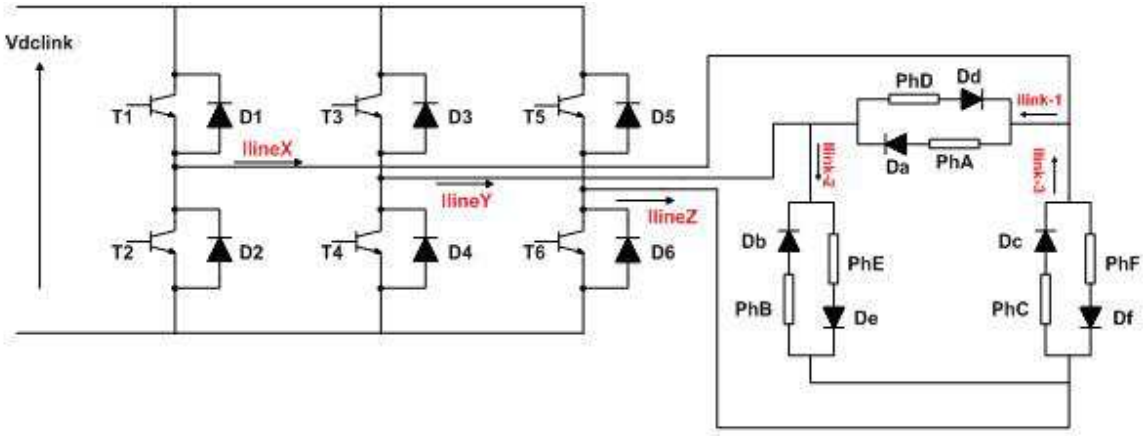

Figure 138 Delta-connected six-phase SRM operated from a conventional 3-phase bridge circuit

Section 9.3 comprises the dynamic measurement results of the six-phase prototype segmental rotor machine. Several examples have been given for low speed and high speed operation. When the machine is under voltage control at high speeds, the line current

waveforms were used to derive the currents flowing through the power devices and diodes in the 3-phase full bridge circuit. These currents, along with the dc-link voltage during testing, were used to estimate the VA-rating of the inverter. Finally, in section 9.4, the findings of the chapter are summarised.

9.2 DYNAMIC SIMULATION RESULTS

The measurements taken from the star-connected six-phase segmental rotor machine driven from the three phase full bridge circuit are given in section 9.3.

As part of this PhD project a six-phase conventional rotor SRM was also designed. The phases of this machine were magnetically de-coupled, meaning the phases could be analysed in isolation in the simulation (Flux linking any phase is assumed to be solely due to the rotor position and the current in that phase only). Thus, it was still believed to be a useful exercise to realise the simulation models for the six-phase machine with mutually de-coupled phases when driven from the 3-phase full bridge circuit and connected in star and delta configurations. This exercise will be beneficial in understanding the operation of the 3-phase bridge circuit with the 6-phase machine topology when there were no mutual coupling effects in the control of the drive. The following two subsections summarise the simulation results obtained from the dynamic simulation for a six-phase SRM with mutually de-coupled phases, driven from the 3-phase bridge circuit. FEA generated flux-linkage characteristics of the prototype 6-phase machine with a conventional toothed rotor structure were used in the dynamic simulation.

9.2.1 Mutually De-Coupled Star Connected Line Current Controlled Six-Phase Drive

Previously in [89] a switched reluctance motor driven from a 3-phase bridge circuit has been demonstrated and various switching waveforms were analysed. In [89] the controller was able to control the phase currents directly, however, when the phases of the prototype 6-phase machine are connected in star and driven from the 3-phase bridge circuit, phase currents can no longer be directly regulated by the controller that is linked to the line currents of the drive. Results in this section were obtained from the dynamic simulation of

the six phase conventional machine with the phase windings connected in star configuration (see *Chapter 6 – Simulation Models*). The model presented is for machines with mutually de-coupled phases. Examples at low and high speed are given, with the results summarised in Table 23 and Table 24. Torque ripple values given in Table 23 and Table 24 are calculated by using Equation 32 in *Chapter 7 – Machine Operation and Comparison to Simulation – Two Phase Drives*. Negative advance angle denotes energising before the unaligned rotor position and zero advance angle stands for energising at the unaligned rotor position. For explanation of some of the variables in Table 23 and Table 24 see Table 16 in *Chapter 7 – Machine Operation and Comparison to Simulation – Two Phase Drives*.

9.2.1.1 Drive under Current Control

Here, the six-phase machine is connected in star configuration and driven from the 3-phase full bridge converter. The three line currents were the controlled parameters and each line had its own PID and PWM controllers, with the current demand set to 30A and the machine rotating at 250rpm. At this speed, the machine BEMF is low and the controller has enough time to build the current from zero to the demanded level. Thus, the controller works in the current control mode. The phases were energised at the unaligned rotor position. The conduction period was fixed to 120^o and the dc-link voltage was set to 175.0V. The results from the dynamic simulation are depicted from Figure 139 to Figure 148. At this speed, the line currents are very close to those expected from the ideal 120^o conduction. In Figure 139, the black trace is the instantaneous phase voltage waveform obtained directly from the simulation. However, it is quite difficult to use the simulated phase voltage waveform to explain the operation of the drive. For this purpose the red trace (*Vphase Filtered*) in Figure 139 is generated after post-processing the simulated phase voltage via a simple moving average based filter.

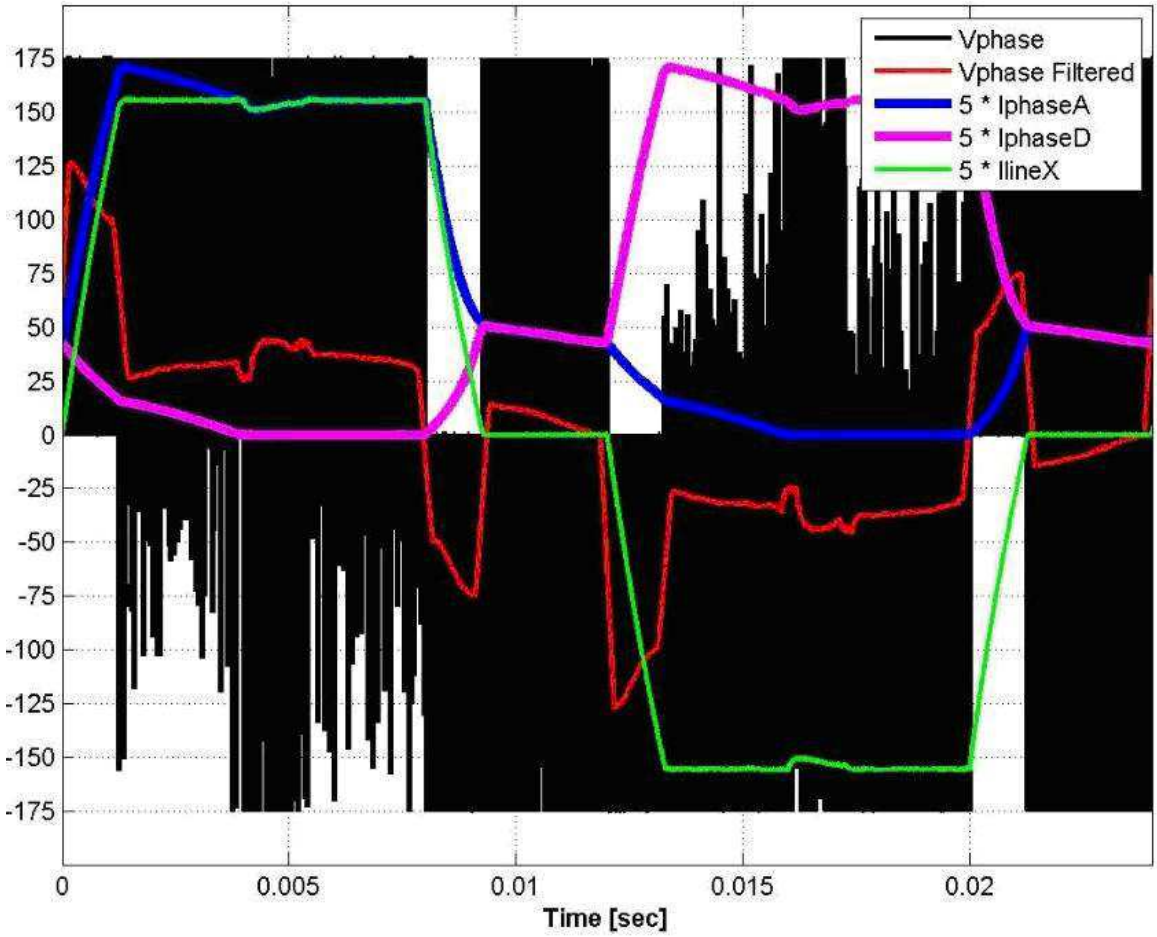

Figure 139 Simulated phase voltage (in black), phase-A current (x5 in blue), phase-D current (x5 in magenta), line-X current (x5 in green) and filtered phase voltage (in red) for the 3-phase bridge circuit driven star connected 6-phase conventional rotor SRM with mutually de-coupled phase windings running at 250rpm

In Figure 139 it is quite clear that the phase currents have a two-stage tail-off period. There are two reasons for this:

- Not all the dc-link voltage is available to de-flux the phase windings. This is a virtue of the star-connected three phase system and can be explained with the help of Figure 140. Across a pair of parallel connected phases (phaseA / phaseD, phaseB / phaseE or phaseC / phaseF in Figure 140), the controller is only able to control the potential at one end of the circuit (Vx, Vy or Vz in Figure 140), the other end is the uncontrolled star-point potential (Vs in Figure 140).

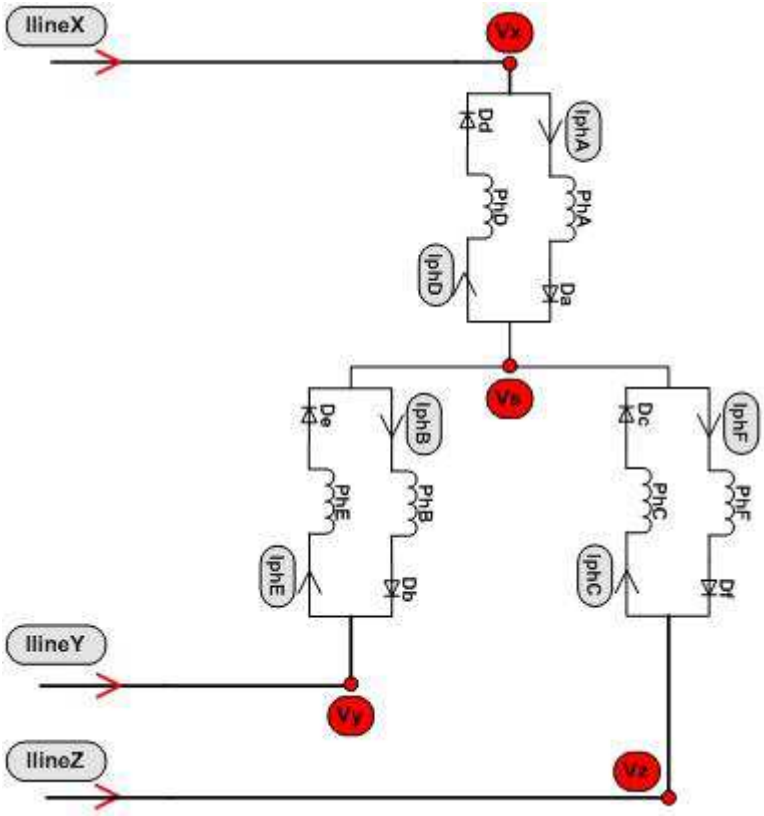

Figure 140 Six phase machine is star configuration

- The controller is not able to control the phase currents directly. Instead, the line currents are controlled. When the line current falls to zero the controller aims to keep it at zero. This effectively means no voltage is applied across the phase windings and the decay in the phase current is very small.

As the controller is only able to regulate the line potential directly in order to control the line current, it is hard to see that the controller is under current control by observing the phase voltage waveform in Figure 139. With respect to Figure 140, Figure 141 depicts the line-X potential (Vx) and current (IlineX). In Figure 141, the controller is clearly under current control and the Vx potential swings between positive and negative Vdclink / 2 (i.e. 87.5V). All of the available line potential is applied at point Vx in Figure 141. This continues until the line current reaches the demanded level. Once the demanded level is reached the controller chops the voltage between positive and negative values until the end of the conduction period. Once the conduction period elapses the controller applies the full negative voltage at point Vx to reduce the line current back down to zero.

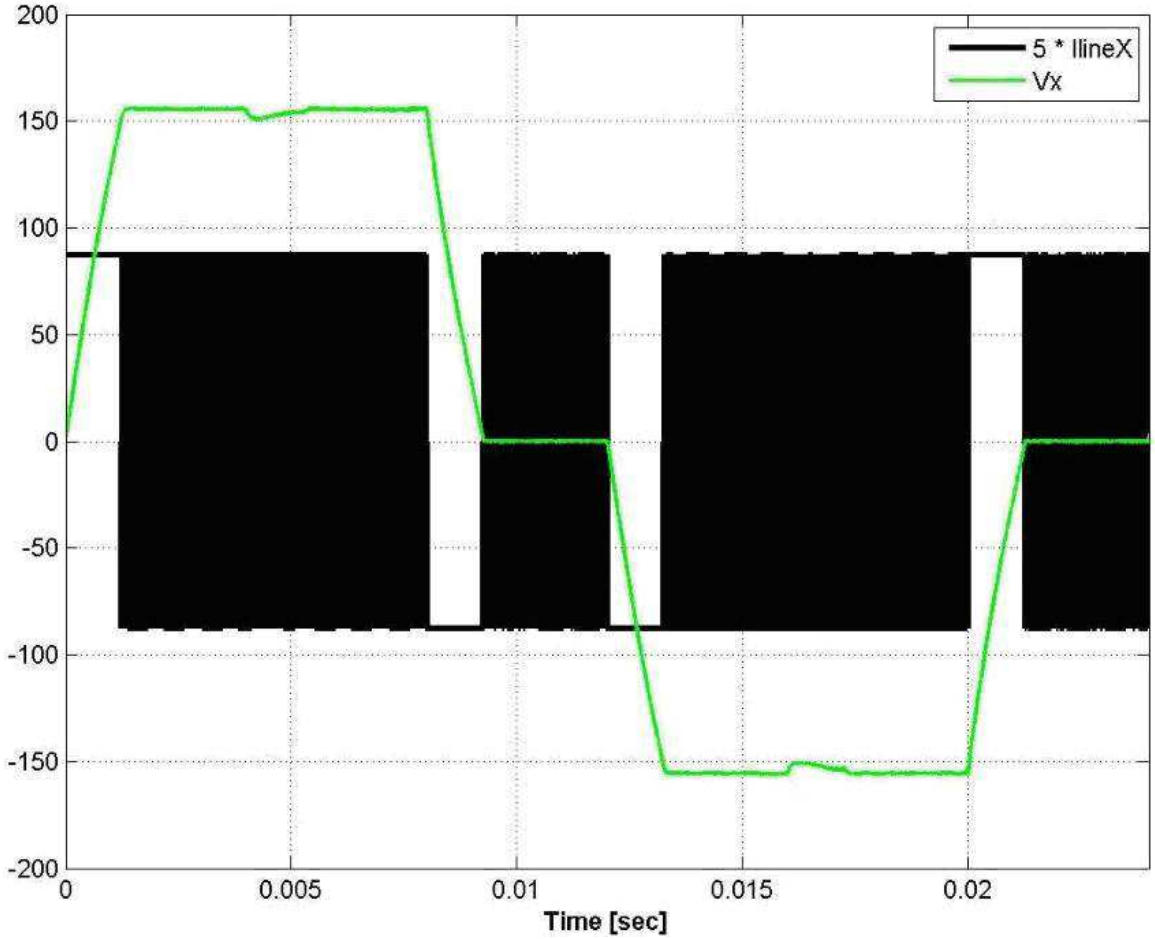

Figure 141 Simulated line potential (in black) and current (x5 in green) for the 3-phase bridge circuit driven star connected 6-phase conventional rotor SRM with mutually de-coupled phase windings running at 250rpm

To clarify the operation of the star-connected drive under current control Figure 142 has been generated.

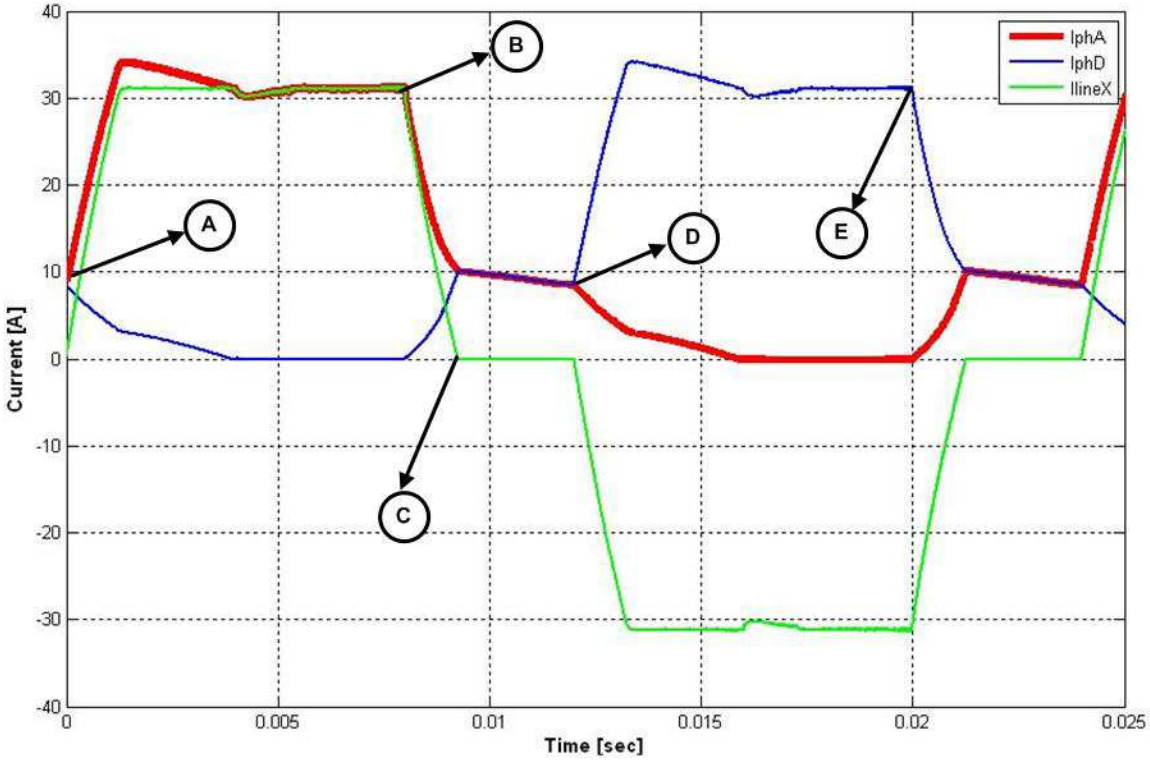

Figure 142 Simulated phase-A current (in red), phase-D current (in blue), line-X current (in green) for the 3-phase bridge circuit driven star connected 6-phase conventional rotor SRM with mutually de-coupled phase windings running at 250rpm

The operating states in Figure 142 are summarised below with respect to the circuit diagram in Figure 137:

Point A : Phase-A is turned on.

Point B : Phase-A is turned off.

Point C : Line current (IlineX) falls to zero.

Point D : Phase-D is turned on.

Point E : Phase-D is turned off.

It is quite clear from Figure 142 that the peak phase current is higher than the demanded current level of 30A. However, this current is not seen by the power devices in the full bridge as it circulates around the parallel connected phases (note the balancing current flowing in phase-D between points B and C in Figure 142 as well). Once the current in phase-D falls to zero the line current equals phase-A current (the phase current that is in its conduction period). As mentioned earlier, when the line current falls to zero, the controller aims to keep this at zero. The currents in phases A and D circulate around the

phase windings and the phase diodes. Between points C and D in Figure 142, the Line-X and the star point potentials are zero (see bottom trace of Figure 146).

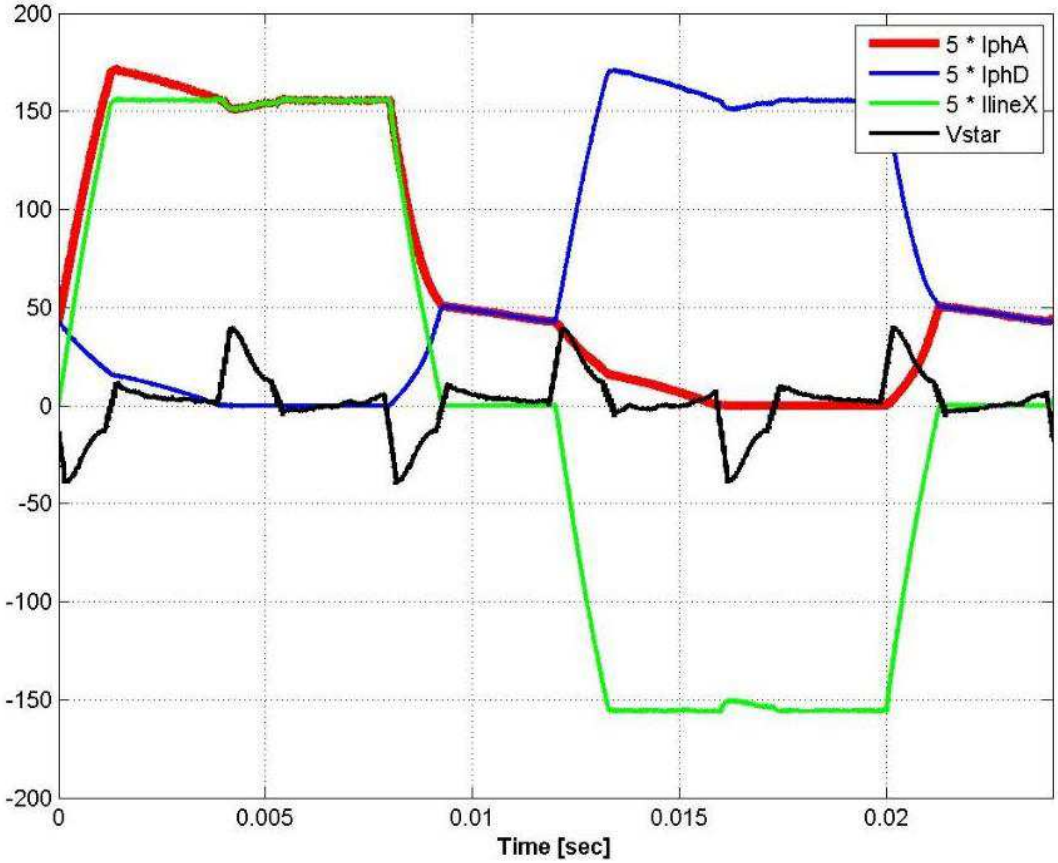

Figure 143 Simulated phase-A current (x5 in red), phase-D current (x5 in blue), line-X current (x5 in green) and star-point potential (in black) for the 3-phase bridge circuit driven star connected 6-phase conventional rotor SRM with mutually de-coupled phase windings running at 250rpm

From Figure 143, there are six distinct periods of star point potential, each corresponding to a phase commutation point. This ensures that the currents flowing into the star point sum up to zero. The effect of this star point potential can be seen in the phase and line current waveforms, as a dip appears in the figures approximately half way through the conduction period. The positive star point potential effectively reduces the available voltage across phase-A windings when the line current is flowing in the positive direction and the Line-X potential is connected to the positive dc-link rail (Figure 144-a). The reduction in the available phase voltage can also be seen in Figure 139. The same applies when phase-D conducts. Negative star point potential reduces the voltage available to drive the phase-D current, as in this period the Line-X is connected to the negative dc-link rail (Figure 144-b). These waveforms are very similar to those experienced with the h-

bridge driven two-phase drive, apart from the dip during phase commutation. This is of no surprise, as the only difference between the two drives is the fact that the six phase drive can only control the potential at one end of the module (e.g. comprising phases A and D with the phase diodes in series with the phase windings). The other end is the uncontrolled star point potential that regulates the star point current.

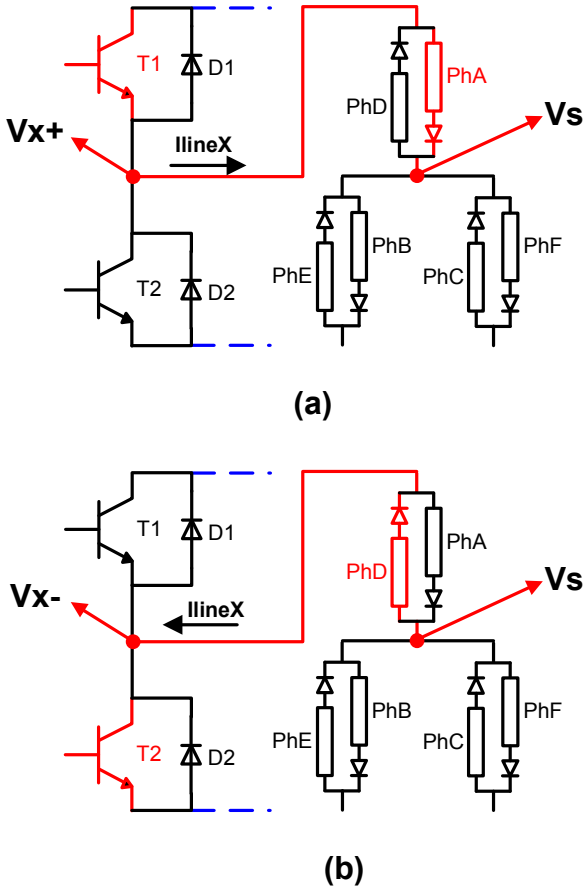

Figure 144 Schematic explanation of inverter states for the 3-phase bridge circuit driven star connected 6-phase conventional rotor SRM: a-) PhA conducting and line current in positive direction, b-) PhD conducting and line current in negative direction. Conductive paths in red

In Figure 145, the simulated instantaneous star point potential and current are depicted. The black traces are taken directly from the dynamic simulation and the green traces are simply the filtered versions of these simulated waveforms. As before, filtering is achieved by a simple moving average method. It is obvious from the bottom trace in Figure 145 that the error in the current flowing into the star point voltage (i.e. sum of all phase currents) is at its maximum during phase commutation. However, even during phase commutation the error is only 0.1% of the demand current level. It can be said that the

calculation of the star point potential based on the trial of a set of predetermined values explained in *Chapter 6 – Simulation Models* works adequately.

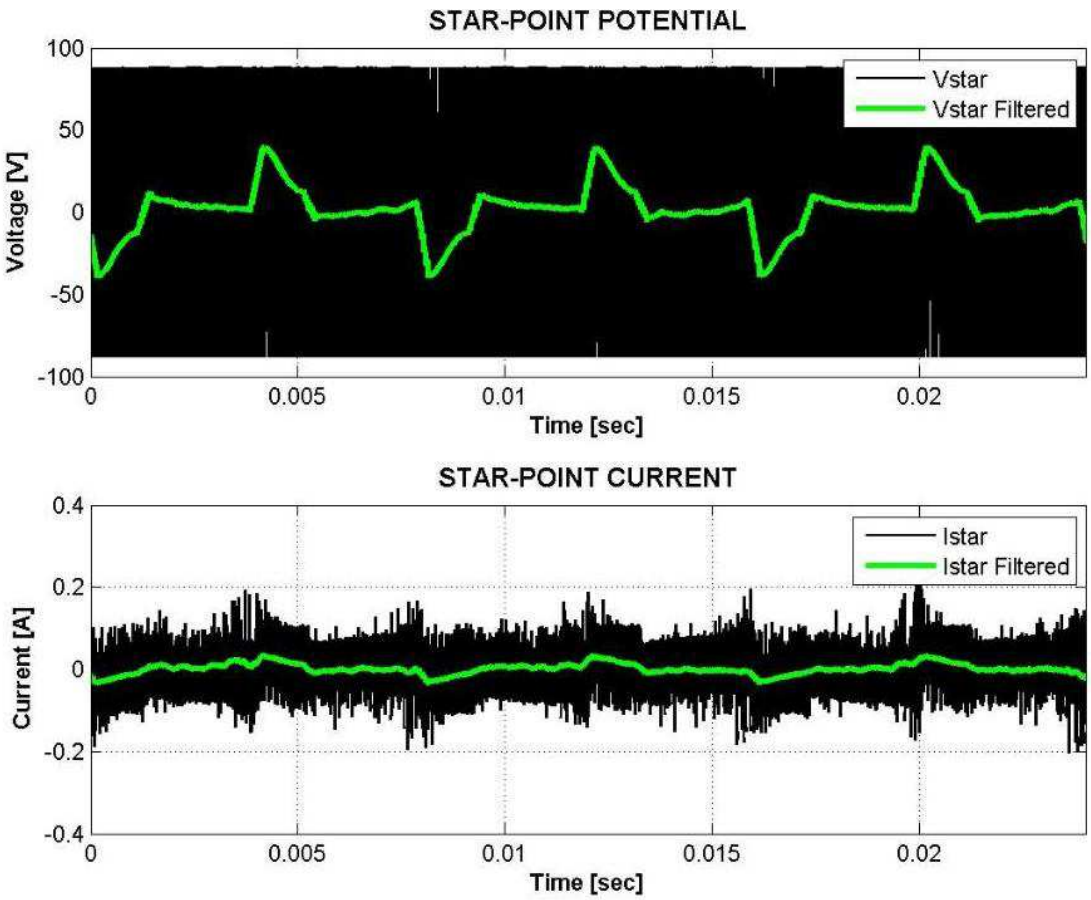

Figure 145 Simulated star-point potential (top trace) and star-point current (bottom trace) for the 3-phase bridge circuit driven star connected 6-phase conventional rotor SRM with mutually de-coupled phase windings running at 250rpm

In Figure 139, it is also interesting to note that the filtered phase voltage never reaches the full dc-link rail voltage. This can be explained with the help of the two traces given in Figure 146. The top trace in Figure 146 depicts the phase voltage, line potential and the star point potential that are generated by the simulation. The bottom trace contains the filtered (with a simple moving average method) versions of the same waveforms. As mentioned earlier, with the machine connected in the star configuration, the controller is unable to regulate the phase voltage. The phase voltage depends on the star point potential, which in turn varies in order to keep the sum of the currents flowing into it at zero. As the filtered star point potential never reaches the full negative voltage neither does the phase voltage.

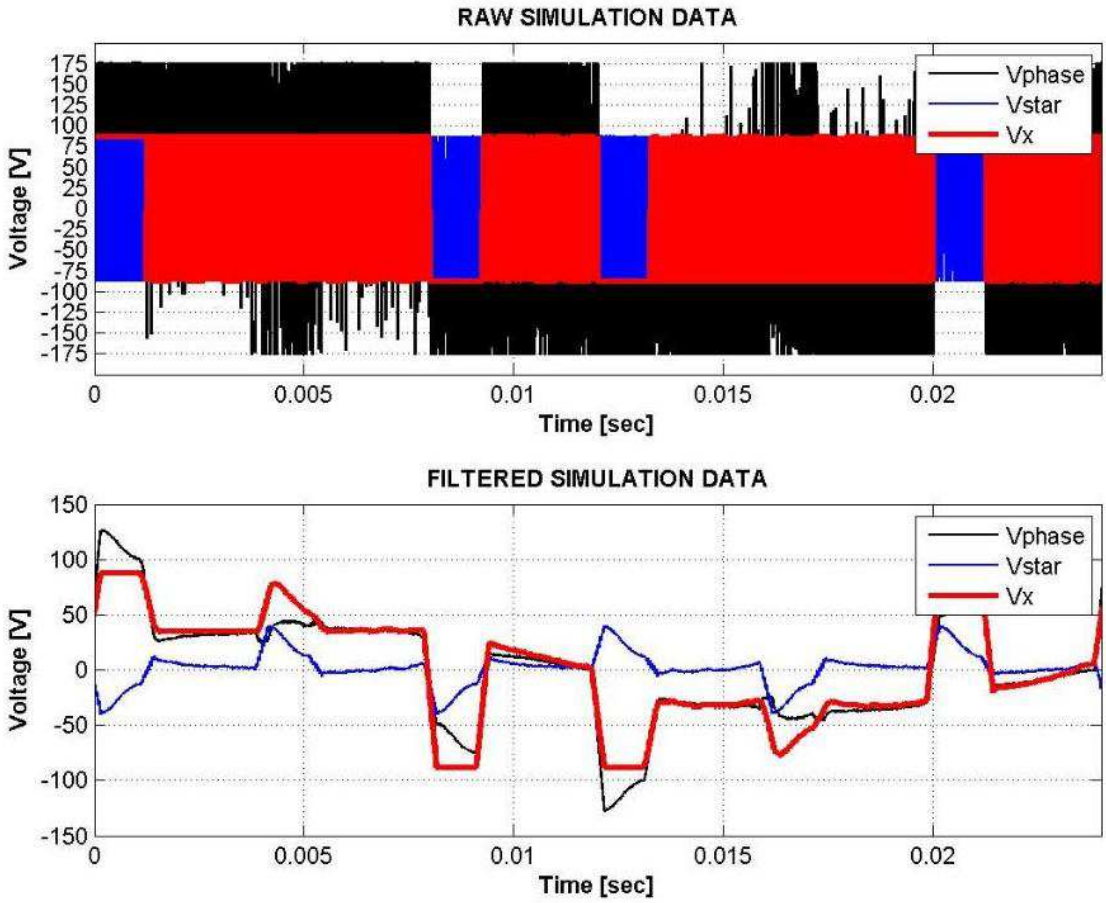

Figure 146 Simulated raw phase, line and star point voltages (top trace) and filtered phase, line and star point voltages (bottom) for the 3-phase bridge circuit driven star connected 6-phase conventional rotor SRM with mutually de-coupled phase windings running at 250rpm

In Figure 147, the phase currents are displayed along with all three line currents.

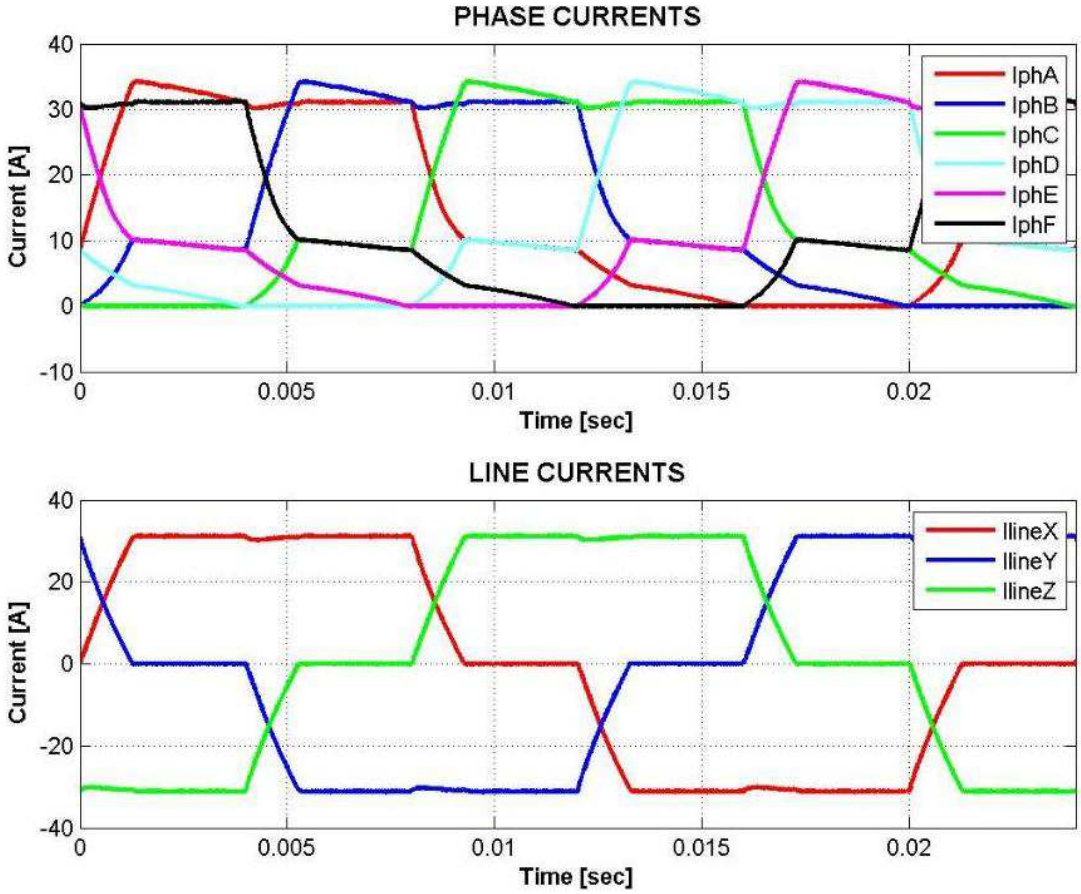

Figure 147 Simulated phase currents (top trace) and line currents (bottom trace) for the 3-phase bridge circuit driven star connected 6-phase conventional rotor SRM with mutually de-coupled phase windings running at 250rpm

Figure 148 depicts the contribution of each machine phase to the total output torque. The dip during phase commutation approximately half-way through a phase's conduction period is visible in the phase torque waveforms in Figure 148.

Table 23 summarises some of the simulation input parameters along with the results of some of the performance parameters generated by the simulation for the star connected drive running at 250rpm under current control.

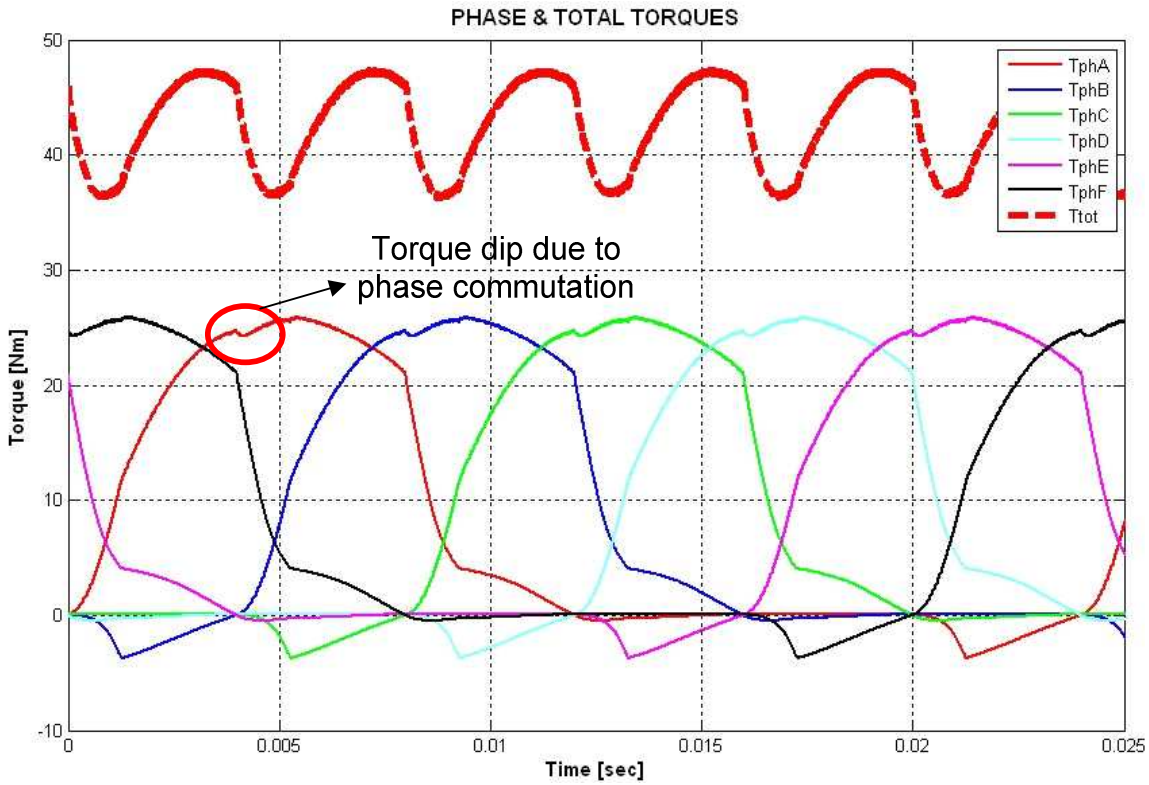

Figure 148 Simulated phase torques and resulting total output torque for the 3-phase bridge circuit driven star connected 6-phase conventional rotor SRM with mutually de-coupled phase windings running at 250rpm

Table 23 Summary of simulated performance parameters for the 3-phase bridge circuit driven star connected 6-phase conventional rotor SRM with mutually de-coupled phase windings running at 250rpm.

Speed [RPM]	250	**Swt_VARating_Peak [kVA / kW]**	29.37
Current Demand [A]	30	**Swt_VARating_RMS [kVA / kW]**	13.69
Advance Angle [Deg]	0	**Dio_VARating_Peak [kVA / kW]**	29.32
Conduction Angle [Deg]	60	**Dio_VARating_RMS [kVA / kW]**	8.85
DC-Link Voltage [V]	175	**Total Peak VA Rating [kVA / kW]**	58.69
Average Output Torque [Nm]	42.8	**Total RMS VA Rating [kVA / kW]**	22.54
Average Output Power [Nm]	1120.4		
Maximum Output Torque [Nm]	47.4		
Minimum Output Torque [Nm]	36.3		
Output Torque Ripple - Pk2Pk [%]	23.33		
RMS Phase Current [A]	18.79		
Peak Phase Current [A]	34.28		
Total Machine Copper Losses [W]	961.7		
Total Inverter Losses [W]	240.5		
Total Phase Diode Losses [W]	50		
Drive Efficiency [%]	47.2		

9.2.1.2 Drive under Voltage Control

The current demand was kept at 30A, but this time, the machine was run at 1200rpm. At this speed, the machine BEMF is relatively high and the controller does not have enough time to build the line current from zero to the demanded level against the rapid change in the machine inductance between the unaligned and aligned rotor positions. Thus, the current demand is never reached and the controller works under full voltage control mode. In this case, the values for the PID gains are irrelevant. The energisation of the phases was advanced by 40^o in order to help with the torque production. Similar to the low speed operation, the conduction period was fixed to 120^o and the dc-link voltage was set to 175.0V. The results from the dynamic simulation are depicted from Figure 149 to Figure 156.

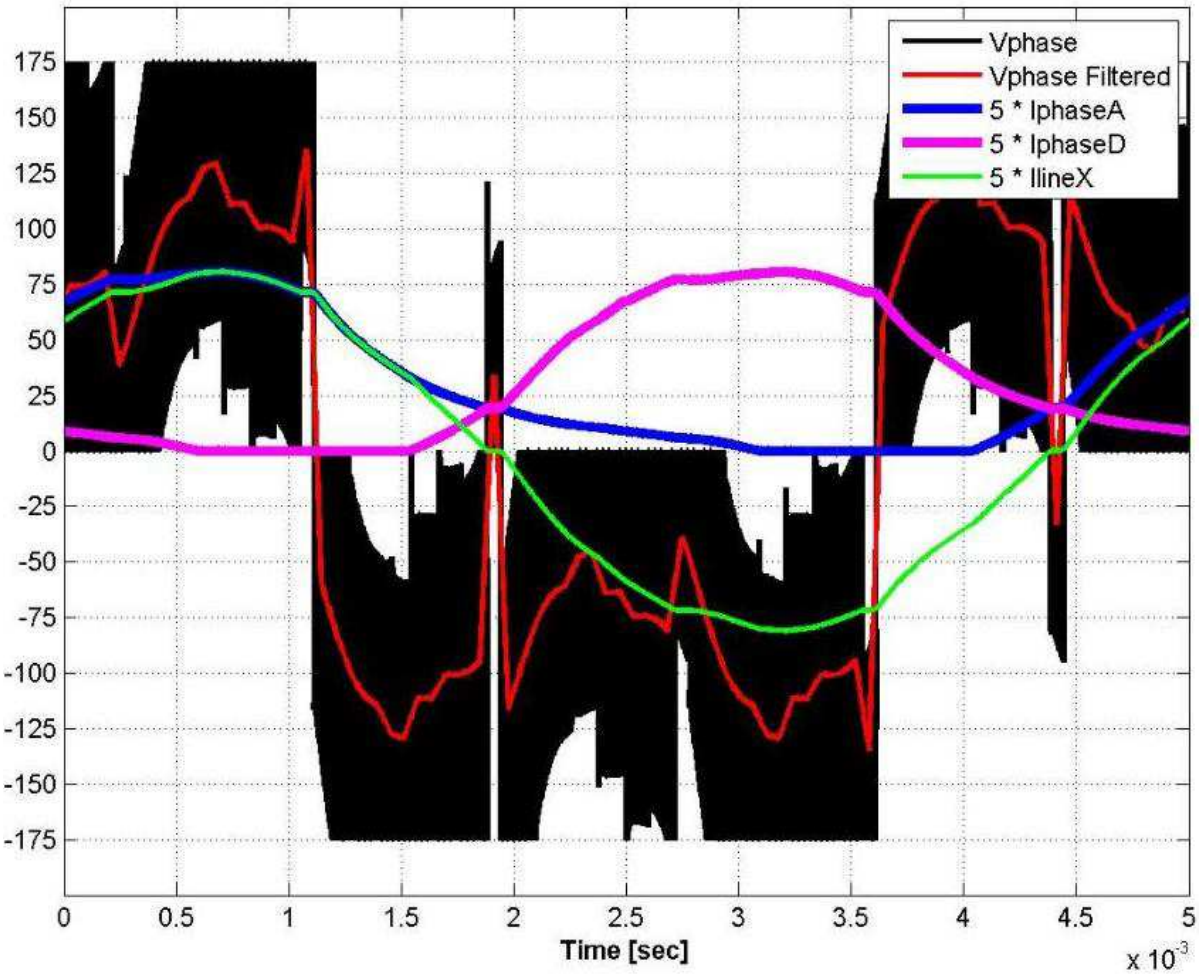

Figure 149 Simulated phase voltage (in black), phase-A current (x5 in blue), phase-D current (x5 in magenta), line-X current (x5 in green) and filtered phase voltage (in red) for the 3-phase bridge circuit driven star connected 6-phase conventional rotor SRM with mutually de-coupled phase windings running at 1200rpm

It is clear from Figure 149 that the line current waveform deviates significantly from the ideal 120^o as it is almost continuous with a very narrow zero period (between points B and C in Figure 151).

Figure 150 clearly demonstrates that the controller is under full voltage control and the Vx potential swings between positive and negative dc-link voltage (i.e. 87.5V). All of the available line potential is applied at point Vx (see Figure 140) until the end of the conduction period. Once the conduction period elapses the controller applies the full negative voltage at point Vx to reduce the line current back down to zero.

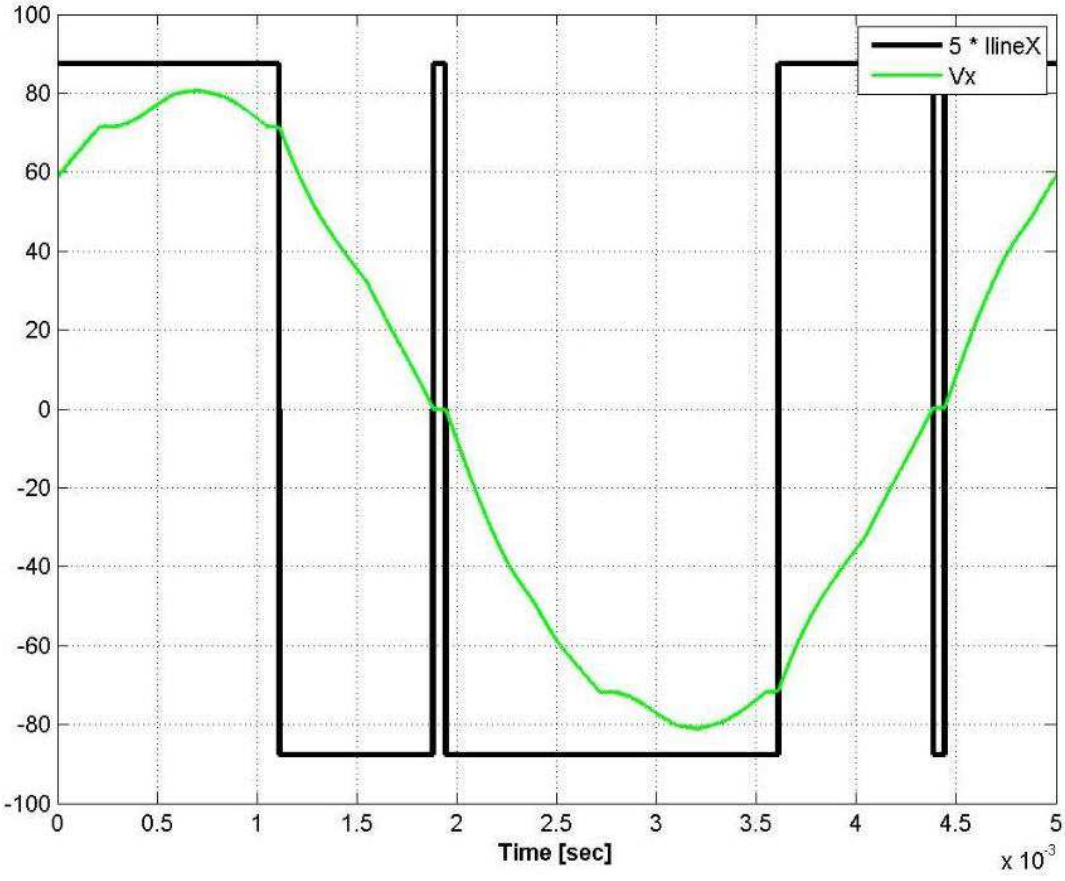

Figure 150 Simulated line potential (in black) and current (x5 in green) for the 3-phase bridge circuit driven star connected 6-phase conventional rotor SRM with mutually de-coupled phase windings running at 1200rpm

Once again, to help with the understanding of the operation of the star-connected drive under voltage control, Figure 151 has been generated. States in Figure 151 are summarised below:

Point A : Phase-A is turned off.

Point B : Line current (IlineX) falls to zero.

Point C : Phase D is turned on.

Point D : Phase D is turned off.

Point E : Phase A is turned on.

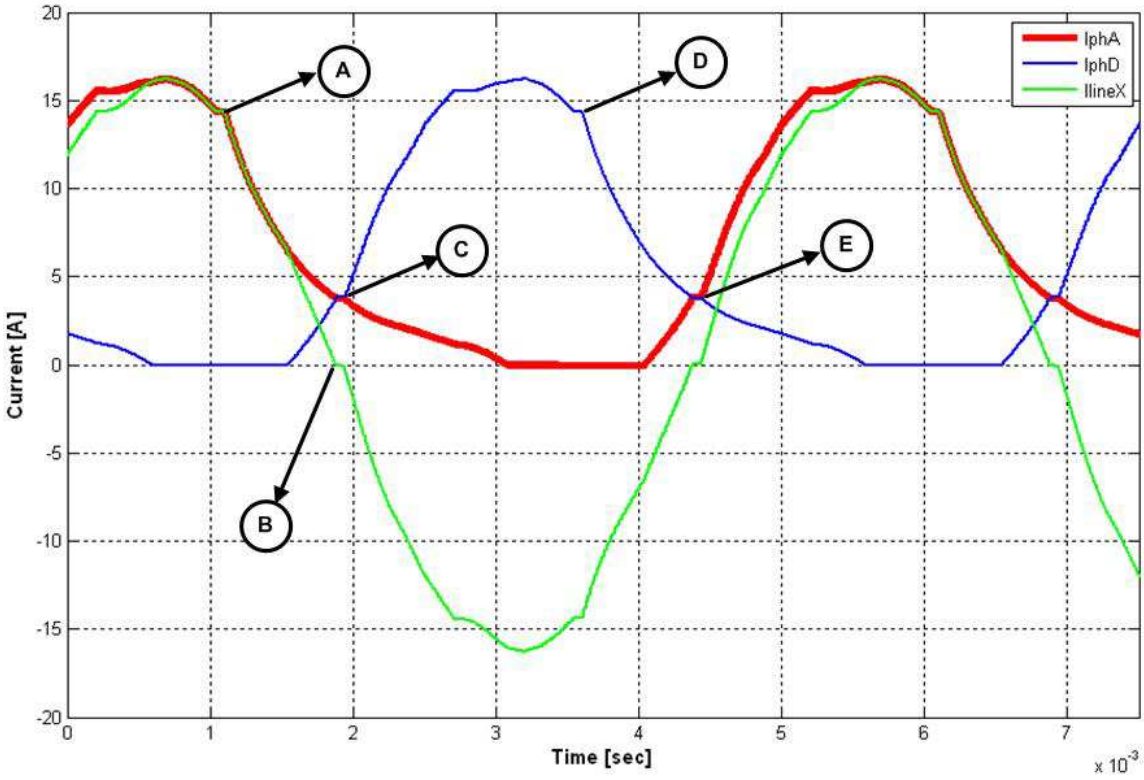

Figure 151 Simulated phase-A current (in red), phase-D current (in blue), line-X current (in green) for the 3-phase bridge circuit driven star connected 6-phase conventional rotor SRM with mutually de-coupled phase windings running at 1200rpm

Once again the filtered phase voltage fails to reach the full dc-link rail voltage in Figure 149. The situation is similar to the current controlled drive and illustrated in Figure 152. In the bottom trace of Figure 152 the potential at point X (Vx) has a triangular characteristic for short periods of time. This triangular characteristic is a result of moving average filtering as the filter does not produce good results with signals which have very quickly changing sharp edges.

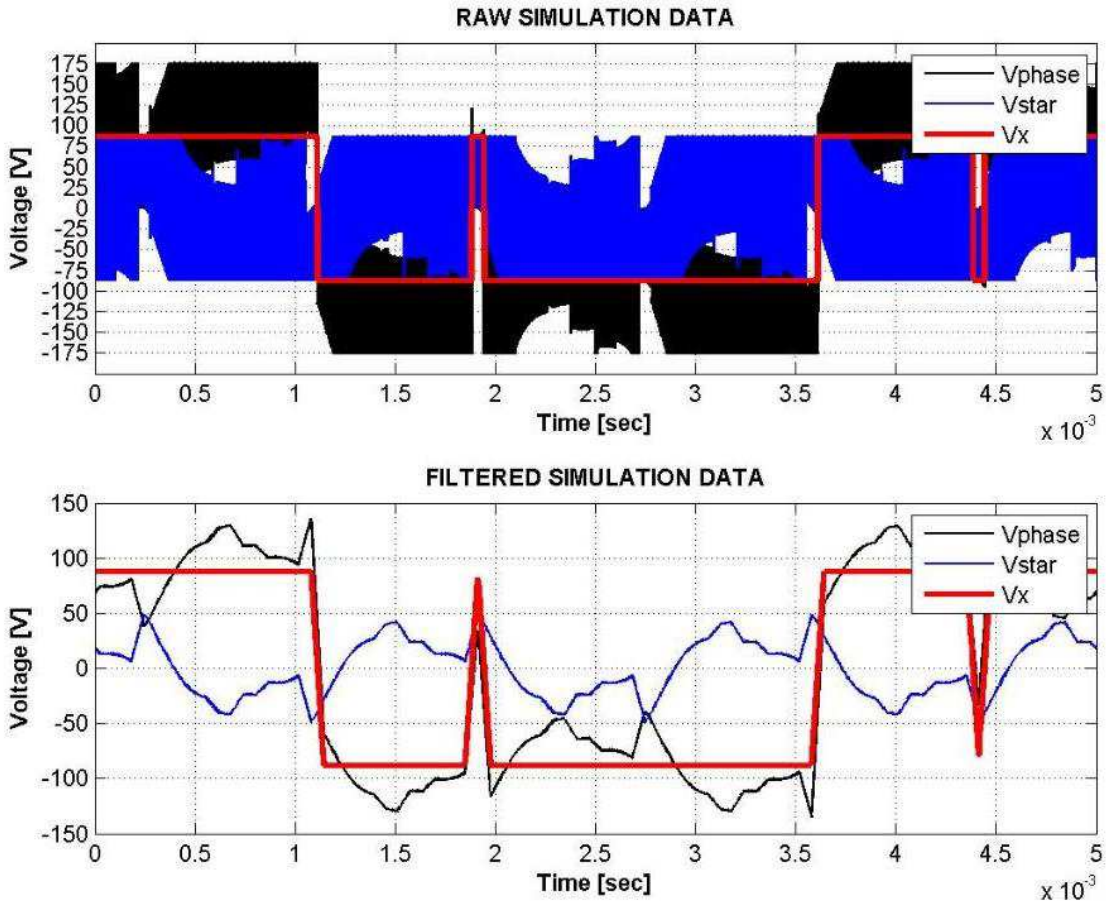

Figure 152 Simulated raw phase, line and star point voltages (top trace) and filtered phase, line and star point voltages (bottom) for the 3-phase bridge circuit driven star connected 6-phase conventional rotor SRM with mutually de-coupled phase windings running at 1200rpm

From Figure 153, there are six distinct periods of star point potential, each corresponding to a phase commutation point. Similar to the current controlled situation, significant changes in the star point potential appear around the phase commutation points.

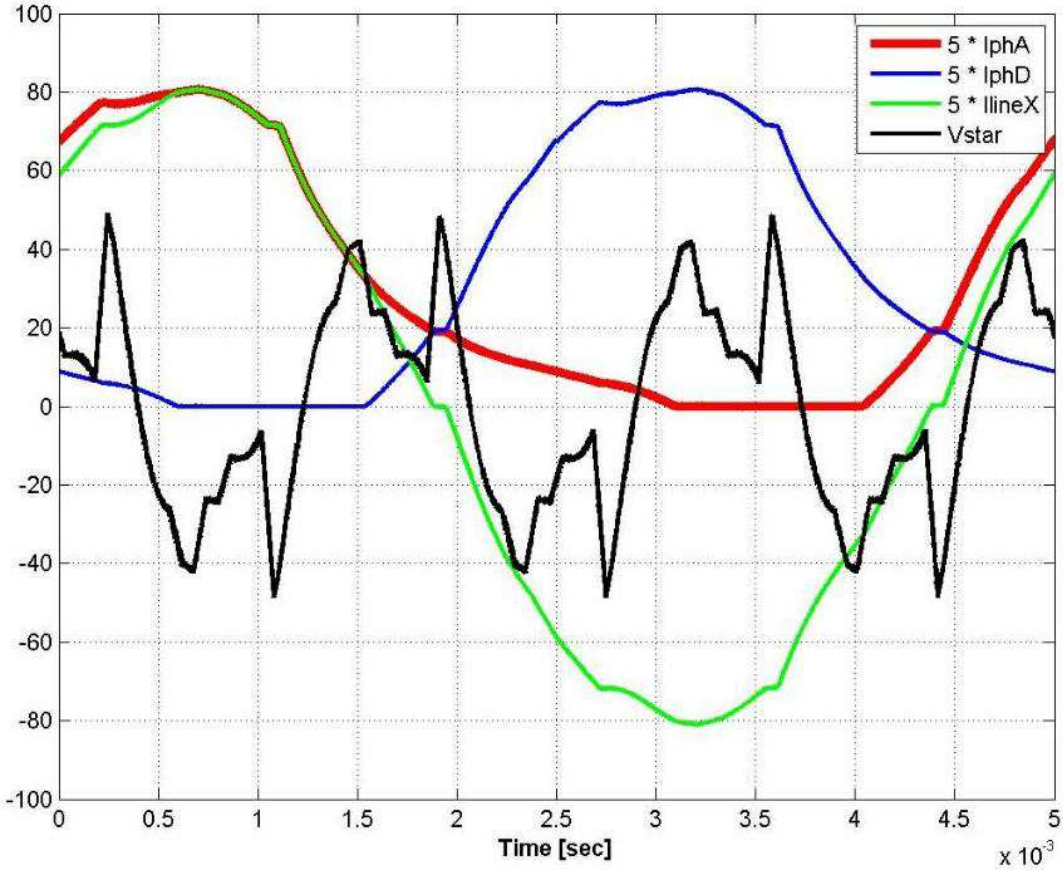

Figure 153 Simulated phase-A current (x5 in red), phase-D current (x5 in blue), line-X current (x5 in green) and star-point potential (in black) for the 3-phase bridge circuit driven star connected 6-phase conventional rotor SRM with mutually de-coupled phase windings running at 1200rpm

From Figure 154, unlike the drive under current control, the (filtered) star point potential varies continuously with the drive under voltage control. Once again the error in the star point current is small compared to the demand current level, which suggests that the simulation is behaving well in controlling the line currents under full voltage control.

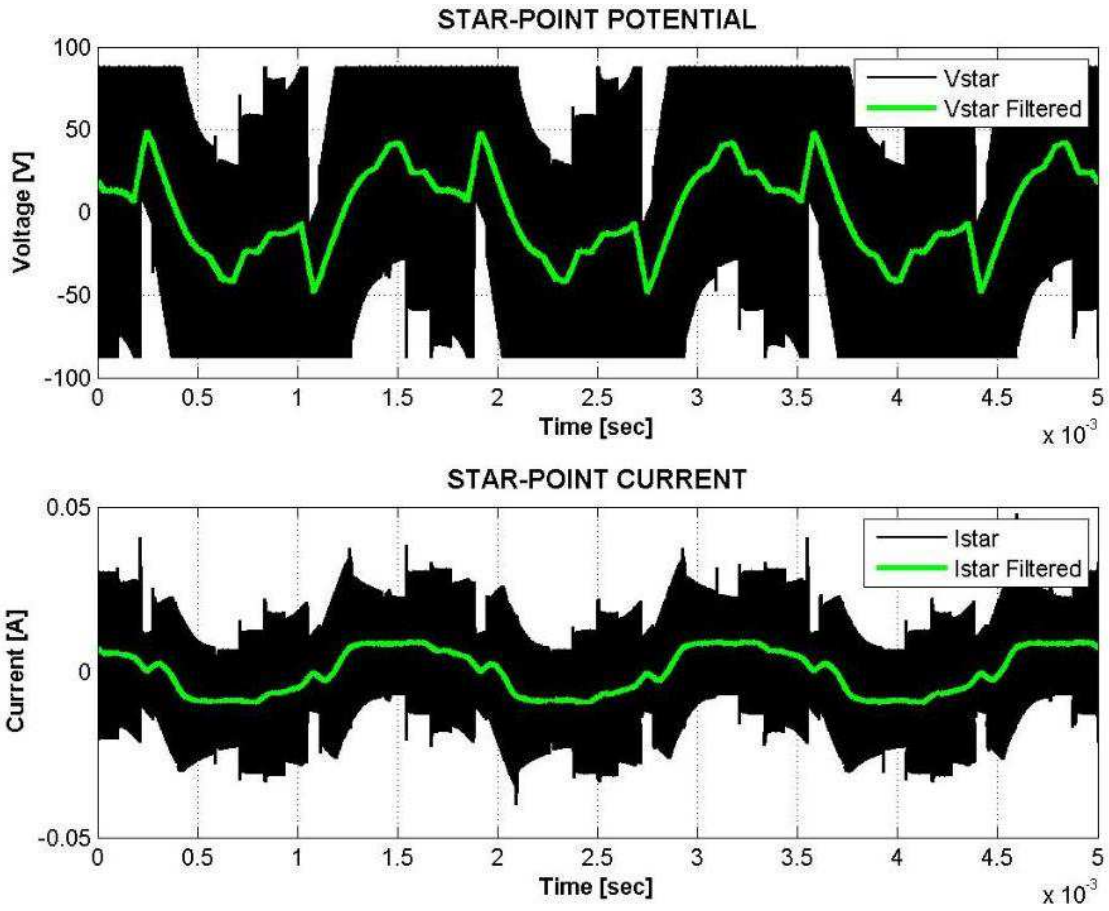

Figure 154 Simulated star-point potential (top trace) and star-point current (bottom trace) for the 3-phase bridge circuit driven star connected 6-phase conventional rotor SRM with mutually de-coupled phase windings running at 1200rpm

Figure 155 depicts the phase and line currents when the drive is under voltage control in the simulation.

Figure 156 suggests that - compared to current controlled drive - a larger proportion of the instantaneous torque per phase is negative. This is also apparent when comparing the torque ripple figure in Table 24 to that in Table 23. This is typical of high speed operation where the peak to peak variation of output torque is compromised for a greater average value.

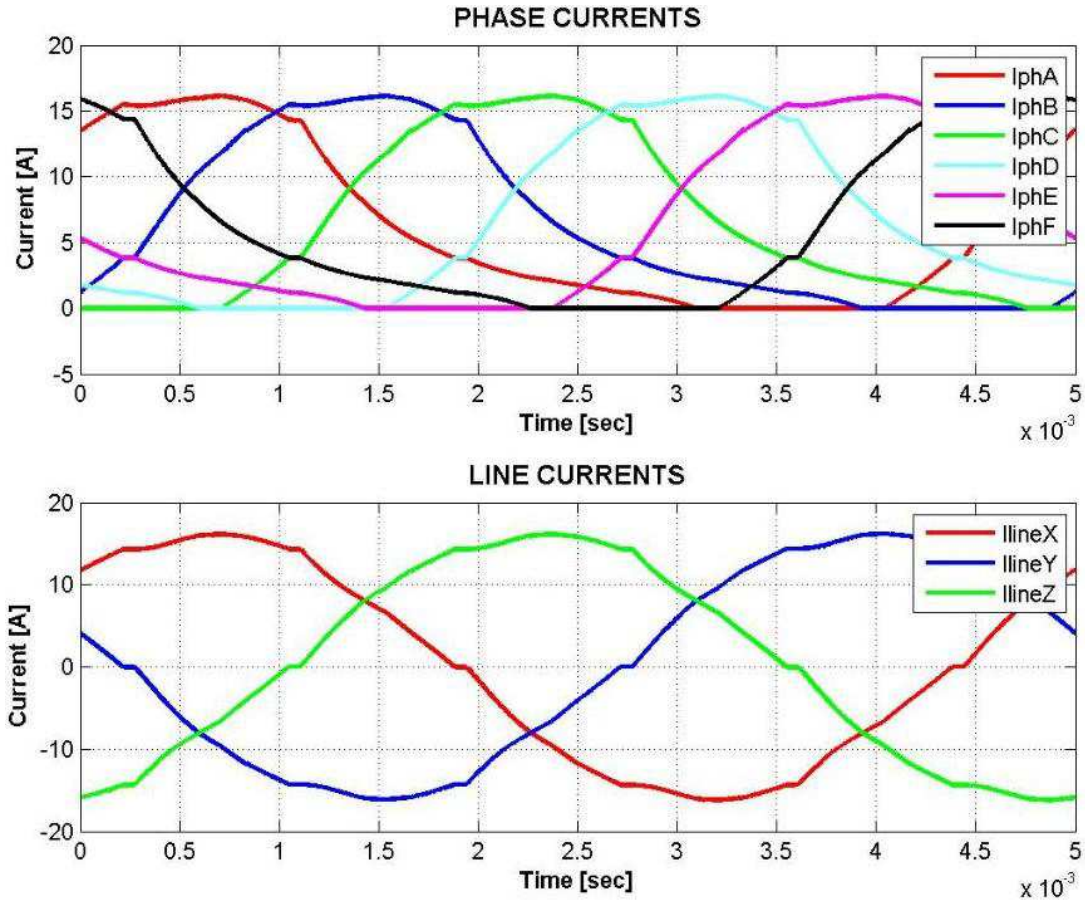

Figure 155 Simulated phase currents (top trace) and line currents (bottom trace) for the 3-phase bridge circuit driven star connected 6-phase conventional rotor SRM with mutually de-coupled phase windings running at 1200rpm

Table 24 summarises some of the simulation input parameters along with the results of some of the performance parameters generated by the simulation for the star connected drive running at 1200rpm under full voltage control.

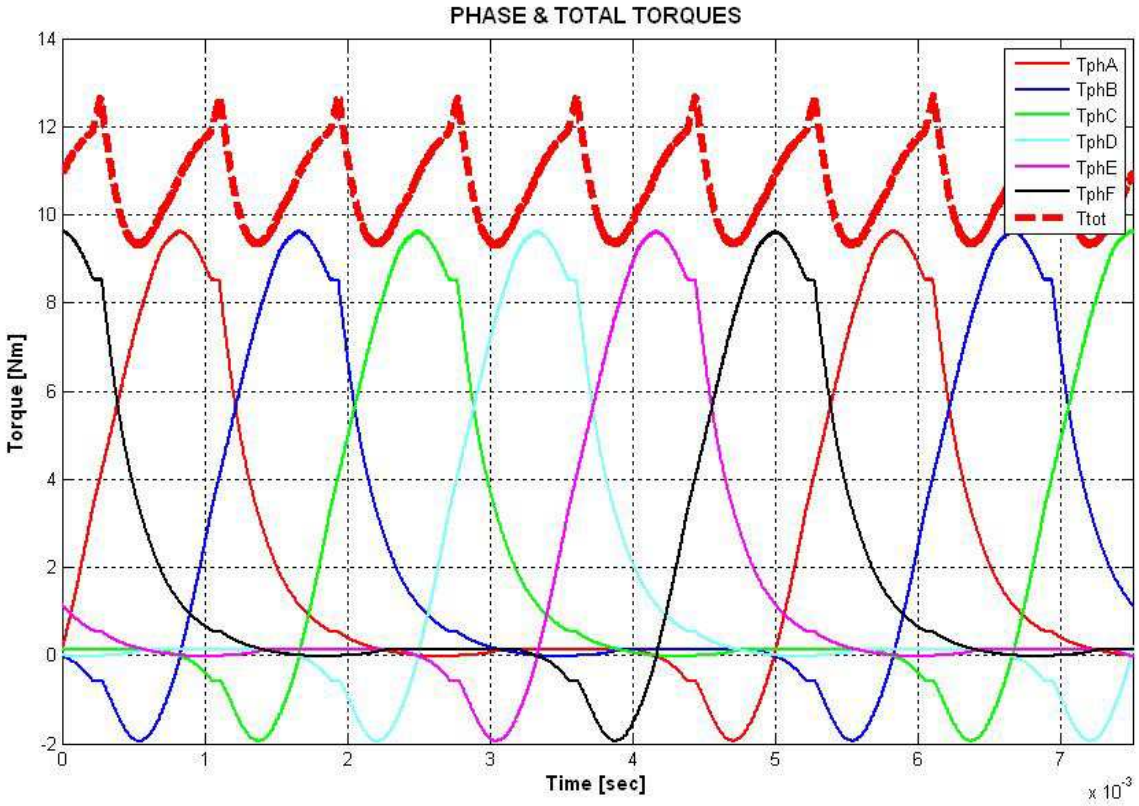

Figure 156 Simulated phase torques and resulting total output torque for the 3-phase bridge circuit driven star connected 6-phase conventional rotor SRM with mutually de-coupled phase windings running at 1200rpm

Table 24 Summary of simulated performance parameters for the 3-phase bridge circuit driven star connected 6-phase conventional rotor SRM with mutually de-coupled phase windings running at 1200rpm

Speed [RPM]	1200	**Swt_VARating_Peak [kVA / kW]**	12.75
Current Demand [A]	30	**Swt_VARating_RMS [kVA / kW]**	5.85
Advance Angle [Deg]	-40	**Dio_VARating_Peak [kVA / kW]**	11.26
Conduction Angle [Deg]	60	**Dio_VARating_RMS [kVA / kW]**	2.46
DC-Link Voltage [V]	175	**Total Peak VA Rating [kVA / kW]**	24.01
Average Output Torque [Nm]	10.6	**Total RMS VA Rating [kVA / kW]**	8.31
Average Output Power [Nm]	1336.8		
Maximum Output Torque [Nm]	12.7		
Minimum Output Torque [Nm]	9.2		
Output Torque Ripple - Pk2Pk [%]	27.06		
RMS Phase Current [A]	8.66		
Peak Phase Current [A]	16.23		
Total Machine Copper Losses [W]	204.6		
Total Inverter Losses [W]	60.5		
Total Phase Diode Losses [W]	21		
Drive Efficiency [%]	82.4		

From Table 24, compared to the drive under current control, the inverter VA rating is significantly reduced when the drive is under full voltage control. This is due to the reduced currents flowing in the system, which also results in reduced total machine copper losses. The drive efficiency is significantly improved. This is typical of SR drives, where the output power is kept almost constant even though the phase currents and the total average output torque are reduced with increasing operating speeds. As mentioned earlier, compared to the star connected drive under current control, the torque ripple is increased, which is due to the peaky nature of individual phase torque waveforms (see Figure 156). Nevertheless, the torque ripple is still relatively low at approximately 26.7%.

9.2.2 Mutually De-Coupled Delta Connected Line Current Controlled Six-Phase Drive

The control of the 6-phase machine can also be achieved when the phase connection is changed to a delta configuration. Similar to the simulation where the phases were star-connected, the control was based on the three line currents (IlineX, IlineY and IlineZ in Figure 157). Separate PID and PWM controllers were needed for controlling each line current. Unlike the star-connected drive where module currents must sum up to zero at the star point, with the delta configuration module voltages must sum up to zero (once again a module is formed by two back-to-back connected phases e.g. PhA and PhD in Figure 157). Like the star-connected drive two examples are given; one for low, and the other for high speed operation. Some of the performance results obtained from the simulations are tabulated inTable 25 and Table 26 for low speed and high speed operation, respectively.

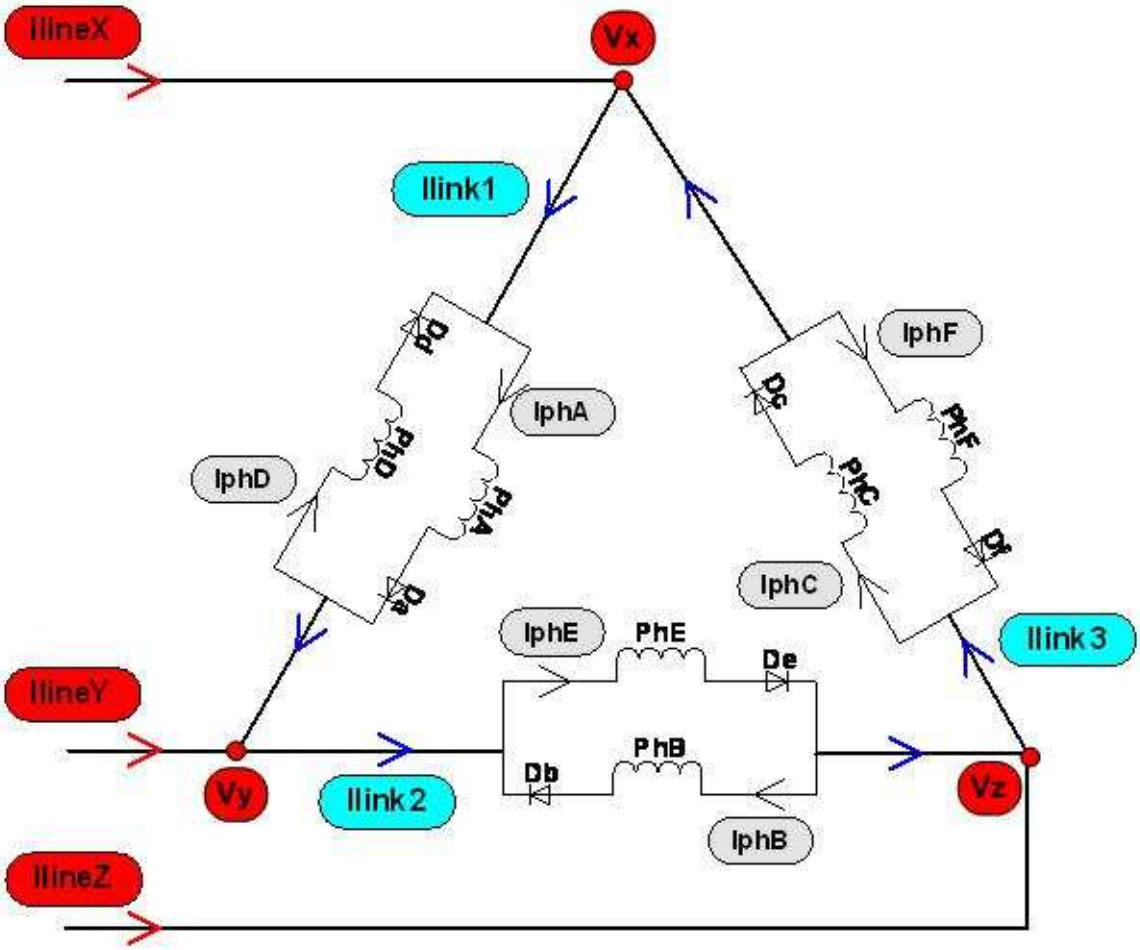

Figure 157 Graphical illustration of the line, link and phase currents of the 6-phase delta connected machine with back-to-back connected phase windings driven from 3-phase full bridge circuit

Line currents (IlineX, IlineY, and IlineZ), phase currents (IphA, IphB, IphC, IphD, IphE, and IphF) and link currents (Ilink1, Ilikn2, and Ilink3) in Figure 158 to Figure 170 are all illustrated in Figure 157. In order to clearly demonstrate the mode of operation for the controller, Figure 159 and Figure 166 are presented for the drive under current and full voltage control, respectively.

9.2.2.1 Drive under Current Control

The same simulation conditions explained in section 2.1.1 of this chapter are used here. The results from the dynamic simulation are depicted from Figure 158 to Figure 164. Clearly visible in Figure 157, unlike the star-connected drive, the line currents are a result of two link currents. This can be formulated as follows:

$$IlineX = Ilink1 - Ilink3$$
$$IlineY = Ilink2 - Ilink1$$
$$IlineZ = Ilink3 - Ilink2$$

Equation 34

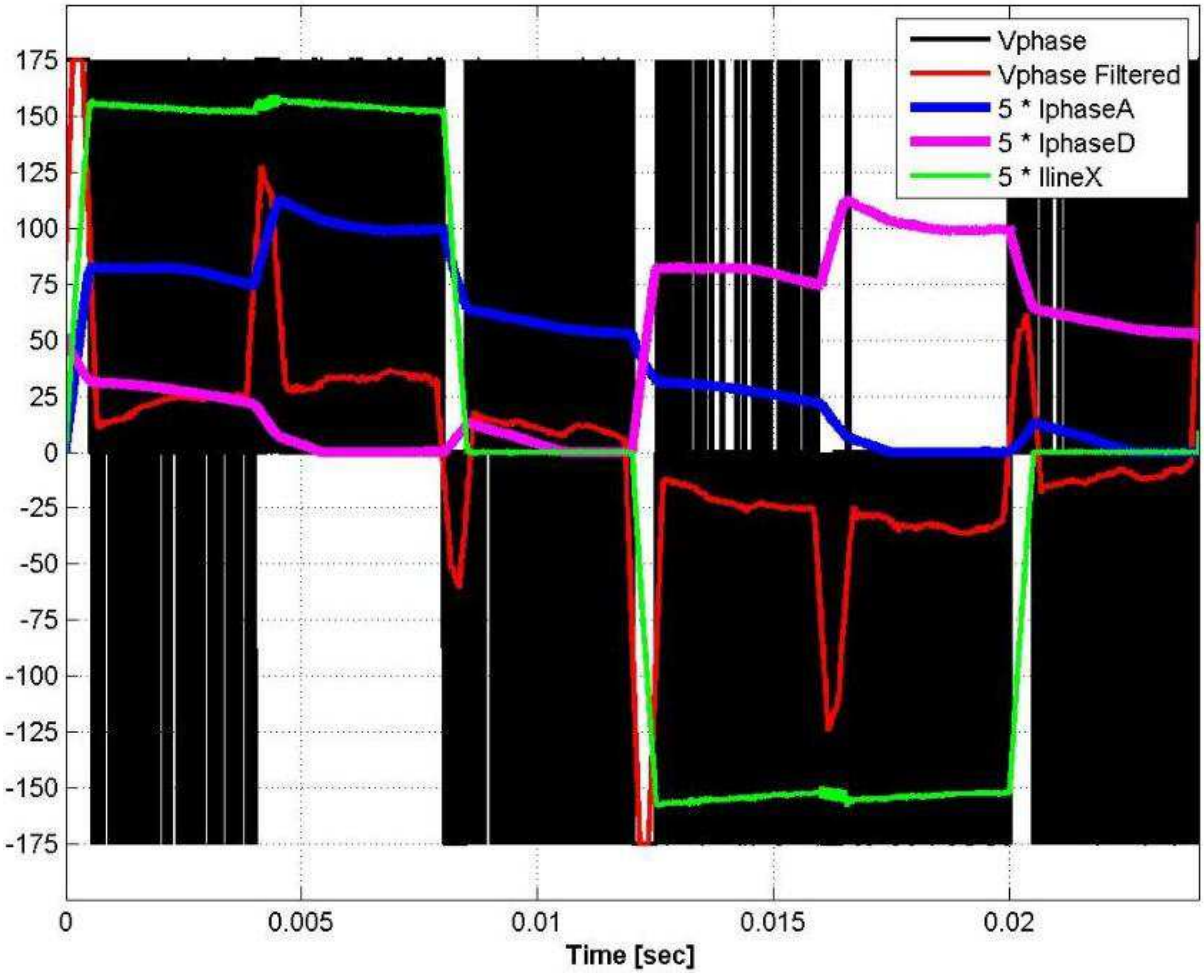

Figure 158 Simulated phase voltage (in black), phase-A current (x5 in blue), phase-D current (x5 in magenta), line-X current (x5 in green) and filtered phase voltage (in red) for the 3-phase bridge circuit driven delta connected 6-phase conventional rotor SRM with mutually de-coupled phase windings running at 250rpm

Unlike the machine connected in star configuration, it is clear from Figure 158 that the filtered phase voltage is now able to reach the full dc-link voltage as the controller can control the two potentials at each end of a phase connection (e.g. Vx and Vy through IlineX and IlineY in Figure 157).

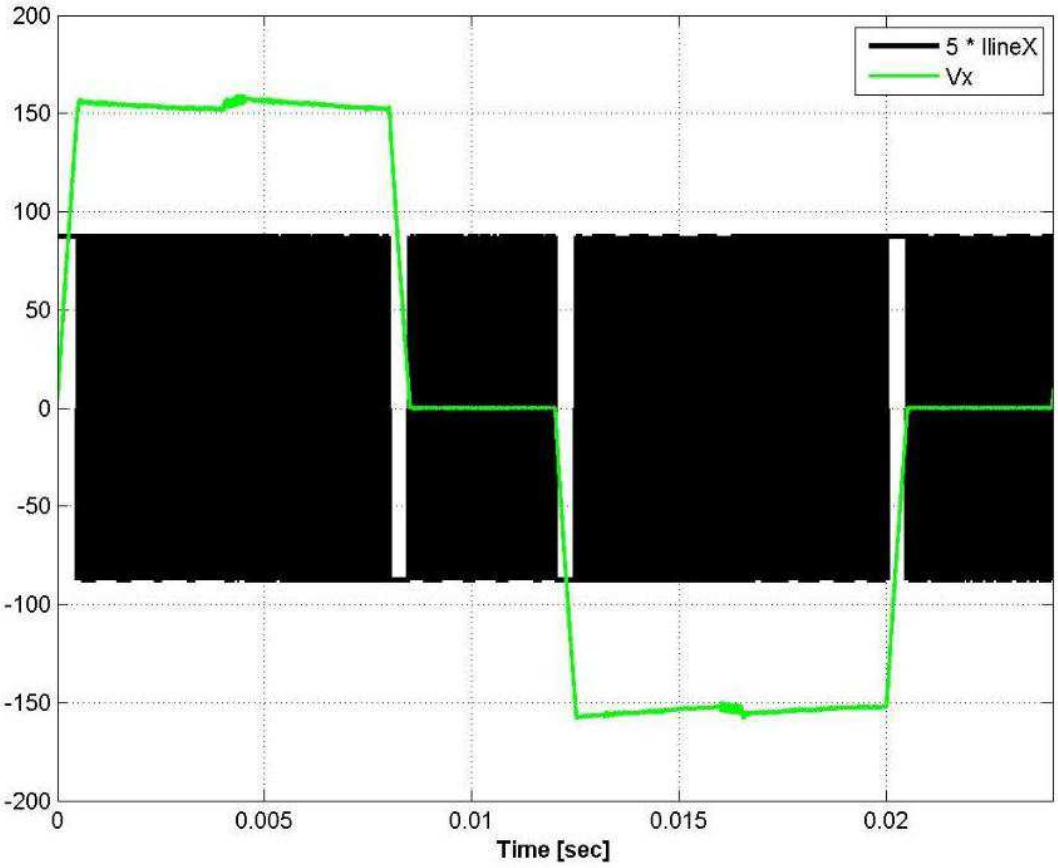

Figure 159 Simulated line potential (in black) and current (x5 in green) for the 3-phase bridge circuit driven delta connected 6-phase conventional rotor SRM with mutually de-coupled phase windings running at 250rpm

In helping to explain Figure 158, Figure 160 and Figure 161 have been generated. In Figure 158, until the line current (IlineX) reaches the demanded level, the full dc-link voltage is available across the phase windings (Vphase Filtered). Once the line current reaches the demand, the controller aims to keep it at this level. As a result, the phase currents (phase-A and phase-D) remain approximately the same, i.e. the current circulates around the parallel connected phases and the phase diodes. The slight drop in both phase currents is due to the resistive voltage drop across each phase. Once phase-B is turned on (around 0.004sec in Figure 158 and Figure 161), the controller keeps phase-C off by applying positive potentials at point X and Z (Figure 160) and negative potential at points Y, which result in positive voltage across phase-A. Consequently, current in phase-A rises again until the current flowing in line-Y reaches its demand level. Comparing Figure 158 to Figure 139 reveals that the phase current tail-off period is significantly longer than with the star connected drive. From Figure 161 and Figure 162, it is apparent that the link current has a six step characteristic. Compared to the star-connected drive, where the demand current was set to the same value, the peak phase current is significantly lower in

the delta-connected drive. This is due to the fact that two phase currents formed one line current in the star-connected drive whereas four phase currents are needed in the delta-connected drive.

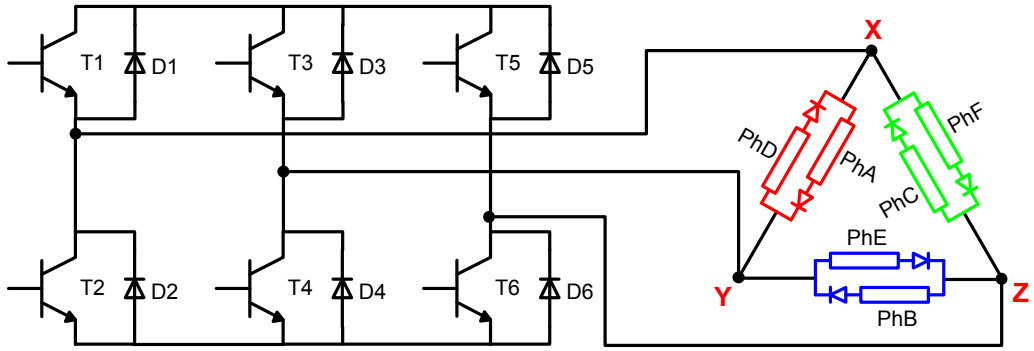

Figure 160 Delta-connected six-phase machine driven from 3-phase full bridge inverter

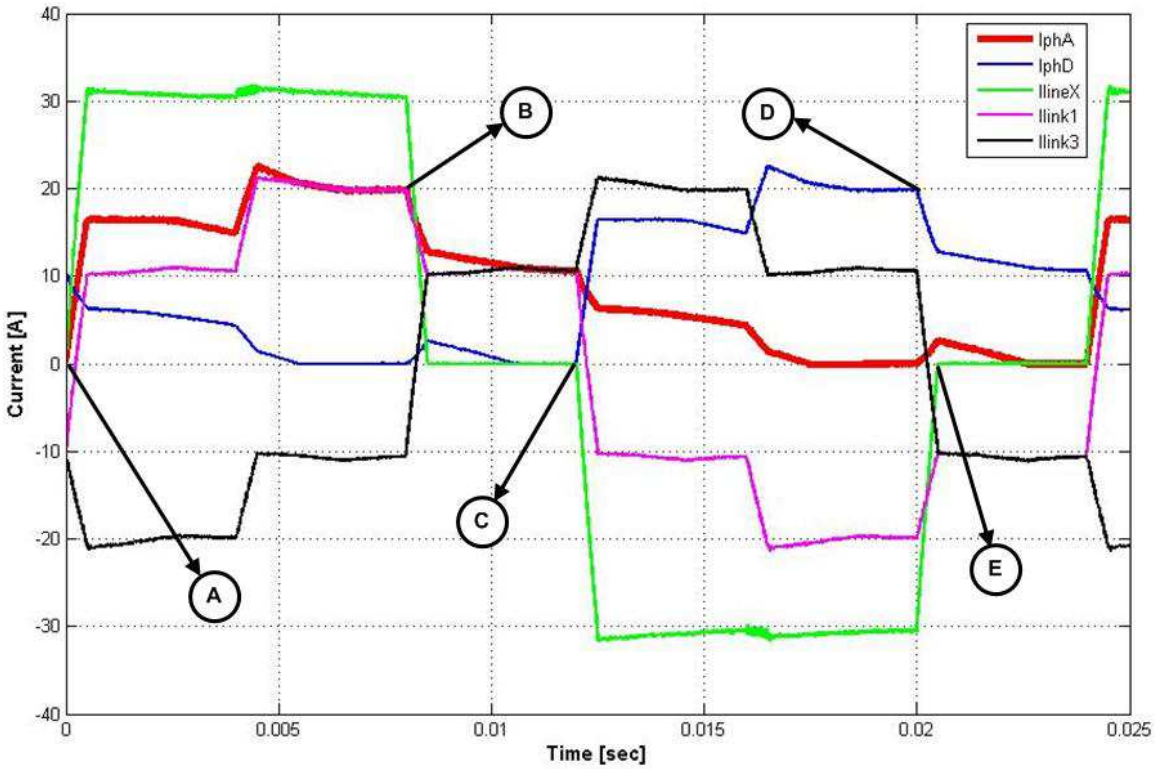

Figure 161 Simulated phase-A current (in red), phase-D current (in blue), line-X current (in green), link-1 current (in magenta) and link-3 current (in black) for the 3-phase bridge circuit driven delta connected 6-phase conventional rotor SRM with mutually de-coupled phase windings running at 250rpm

The operating states in Figure 161 are summarised below with respect to the circuit diagram in Figure 160:

Point A : Phase-A is turned on.

Point B : Phase-A is turned off.

Point C : Phase-D is turned on.

Point D : Phase-D is turned off.

Point E : Line current (IlineX) falls to zero. Current in link-1 (Ilink-1) equals that in link-3 (Ilink-3).

Between points D and E, phase-A current rises even though it is in its off period. This is due to the negative voltage applied across the windings of phase-D appearing as positive voltage across the windings of phase-A. The series connected phase diode becomes forward biased and phase-A starts conducting current. This lasts until the line current falls to zero. The current in phase-A gradually falls back to zero before the start of the next energisation cycle (point A in Figure 161).

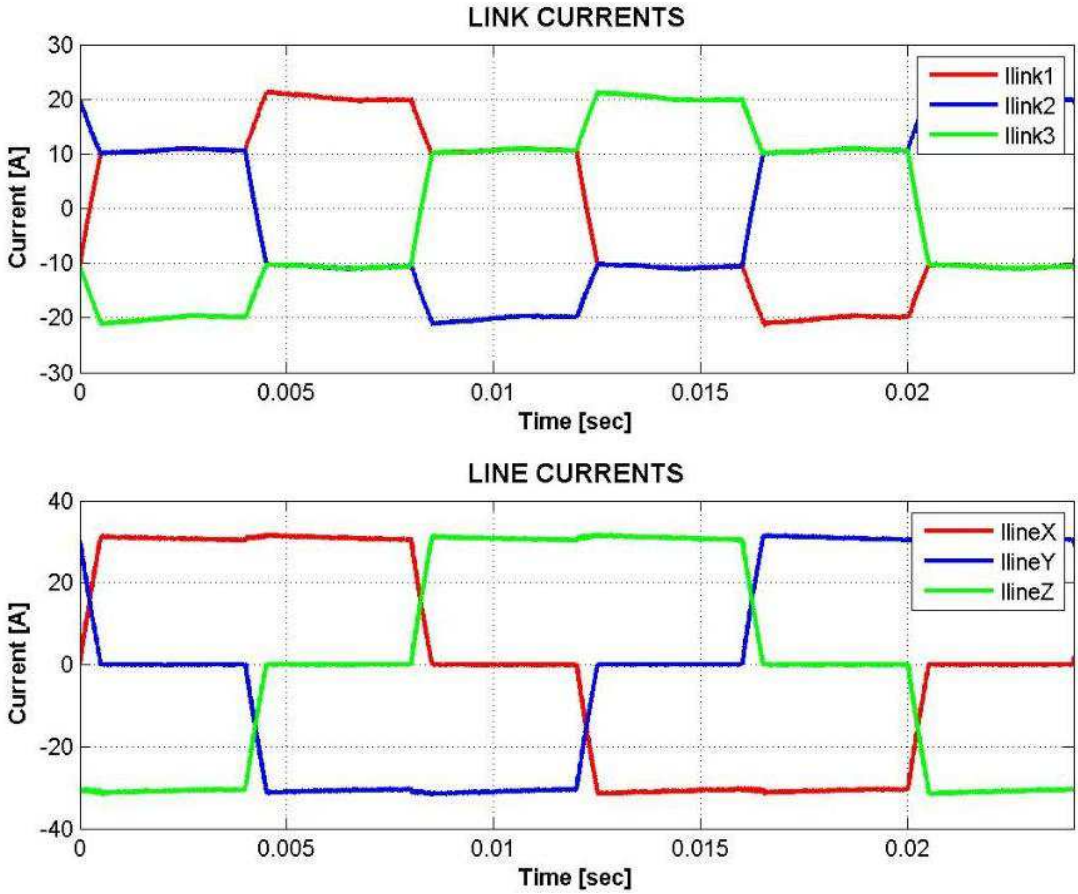

Figure 162 Simulated link currents (top trace) and line currents (bottom trace) for the 3-phase bridge circuit driven delta connected 6-phase conventional rotor SRM with mutually de-coupled phase windings running at 250rpm

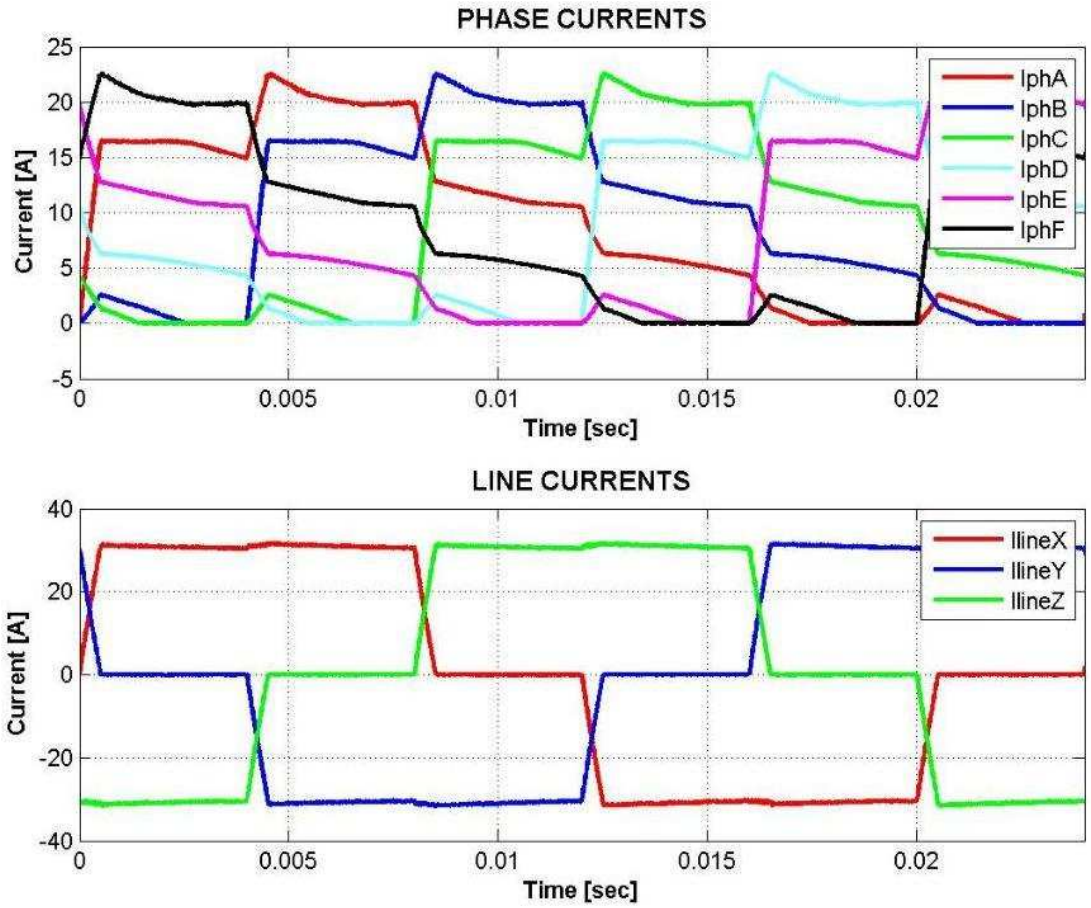

Figure 163 Simulated phase currents (top trace) and line currents (bottom trace) for the 3-phase bridge circuit driven delta connected 6-phase conventional rotor SRM with mutually de-coupled phase windings running at 250rpm

As mentioned earlier, with the delta-connected drive the phases conduct current for long periods although the actual energisation period for each phase is relatively low (i.e. 120^{o}). Having long periods of current in each phase results in negative torque generated by each phase as there is still current flowing in the phase windings even when the rate of change phase inductance changes its sign, i.e. the phase inductance starts to reduce once the rotor passes the aligned position. However, the generated negative torque is small, as the phase current has fallen to a small value by the time the rotor passes the aligned rotor position. As each phase conducts current for longer periods there is significant overlap between phase output torque waveforms. This results in long periods of flat total output torque that is visible in Figure 164.

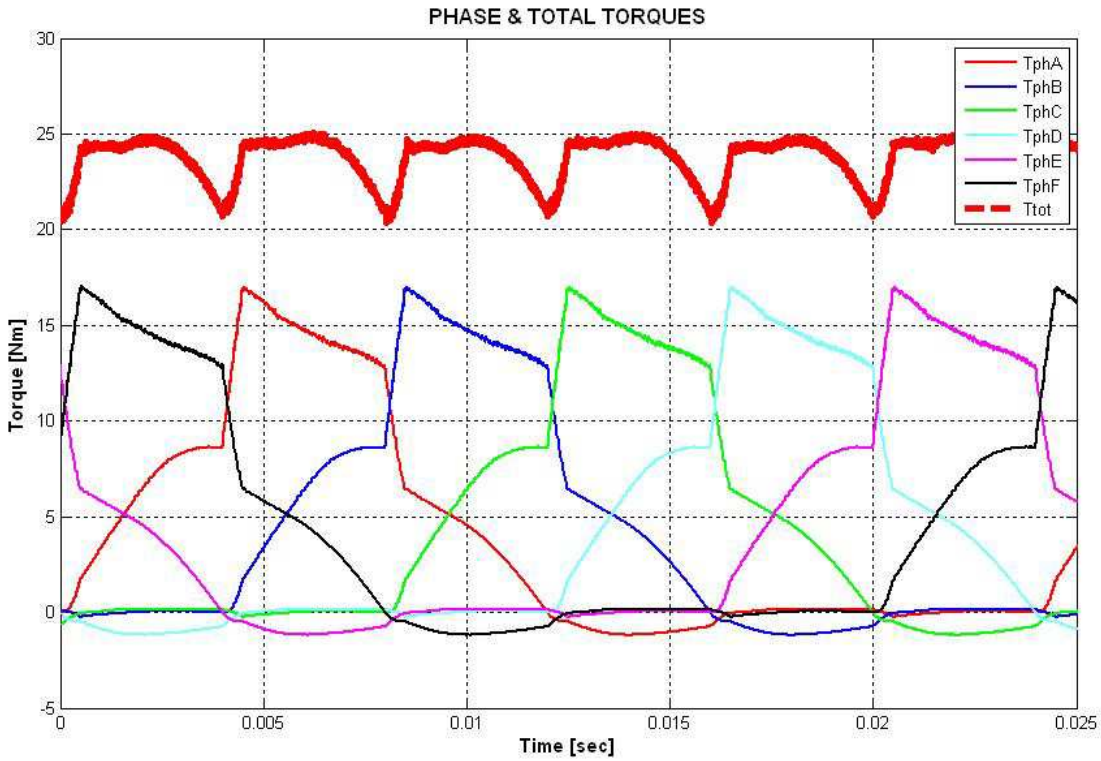

Figure 164 Simulated phase torques and resulting total output torque for the 3-phase bridge circuit driven delta connected 6-phase conventional rotor SRM with mutually de-coupled phase windings running at 250rpm

Although the simulations for the star and delta configured drives were run at the same speed, when both were under current control they resulted in different average output torques. This makes it hard to compare the output torque ripple values and draw a conclusion. Although both the star and delta connected drives have similar amount of line currents, i.e. the current flowing through devices is similar and the dc-link voltage is kept the same, the inverter VA rating of the delta-connected drive is significantly higher. This is due to the fact that lower levels of currents circulate in the phases and consequently the output torque is reduced. As both drives run at the same speed the reduced output power results in increased inverter VA. Comparison of the inverter ratings of the star and delta connected drives will be a topic of the next chapter On the other hand, the voltage that can be applied to each phase of the delta connected drive is higher, so the peak speed of the machine can be higher with the delta connected drive. The efficiency of the delta-connected drive is slightly higher than the star-connected drive. This is due to the reduced ohmic losses as a result of lower current levels in the delta-connected drive.

Table 25 Summary of simulated performance parameters for the 3-phase bridge circuit driven delta connected 6-phase conventional rotor SRM with mutually de-coupled phase windings running at 250rpm

Speed [RPM]	250	**Swt_VARating_Peak [kVA / kW]**	53.81
Current Demand [A]	30	**Swt_VARating_RMS [kVA / kW]**	22.97
Advance Angle [Deg]	0	**Dio_VARating_Peak [kVA / kW]**	53.74
Conduction Angle [Deg]	60	**Dio_VARating_RMS [kVA / kW]**	18.88
DC-Link Voltage [V]	175	**Total Peak VA Rating [kVA / kW]**	107.55
Average Output Torque [Nm]	23.7	**Total RMS VA Rating [kVA / kW]**	41.85
Average Output Power [Nm]	621.7		
Maximum Output Torque [Nm]	25.3		
Minimum Output Torque [Nm]	20.4		
Output Torque Ripple - Pk2Pk [%]	19.53		
RMS Phase Current [A]	11.79		
Peak Phase Current [A]	22.66		
Total Machine Copper Losses [W]	379		
Total Inverter Losses [W]	242.6		
Total Phase Diode Losses [W]	31.4		
Drive Efficiency [%]	48.8		

9.2.2.2 Drive under Voltage Control

In order to achieve an operation that is under full voltage control, the speed of the motor has been increased to 1500rpm. This is 300rpm faster than the speed setting for the simulation with the star configuration. This is due to the fact that there is more voltage available across the phase windings with a delta configuration than a star configuration. All other simulation inputs are kept the same as those used for the high speed simulation of the star configuration. Similar to operation in the current control mode, the phase voltage is able to reach the full dc-link voltage with voltage control. Figure 166 confirms that the drive is under full voltage control.

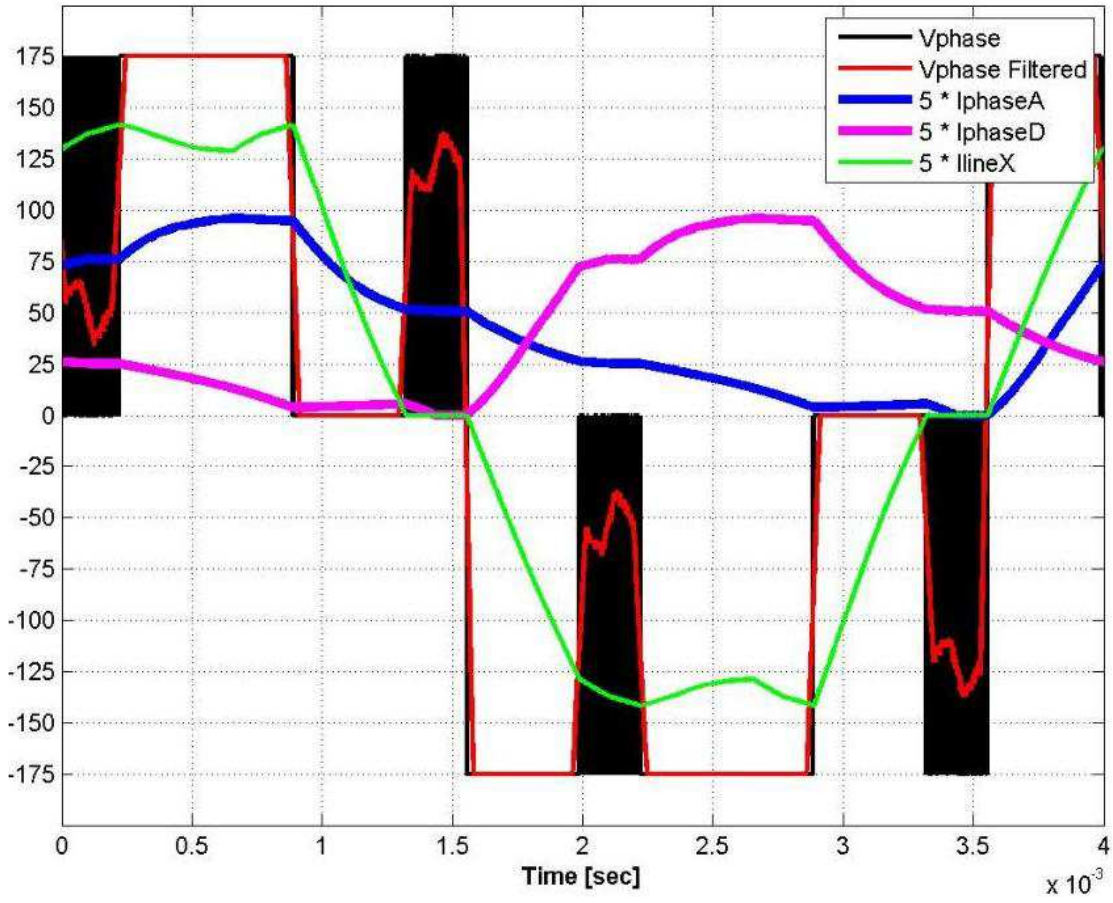

Figure 165 Simulated phase voltage (in black), phase-A current (x5 in blue), phase-D current (x5 in magenta), line-X current (x5 in green) and filtered phase voltage (in red) for the 3-phase bridge circuit driven delta connected 6-phase conventional rotor SRM with mutually de-coupled phase windings running at 1500rpm

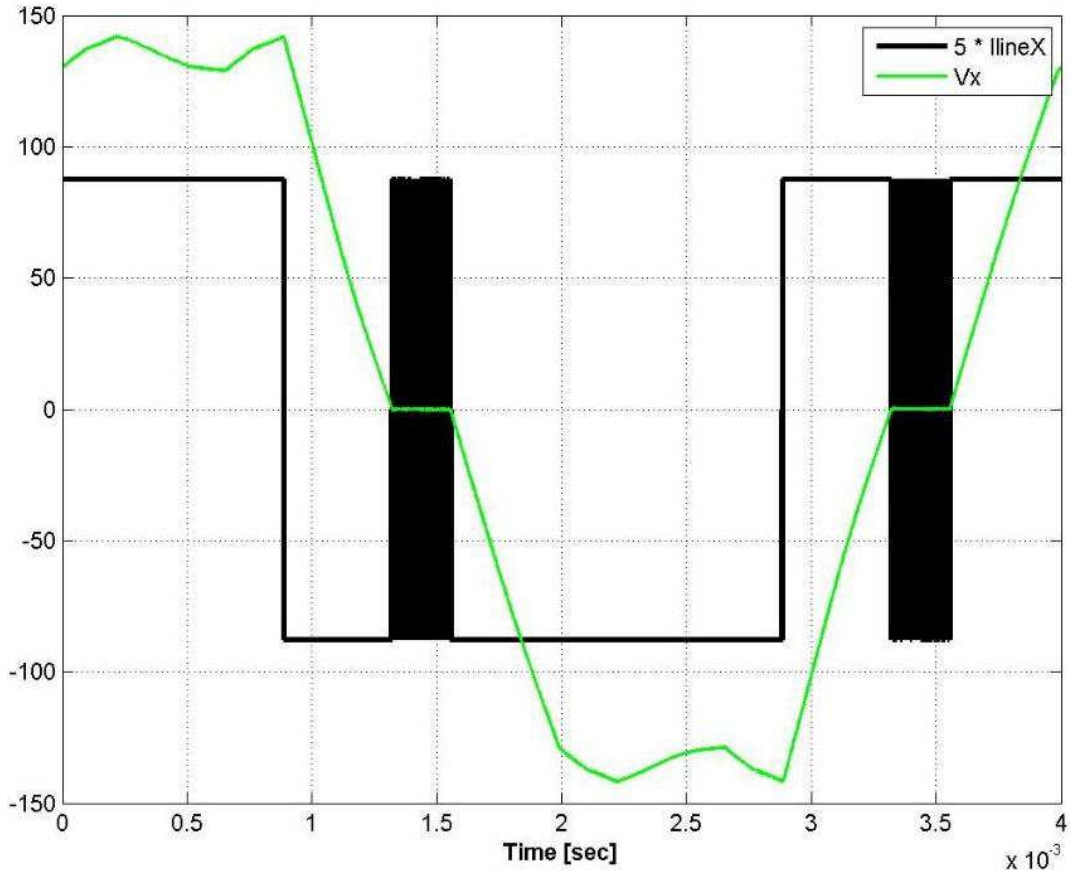

Figure 166 Simulated line potential (in black) and current (x5 in green) for the 3-phase bridge circuit driven delta connected 6-phase conventional rotor SRM with mutually de-coupled phase windings running at 1500rpm

The operating states in Figure 167 are summarised below:

Point A : Phase-A is turned off.

Point B : Phase D is turned on.

Point C : Phase D is turned off.

Point D : Line current falls to zero. Current in link-1 current equals that in link-3

Point E : Phase A is turned on.

Similar to the drive under current control, the two-stage rise in the phase currents is still visible in Figure 167. However, the rate of change of current is slower in the second stage although the same amount of voltage is available across the phase windings. This is believed to be due to the rapid increase in phase inductance as the rotor position approaches alignment.

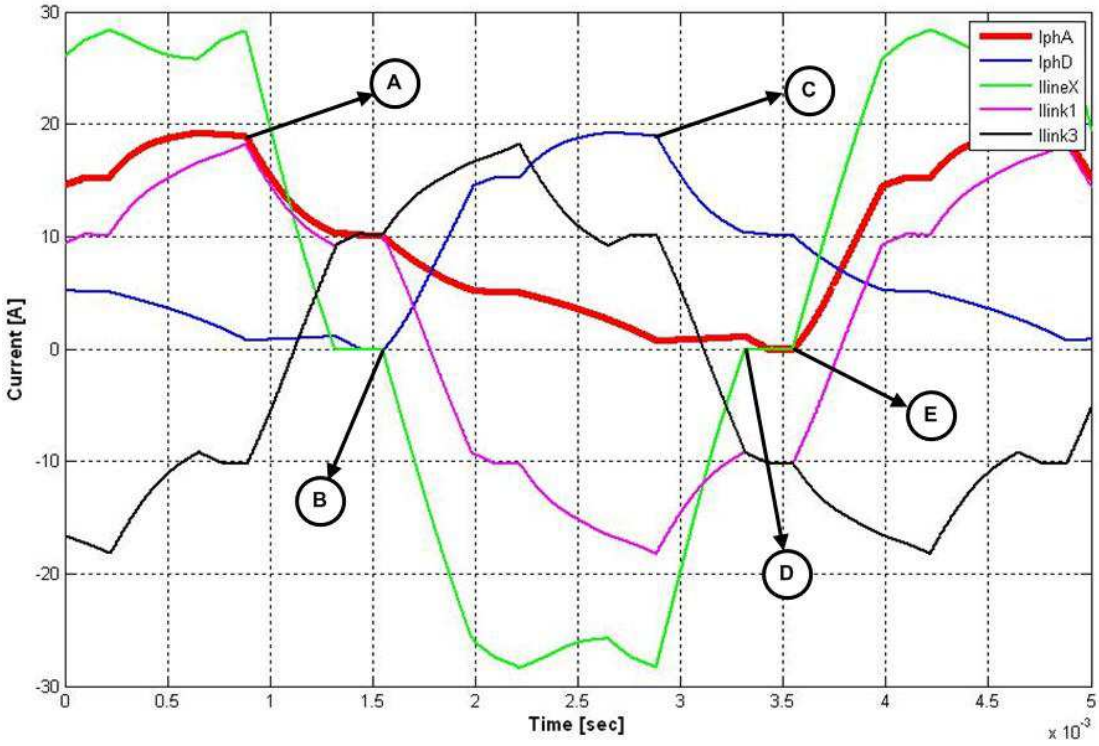

Figure 167 Simulated phase-A current (in red), phase-D current (in blue), line-X current (in green), link-1 current (in magenta) and link-3 current (in black) for the 3-phase bridge circuit driven delta connected 6-phase conventional rotor SRM running at 1500rpm

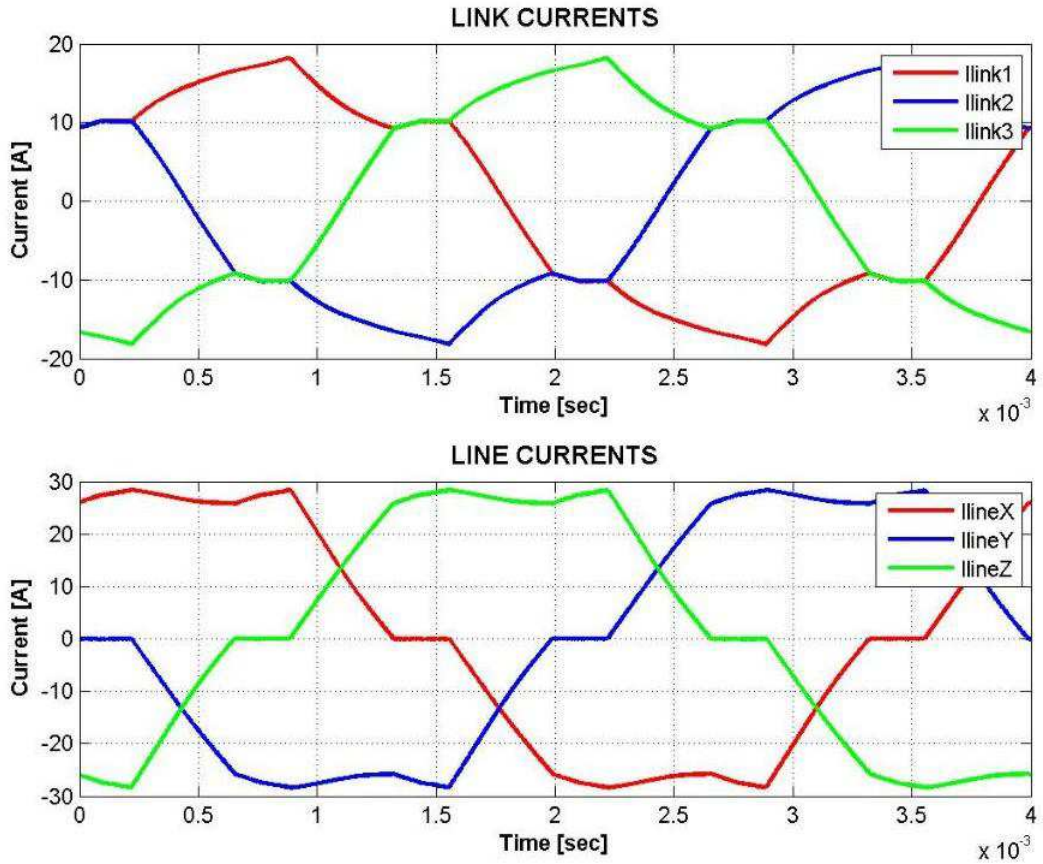

Figure 168 Simulated link currents and line currents for the 3-phase bridge circuit driven delta connected 6-phase conventional rotor SRM running at 1500rpm

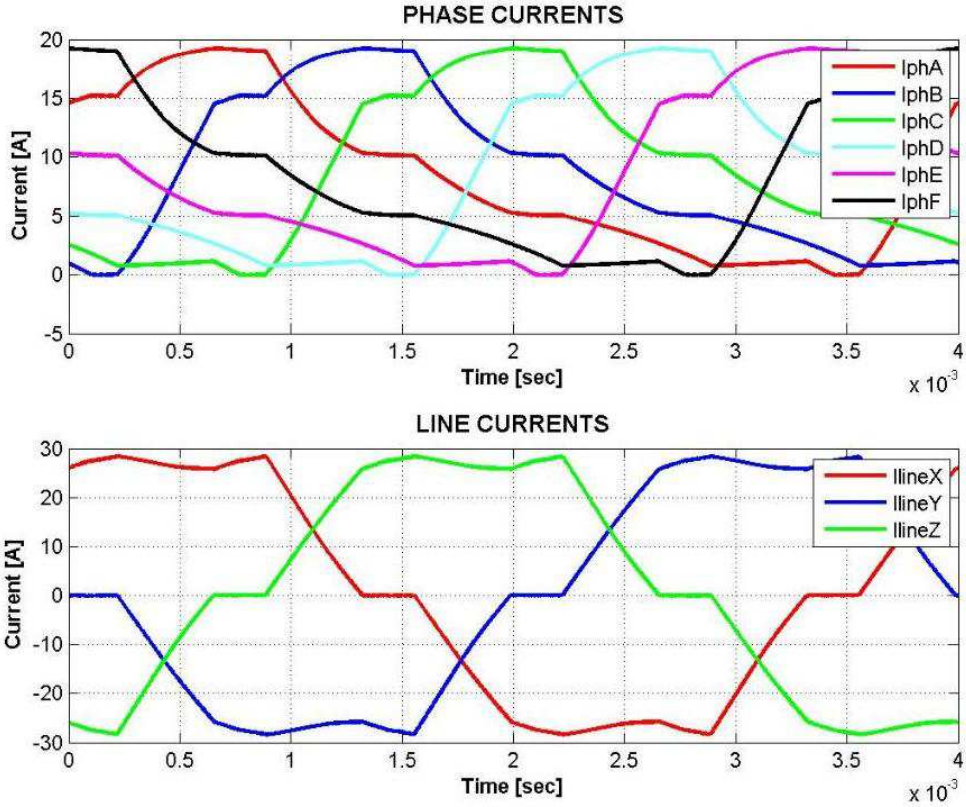

Figure 169 Simulated phase currents (top trace) and line currents (bottom trace) for the 3-phase bridge circuit driven delta connected 6-phase conventional rotor SRM running at 1500rpm

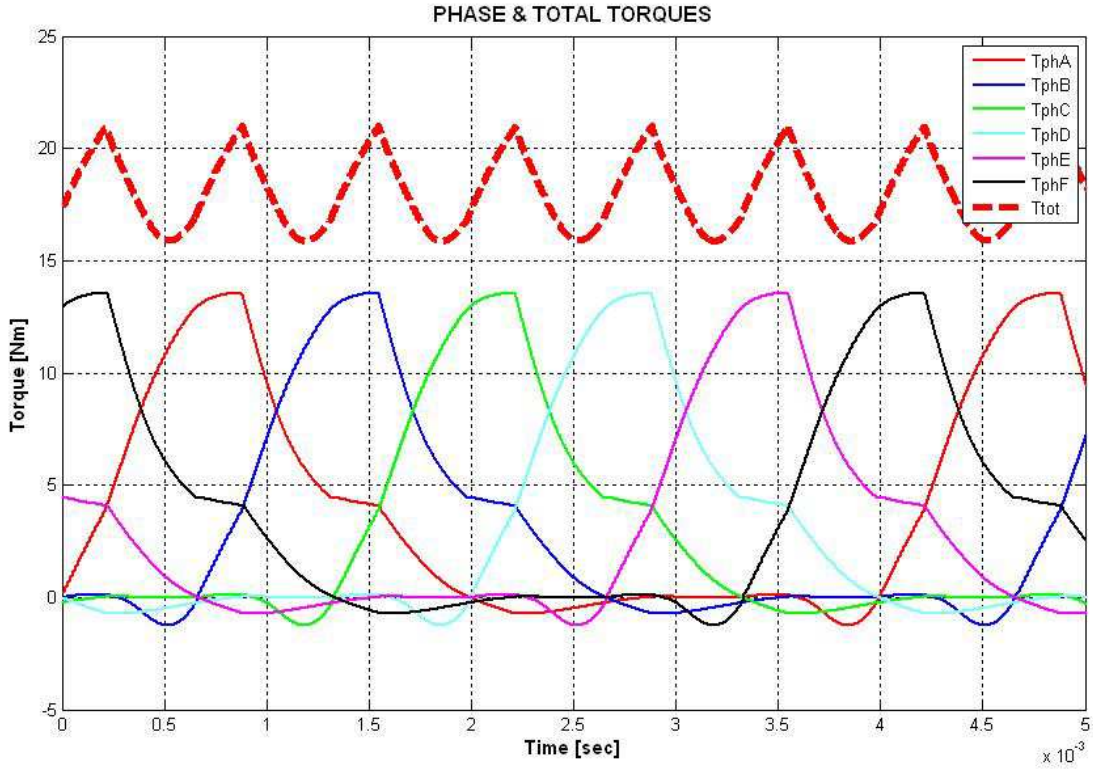

Figure 170 Simulated phase torques and resulting total output torque for the 3-phase bridge circuit driven delta connected 6-phase conventional rotor SRM running at 1500rpm

In Figure 165, Figure 167 and Figure 169 it is interesting to note that the phase current is almost continuous. This is believed to be a result of the anti-parallel connection of phase windings. Negative voltage applied across one of the phases of a module appears as positive across the anti-parallel phase in the same module. This results in the off-phase in a module conducting current even out of its conduction period. Moreover, compared to low speed operation, at high speed there is even less time to de-flux a phase completely before the next energisation cycle. At point C in Figure 167, before the phase-A current completely falls to zero the anti-parallel connected phase (phase-D in this case) is turned off and negative voltage appears across this phase. Negative voltage across phase-D appears as positive across phase-A and the phase diode connected in series with the phase windings becomes forward biased. Consequently at point C in Figure 167, the current in phase-A starts rising again. The current in phase-A eventually falls to zero once the line current is zero and (in simulation) the current decays due to resistive voltage drops across the windings of phase-A and phase-D.

Table 26 Summary of simulated performance parameters for the 3-phase bridge circuit driven delta connected 6-phase conventional rotor SRM with mutually de-coupled phase windings running at 1500rpm

Speed [RPM]	1500	**Swt_VARating_Peak [kVA / kW]**	10.54
Current Demand [A]	30	**Swt_VARating_RMS [kVA / kW]**	5.12
Advance Angle [Deg]	-40	**Dio_VARating_Peak [kVA / kW]**	10.54
Conduction Angle [Deg]	60	**Dio_VARating_RMS [kVA / kW]**	1.93
DC-Link Voltage [V]	175	**Total Peak VA Rating [kVA / kW]**	21.08
Average Output Torque [Nm]	18	**Total RMS VA Rating [kVA / kW]**	7.05
Average Output Power [W]	2826.2		
Maximum Output Torque [Nm]	21		
Minimum Output Torque [Nm]	15.9		
Output Torque Ripple - Pk2Pk [%]	24.29		
RMS Phase Current [A]	10.63		
Peak Phase Current [A]	19.2		
Total Machine Copper Losses [W]	307.8		
Total Inverter Losses [W]	130.2		
Total Phase Diode Losses [W]	30.1		
Drive Efficiency [%]	85.8		

In simulations of both the star and delta connected drives presented in the preceding sections, the phase currents conduct current even when they are not in their respective conduction periods. This is similar to what was seen with the 2-phase machine driven from the h-bridge inverter. The duration of time a phase is conducting current (even if it is not in its conduction period) seems to be longer when the machine is in delta configuration. The star connected drive suffers from higher machine copper losses compared to the delta connected drive when under current control. This is simply because of the increased phase currents in the star connected configuration even when the conduction period and the line current demand are the same as those of the delta connected drive. This can be related to the fact that the phases forming a module in the star connected drive also make up the line current, whereas two modules make up a line current in the delta configuration.

9.3 DYNAMIC MEASUREMENTS OF THE PROTOTYPE SIX-PHASE SEGMENTAL ROTOR SRM

9.3.1 Dynamic Torque against Speed Characteristics

Torque/speed characteristics of the prototype 6-phase segmental rotor SRM were measured on the test rig for different conduction angles. The machine phases were connected in star and driven from a 3-phase bridge circuit (Figure 137). The advance angle has been varied and measurements taken at different speeds for each advance angle. The speed was varied by varying the load. The measurements were taken with a dc-link voltage of 175V. Line currents were controlled and the demand current level was set to 15A and then 30A. The results are presented in Figure 171. The conduction angle was fixed at 120^{o}. “Adv” in Figure 171 represents switching angle that is before the unaligned rotor position and “Del” represents switching angle that is after the unaligned rotor position. The unaligned position in the case of the 6-phase machine driven from the 3-phase bridge circuit where two adjacent phases conduct current simultaneously is

somewhat different to the 3-phase machine. This will be explained in detail in the next section. There are no unexpected conclusions from Figure 171 and Figure 172.

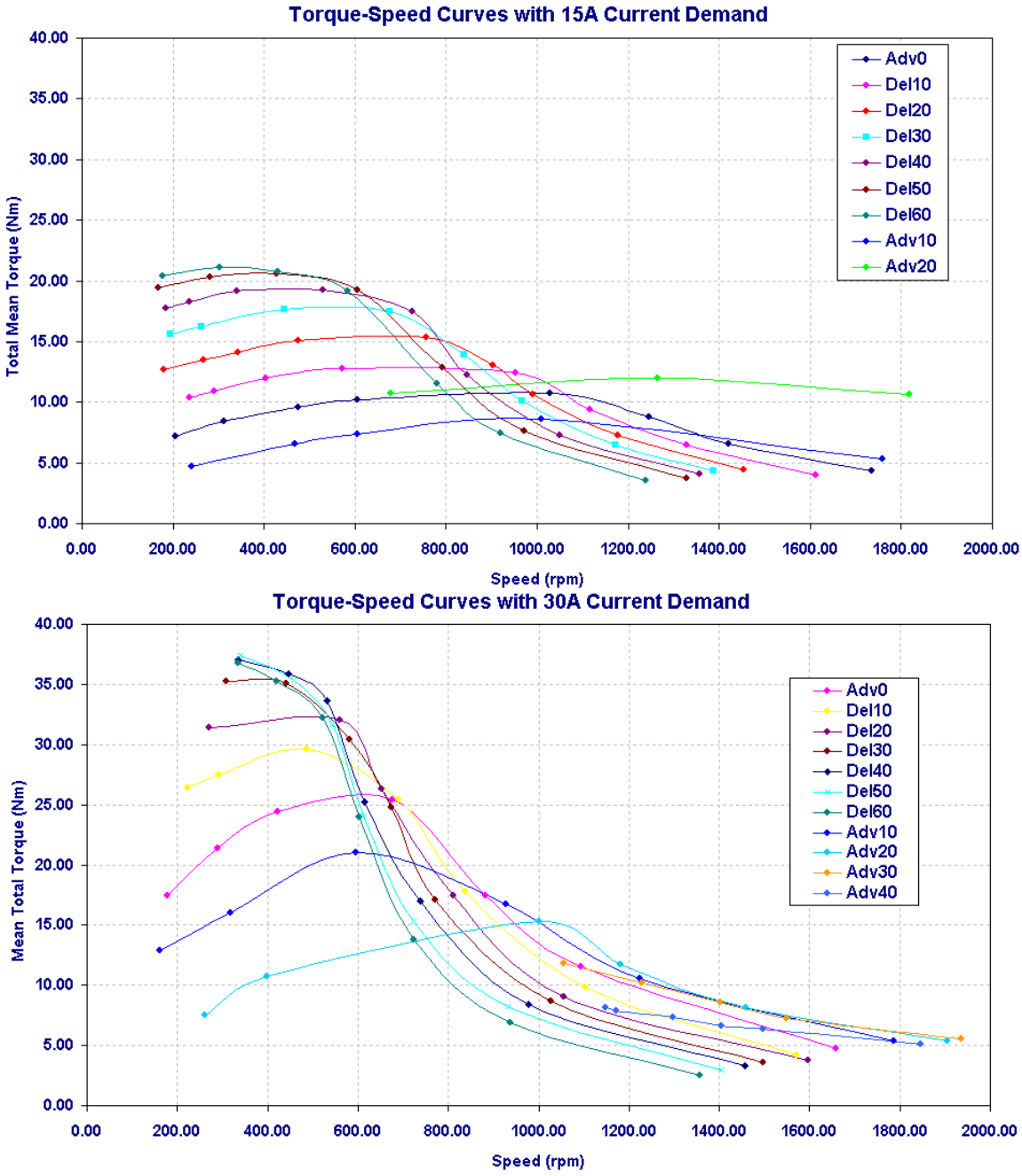

Figure 171 Torque-Speed curves of the prototype segmental rotor star-connected 6-phase SRM driven from a 3-phase bridge circuit. Top trace is when the line current demand is 15A and bottom trace is when the line current demand is 30A

For each point in the curves presented in the top and bottom traces of Figure 171 the total machine copper losses were also calculated (rms phase current was measured via an oscilloscope). In Figure 172 each curve is plotted for a fixed energisation angle (advanced or delayed with respect to the unaligned rotor position) and calculated total machine

copper losses were given against the total machine output torque. Each point in the top and bottom traces of Figure 172 is therefore at a different operating speed. The measured results are for two different current demands: 15A and 30A. In general, advancing the phase energisation instance with respect to the unaligned position of the phase is beneficial in torque production as the speed increases. As the speed reduces, delaying the phase energisation instance after the unaligned position helps with torque production.

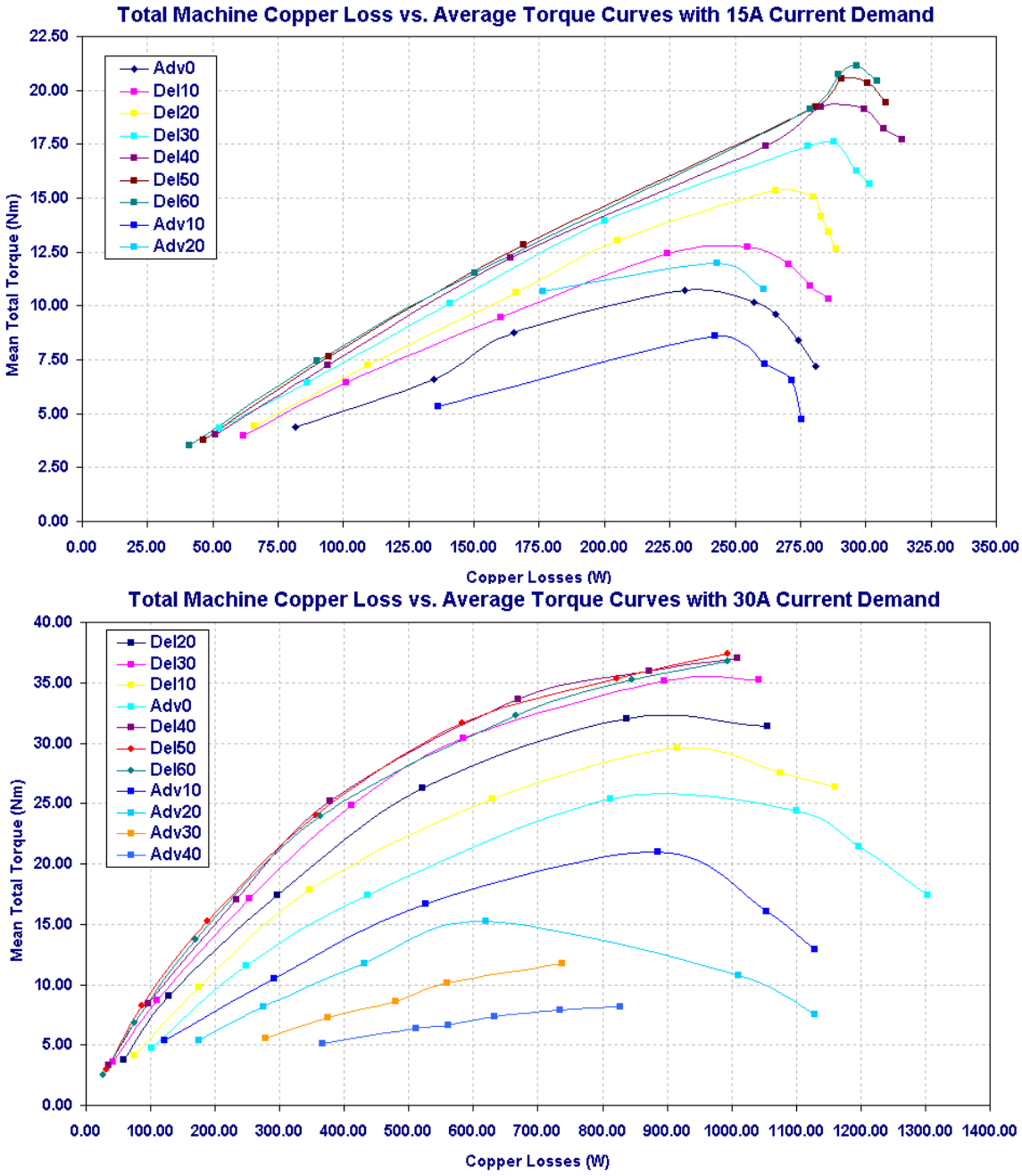

Figure 172 Total machine copper loss vs. Total mean output torque curves of the prototype segmental rotor star-connected 6-phase SRM driven from a 3-phase bridge circuit. Top trace = 15A current demand and bottom trace = 30A current demand

Mechanical losses (friction and windage) of the prototype machine were also measured and the results are presented in Figure 173. During this test, the phases of the machine were not energised. The machine was run from the load (dc-machine with controlled field and armature windings). The dc voltage to the field terminals of the dc-machine was adjusted to increase and reduce the speed of the dc-machine and hence the speed of the prototype 6-phase SRM. The speed and torque were measured by a handheld tachometer and a torque transducer coupled in between the dc-machine and the SRM, respectively. Before the measurements were taken the machine was run for 15 minutes to allow for the warming of the couplings and bearings. The measurements were taken up to around 1800rpm as this was the rated speed of the load machine.

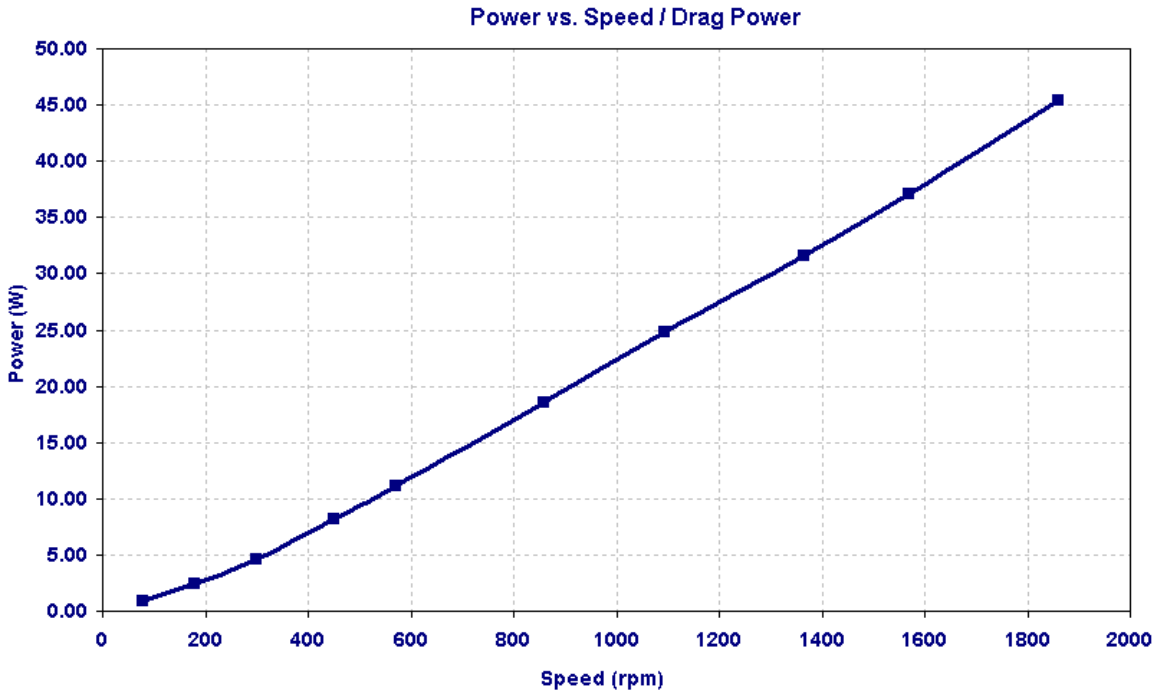

Figure 173 Mechanical losses vs. speed of the prototype 6-phase segmental rotor machine

9.3.2 Dynamic Measurements

This section summarises the measurements taken from the six-phase star connected drive system and the estimated drive performance derived from the captured phase current and rotor position information. Unlike the 2-phase and 3-phase drives analysed in previous chapters where magnetic coupling between phase windings was negligible (and hence

was ignored) the phase current and static flux-linkage characteristics of the 6-phase segmental machine cannot be used to predict the instantaneous torque waveforms and hence performance parameters relating to the machine torque i.e. average torque, torque ripple and shaft power cannot easily be determined. The phase windings of the prototype 6-phase segmental rotor SRM are connected in star and driven from the 3-phase bridge inverter whereby two adjacent phases are energised simultaneously, resulting in magnetically coupled phases. As the phases are magnetically coupled, the flux linking a phase is a non-linear function of seven variables: the six phase currents, and the rotor position. However, by using the equivalent slot quantities it is possible to predict the instantaneous output torque.

By using the transformation matrices presented in *Chapter 6 – Simulation Models* along with the flux-linkage characteristics per machine slot, it is possible to calculate the instantaneous flux-linkage and torque contribution of each slot. The total output torque is then the sum of all slot torques. A section of the FE model of the 6-phase segmental machine that is used to generate the Flux vs. MMF characteristics of a slot is depicted in Figure 174. In Figure 174, phases A and F are energised simultaneously. The motor is in the aligned position with respect to phases A and F and the Slot1 permeance is at its maximum. Unlike the 3-phase segmental machine where the aligned and unaligned positions of the motor can be related directly to the phases of the machine it is more appropriate for the 6-phase segmental machine to refer to the aligned and unaligned positions with respect to stator slots. In Figure 174 MMFs of Slot6 and Slot2 are not zero but the motor is clearly not in the aligned position with respect to either of these slots. By using the core-back flux density (along the black line in Figure 174), the core-back depth and the lamination packing factor, Flux vs. MMF characteristics for a single slot can be generated.

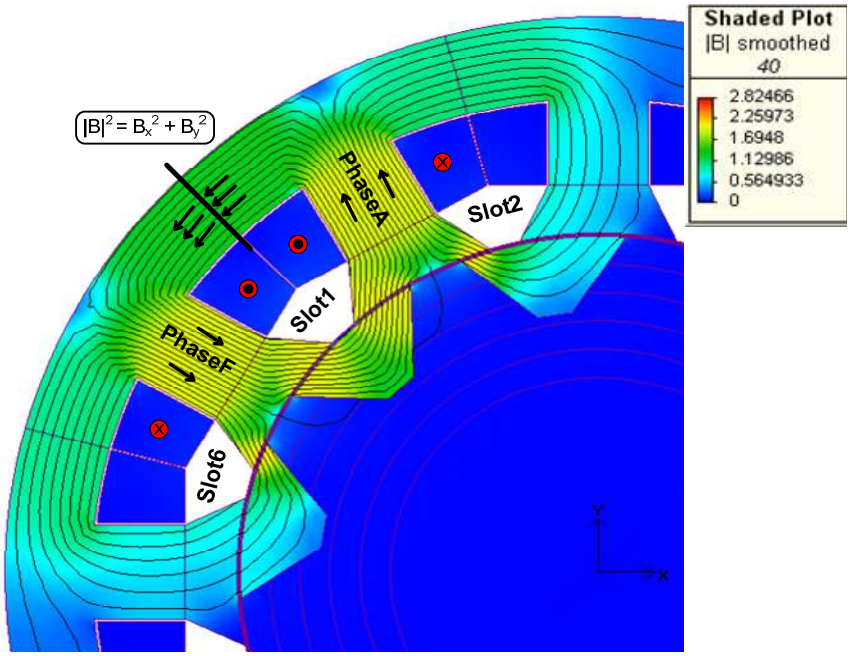

Figure 174 Flux density plot of the 6-phase segmental rotor SRM in the aligned position

Current per coil was varied from 0A to 40A with 1A steps and the rotor position was varied from the unaligned to aligned position with 2 degree steps. The average flux density across the core-back of the slot (along the black line in Figure 174**)** was then calculated with the FE simulation at every position and phase current**.** Using the number of turns per coil, the core-back depth and the stator lamination packing factor the Flux vs. MMF characteristics of the slot were generated. The generated Flux vs. MMF characteristics for Slot1 (in Figure 174) are given in Figure 175. Flux-MMF-Position characteristics of the slot were then used to calculate the Torque-MMF-Position characteristics. This is given in Figure 176.

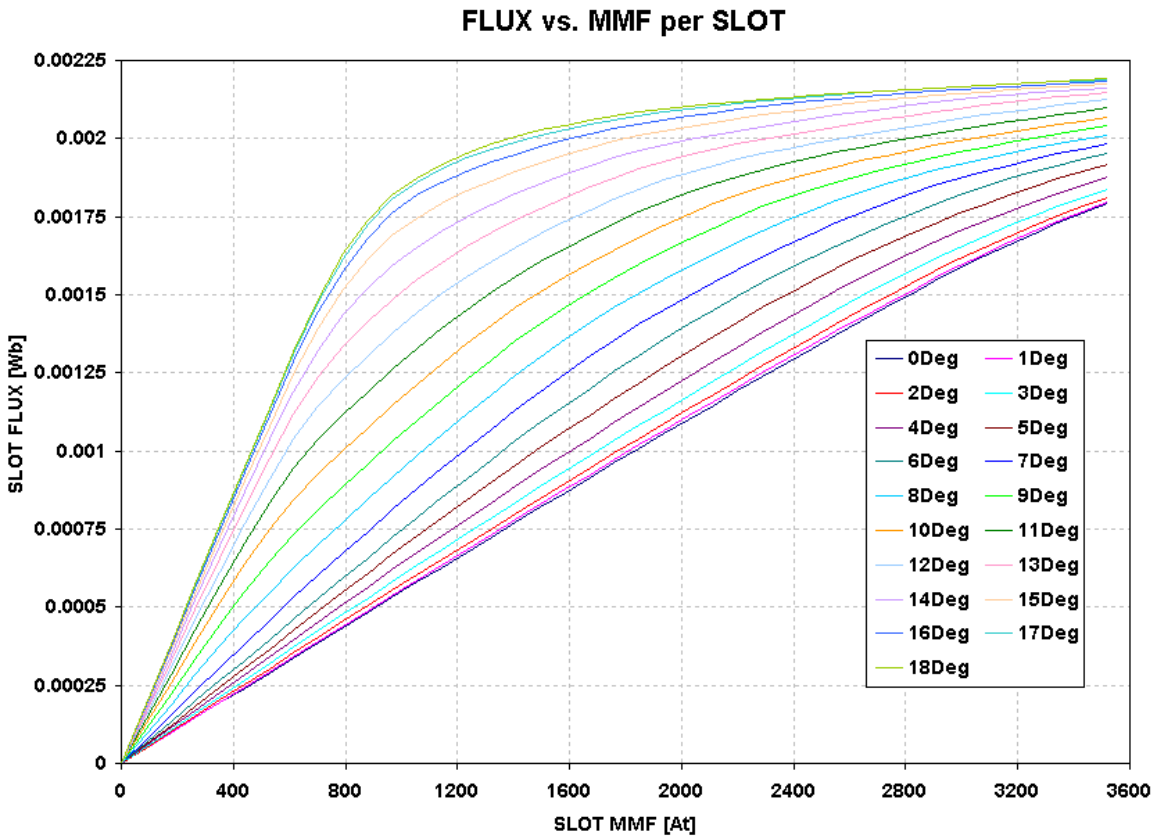

Figure 175 Slot (Slot1 in Figure 18) Flux vs. MMF characteristics from unaligned position to aligned position with 1 degree steps up to 3520 ampere-turns

The 6-phase machine was connected in star and driven from the 3-phase bridge circuit (see Figure 137). Phase-A current, rotor position with respect to Slot1, line current, line-to-line voltage and line-to-star point voltage were all captured with an oscilloscope. The slot position was captured by using the DSP measured encoder feedback and the digital-to-analog conversion card of the drive system.

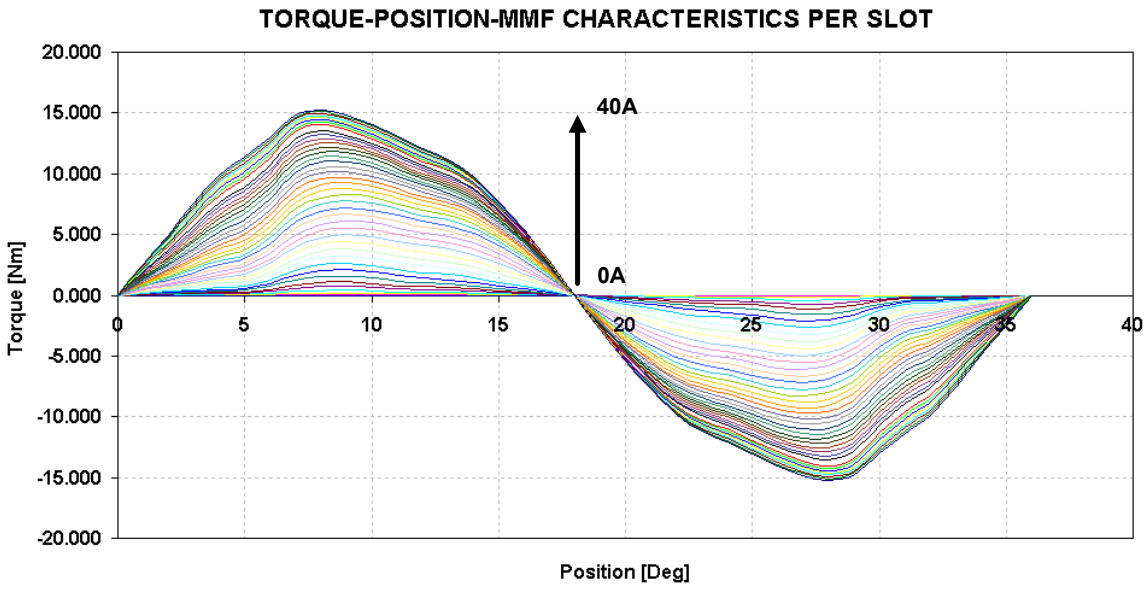

Figure 176 Torque-Position-MMF characteristics per slot generated from the Flux-MMF-Position characteristics per slot

Similar to the 2-phase and 3-phase drives a Matlab® based script was written to analyse the captured waveforms to determine some of the machine performance parameters, such as copper losses and the instantaneous torque waveform. Instantaneous output torque was then used to determine the machine output torque ripple. The phase current was used to calculate the copper losses and the speed of operation. The speed was then used to calculate the required amount of phase shift to generate all the other five phase current waveforms. Similarly by phase shifting, all slot positions were determined. The slot positions and the phase currents were then used along with the transformation matrices to calculate the instantaneous machine torque. The instantaneous torque waveform was then further analysed to estimate the machine average torque and the torque ripple. To validate the Matlab® script, the average torque and the running speed estimations obtained from the script were compared to those measured. The results are divided into two sections: low speed measurements (current controlled drive) and high speed measurements (voltage controlled drive). Several examples are given for each control mode (current or voltage control). Three figures are presented for each example for measurements of both control modes. These are:

- Six phase currents (top trace of first figure) and three line currents (bottom trace of first figure).
- Six slot torques and the total machine output torque (second figure).
- One of the line currents (top trace of third figure), line-to-line voltage (middle trace of third figure) and line-to-star point voltage (bottom trace of third figure). Red traces in the middle and bottom figures are the filtered waveforms for the line-to-line and line-to-star point voltages. (A simple moving average filter was used).

A table where some of the measured and script estimated performance parameters are presented is also given for each example (Table 27 to Table 36). In these tables;

- *Adv Angle [Deg.]* is the point where the phase is energised in advance with respect to the unaligned rotor position.
- *Idemand [A]* is the demand current. In case of the six-phase machine driven from the 3-phase bridge circuit, this is the line current demand.
- *Speed [RPM]* is the speed of operation at which the measurement was taken.
- *Taverage [Nm]* is the average total machine output torque
- *IphRMS [A]* is the root mean square of the phase current.
- *IphPEAK* is the peak value of the phase current.
- *Cu Loss [W]* is the total machine copper losses. 100^{o}C was assumed for the winding operating temperature for copper loss calculations.
- *Tripple – MEAN [%]* is calculated by Equation 31 in Chapter 7. This is the torque ripple based on peak-to-peak instantaneous torque variation and the average output torque.
- *Tripple – MAX [%]* is calculated by Equation 32 in Chapter 7. This is the torque ripple based on peak-to-peak instantaneous torque variation and the maximum output torque.
- *Pshaft [W]* is the total machine shaft power calculated by Equation 35.
- *Efficiency [%]* is the machine efficiency calculated by $100 \times (Pshaft / (Pshaft + Cu\ Loss))$

$$Pshaft = \frac{2 \times \pi}{60} \times Speed \times Torque$$ **Equation 35**

9.3.2.1 Low Speed Measurements of the Prototype Six-Phase Star-Connected Segmental Rotor Machine Driven by the Three-Phase Bridge Circuit

9.3.2.1.1 Low Speed Measurement-1:

Captured results for this low speed measurement are presented from Figure 177 to Figure 179. Table 27 summarises the measured and "script" estimated performance parameters based on the captured data.

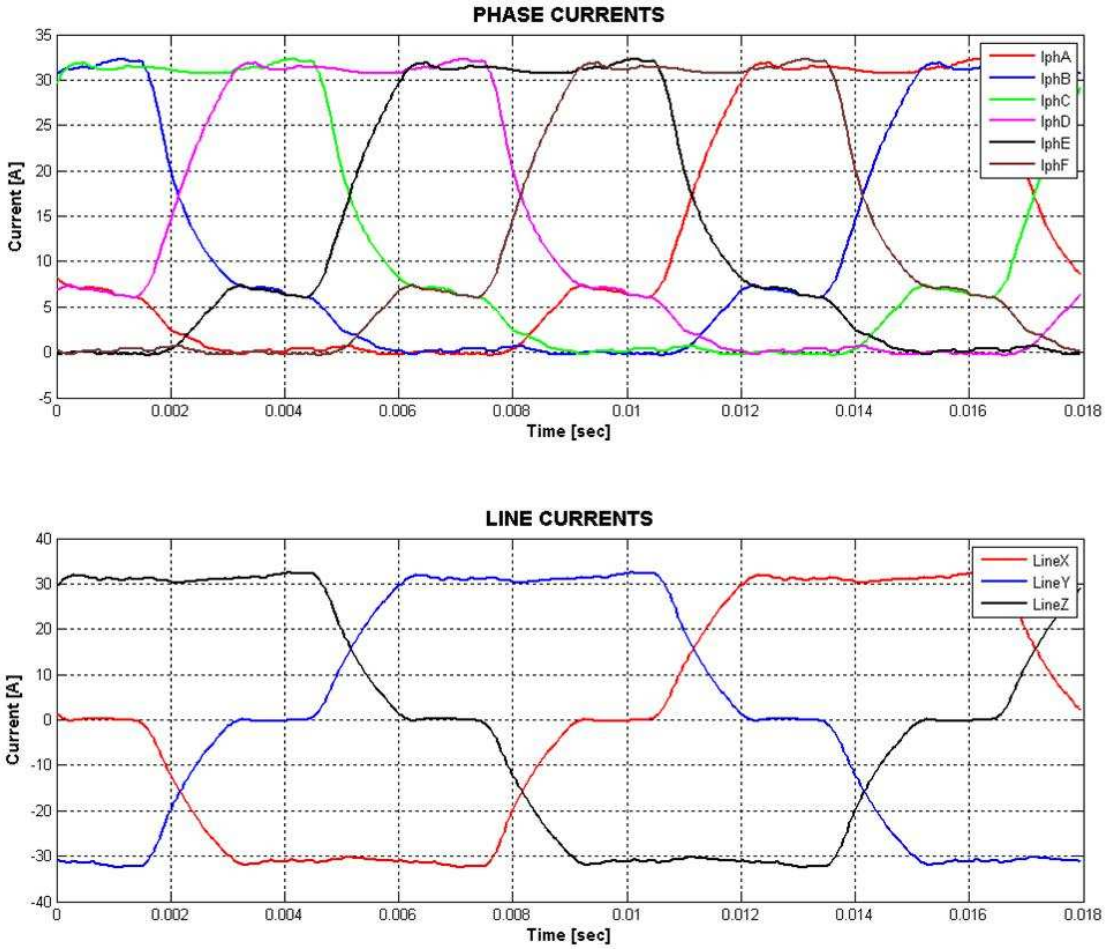

Figure 177 Phase currents (top trace) and line currents (bottom trace) with Advance Angle = -30°; Line Current Demand = 30A; Speed = 335.57RPM; DC-Link Voltage = 175V

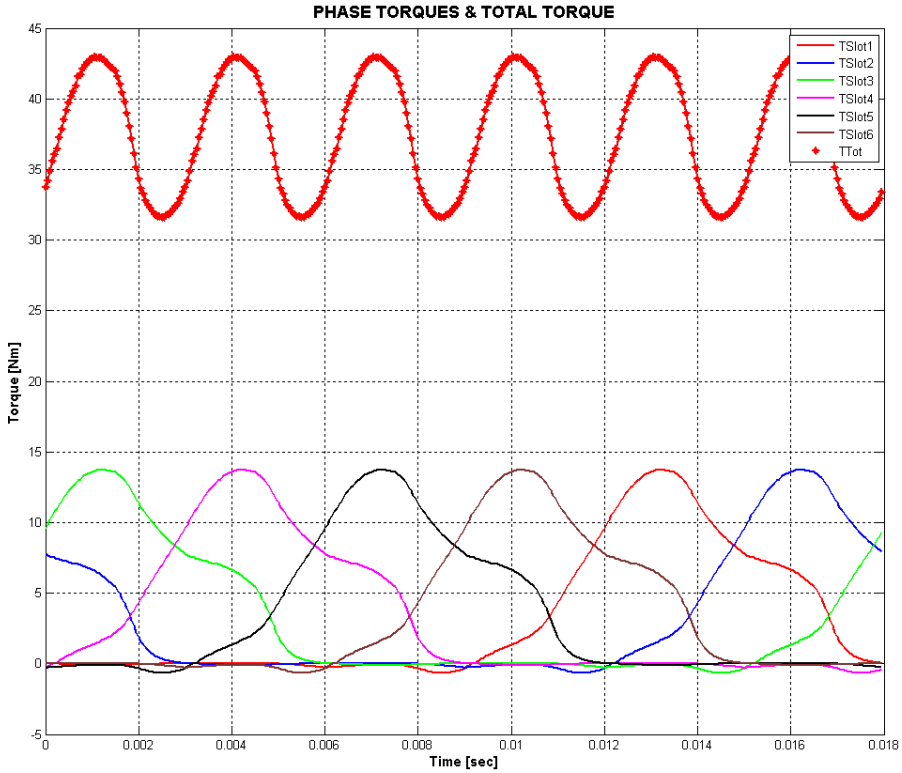

Figure 178 Instantaneous slot torques and total machine output torque (in red) with Advance Angle = -30°; Line Current Demand = 30A; Speed = 335.57RPM; DC-Link Voltage = 175V

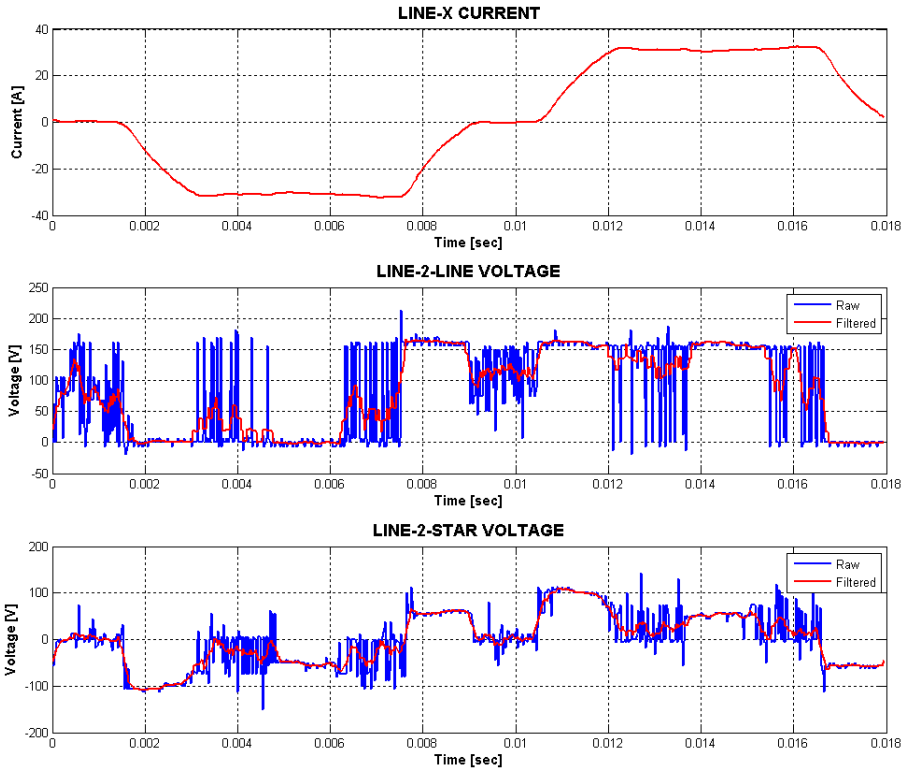

Figure 179 Line current (top trace), line-to-line voltage (middle trace) and line-to-star point voltage (bottom trace) with Advance Angle = -30°; Line Current Demand = 30A; Speed = 335.57RPM; DC-Link Voltage = 175V

Clearly, the motor is running slowly and the controller has enough time to build the line current from zero to the demanded level and therefore is under current control. Although there is strong mutual coupling between machine phases, at this speed, the line currents are very close to those expected from the ideal 120^o conduction. It is fair to say that the controller works reasonably well controlling a machine with mutually coupled phase windings.

It is apparent from Figure 177 that the phase currents have two-stage rise and fall periods. This is similar to what was seen with the simulated results of the six phase machine with no mutually coupled phases. The reason for the rise at the beginning of the phase current waveform is the same: the negative voltage applied across the phase that is switched-off appears as positive voltage across the phase that is not in its conduction period. The phase diode becomes forward biased and the phase starts conducting current even though it is not in its conduction period. Once the line current falls to zero, there is still current in both of the phases in a module (formed by a pair of phases connected back to back with series connected phase diodes) that circulates around the phase diodes and the phase windings. In this period where the line current is zero, the phase currents have a slow decay due to resistive voltage drop across the phases and the forward voltage drops across the phase diodes.

When the phase energisation cycle starts positive voltage is applied across the newly conducting phase. The phase current has a second rise period until the line current hits the demand current level and the controller starts chopping the line voltage. During the chopping period, one of the phase currents has already fallen to zero. The line current equals the phase current that is in its conduction period. Once the conducting phase gets to the end of its energisation cycle, it is turned off and both the phase and line current decay. Once the line current hits zero, the controller reacts to keep it at this level until the beginning of the next energisation cycle of one of the anti-parallel connected phases. It is also quite apparent from the individual torque waveforms (Figure 178) that the phases go through two level energisation and de-fluxing periods.

Table 27 Summary of measured and predicted performance parameters for the star-connected 6-phase segmental rotor SRM when driven from 3-phase bridge circuit with Advance Angle = -30°; Line Current Demand = 30A; Speed = 335.57RPM; DC-Link Voltage = 175V

	MEASURED	ESTIMATED
Adv Angle [Deg.]	-30	
Idemand [A]	30	
Speed [RPM]	335.57	333.3
Taverage [Nm]	37.02	38.36
IphRMS [A]		17.8
IphPEAK [A]		32.3
Cu Loss [W]		1095
Tripple - MEAN [%]		27.0
Tripple - MAX [%]		24.2
Pshaft [W]	1300.915	1339.1
Efficiency [%]		55.02

According to Table 27, measured and estimated values for the average torque and shaft power are in good correlation. Therefore the torque ripple estimation can be viewed as quite reasonable. Although the drive works well and the motor is able to generate approximately 38.0Nm of average output torque, the machine copper losses are considerably high compared to the generated shaft power. This is believed to be due to the two-stage rise and fall periods visible in phase current waveforms that result in increased rms phase currents. The efficiency value of 55.02% in Table 27 is reasonable for an SR machine under current control running at low speed. Moreover, in the case of *Low Speed Measurement-1* the machine is pushed close to its limits of torque output affecting the drive efficiency. Even with this high advance angle, torque ripple is quite favourable at 27.0% with plenty of overlapping between adjacent slot torque waveforms.

9.3.2.1.2 Low Speed Measurement-2:

For the second example, the current demand is kept at 30A and the machine was run at approximately 342 rpm with a dc-link voltage of 175V. The phase energisation instance was increased to 50° before the unaligned rotor position. The captured results are presented from Figure 180 to Figure 182.

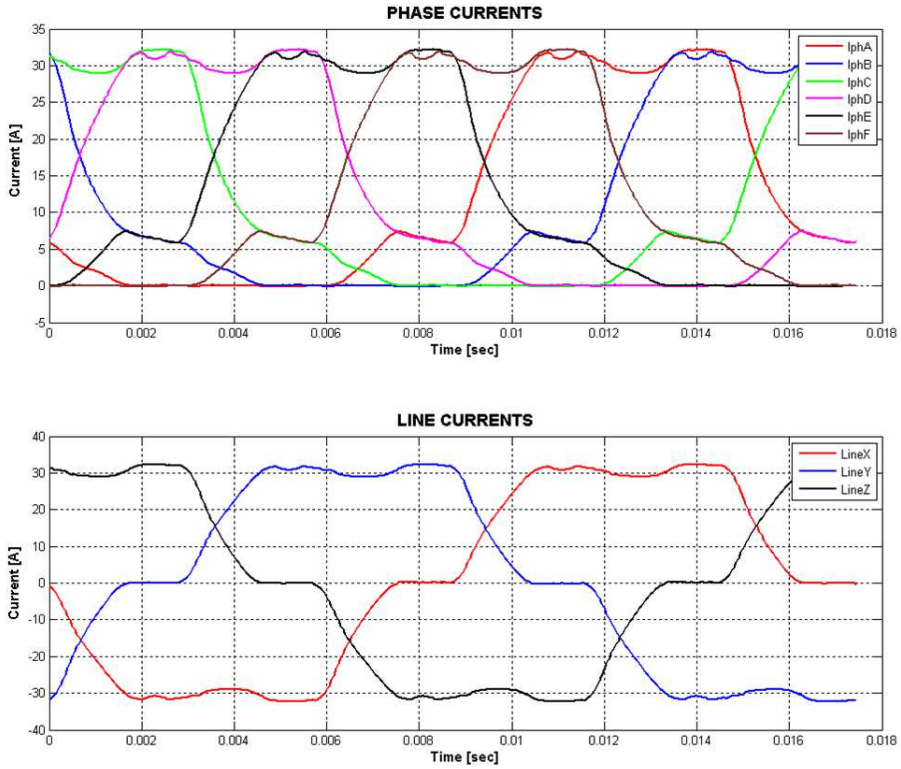

Figure 180 Phase currents (top trace) and line currents (bottom trace) with Advance Angle = -50^o; Line Current Demand = 30A; Speed = 341.67RPM; DC-Link Voltage = 175V

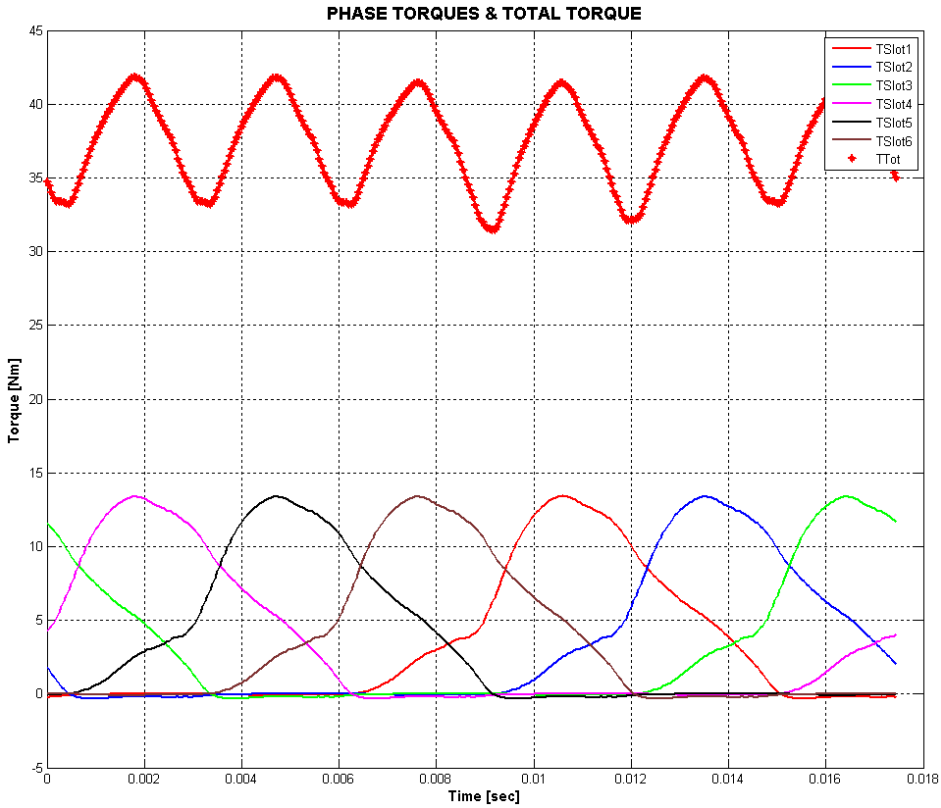

Figure 181 Instantaneous slot torques and total machine output torque (in red) with Advance Angle = -50^o; Line Current Demand = 30A; Speed = 341.67RPM; DC-Link Voltage = 175V

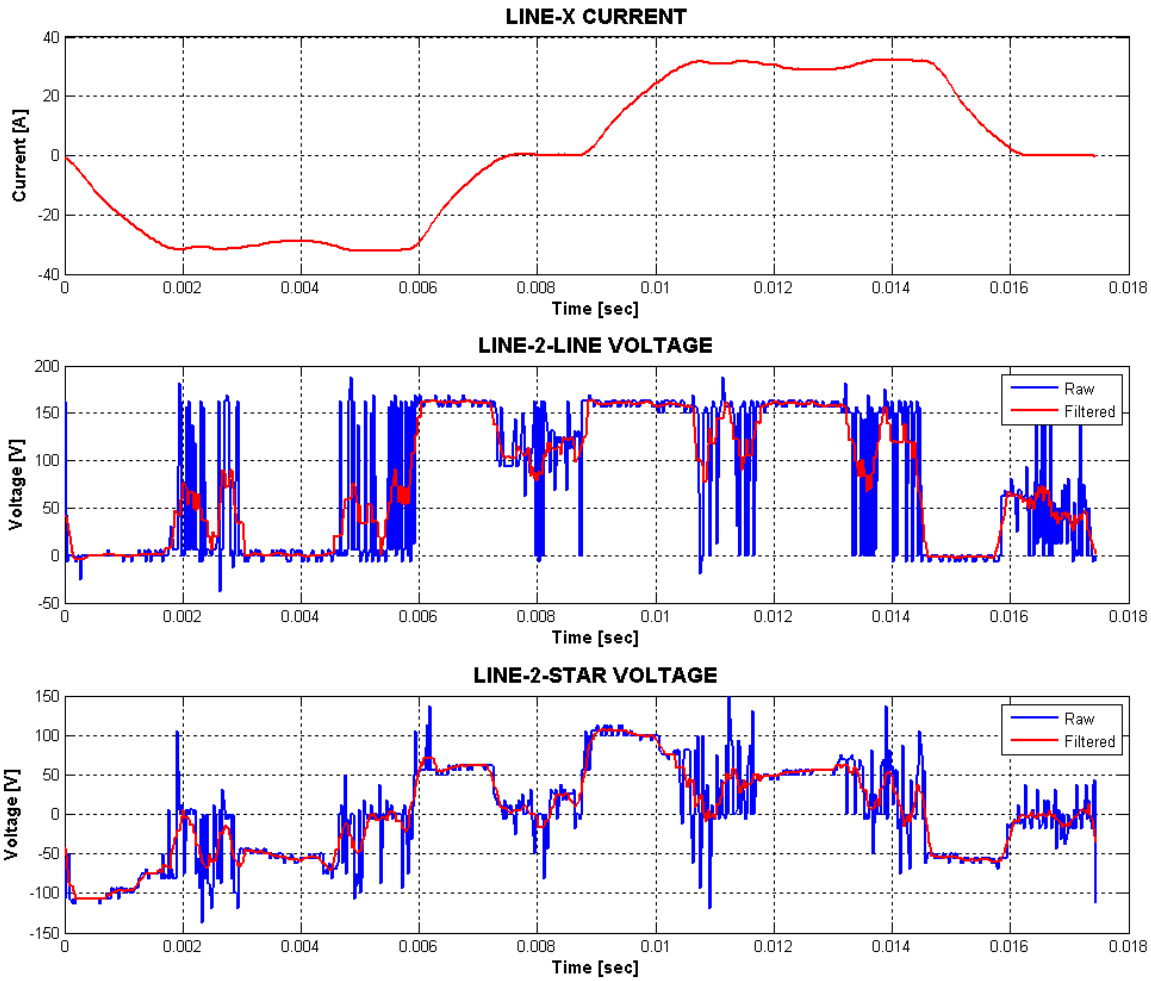

Figure 182 Line current(top trace), line-2-line voltage (middle trace) and line-2-star point voltage (bottom trace) with Advance Angle = -50^{o}; Line Current Demand = 30A; Speed = 341.67RPM; DC-Link Voltage = 175V

From the above figures, it is clear that the controller is still under current control. The two-stage rise and fall time periods in the phase current waveforms are also visible. Table 28 tabulates the measured against estimated performance parameters. The correlation between measured and estimated torques is within 1%. Still operating at a reasonably low speed and generating similar amounts of output torque, the efficiency of *Low Speed Measurement-2* is similar to that of *Low Speed Measurement-1*.

Table 28 Summary of measured and predicted performance parameters for the star-connected 6-phase segmental rotor SRM when driven from 3-phase bridge circuit with Advance Angle = -50°; Line Current Demand = 30A; Speed = 341.67RPM; DC-Link Voltage = 175V

	MEASURED	ESTIMATED
Adv Angle [Deg.]	-50	
Idemand [A]	30	
Speed [RPM]	341.7	342.8
Taverage [Nm]	37.2	37.4
IphRMS [A]		17.5
IphPEAK [A]		32.2
Cu Loss [W]		1058.8
Tripple - MEAN [%]		27.6
Tripple - MAX [%]		24.7
Pshaft [W]	1331.8	1344.4
Efficiency [%]		55.9

9.3.2.1.3 Low Speed Measurement-3:

In the final low speed example the current demand was reduced to 15A. The machine was run slower at approximately 255.3rpm with a dc-link voltage of 175V. The phases were energised 40° before the unaligned rotor position was reached. The captured results are presented from Figure 183 to Figure 185. The controller is again under current control and the operation is similar to that with 30A current demand with the two-stage rise and fall periods in all phase currents. It is interesting to note that the behaviour of the phase currents in the first part of the rise period is very similar to that seen with the examples with 30A current demand. The phase currents initially rise to approximately 6.0A and then fall to around 5.0A. This is due to the fact that the first rise period in the phase currents is not controlled by the controller but is a result of negative voltage applied across the anti-parallel phase appearing as positive voltage across the phase windings and forward-biasing of the phase diode. The rate of change of phase current is faster with the 15A current demand as the controller only needs to elevate the line current to 15A rather than 30A with the same dc-link voltage available. This is reflected in the individual phase torque waveforms. As a result the total output torque waveform has more torque ripple (see Table 29).

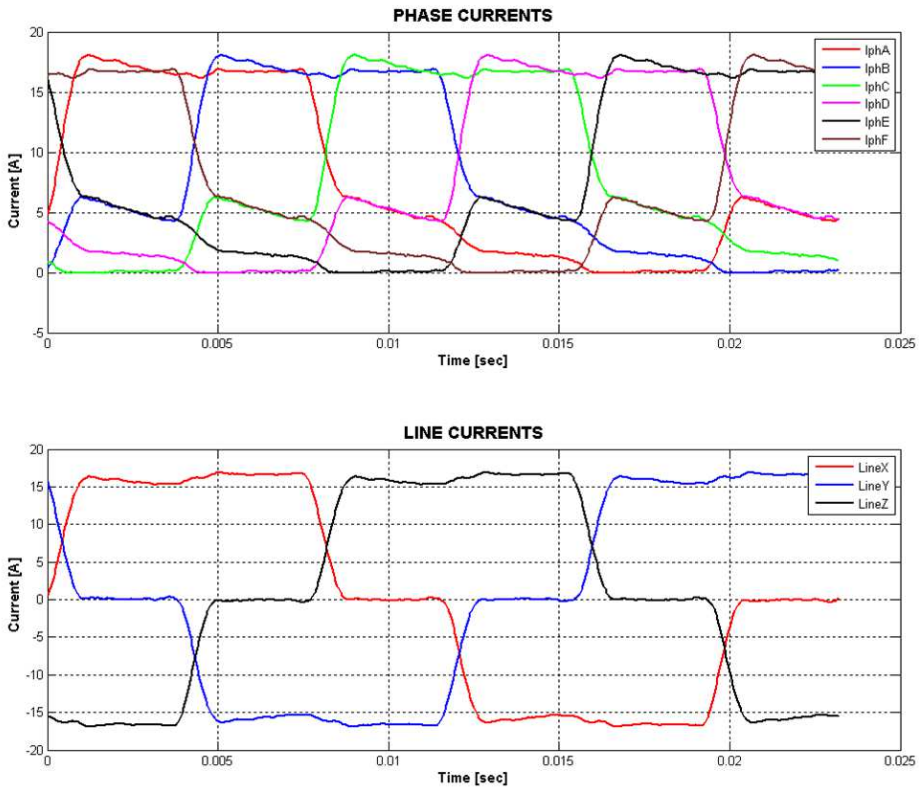

Figure 183 Phase currents (top trace) and line currents (bottom trace) with Advance Angle = -40^{o}; Line Current Demand = 15A; Speed = 255.32RPM; DC-Link Voltage = 175V

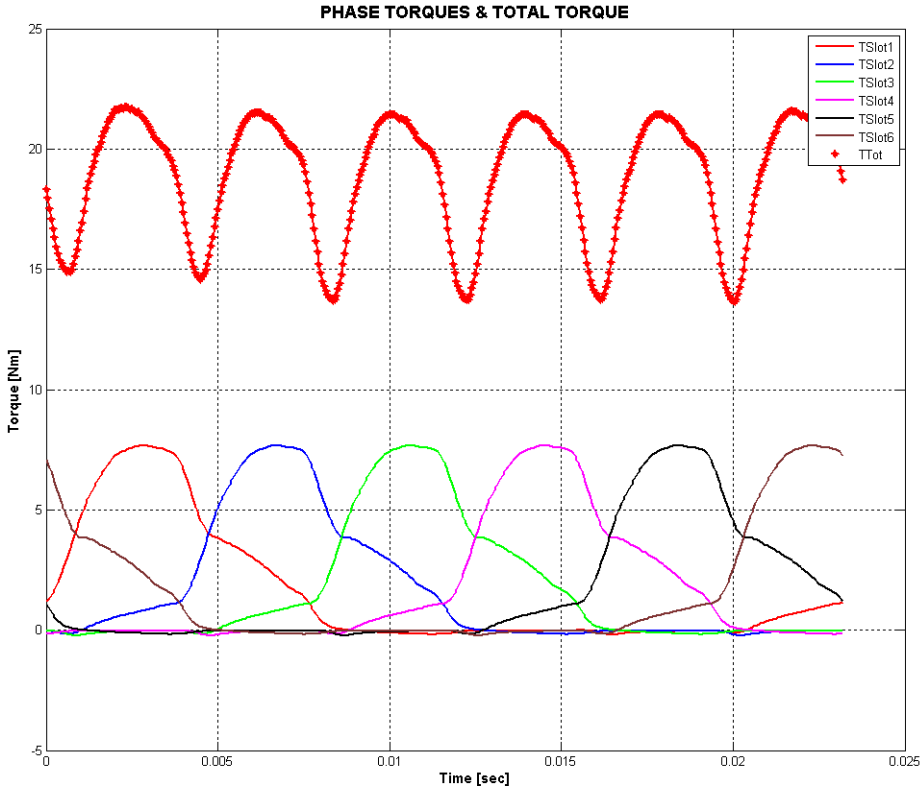

Figure 184 Instantaneous slot torques and total machine output torque (in red) with Advance Angle = -40^{o}; Line Current Demand = 15A; Speed = 255.32RPM; DC-Link Voltage = 175V

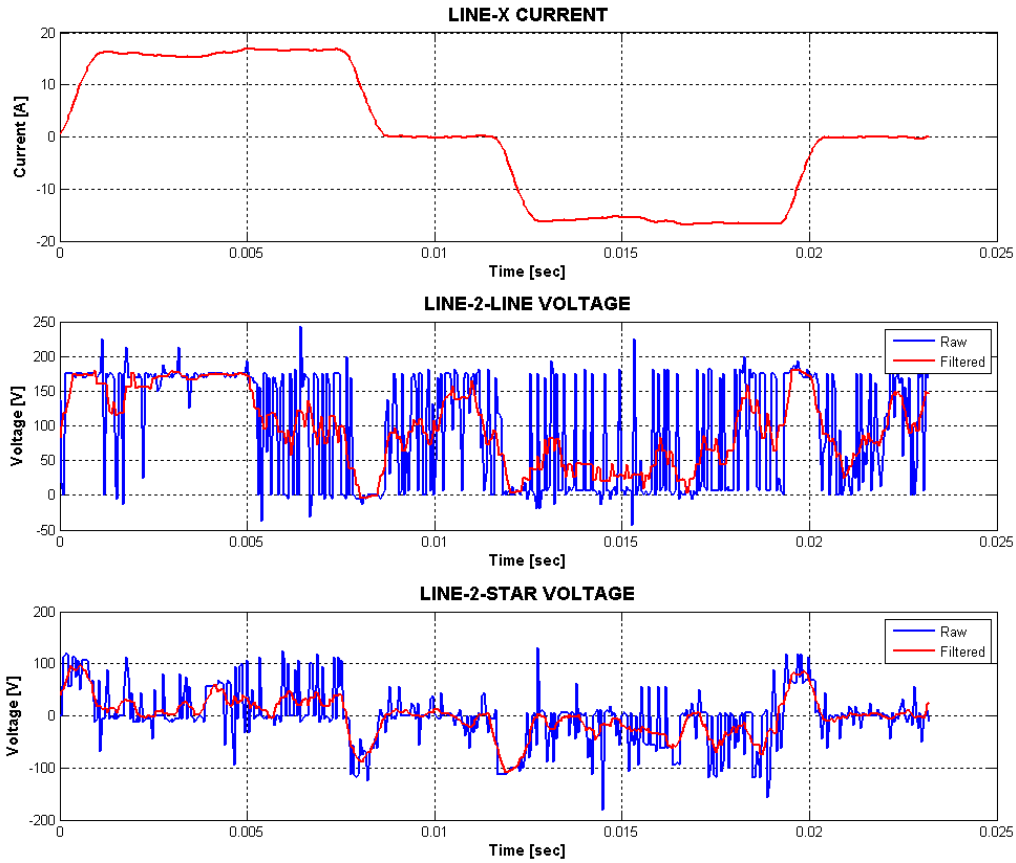

Figure 185 Line current(top trace), line-2-line voltage (middle trace) and line-2-star point voltage (bottom trace) with Advance Angle = -40^{o}; Line Current Demand = 15A; Speed = 255.32RPM; DC-Link Voltage = 175V

Table 29 Summary of measured and predicted performance parameters for the star-connected 6-phase segmental rotor SRM when driven from 3-phase bridge circuit with Advance Angle = -40^{o}; Line Current Demand = 15A; Speed = 255.32RPM; DC-Link Voltage = 175V

	MEASURED	ESTIMATED
Adv Angle [Deg.]	-40	
Idemand [A]	15	
Speed [RPM]	255.3	258
Taverage [Nm]	19.7	18.8
IphRMS [A]		10.1
IphPEAK [A]		18.1
Cu Loss [W]		350
Tripple - MEAN [%]		42.9
Tripple - MAX [%]		37.2
Pshaft [W]	525.6	508.9
Efficiency [%]		59.2

As the demand current is lower (15A as opposed to 30A) it is not surprising to see that the average output torque and the total machine copper losses are reduced. At the same time the efficiency is slightly higher than those experienced during *Low Speed Measurement-1* and *Low Speed Measurement-2*.

The flux vs. MMF loci of all three low speed measurements are displayed against the aligned and unaligned magnetisation curves (see Figure 175) of a single slot in Figure 186.

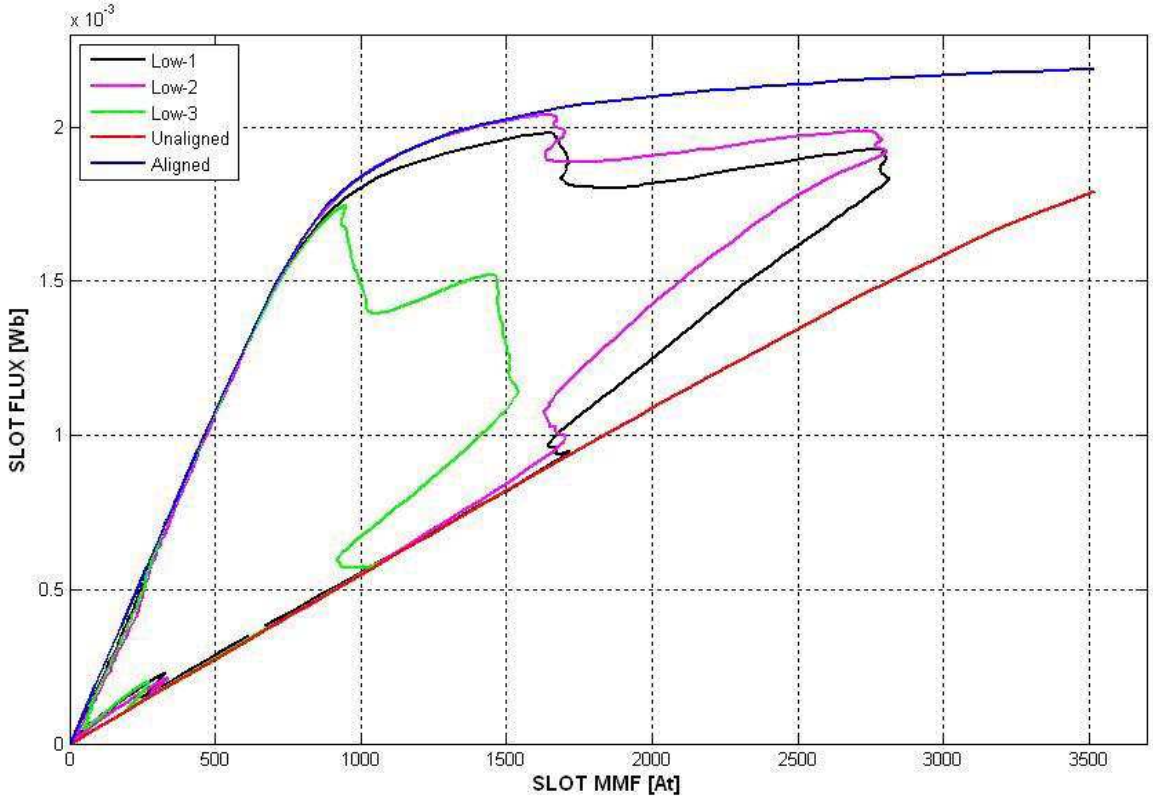

Figure 186 Flux vs. MMF loci for the low speed measurements

9.3.2.2 High Speed Measurements of the Prototype Six-Phase Star-Connected Segmental Rotor Machine Driven by the Three-Phase Bridge Circuit

With the examples in the next four subsections, the machine BEMF is relatively high and the controller does not have enough time to achieve the demanded current level. The

machine therefore operates under full voltage control. This is apparent from the line-to-line and line-to-star point voltage waveforms given in Figure 189, Figure 193, Figure 197 and Figure 201.

The current demand was set to 30A for *High Speed Measurement-1* and *High Speed Measurement-2* and to 15A for *High Speed Measurement-3* and *High Speed Measurement-4*. A summary of the results will be given at the end of this subsection.

9.3.2.2.1 High Speed Measurement-1:

Here the machine was run at approximately 1271rpm. The phases were energised at the unaligned rotor position. The results are presented from Figure 187 to Figure 189. Table 30 summarises the predicted and measured performance parameters such as average output torque for the *High Speed Measurement-1*. The power device and diode current waveforms of the measurement are illustrated in Figure 190. Based on the measured line currents, the VA ratings of the power devices and diodes have been estimated and the results are presented in Table 31.

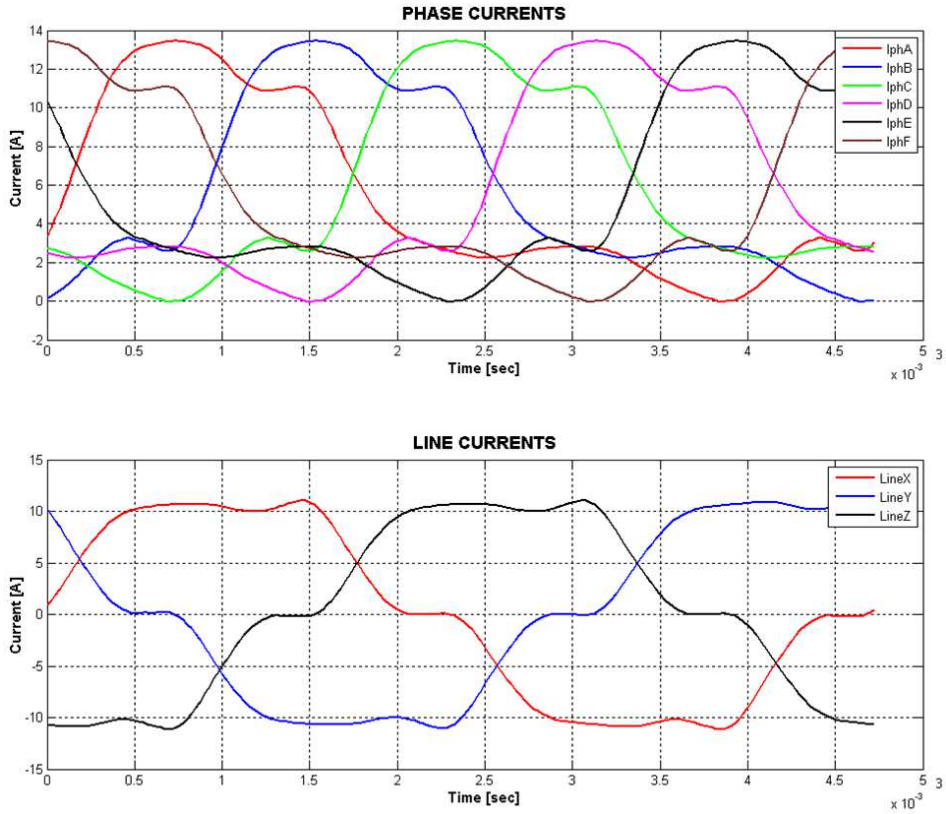

Figure 187 Phase currents (top trace) and line currents (bottom trace) with Advance Angle = 0^0; Line Current Demand = 30A; Speed = 1271.19RPM; DC-Link Voltage = 175V

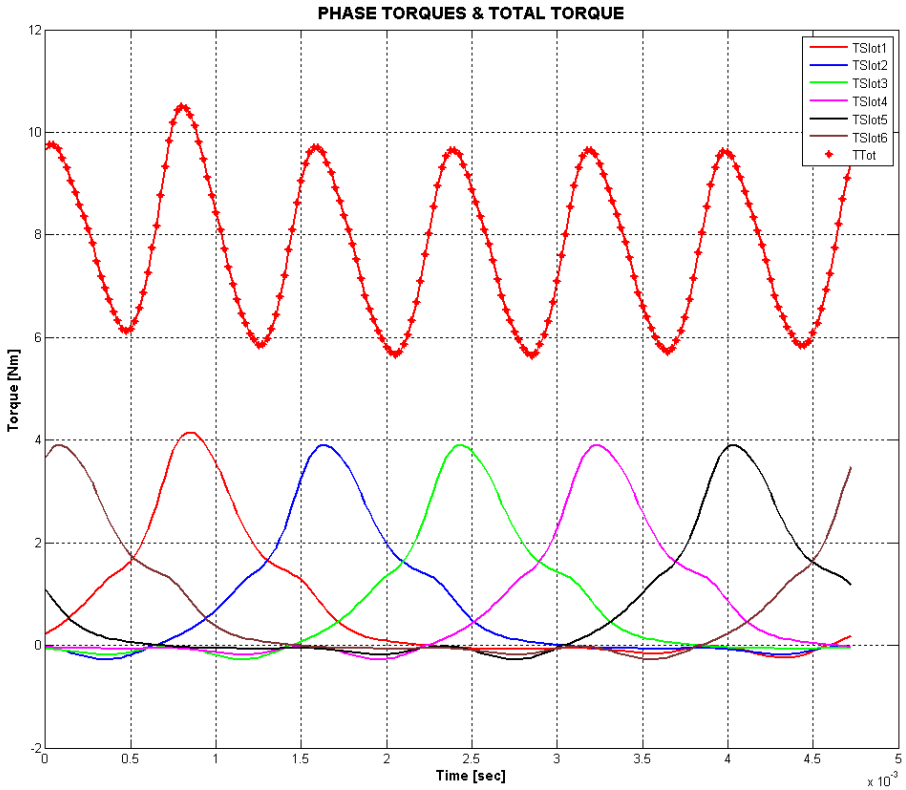

Figure 188 Instantaneous slot torques and total machine output torque (in red) with Advance Angle = 0^o; Line Current Demand = 30A; Speed = 1271.19RPM; DC-Link Voltage = 175V

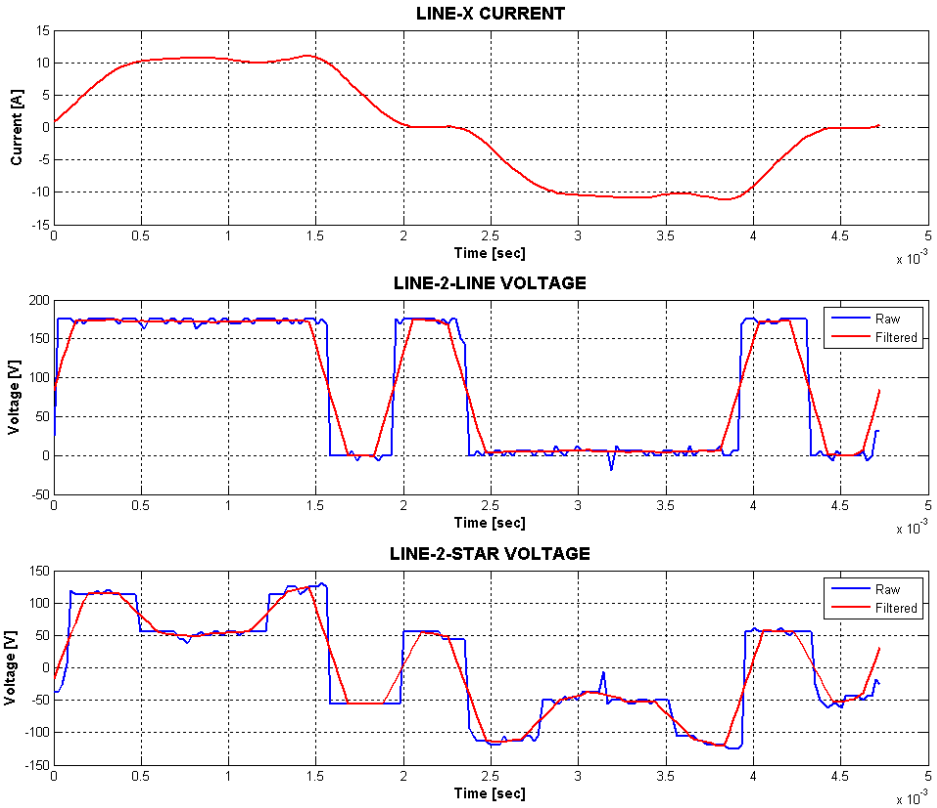

Figure 189 Line current (top trace), line-2-line voltage (middle trace) and line-2-star point voltage (bottom trace) with Advance Angle = 0^o; Line Current Demand = 30A; Speed =1271.19RPM; DC-Link Voltage = 175V

Table 30 Summary of measured and predicted performance parameters for the star-connected 6-phase segmental rotor SRM when driven from 3-phase bridge circuit with Advance Angle = 0°; Line Current Demand = 30A; Speed = 1271.19RPM; DC-Link Voltage = 175V

	MEASURED	ESTIMATED
Adv Angle [Deg.]	0	
Idemand [A]	30	
Speed [RPM]	1271.2	1263.2
Taverage [Nm]	7.3	7.7
IphRMS [A]		7.0
IphPEAK [A]		13.5
Cu Loss [W]		170.5
Tripple - MEAN [%]		62.7
Tripple - MAX [%]		46.2
Pshaft [W]	974.4	1023.1
Efficiency [%]		85.7

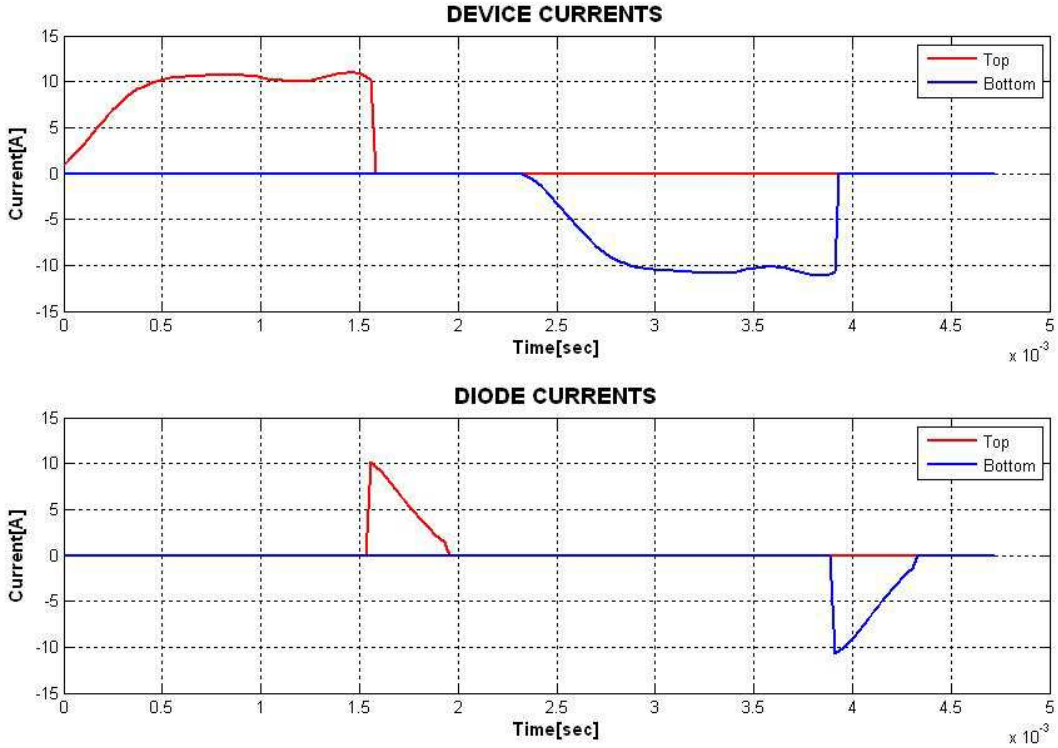

Figure 190 IGBT currents (top trace) and reverse recovery diode currents (bottom trace) based on the measured line currents presented in Figure 187

Table 31 Summary of estimated power electronic performance parameters based on measured line currents with Advance Angle = 0°; Line Current Demand = 30A; Speed = 1271.19RPM; DC-Link Voltage = 175V

Top Device RMS Current [A]	5.48
Top Device Peak Current [A]	11.02
Bottom Device RMS Current [A]	5.42
Top Device RMS Current [A]	11.11
Top Diode RMS Current [A]	1.83
Top Diode Peak Current [A]	10.14
Bottom Diode RMS Current [A]	2.05
Bottom Diode Peak Current [A]	10.77
Device VA Rating - PEAK [kVA / kW]	11.35
Device VA Rating - RMS [kVA / kW]	5.6
Diode VA Rating - PEAK [kVA / kW]	10.73
Diode VA Rating - RMS [kVA / kW]	2.0

9.3.2.2.2 High Speed Measurement-2:

Here the machine was run at approximately 1342rpm. The phases were energised 30° prior to the unaligned rotor position. The results are presented from Figure 191 to Figure 193.

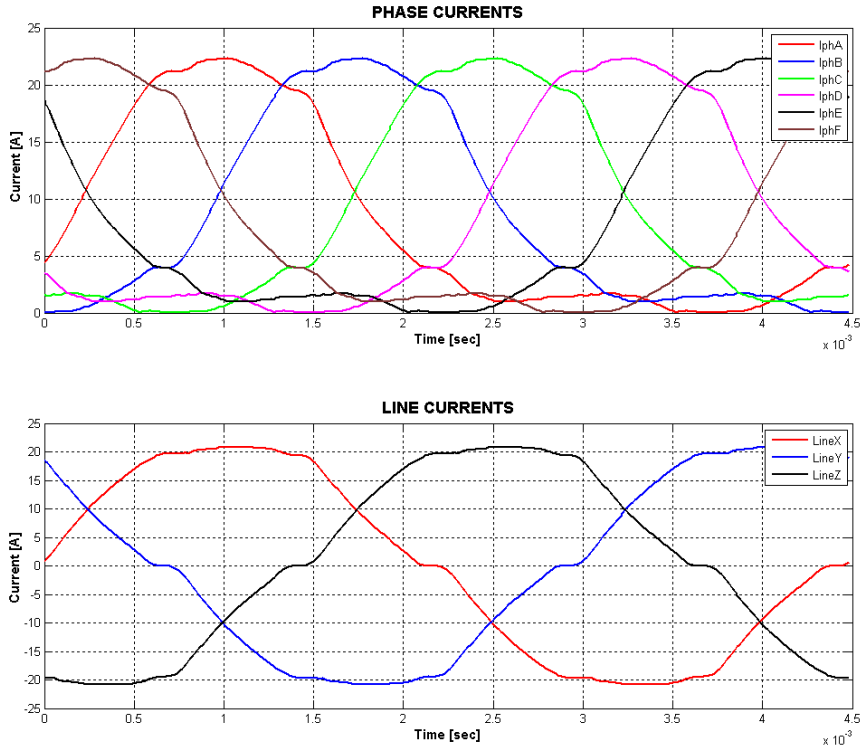

Figure 191 Phase currents (top trace) and line currents (bottom trace) with Advance Angle = 30°; Line Current Demand = 30A; Speed = 1342.28RPM; DC-Link Voltage = 175V

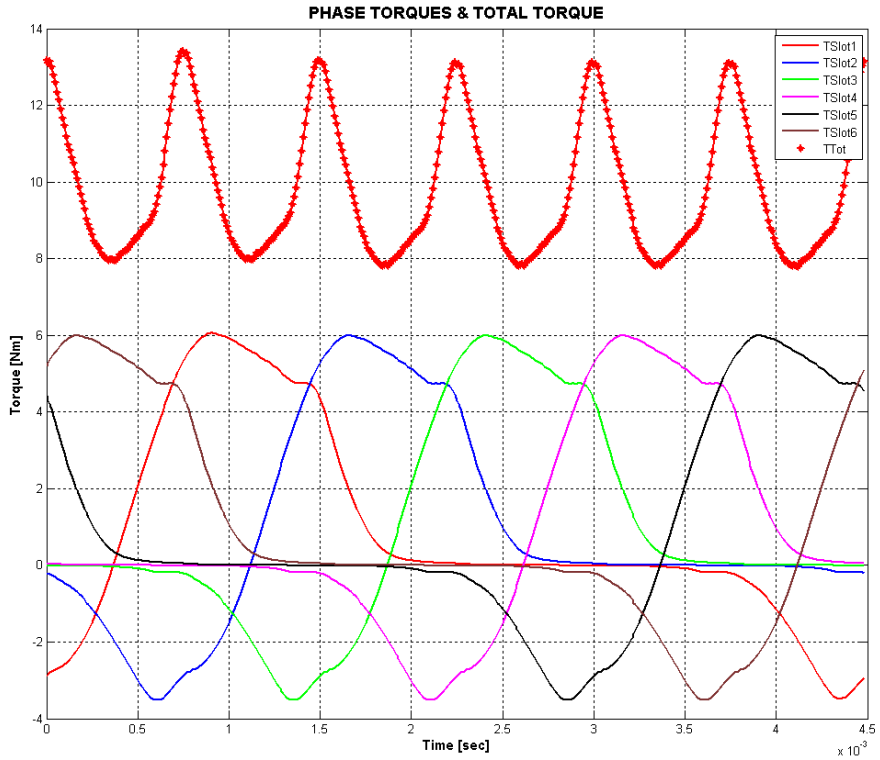

Figure 192 Instantaneous slot torques and total machine output torque (in red) with Advance Angle = 30^{o}; Line Current Demand = 30A; Speed = 1342.28RPM; DC-Link Voltage = 175V

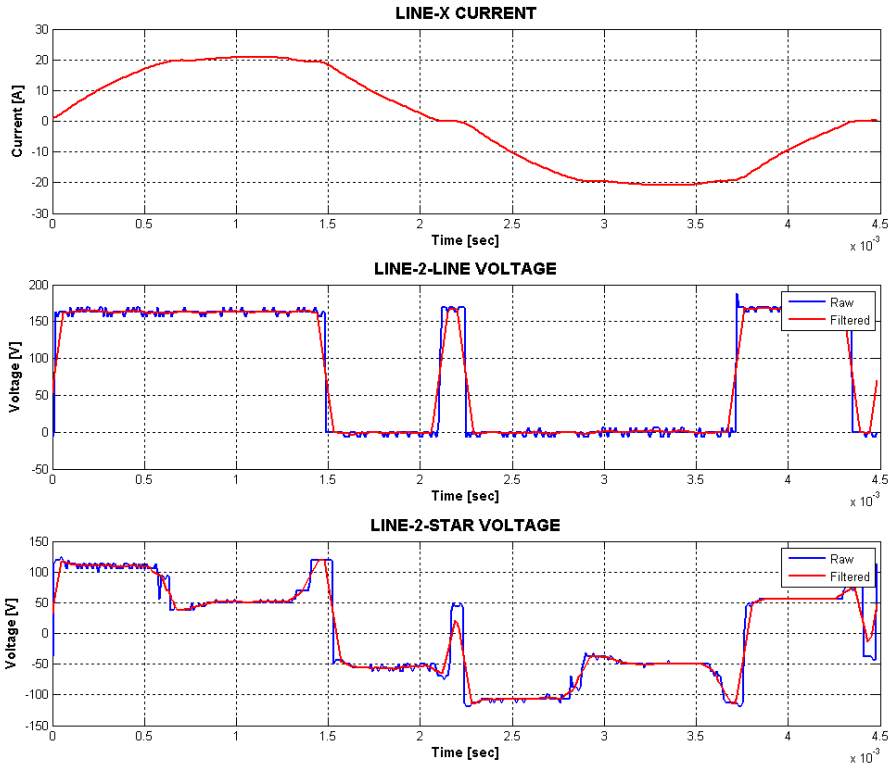

Figure 193 Line current(top trace), line-2-line voltage (middle trace) and line-2-star point voltage (bottom trace) with Advance Angle = 30o; Line Current Demand = 30A; Speed =1342.28RPM; DC-Link Voltage = 175V

Table 32 Summary of measured and predicted performance parameters for the star-connected 6-phase segmental rotor SRM when driven from 3-phase bridge circuit with Advance Angle = 30°; Line Current Demand = 30A; Speed = 1342.28RPM; DC-Link Voltage = 175V

	MEASURED	ESTIMATED
Adv Angle [Deg.]	30	
Idemand [A]	30	
Speed [RPM]	1342.3	1336.3
Taverage [Nm]	9.1	9.8
IphRMS [A]		11.4
IphPEAK [A]		22.3
Cu Loss [W]		449.2
Tripple - MEAN [%]		57.2
Tripple - MAX [%]		41.9
Pshaft [W]	1281.9	1373.1
Efficiency [%]		75.35

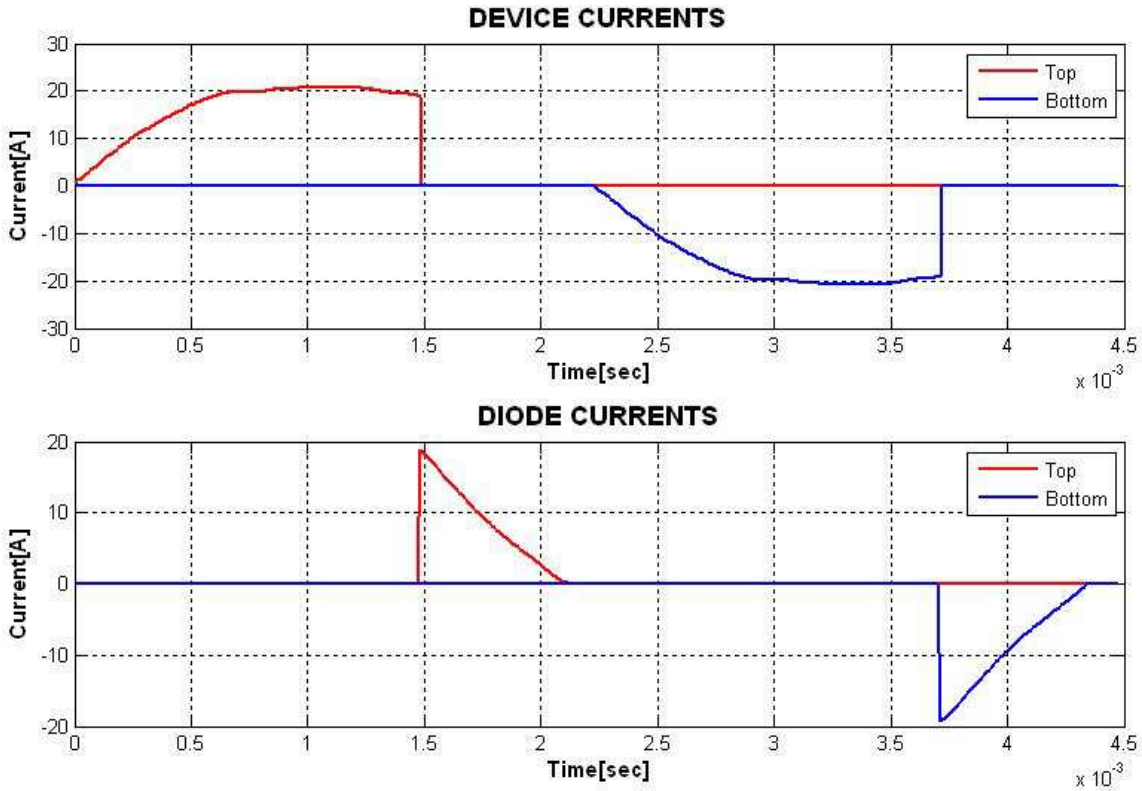

Figure 194 IGBT currents (top trace) and reverse recovery diode currents (bottom trace) based on the measured line currents presented in Figure 191

Table 33 Summary of estimated power electronic performance parameters based on measured line currents with Advance Angle = 30°; Line Current Demand = 30A; Speed = 1342.28RPM; DC-Link Voltage = 175V

Top Device RMS Current [A]	10.00
Top Device Peak Current [A]	20.83
Bottom Device RMS Current [A]	9.93
Top Device RMS Current [A]	20.86
Top Diode RMS Current [A]	3.88
Top Diode Peak Current [A]	18.85
Bottom Diode RMS Current [A]	4.07
Bottom Diode Peak Current [A]	19.20
Device VA Rating - PEAK [kVA / kW]	15.37
Device VA Rating - RMS [kVA / kW]	7.35
Diode VA Rating - PEAK [kVA / kW]	14.03
Diode VA Rating - RMS [kVA / kW]	2.93

9.3.2.2.3 High Speed Measurement-3:

Here the machine was run at approximately 1470rpm with a reduced current demand value of 15A. The phases were energised 20° prior to the unaligned rotor position. The results are presented from Figure 195 to Figure 197.

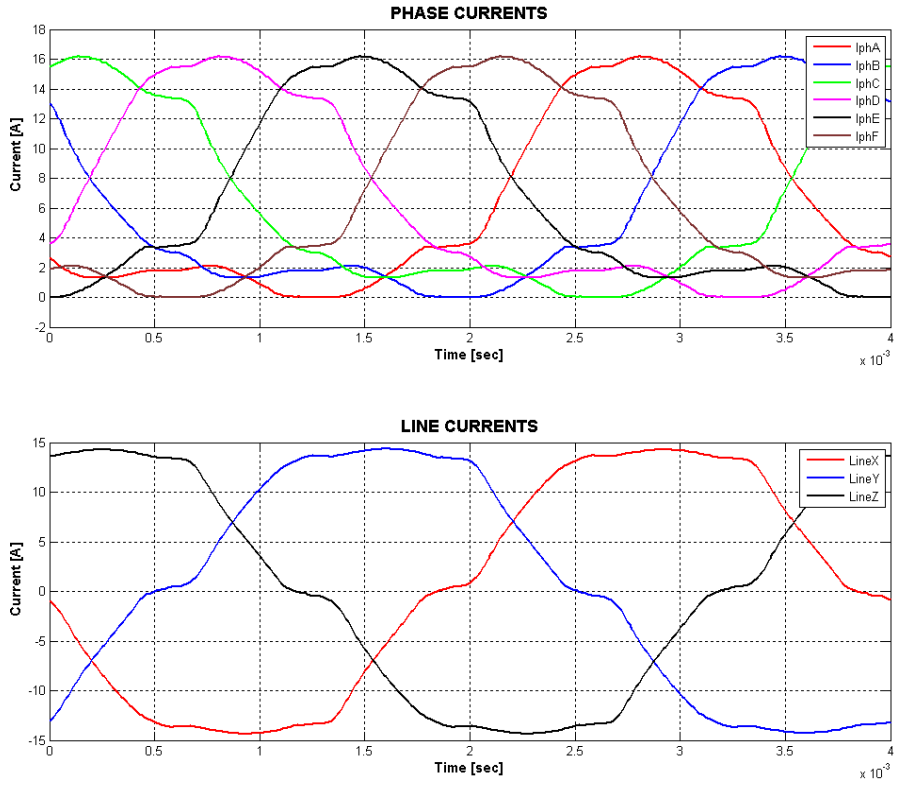

Figure 195 Phase currents (top trace) and line currents (bottom trace) with Advance Angle = 20°; Line Current Demand = 15A; Speed = 1474.20RPM; DC-Link Voltage = 175V

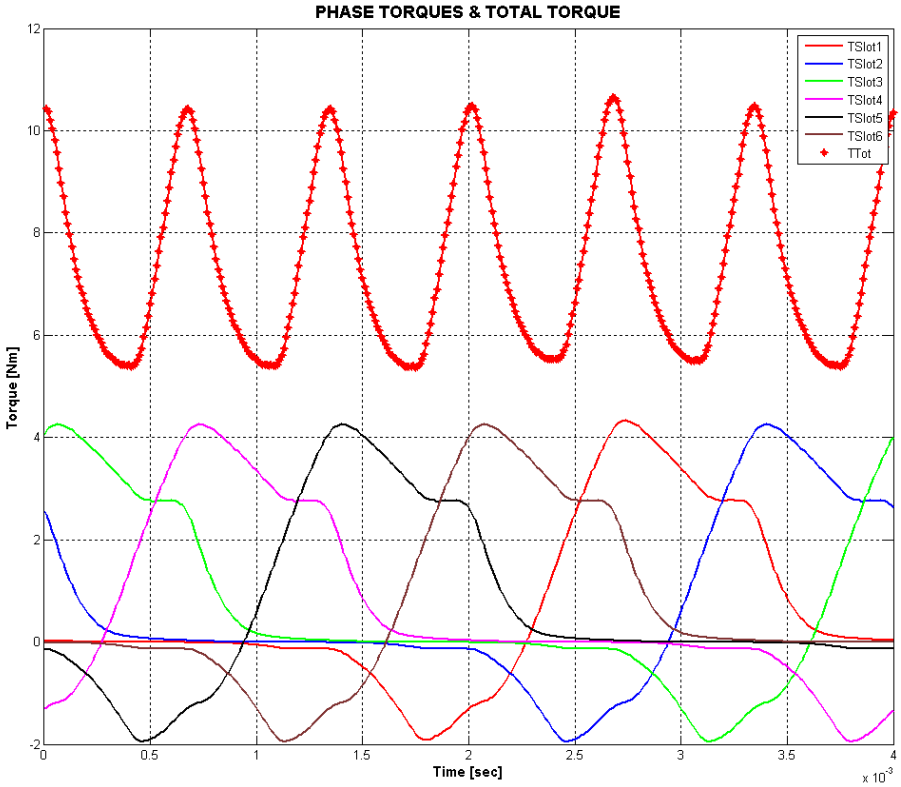

Figure 196 Instantaneous slot torques and total machine output torque (in red) with Advance Angle = 20^o; Line Current Demand = 15A; Speed = 1474.20RPM; DC-Link Voltage = 175V

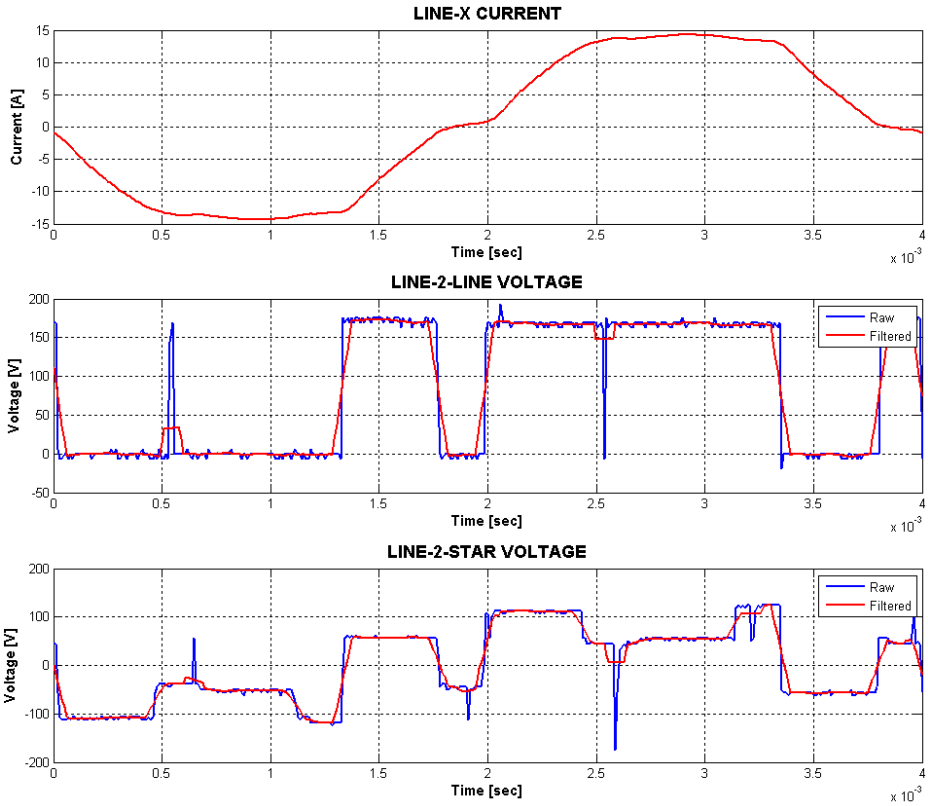

Figure 197 Line current(top trace), line-2-line voltage (middle trace) and line-2-star point voltage (bottom trace) with Advance Angle = 20^o; Line Current Demand = 15A; Speed =1474.20RPM; DC-Link Voltage = 175V

Table 34 Summary of measured and predicted performance parameters for the star-connected 6-phase segmental rotor SRM when driven from 3-phase bridge circuit with Advance Angle = 20°; Line Current Demand = 15A; Speed = 1474.20RPM; DC-Link Voltage = 175V

	MEASURED	ESTIMATED
Adv Angle [Deg.]	20	
Idemand [A]	15	
Speed [RPM]	1474.2	1496.3
Taverage [Nm]	7.0	7.4
IphRMS [A]		8.3
IphPEAK [A]		16.2
Cu Loss [W]		239.6
Tripple - MEAN [%]		71.5
Tripple - MAX [%]		49.5
Pshaft [W]	1074.5	1155.8
Efficiency [%]		82.8

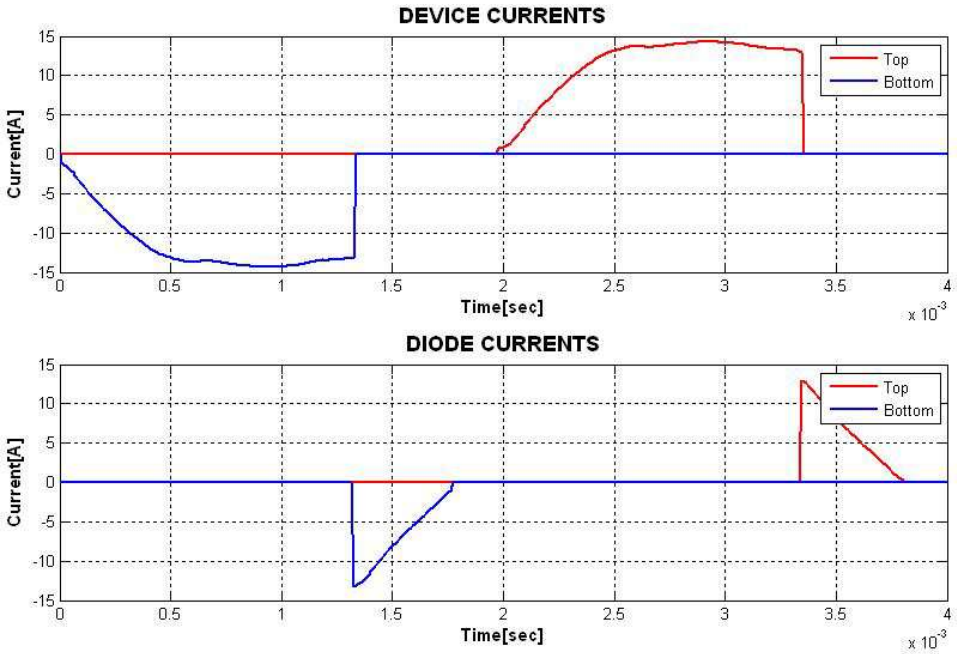

Figure 198 IGBT currents (top trace) and reverse recovery diode currents (bottom trace) based on the measured line currents presented in Figure 196

Compared to the previous high speed measurement results, significant negative torque is present in the individual phase torque waveforms (see Figure 196). This is reflected in the torque ripple values presented in Table 34. This can be related to the speed of operation and the selected advance angle. As the operating speed is faster there is even less time for the controller to de-flux the phases completely before the aligned rotor position is reached and the machine starts generating negative torque.

Table 35 Summary of estimated power electronic performance parameters based on measured line currents with Advance Angle = 20°; Line Current Demand = 15A; Speed = 1474.20RPM; DC-Link Voltage = 175V

Top Device RMS Current [A]	7.05
Top Device Peak Current [A]	14.30
Bottom Device RMS Current [A]	7.00
Top Device RMS Current [A]	14.37
Top Diode RMS Current [A]	2.53
Top Diode Peak Current [A]	12.96
Bottom Diode RMS Current [A]	2.68
Bottom Diode Peak Current [A]	13.21
Device VA Rating - PEAK [kVA / kW]	14.41
Device VA Rating - RMS [kVA / kW]	7.06
Diode VA Rating - PEAK [kVA / kW]	13.16
Diode VA Rating - RMS [kVA / kW]	2.62

9.3.2.2.4 High Speed Measurement-4:

Here the machine was run at approximately 1357rpm with reduced current demand value of 15A. The phases were energised at the unaligned rotor position. The results are presented from Figure 199 to Figure 201.

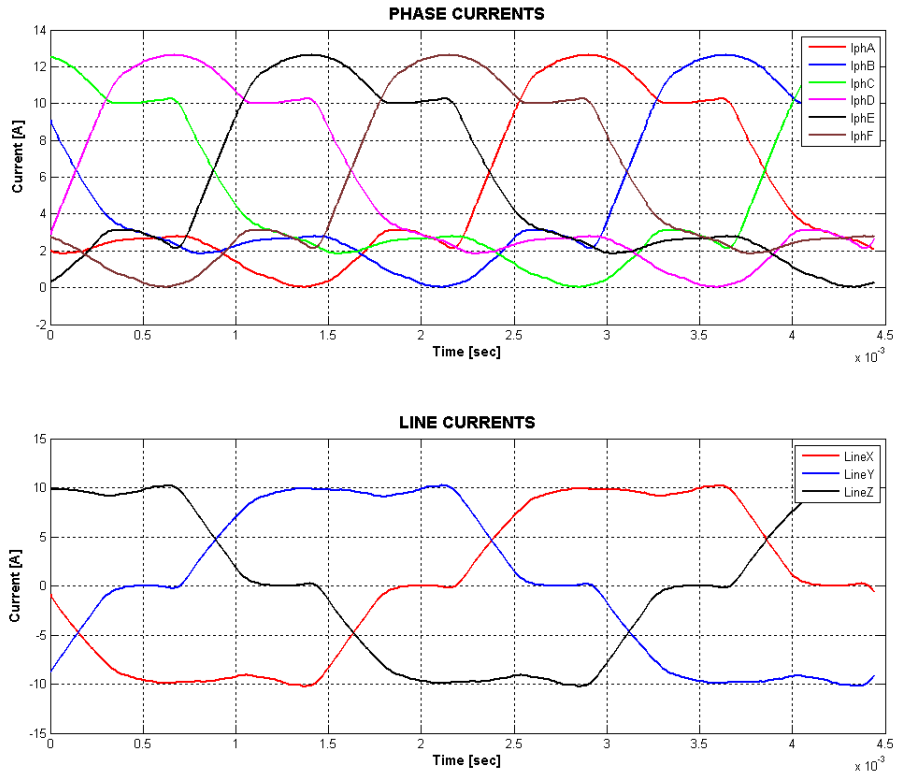

Figure 199 Phase currents (top trace) and line currents (bottom trace) with Advance Angle = 0°; Line Current Demand = 15A; Speed = 1357.47RPM; DC-Link Voltage = 175V

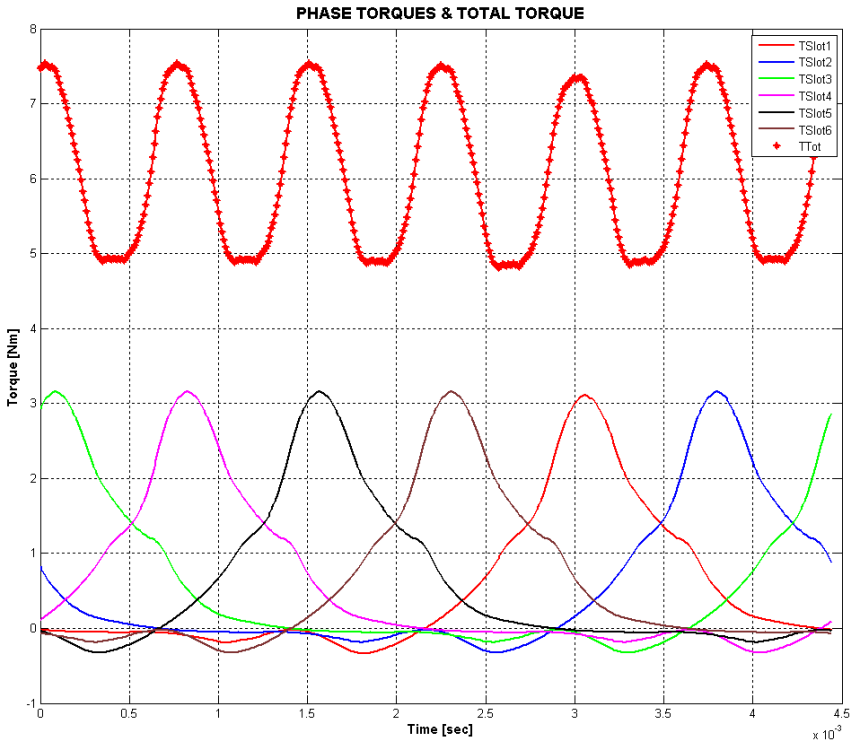

Figure 200 Instantaneous slot torques and total machine output torque (in red) with Advance Angle = 0^o; Line Current Demand = 15A; Speed = 1357.47RPM; DC-Link Voltage = 175V

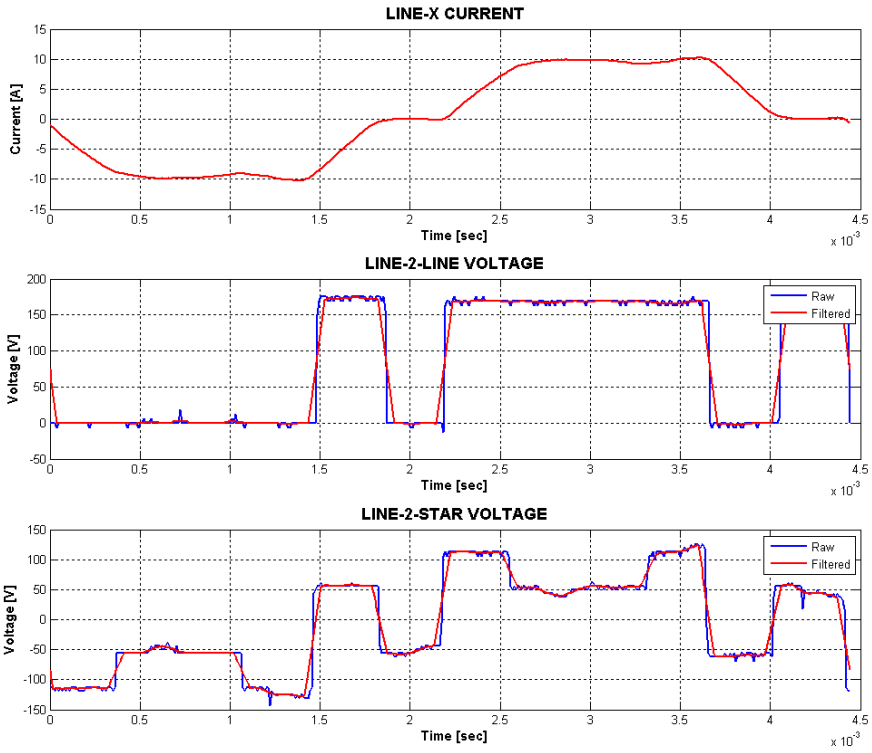

Figure 201 Line current (top trace), line-2-line voltage (middle trace) and line-2-star point voltage (bottom trace) with Advance Angle = 0^o; Line Current Demand = 15A; Speed =1357.47RPM; DC-Link Voltage = 175V

Table 36 Summary of measured and predicted performance parameters for the star-connected 6-phase segmental rotor SRM when driven from 3-phase bridge circuit with Advance Angle = 0°; Line Current Demand = 15A; Speed = 1357.47RPM; DC-Link Voltage = 175V

	MEASURED	ESTIMATED
Adv Angle [Deg.]	0	
Idemand [A]	15	
Speed [RPM]	1357.5	1348.3
Taverage [Nm]	6.4	6.0
IphRMS [A]		6.5
IphPEAK [A]		12.6
Cu Loss [W]		147.3
Tripple - MEAN [%]		45.3
Tripple - MAX [%]		36.2
Pshaft [W]	912.6	851.0
Efficiency [%]		85.2

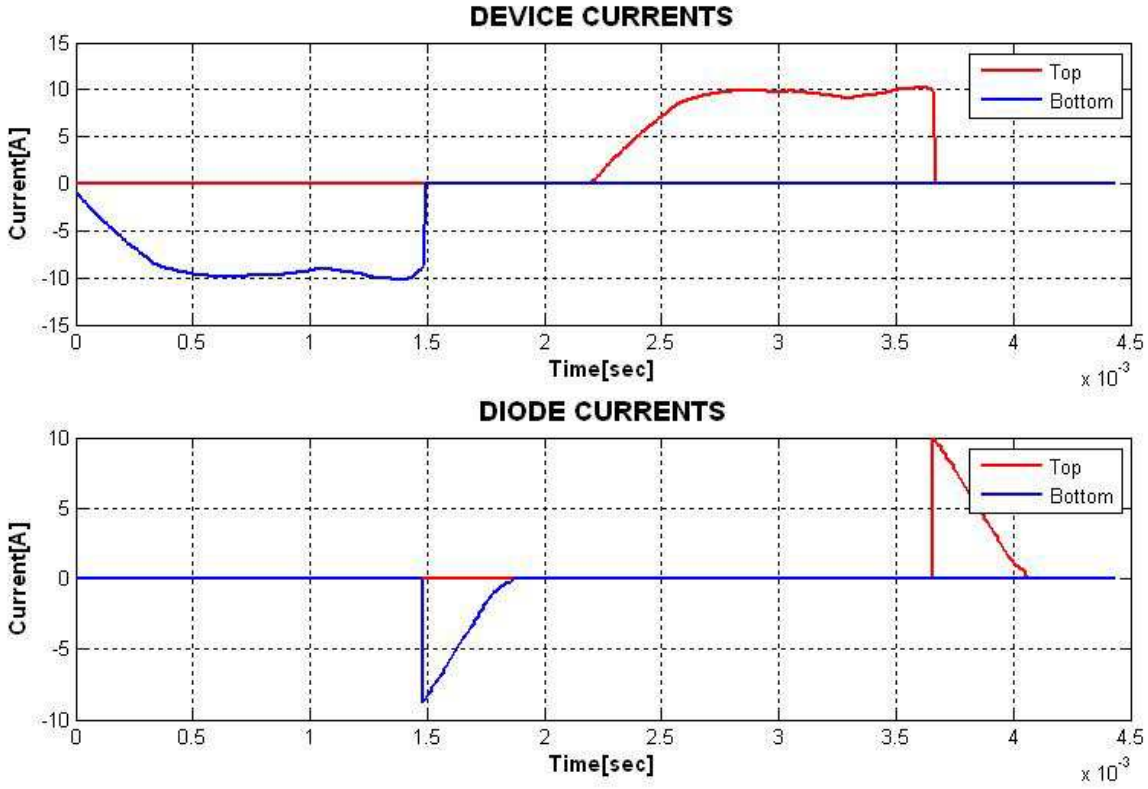

Figure 202 IGBT currents (top trace) and reverse recovery diode currents (bottom trace) based on the measured line currents presented in Figure 199

Table 37 Summary of estimated power electronic performance parameters based on measured line currents with Advance Angle = 0^o; Line Current Demand = 15A; Speed =1357.47RPM; DC-Link Voltage = 175V

Top Device RMS Current [A]	5.00
Top Device Peak Current [A]	10.22
Bottom Device RMS Current [A]	5.10
Top Device RMS Current [A]	10.24
Top Diode RMS Current [A]	1.745
Top Diode Peak Current [A]	9.92
Bottom Diode RMS Current [A]	1.41
Bottom Diode Peak Current [A]	8.72
Device VA Rating - PEAK [kVA / kW]	12.62
Device VA Rating - RMS [kVA / kW]	6.24
Diode VA Rating - PEAK [kVA / kW]	11.5
Diode VA Rating - RMS [kVA / kW]	1.95

Compared to the low speed measurements, the motor efficiency was significantly improved throughout the high speed measurements. This is again of no surprise for an SR machine running under voltage control at high speeds. Although the output torque is reduced the output power remains relatively high with speed resulting in improved motor efficiency. As the machine was running under full voltage control with all the high speed examples presented in the preceding subsections, the currents flowing through the IGBTs and the reverse recovery diodes could be determined from the line currents. Once the instantaneous IGBT and diode currents were determined, the peak and rms IGBT and diode currents and the inverter VA ratings could be calculated. These are presented in Table 31, Table 33, Table 35 and Table 37 for High Speed Measurement-1, High Speed Measurement-2, High-Speed Measurement-3, and High Speed Measurement-4, respectively. The VA ratings for the IGBTs and the diodes are very similar when the calculations are based on the device peak currents. However, there is a significant difference in VA ratings of IGBTs and recovery diodes when the rms device currents are used. This can easily be explained by analysing the device current waveforms in Figure 190, Figure 194, Figure 198, and Figure 202. The peak currents flowing through the IGBTs and the diodes are very similar in all of the four figures. However, the conduction periods of the diodes are significantly lower than IGBTs. This results in significantly less rms diode currents and hence significantly less VA ratings based on rms currents. It can be said that the correlation between the measured and estimated average torque output is very good in Table 30, Table 32, Table 34, and Table 36. The Matlab script used for post processing the measured data is still able to predict the instantaneous output torque

reasonably well, even when the operating speed of the machine is increased and the drive enters into full voltage control.

The periods where the phase currents are zero are shorter than under current control due to a reduced amount of time available to de-flux the phase and at the same time control the line currents. The torque waveforms appear to be peaky with more negative torque generated. As a result, the torque ripple is higher at high speeds than low speeds. This is typical of high speed operation where the torque ripple is compromised in order to achieve high average output torque. The flux vs. MMF loci of all four high speed measurements are displayed against the aligned and unaligned magnetisation curves (see Figure 175) of a single slot in Figure 203.

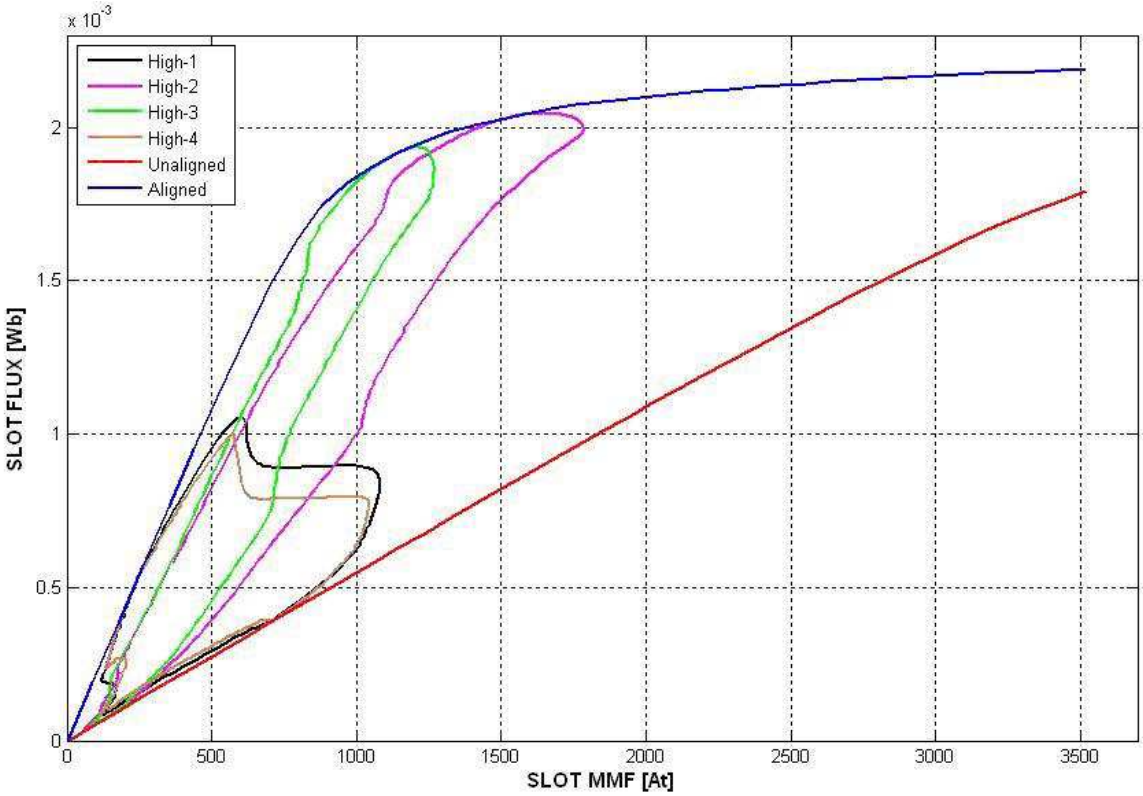

Figure 203 Flux vs. MMF loci for the high speed measurements

Attempts for simulating the six-phase drives with mutually coupled phase windings have been unsuccessful. The following points have yet to be resolved:

- Switching states and phase voltages / phase diode states when the phase currents fall to zero.

- Star point voltage. When there is no mutual coupling a vector definition of the star point voltage has been successful. However, the same approach has not been successful when simulating the machine with mutually coupled phase windings.

- Transformation matrices. As the simulation model has not been successful it is unknown how well the transformation matrices represent the machine dynamics.

9.4 SUMMARY

A method of keeping the size and cost of the power electronics down and increase the number of phases in an attempt to reduce the output torque ripple of SRM drives is to make use of the 3-phase full-bridge circuit and drive a 6-phase machine. To achieve unipolar phase currents additional phase diodes were connected in series with each phase winding. A pair of phases was connected back-to-back to form a module of phases. Three current transducers were required to achieve control of the drive system based on line currents. Each line current control required separate PID and PWM controllers.

Simulation of the six-phase SRM from a 3-phase full bridge circuit has been successfully achieved when the phase windings were magnetically de-coupled. Unfortunately the simulation of the 6-phase machine with magnetically coupled phase windings could not be finalised and verified against measurements. Although the waveforms from the simulation models of the star and delta connected 6-phase drives with magnetically de-coupled phases looked favourable they need to be validated against measurements in future work.

Using the test rig explained in *Chapter 5 – Machine Construction Techniques and Test Rig Description* the star-connected six phase segmental rotor SRM has been successfully driven from the 3-phase full bridge circuit. The line currents were the controlled parameters.

The machine was run under voltage and current control and the measurements have been presented. Matlab® scripts were written to analyse captured waveforms. The scripts were able to estimate some of the performance parameters such as phase RMS currents, running speed (from the period of phase current), instantaneous phase torques, average total output torque, torque ripple, shaft power and total machine copper losses (assuming

steady-state winding temperature of 100^{o}C). Although estimated performance parameters were based on the 2D FE simulated flux-MMF characteristics of a slot of the machine, the predicted values for the average total output torque correlated reasonably well with the measurements when the machine was run at both high and low speeds.

It is believed that the higher-than-expected torque ripple values experienced with the 6-phase segmental rotor SRM drive were due to the slot MMF pattern resulting in peaky output torque characteristics. Unlike the conventional toothed rotor SRMs, where stator tooth permeance is regulated by the positioning of the rotor teeth, for the segmental rotor SRM the slot permeance is regulated by the position of the rotor segments. Therefore in terms of machine torque, the total output torque is the sum of the individual slot torques as opposed to the sum of the individual tooth torques in the conventional toothed rotor SRM.

CHAPTER 10

10 – Comparison of Machines and Drives

10.1 ELECTROMAGNETIC PERFORMANCE COMPARISON

This section summarises the comparison made between the 6-phase segmental and toothed rotor SRMs with 12 stator teeth and 10 rotor poles and the 3-phase single-tooth winding (also a 12-10 machine) segmental rotor SRM. Comparisons given in this section of the chapter are based on finite element analysis obtained for each machine and are based on torque per copper loss. For the sake of comparison it is assumed that the phase currents are under perfect current control for each machine (illustrated for 6-phase machines in Figure 204 and for 3-phase machine in Figure 205).

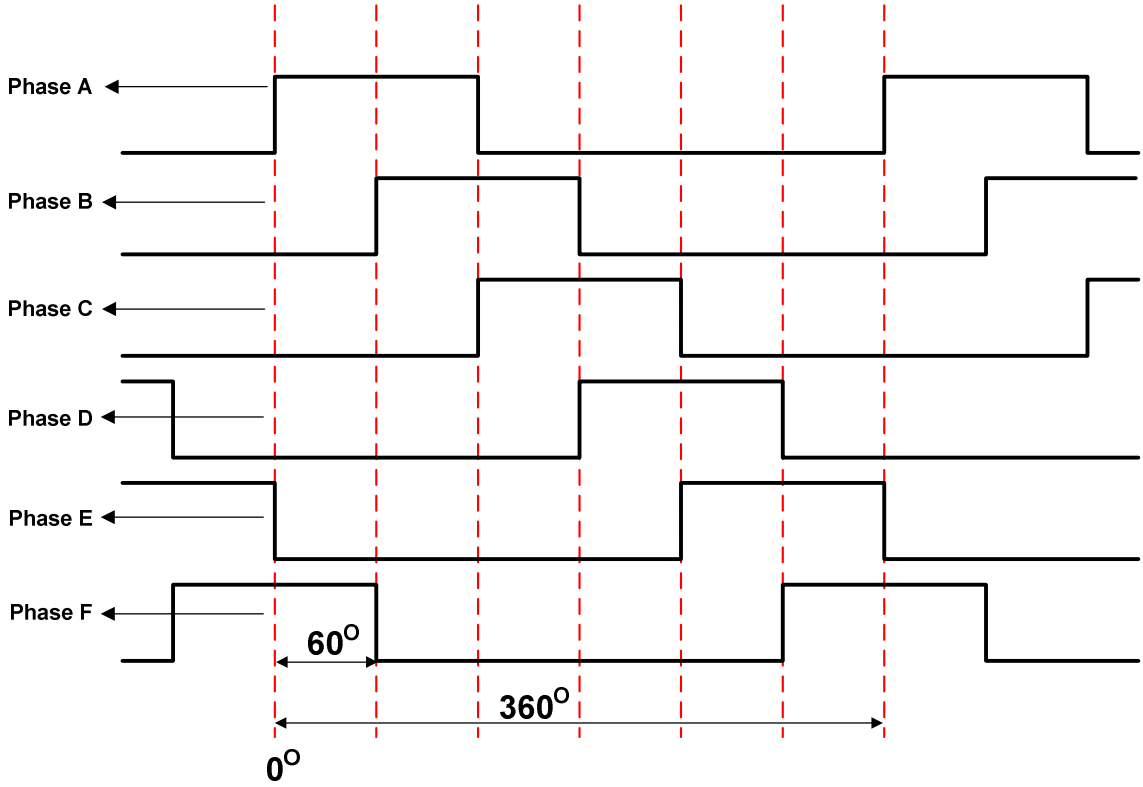

Figure 204 6-phase 12-10 SRM phase current waveforms under perfect current control

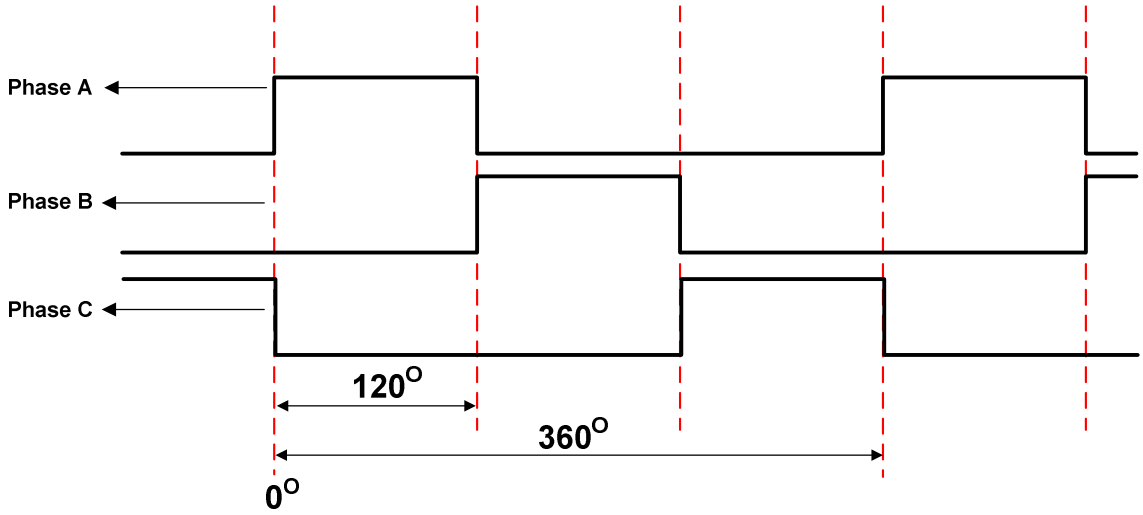

Figure 205 3-phase 12-10 SRM phase current waveforms under perfect current control

10.1.1 Number of turns per slot, slot fill factor and conductor diameter as designed

In this section comparison will be made based on the ability to produce torque for a given total copper loss. Measured phase resistances are used throughout except for the 6 phase conventional SRM, which was not completed. Total average torque has been calculated by

$$Torque = \left(A\_Pos(X) - A\_Pos(X - \frac{360^o}{Nph * Nr}) \right) \times \frac{Nph \times Nr}{2 \times \pi} \qquad \textbf{Equation 36}$$

where $A\_Pos(X)$ is the area below the magnetisation curve at X degrees after the unaligned position, $A\_Pos(X - \frac{360^o}{Nph * Nr})$ is the area below the magnetisation curve at $(X - \frac{360^o}{Nph * Nr})$ after the unaligned position, Nph is the number of phases, and Nr is the number of rotor poles.

Torque per unit copper loss for each machine has been tabulated in Table 38.

Table 38 Summary of torque per copper loss as per machine design for the 6-phase and 3-phase segmental and 6-phase conventional machines

	6-phase Segmental	3-phase Segmental	6-phase Conventional
Conductor Diameter [mm]	1.40	1.00	1.40
Slot Fill Factor [%]	49.51	40.98	48.86
Number of Turns per Slot	88.00	135.00	100.00
Phase Resistance [Ω]	0.44	2.56	0.45
Total Copper Loss [W]	**300.00**	**300.00**	**300.00**
Iphase [A]	**18.48**	**10.83**	**18.17**
Max Torque [Nm]	**20.99**	**28.72**	**22.81**
Torque per Copper Loss [Nm / W]	**0.0700**	**0.0957**	**0.0760**

In Table 38 each machine is given as they are designed and it is obvious that each has a different slot fill factor and number of turns. According to Table 38, the 3-phase segmental machine is able to produce approximately 36.8% more torque per copper loss than the 6-phase segmental machine. Also the 6-phase conventional machine is able to generate approximately 8.7% more torque per copper loss than the 6-phase segmental machine.

10.1.2 Number of turns per slot, slot fill factor kept the same

In this case the number of turns per slot and the slot fill factor of all three machines have been fixed to those of the 3-phase segmental machine (135 turns per slot and 41% slot fill factor). Table 39 summarises the torque per copper loss comparison.

Table 39 Comparison of torque per copper loss of 6-phase and 3-phase segmental and 6-phase conventional machines for fixed number of turns per slot and slot fill factor

	6-PHASE SEGMENTAL	3-PHASE SEGMENTAL	6-PHASE CONVENTIONAL
Total Available Slot Area [mm ^ 2]	273.59	258.74	315.06
Nturns	136	135	136
Intended Slot Fill Factor	0.41	0.41	0.41
Conductor CSA [mm ^ 2]	0.82	0.79	0.95
Calculated Dcond [mm]	1.0248	1.0003	1.0997
Realistic Dcond [mm]	1.00	1.00	1.10
Achieved Slot Fill Factor	0.39	0.41	0.41
PHASE RESISTANCE [Ω]	**1.37**	**2.56**	**1.02**
TOTAL COPPER LOSS [W]	**300.00**	**300.00**	**300.00**
PHASE CURRENT [A]	**10.46**	**10.83**	**12.12**
MAXIMUM TORQUE [Nm]	**17.59**	**28.72**	**19.63**
TORQUE per unit COPPER LOSS [Nm]	**0.0586**	**0.0957**	**0.0654**

According to Table 39, the 3-phase segmental machine is able to produce approximately 63.3% more torque per copper loss than the 6-phase segmental machine. The 6-phase segmental machine is still inferior to the 6-phase conventional machine, this time, by approximately 11.6%.

The performances of the machines can also be compared using MMF vs. flux characteristics. The numbers of turns per coil, the number of active coils and the stator tooth widths for all three prototype machines are tabulated in Table 40.

Table 40 Number of turns, number of active coils and stator tooth widths of all three machines

	6-phase Segmental	3-phase Segmental	6-phase Conventional
Number of Turns per Coil	68	135	68
Active Number of Coils	4	2	4
Stator Tooth Width - Narrow [mm]	n/a	10	n/a
Stator Tooth Width - Wide [mm]	12.68	20	11.41

As both the segmental and conventional rotor 6-phase machines have two phases conducting at any one time, the number of active machine coils is 4 for both machines. Only the wide teeth of the 3-phase segmental rotor machine are wound resulting in 2 active coils at any one time. In order to have the same MMF in each machine, the numbers of turns per coil of both 6-phase machines are adjusted to 68. The coils of each machine are energised in 2D FE and the MMF vs. flux curves in the aligned and unaligned rotor positions are plotted for each machine in Figure 206.

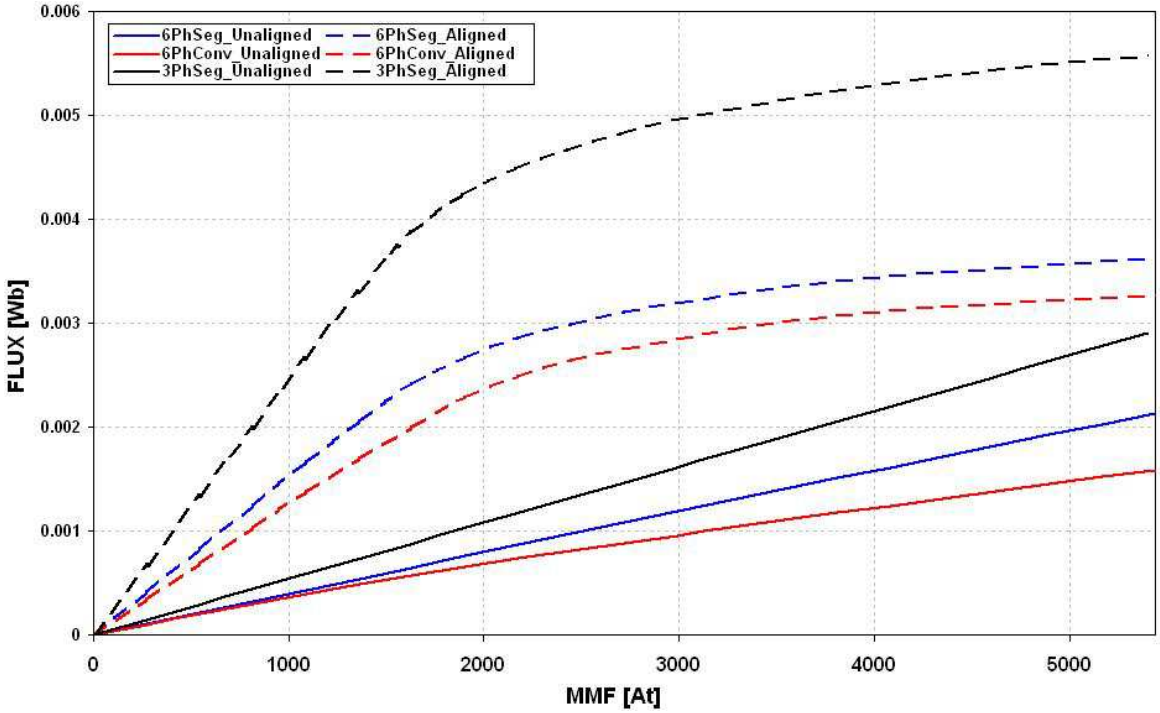

Figure 206 MMF vs. flux plots of the 3-phase segmental (in black), 6-phase segmental (in blue) and 6-phase conventional (in red) rotor machines in the aligned and unaligned (dotted curves) positions

From Figure 206, the area between the aligned and unaligned curves can be calculated and used to assess the output torque capability of each machine. This is tabulated in Table 41.

Table 41 Table of the areas covered by the magnetisation curves of all three machines

	6-phase Seg	3-phase Seg	6-phase Conv
AREA between ALIGNED and UNALIGNED curves	8.54	14.4	8.05

According to Table 41, the 3-phase segmental machine is approximately 68.0% better than the 6-phase segmental and the 6-phase segmental is only about 6.0% better than the 6-phase conventional machine. In Figure 206, it is clear that the saturation point of the aligned magnetisation curve of the 3-phase machine is considerably higher than those of the 6-phase machines. This is due to the difference in the stator tooth widths of the machines (Table 40). The linear inductances of the 3-phase segmental machine in the aligned and unaligned positions are also considerably higher than those of the 6-phase machines. This can be explained with the help of Figure 207. In Figure 207, the flux plots

of all three machines are presented in the aligned position. Clearly, the overlap between the stator teeth (slots) and the rotor segments of the 3-phase segmental machine is considerably larger than that seen in the segmental and conventional rotor 6-phase machines resulting in increased linear inductance in the aligned and unaligned rotor positions for the 3-phase machine.

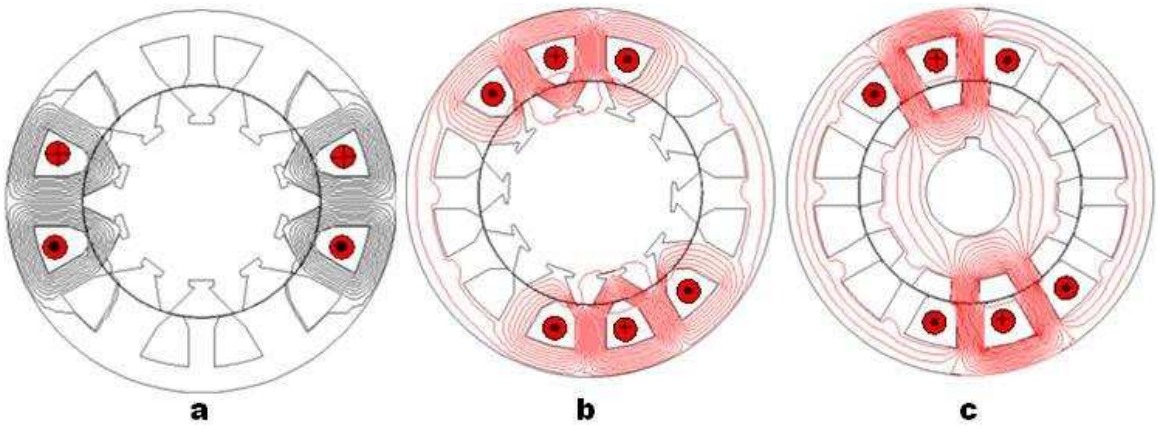

Figure 207 2D flux plots of a-) 3-phase segmental rotor b-) 6-phase segmental rotor c-) 6-phase conventional rotor machines in the aligned position

It is apparent from the analysis above that the 6-phase segmental machine is not significantly better than its conventional counterpart. This is believed to be due to the machine design; having short pitched coils wound around each stator teeth. Note that a machine design approach similar to that of the 3-phase single-tooth segmental rotor design could be undertaken with the 6-phase segmental machine, where the machine stator could be formed by narrow and wide teeth and coils wound only around the wide ones. However, this would result in unbalanced forces during machine operation, increasing noise and vibration of the machine and reducing bearing life.

10.2 TORQUE RIPPLE COMPARISON OF THREE AND SIX PHASE DRIVES

In chapters 7, 8 and 9 measured waveforms for the 2-phase, 3-phase and 6-phase drives were used to estimate the instantaneous total machine output torque waveforms. The estimated waveforms were verified against measurements by comparing the values for speed and total average torque output. The aim of this PhD project was to achieve a low torque ripple SRM drive without the need for complicated control algorithms and / or expensive and complicated power electronics. It is quite apparent (and as expected) from the waveforms and tables given in the preceding chapters (7, 8 and 9) that the two-phase drive has the highest torque ripple. However comparing the instantaneous torque waveforms of the 3-phase segmental machine driven from the asymmetric half-bridge inverter to those of the 6-phase segmental machine connected in star and driven from the 3-phase bridge circuit the conclusion is not as apparent as one expects. Out of the four examples given for the 3-phase segmental rotor drive driven from the asymmetric half-bridge inverter the one with the highest conduction angle has the lowest torque ripple. This is not unexpected, as an increased conduction angle results in increased overlapping between torque contributions of individual phases. Higher conduction angles are advantageous for reducing the machine output torque ripple but result in increased copper losses and potentially reduced average torque output per copper loss. The other two examples given for the 3-phase drive where the torque ripple is relatively high are when the conduction angles are as low as (approximately) 120^o.

The star connected 3-phase full bridge circuit driven 6-phase machine is restricted to 120^o conduction angle. Comparing the 3-phase drive example with the high conduction angle of 164.6^o to the high and low speed examples given for the 6-phase star connected drive examples suggest that in terms of torque ripple, no considerable gain has been achieved with designing and using a 6-phase machine. Arriving to a final conclusion based on one example would not be justifiable. Therefore, theoretical analysis of the average total torque, torque ripple and copper loss of the 3-phase and the 6-phase 12-10 segmental rotor machines has been carried out in Matlab® by a simple m-file script simulation. The analysis was extended to include the 6-phase 12-10 machine with conventional toothed rotor. The analysis assumes that all of the machines are under perfect current control and have the pattern shown in Figure 208.

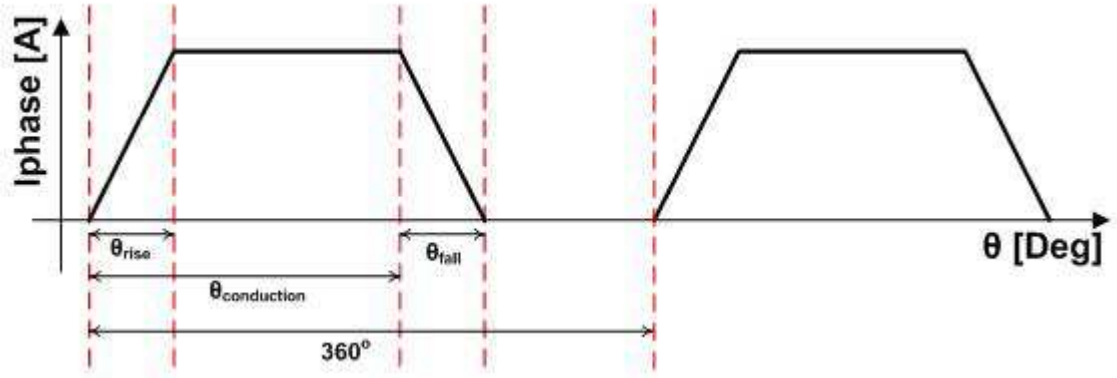

Figure 208 Assumed phase current pattern for the torque ripple comparison study

In Figure 208:

θ_{rise} is the angle corresponding to the rise time for the phase current from zero to the demand level. This is set to 20^o for all of the machines.

$\theta_{conduction}$ is the conduction angle. This is fixed at 120^o for the six phase drives driven from the 3-phase full bridge circuit.

θ_{fall} is the angle corresponding to the fall time for the phase current from the demand level back down to zero. This is again set to 20^o for all of the machines.

As introduced in the previous chapter, the total output torque of the 6-phase segmental drive is the sum of the contribution of each slot torque. Therefore the slot MMF pattern of the 6-phase segmental drive has a direct contribution to the instantaneous output torque waveform and hence the machine output torque ripple. The stator slots of the 6-phase segmental rotor machine share windings of two adjacent phases. Once the phase current demand is defined as given in Figure 208 the slot MMF pattern has the form depicted in Figure 209. This is significantly different to the phase current pattern in Figure 208 that is useful for the 6-phase conventional and 3-phase segmental rotor machines. In Figure 209, as each phase is energised for 120^o, each slot is energised for 200^o in total.

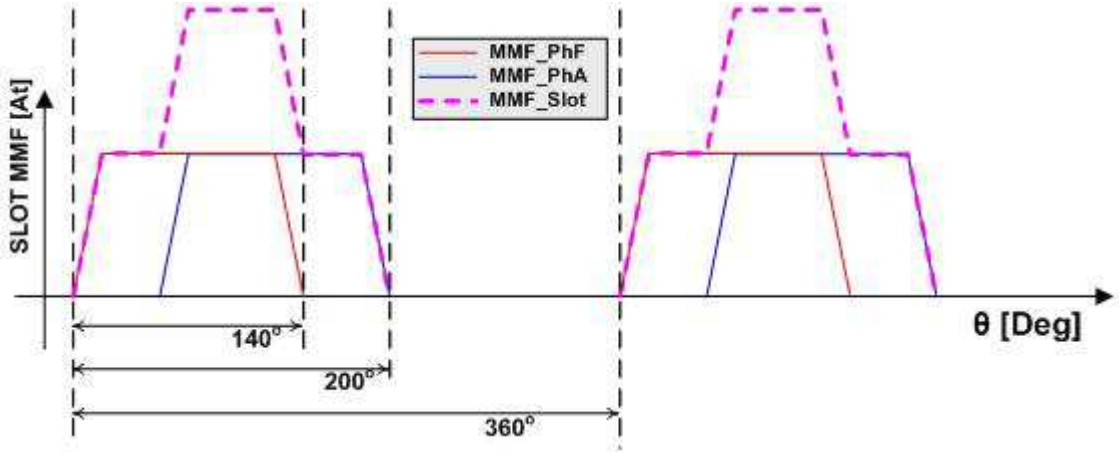

Figure 209 Graphical explanation of the total conduction period for the slot MMF

The Matlab® script was configured to go through batch-runs where advance angle, conduction angle and current demand could be varied over a wide range of values for each machine. The set-ups for batch-runs for each machine are given below:

1. ***6-phase 12-10 Segmental Rotor Machine:***
   Conduction angle was fixed at 120^o. Advance angle was varied from -60^o to $+60^o$ and current demand from 5A to 40A, respectively.

2. ***3-phase 12-10 Segmental Rotor Machine:***
   Conduction angles of 120^o, 150^o and 180^o were analysed. For each conduction angle advance angle was varied from -60^o to $+60^o$ and the current demand from 2A to 28A.

3. ***6-phase 12-10 Conventional Toothed Rotor Machine:***
   Conduction angle was first fixed at 120^o and then 150^o was analysed in order to asses the improvement in output torque ripple with higher values of conduction angle. Similar to the 6-phase segmental machine, advance angle was varied from -60^o to $+60^o$ and the current demand from 5A to 40A.

The results heavily depend on the magnetic characteristics of the machine. In order to have a fair comparison, the magnetic characteristics for each machine should be generated by using the same method, i.e. FE or measurements (assuming FE models and measurements for each machine have similar accuracy). The analysis presented in this

section uses the magnetic characteristics for all machines generated from 2D FE analysis. Also it is assumed that from one machine to the next, the errors in magnetic characteristics are not a significant factor on the final results, i.e. all FE models have sufficient detail to achieve similar amounts of accuracy. Although already presented in the relevant chapters, it is beneficial to have the static torque characteristics of each machine in this chapter as well in order to aid with the understanding of the torque ripple comparison analysis. The static torque characteristics of the 6-phase segmental, 6-phase conventional and 3-phase segmental rotor machines are presented in Figure 210, Figure 211 and Figure 212, respectively. The static torque characteristics of the 6-phase segmental rotor machine in Figure 210 are therefore given for a single slot.

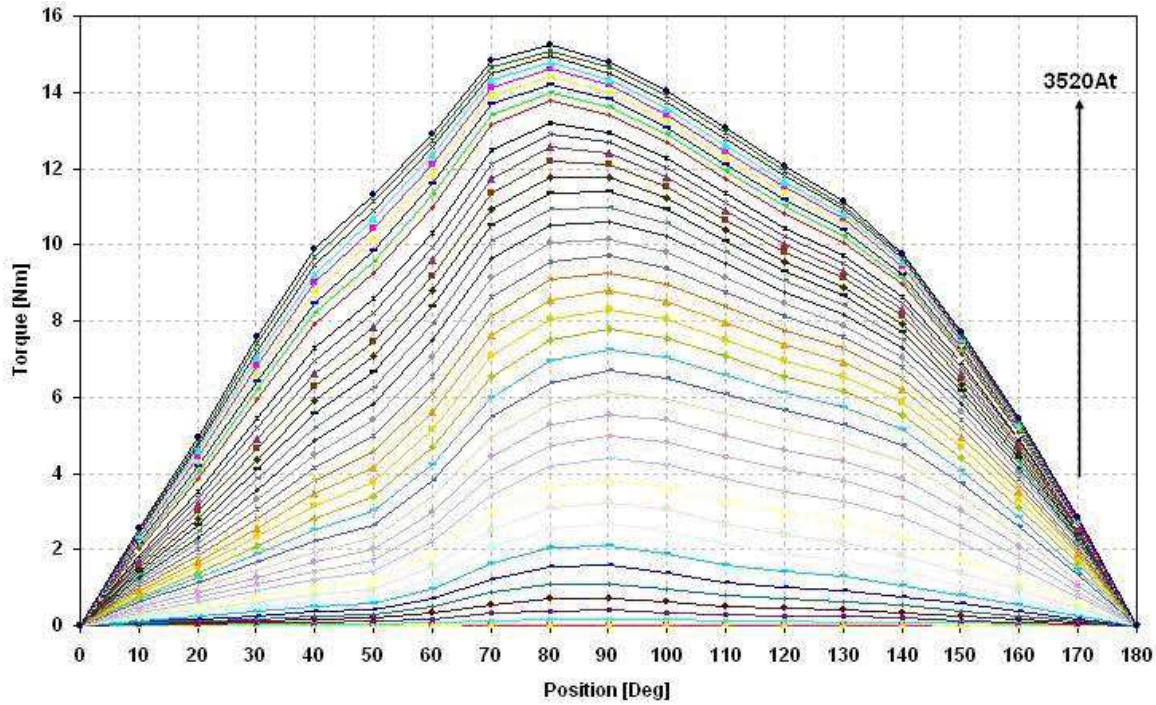

Figure 210 Static torque characteristics of the 6-phase 12-10 segmental rotor machine from 0At to 3520At

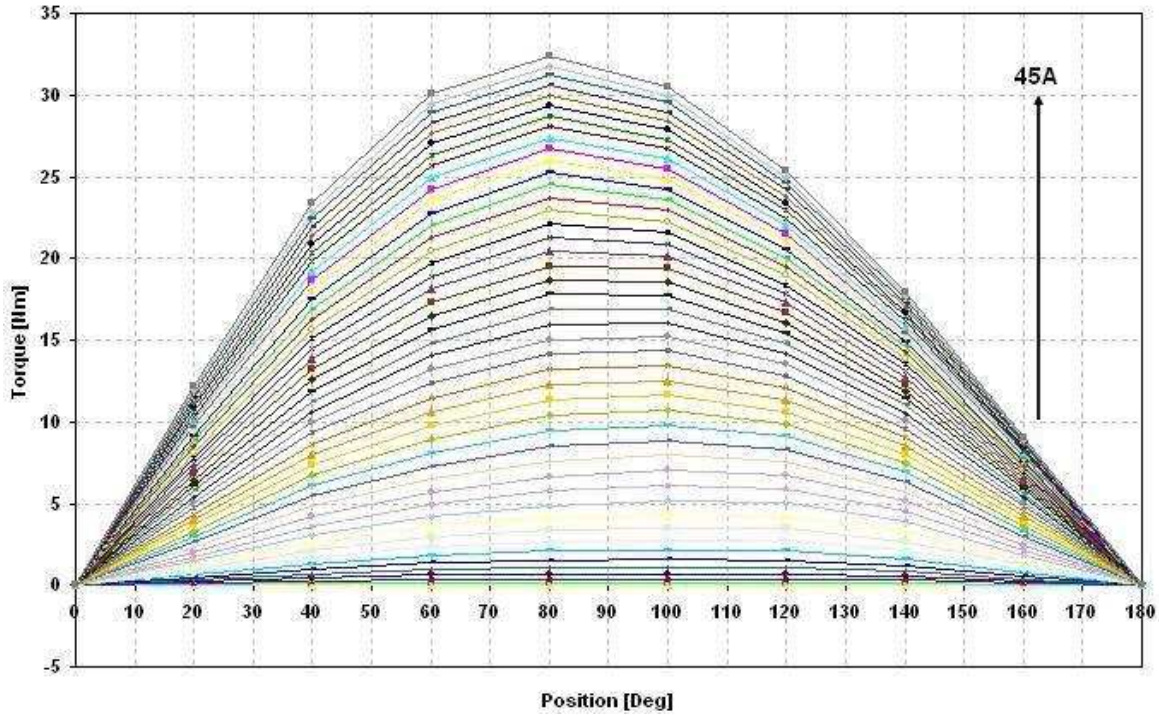

Figure 211 Static torque characteristics of the 6-phase 12-10 conventional rotor machine from 0A to 45A

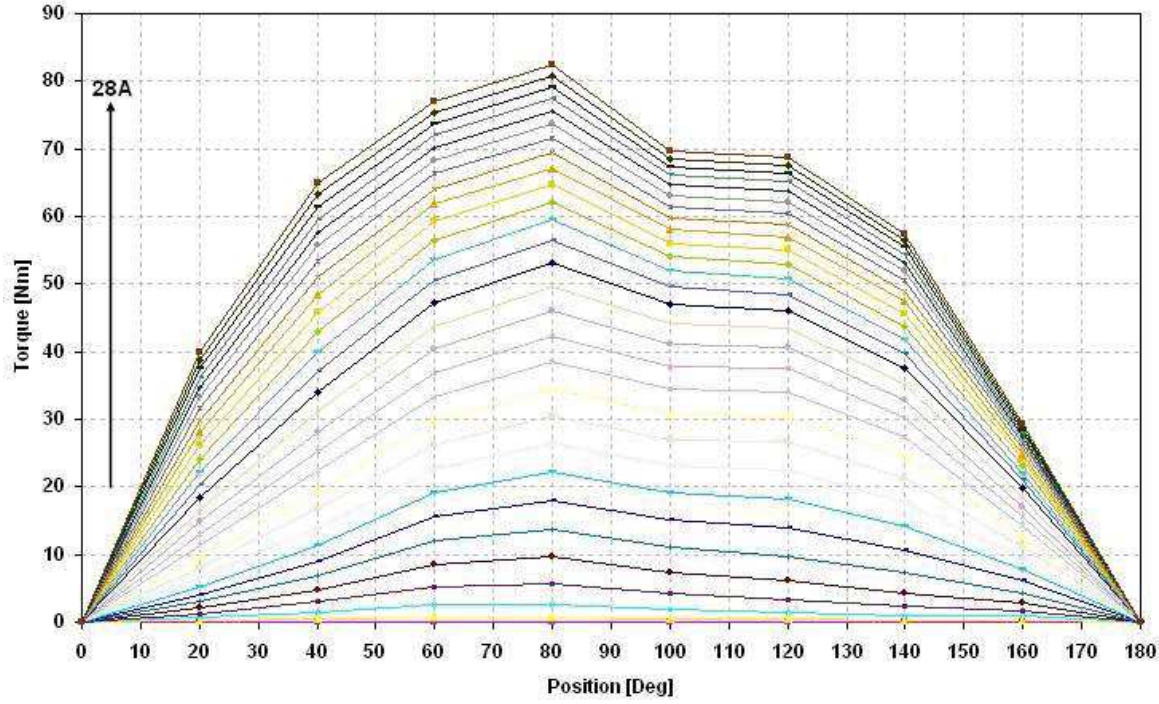

Figure 212 Static torque characteristics of the 3-phase 12-10 single-tooth winding segmental rotor machine from 0A to 28A

It is clear from the figures presented above that the 6-phase machine with a conventional rotor has more sinusoidal static torque characteristic compared to both the 3-phase and 6-phase segmental rotor machines. Moreover, at low excitation levels, as the magnetic permeance rises almost linearly with angle of overlap of the teeth, torque is almost constant. In the segmental machines, as the area of overlap on one side of the magnetic circuit increases, it decreases on the other resulting in non-constant torque even at low excitation levels [12]. At high excitation levels, the difference in the static torque characteristics of a segmental and a conventional machine is small.

The results are then used across a range of torque values to find the minimum torque ripple which can be achieved with each drive. The process is explained in a simple flow-chart format in Figure 213.

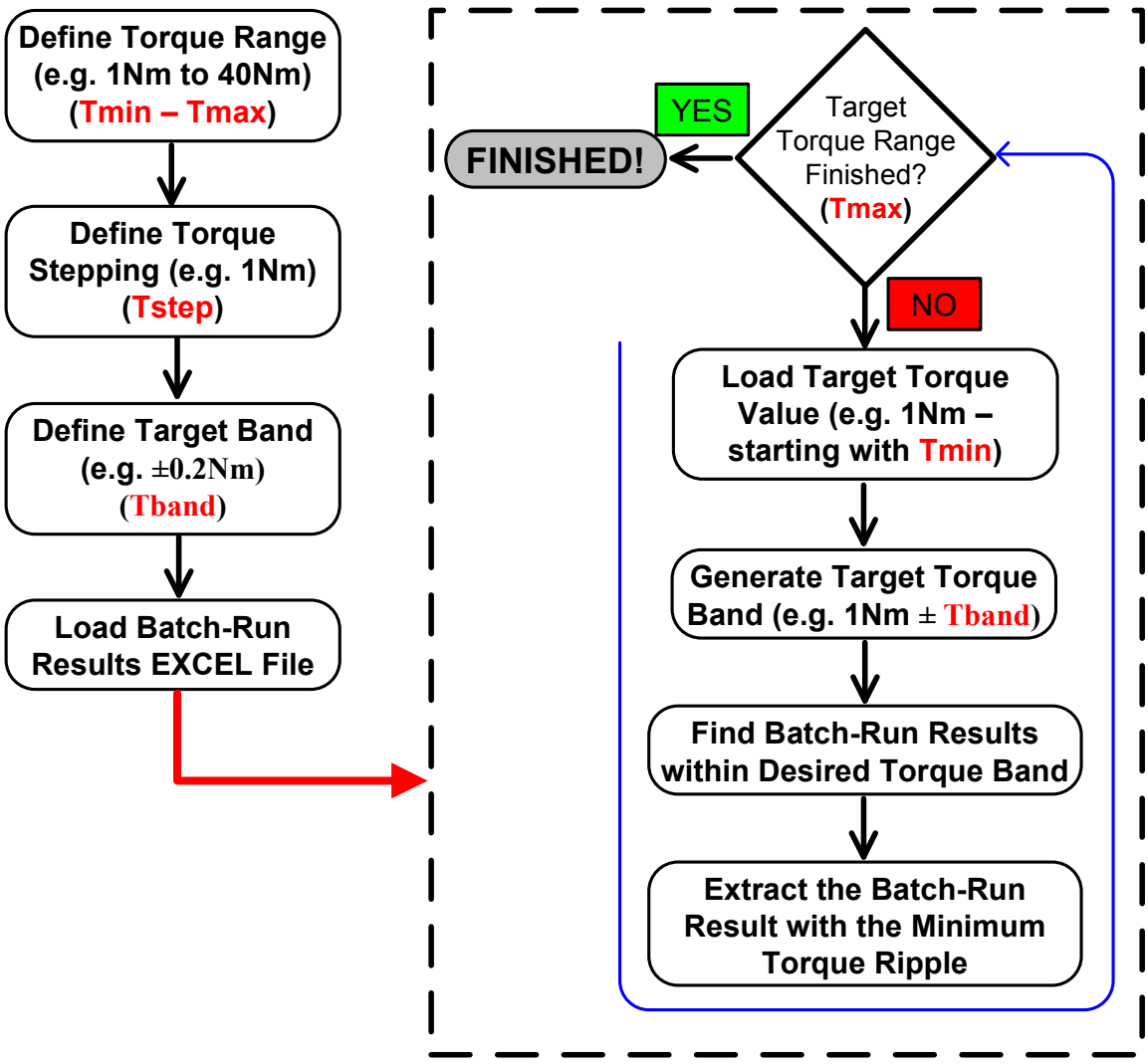

Figure 213 Simple flow-chart explanation of the Matlab® script analysing the batch-run results of the perfect current control simulation

In Figure 214 a graphical comparison of torque ripple against average output torque for the 6-phase segmental, 3-phase segmental and 6-phase conventional 12-10 SRM drives is given. The results are shown from 6.0Nm up to 43.0Nm of average output torque. In Figure 215 and Figure 216, the variations of demand current and the advance angle corresponding to each point in Figure 214 are given. In Figure 216 negative advance angle corresponds to energisation before the unaligned rotor position whereas positive advance angle corresponds to energisation after the unaligned rotor position.

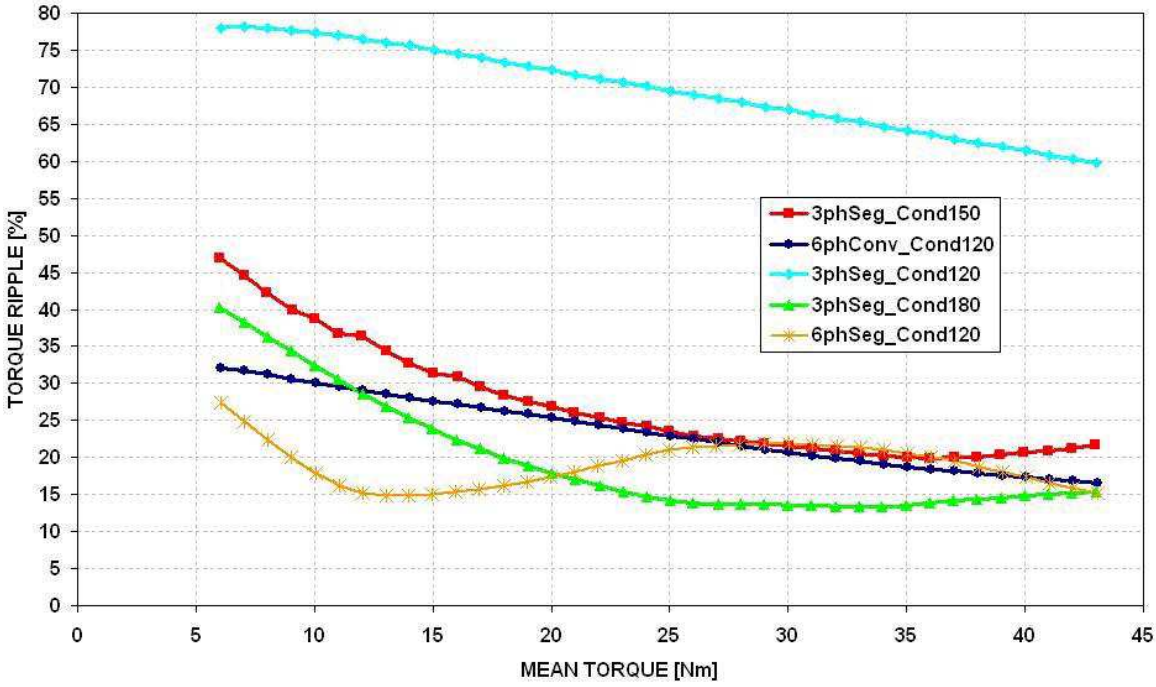

Figure 214 Torque ripple vs. average output torque characteristics for the 6-phase conventional toothed rotor drive, 6-phase segmental rotor drive and 3-phase segmental rotor drive (with three different conduction angles)

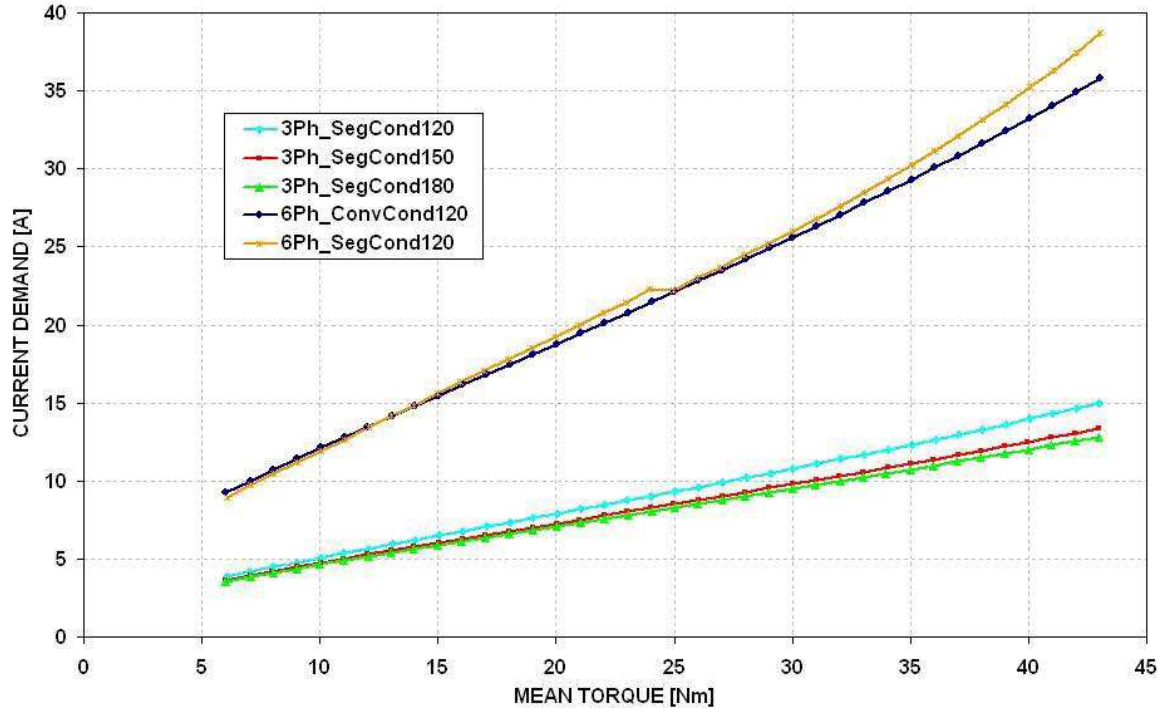

Figure 215 Current demand vs. average output torque characteristics for the 6-phase conventional toothed rotor drive, 6-phase segmental rotor drive and 3-phase segmental rotor drive (with three different conduction angles)

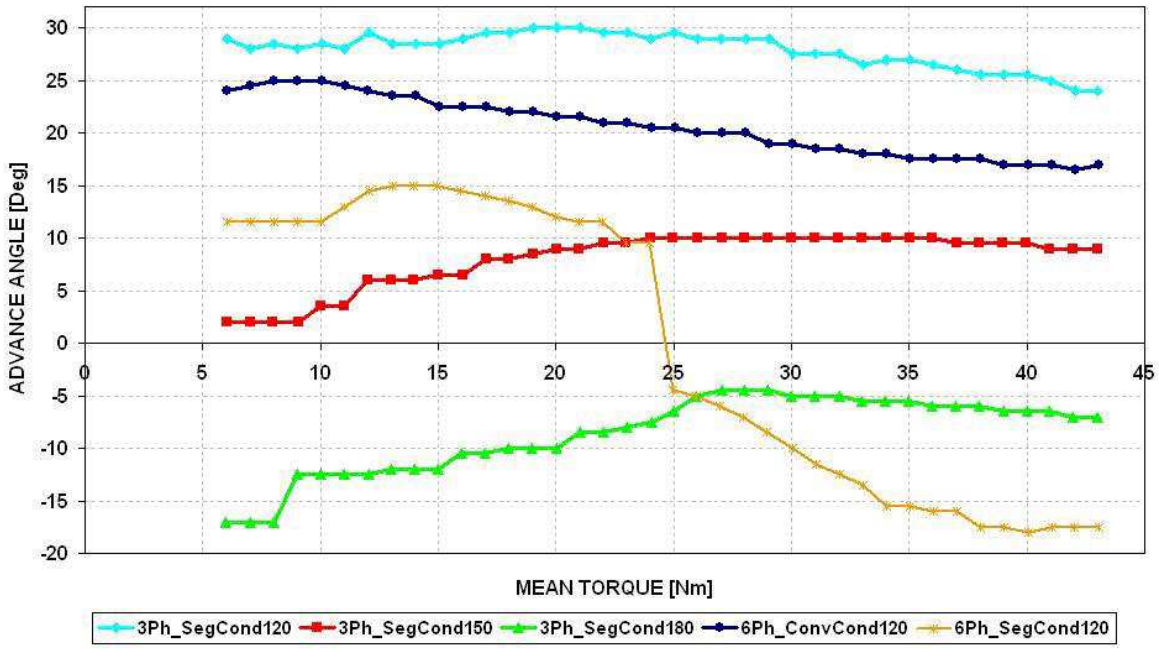

Figure 216 Advance angle vs. average output torque characteristics for the 6-phase conventional toothed rotor drive, 6-phase segmental rotor drive and 3-phase segmental rotor drive (with three different conduction angles)

In terms of output torque ripple, the following can be concluded from the above figures:

- The 6-phase conventional machine suffers from restricted conduction angle of 120^o. If the conduction angle could be further increased the torque ripple would be further reduced for the 6-phase conventional drive. Of course increased conduction angle will inevitably result in increased copper losses and consequently reduce the average output torque per unit machine copper loss.
- The 6-phase segmental machine suffers from the two-stage slot MMF pattern which results in peaky output torque characteristics. This is demonstrated with a theoretical example in Figure 217.
- The 3-phase segmental machine with 120^o conduction angle is significantly worse than both of the 6-phase drives. However, when the conduction angle of the 3-phase drive is increased beyond 120^o the torque ripple characteristics of the 3-phase segmental drive improve dramatically. When the conduction angle is set to 1/2 of an electrical cycle for the 3-phase drive, it is able to compete very well against both 6-phase drives throughout the torque range demonstrated in Figure 214.
- In reality, higher torque can be achieved under current control at low speeds and lower torque under voltage control at high speeds. The conduction angle is generally limited to 120^o under current control in order to maximise the torque per copper loss. This can compromise the torque ripple characteristic of the 3-phase drive as it is likely to have more torque ripple than that shown in Figure 214 at higher torque levels.
- In the first part of this chapter, it was shown that both the conventional and the segmental rotor 6-phase drives are significantly inferior to the 3-phase segmental drive in terms of torque per copper loss. As a result, the 3-phase drive is able to achieve the same output torque with significantly less current (see Figure 215) even with 120^o conduction. If all three drives were designed to have similar output torque capability the author believes that the torque ripple difference between the 6-phase and 3-phase drives would be more pronounced even when the phases of the 3-phase drive were energised for longer periods of time. Of course, this would result in a significantly smaller 3-phase machine design.

- The 6-phase segmental rotor machine still performs better than the 3-phase drive with 180^o conduction up to 20Nm. This is believed to be the result of having 200^o of effective slot energisation due to 120^o of phase energisation, which results in significant overlap between individual slot torques. On the other hand, the 6-phase conventional machine is better than the 3-phase drive with 180^o conduction only up to 11Nm.
- As seen in Figure 214, the torque ripple characteristics of the 6-phase and 3-phase segmental drives (at 150^o and 180^o) first reduce with increased average output torque and then increase. This is believed to be a result of the static torque characteristics of both of the segmental machines. The trend is more pronounced with the 6-phase segmental drive but can also be seen in the 3-phase drive, especially when the conduction angle is changed to 180^o (only the beginnings of this characteristic can be seen in the 3-phase drive with 180^o).

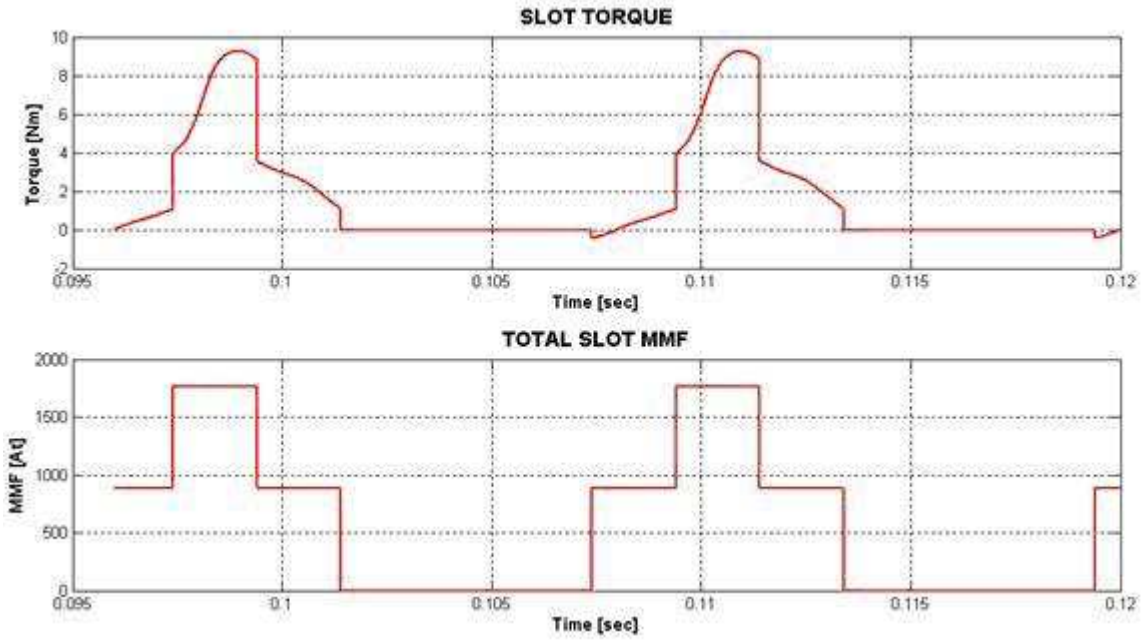

Figure 217 a-) Instantaneous slot torque (top trace) and slot MMF (bottom trace) waveforms for the 6-phase segmental rotor drive with ~47% torque ripple

The idea of what would happen to the torque ripple if the conduction angle of the 6-phase drives could be increased beyond 120^o was investigated using the 6-phase conventional toothed rotor machine. For this purpose, the conduction angle of this machine was further increased to 150^o. The results are illustrated from Figure 218 to Figure 220.

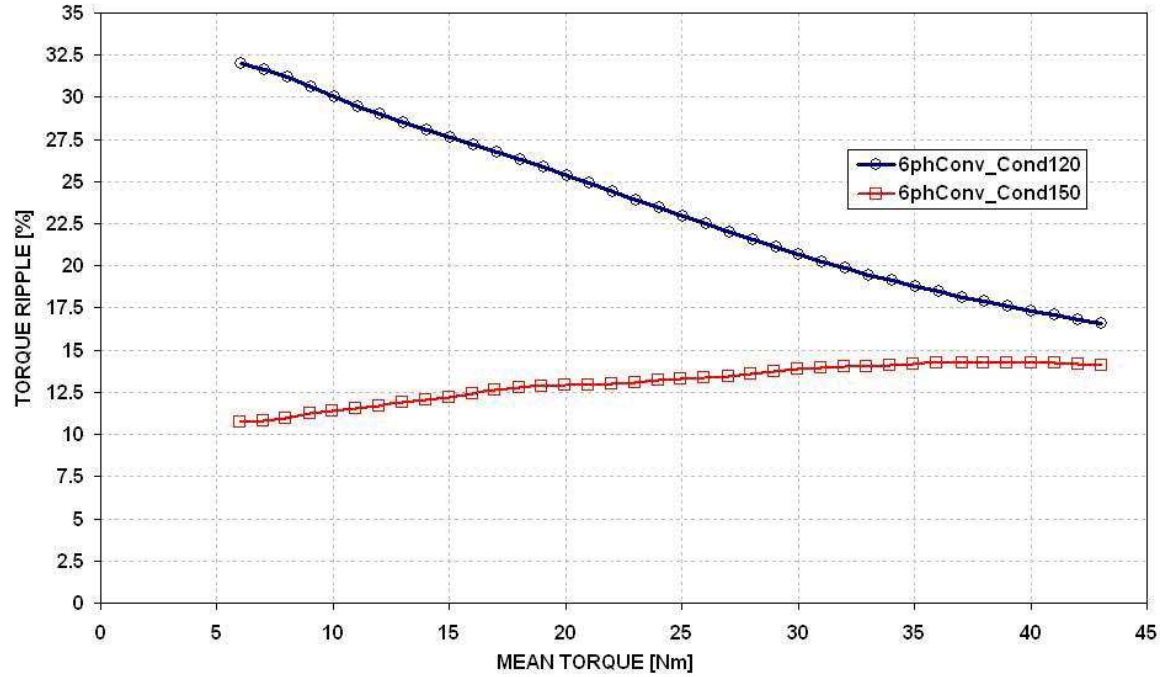

Figure 218 Torque ripple vs. average output torque characteristics for the 6-phase conventional toothed rotor drive. Blue trace when conduction angle = 120^o and red trace when conduction angle = 150^o

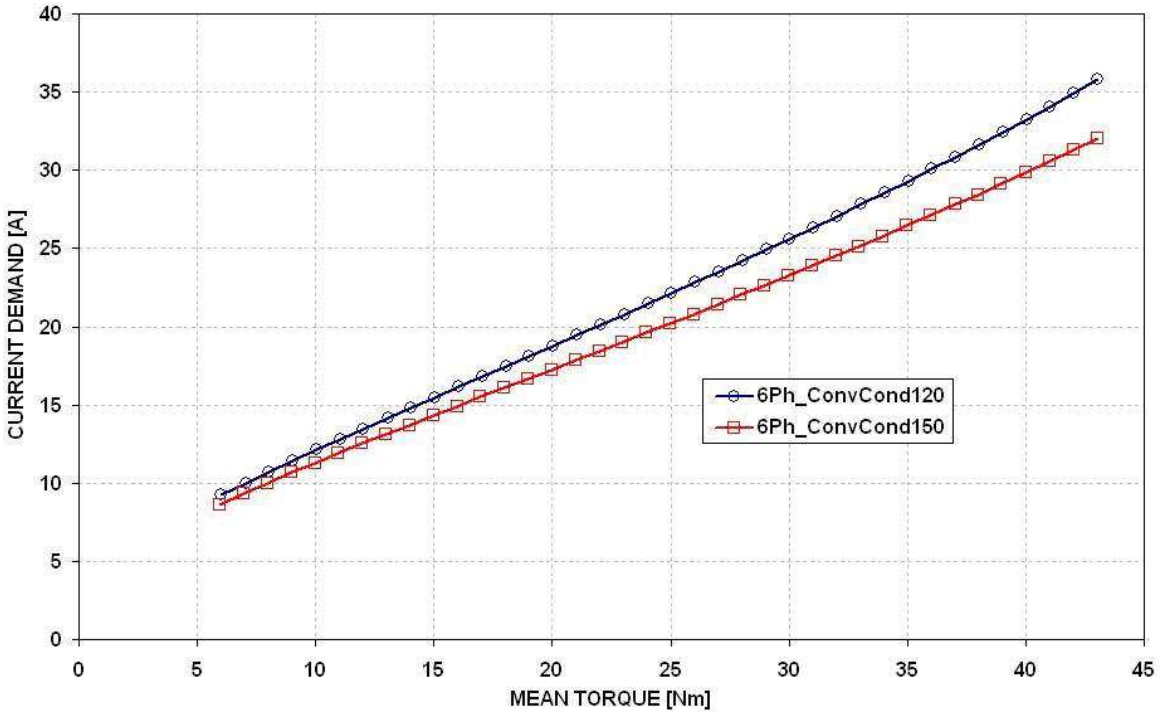

Figure 219 Current demand vs. average output torque characteristics for the 6-phase conventional toothed rotor drive. Blue trace when conduction angle = 120^o and red trace when conduction angle = 150^o

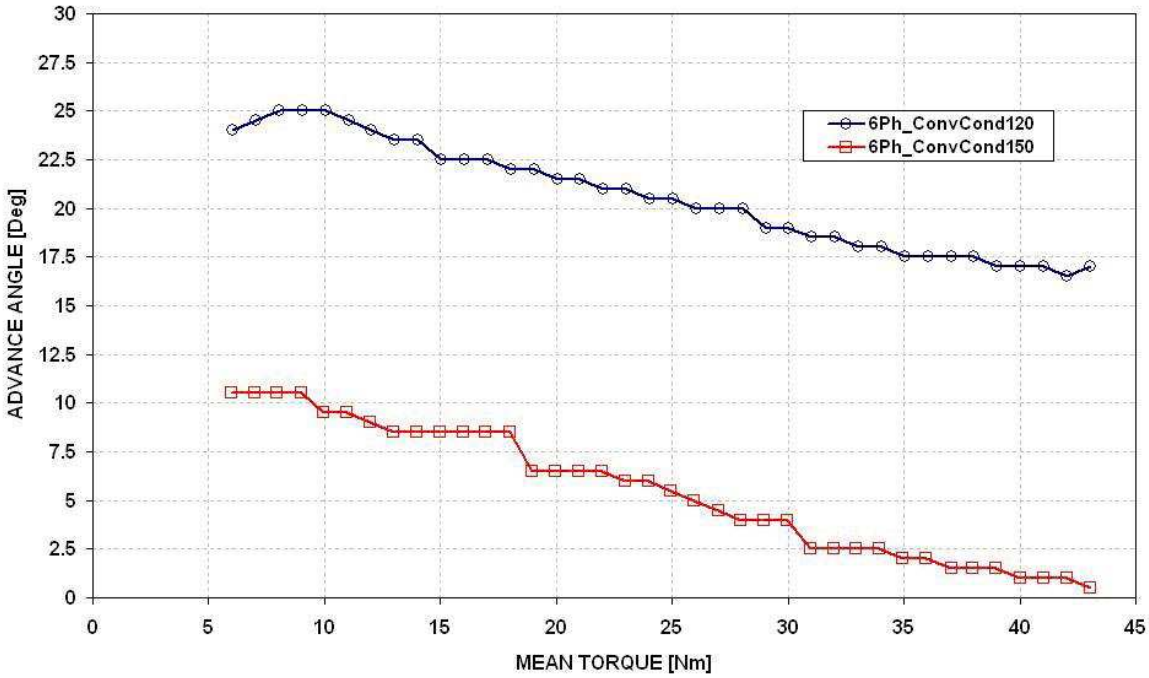

Figure 220 Advance angle vs. average output torque characteristics for the 6-phase conventional toothed rotor drive. Blue trace when conduction angle = 120^o and red trace when conduction angle = 150^o

It is quite clear from Figure 218 that increasing the conduction angle beyond 120^o improves the torque ripple performance of the 6-phase conventional toothed rotor drive. It is not surprising to see that the current demand and the advance angle profiles are shifted downwards with increased conduction angle in Figure 219 and Figure 220, respectively.

It must be stressed here that in practice, it is not possible to achieve perfect current control and the shape of the currents will deviate significantly from those presented in Figure 208 and Figure 209, especially at high speeds when the controller cannot achieve the desired current level and enters into full voltage control. The required advance angle and the converter topology will also significantly influence the shape of the output torque. Therefore the practical limitations will affect the torque ripple for all of the drives.

10.3 COMPARISON OF INVERTER VA-RATINGS

Measurements and simulation results of the 3-phase segmental rotor machine, driven from the asymmetric half-bridge inverter were presented in Chapter 8. Measurements taken when the drive was operating under full voltage control were used to estimate the converter VA rating of the 3-phase drive. Similarly, measurements of the 6-phase segmental rotor machine driven from the 3-phase full bridge circuit when connected in star configuration were used to estimate the converter VA rating of the 6-phase segmental rotor drive. However, no direct comparison could be made between the 3-phase and 6-phase drives in terms of converter VA ratings as the measured operating speed and the average output torque values were different.

Unfortunately, as far as the 6-phase segmental rotor machine is concerned, analysis concerning converter VA ratings could not be advanced any further as the efforts to generate dynamic simulation models of the drive were unsuccessful (see Chapter 9). Although not verified against measurements, the six-phase drive simulations with star and delta configurations were generated and run successfully when the machine with no mutual coupling was modelled. It was believed that a comparison of converter VA ratings between the 3-phase and 6-phase drives would be beneficial. For this purpose, the dynamic simulation models for the 3-phase and 6-phase drives were used. The 3-phase 12-10 single-tooth winding segmental rotor and the 6-phase 12-10 conventional rotor machine with no mutually coupled phases were modelled. The 6-phase machine was connected in star and delta configurations and driven from the 3-phase full bridge circuit, whereas the 3-phase machine was driven from the asymmetric half-bridge circuit. The comparison was divided into two sections. The first section below is the comparison of inverter VA-ratings of the 3-phase and 6-phase drives when both drives were operating under full voltage control (high speed operation). The second section follows on from the first one but looks at the comparison when both drives were operating under current control (low speed operation). For all simulations the dc-link voltage is fixed at 175V.

10.3.1 Drive under Voltage Control

For the purposes of this comparison, all three drives have been simulated at 1200rpm and the current demands were set to 50A in order to ensure operation under full voltage control. It should be noted that the current demand for the 3-phase drive is for the phase current and for the 6-phase drives it is the line current demand. The numbers of turns of the machines and the advance angles were then adjusted (by using the simulation GUI) in order to achieve 20Nm at 1200rpm with all three drives. The conduction angles of the 6-phase drives were limited to 120^o, however, in order to maximise the output torque at high speed, the conduction angle was set to 180^o for the 3-phase drive. As explained in Chapter 7, the aim here is to maximise the number of turns for the given speed and torque requirements in order to minimise the current in the circuit. This way, the inverter and machine losses are minimised for the given operating point. Once again, any change in the number of turns does not affect the machine copper losses (the same amount of stator slot area with the same slot fill factor is available to fill with copper). Table 42 summarises the simulation results for the 6-phase delta connected drive, 6-phase star connected drive and 3-phase drive under voltage control.

For the definition of the parameters in Table 42 readers are referred to Chapter 7.

Table 42 Summary of dynamic simulation results with the delta and star connected six-phase conventional rotor SRM driven from the 3-phase full bridge inverter and the three-phase single-tooth winding segmental rotor SRM driven from the asymmetric half-bridge inverter at 1200 rpm generating approximately 20Nm average output torque

	Six-Phase Delta Connected 3-Phase Full Bridge	Six-Phase Star Connected 3-Phase Full Bridge	Three-Phase Asymmetric Half-Bridge
Vdc_Link [V]	175	175	175
Number of Motor Phases	6	6	3
Speed [RPM]	1200	1200	1200
Tave [Nm]	20.01	20.00	20.01
Output Power [W]	2514.25	2512.80	2513.93
Demand Current [A]	50	50	50
Nturns per coil - ORIGINAL	**50**	**50**	**135**
Nturns per coil – FINAL	**64**	**39**	**66**
R_Phase [Ohms]	0.744	0.276	0.612
Advance [Deg.]	**-59.9**	**-38.2**	**-85**
Conduction [Deg.]	**120**	**120**	**180**
Iphase_RMS [A]	9.71	16.24	12.26
Winding Cu Losses [W]	420.55	436.67	275.83
Iphase_PEAK [A]	19.29	29.97	22.58
Total Inverter Losses [W]	128.89	136.75	117.00
Total Phase Diode Losses [W]	25.81	41.11	0.00
Total Power Electronic Losses [W]	154.69	177.86	117.00
Drive Efficiency [%]	81.38	80.35	86.49
Swt_VARating_Peak [kVA / kW]	11.71	12.53	9.43
Swt_VARating_RMS [kVA / kW]	5.68	5.89	4.89
Dio_VARating_Peak [kVA / kW]	11.65	11.73	6.83
Dio_VARating_RMS [kVA / kW]	2.36	2.44	1.52
Total Peak VA Rating [kVA / kW]	23.36	24.26	16.26
Total RMS VA Rating [kVA / kW]	8.04	8.33	6.41
Torque Ripple Pk-2-Pk [%]	27.1	32	85.2
Torque Ripple Ave-2-Pk [%]	32.6	39.5	143.8

10.3.2 Drive under Current Control

Here, the motor speed was reduced to 100rpm. The numbers of turns determined when the drives were under voltage control (in the previous section) were used in the simulations for each drive. The controllers now work under current control. All three drives use the same PID controller parameters. In order to maximise the torque per unit copper loss the conduction angle of the 3-phase drive is now reduced to 120^{o}. The current demands and the advance angles for all three drives were then optimised in order to achieve the required output torque (same as the previous section – 20Nm). Simulation results for the 6-phase delta and star connected and the 3-phase drive are summarised in Table 43.

Table 43 Summary of dynamic simulation results with the delta and star connected six-phase conventional rotor SRM driven from the 3-phase full bridge inverter and the three-phase single-tooth winding segmental rotor SRM driven from the asymmetric half-bridge inverter at 100 rpm generating approximately 20Nm average output torque

	Six-Phase Delta Connected 3-Phase Full Bridge	Six-Phase Star Connected 3-Phase Full Bridge	Three-Phase Asymmetric Half-Bridge
Vdc_Link [V]	175	175	175
Number of Motor Phases	6	6	3
Speed [RPM]	100	100	100
Tave [Nm]	20.06	20.06	20.00
Output Power [W]	210.08	210.04	209.42
Demand Current [A]	21.5	20.5	14.4
Nturns per coil - ORIGINAL	**50**	**50**	**135**
Nturns per coil - FINAL	**64**	**39**	**66**
R_Phase [Ohms]	0.744	0.276	0.612
Advance [Deg.]	**3**	**30**	**30**
Conduction [Deg.]	**120**	**120**	**120**
Iphase_RMS [A]	8.24	13.84	8.54
Winding Cu Losses [W]	302.87	317.30	133.98
Iphase_PEAK [A]	15.39	26.05	15.78
Total Inverter Losses [W]	163.91	158.95	122.29
Total Phase Diode Losses [W]	20.72	37.79	0.00
Total Power Electronic Losses [W]	184.63	196.74	122.29
Drive Efficiency [%]	30.12	29.01	44.97
Swt_VARating_Peak [kVA / kW]	114.95	109.80	79.09
Swt_VARating_RMS [kVA / kW]	47.42	45.29	32.54
Dio_VARating_Peak [kVA / kW]	114.93	109.61	79.09
Dio_VARating_RMS [kVA / kW]	41.30	38.80	32.54
Total Peak VA Rating [kVA / kW]	229.88	219.41	158.18
Total RMS VA Rating [kVA / kW]	88.71	84.09	65.08
Torque Ripple Pk-2-Pk [%]	25.7	25.8	75.8
Torque Ripple Ave-2-Pk [%]	27.9	29.6	99.3

10.3.3 Discussion on Converter VA-Rating Comparison

In the preceding two sections the simulation results of the star and delta connected six-phase drives and the three-phase drive under voltage and current control were given in tabulated formats. In this section, these simulation results will be scrutinised.

Although the rms phase current seen in the star connected six-phase drive is approximately 1.67 times more than the delta connected six-phase drive, the total machine copper losses of both drives are very similar. This is due to the difference in machine phase resistances between the star and delta connected drives. Phase resistance of the star connected six-phase machine is almost 1/3 of the phase resistance of the delta connected six-phase machine.

The six-phase delta connected drive has approximately 1.32 times the power electronic losses of the three-phase drive and the star connected drive has approximately 1.52 times the power electronic losses of the three-phase drive. According to the inverter VA ratings comparison (based on peak currents), under voltage control, the six-phase delta connected drive requires approximately 1.43 times and the star connected drive requires an approximately 1.5 times bigger inverter than the three-phase drive. When the same comparison is based on the rms currents the difference is smaller. Inverter VA rating comparison based on rms currents reveals that the inverter of the star connected drive is 1.25 times and the inverter of the delta connected drive is 1.3 times larger than the inverter of the three-phase drive under voltage control. Similar results are observed when the drives are under current control. The main difference under current control in terms of inverter VA ratings is that the star-connected drive outperforms the delta-connected drive. However, the difference is only about 5.0% and is unlikely to result in a bigger inverter requirement for the delta connected drive as the ratings of the devices will have quantised characteristics.

Overall, the three-phase drive is approximately 6% more efficient than the six-phase star connected drive when both drives are under full voltage control. The difference is larger when the drives are under current control. The three-phase drive is approximately 15% more efficient than the six-phase star connected drive when both drives are under current control. The increase in the efficiency difference under current control is mainly due to the increased circulating currents in the six-phase drives. The efficiencies of the star and delta connected six phase drives are very similar, both under current and voltage controlled situations. In both cases the delta connected drive is approximately 1.0% more

efficient than the star connected drive. It is interesting to note that the delta connected drive generates more inverter losses compared to the star connected drive when the drives are under current control but the total power electronics losses generated by the delta connected drive is still lower than the star connected drive. The difference is due to the additional phase diode losses. The delta connected drive is more efficient in terms of the phase diode losses. The star connected drive generates approximately 16.0W more phase diode conduction losses compared to the delta connected drive under voltage and current control situations. This can be related to the reduced rms phase currents achieved with the delta connected drive.

10.4 DISCUSSION ON TORQUE RIPPLE COMPARISON

As a result of the analysis presented in section 10.2, it was concluded that compared to the 3-phase segmental rotor drive, there was no real advantage of employing either of the 6-phase drives in terms of output torque ripple across a wide range of average torque levels. However, at the end of the same section, it was also briefly mentioned that – *due to practical limitations- the phase current shape would deviate significantly from the ideal case affecting the output torque waveform. Also the advance angle and the desired current level used in practice would also affect the overall output torque ripple of the drive system.*

In terms of the aim of this PhD project, it is certainly worth mentioning that unlike the results obtained with the theoretical analysis in section 10.2 of this chapter, it is obvious from Table 42 and Table 43 that both the star and delta connected six phase drives have significantly better output torque ripple characteristics compared to the three-phase drive under both voltage and current control modes: peak-to-peak torque ripple performances of the six-phase drives are approximately 1/3 of the three-phase drive under both control modes. It is also interesting to note that in Table 42, despite the fact that the 3-phase segmental drive operates with a conduction angle of 180^o, the generated output torque has significantly more ripple compared to those generated by both of the 6-phase drives. The reasons can be explained with the help of Figure 221 to Figure 224. Note that the current and torque waveforms in Figure 221 and Figure 223 are scaled to the level of rotor position for visual clarity.

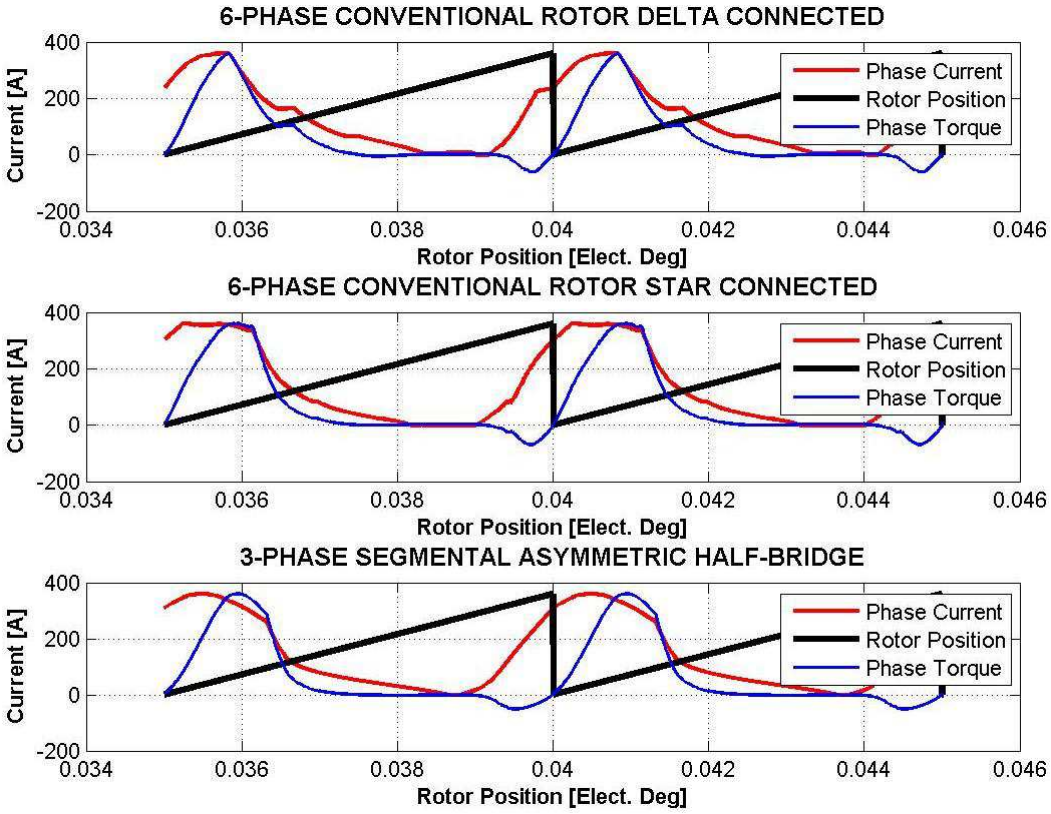

Figure 221 Phase current, phase torque and rotor position waveforms for drives tabulated in Table 42

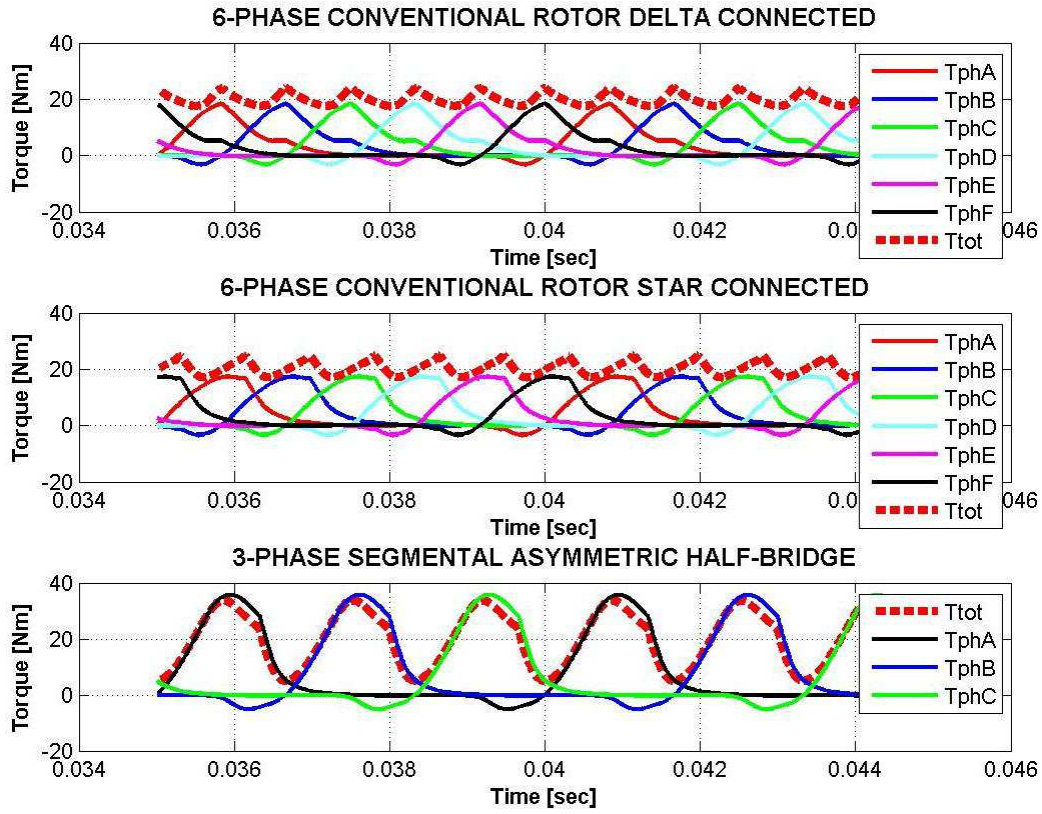

Figure 222 Phase torques and total torque waveforms for drives tabulated in Table 42

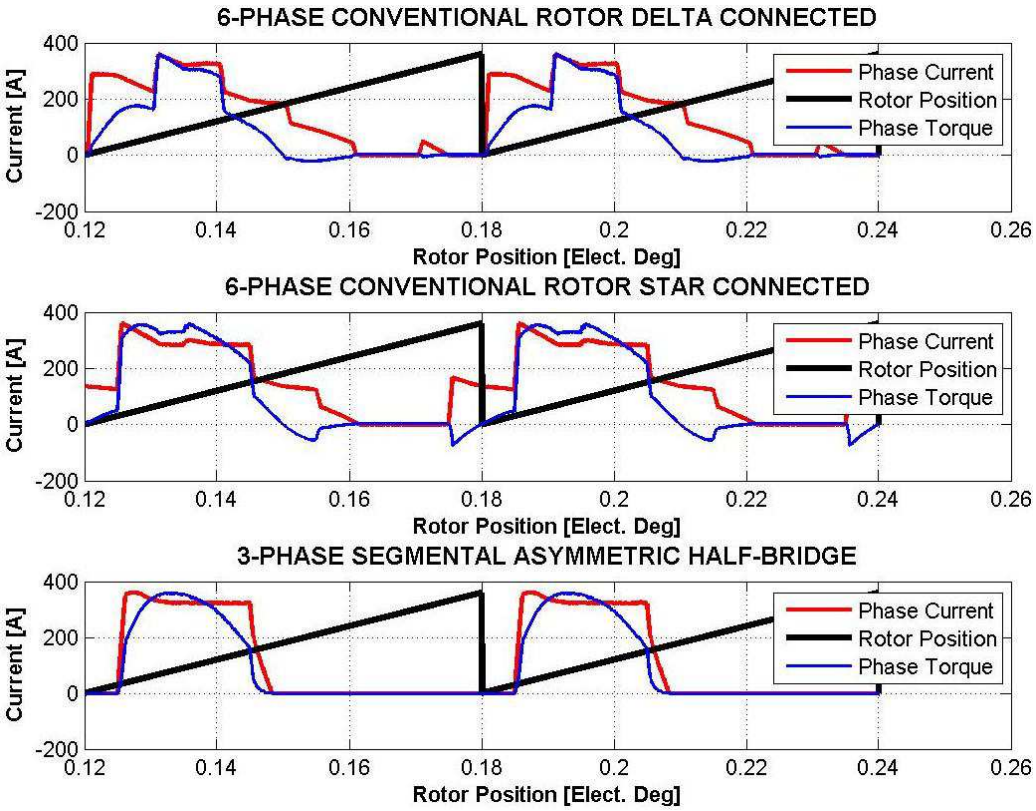

Figure 223 Phase current, phase torque and rotor position waveforms for drives tabulated in Table 43

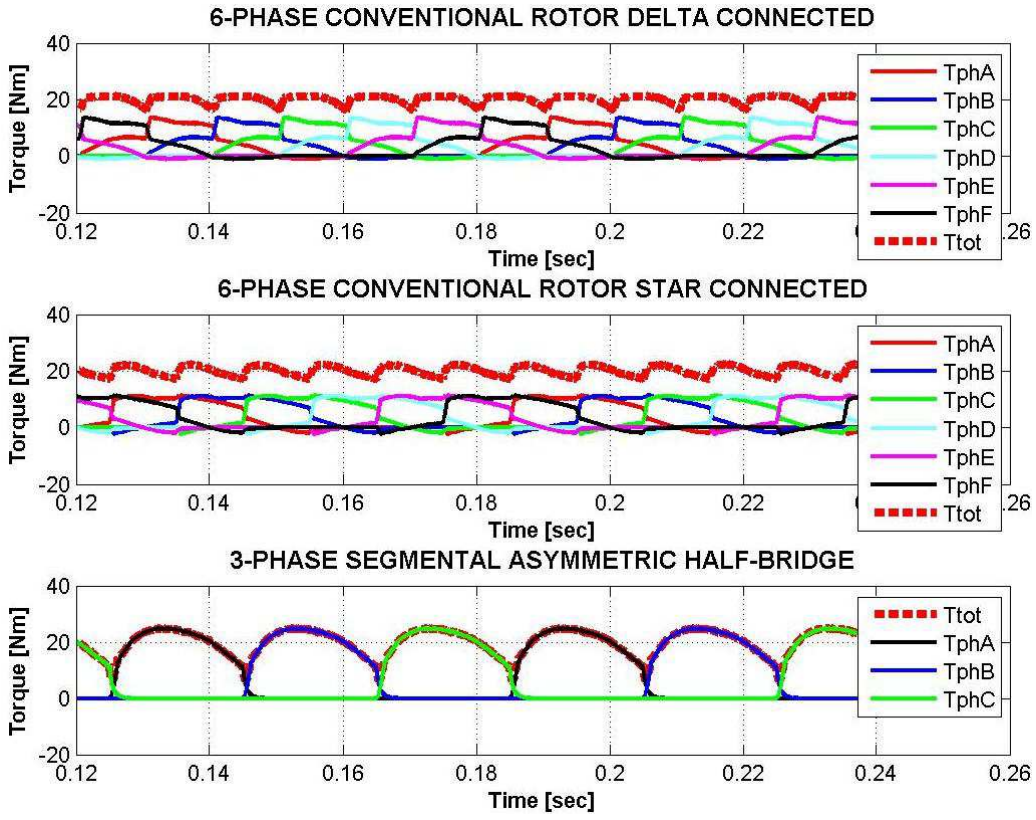

Figure 224 Phase torques and total torque waveforms for drives tabulated in Table 43

It is not surprising to see that the output torque of the 3-phase drive has significant torque ripple component when the conduction angle is set to 120^o. This can also be observed from Figure 214 in the theoretical torque ripple analysis work carried out in section 10.2. As already discussed, this is because of the relatively low overlap angle between individual phase torque waveforms (see bottom trace in Figure 224). Even though the conduction angles of both of the 6-phase drives are limited to 120^o both maintain a high degree of overlap between individual phase torque waveforms which results in relatively low output torque ripple under both voltage and current control modes. This is due to a combination of increased number of phases and phases conducting current for long periods of time over an electrical cycle (see first two traces in Figure 221 and Figure 223). It should also be noted that the static torque characteristics that are used to generate the results in section 10.2 are now different due to the changes made to the numbers of turns for each drive. When the drives are under voltage control, the phase current waveforms are significantly different to those simulated in the theoretical torque ripple analysis presented in section 10.2. Another reason for the high torque ripple observed with the 3-phase drive is believed to be the required advance angle and the current demand for the given torque level to achieve minimum converter VA-rating.

10.5 SUMMARY

In this chapter both 6-phase designs have been compared against the 3-phase, single-tooth winding segmental rotor design, based on torque per copper loss. The comparison revealed that both 6-phase designs were significantly inferior to the 3-phase design. This was attributed to two factors; firstly, the stator teeth of the 3-phase machine that carry the windings of the coils are considerably wider than those of the 6-phase machines. Secondly, the overlap between the stator teeth and the rotor segments of the 3-phase machine is larger than that seen in the 6-phase machines.The comparison based on the torque per unit copper loss suggested a slight advantage for the 6-phase toothed rotor machine compared to the 6-phase segmental rotor machine.

In the second part of this chapter, theoretical analysis of torque ripple vs. average output torque of the 3-phase and the 6-phase 12-10 segmental rotor machines and the 6-phase conventional rotor machine has been carried out in Matlab® by a simple m-file script

simulation. For the six-phase drives, the conduction angles were fixed to 120^o, current demands and the advance angles were varied. For the three-phase drive, the conduction angle was also varied. Once the average torques for all of the three drives were calculated, the script then searched for the result with the lowest torque ripple for each average output torque level from 6.0Nm to 43.0Nm. It was shown that with the same conduction angle, the output torque ripple could be significantly improved with both conventional and segmental rotor 6-phase drives. However, as the 3-phase drive can operate with conduction angles of up to 180^o, the output torque ripple of the 3-phase drive can be improved to a level comparable to that of both 6-phase drives throughout the torque range (that was analysed in this chapter). It was also shown that the 6-phase segmental rotor machine can still outperform the 3-phase drive with 180^o of conduction angle up to 20Nm mean output torque.

The VA-ratings of the 6-phase conventional rotor machine connected in star and delta configurations and driven from the 3-phase full bridge circuit has been compared to that of the 3-phase segmental rotor machine driven from the asymmetric half-bridge circuit in the dynamic simulation. The numbers of turns of the machines were adjusted in order to achieve 20Nm at 1200 rpm when all of the drives were under full voltage control. The same numbers of turns were then used at 100 rpm and the current demands were adjusted in order to achieve the same output torque level of 20Nm from all of the drives. The three-phase drive outperformed both the star and delta connected six-phase drives. Comparison of the star and delta connected six-phase drives revealed that similar VA-ratings can be achieved. However, the delta connected drive was 1.0% more efficient than the star connected drive under both voltage and current controlled situations.

Although the VA comparison of the drives was in favour of the 3-phase one, the same comparison was also beneficial in realising that both the star and delta connected six phase drives significantly outperformed the 3-phase drive in terms of output torque ripple. This was a result of the practical phase current waveforms that deviated significantly from the idealised ones used in the theoretical torque ripple analysis that was presented in the second part of this chapter. In terms of the torque ripple comparison, the simulated results obtained from the dynamic simulation package are believed to be more relevant and they clearly show the inadequacy of the theoretical approach presented in section 10.2.

CHAPTER 11

11 – Conclusions and Future Work

11.1 CONCLUSIONS

The principle aim of the work presented here was to design a 6-phase segmental rotor machine drive capable of generating torque ripple levels comparable to a 3-phase AC machine without the need for complicated circuit topologies or control methods. For this purpose a prototype 6-phase segmental rotor machine was built and tested. The static torque and flux-linkage characteristics were correlated against FE predictions and were in good agreement. For direct comparison, a 6-phase conventional toothed rotor machine of the same inner diameter, outer diameter and stack length was also designed. The segmental machine design was based on the principles that were used to design the 3-phase segmental rotor designs. On the other hand the conventional toothed rotor 6-phase machine was designed using simple and well-known conventional SRM design equations. Both 6-phase machines were also compared to a 3-phase single-tooth winding segmental rotor machine of the same outer diameter, inner diameter and stack length.

The optimal machine design for the 6-phase segmental rotor machine was chosen using an equation that was based on the average machine output torque, output torque per copper loss, output torque per machine mass and the inverter VA rating that was indirectly derived from the unaligned inductance of the machine. 2D FE analysis was used for the initial and refined designs for both toothed and segmental rotor machines. In terms of comparative study of different design options, use of 2D FE was believed to be

valid. Furthermore, the stack length of the machine is believed to be large enough to keep the 3D end effects low, hence permitting the use of 2D FE analysis to predict the measured values. The discrepancies between the measured and 2D FE generated results are more obvious in the unaligned position where the axial fringing flux is at its highest level. In the aligned position the saturation characteristic is predicted well with 2D studies. The difference in the linear region of the magnetisation curves in the aligned position is believed to be due to the difference in the final machine air-gap compared to the design intent value of 0.3mm.

11.1.1 Machine Performance

In terms of machine performance comparison between the 3-phase segmental and the 6-phase segmental and conventional machines, the results are summarised in the following three sub-sections.

Based on all three machines having the same total slot MMF, the 3-phase segmental rotor machine requires the least amount of copper for a given average output torque. For a kilogram of copper, the 3-phase machine is able to generate twice the amount of torque compared to 6-phase segmental rotor machine whereas the 6-phase machine with the segmental rotor is only marginally better than the 6-phase machine with the conventional rotor.

For a given amount of total machine copper losses, the 3-phase machine is found to be more favourable than both 6-phase machines. The 3-phase machine is able to generate approximately 50% more torque compared to the 6-phase machines for 300W of machine copper loss. The comparison between the two 6-phase designs is unlike that experienced with the three phase machines, where the 3-phase segmental rotor design proved to generate significantly more torque for a given copper loss compared to a 3-phase conventional rotor machine of similar dimensions. In the case of the 6-phase designs, the conventional rotor machine is able to generate marginally more torque than the segmental rotor machine.

Similar conclusions can be drawn from the comparison of the MMF vs. flux curves of each machine in the aligned and unaligned rotor positions. The 3-phase segmental rotor machine is more than 50% better than both 6-phase machines and there is no significant difference between the segmental and conventional rotor 6-phase machines.

11.1.2 Machine Construction Techniques

The stator of the 6-phase segmental machine was constructed from separate cores. This was somewhat different to the conventional single lamination construction. The use of separate cores for the stator construction has allowed an easier winding operation and consequently improved the machine slot fill factor beyond the typical values of 0.4 achieved with conventional single lamination designs. Although higher than usual slot fill factor was achieved by the separate stator core construction, the author believes that there is scope to further improve the slot fill factor with a more careful winding operation that focuses on reducing the bulging of long and thick conductors. Also for designs where conductors with small diameters and a short machine stack length are required, the winding operation is expected to be easier with less bulging and curving of conductors, which in turn is expected to further improve the slot fill factor.

It should be mentioned that the increased component count associated with using separate stator cores is likely to limit the use of this construction technique. However, in this work, increasing the slot fill factor has been the main focus. Furthermore, the separation of cores can be achieved in a similar fashion to the technique used by the Mitsubishi Motors group [156], where the entire stator can be opened up to ease the winding operation and to increase the slot fill factor.

11.1.3 Drive Modelling

A set of transformation equations allowing phase quantities in the 6-phase segmental rotor SRM related to the machine slot quantities has been developed in order to aid with the understanding and simulation of the drive system. By de-coupling the windings of the prototype machine, these transformations allow the machine to be modelled in a conventional way (i.e. each phase can be analysed separately), and are a very useful tool for simulation and performance analysis of the drive system. However, because the terminal equations for all phases are effectively coupled with the introduction of the transformation matrices, all phase flux-linkages are needed to be solved simultaneously. Compared to the machines with naturally de-coupled phase windings, the computation time is substantially increased, but this is unavoidable.

11.1.4 Inverter VA-Ratings and Drive Testing

Using a power circuit which (by control of device signals) can emulate several common configurations and by implementing control functions in software, it has been possible to explore several circuit configurations and control strategies without extensive hardware modifications. To aid with the simulation and understanding of the more complex 6-phase drive, the 6-phase machine was also configured to run as a 2-phase machine. In both cases standard recovery type diodes were connected in series with each phase winding to prevent phase currents becoming bipolar. In this case, the standard rectifier grade recovery diodes are low cost. It should be noted that these diodes never experience a large di/dt as they are placed in series with the phase windings. It is also believed that the phase diodes do not contribute to turn on losses in the active power devices due to stored charge effects. The drive circuitry was configured to run the two-phase machine from both an asymmetric half-bridge and h-bridge circuit configurations. Performance comparison between the two inverter topologies for the two-phase machine has been carried out in the dynamic simulation, once the simulations of both topologies were correlated with the measurements.

With the H-bridge circuit there is a restriction that the sum of the voltages applied to the two phases is equal and opposite. A scheme is adapted where the on-coming phase current is used to determine the voltage demand. This reduces the voltage applied to the phase switching off and consequently gives a long current tail during a period when the phase produces negative torque. This is a fundamental disadvantage of the H-bridge arrangement, resulting in a small reduction in torque and a small increase in winding loss. However, there is a reduction in power device losses because current in an off-going phase is transferred to the on-coming phase without it flowing through the power switches.

The two-phase drives were compared in the dynamic simulation at two different operating speeds (1200 rpm and 100 rpm) where the drives were under voltage and current control, respectively. When the drives were under voltage control with phases conducting half the electrical cycle, both drives operate at similar efficiencies (around 82-83%). However, under current control the asymmetric half-bridge driven drive is slightly more efficient than the h-bridge driven drive. This is due to increased copper losses and additional phase diode losses of the h-bridge drive. In terms of total inverter losses, the h-bridge drive

performs better than the asymmetric half-bridge drive. However, this is somehow counterbalanced by extra conduction losses incurred due to the use of the phase diodes in the h-bridge drive for ensuring unipolar phase currents. Even under current control, the total inverter losses are not worse with the h-bridge drive as the power devices in the h-bridge inverter experience the difference between two phase currents. In terms of the total inverter VA-ratings (including reverse recovery diodes and IGBTs), the h-bridge drive is only slightly favourable under current control. However, based on rms device currents, the advantage of the h-bridge drive in terms of total VA-ratings is elevated when both drives are under full voltage control. The other advantages of the h-bridge driven two-phase drive over the asymmetric half-bridge driven two-phase drive can be summarised as follows:

- The number of connections between the motor and the converter is reduced from 4 to 2. This assumes that the phase diodes can be mounted at the motor end of the drive system.
- Adequate control can be achieved by a single current transducer.
- The reverse recovery diodes needed for the h-bridge drive can be part of the power devices, potentially reducing the required board space for the electronics. Once again this assumes that the phase diodes are located at the motor end of the drive system.

Furthermore, machines with two or less phases are preferred for high speed applications. At high speeds the drive is more than likely to be operating under full voltage control where use of h-bridge topology might be advantageous.

Switched reluctance machines suffer from high torque ripple. A major cause of this is that each phase produces one torque pulse per electrical cycle, whereas other machine types produce two. Hence, to reduce the torque ripple of an SRM towards that of a three phase a.c. machine, it is necessary to have a six-phase SRM. Existing SRM concepts have not been able to do this in an economical fashion because there are two wires per phase connecting the machine to the power converter and two controlled power electronic switches per phase. This research has shown that a six phase SRM can be successfully driven from a three phase bridge with only three connections between the inverter and the motor. The number of controlled devices per phase has been reduced from two to one and

the number of connections between inverter and machine has been reduced from twelve to three.

Prior to this PhD work it was shown that the utilisation of basic star and delta connections were somewhat limited for the 3-phase SR machines. For the star connection each phase was required to conduct for 2/3 of the electrical cycle resulting in significant periods of negative torque. The extended period of conduction also increased the machine copper losses. For the delta connected machine there cannot be a net voltage applied around the delta. There is a circulating current which cannot be maintained and the phase currents are required to be bipolar, which results in the same problems as the star connection. Experimental operation of the 6-phase segmental rotor switched reluctance drive has been explored with star-connected windings driven from a 3-phase bridge circuit.

In terms of inverter VA-rating and total power electronics losses (in the case of the 6-phase drives total power electronics losses include the conduction losses incurred across the series connected phase diodes) of the six-phase and three phase drives, both the delta and star connected six-phase drives are inferior to the three-phase drive under voltage and current control conditions. The delta connected drive was found to be slightly better than the star-connected one. The gain with the 3-phase drive was smaller when the comparison was based on the rms device currents.

A set of transformation matrices has been used to determine the torque produced by a segmental rotor SRM with mutual coupling between phases. Considering the likelihood of a difference between the dynamic and static torque characteristics and the strong mutual coupling experienced in this machine, the good correlation achieved between the measured and predicted average torque values based on the estimated instantaneous torque waveforms suggest that the transformation matrices work well and are useful in explaining / predicting the performance of the 6-phase segmental rotor machine with mutually coupled phase windings.

11.1.5 Torque Ripple

Torque ripple results based on the limited number of measurements made upon the 3-phase and 6-phase segmental rotor machines were not conclusive. As one might expect the 3-phase machine driven from the asymmetric half-bridge circuit has the advantage of being able to run with conduction angles exceeding 1/3 of an electrical cycle. As the conduction angle is increased towards 1/2 of an electrical cycle the overlap angle between individual phase torques increases, resulting in reduced torque ripple at the expense of increased machine copper losses. For this reason a theoretical torque ripple comparison was carried out between the 3-phase segmental rotor and the 6-phase segmental and conventional rotor machines. The analysis was based on perfect current control and the FE generated torque characteristics were used to calculate the instantaneous torque values for many combinations of advance angle, conduction angle and current demand. Comparisons were made between 6.0Nm and 43.0Nm of average output torque. For every value of average output torque, the solution with the lowest torque ripple was chosen for each machine. The relatively marginal improvement made with the 6-phase segmental machine was attributed to the slot MMF pattern and the way the torque is generated in the 6-phase segmental machine. For the segmental rotor machine the slot permeances are regulated by the rotation of the rotor segments and the slot torque is generated as a result of the slot MMF. As each slot carries windings of two adjacent phases and in the star connected configuration two adjacent phases are energised simultaneously the MMF pattern has a double step characteristic. As a result the torque generated per slot also takes a profile with two steps. The resulting output torque waveform has more peaky characteristics, which consequently means increased torque ripple. On the other hand, the output torque ripple of the 6-phase conventional rotor machine driven from the 3-phase full bridge converter suffers from the limited conduction angle of 120^{o}. Overall, when all three drives were limited to 120^{o} of phase conduction periods, both 6-phase drives significantly outperform the 3-phase drive in terms of output torque ripple. However, when the conduction angle of the 3-phase drive was increased towards 1/2 of an electrical cycle, the output torque ripple of all three drives was comparable. Nevertheless, compared to the 3-phase drive, the 6-phase segmental drive was still able to generate torque with a lower ripple component up to 20Nm.

During the inverter VA-rating comparison, it was found that both star and delta connected 6-phase drives with a conventional rotor outperform the 3-phase segmental rotor drive in terms of output torque ripple; generating only 1/3 of the torque ripple seen in the 3-phase drive under voltage and current control conditions. This was due to a combination of factors; required current demand and phase commutation angle for the given output torque in order to keep the VA-rating of the drive to a minimum, the changes made to the numbers of turns of each drive and hence the static torque characteristics and the resulting non-ideal phase current waveforms. In the case of the current control mode, the majority of the difference is due to the low conduction angle used for the 3-phase drive in order to maximise the torque per copper loss of the machine. The analysis in the dynamic simulation shows the inadequacy of the theoretical approach where the ideal current waveforms are used.

Considering the aim of this PhD work, it can be concluded that the torque ripple of an SRM can be reduced by increasing the number of phases to six. In doing so, the number of power electronic devices, current transducers and the number of connections between the machine and the converter can still be kept to a minimum. This can be achieved by driving the machine from a conventional 3-phase bridge converter and connecting the phase windings of the machine back-to-back through diodes. Compared to a conventional toothed rotor machine topology, segmental rotor SRM results in a smaller reduction in the torque ripple. This is believed to be due to the way the phase windings are arranged within the machine slots and the way the torque is generated in segmental rotor SRMs.

11.2 FUTURE WORK

Although several simulation models have been successfully generated throughout the course of this project, without a doubt one of the first steps of a future project would be the generation of a working dynamic simulation model of the six-phase machine with mutually coupled phase windings. Once this dynamic simulation model is correlated against the measurements, a much more detailed analysis of the 6-phase segmental rotor SR drives can be investigated.

The aim was to have an SR drive capable of achieving torque ripple levels that are comparable to the 3-phase brushless dc machines. Due to time restrictions and unavailability of the characteristics of such a 3-phase BLDC machine the comparison has not been done in this thesis. A direct comparison of the torque ripple with a 3-phase brushless dc machine is therefore something to pursue in the future.

The 6-phase conventional toothed rotor design, once built, will have mutually de-coupled phases. The simulation models of the star and delta connected 6-phase machine driven from the 3-phase bridge circuit with mutually de-coupled phase windings can then be correlated against the measurements made upon this machine. A direct comparison can then be made between the performances of the 6-phase conventional toothed and segmental rotor machines when driven from a 3-phase bridge inverter in star and delta connected configurations.

Instead of trying to control the phase currents to a fixed current demand, it is possible instead to control the line currents to a sinusoidal shape. Sinusoidal phase current excitation was previously used for driving a 3-phase conventional toothed rotor machine with fully-pitched phase windings. The machine was connected in star and hence the phase currents were also the line currents. The sinusoidal excitation pattern resulted in reduced peak-to-peak torque ripple in the 3-phase conventional machine with fully-pitched windings. This brings the SR drive another step closer to the inverter fed induction motor in terms of the hardware and software required to drive the motor [89]. The same sinusoidal excitation pattern can be used with the 6-phase machine drive. This time the controlled currents are the line currents. It would be interesting to see the resulting shape of the phase currents and the effect of the sinusoidal excitation pattern on the machine output torque for a given loss and more importantly on the ripple component of the output torque.

The ability to use a 3-phase full bridge circuit to drive an SRM has many advantages, such as reduced number of power connections to the machine, ability to use devices with internally packaged diodes and three current transducers (or even only two if the current transducers can be placed at the power converter end of the drive) instead of six but perhaps the most promising benefit comes with the volume of production of standard 3-phase drives. With minimal modification to the standard drives the integration of SRMs

into the drives market will be considerably eased if the use of 3-phase bridge circuitry is made a reality without compromising the performance of the machine. It would therefore be an interesting and a very useful study to use a commercially available off-the-shelf 3-phase drive to run the 6-phase conventional toothed and segmental rotor machines.

APPENDIX A

A. Flux-Linkage Measurements & Post-Processing of Data

A.1 FLUX-LINKAGE MEASUREMENTS

Locked rotor tests were used to determine the flux-linkage/current/position characteristics of the prototype machine. As mentioned in Chapter 4, Flux-linkage measurements in this project are based on the "Volt-Seconds" method.

In order to collect the flux-linkage characteristics with the volt-seconds method, it is necessary to supply the machine phase windings with a known voltage for a specified length of time. A signal generator can supply a voltage pulse and this would work for a small machine. However for larger machines the current supplied by a signal generator would be rather small to obtain any sensible readings from the machine. Here, output from a signal generator is used to switch on a high voltage high current power MOSFET which in turn turns a larger power supply on. The signal generator is protected by an opto-isolator against any faults at the high voltage high current end of the test set-up. Full rated voltage is required over the entire time period of the voltage pulse. Such a supply can be produced by either having an ac rectifier or having bench-top dc power supply being used to charge some large capacitors. Due to the size and cost of the required rectifier and time associated with the building of such a rectifier a bench-top dc power supply along with two parallel connected high-voltage electrolytic capacitors (4700uF –

400V) are used. The pulse width of the signal generator is used to adjust the achievable peak current. A 100Ω resistor is also placed in the circuit to safely discharge the large capacitors once the testing is finished. Two phases of the prototype are connected in series and excited simultaneously whilst the rotor of the machine is locked at a desired position. The frequency of the signal generator output is adjusted until the required peak current is attained. Voltage and current waveforms are monitored and recorded in excel spreadsheet format for a series of rotor positions. The DSP of the drive system was arranged so that it could process the 12- bit encoder readings and output the rotor position to a display on the PC. It must be reminded here that the rotor clamping action must be strong enough to hold the rotor through the impulse torque which is the force trying to align the rotor pole(s) with the nearest stator pole(s), when current is applied. This will ensure errors in rotor position are minimised. As the prototype machine had 10 rotor segments, measurements are taken for 18 mechanical degrees to obtain the full flux-linkage characteristics from unaligned to aligned position. A position stepping of 2 degrees was decided to be sufficient enough to predict the performance of the motor either manually or in simulation with a high accuracy.

In the proceeding section, the GUI that processes the voltage and current data in order to generate the set of flux-linkage characteristics is explained.

A.2 FLUX-LINKAGE VIEWER GUI FOR DATA POST-PROCESSING

To overcome problems of noise on the measured data and twisting of shafts, with large torques, the measured data is post processed in MATLAB environment. As both voltage and current affect the flux-linkage calculation, any noise or offset present in these waveforms will be reflected into the flux-linkage as well. The large number of data points captured by the oscilloscope meant that minute variations in current being captured were also magnified through the calculation process. Therefore, the raw flux-linkage characteristics were found to be erratic and a method of filtering was applied to the current data. A GUI has been created to assist with the calculation of the flux-linkage characteristics of the prototype motor from captured voltage and current scope traces. The GUI is able to remove offsets from measured waveforms, apply a moving average filter to

remove any noise effects and plot and save the flux-linkage characteristics of an SRM. The GUI can also generate torque characteristics based on calculated flux-linkage characteristics and plot and save this data as well. A screen-shot of the GUI is presented in Figure A. 1.

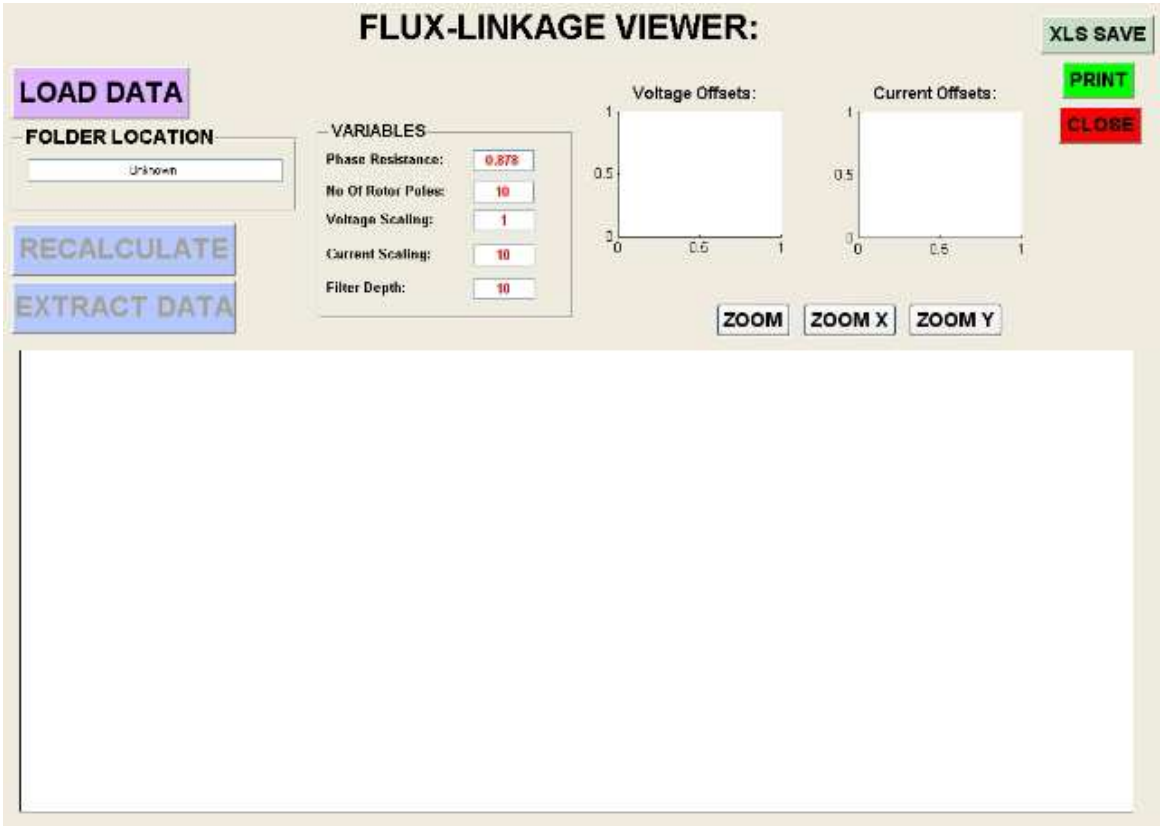

Figure A. 1 Screenshot of the GUI used to post-process the voltage and current measurements and generate flux-linkage characteristics of the prototype machine

The user can change the phase resistance, number of rotor poles, voltage scaling, current scaling, and filter depth in the GUI window. Voltage and current scaling are there to scale the captured waveforms to get the real values (due to current transducer and the voltage probe settings). Filter depth denotes the order of the moving average filter. The GUI is also able to plot offset values for each set of measurements (each set meaning, a set of current and voltage measurements at a specific rotor position) for current and voltage separately. Once the folder containing all captured waveforms is loaded the GUI calculates the flux-linkage characteristics for each rotor position and plots the results in the axis provided within the GUI window. Users can print the contents of GUI window by pressing the “Print” pushbutton at the right hand corner of the GUI window. By pressing

the XLS button users can also save the calculated flux-linkage data in excel spreadsheet format. The GUI not only computes the flux-linkage for the filtered voltage and current waveforms but also for the unfiltered (raw) voltage and current waveforms as well. Both flux-linkage results for each rotor position are plotted in the axis provided in the GUI window. In Figure A. 2 the effects of unfiltered voltage and current waveforms can clearly be seen. If the user wants to see the effect of phase resistance value or wants to use a different filter depth, he can do so by changing the corresponding values under the "VARIABLES" panel of the GUI window and pressing the "RECALCULATE" pushbutton on the left hand side of the GUI window just above the flux-linkage plots.

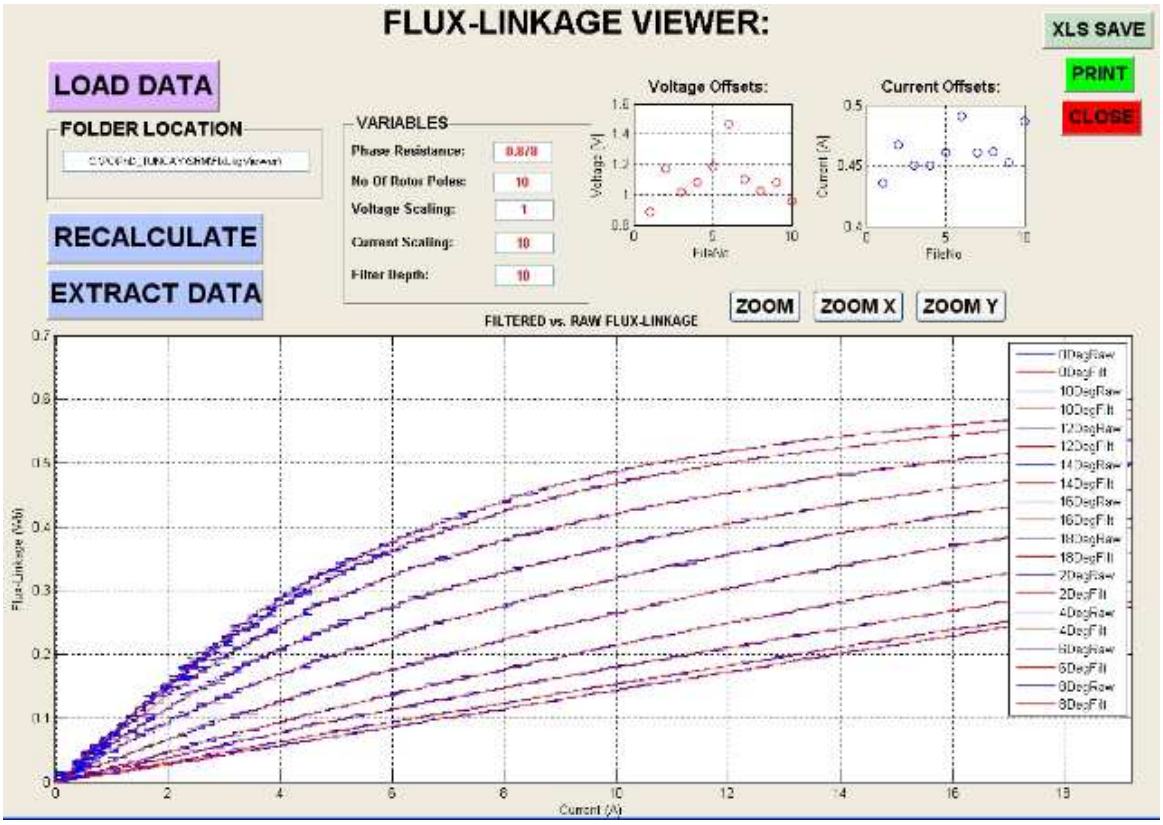

Figure A. 2 Effects of undesirable voltage and current waveforms on the calculated flux-linkage characteristics

APPENDIX B

B. Lamination Drawings of the Six Phase Segmental and Conventional Rotor Machines

This appendix gives mechanical details of the six-phase 12-10 switched reluctance machine prototypes with conventional toothed and segmental rotor structures. The information here is intended to compliment the details of the design stages for both prototype machines in *Chapter 4 – Machine Design*.

Note that the drawings of both prototypes in the following sections are not to scale. The drawings were generated using AutoCad® technical drawing software package. The first two sections below detail the lamination drawings for the stator and the rotor of the segmental rotor machine and the last two sections detail those for the stator and rotor of the conventional toothed rotor machine.

B.1 STATOR SEGMENT LAMINATION DRAWING OF THE SEGMENTAL ROTOR SIX-PHASE MACHINE

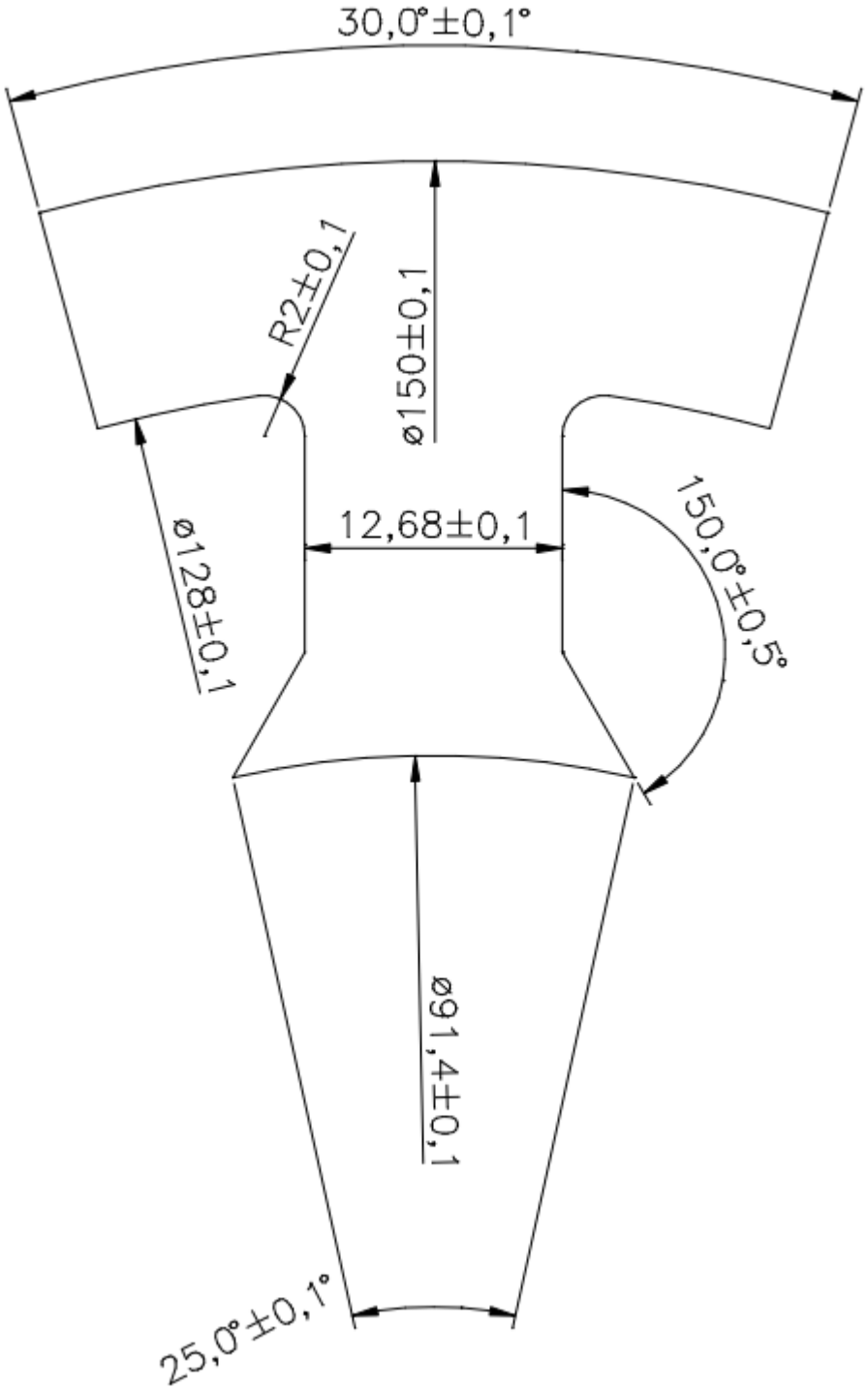

Figure B. 1 Stator segment lamination of the segmental rotor six-phase switched reluctance machine

B.2 ROTOR SEGMENT LAMINATION DRAWING OF THE SEGMENTAL ROTOR SIX-PHASE MACHINE

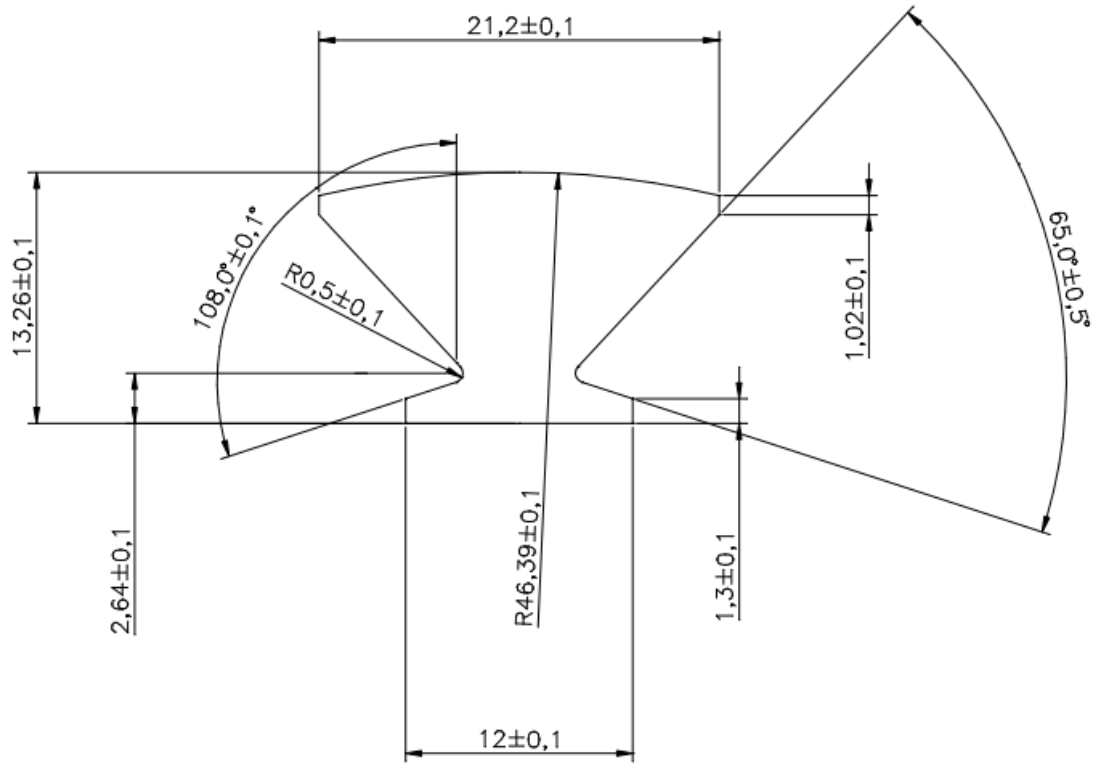

Figure B. 2 Rotor segment lamination of the segmental rotor six-phase switched reluctance machine

B.3 STATOR SEGMENT LAMINATION DRAWING OF THE TOOTHED ROTOR SIX-PHASE MACHINE

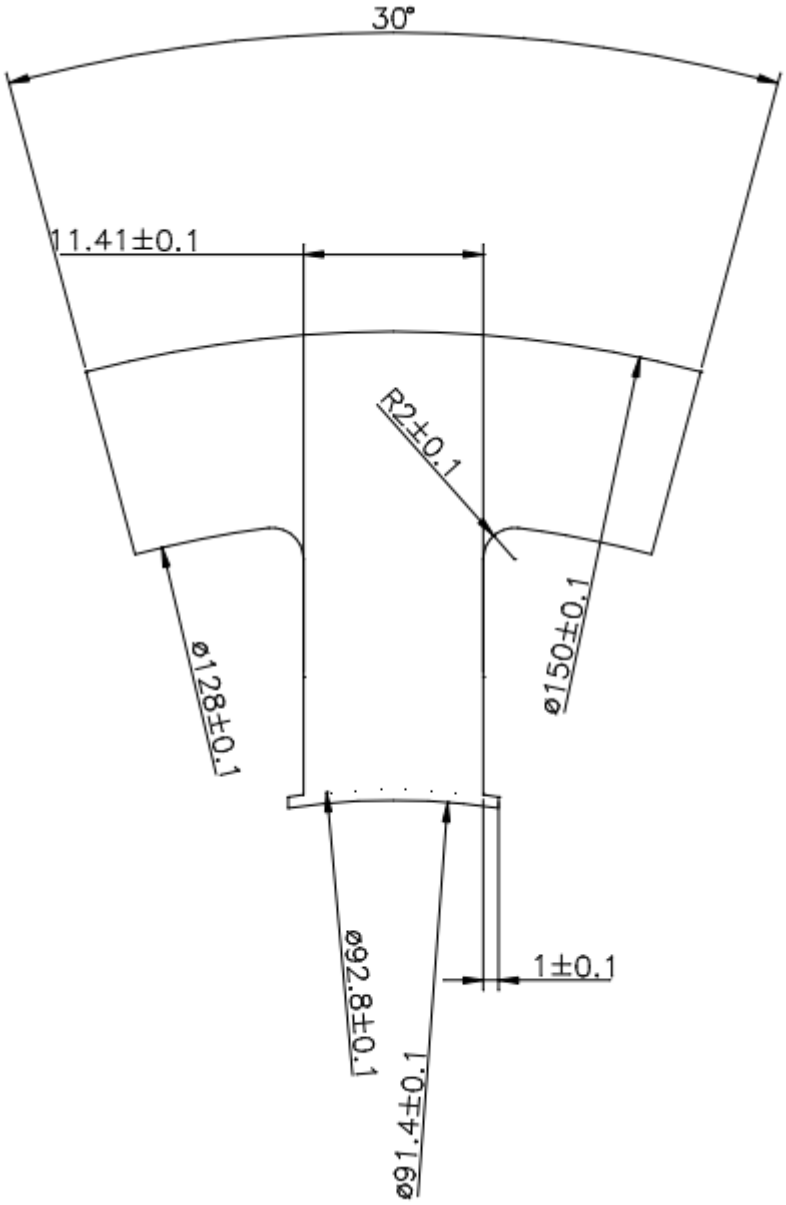

Figure B. 3 Stator segment lamination of the toothed rotor six-phase switched reluctance machine

B.4 ROTOR LAMINATION DRAWING OF THE TOOTHED ROTOR SIX-PHASE MACHINE

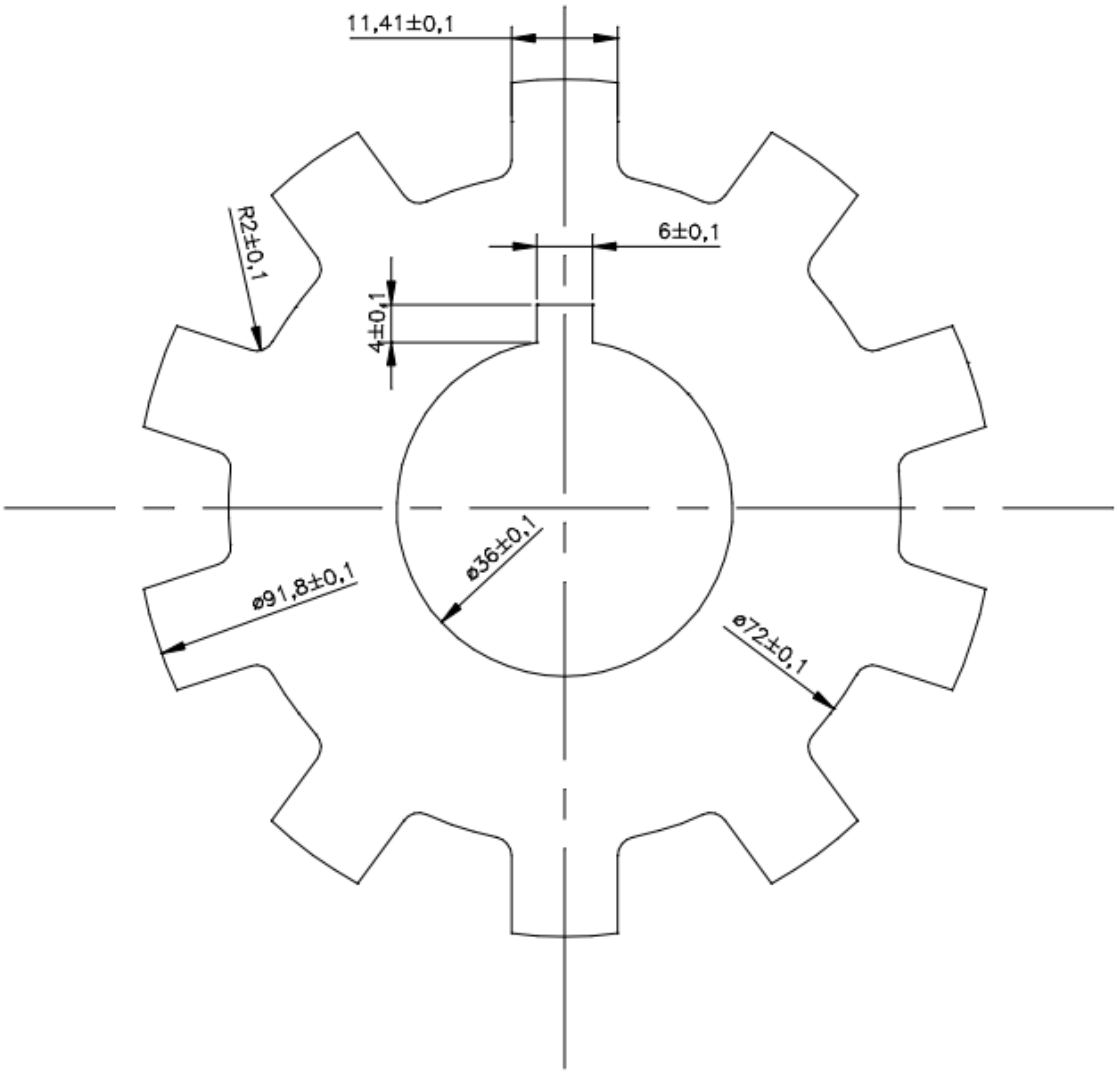

Figure B. 4 Rotor lamination of the toothed rotor six-phase switched reluctance machine

APPENDIX C

C. Simulation Package and Graphical User Interface

C.1 INTRODUCTION

This appendix details the Graphical User Interface (GUI) created for the simulation package (details of which was presented in *Chapter 6- Simulation Models*). The motivation to create a GUI for the simulation was to simplify the entry points to the simulation and encapsulate simulation's functional behaviour. Effectively, interfacing the simulation models generated in the Simulink® environment with a GUI makes it easier for end-users to change key parameters. Having a GUI also helps to minimise the user's efforts to run simulations and view results.

The GUI for the simulation package presented in this thesis was created in Matlab® environment. GUIs in Matlab® are created using a tool called ***Guide***, Java-based GUI development environment. This tool allows the programmer to layout the GUI, to select and align the components to be placed in the GUI. Once the components are in place, the programmer can then edit their properties such as name, colour, size, font, text to display, etc. When ***Guide*** saves the GUI, it creates a working program (in m-file format) including skeleton functions that the programmer can modify to implement the behaviour of the GUI. A screenshot to show how ***Guide*** in Matlab® looks like along with some of its key parts is depicted in Figure C. 1.

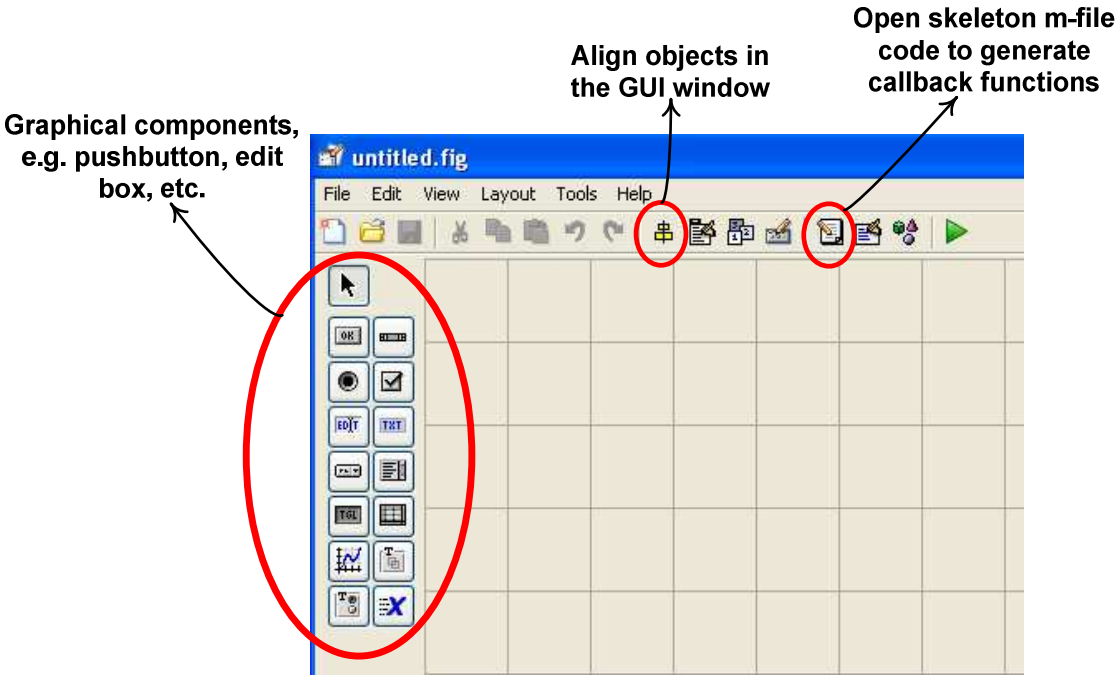

Figure C. 1 A screenshot of GUIDE in Matlab® environment for creating GUIs

The three principal elements required to create a Matlab® GUI are:

1. Components: Each item on a Matlab® GUI is a graphical component. The types of components include graphical controls (pushbuttons, edit boxes, lists, sliders, etc.), static elements (frames and text strings), menus, and axes.

2. Figures: The components of a GUI must be arranged within a figure, which is a window on the computer screen.

3. Callbacks: A mouse click or a key press is an event, and the Matlab® program must respond to each event if the program is to perform its function. The code executed in response to an event is known as a callback. There must be a callback to implement the function of each graphical component on the GUI. Once a callback has been assigned to an object, the control flow of the program will be passed to the assigned callback. If a button has been assigned the callback named "*close*", then once that button is pressed, the code under "*close*" *will* be executed.

As a rule of thumb, if a user is able to use an interface without intervention and understand what happens behind the GUI and is able to interpret the results then the GUI is said to have accomplished its goal.

C.2 SIMULATION DATABASE

GUI created for this project is conveniently named as "SRMSim" and it is flexible enough to accommodate new functionalities if required in the future. GUI used here has a consistent appearance and armed with intuitive controls like pushbuttons and edit boxes, and, behaves in an understandable and predictable manner. Data flow between the functions of the main simulation GUI, the main simulation GUI window and the post-processing GUI windows like the *Results* GUI and the *Flux-Linkage Locus* GUI is transferred through the use of handles structure. In Matlab, handle is the unique identifier that gives direct access to each instance of any graphics object's properties. By providing access to each graphics object, handles enable the designer/user to access, explore, and modify the characteristics that define said objects. These characteristics are called ***properties***. A graphics object's properties control many aspects of its appearance and behaviour. Properties include general information such as the object's type, its parent and children, and whether it is visible, as well as information unique to the particular class of object.

The variables for the Simulink models need to be identified before any of the simulation models can be run. This is done via the GUI. GUI passes the simulation parameters (defined as variable names rather than actual numbers) into the model workspace rather than the base workspace. One can have access to the model workspace and check the variables and make sure the desired values are being used by the simulation. On start-up the main GUI window is displayed as in Figure C. 2.

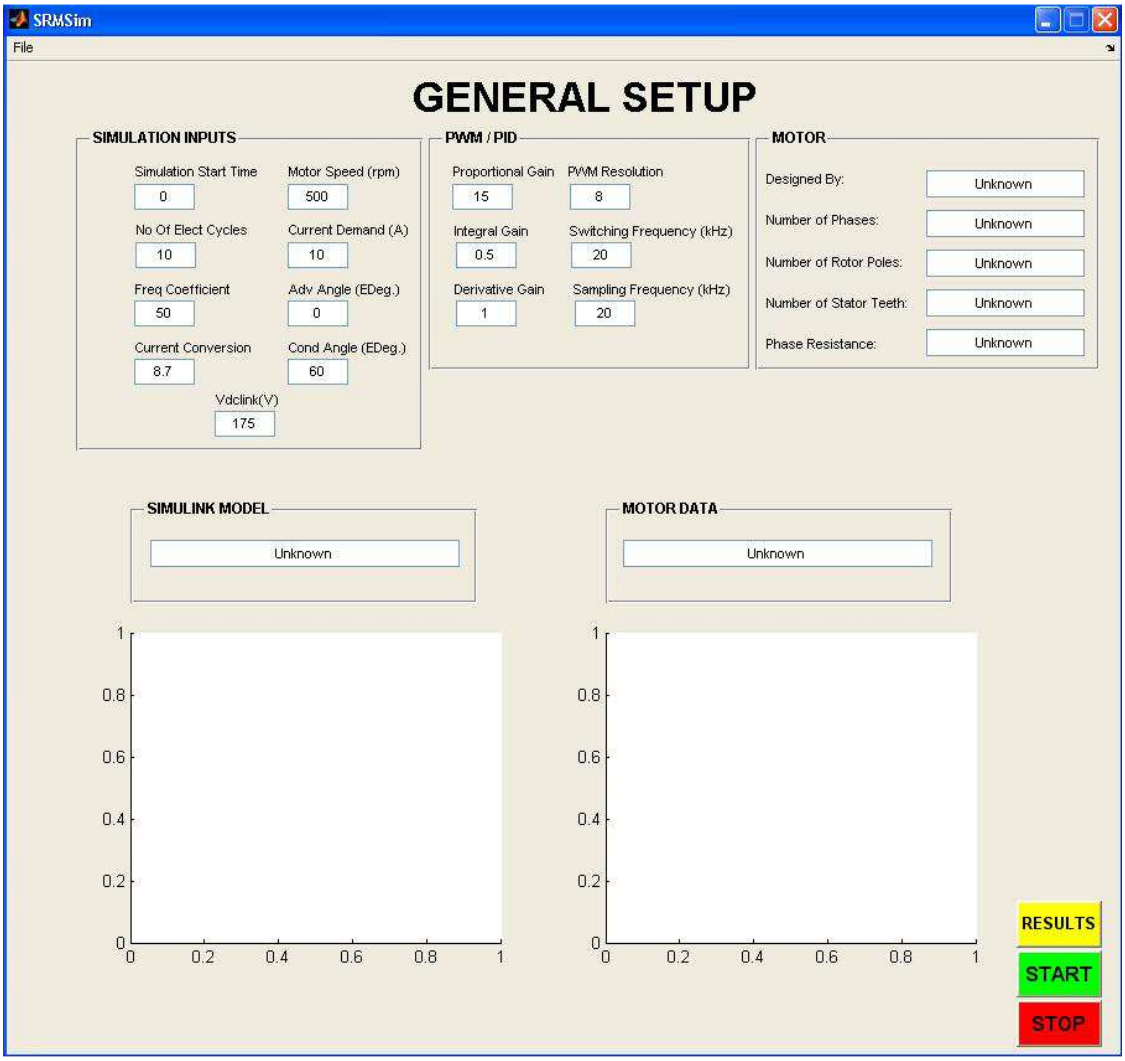

Figure C. 2 SRMSim Database Main GUI Window Initial State

The main GUI window is divided into several sub-sections. These are:

1. **SIMULATION INPUTS**: This is where information relating to the rotor speed, current demand, advance and conduction angles and dc-link voltage are entered. Here the user can also choose the number of electrical cycles the simulation is required to run for. Depending on the speed of the machine and the number of electrical cycles in the simulation the total length of each simulation run will vary.
2. **PWM / PID**: This is where parameters relating to the PID and PWM controllers are entered.
3. **MOTOR**: This is where basic information for the motor being simulated is displayed. This is more of an informative section. Manually changing values in this section will not change the parameters used in the simulation model.

4. **SIMULINK MODEL**: This is an informative section where the name of the simulink model being simulated is displayed. Again manually changing this will affect the simulation results.
5. **MOTOR DATA**: This is again an informative section where the name of the excel spreadsheet for the motor parameters such as flux-linkage / current / position and phase resistance is displayed.

The user can choose the simulation model and the motor parameters associated with that model by clicking the ***File*** menu at the top left corner of the main GUI window. This is shown in Figure C. 3.

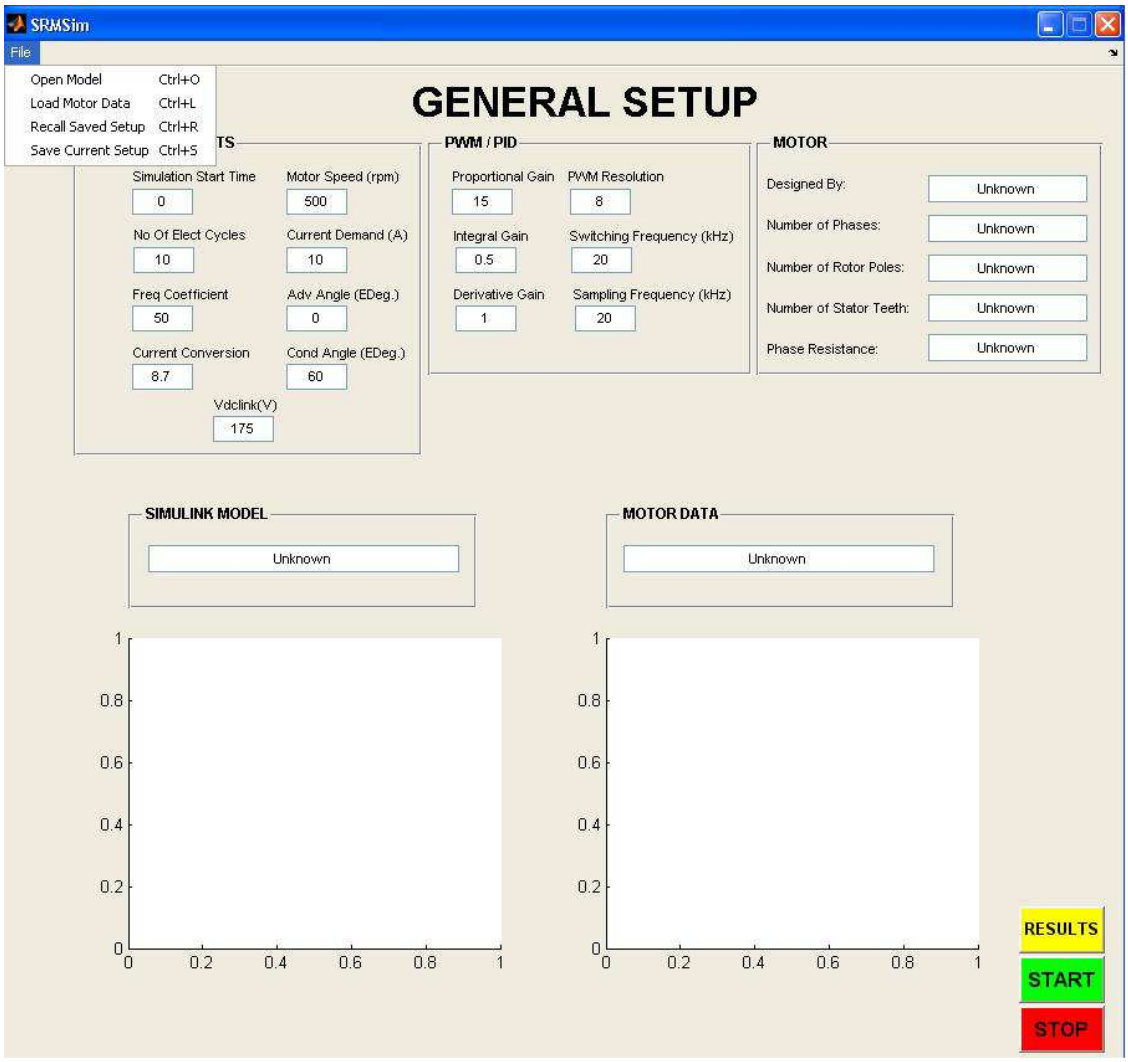

Figure C. 3 SRMSim Database Main GUI Window "File" Menu List

Once the user selects a spreadsheet that stores the flux-linkage characteristics of a particular motor, the GUI then calculates the torque / current / rotor position information. Algorithms employed for generating the torque characteristics from the flux-linkage characteristics are explained in Chapter 6. Both the flux-linkage (axis on the left) and the torque (axis on the right) characteristics are displayed in 3D surface plot format within the GUI window. The designer of the motor, the number of phases, rotor poles and the stator teeth along with the phase resistance are displayed in the ***MOTOR*** sub-section. All of these are depicted in Figure C. 4.

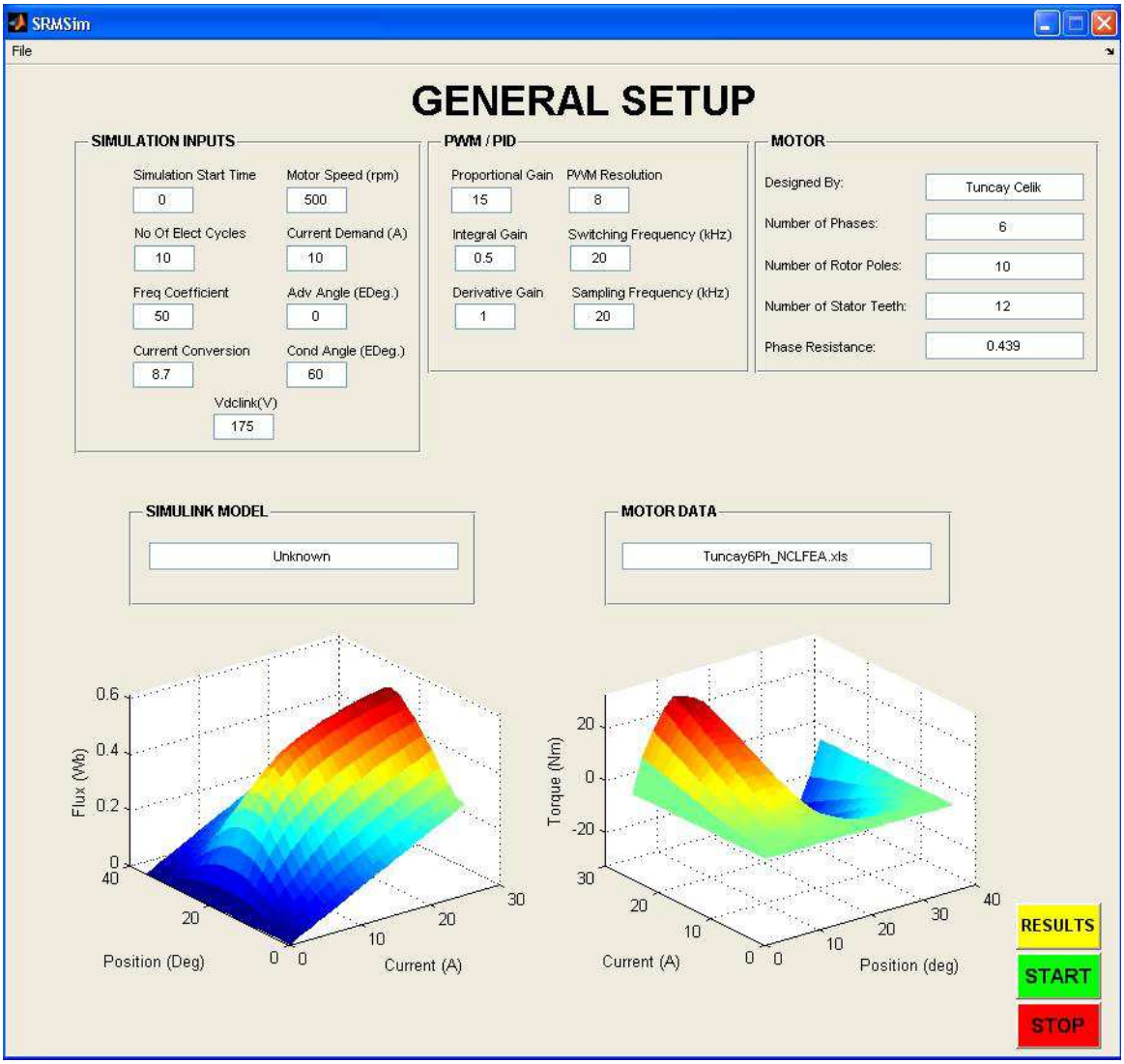

Figure C. 4 SRMSim Database Main GUI Window Once Motor Data Loaded

Once the simulink model is selected the GUI window displays the name of the model to be simulated. This is shown in Figure C. 5.

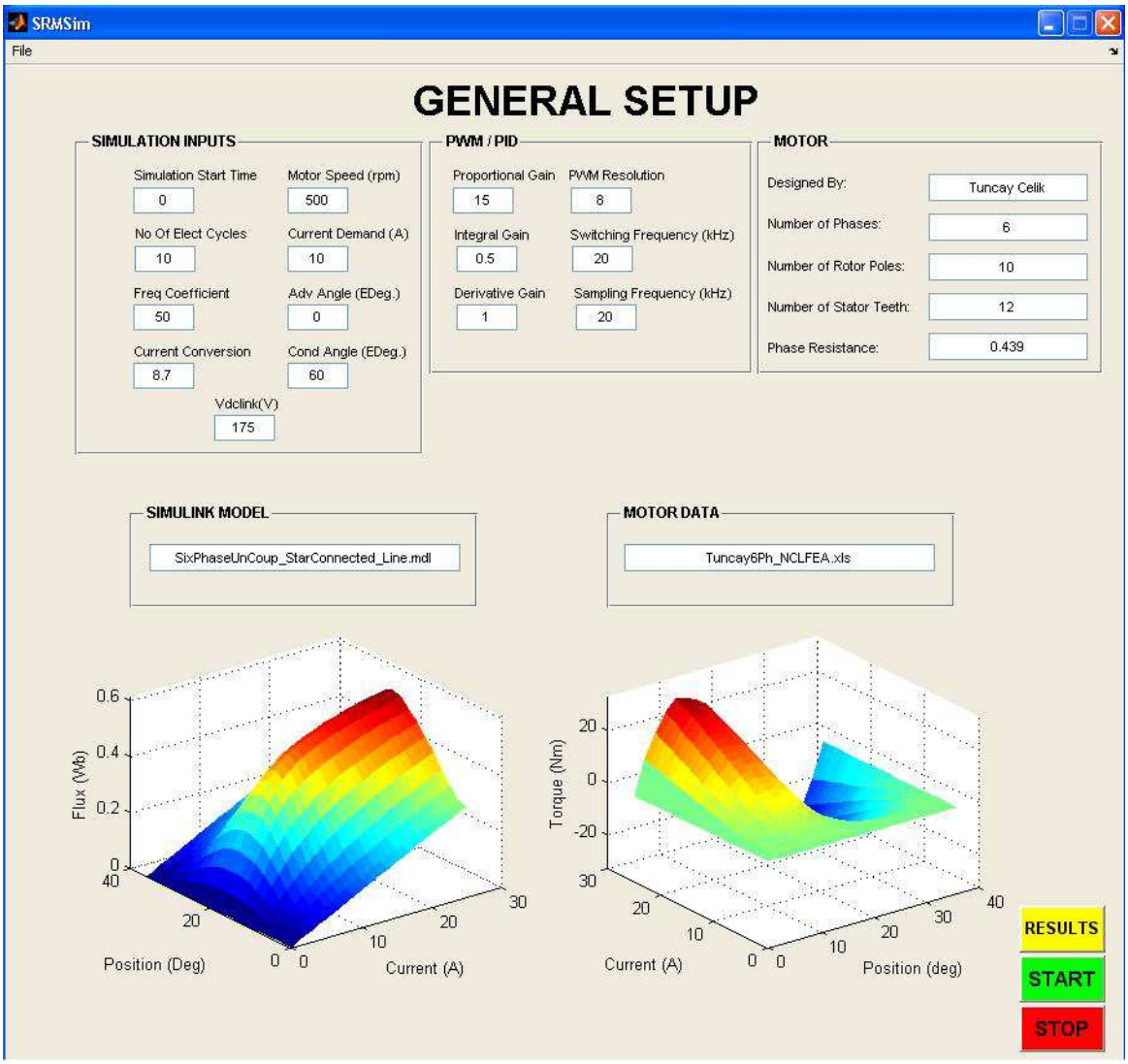

Figure C. 5 SRMSim Database Main GUI Window Once Simulink® Model Loaded

Once the simulation is completed, the ***RESULTS*** GUI is loaded. This is shown in Figure C. 6. ***RESULTS*** GUI displays the results of the performance calculations carried out once the simulation is completed such as total copper losses, inverter VA-rating, total inverter losses, output torque and torque ripple, etc. In ***RESULTS*** GUI there are two more GUIs available both of which can be loaded by clicking the pushbuttons; ***Vstar*** and ***FlxLkgLOCUS***. ***FlxLkgLocus*** GUI window displays the flux-linkage locus of the motor during simulation for one electrical cycle. This is displayed in Figure C. 7. ***Vstar*** pushbutton only becomes available if the motor is connected in star configuration. Once the ***Vstar*** pushbutton is pressed the ***Vstar*** GUI is displayed. In this GUI the user can view the simulated and filtered waveforms for the star point potential and the current flowing into the star point to further validate the simulation. This is displayed in Figure C. 8.

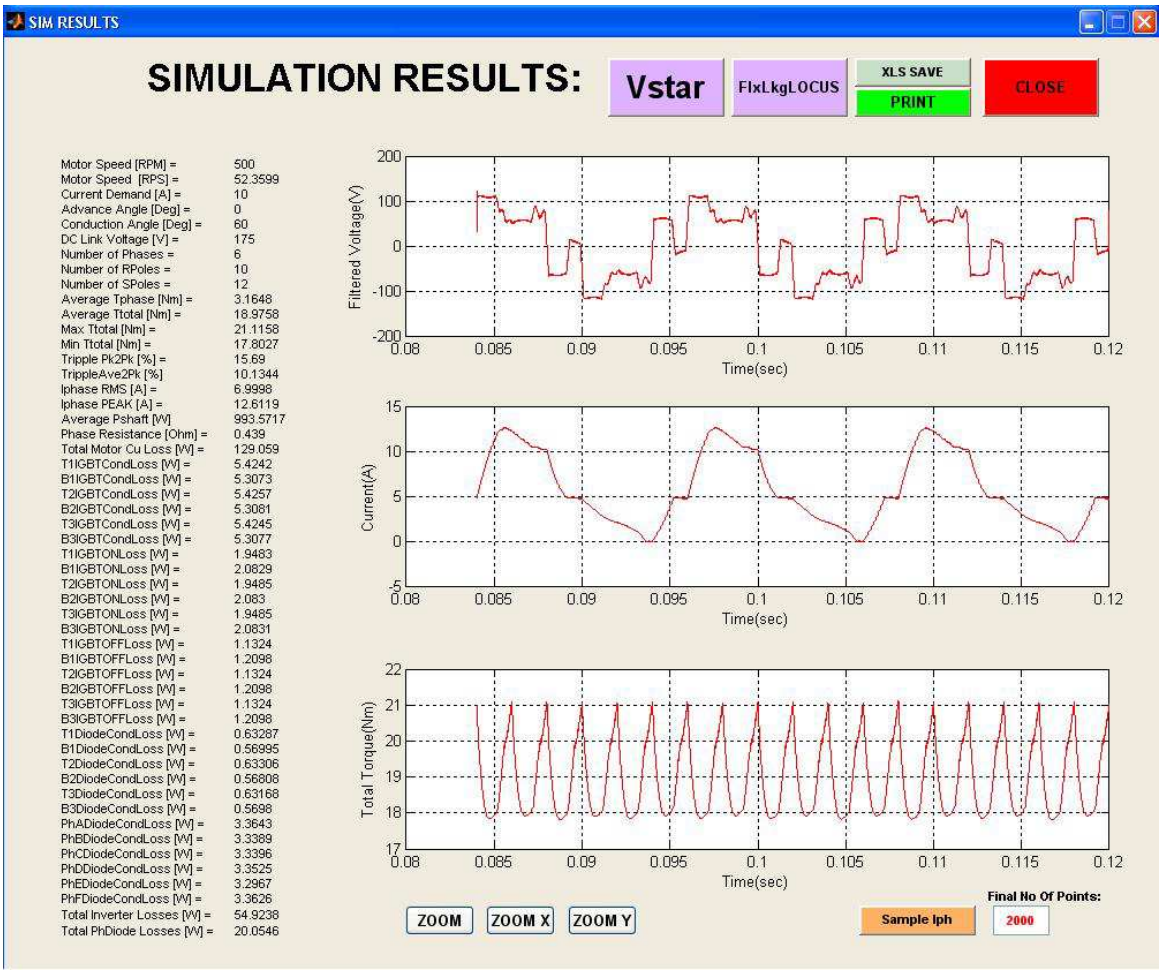

Figure C. 6 SIM RESULTS GUI Window (Left-Hand Side = Statistics Calculation Results; First Figure = Filtered Phase Voltage; Second Figure = Phase Current; Third Figure = Total Machine Torque)

Figure C. 7 FlxLkgLocus GUI Window depicting Phase Flux-Linkage vs. Phase Current

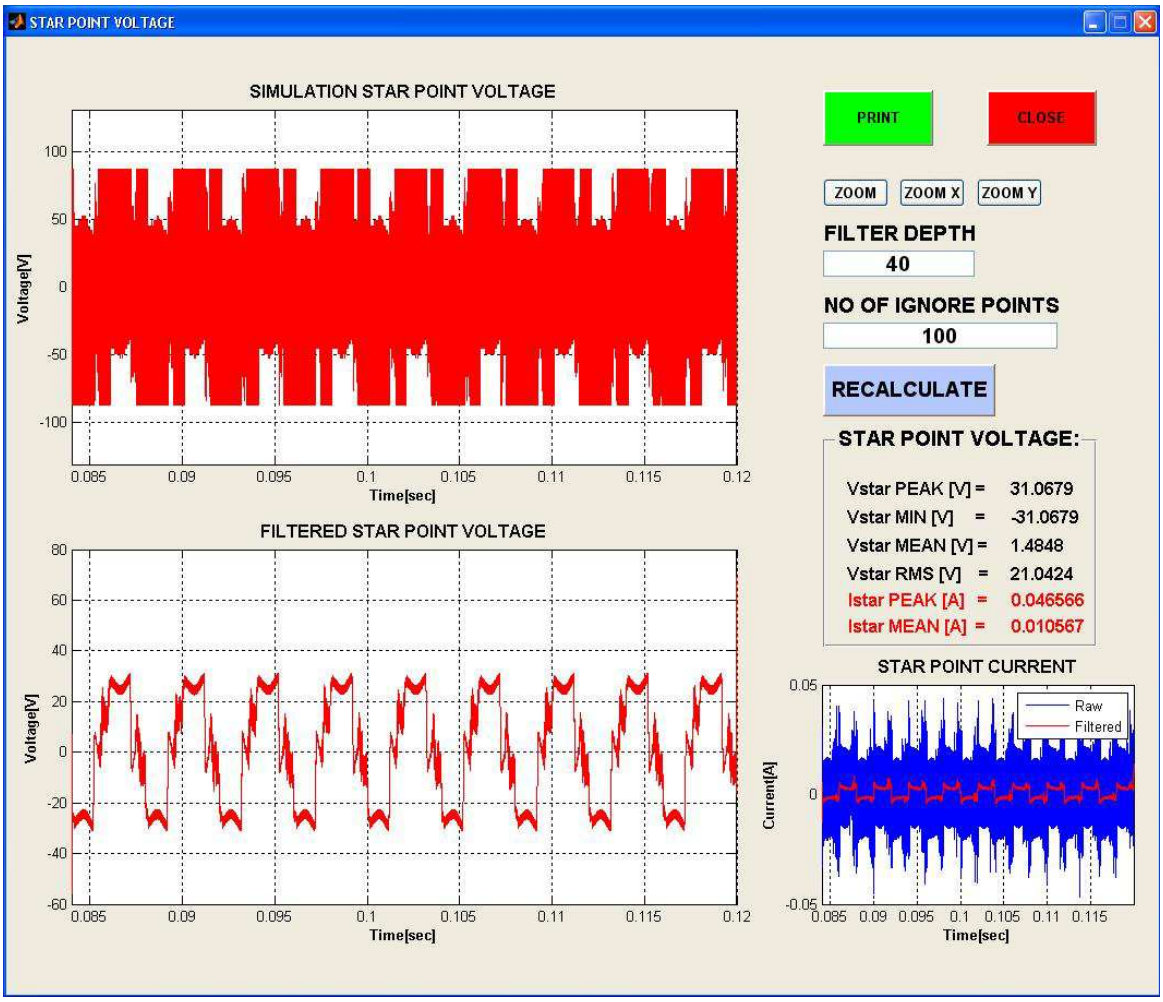

Figure C. 8 STAR POINT VOLTAGE GUI Window

APPENDIX D

D. Estimation of Machine Slot Area and Phase Resistance

This appendix details the derivation of mathematical equations that were used to calculate the slot area and consequently, estimate the phase resistance of the six phase 12-10 segmental rotor prototype switched reluctance machine. The information presented here was used to generate some of the results and discussions detailed in *Chapter 4 – Machine Design*. This appendix has been divided into two parts. The first part details the calculation of the slot area using machine design variables. The second part, on the other hand, details the estimation of the machine phase resistance using the calculated slot area from the first part.

D.1 CALCULATION OF MACHINE SLOT AREA

In Figure D. 1 a stator tooth segment of the six phase segmental rotor machine is outlined by the vertex points S_V0, S_V1, S_V2, S_V3, S_V4, S_V5, S_V6, S_V7, S_V8, and S_V9. It is a 30^o section of the full machine.

Coordinates of each vertex point in Figure D. 1 can be calculated by using the machine design variables. Machine design variables are explained graphically in Figure D. 2 and Figure D. 3. In Figure D. 2, BCD is the z-axis insulation layer thickness (separating the conductors from touching the inner surface of the stator tooth) and BCW is the x-axis

insulation layer thickness. Obvious from its definition, BCD will affect the total axial length of the machine. The insulation layer was formed by wrapping slot liners around each stator tooth. Table D. 1 lists the machine design variables depicted in Figure D. 2 and Figure D. 3. Coil gap angle in Table D. 1 (Θ_5 in Figure D. 3) defines the gap between the two coils (of neighbouring phases) wrapped around two adjacent stator teeth. In reality, coil gap is a linear dimension in [128]. However, during the modelling of the machine in the FE package it was represented in mechanical degrees in order to ease the generation of the machine in the FE environment.

Coordinates for each vertex point defining the area of a single stator tooth segment are calculated by using the equations listed below (Eq.D. 1 to Eq.D. 20).

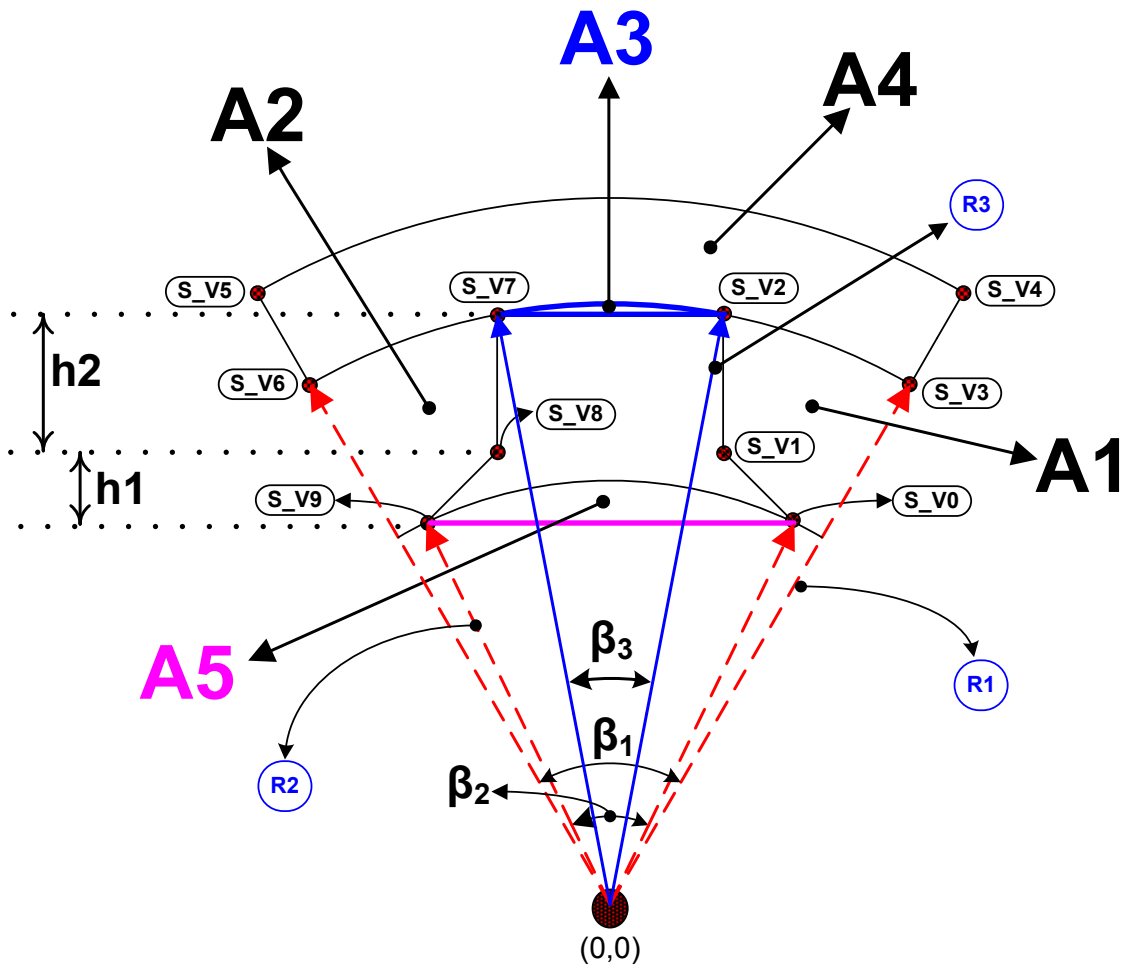

Figure D. 1 2D illustration of the stator segment area and the total slot area

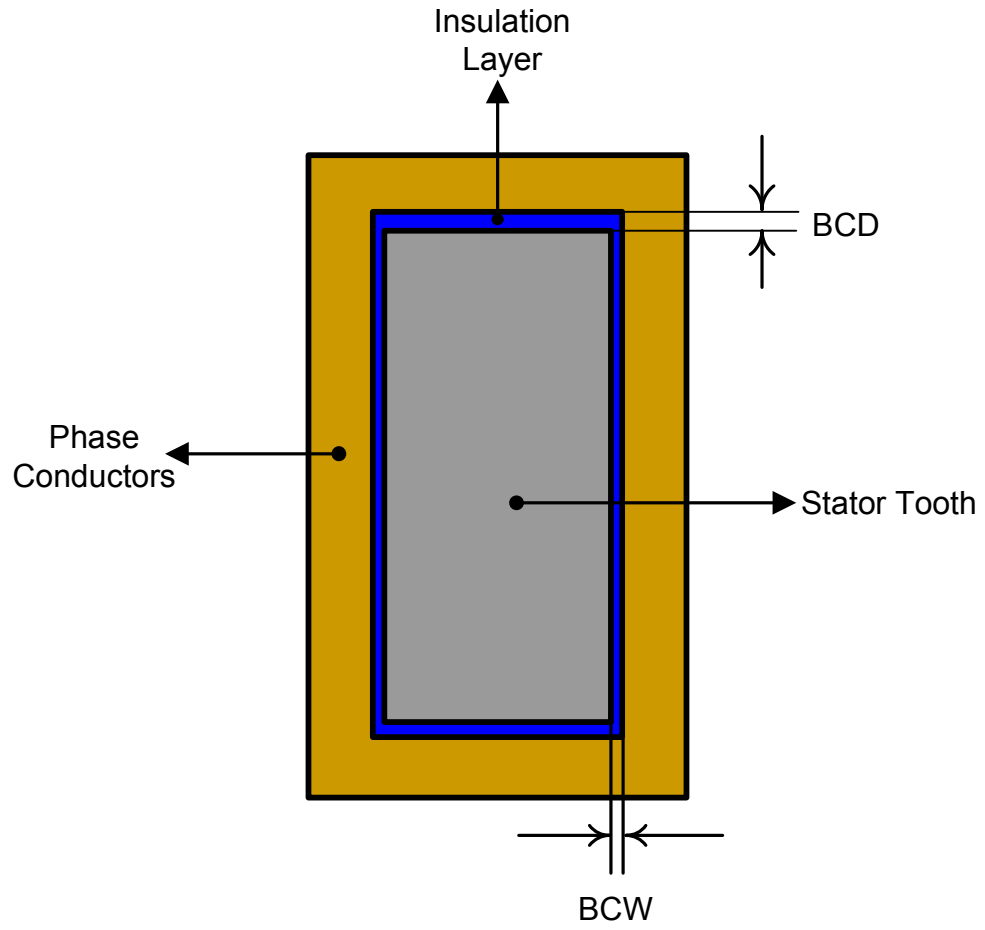

Figure D. 2 Figure showing dimensions of insulation layer between the stator core and the phase conductors (View from the top – positive y-axis)

Table D. 1 Table of machine design variables

CBD	Stator core-back depth
SD	Rotor segment depth
BCH	y-axis insulation layer thickness
BCW	x-axis insulation layer thickness
BCD	z-axis insulation layer thickness
TW	Stator tooth width
Lg	Air-gap length
Φ_1	Stator outside diameter
Φ_2	Stator bore-diameter
Φ_3	Rotor outside diameter
Θ_1	Stator tooth tang angle
Θ_2	Rotor segment angle
Θ_3	Stator tooth tip arc angle
Θ_4	Rotor segment arc angle
Θ_5	Coil gap angle
N_s	Total number of stator teeth
N_r	Total number of rotor segments

Appendix D – ESTIMATION OF MACHINE SLOT AREA & PHASE RESISTANCE

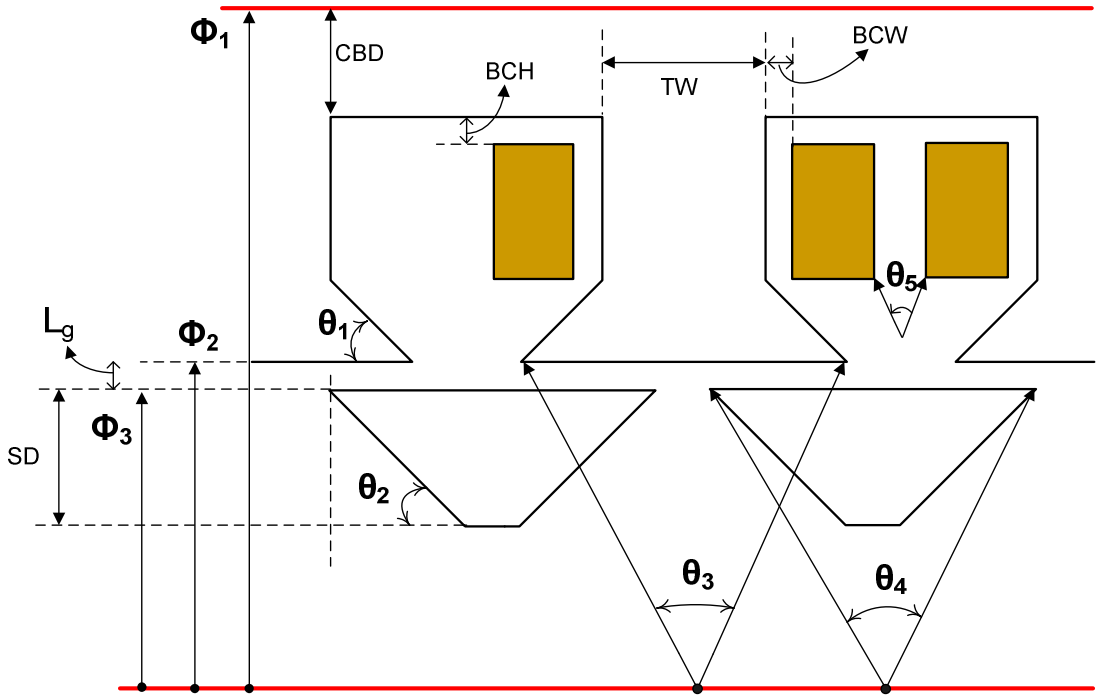

Figure D. 3 Rectilinear representation of the segmented rotor machine design variables

$$S\_V0(x) = \frac{\phi_2}{2} \times \cos(90 - \frac{\theta_3}{2}) \quad \textbf{Eq.D. 1}$$

$$S\_V0(y) = \frac{\phi_2}{2} \times \sin(90 - \frac{\theta_3}{2}) \quad \textbf{Eq.D. 2}$$

$$S\_V1(x) = \frac{TW}{2} \quad \textbf{Eq.D. 3}$$

$$S\_V1(y) = \frac{S\_V0(y) + ((S\_V0(x) - \frac{TW}{2}))}{\tan(\theta_1)} \quad \textbf{Eq.D. 4}$$

$$S\_V2(x) = S\_V1(x) \quad \textbf{Eq.D. 5}$$

$$S\_V2(y) = \sqrt{((\frac{\phi_1}{2} - CBD)^2 - (\frac{TW}{2})^2)} \quad \textbf{Eq.D. 6}$$

$$S\_V3(x) = (\frac{\phi_1}{2} - CBD) \times \cos(90 - \frac{360}{2 \times N_s}) \quad \textbf{Eq.D. 7}$$

$$S\_V3(y) = (\frac{\phi_1}{2} - CBD) \times \sin(90 - \frac{360}{2 \times N_s}) \quad \textbf{Eq.D. 8}$$

$$S\_V4(x) = (\frac{\phi_1}{2}) \times \cos(90 - \frac{360}{2 \times N_s}) \quad \textbf{Eq.D. 9}$$

$$S\_V4(y) = (\frac{\phi_1}{2}) \times \sin(90 - \frac{360}{2 \times N_s}) \quad \textbf{Eq.D. 10}$$

$$S\_V5(x) = -S\_V4(x) \quad \textbf{Eq.D. 11}$$

$$S\_V5(y) = S\_V4(y) \quad \textbf{Eq.D. 12}$$

$$S\_V6(x) = -S\_V3(x) \quad \textbf{Eq.D. 13}$$

$$S\_V6(y) = S\_V3(y) \quad \textbf{Eq.D. 14}$$

$$S\_V7(x) = -S\_V2(x) \quad \textbf{Eq.D. 15}$$

$$S\_V7(y) = S\_V2(y) \quad \textbf{Eq.D. 16}$$

$$S\_V8(x) = -S\_V1(x) \quad \textbf{Eq.D. 17}$$

$$S\_V8(y) = S\_V1(y) \quad \textbf{Eq.D. 18}$$

$$S\_V9(x) = -S\_V0(x) \quad \textbf{Eq.D. 19}$$

$$S\_V9(y) = S\_V0(y) \quad \textbf{Eq.D. 20}$$

The total slot area can now be calculated by using the equations listed below (Eq.D. 21 to Eq.D. 32).

$$h2 = S\_V2(y) - S\_V1(y) \quad \textbf{Eq.D. 21}$$

where $h2$ is the stator body height and, $S\_V2(y)$ and $S\_V1(y)$ are the stator vertex coordinates given in Eq.D. 6 and Eq.D. 4, respectively. Using Eq.D. 21, the stator body area can be calculated by Eq.D. 22.

$$A_{body} = h2 \times TW \quad \textbf{Eq.D. 22}$$

where A_{body} is the stator body area enclosed by the vertex points S_V1, S_V2, S_V7, and S_V8.

$$h1 = S\_V1(y) - S\_V0(y) \quad \textbf{Eq.D. 23}$$

where $h1$ is the stator tooth tip height and, $S\_V1(y)$ and $S\_V0(y)$ are the stator vertex coordinates given in Eq.D. 4 and Eq.D. 2 , respectively.

$$A5 = 0.5 \times (\frac{\phi_2}{2})^2 \times (\frac{\pi \times \theta_3}{180} - \sin(\theta_3)) \quad \textbf{Eq.D. 24}$$

where $A5$ is the stator tooth tip segment area as shown in Figure D. 1. ϕ_2 (R2 in Figure D. 1) and θ_3 (β_2 in Figure D. 1) are illustrated in Figure D. 3.

$$A_{trap} = 0.5 \times h1 \times (\frac{TW}{2} + (S\_V0(x) - S\_V9(x))) \quad \textbf{Eq.D. 25}$$

where A_{trap} is the area of the stator tooth tip trapezoid enclosed by the vertex points S_V0, S_V1, S_V8, and S_V9 in Figure D. 1. $h1$ is the stator tooth tip height shown in Figure D. 1. Definitions for $S\_V0(x)$ and $S\_V9(x)$ are given in Eq.D. 1 and Eq.D. 19, respectively.

$$A4 = \frac{\pi}{N_s} \times ((\frac{\phi_1}{2})^2 - (\frac{\phi_1}{2} - CBD)^2) \quad \textbf{Eq.D. 26}$$

where $A4$ is the area of the stator core-back segment as shown in Figure D. 1.

$$A3 = 0.5 \times (\frac{\phi_1}{2} - CBD)^2 \times (\frac{\pi \times \beta_3}{180} - \sin(\beta_3)) \quad \textbf{Eq.D. 27}$$

where $A3$ is the area of the stator core-back sector as shown in Figure D. 1. β_3 is the core-back sector area angle depicted in Figure D. 1 and is calculated by Eq.D. 28.

$$\beta_3 = 2 \times \arctan\left(\frac{S\_V2(x)}{S\_V2(y)}\right) \quad \textbf{Eq.D. 28}$$

The total stator tooth area can be calculated by Eq.D. 29.

$$A_{Tstator} = A3 + A4 + A_{body} + A_{trap} - A5 \quad \textbf{Eq.D. 29}$$

where $A_{TStator}$ is the total stator tooth area. The area enclosed by points (0,0), S_V4 and S_V5 in Figure D. 1 is called the total segment area and is calculated by Eq.D. 30.

$$A_{TSegment} = \frac{\pi}{N_s} \times \left(\frac{\phi_1}{2}\right)^2 \quad \textbf{Eq.D. 30}$$

The area enclosed by points (0,0), S_V0 and S_V9 in Figure D. 1 is called the inner segment area and is calculated by Eq.D. 31.

$$A_{ISegment} = \frac{\pi}{N_s} \times \left(\frac{\phi_2}{2}\right)^2 \quad \textbf{Eq.D. 31}$$

Finally the total slot area is calculated by Eq.D. 32.

$$A_{TSlot} = A1 + A2 = A_{TSegment} - A_{ISegment} - A_{TStator} \quad \textbf{Eq.D. 32}$$

Areas $A1$ and $A2$ are both illustrated in Figure D. 1. If the total number of turns per coil and the total conductor diameter (including conductor insulation layer) are known, the slot fill factor can be calculated by Eq.D. 33.

$$SFF = \frac{2 \times N_{turns} \times \pi \times \frac{D_{cond}^{\ 2}}{4}}{A_{TSlot}} \quad \textbf{Eq.D. 33}$$

where SFF is the slot fill factor, N_{turns} is the number of turns per coil, D_{cond} is the total conductor diameter (including insulation layer), and A_{TSlot} is the total slot area calculated by Eq.D. 32. Estimation of phase resistance is given in the following section.

D.2 ESTIMATION OF MACHINE PHASE RESISTANCE

Coil resistance can be calculated by Eq.D. 34.

$$R_{coil} = \rho \frac{L_{tot}}{A_{cond}} \quad \textbf{Eq.D. 34}$$

where R_{coil} is the coil resistance in [Ω], ρ is the electrical resistivity in [Ω.m], L_{tot} is the total length of the conductors forming the coil in [m], and A_{cond} is the bare conductor cross-sectional area in [m^2]. Bare conductor cross-sectional area is given by Eq.D. 35.

$$A_{cond} = \pi \times \frac{(D_{total} - 2 \times L_{insulation})^2}{4} \quad \textbf{Eq.D. 35}$$

where D_{total} is the total conductor diameter and $L_{insulation}$ is the conductor insulation layer thickness. Apparent from Eq.D. 34, an accurate estimate for the total length of the conductors forming the coil is required for an accurate estimation of coil resistance.
The total length of conductors (forming a coil) can be estimated by Eq.D. 36.

$$L_{tot} = N_{turns} \times MPL \quad \textbf{Eq.D. 36}$$

where N_{turns} is the total number of turns per coil and MPL is the mean path length of a single coil turn.

The mean path length of a single coil turn can be estimated by Eq.D. 37.

$$MPL = 2 \times (L_{stk} + L_{endwinding}) \quad \textbf{Eq.D. 37}$$

where L_{stk} is the total lamination stack length and $L_{endwinding}$ is the end-winding length. To ease the calculation process the winding area is assumed to be a square as in Figure D. 4-a where in fact it is more of the form given in Figure D. 4-b.

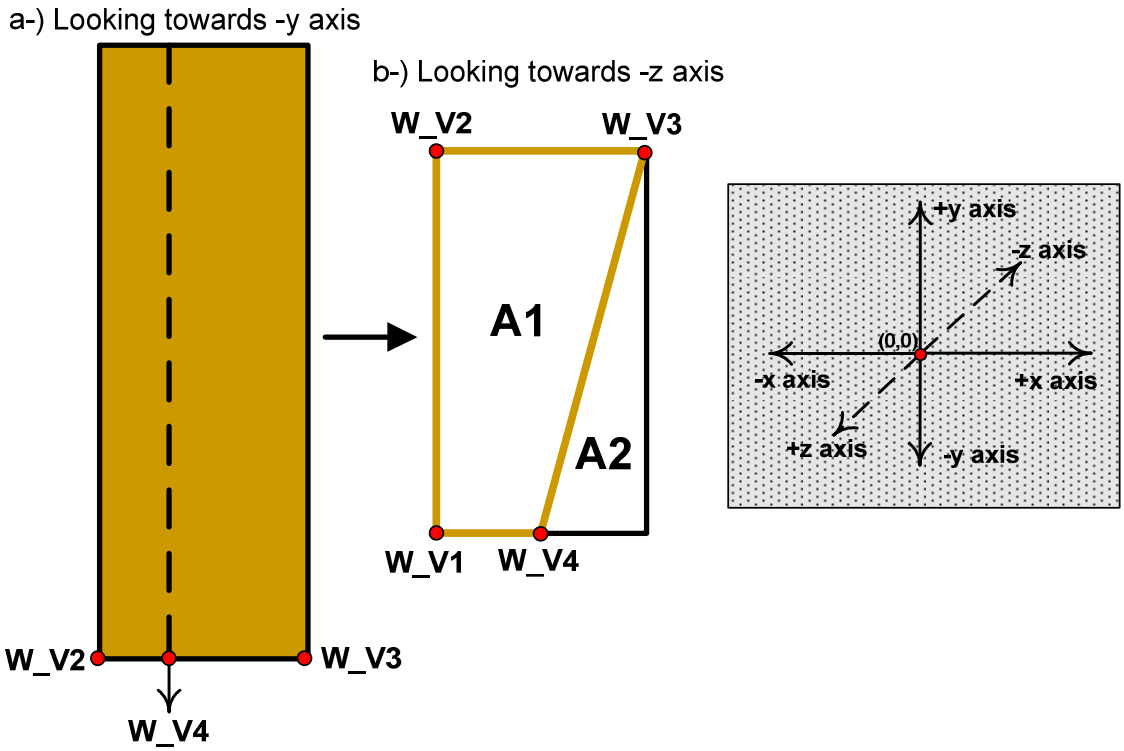

Figure D. 4 Rectilinear view of the winding area looking from the top (towards –y axis) and the front (towards –z axis) of the machine showing vertex points that outline the winding area

The end-winding length can be estimated by Eq.D. 38.

$$L_{endwinding} = TW + C \qquad \textbf{Eq.D. 38}$$

where TW is the stator tooth width and C is the length of the arc, both depicted in Figure D. 5. The length of the arc C can be approximated by a straight line (Z in Figure D. 5) and a correction factor as in Eq.D. 39.

$$C = k \times Z = k \times \sqrt{\left(X^2 + Y^2\right)} \qquad \textbf{Eq.D. 39}$$

where k is the correction factor, and X and Y are the straight lines shown in Figure D. 5. Correction factor k in Eq.D. 39 is used to account for the linearization of the arc length C into the straight line Z (Figure D. 5).

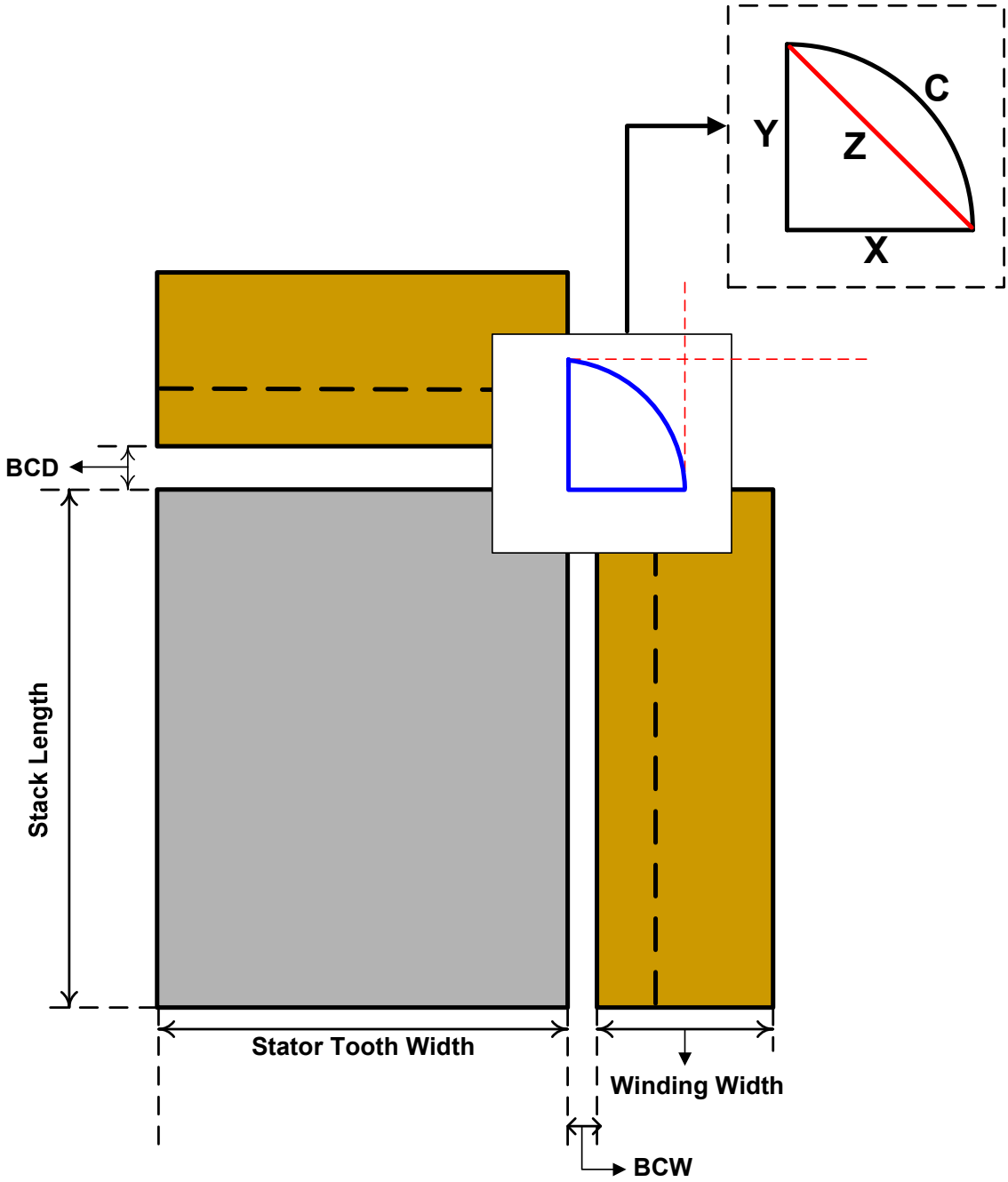

Figure D. 5 Graphical explanation of end-winding length estimation in rectilinear form (Top view of machine stator tooth and coil windings)

To be able to calculate X and Y, the coordinates of vertex points defining the winding area need to be defined. Figure D. 4-b is the graphical representation of the winding area vertex points showing V_W1, V_W2, V_W3 and V_W4. The coordinates of these vertex points can be calculated by using the following equations (Eq.D. 40 to Eq.D. 47). Note that equations from Eq.D. 40 to Eq.D. 47 are not for the rectangular winding area model given in Figure D. 4-b but they are for the actual machine geometry.

$$W\_V1(x) = \frac{TW}{2} + BCW \quad \textbf{Eq.D. 40}$$

$$W\_V1(y) = \sqrt{((\frac{\phi_1}{2} - CBD)^2 - (\frac{TW}{2})^2)} \quad \textbf{Eq.D. 41}$$

$$W\_V2(x) = \frac{TW}{2} + BCW \quad \textbf{Eq.D. 42}$$

$$W\_V2(y) = \sqrt{\left(\frac{\phi_1}{2} - CBD - BCH\right)^2 - \left(\frac{TW}{2} + BCW\right)^2} \quad \textbf{Eq.D. 43}$$

$$W\_V3(x) = (\frac{\phi_1}{2} - CBD - BCH) \times \cos(90 - \frac{360}{N_s \times 2} + \theta_5) \quad \textbf{Eq.D. 44}$$

$$W\_V3(y) = (\frac{\phi_1}{2} - CBD - BCH) \times \sin(90 - \frac{360}{N_s \times 2} + \theta_5) \quad \textbf{Eq.D. 45}$$

$$W\_V4(x) = \frac{W\_V1(y)}{\tan(90 - \frac{360}{N_s \times 2} + \theta_5)} \quad \textbf{Eq.D. 46}$$

$$W\_V4(y) = W\_V1(y) \quad \textbf{Eq.D. 47}$$

X and Y in Eq.D. 39 can now be calculated by using Eq.D. 48 and Eq.D. 49, respectively.

$$X = \frac{W\_V3(x) - W\_V2(x)}{2} + BCD \quad \textbf{Eq.D. 48}$$

and

$$Y = \frac{W\_V3(x) - W\_V2(x)}{2} + BCW \quad \textbf{Eq.D. 49}$$

The correction factor k in Eq.D. 39 is set to 1.05. Equations from Eq.D. 38 to Eq.D. 49 assume that the windings cover a rectangular area (A1 + A2 in Figure D. 4-b). However, in reality, windings cover the area A1 in Figure D. 4-b. Therefore once the coil resistance

is calculated a correction factor must be added to account for this fact. This is achieved by using Eq.D. 50.

$$R\_Coil = Area\_Factor \times R\_Coil\,\mathrm{Re}\,ct \qquad \textbf{Eq.D. 50}$$

where R_Coil is the actual coil resistance, $R\_Coil\,\mathrm{Re}\,ct$ is the coil resistance calculated by using equations from Eq.D. 38 to Eq.D. 49 and $Area\_Factor$ is the ratio of the areas A1 and A2 in Figure D. 4-b. $Area\_Factor$ is calculated by Eq.D. 51.

$$Area\_Factor = \frac{A1}{A1 + A2} \qquad \textbf{Eq.D. 51}$$

Once the machine dimensions and the bare conductor diameter are known the coil resistance can be calculated. Depending on the coil connections (either parallel or series) estimation for the phase resistance can be made. The following steps explain how the conductor diameter has been determined for the prototype 6-phase segmented rotor machine.

Peak current density of 10.0 [A/mm^2] and peak phase current of 25.0 [A] are assumed. From Eq.D. 52 (any one phase of the machine phase is assumed to be conducting for one third of the electrical cycle) 25.0 [A] of peak phase current equates to approximately 14.4 [A] of RMS phase current.

$$I_{phRMS} = \frac{I_{phPEAK}}{\sqrt{3}} \qquad \textbf{Eq.D. 52}$$

The required conductor cross sectional area (A_{cond}) can then be calculated by Eq.D. 53

$$A_{cond} = \frac{I_{phRMS}}{J_{PEAK}} \qquad \textbf{Eq.D. 53}$$

where J_{PEAK} is the maximum current density. A_{cond} is calculated to be approximately 1.443 [mm^2] which equates to a conductor diameter of approximately 1.36[mm]. The closest available conductor diameter was 1.4 [mm] so this was chosen as the conductor diameter.

List of References

[1] Cardenas, R.; Pena, R.; Perez, M.; Clare, J.; Asher, G.; Wheeler, P.;, "Control of a switched reluctance generator for variable-speed wind energy applications," *Energy Conversion, IEEE Transactions on*, vol. 20, pp. 781-791, 2005.

[2] Cardenas, R.; Ray, W.F.; Asher, G.M.;, "Switched reluctance generators for wind energy applications," in *Power Electronics Specialists Conference, 1995. PESC '95 Record., 26th Annual IEEE*, 1995, pp. 559-564 vol.1.

[3] Mese, E.; Sozer, Y.; Kokernak, J.M.; Torrey, D.A.;, "Optimal excitation of a high speed switched reluctance generator," in *Applied Power Electronics Conference and Exposition, 2000. APEC 2000. Fifteenth Annual IEEE*, 2000, pp. 362-368 vol.1.

[4] M. A. Mueller, "Design of low speed switched reluctance machines for wind energy converters," in *Electrical Machines and Drives, 1999. Ninth International Conference on (Conf. Publ. No. 468)*, 1999, pp. 60-64.

[5] "Offshore Wind Power Market Potential," *Energy Business Reports, April 2008.*

[6] "U.S., China Lead Global Wind Installation," *North American Wind Power, February 2009.*

[7] Powell, D.J.; Jewell, G.W.; Calverley, S.D.; Howe, D.;, "Iron loss in a modular rotor switched reluctance machine for the "More-Electric" aero-engine," *Magnetics, IEEE Transactions on*, vol. 41, pp. 3934-3936, 2005.

[8] Hall, R.; Jack, A.G.; Mecrow, B.C.; Mitcham, A.J.;, "Design and initial testing of an outer rotating segmented rotor switched reluctance machine for an aero-engine shaft-line-embedded starter/generator," in *Electric Machines and Drives, 2005 IEEE International Conference on*, 2005, pp. 1870-1877.

[9] S. R. MacMinn and W. D. Jones, "A very high speed switched-reluctance starter-generator for aircraft engine applications," in *Aerospace and Electronics Conference, 1989. NAECON 1989., Proceedings of the IEEE 1989 National*, 1989, pp. 1758-1764 vol.4.

[10] E. Richter, "High Temperature, Lightweight, Switched Reluctance Motors and Generators for Future Aircraft Engine Applications," in *American Control Conference, 1988*, 1988, pp. 1846-1851.

[11] S. Shoujun, L.Weiguo, D. Peitsch, U. Schaefer;, "Detailed Design of a High Speed Switched Reluctance Starter/Generator for More/All Electric Aircraft," *Chinese Journal of Aeronautics*, vol. 23, pp. 216-226, 2010.

[12] Mecrow, B.C.; Finch, J.W.; El-Kharashi, E.A.; Jack, A.G.;, "Switched reluctance motors with segmental rotors," *Electric Power Applications, IEE Proceedings -*, vol. 149, pp. 245-254, 2002.

[13] A. C. Clothier and B. C. Mecrow, "Inverter topologies and current sensing methods for short pitched and fully pitched winding SR motors," in *Applied Power Electronics Conference and Exposition, 1999. APEC '99. Fourteenth Annual*, 1999, pp. 416-423 vol.1.

[14] Mecrow, B.C.; Jack, A.G.; Atkinson, D.J.; Green, S.R.; Atkinson, G.J.; King, A.; Green, B.;, "Design and testing of a four-phase fault-tolerant permanent-magnet machine for an engine fuel pump," *Energy Conversion, IEEE Transactions on*, vol. 19, pp. 671-678, 2004.

[15] D. Kennedy, "Rare Earth Permanent Magnet Raw Materials Supply," *magnews - The international publication of the UK Magnetics Society, UKMAG one-day seminar Cutting Costs by Optimised Machine Design, April 2009,* 2009.

[16] B. D. Bedford, ""Compatible Permanent Magnet or Reluctance Brushless Motors and Controlled Switch Circuits", US Patent No 3678352, 18 July 1972.."

[17] B. D. Bedford, ""Compatible Brushless Reluctance Motors and Controlled Switch Circuits", US Patent No 3679953, 25 July 1972.."

[18] Lawrenson, P.J.; Stephenson, J.M.; Fulton, N.N.; Blenkinsop, P.T.; Corda, J.;, "Variable-speed switched reluctance motors," *Electric Power Applications, IEE Proceedings B,* vol. 127, pp. 253-265, 1980.

[19] L. J. G. Byrn J. V., "Characteristics of saturable stepper and reluctance motors," in *Small Electrical Machines, 1976 IEEE International Conference on.*, 1976.

[20] W. F. Ray and R. M. Davis, "Inverter Drive for Doubly Salient Reluctance Motor: Its Fundamental Behaviour, Linear Analysis and Cost Implications," *Electric Power Applications, IEE Journal on,* vol. 2, pp. 185-193, 1979.

[21] R. T. Fingers and C. S. Rubertus, "Application of high temperature magnetic materials," *Magnetics, IEEE Transactions on,* vol. 36, pp. 3373-3375, 2000.

[22] Mecrow, B.; Bennett, J.; Jack, A.; Atkinson, D.; Freeman, A.;, "Very high efficiency drives for solar powered unmanned aircraft," in *Electrical Machines, 2008. ICEM 2008. 18th International Conference on*, 2008, pp. 1-6.

[23] Mecrow, B.C.; El-Kharashi, E.A.; Finch, J.W.; Jack, A.G.;, "Segmental rotor switched reluctance motors with single-tooth windings," *Electric Power Applications, IEE Proceedings -*, vol. 150, pp. 591-599, 2003.

[24] T. J. E. Miller, *"Electronic Control of Switched Reluctance Machines", Newnes Press, Oxford, 2001.*

[25] Yong Kwon Choi; Hee Sung Yoon; Chang Seop Koh;, "Pole-Shape Optimization of a Switched-Reluctance Motor for Torque Ripple Reduction," *Magnetics, IEEE Transactions on,* vol. 43, pp. 1797-1800, 2007.

[26] Johnson, J.P.; Rajarathnam, A.V.; Toliyat, H.A.; Gopalakrishnan, S.; Fahimi, B.;, "Torque optimization for a SRM using winding function theory with a gap-dividing surface," in *Industry Applications Conference, 1996. Thirty-First IAS Annual Meeting, IAS '96., Conference Record of the 1996 IEEE*, 1996, pp. 753-760 vol.2.

[27] T. A. Lipo, "Novel reluctance machine concepts for variable speed drives," in *Electrotechnical Conference, 1991. Proceedings., 6th Mediterranean*, 1991, pp. 34-43 vol.1.

[28] Van der Giet, M.; Lange, E.; Corrêa, D.A.P.; Chabu, I.E.; Nabeta, S.I.; Hameyer, K.;, "Acoustic Simulation of a Special Switched Reluctance Drive by Means of Field-Circuit Coupling and Multiphysics Simulation," *Industrial Electronics, IEEE Transactions on,* vol. 57, pp. 2946-2953, 2010.

[29] Pengov, W.; Hendershot, J.R.; Miller, T.J.E.;, "A new low-noise two-phase switched reluctance motor," in *Electric Machines and Drives, 2005 IEEE International Conference on*, 2005, pp. 1281-1284.

[30] Moallem, M.; Ong, C.-M.; Unnewehr, L.E.;, "Effect of rotor profiles on the torque of a switched-reluctance motor," *Industry Applications, IEEE Transactions on,* vol. 28, pp. 364-369, 1992.

[31] D. P. Tormey and D. A. Torrey, "A comprehensive design procedure for low torque-ripple variable-reluctance motor drives," in *Industry Applications Society Annual Meeting, 1991., Conference Record of the 1991 IEEE*, 1991, pp. 244-251 vol.1.

[32] Ozoglu, Y.; Garip, M.; Mese, E.;, "New pole tip shapes mitigating torque ripple in short pitched and fully pitched switched reluctance motors," in *Industry Applications Conference, 2002. 37th IAS Annual Meeting. Conference Record of the*, 2002, pp. 43-50 vol.1.

[33] R. T. Naayagi and V. Kamaraj, "Optimum Pole Arcs for Switched Reluctance Machine with Reduced Ripple," in *Power Electronics and Drives Systems, 2005. PEDS 2005. International Conference on*, 2005, pp. 761-764.

[34] N. K. Sheth and K. R. Rajagopal, "Optimum pole arcs for a switched reluctance motor for higher torque with reduced ripple," *Magnetics, IEEE Transactions on*, vol. 39, pp. 3214-3216, 2003.

[35] Bhiwapurkar, N.; Jain, A.K.; Mohan, N.;, "Study of new stator pole geometry for improvement of SRM torque profile," in *Electric Machines and Drives, 2005 IEEE International Conference on*, 2005, pp. 516-520.

[36] Krishnan, R.; Arumugan, R.; Lindsay, J.F.;, "Design procedure for switched-reluctance motors," *Industry Applications, IEEE Transactions on*, vol. 24, pp. 456-461, 1988.

[37] Anwar, M.N.; Husain, I.; Radun, A.V.;, "A comprehensive design methodology for switched reluctance machines," *Industry Applications, IEEE Transactions on*, vol. 37, pp. 1684-1692, 2001.

[38] J. Faiz and J. W. Finch, "Aspects of design optimisation for switched reluctance motors," *Energy Conversion, IEEE Transactions on*, vol. 8, pp. 704-713, 1993.

[39] Finch, J.W.; Faiz, J.; Metwally, H.M.B.;, "Design study of switched reluctance motor performance," in *Industry Applications Society Annual Meeting, 1992., Conference Record of the 1992 IEEE*, 1992, pp. 242-248 vol.1.

[40] T. J. E. Miller, "Optimal design of switched reluctance motors," *Industrial Electronics, IEEE Transactions on*, vol. 49, pp. 15-27, 2002.

[41] A. V. Radun, "Design considerations for the switched reluctance motor," *Industry Applications, IEEE Transactions on*, vol. 31, pp. 1079-1087, 1995.

[42] Vijayakumar, K.; Karthikeyan, R.; Paramasivam, S.; Arumugam, R.; Srinivas, K.N.;, "Switched Reluctance Motor Modeling, Design, Simulation, and Analysis: A Comprehensive Review," *Magnetics, IEEE Transactions on*, vol. 44, pp. 4605-4617, 2008.

[43] R. M. Davis, "A comparison of switched reluctance rotor structures," *Industrial Electronics, IEEE Transactions on*, vol. 35, pp. 524-529, 1988.

[44] R. M. Davis, "Variable reluctance rotor structures-their influence on torque production," *Industrial Electronics, IEEE Transactions on*, vol. 39, pp. 168-174, 1992.

[45] Neagoe, C.; Foggia, A.; Krishnan, R.;, "Impact of pole tapering on the electromagnetic torque of the switched reluctance motor," in *Electric Machines and Drives Conference Record, 1997. IEEE International*, 1997, pp. WA1/2.1-WA1/2.3.

[46] A. Pelikant and S. Wiak, "The influence of the rotor pole shape on the static and dynamic characteristics of the switched reluctance motor," *Magnetics, IEEE Transactions on*, vol. 32, pp. 1529-1532, 1996.

[47] N. K. Sheth and K. R. Rajagopal, "Torque profiles of a switched reluctance motor having special pole face shapes and asymmetric stator poles," *Magnetics, IEEE Transactions on*, vol. 40, pp. 2035-2037, 2004.

[48] H. C. Lovatt and J. M. Stephenson, "Influence of number of poles per phase in switched reluctance motors," *Electric Power Applications, IEE Proceedings B*, vol. 139, pp. 307-314, 1992.

[49] T. J. E. Miller, *"Switched Reluctance Motors and Their Controls", Clarendon Press, Oxford, 1993.*

[50] B. C. Mecrow, "Fully pitched-winding switched-reluctance and stepping-motor arrangements," *Electric Power Applications, IEE Proceedings B,* vol. 140, pp. 61-70, 1993.

[51] Feng Liang; Yuefeng Liao; Lipo, T.A.;, "A new variable reluctance motor utilizing an auxiliary commutation winding," in *Industry Applications Society Annual Meeting, 1992., Conference Record of the 1992 IEEE,* 1992, pp. 219-225 vol.1.

[52] Arumugam, R.; Lowther, D.; Krishnan, R.; Lindsay, J.;, "Magnetic field analysis of a switched reluctance motor using a two dimensional finite element model," *Magnetics, IEEE Transactions on,* vol. 21, pp. 1883-1885, 1985.

[53] V. Kamaraj and C. Aravind Vaithilingam, "Modelling and simulation of switched reluctance machine (SRM) using MAGNET6.0," in *Power Electronics and Drive Systems, 2003. PEDS 2003. The Fifth International Conference on,* 2003, pp. 480-484 Vol.1.

[54] Koibuchi, K.; Ohno, T.; Sawa, K.;, "A basic study for optimal design of switched reluctance motor by finite element method," *Magnetics, IEEE Transactions on,* vol. 33, pp. 2077-2080, 1997.

[55] Murthy, S.S.; Singh, B.; Sharma, V.K.;, "Finite element analysis to achieve optimum geometry of switched reluctance motor," in *TENCON '98. 1998 IEEE Region 10 International Conference on Global Connectivity in Energy, Computer, Communication and Control,* 1998, pp. 414-418 vol.2.

[56] Ohdachi, Y.; Kawase, Y.; Miura, Y.; Hayashi, Y.;, "Optimum design of switched reluctance motors using dynamic finite element analysis," *Magnetics, IEEE Transactions on,* vol. 33, pp. 2033-2036, 1997.

[57] Wei Wu; Dunlop, J.B.; Collocott, S.J.; Kalan, B.A.;, "Design optimization of a switched reluctance motor by electromagnetic and thermal finite-element analysis," *Magnetics, IEEE Transactions on,* vol. 39, pp. 3334-3336, 2003.

[58] A. M. Michaelides and C. Pollock, "Effect of end core flux on the performance of the switched reluctance motor," *Electric Power Applications, IEE Proceedings -,* vol. 141, pp. 308-316, 1994.

[59] Fahimi, B.; Suresh, G.; Ehsani, M.;, "Large switched reluctance machines: a 1 MW case study," in *Electric Machines and Drives, 1999. International Conference IEMD '99,* 1999, pp. 84-86.

[60] Lobo, N.S.; Hong Sun Lim; Krishnan, R.;, "Comparison of Linear Switched Reluctance Machines for Vertical Propulsion Application: Analysis, Design, and Experimental Correlation," *Industry Applications, IEEE Transactions on,* vol. 44, pp. 1134-1142, 2008.

[61] M. F. Momen and I. Husain, "Design and performance analysis of a switched reluctance motor for low duty cycle operation," *Industry Applications, IEEE Transactions on,* vol. 41, pp. 1612-1618, 2005.

[62] K. M. Rahman and S. E. Schulz, "Design of high-efficiency and high-torque-density switched reluctance motor for vehicle propulsion," *Industry Applications, IEEE Transactions on,* vol. 38, pp. 1500-1507, 2002.

[63] S. S. Ramamurthy and J. C. Balda, "Sizing a switched reluctance motor for electric vehicles," *Industry Applications, IEEE Transactions on,* vol. 37, pp. 1256-1264, 2001.

[64] Schofield, N.; Long, S.A.; Howe, D.; McClelland, M.;, "Design of a Switched Reluctance Machine for Extended Speed Operation," *Industry Applications, IEEE Transactions on,* vol. 45, pp. 116-122, 2009.

[65] J. M. Stephenson and G. C. Jenkinson, "Single-phase switched reluctance motor design," *Electric Power Applications, IEE Proceedings* -, vol. 147, pp. 131-139, 2000.

[66] J. R. Suriano and O. Chee-Mun, "Variable reluctance motor structures for low-speed operation," *Industry Applications, IEEE Transactions on,* vol. 32, pp. 345-353, 1996.

[67] T. Suzuki, Ito, S., Tanaka, N., Chiba, A., Fukao, T. and Ninomiya, H., "Development of high-efficiency switched reluctance motor," *Electrical Engineering in Japan,* vol. 162, pp. 73–82, 2008.

[68] K. S. Chai and C. Pollock, "Evolutionary computer controlled design of a reluctance motor drive system," in *Industry Applications Conference, 2003. 38th IAS Annual Meeting. Conference Record of the,* 2003, pp. 1480-1487 vol.3.

[69] Kosaka, T.; Pollock, C.; Shikayama, T.; Nakagami, T.; Kano, Y.; Matsui, N.;, "GA-based computer aided autonomous electromagnetic design of switched reluctance servomotor drives," in *Industry Applications Conference, 2004. 39th IAS Annual Meeting. Conference Record of the 2004 IEEE,* 2004, p. 423 Vol.1.

[70] Mirzaeian, B.; Moallem, M.; Tahani, V.; Lucas, C.;, "Multiobjective optimization method based on a genetic algorithm for switched reluctance motor design," *Magnetics, IEEE Transactions on,* vol. 38, pp. 1524-1527, 2002.

[71] N. R. Matveev A., Undeland T., "Design optimization of switched reluctance drives using artificial neural networks," in *Power Electronics and Motion Control, 2002. EPE-PEMC 2002. 10th International Conference on.*, Cavtat & Dubrovnik, 2002.

[72] S. Brisset and P. Brochet, "Optimization of switched reluctance motors using deterministic methods with static and dynamic finite element simulations," *Magnetics, IEEE Transactions on,* vol. 34, pp. 2853-2856, 1998.

[73] J. R. Hendershot. (1989, Short flux loops cool SR motors. *Machine Design,* pp. 106-111.

[74] A. Michaelides and C. Pollock, "Design and performance of a high efficiency 5-phase switched reluctance motor," in *Electrical Machines and Drives, 1995. Seventh International Conference on (Conf. Publ. No. 412),* 1995, pp. 266-270.

[75] A. M. Michaelides and C. Pollock, "Modelling and design of switched reluctance motors with two phases simultaneously excited," *Electric Power Applications, IEE Proceedings* -, vol. 143, pp. 361-370, 1996.

[76] Lobo, N.S.; Swint, E.; Krishnan, R.;, "M-Phase N-Segment Flux-Reversal-Free Stator Switched Reluctance Machines," in *Industry Applications Society Annual Meeting, 2008. IAS '08. IEEE,* 2008, pp. 1-8.

[77] O. Seok-Gyu and R. Krishnan, "Two-Phase SRM With Flux-Reversal-Free Stator: Concept, Analysis, Design, and Experimental Verification," *Industry Applications, IEEE Transactions on,* vol. 43, pp. 1247-1257, 2007.

[78] W. Pengov, ""Staggered Pole Switched Reluctance Motor", US Patent No 6060809, 9 May 2000.."

[79] Cheewoo Lee; Krishnan, R.; Lobo, N.S.;, "Novel Two-Phase Switched Reluctance Machine Using Common-Pole E-Core Structure: Concept, Analysis, and Experimental Verification," *Industry Applications, IEEE Transactions on,* vol. 45, pp. 703-711, 2009.

[80] C. Pollock and M. Wallace, "The flux switching motor, a DC motor without magnets or brushes," in *Industry Applications Conference, 1999. Thirty-Fourth IAS Annual Meeting. Conference Record of the 1999 IEEE*, 1999, pp. 1980-1987 vol.3.

[81] Pollock, C.; Pollock, H.; Barron, R.; Coles, J.R.; Moule, D.; Court, A.; Sutton, R.;, "Flux-Switching Motors for Automotive Applications," *Industry Applications, IEEE Transactions on*, vol. 42, pp. 1177-1184, 2006.

[82] J. D. Wale and C. Pollock, "Novel converter topologies for a two-phase switched reluctance motor with fully pitched windings," in *Power Electronics Specialists Conference, 1996. PESC '96 Record., 27th Annual IEEE*, 1996, pp. 1798-1803 vol.2.

[83] Corda, J.; Tataru, A.M.; Rasmussen, P.O.; Ritchie, E.;, "Analytical estimation of torque enhancement of the SR machine with saw-shaped (shark) pole surfaces," *Electric Power Applications, IEE Proceedings* -, vol. 151, pp. 223-229, 2004.

[84] A. M. T. Kjaer, ""Shark, New Motor Design Concept for Energy Saving Applied to Switched Reluctance Motor", Thesis submitted for Doctor of Philosophy," Institute of Energy Technology, 2004., Aalborg University.

[85] Rasmussen, P.O.; Blaabjerg, F.; Pedersen, J.K.; Jensen, F.;, "Switched reluctance-shark machines-more torque and less acoustic noise," in *Industry Applications Conference, 2000. Conference Record of the 2000 IEEE*, 2000, pp. 93-98 vol.1.

[86] Faiz, J.; Harris, M.R.; Finch, J.W.;, "Two-dimensional finite element analysis of multi-tooth per stator pole switched reluctance motor-four teeth per stator pole," in *Industry Applications Society Annual Meeting, 1990., Conference Record of the 1990 IEEE*, 1990, pp. 234-240 vol.1.

[87] J. R. Hendershot, ""A five phase switched reluctance brushless DC motor with a low loss magnetic circuit"," ed: Magna Physics Corp., 1989., 1989.

[88] Faiz, J.; Raddadi, J.; Finch, J.W.;, "Spice-based dynamic analysis of a switched reluctance motor with multiple teeth per stator pole," *Magnetics, IEEE Transactions on*, vol. 38, pp. 1780-1788, 2002.

[89] A. C. Clothier, ""Switched Reluctance Motor Drives with Fully Pitched Windings", Thesis submitted for Doctor of Philosophy," School of Electrical, Electronic and Computer Engineering, University of Newcastle upon Tyne, 2001.

[90] P. G. Barrass, ""High Performance Switched Reluctance Drives", Thesis submitted for Doctor of Philosophy," School of Electrical, Electronic and Computer Engineering, University of Newcastle upon Tyne, 1995.

[91] Mecrow, B.C.; Weiner, C.; Clothier, A.C.;, "The modeling of switched reluctance machines with magnetically coupled windings," *Industry Applications, IEEE Transactions on*, vol. 37, pp. 1675-1683, 2001.

[92] Li, S.-Y.H.; Feng Liang; Yifan Zhao; Lipo, T.A.;, "A doubly salient doubly excited variable reluctance motor," *Industry Applications, IEEE Transactions on*, vol. 31, pp. 99-106, 1995.

[93] B. C. Mecrow, ""Switched Reluctance Motor", European Patent No EP1359660A2, 5 November 2003."

[94] Mecrow, B.C.; El-Kharashi, E.A.; Finch, J.W.; Jack, A.G.;, "Performance evaluation of switched reluctance motors with segmental rotors," in *Electric Machines and Drives Conference, 2003. IEMDC'03. IEEE International*, 2003, pp. 568-574 vol.1.

[95] Xu, L.; Lipo, T.A.; Rao, S.C.;, "Analysis of a new variable-speed singly salient reluctance motor utilizing only two transistor switches," *Industry Applications, IEEE Transactions on*, vol. 26, pp. 229-236, 1990.

[96] G. A. Horst, ""Isolated Segmental Switched Reluctance Motor", US Patent No 5111096, 5 May 1992.."

[97] E. A. El-Kharashi, ""Segmented Rotor Switched Reluctance Motors", Thesis submitted for Doctor of Philosophy," Thesis submitted for Doctor of Philosophy, School of Electrical, Electronic and Computer Engineering, University of Newcastle upon Tyne, 2003.

[98] Oyama, J.; Higuchi, T.; Abe, T.; Tanaka, K.;, "The fundamental characteristics of novel switched reluctance motor with segment core embedded in aluminum rotor block," in *Electrical Machines and Systems, 2005. ICEMS 2005. Proceedings of the Eighth International Conference on*, 2005, pp. 515-519 Vol. 1.

[99] Vattikuti, N.; Rallabandi, V.; Fernandes, B.G.;, "A novel high torque and low weight segmented switched reluctance motor," in *Power Electronics Specialists Conference, 2008. PESC 2008. IEEE*, 2008, pp. 1223-1228.

[100] J. C. Zolper, "Emerging silicon carbide power electronics components," in *Applied Power Electronics Conference and Exposition, 2005. APEC 2005. Twentieth Annual IEEE*, 2005, pp. 11-17 Vol. 1.

[101] C. Pollock and W. Chi-Yao, "Acoustic noise cancellation techniques for switched reluctance drives," *Industry Applications, IEEE Transactions on*, vol. 33, pp. 477-484, 1997.

[102] I. Husain, "Minimization of torque ripple in SRM drives," *Industrial Electronics, IEEE Transactions on*, vol. 49, pp. 28-39, 2002.

[103] Sahoo, N.C.; Xu, J.X.; Panda, S.K.;, "Determination of current waveforms for torque ripple minimisation in switched reluctance motors using iterative learning: an investigation," *Electric Power Applications, IEE Proceedings* -, vol. 146, pp. 369-377, 1999.

[104] Ilic-Spong, Marija; Miller, Timothy J. E.; Macminn, Stephen R.; Thorp, James S.;, "Instantaneous Torque Control of Electric Motor Drives," *Power Electronics, IEEE Transactions on*, vol. PE-2, pp. 55-61, 1987.

[105] R. S. Wallace and D. G. Taylor, "Low-torque-ripple switched reluctance motors for direct-drive robotics," *Robotics and Automation, IEEE Transactions on*, vol. 7, pp. 733-742, 1991.

[106] R. S. Wallace and D. G. Taylor, "A balanced commutator for switched reluctance motors to reduce torque ripple," *Power Electronics, IEEE Transactions on*, vol. 7, pp. 617-626, 1992.

[107] Mir, S.; Elbuluk, M.E.; Husain, I.;, "Torque-ripple minimization in switched reluctance motors using adaptive fuzzy control," *Industry Applications, IEEE Transactions on*, vol. 35, pp. 461-468, 1999.

[108] M. S. Islam and J. Husain, "Torque-ripple minimization with indirect position and speed sensing for switched reluctance motors," *Industrial Electronics, IEEE Transactions on*, vol. 47, pp. 1126-1133, 2000.

[109] Russa, K.; Husain, I.; Elbuluk, M.E.;, "Torque-ripple minimization in switched reluctance machines over a wide speed range," *Industry Applications, IEEE Transactions on*, vol. 34, pp. 1105-1112, 1998.

[110] P. G. Barrass and B. C. Mecrow, "Flux and torque control of switched reluctance machines," *Electric Power Applications, IEE Proceedings* -, vol. 145, pp. 519-527, 1998.

[111] Xue, X.D.; Cheng, K.W.E.; Ho, S.L.;, "A Control Scheme of Torque Ripple Minimization for SRM Drives Based on Flux Linkage Controller and Torque Sharing Function," in *Power Electronics Systems and Applications, 2006. ICPESA '06. 2nd International Conference on*, 2006, pp. 79-84.

[112] Reay, D.S.; Mirkazemi-Moud, M.; Green, T.C.; Williams, B.W.;, "Switched reluctance motor control via fuzzy adaptive systems," *Control Systems Magazine, IEEE*, vol. 15, pp. 8-15, 1995.

[113] Rochford, C.; Kavanagh, R.C.; Egan, M.G.; Murphy, J.M.D.;, "Development of smooth torque in switched reluctance motors using self-learning techniques," in *Power Electronics and Applications, 1993., Fifth European Conference on*, 1993, pp. 14-19 vol.6.

[114] L. Henriques, Branco, P. J. C., Rolim, L., Suemitsu, W., "Automatic Learning of Pulse Current Shape for Torque Ripple Minimisation in Switched Reluctance Machines," in *European Control Conference, ECC'01*, Porto, Portugal, 2001., 2001, pp. pp. 232-237.

[115] J. C. Moreira, "Torque ripple minimization in switched reluctance motors via bi-cubic spline interpolation," in *Power Electronics Specialists Conference, 1992. PESC '92 Record., 23rd Annual IEEE*, 1992, pp. 851-856 vol.2.

[116] Cailleux, H.; Le Pioufle, B.; Multon, B.; Sol, C.;, "A precise analysis of the phase commutation for the torque nonlinear control of a switched reluctance motor - torque ripples minimization," in *Industrial Electronics, Control, and Instrumentation, 1993. Proceedings of the IECON '93., International Conference on*, 1993, pp. 1985-1990 vol.3.

[117] Ilic'-Spong, M.; Marino, R.; Peresada, S.; Taylor, D.;, "Feedback linearizing control of switched reluctance motors," *Automatic Control, IEEE Transactions on*, vol. 32, pp. 371-379, 1987.

[118] H. C. Lovatt and J. M. Stephenson, "Computer-optimised smooth-torque current waveforms for switched-reluctance motors," *Electric Power Applications, IEE Proceedings -*, vol. 144, pp. 310-316, 1997.

[119] Malesani, L.; Leonardi, F.; Speranza, R.; Scandellari, A.;, "Switched reluctance motor: a reduced torque ripple drive," in *Industrial Electronics, Control, and Instrumentation, 1993. Proceedings of the IECON '93., International Conference on*, 1993, pp. 1764-1769 vol.3.

[120] Xue, X.D.; Cheng, K.; Cheung, N.C.;, "Evaluation of torque sharing functions for torque ripple minimization of switched reluctance motor drives in electric vehicles," in *Power Engineering Conference, 2008. AUPEC '08. Australasian Universities*, 2008, pp. 1-6.

[121] Bizkevelci, E.; Leblebicioglu, K.; Ertan, H.B.;, "A sliding mode controller to minimise SRM torque ripple and noise," in *Industrial Electronics, 2004 IEEE International Symposium on*, 2004, pp. 1333-1338 vol. 2.

[122] I. Husain and M. Ehsani, "Torque ripple minimization in switched reluctance motor drives by PWM current control," *Power Electronics, IEEE Transactions on*, vol. 11, pp. 83-88, 1996.

[123] H. Ishikawa, Kamada, Y. and Naitoh, H., "Instantaneous current profile control for flat torque of switched reluctance motors," *Electrical Engineering in Japan*, vol. 163, pp. 78–87, 2008.

[124] T. Kosaka, Matsui, N., Taniguchi, Y.-I. and Do-meki, H., "Some considerations on torque ripple suppression in reluctance motors," *Electrical Engineering in Japan*, vol. 130, pp. 118–128, 2000.

[125] N. T. Shaked and R. Rabinovici, "New procedures for minimizing the torque ripple in switched reluctance motors by optimizing the phase-current profile," *Magnetics, IEEE Transactions on*, vol. 41, pp. 1184-1192, 2005.

[126] Stephenson, J.M.; Hughes, A.; Mann, R.;, "Torque ripple minimisation in a switched reluctance motor by optimum harmonic current injection," *Electric Power Applications, IEE Proceedings* -, vol. 148, pp. 322-328, 2001.

[127] Zhengyu Lin; Reay, D.S.; Williams, B.W.; Xiangning He;, "Torque Ripple Reduction in Switched Reluctance Motor Drives Using B-Spline Neural Networks," *Industry Applications, IEEE Transactions on*, vol. 42, pp. 1445-1453, 2006.

[128] D. S. Schramm and B. W. Williams, "High bandwidth measurement of SRM torque ripple," in *Electrical Machines and Drives, 1993. Sixth International Conference on (Conf. Publ. No. 376)*, 1993, pp. 647-651.

[129] Corda, J.; Masic, S.; Stephenson, J.M.;, "Computation and experimental determination of running torque waveforms in switched-reluctance motors," *Electric Power Applications, IEE Proceedings B*, vol. 140, pp. 387-392, 1993.

[130] A. C. Koenig and S. D. Pekarek, "Measurement of torque ripple in mass-produced switched-reluctance motor drives," in *Electric Machines and Drives, 2005 IEEE International Conference on*, 2005, pp. 6 pp.-509.

[131] Ehsani, Mehrdad; Bass, James T.; Miller, Timothy J. E.; Steigerwald, Robert L.;, "Development of a Unipolar Converter for Variable Reluctance Motor Drives," *Industry Applications, IEEE Transactions on*, vol. IA-23, pp. 545-553, 1987.

[132] Ehsani, M.; Husain, I.; Ramani, K.R.; Galloway, J.H.;, "Dual-decay converter for switched reluctance motor drives in low-voltage applications," *Power Electronics, IEEE Transactions on*, vol. 8, pp. 224-230, 1993.

[133] R. Krishnan and P. N. Materu, "Analysis and design of a low-cost converter for switched reluctance motor drives," *Industry Applications, IEEE Transactions on*, vol. 29, pp. 320-327, 1993.

[134] Mir, S.; Husain, I.; Elbuluk, M.E.;, "Energy-efficient C-dump converters for switched reluctance motors," *Power Electronics, IEEE Transactions on*, vol. 12, pp. 912-921, 1997.

[135] Jun-Ho Kim; Eun-Woong Lee; Jong-Han Lee;, "Design of the Starting Device Installed in the Single-Phase Switched Reluctance Motor," *Magnetics, IEEE Transactions on*, vol. 43, pp. 1741-1744, 2007.

[136] B. C. Mecrow, Bedford, T. J., Bennet, J. W., and Celik, T. , "The use of segmental rotors for 2 phase flux-switching motors," in *Electrical Machines, 2006. ICEM '06. 17th International Conference on.* , 2006.

[137] C. Weiner, ""High Performance Switched Reluctance Drives for Electric Vehicle Applications", Thesis submitted for Doctor of Philosophy," Thesis submitted for Doctor of Philosophy, School of Electrical, Electronic and Computer Engineering, University of Newcastle upon Tyne, 2000.

[138] Acarnley, Paul P.; Hill, Roland J.; Hooper, Clive W.;, "Detection of Rotor Position in Stepping and Switched Motors by Monitoring of Current Waveforms," *Industrial Electronics, IEEE Transactions on*, vol. IE-32, pp. 215-222, 1985.

[139] J. P. Lyons, Macminn, S. R., Preston, M. A., ""Discrete position estimator for switched reluctance machine using a flux-current map calculator", US Patent No 5140243, 18 August 1992.."

[140] A. Lumsdaine and J. H. Lang, "State observers for variable-reluctance motors," *Industrial Electronics, IEEE Transactions on*, vol. 37, pp. 133-142, 1990.

[141] P. K. Sood, Skinner, J. L., Petty, D. M. , ""Method and apparatus of operating a dynamoelectric machine using DC bus current profile", US Patent No5420492, 30 May 1995.."

[142] R. Krishnan, *"Switched Reluctance Motor Drives: Modeling, Simulation, Analysis, Design, and Applications"*: CRC Press, Boca Raton, 2001.

[143] Blaabjerg, F.; Kjaer, P.C.; Rasmussen, P.O.; Cossar, C.;, "Improved digital current control methods in switched reluctance motor drives," *Power Electronics, IEEE Transactions on,* vol. 14, pp. 563-572, 1999.

[144] Miller, T.J.E.; Bower, P.G.; Becerra, R.; Ehsani, M.;, "Four-quadrant brushless reluctance motor drive," in *Power Electronics and Variable-Speed Drives, Third International Conference on,* 1988, pp. 273-276.

[145] Hava, A.M.; Blasko, V.; Lipo, T.A.;, "A modified C-dump converter for variable-reluctance machines," *Industry Applications, IEEE Transactions on,* vol. 28, pp. 1017-1022, 1992.

[146] King-Jet Tseng; Shuyu Cao; Jijiu Wang;, "A new hybrid C-dump and buck-fronted converter for switched reluctance motors," *Industrial Electronics, IEEE Transactions on,* vol. 47, pp. 1228-1236, 2000.

[147] Barrass, P.G.; Mecrow, B.C.; Clothier, A.C.;, "Bipolar operation of fully-pitched winding switched reluctance drives," in *Electrical Machines and Drives, 1995. Seventh International Conference on (Conf. Publ. No. 412),* 1995, pp. 252-256.

[148] Oliveira, A.C.; Lima, A.M.N.; Jacobina, C.B.; Salvadori, F.;, "Startup and Fault Tolerance of the SRM Drive with Three-Phase Bridge Inverter," in *Power Electronics Specialists Conference, 2005. PESC '05. IEEE 36th,* 2005, pp. 714-719.

[149] Sadeghi, S.; Milimonfared, J.; Mirsalim, M.; Jalalifar, M.;, "Dynamic Modeling and Simulation of a Switched Reluctance Motor in Electric Vehicles," in *Industrial Electronics and Applications, 2006 1ST IEEE Conference on,* 2006, pp. 1-6.

[150] Kartono, I.R.; Kajiwara, K.; Dohmeki, H.;, "Dynamic simulation of maximizing the starting torque for super-high-speed drive of a 4/2 Switched Reluctance Motor," in *Electrical Machines, 2008. ICEM 2008. 18th International Conference on,* 2008, pp. 1-6.

[151] Y. Hayashi and T. J. E. Miller, "A new approach to calculating core losses in the SRM," *Industry Applications, IEEE Transactions on,* vol. 31, pp. 1039-1046, 1995.

[152] P. N. Materu and R. Krishnan, "Estimation of switched reluctance motor losses," *Industry Applications, IEEE Transactions on,* vol. 28, pp. 668-679, 1992.

[153] S. Vukosavic and V. R. Stefanovic, "SRM inverter topologies: a comparative evaluation," *Industry Applications, IEEE Transactions on,* vol. 27, pp. 1034-1047, 1991.

[154] Z. Jinhui and A. V. Radun, "A New Method to Measure the Switched Reluctance Motor's Flux," *Industry Applications, IEEE Transactions on,* vol. 42, pp. 1171-1176, 2006.

[155] R. Krishnan and P. Materu, "Measurement and instrumentation of a switched reluctance motor," in *Industry Applications Society Annual Meeting, 1989., Conference Record of the 1989 IEEE,* 1989, pp. 116-121 vol.1.

[156] Akita, H.; Nakahara, Y.; Miyake, N.; Oikawa, T.;, "A new core," *Industry Applications Magazine, IEEE,* vol. 11, pp. 38-43, 2005.

[157] U. Hoefer, ""Design and Development of a High-Speed Motor for a Vacuum Pump", Thesis submitted for Engineering Doctorate," School of Electrical, Electronic and Computer Engineering, University of Newcastle upon Tyne, 2008.

[158] Akita, H.; Nakahara, Y.; Miyake, N.; Oikawa, T.;, "New core structure and manufacturing method for high efficiency of permanent magnet motors," in

Industry Applications Conference, 2003. 38th IAS Annual Meeting. Conference Record of the, 2003, pp. 367-372 vol.1.

[159] Y. Fujita, Hazeyama, M., ""Electromagnetic Driving Technology of DC Motor for EGR Valve"," Mitsubishi Electric Technical Reports, December 2006, Japan.

[160] K. Inoue, Miyake, N., ""New Traction Machine for Machine Room-Less Elevators," Mitsubishi Electric Technical Reports, September 2002, Japan.

[161] H. Kawaguchi, Oikawa, T., ""High-Efficiency Motors for Air-Conditioner Compressors"," Mitsubishi Electric Technical Reports, September 2003, JapanSeptember 2003.

[162] C. E. Carstensen, Bauer, S. E., Inderka, R. B. & De Doncker, R. W. , "Efficiency Comparison of Different Winding Configurations for Switched Reluctance Vehicle Propulsion Drives," in *In 20th International Electric Vehicle Symposium (EVS-20)*, Long Beach, USA, 2003.

[163] "Beacon Adhesives Co. Inc.," in *Magna-Tac E645, Stack Lamination Epoxy datasheet*, ed.

[164] I. Husain and S. A. Hossain, "Modeling, Simulation, and control of switched reluctance motor drives," *Industrial Electronics, IEEE Transactions on,* vol. 52, pp. 1625-1634, 2005.

[165] J. A. Haylock, ""Fault Tolerant Drives for Safety Critical Applications", Thesis submitted for Doctor of Philosophy," School of Electrical, Electronic and Computer Engineering, University of Newcastle upon Tyne, 1998.

[166] C. French, ""Real Time Control of Electric Drives", Thesis submitted for Doctor of Philosophy," School of Electrical, Electronic and Computer Engineering, University of Newcastle upon Tyne, 2001.

[167] J. M. Stephenson and J. Corda, "Computation of torque and current in doubly salient reluctance motors from nonlinear magnetisation data," *Electrical Engineers, Proceedings of the Institution of,* vol. 126, pp. 393-396, 1979.

[168] J. M. Stephenson and M. A. El-Khazendar, "Saturation in doubly salient reluctance motors," *Electric Power Applications, IEE Proceedings B,* vol. 136, pp. 50-58, 1989.

[169] M. Ehsani, Abourida, S., ""Real time Simulation of Switched Reluctance Motor Drives"," in *Technical Documents*, ed: Opal-RT Technologies, Sep 2003.

[170] T. Tsukii, Nakamura, K. and Ichinokura, O., "SPICE simulation of SRM considering nonlinear magnetization characteristics," *Electrical Engineering in Japan*, vol. 142, pp. 50-56, 2003.

[171] Phillips, N.W.; Bolton, H.R.; Lewis, J.D.; Pollock, C.; Barnes, M.;, "Simulation of switched reluctance drive system using a commercially available simulation package," in *Electrical Machines and Drives, 1995. Seventh International Conference on (Conf. Publ. No. 412)*, 1995, pp. 257-260.

[172] D. W. J. Pulle, "New database for switched reluctance drive simulation," *Electric Power Applications, IEE Proceedings B*, vol. 138, pp. 331-337, 1991.

[173] A. Radun, "Analytical calculation of the switched reluctance motor's unaligned inductance," *Magnetics, IEEE Transactions on,* vol. 35, pp. 4473-4481, 1999.

[174] A. Radun, "Analytically computing the flux linked by a switched reluctance motor phase when the stator and rotor poles overlap," *Magnetics, IEEE Transactions on,* vol. 36, pp. 1996-2003, 2000.

[175] D. A. Torrey and J. H. Lang, "Modelling a nonlinear variable-reluctance motor drive," *Electric Power Applications, IEE Proceedings B,* vol. 137, pp. 314-326, 1990.

[176] Torrey, D.A.; Niu, X.-M.; Unkauf, E.J.;, "Analytical modelling of variable-reluctance machine magnetisation characteristics," *Electric Power Applications, IEE Proceedings -*, vol. 142, pp. 14-22, 1995.

[177] T. J. E. Miller and M. McGilp, "Nonlinear theory of the switched reluctance motor for rapid computer-aided design," *Electric Power Applications, IEE Proceedings B,* vol. 137, pp. 337-347, 1990.

[178] Xue, X. D.; Cheng, K. W. E.; Ho, S. L.;, "Simulation of switched reluctance motor drives using two-dimensional bicubic spline," *Energy Conversion, IEEE Transactions on,* vol. 17, pp. 471-477, 2002.

[179] J. C. Moreira and T. A. Lipo, "Simulation of a four phase switched reluctance motor including the effects of mutual coupling," *Electric Machines & Power Systems,* vol. 16, pp. 281 - 299, 1989.

[180] C. Shuyu and K. J. Tseng, "Evaluation of neighboring phase coupling effects of switched reluctance motor with dynamic modeling approach," in *Power Electronics and Motion Control Conference, 2000. Proceedings. IPEMC 2000. The Third International*, 2000, pp. 881-886 vol.2.

[181] Y. Xu and D. A. Torrey, "Study of the mutually coupled switched reluctance machine using the finite element-circuit coupled method," *Electric Power Applications, IEE Proceedings -*, vol. 149, pp. 81-86, 2002.

[182] J. M. Kokernak and D. A. Torrey, "Magnetic circuit model for the mutually coupled switched-reluctance machine," *Magnetics, IEEE Transactions on,* vol. 36, pp. 500-507, 2000.

[183] M. Stiebler and L. Ke, "An analytical model of switched reluctance machines," *Energy Conversion, IEEE Transactions on,* vol. 14, pp. 1100-1107, 1999.

[184] S. A. Hossain and I. Husain, "A geometry based simplified analytical model of switched reluctance machines for real-time controller implementation," *Power Electronics, IEEE Transactions on,* vol. 18, pp. 1384-1389, 2003.

[185] Vejian Rajanran, R.; Sahoo, N.C.; Gobbi, R.;, "Mathematical Modeling of Flux-Linkage Characteristics of Switched Reluctance Motors Using Polynomial Neural Networks," in *Power and Energy Conference, 2006. PECon '06. IEEE International*, 2006, pp. 378-382.

[186] Yan Cai; Qingxin Yang; Yanbin Wen; Lihua Su;, "Nonlinear modeling and simulating of switched reluctance motor and its drive," in *Computer and Automation Engineering (ICCAE), 2010 The 2nd International Conference on*, 2010, pp. 465-469.

[187] Zhengyu Lin; Reay, D.S.; Williams, B.W.; Xiangning He;, "Online Modeling for Switched Reluctance Motors Using B-Spline Neural Networks," *Industrial Electronics, IEEE Transactions on,* vol. 54, pp. 3317-3322, 2007.

[188] Owatchaiphong, S.; Carstensen, C.; De Doncker, R.W.;, "Optimization of Predesign of Switched Reluctance Machines Cross Section Using Genetic Algorithms," in *Power Electronics and Drive Systems, 2007. PEDS '07. 7th International Conference on*, 2007, pp. 707-711.

[189] Carstensen, C.E.; Fuengwarodsakul, N.H.; De Doncker, R.W.;, "Flux Linkage Determination for Correct Modeling of Switched Reluctance Machines - Dynamic Measurement versus Static Computation," in *Electric Machines & Drives Conference, 2007. IEMDC '07. IEEE International*, 2007, pp. 1317-1323.

[190] Charton, J.T.; Corda, J.; Stephenson, J.M.; Randall, S.P.;, "Dynamic modelling of switched reluctance machines with iron losses and phase interactions," *Electric Power Applications, IEE Proceedings -*, vol. 153, pp. 327-336, 2006.

[191] Khotpanya, S.; Kittiratsatcha, S.; Kazuhisa, I.;, "A Magnetic Model of a Three-Phase Switched-Reluctance Machine using Cubic Spline Interpolation Technique," in *Power Electronics and Drives Systems, 2005. PEDS 2005. International Conference on*, 2005, pp. 1167-1170.

[192] Ling Yuelun; Wang Mianhua; Wang Yan; Wang Fenli;, "Simulation Research on Switched Reluctance Motor Modeling and Control Strategy Based on ANSOFT," in *Measuring Technology and Mechatronics Automation (ICMTMA), 2010 International Conference on*, 2010, pp. 374-377.

[193] Bingni Qu; Jiancheng Song; Hongda Zhang;, "Simulation for Switched Reluctance Drive Based on the Measured Flux Linkage Characteristics," in *Power and Energy Engineering Conference, 2009. APPEEC 2009. Asia-Pacific*, 2009, pp. 1-4.

[194] Zhengang Sun; Cheung, N.C.; Jianfei Pan; Shiwei Zhao; Wai-Chuen Gan;, "Design and simulation of a magnetic levitated switched reluctance linear actuator system for high precision application," in *Industrial Electronics, 2008. ISIE 2008. IEEE International Symposium on*, 2008, pp. 624-629.

[195] Woothipatanapan, S.; Chancharoensook, P.; Jangwanitlert, A.;, "Efficiency improvement of converter for switched reluctance motor drives at low speed operation," in *Power Electronics and Drive Systems, 2009. PEDS 2009. International Conference on*, 2009, pp. 488-493.

[196] M. T. Khor and R. Sotudeh, "A 3-phase 12/10 asymmetrical switched reluctance motor," in *Power Electronics and Applications, 2005 European Conference on*, 2005, pp. 9 pp.-P.9.

[197] Lin, D.; Zhou, P.; Stanton, S.; Cendes, Z.J.;, "An Analytical Circuit Model of Switched Reluctance Motors," *Magnetics, IEEE Transactions on*, vol. 45, pp. 5368-5375, 2009.

[198] Qiong-zhong Chen; Guang Meng; Yu-feng Mo; Ting-xing Wang;, "Analytical nonlinear modeling of SRM and its system-level simulation with airborne power system," in *Industrial Technology, 2008. ICIT 2008. IEEE International Conference on*, 2008, pp. 1-8.

[199] D. Wen and L. Deliang, "Fourier series and ANFIS-based modeling and prediction for switched reluctance motor," in *Electrical Machines and Systems, 2008. ICEMS 2008. International Conference on*, 2008, pp. 3362-3366.

[200] A. Khalil and I. Husain, "A Fourier Series Generalized Geometry-Based Analytical Model of Switched Reluctance Machines," *Industry Applications, IEEE Transactions on*, vol. 43, pp. 673-684, 2007.

[201] Z. Suying and L. Hui, "Modeling and Simulation of Switched Reluctance Motor Double Closed Loop Control System," in *Intelligent Control and Automation, 2006. WCICA 2006. The Sixth World Congress on*, 2006, pp. 6151-6155.

[202] Xia, C.L.; Xue, M.; Shi, T.N.;, "A New Rapid Nonlinear Simulation Method for Switched Reluctance Motors," *Energy Conversion, IEEE Transactions on*, vol. 24, pp. 578-586, 2009.

[203] Ding Wen; Liang Deliang; Cheng Zhuping;, "Dynamic Model and Simulation for a 6/4 Switched Reluctance Machine System Assisted by Maxwell SPICE and Simplorer," in *Mechatronics and Automation, 2007. ICMA 2007. International Conference on*, 2007, pp. 1699-1704.

[204] C. Yanbo and K. W. E. Cheng, "Real-time Simulation and Experiment Platform for Switched Reluctance Motor," in *Power Electronics Systems and Applications, 2006. ICPESA '06. 2nd International Conference on*, 2006, pp. 244-249.

[205] Dufour, C.; Paquin, J.-N.; Blanchette, H.; Belanger, J.;, "Specifications for real-time simulation of switched reluctance drives using microprocessors and FPGAs as computational engines," in *Electric Machines and Drives Conference, 2009. IEMDC '09. IEEE International*, 2009, pp. 750-754.

[206] T. J. E. Miller, "Converter Volt-Ampere Requirements of the Switched Reluctance Motor Drive," *Industry Applications, IEEE Transactions on,* vol. IA-21, pp. 1136-1144, 1985.